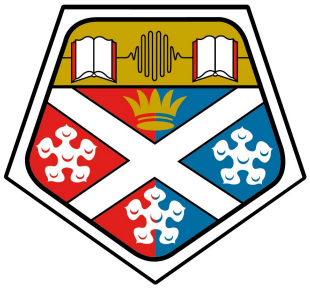

University of Strathclyde Glasgow

Numerical analysis and simulation of magnetoelastic, antiferromagnetic, and ultrafast magnetic materials

University of Strathclyde,

Glasgow, UK

A thesis submitted for the degree of

Doctor of Philosophy

Hywel Normington

Under the supervision of

Dr. Michele Ruggeri, University of Bologna, Bologna, Italy

Dr. Gabriel R. Barrenechea, University of Strathclyde, Glasgow, UK

April 11, 2026

Declaration of Authenticity

This thesis is the result of the author's original research. It has been composed by the author and has not been previously submitted for examination which has led to the award of a degree.

Signed: *Hywel Normington*

Date: April 11, 2026

Previously Published Material

Parts of this thesis have been previously published:

- *A decoupled, convergent and fully linear algorithm for the Landau–Lifshitz–Gilbert equation with magnetoelastic effects*, by Hywel Normington and Dr. Michele Ruggeri. Published in *Computers & Mathematics With Applications* in 2025 under the CC-BY 4.0 license (see [NR25c] for more details).
- *Convergent finite element methods for antiferromagnetic and ferrimagnetic materials*, by Hywel Normington and Dr. Michele Ruggeri. Published in *ESAIM: Mathematical Modelling and Numerical Analysis* in 2025 under the CC-BY 4.0 license (see [NR25b] for more details).

Parts of the thesis are available as preprints:

- *A decoupled, unconditionally stable and second-order integrator for the Landau–Lifshitz–Gilbert equation with magnetoelastic effects*, by Prof. Martin Kružík, Hywel Normington and Dr. Michele Ruggeri. Appeared on arXiv in 2025 under the CC BY-NC-ND 4.0 license (see [KNR25] for more details).

Abstract

For modern technological applications, magnetic materials and their underlying magnetization dynamics are of great interest for data storage, spintronic devices, and various magnetic sensors. The dynamics of magnetization are typically modelled by the Landau–Lifshitz–Gilbert (LLG) equation, which is a highly nonlinear, time-dependent partial differential equation, subject to a non-convex unit length constraint, and governed by an intrinsic dissipative energy law. The LLG equation is often extended to include additional effects, such as magnetoelastic coupling, where the magnetic and elastic behaviour of the material are coupled through the conservation of momentum equation, antiferromagnetic/ferrimagnetic interactions where multiple LLG equations are coupled together, and ultrafast dynamics where the LLG equation includes a higher derivative term in time yielding high frequency nutation behaviour on short time-scales. Each of these extensions introduces additional complications to the analysis and efficient numerical simulation of the respective models. In this thesis, we develop finite element numerical schemes based upon a projection-free tangent plane scheme, with first-order finite elements for the spatial discretization where the LLG equation is reformulated in its tangent space, and the unit length constraint is not enforced via a nodal projection to the sphere. Despite this, the schemes are fully linear, decoupled, unconditionally stable, and, under suitable assumptions, convergent to weak solutions. Importantly, we do not require restrictive geometric conditions on the meshes used in the numerical schemes. Particular attention is paid to the energetic behaviour of the discrete schemes, with a focus on mimicking the energy law satisfied by the continuous problem at the discrete level. Numerical experiments are provided to demonstrate the performance of the schemes and to support our theoretical findings.

Dedication

To my two parents, Helen and James Normington.

Acknowledgements

I would firstly like to thank my supervisor Dr. Michele Ruggeri for whom without this thesis would have never made it past this page, and Dr. Gabriel Barrenechea for taking up the mantle. I would also like to thank Lauren Schofield and Ann Paterson for preventing me from bouncing off of the ceiling in my office every week. Furthermore, I would like to thank Michele Aldé for his collaboration, Shuo Yang for several useful conversations about higher order tangent plane schemes, and Professor Martin Kružík for the kind hospitality of the Institute of Information Theory and Automation of the Czech Academy of Sciences in Prague and his discussions about magnetoelastic materials.

The support of the Royal Society (grant IES\R2\222118) is thankfully acknowledged. I am grateful for support from the London Mathematical Society (grants ECR-2324–46 and ECR-2223–44), and from the European Cooperation in Science & Technology (COST) through the COST Action CA23134 — Topological Textures in Condensed Matter (Polytopo).

Contents

List of Figures

List of Tables

Chapter 1

Introduction

1.1 Motivation

Manipulation of ferromagnetic (FM) materials is a central topic in data storage, spintronics, nanotechnologies and information processing. For the case of storage devices, in 1988 the discovery of Giant Magneto-Resistance (GMR) increased the interest in spin dynamics for the fast, and low energy, recording of information on magnetic materials, with products introduced in 1997 and now used in nearly all hard disk drives [CFVD07, HB05]. As technology advances and applications broaden, more effects must be included during the modelling stage of production to accurately and precisely predict behaviour for the variety of materials considered, especially as physical dimensions become smaller, and timescales become faster.

- Antiferromagnetic (AFM) materials are similar to ferromagnetic materials, but have a variety of advantages over typical ferromagnetic materials in applications. Unlike FM materials, AFM materials are much harder to perturb with external magnetic fields, generally do not produce their own magnetic fields, and undergo much faster dynamics. As a result they are extremely attractive materials for data storage and may well replace ferromagnets in many areas in the future [BMT$^+$18, DDAWE24]. They are therefore extremely important materials to develop accurate models for, along with fast and efficient numerical schemes for simulating their behaviour.
- In a hard disk drive, to change the information stored, a dynamical process must occur. As the speed of data storage increases, the older models of magnetic dynamics become less accurate on very short timescales (e.g. subpicoseconds) making reading and writing at these speeds impossible. Recently a new model has been developed which correctly models this behaviour [NAK$^+$21] within the "inertial regime". This opens the gates for "ultrafast" magnetic materials, that take advantage of these fast processes to switch the magnetic state extremely quickly [MRF$^+$23].
- Magnetic materials are not only used in data storage, and are often used in mechanical applications as a type of smart material, relying upon various

magnetoelastic effects. Magnetoelastic effects refer to the coupling between the magnetic properties, and the elastic properties, of a material, whereby influencing the magnetic state of a material will distort the physical dimensions of the material, and vice versa. All ferromagnetic materials exhibit some level of magnetostriction, but in many materials it has a very small effect. The magnetoelastic effects are key to a variety of applications, such as in many types of actuators, energy harvesters, and various sensors [Pas03]. Magnetoelastic materials are often in the form of thin films and strips, and may be coupled with multiple layers of piezoelectric or magnetoelastic materials [LDC$^+$20].

These three topics do not occur independently. As mentioned, antiferromagnetic materials are generally quicker to change their magnetic state than ferromagnetic materials, and this holds for the inertial regime as well, giving potential for much higher writing and reading speeds than currently possible [MGRN21]. Antiferromagnetic materials, like ferromagnetic materials, are also magnetoelastic, so for precise simulation the magnetoelastic effect should be included for accurate modelling. Models of magnetoelastic effects have also recently began including the effects of ultrafast dynamics [DMD24, DHD24]. It is therefore possible to consider a material and model that incorporates all three of these properties into practice, i.e., considering an ultrafast antiferromagnetic material with magnetoelastic effects. The physical description of magnetic materials in a continuum setting lies within the paradigm of "Micromagnetics", an energy functional based theory where the main quantity is the magnetization $\boldsymbol{m}$, that satisfies a non-convex unit length constraint $|\boldsymbol{m}| = 1$. As a result, micromagnetics involves solving highly non-linear problems, where exact solutions rarely exist beyond extremely simple limiting cases, often restricted to two-dimensional thin-films. In three dimensions, numerical methods are the primary means of investigation of magnetic materials, and accurate modelling therefore requires accurate, precise, and stable numerical methods to be developed.

1.2 State of the art

1.2.1 History

The origins of micromagnetics[1] lies with the 1935 paper [LL35] by L. Landau and E. Lifshitz [Aha01, Bro78b, BI15]. Through pioneering work by P. Weiss, F. Bloch, W. Heisenberg, Ya. G. Dorfman, Ya. I. Frenkel, and many others, the so-called exchange interaction, fundamental to ferromagnets, came to be well understood through "Domain Theory" between 1908 and 1931. The paper [LL35] only dealt with a single dimension, but the energy term associated with the exchange interaction was described further in [Elm38] by W. C. Elmore, and then expanded upon by Brown [BJ40, BJ57], including a general theory for 3D,

[1]To the author's knowledge, the first time that W. F. Brown Jr. used "micromagnetics" in his published works was in 1958 [Bro58, p.471], writing "I hope that others will join us in developing this new field — micromagnetics, successor to domain theory".

using a variational approach to derive conditions for static equilibria. When the micromagnetic system is out of equilibrium, the dynamical Landau–Lifshitz–Gilbert (LLG) equation is required [LL35, Gil04], combining the contributions of Landau, Lifshitz, (who originally produced the Landau–Lifshitz equation) and T. Gilbert, who provided the modern form of the LLG equation. The work [BI15] explains the long 80+ year history of the dynamical equation, and a few of the various extensions to e.g. antiferromagnetic materials, spin electronics (spintronics), and dynamics of magnetic skyrmions.

For a reflective essay on the development of micromagnetics given by Brown, see [Bro78b]. For a history of the development of micromagnetics from the perspective of Brown, see [Bro78a, Chapter 2], or for a more critical history by A. Aharoni see [Aha01]. We note that according to [Aha01], the field of micromagnetics was not well accepted until experiments involving magnetic recording devices were found to be well described by micromagnetic calculations. For the history of micromagnetics in the context of recording materials, see [Wei12, Section 2.3.3].

1.2.2 Numerical Schemes

Before discussing the types of integrators available, we first list some desired properties of numerical algorithms which generally cannot all be met at once:

- Maintains the unit length constraint on the magnetization. This must hold in the limit almost everywhere, but approximations generally will not satisfy this except at finitely many places, and perhaps not anywhere. Of any requirement, this is the most fundamental. If this constraint is not considered, then the solver is not appropriate for micromagnetics.
- The very expensive magnetostatic contribution should be handled efficiently [Bro62, FSD$^+$03]. This will typically take up most of the computation time, and requires special methods depending upon the approach chosen, finite element, or finite difference, and so on.
- Requires only linear solvers. Non-linear equations require more expensive computation, and can be more difficult to analyse. This typically conflicts with the unit length constraint.
- Satisfies the Lyapunov structure, with the energy functional decreasing over time according to an energy law, which suggests that the magnetic state will evolve towards a stationary point of the energy. This law may be weakened to the energy being non-increasing, or just bounded. Furthermore, if the damping is eliminated, the energy should be conserved throughout time.
- Analysis should exist proving that the method is stable to show that quantities that should be finite do not diverge to infinity, and convergence analysis should be available proving that the algorithm approaches a solution in some sense, either weak or strong. In particular, existence, stability, and convergence should be "unconditional" if possible, without restrictive relationships between the mesh size h and time-step size k.
- Coupled systems should be decoupled where possible. Decoupled systems

are generally easier to solve, and in some cases decoupling allows for old algorithms and code to be reused.

1.2.3 Integrators

There are many integrators for the LLG equation, but most commercial software and especially those used in physical investigations rely upon black box or out-of-the-box integrators such as the four step Runge–Kutta (RK4) method or Adams type predictor corrector methods [DP99, Abe19, Cim07b]. These methods are fast, but often require extremely tiny time-steps for numerical stability. Furthermore, these types of integrators do not attempt to take the unit length structure of the equation into account (typically resorting to a non-linear projection step), nor the Lyapunov structure.

Many numerical integrators for the LLG equation have been proposed over the years, and for a more comprehensive view of these we recommend the following review articles [KP06, Cim07b, Abe19, RXS22, NR25a]. Some methods directly preserve the unit length by relying upon an exponential mapping via a rotation vector [LN03, ME12, DW23b], but these are not linear. Other methods apply implicit treatment such as in [BP06] to avoid restrictively small time-steps as with the RK4 methods, and have been extended to implicit-explicit (IMEX) techniques for handling the computationally expensive terms [PRS18, DFPPR23].

An attractive type of integrator is known as the midpoint scheme [dSM05]. Various extensions to [dSM05] have been considered [EMSS17, dPS24]. This type of integrator applies the symplectic midpoint time-stepping scheme to the LLG equation, which inherently preserves the Lyapunov structure, and also conserves the unit length constraint. The price paid for these nice features is that the resulting discrete system is non-linear, requiring further linearization techniques to make solving the non-linear system efficient. A similar integrator is used for the angular momentum method [KW14] applied for the iLLG problem [Rug22], where the non-linear solve introduces a Courant–Friedrichs–Lewy (CFL) condition of the form $k = O(h)$.

The integrator of choice for this thesis is known as a "tangent plane scheme", based on the θ-method for the LLG equation proposed in [Alo08] by F. Alouges, itself based on previous work [Alo97] for harmonic maps, and an explicit (i.e. conditionally convergent) form of the algorithm was given in [AJ06, BKP08], and the algorithm was later extended in [AKT12, BFF$^+$14] to include more micromagnetic terms than exchange. The θ-method is unconditionally stable and convergent, with no CFL condition. Including lower order terms however may introduce a CFL condition, and CFL conditions are typically required when proving that an energy law holds.

The tangent plane type integrator uses first-order finite elements in space, and an implicit first-order time-stepping method in time. The resulting discretization is a linear system similar to that of the heat equation, but a non-linear nodal projection correction step may be applied to the solution to impose the unit length constraint as in e.g. [Rug22, BPPR14, KPP$^+$19, HPP$^+$19].

To get the linearization, the "tangent plane" orthogonality constraint $\boldsymbol{m} \cdot \boldsymbol{\phi}$ must be imposed, where $\boldsymbol{\phi}$ is a test function and $\boldsymbol{m}$ is the function of interest. This requires either a Lagrange multiplier approach [PRS16, AEB$^+$13, GHPS12], or the use of a null-space method [RGJ13], both of which involve building additional matrices per linear solve. To guarantee the stability of this nodal projection step, the mesh used for the spatial discretization must be assumed to be weakly acute (see Proposition 3.3.3), a condition first given in [Bar05]. If the nodal projection is omitted from [Alo08] as considered in [Bar16, AHP$^+$14, KPP$^+$19, HPP$^+$19] then the unit length constraint violation is controlled linearly by the time-step.

Various extensions to the method and analysis in [Alo08] have been considered, e.g. the ultrafast version of the LLG equation [Rug22], including magnetoelasticity [BPPR14], the quasi-static Maxwell–Heaviside equations [LT13, LPPT15, DFPP$^+$20, CCV$^+$17] magnetostatics and other lower order terms [PRS18], magnetic skyrmions [HPP$^+$19, DDFPR22], multiscale models [BFF$^+$14], and more recently a rigorous error analysis has been developed [ALS24] for the projected tangent plane scheme, although the error analysis for the projection-free scheme has existed much longer [FT17a].

When it comes to second-order formulations of the tangent plane scheme, a decent attempt was made in [AKST14] with similar work in [KVBP$^+$14], where the schemes are above first-order, but not quite second-order in time. This additionally comes at the cost of the linearity that was gained by applying the tangent plane scheme.

A second-order in time tangent plane scheme has recently been given in [ABP24, AFP25], which utilizes a two-step backwards differentiation formula (BDF2) — previously considered in [AFKL21] for a spatially averaged tangent plane scheme — to impose a second-order constraint violation on the unit length. This also provides second-order convergence in time, and also does not give up the linearity of the tangent plane scheme, nor does it require weakly acute meshes due to the lack of a nodal projection step. The second-order constraint violation is dependent upon a discrete regularity condition, but an unconditional linear violation can be proven in analogy with [Bar16]. This second-order violation can be upgraded to be unconditional, with a conditional third-order constraint, as seen in [DGXY24] in the context of accelerated gradient descent but still applying a tangent plane scheme. A similar method was designed in [ABRW25], where instead of applying BDF2 discretizations, a midpoint scheme yielded second-order constraint violation, subject to a similar discrete regularity condition.

1.2.4 Recent Developments

Recent focuses in micromagnetics are on extensions of micromagnetic phenomena to ultrafast micromagnetic dynamics [NAK$^+$21, CRW11, OLW12, MGRN21, Mon21, dPS24, Rug22], or to coupled systems, such as magnetoelastic phenomena [TdL93, Ens09, JW98, DDCF16, BPPR14, Baň05, BS05, Baň08, VML$^+$21, FKS$^+$25, BHB$^+$14, SLW04, RBJ21a, CEF11], spin transfer torque [AHP$^+$14, Abe19], spin-orbit coupling [STPKA$^+$20, PRS16, GL15, Abe19], or the study

of magnetic skyrmions [FRC17, RCP15, SZT+20, HPP+19, TSTLD+20], thermal effects [LST24, BEA24, ST23], and antiferromagnetic/ferrimagnetic materials [NE15, BMT+18, BCKO21, BCKO22, MGRN21, Mon21, SZT+20, PKC+19, KBL+22, TSTLD+20, MLP16, MRA19],

1.2.5 Existence and uniqueness

We now consider the progression of existence and uniqueness results for the dynamical equations of micromagnetics, but recommend [DL22] or [GD08] for a more in-depth view. Ignoring damping, an early proof of existence of solutions in the one dimensional case was given by [ZG84], and the proof for more than one dimension was given in [SSB86]. A more general mathematical proof of existence of solutions for the LLG equation was given by A. Visintin [Vis85], with proof for the full Maxwell–Heaviside equations and also magnetostriction. Later existence and non-uniqueness of weak solutions followed, in [AS92, GH93], which link the weak solutions of the Landau-Lifshitz equation to the closely related harmonic maps [BCGS92]. Even later, existence of global weak solutions followed for the LLG equation including magnetostriction [CEF11], or the Maxwell–Heaviside equations [Cim07a], or for the related Landau–Lifshitz–Bloch/Landau–Lifshitz–Baryakhtar equations [LST24, ST23]. Strong solutions have also been of interest due to their uniqueness, but are only expected when the initial condition is sufficiently regular, and often small in energy such as in e.g. [CF01b, CF01a, Mel12, FT17b, KKS19]. The two concepts are linked via a "weak-strong uniqueness principle", in which the strong and weak solutions coincide (as long as both exist), as opposed to just coexisting [DFIP20].

1.2.6 Software

There are many finite difference packages available for micromagnetics, of which OOMMF [DP, DP99] is probably the most widely used with over 3800 citing papers at the time of writing [NIS], with a variety of other packages available such as Mumax and its extensions [VVdW11, VLD+14, LDM+18, MLDG+24], or others such as Micromagnum [Sel13], Micromagus [Ber], or MagTense [BPNI21]. Finite differences have the advantage of being relatively simple to implement, e.g. spatial derivatives are just difference approximations, and having fast methods based on the Fast-Fourier Transform (FFT) for dealing with the "magnetostatic contribution", which is a non-local effect taking up most of the simulation time [AES+13, Abe19, MD+07]. The FFT algorithm reduces the problem from $O(N^2)$ to $O(N\log(N))$, where N is related to the number of cells being used, which is a significant decrease in computational effort for large N. Finite differences have the main disadvantage of requiring mainly cuboidal shapes, being restricted to well spaced grids, but many simulations of interest are on thin films for which finite differences are excellent.

Similarly, there are many finite element packages dedicated to micromagnetics, e.g., Nmag [FFBF07], Commics [PRS+20], Magpar [SFS+03], and magnum.fe [AEB+13]. These are usually built upon existing finite element software

such as NGSolve [Sch25], or FEniCS [ABH+15], which handle the construction of the mesh and the assembly of the linear/non-linear system of equations. The packages may also include direct/iterative solvers and preconditioners, or rely on additional packages such as SciPy [VGO+20]. Finite element methods have the advantage of allowing for general (especially curved) shapes, but this lack of regular spacing means special methods are required for computing the magnetostatic contribution efficiently, e.g., using a FEM-BEM coupling approach such as the ones developed by D. Fredkin and T. Koehler [FK90], or by García-Cervera and Roma [GCR06], or with inverted finite elements as developed by T. Boulmezaoud and K. Kaliche [BK24]. FEM-BEM coupling methods usually yield dense matrices that require compression (such as $\mathcal{H}^2$-matrix compression) for the computation to be tractable [SSW, HK14, HCB19, AFF+13]. For more details, see [AES+13, Abe19]. A broader look at the different micromagnetic software available can be found in [Abe19, Bis20]. In addition, there exists Virtual Micromagnetics [VBAF16], a package of micromagnetic codes built around a virtual machine, allowing for easy comparison between the various codes and algorithms.

See [Mag] for a much more inclusive list of the available micromagnetic software.

1.2.7 Extensions to LLG

In addition to the magnetostatic contribution, another non-local effect is the magnetoelastic effect. The partial differential equation system describing these materials, in the small-strain regime, consists of the LLG equation for the magnetization and the conservation of linear momentum law for the displacement (see (5.4)–(5.5) in Chapter 5). The two equations are non-linearly coupled to each other: One of the contributions to the effective field appearing in the LLG equation depends on the mechanical stress in the body (and thus on the displacement) and there is a magnetization-dependent contribution to the strain (usually referred to as the magnetostrain) in the conservation of momentum law. Several versions of this PDE system have been used for physical investigations of magnetoelastic materials; see e.g. [SLW04, MMHH+14, BHB+14, PWH+15, RBJ21b, RBJ21a, DW23a], with the software package [MLDG+24] including an implementation. Literature on numerical approximation for magnetoelastic materials is the focus of L. Baňas and others [Baň05, BS05, Baň08, BPPR14].

Antiferromagnetic (AFM) and ferrimagnetic (FiM) materials, materials in which neighbouring magnetic moments tend to align antiparallel to each other (see Figure 2.1), have been known for many years. However, they have recently gained renewed interest, because several theoretical and experimental studies have shown that AFM and FiM materials have features that could lead to strong improvements of the functionality of spintronic devices, compared to those based on ferromagnetic (FM) materials [BMT+18, KBL+22]. In particular a continuum model has been developed for studying and developing devices based on magnetic processes involving of AFM and FiM materials; see, e.g., the works [NE15, PKC+19, STPKA+20, TSTLD+20, SZT+20] on AFM materials and [MLP16, MRA19, CSTT+21] on FiM materials. These materials essentially

contain two magnetizations, governed by a coupled system of LLG equations, with the constraint that both magnetizations are approximately antiparallel. In general, the mathematical literature on AFM and FiM materials is much less developed than that of FM materials. We refer, e.g., to [BCKO21, BCKO22] for works discussing discrete-to-continuum variational limits of a two-dimensional atomistic model of AFM materials. As far as the continuum model of AFM/FiM materials considered in this work is concerned, to the author's knowledge, the only other work addressing it is [LCDW20], where extensions of the Gauss–Seidel projection method [WGCE01, LXD$^+$20] have been proposed for its numerical approximation (but no convergence analysis is discussed).

A recent extension to the LLG equation is the so called inertial LLG (iLLG) equation, motivated by the discovery of ultrafast dynamics in ferromagnetic Nickel [BMDB96]. The standard LLG equation is not valid at short timescales, where "ultrafast" motion occurs, so the LLG equation must be modified to include a higher order time derivative term, which is highly relevant for the field of ultrafast magnetism [WM16, MRF$^+$23, CBM$^+$22]. The extra derivative term is only relevant on small time-scales, giving a multiscale nature to the iLLG equation, being hyperbolic in the short term and parabolic in the long term. The origin of the inertial term is not clear, with multiple possible derivations available, e.g. [Suh98, FI11] The main qualitative difference between LLG and iLLG governed dynamics is nutation [DSL$^+$25], whereby additional high frequency oscillations are superimposed onto the LLG dynamics, with experimental observation for the inertial dynamics being observed recently [CRW11, WC12, OLW12], with further confirmation in the last few years [NAK$^+$21]. Other differences are noted in [OLM$^+$15], particularly to do with an additional resonance peak associated with the nutation frequency. The field of iLLG dynamics is one of active research, with existence of solutions established in [HT14], and inertial dynamics is often studied in conjunction with magnetoelasticity [Suh98, Suh07, DMD24, DHD24]. In the same way that LLG dynamics are related to the flow of harmonic maps, iLLG dynamics are closely related to the problem of wave maps into the sphere [BFP08, Bar15a, KW14]. Some numerical schemes have been designed for solving the iLLG problem, such as [MT16, LYL$^+$21] which each apply a finite difference scheme. For finite elements, a rigorous numerical analysis, including weak convergence to a solution, for a numerical scheme was given by M. Ruggeri in 2022 [Rug22] using ideas from [Alo08, Bar15b, KW14], followed by d'Aquino et al. in 2024 [dPS24] extending the midpoint scheme of [dSM05]. The scheme by d'Aquino has been used already in the investigation of magnetization switching [NPS$^+$22]. Even more recently, the iLLG equation has been coupled to the Maxwell–Heaviside equations in [KZ25], using similar methods to [Rug22] combined with FEM-BEM techniques. The paper [Rug22] provides two approaches, a first-order in time scheme which requires weakly acute meshes but otherwise involves only linear operations, and a second-order in time non-linear "angular momentum method". Similarly, [dPS24] is of second-order in time but, a non-linear system must be solved at each time-step.

1.3 Contributions and outline

This thesis contributes several algorithms that extend the projection-free variant of the tangent plane scheme [Alo08] given in [Bar16] to magnetoelastic materials, AFM/FiM materials, and to ultrafast timescales in the iLLG equation. We focus on methods that are fully linear, in the sense that each algorithm only solves linear systems at each time-step and does not apply non-linear correction operations such as the nodal projection, despite each problem being very non-linear. For the magnetoelastic problem and ultrafast problem, we develop formally second-order in time algorithms, which are much more valuable for efficient computation of solutions.

The organization of the thesis is as follows:

- In Chapter 2 we describe necessary physical background for understanding each model problem of interest. This includes a brief description of magnetic phenomena, and the Maxwell–Heaviside equations, and then we explain the micromagnetic model of magnetic materials, the energy contributions and their effective field contributions. We describe the different types of time evolution of magnetic materials, such as through the LLG equation, the ultrafast counterpart in the iLLG equation, and the LLG equation coupled with the conservation of momentum equations for elasticity. Special attention is paid to the time evolution of the energy depending upon the model chosen.
- In Chapter 3, we define useful mathematical concepts such as the various Bochner/Hilbert spaces required in the later analysis, and define the common spatial and temporal discretizations to be used in the analysis, as well as the implementation. All methods utilize a first-order finite element scheme in space, but the temporal discretization can vary depending upon the equation being solved, and the order in time (first or second) desired.
- In Chapter 4 we introduce the tangent plane scheme of [Alo08] and the modification [Bar16] within the context of energy minimization. We introduce an energy minimization Algorithm that applies a conditional nodal projection (Algorithm 4.2.1), and a post-processing method (Algorithm 4.3.1) to reduce the unit length constraint violation. We demonstrate the non-linearity of the nodal projection operator through numerical experiments.
- In Chapter 5, we generalize the PDE system considered in [Vis85, CEF11, BPPR14] by including volume and surface forces, as well as a more general expression for the magnetostrain [FCV19], which allows the description of a larger class of magnetoelastic materials. For this generalized system, we propose an integrator which resembles the one in [BPPR14] (same finite element approximation spaces, same time discretization method, same decoupled approach). However, following [Bar16, AHP$^+$14] (and differently from [BPPR14]), we remove the nodal projection from the update of the magnetization (but we keep it in the discretization of the elastic contributions). By doing this, we can avoid the requirement of weakly acute meshes at the expense of not maintaining the unit length constraint on the magnetization

at the vertices of the meshes. However, like in [Bar16, AHP+14], we can uniformly control the violation of the constraint by the time-step size. Despite the strong non-linearity of the problem, the resulting integrator is fully linear (in the sense that it involves only linear operations like solving linear systems and updating the approximations using a linear time-stepping). For this generalized and modified integrator, we show unconditional well-posedness, a discrete energy law satisfied by the approximations, unconditional stability, and unconditional convergence of the approximations towards a weak solution of the problem (here, the adjective "unconditional" refers to the fact that the analysis does not require any restrictive coupling condition between the time and spatial discretization parameters). Moreover, assuming a (very restrictive, but artificial) CFL condition on the time-step size and the spatial mesh size, we can pass the discrete energy law to the limit and show that the weak solution towards which our finite element approximation is converging satisfies an energy inequality. For the published work that this chapter is based on, see [NR25c].

- In Chapter 6, we develop an unconditionally stable, formally second-order in time integrator for the LLG equation with magnetostriction. Recently, projection free tangent plane schemes of second-order in the unit length constraint have been introduced and analysed by [ABP24, ABRW25] and extended by [DGXY24, DGY25, AFP25]. The numerical scheme [ABP24, ABRW25, DGXY24, DGY25] are in the context of numerical gradient descent, whereas [AFP25] is a numerical scheme for the standard LLG equation. In [ABP24, DGXY24, DGY25, AFP25], the improvements to the unit length constraint error order are from applying a two-step backwards differentiation formula (BDF2) time-stepping, instead of the first order time-stepping applied in [Alo08], along with a modification to the solution space of the linear system. The method applied in [ABRW25] only requires a minor modification to the solution space of the linear system used in [Alo08], and does not require the use of any BDF2-adapted norms which are less suited to time-dependent problems, especially when energy laws are desired. For this reason, we apply the "midpoint scheme" of [ABRW25] for this chapter.

  The discretization used in [BPPR14] and Algorithm 5.4.1 for the conservation of linear momentum equation is of first-order, and highly dissipative due to the implicit solver applied. Whilst this is beneficial for the numerical analysis, it can spoil any long-term behaviour of the numerical solution. This numerical dissipation can be directly linked to whether or not the scheme is of second-order when investigated through the Newmark-β scheme [New59]. The Newmark-β takes two parameters, β and γ, and requires $\gamma = 1/2$ to be second-order, and for purely elastic materials requires $\beta \geq 1/4$ for unconditional stability. The discretization for the displacement applied in [BPPR14] and Algorithm 5.4.1 can be matched with a Newmark-β with parameters $\beta = 1, \gamma = 3/2$ and an alternative initialization step.

  We show that coupling between the projection-free midpoint scheme for LLG with the Newmark-β scheme with $\gamma = 1/2, \beta > 1/4$ yields an uncondi-

tionally stable scheme that is formally second-order in time, described in Algorithm 6.3.1. We prove the unconditional stability of the method, and perform numerical simulations to demonstrate the improvements over the algorithm presented in Chapter 5. This chapter is currently in preparation for publication [KNR25].

- In Chapter 7 we consider a continuum model that is the state of the art for micromagnetic simulations of devices based on magnetic processes involving of AFM and FiM materials. The main elements of the model, an extension of the classical micromagnetic model of FM materials [Bro63], are an order parameter, which consists of two unit-length vector fields that can be interpreted as the normalized magnetizations averaging the magnetic moments of two sublattices, and an energy functional, which consists of several contributions, each of them representing a specific physical effect. A key feature of the model, that is necessary to describe the antiparallel alignment of the spins in AFM and FiM materials, is a more complex expression of the exchange energy than in FM materials, which involves not only the classical Heisenberg exchange interaction penalizing non-uniform configurations, but also the interaction of the two fields with each other (see the last two terms in the energy functional (7.1) below). Similarly to the classical micromagnetic theory, the static problem consists of minimizing the energy functional over all pairs of unit-length vector fields, whereas the dynamics of each field out of equilibrium is governed by the LLG equation (see (7.9) below), with the effective field being the Gateaux derivative of the energy with respect to the respective field. However, due to the energy contributions involving the interaction between the two fields, both the Euler–Lagrange equations associated with the minimization problem and the system of LLG equations are non-linearly coupled systems of nonlinear partial differential equations.

  Building on previous work on the approximation of (the heat flow of) harmonic maps [Bar16] and of the classical model of FM materials [Alo08, AHP+14], we propose fully discrete numerical schemes for the approximation of both the static and the dynamic problems.

  For the static problem, we propose a discretization based on first-order finite elements and prove that the discrete energy functional converges to the continuous one in the sense of Γ-convergence [Bra02]. Moreover, we propose two iterative algorithms for the computation of low energy stationary points based on time discretizations of the gradient flow of the energy functional (see Algorithm 7.3.4 and Algorithm 7.3.5 below). These two algorithms differ from each other in the time discretization (fully implicit for Algorithm 7.3.4, semi-implicit for Algorithm 7.3.5). For both algorithms, we prove well-posedness of the iteration, an energy-decreasing property, termination of the iterative loop, an upper bound for the error in the unit-length constraint, and (under a restrictive assumption on the coefficients appearing in the energy functional) convergence toward a stationary point. Moreover, we perform numerical experiments to compare the two algorithms and to assess

their performance.

Then, we extend the best performing algorithm (and its analysis) to the dynamic problem and show that the resulting integrator (Algorithm 7.4.1) is well-posed, stable, and generates approximations that are unconditionally convergent toward a weak solution of the coupled system of LLG equations. For the publication that this chapter is based on, see [NR25b].

- In Chapter 8, we state the extension of the dynamic model for micromagnetic materials to ultrafast materials, and state Algorithm 8.4.1 which is governed by a parameter $\beta \in (0, 1]$ that determines the relative importance of the BDF1 and BDF2 approximations for the time derivative of the velocity. We see that setting this parameter to zero yields a formally second-order in time method, but for non-zero values is significantly more tractable in terms of analysis. In contrast to the midpoint scheme considered in Chapter 6, Algorithm 8.4.1 is based upon BDF2 algorithms for harmonic maps [ABP24] and the LLG equation [AFP25]. We show that Algorithm 8.4.1 is unconditionally stable, and convergent to a weak solution of the ultrafast micromagnetic problem under a suitable CFL condition, and demonstrate that the unit length constraint violation is of at least second-order in time, but third order in practice. Numerical results support our statements.
- In Chapter 9, we state closing remarks and comment on possible extensions to the present work.
- In Appendices A, B and C, we include extra materials.

To summarise, this thesis formulates projection-free tangent plane schemes for three models of micromagnetics: magnetoelastic materials, antiferromagnetic materials, and ultrafast materials. The tangent plane scheme is used to provide a natural linearisation for the solution of the full non-linear three dimensional equations, and the nodal projection normalisation step is removed to eliminate the restrictive assumption of weakly acute meshes. Every discretisation is fully linear, with only one or two linear solving operation required to advance to the next time step, despite each problem being highly non-linear, with a nonconvex unit length constraint. This introduces a unit length constraint violation that is recovered due to the tangent plane scheme in the limit as the time-step approaches zero. Moreover, a focus is placed on the unconditional stability of the numerical schemes, along with the time evolution of the discrete energy, and how the discrete energy law can be passed through to the limit to recover the energy law of the continuous problem. We stress that the energy law is an additional structure placed upon the solution, and requires additional assumptions to eliminate certain defect terms that appear in the discrete energy laws. Despite "CFL-like" conditions being required, these are only required for the proof of convergence to the weak formulation or energy law, and are irrelevant in terms of the stability of the methods. Every algorithm stated is implemented using NGSolve/Netgen in Python.

Chapter 2

Physical Background

Throughout the following section, we will introduce the necessary physical quantities, laws, and relations that describe magnetic materials, and in particular explain the field of micromagnetics.

2.1 The Maxwell–Heaviside equations

The basic quantity of interest in solid-state magnetism is the magnetic moment $\boldsymbol{\mu}$, measured in $\mathrm{A\,m^2}$, associated with the spin and orbital momenta of the electron [Coe10, Section 2.1]. The object of interest within the continuum theory of micromagnetics is the magnetization, $\boldsymbol{M}$, defined by averaging over a suitably small volume $\mathrm{d}V$, that is

$$\boldsymbol{M} = \frac{\mathrm{d}\boldsymbol{\mu}}{\mathrm{d}V}. \tag{2.1}$$

The general theory of electromagnetism is described by the macroscopic Maxwell–Heaviside[1] equations, generally referred to as Maxwell's equations. These are given in differential form by [Coe10, (2.46)–(2.49)]

$$\nabla \cdot \boldsymbol{B} = 0, \tag{2.2a}$$

$$\nabla \cdot \boldsymbol{D} = \rho, \tag{2.2b}$$

$$\nabla \times \boldsymbol{E} = -\frac{\partial \boldsymbol{B}}{\partial t}, \tag{2.2c}$$

$$\nabla \times \boldsymbol{H} = \boldsymbol{J} + \frac{\partial \boldsymbol{D}}{\partial t}, \tag{2.2d}$$

where $\boldsymbol{B}$ is the magnetic flux density (measured in T), $\boldsymbol{H}$ is the magnetic field (measured in A/m), $\boldsymbol{D}$ is the electric displacement field (measured in $\mathrm{C/m^2}$), and $\boldsymbol{E}$ is the electric field (measured in V/m). In order, (2.2a) is Gauss' law for the magnetic flux density, (2.2b) is Gauss' law for the electric displacement, (2.2c) is Faraday's law, and (2.2d) is Ampére's law with Maxwell's contribution. We will

[1] O. Heaviside rewrote the original equations of Maxwell, which were 20 separate equations, into the 4 equations we are familiar with in the modern day. See, for example, [HH12, DSY18] or Chapter II (sections 33-36) and III of [Hea93].

denote the magnetic body by Ω, but the above fields are all defined on the entirety of $\mathbb{R}^3$ in general. For this work, we generally assume that the charge density and current density satisfy $\rho = 0\,\mathrm{C/m^3}$, $\boldsymbol{J} = \boldsymbol{0}\,\mathrm{A/m^2}$ respectively throughout $\mathbb{R}^3$. Furthermore, we have the constitutive law relating the magnetic field, the magnetic flux density, and the magnetization, given by [Coe10, (2.33)]

$$\boldsymbol{B} = \mu_0(\boldsymbol{H} + \chi_\Omega \boldsymbol{M}), \tag{2.3}$$

where the characteristic function χ_Ω serves as a reminder that the magnetization is only non-zero within the material. The value μ_0 is the permeability of free space [YFF13, Appendix F].

2.1.1 Ferromagnetic materials

In [Bro78a, Section 1.1], Brown defines a ferromagnetic (FM) material as a material "that possesses a spontaneous magnetization: that is, sufficiently small volumes of it have a magnetization [of magnitude] $M_\mathrm{s}\ldots$", that is, the magnetization satisfies $|\boldsymbol{M}| = M_\mathrm{s}$ for some positive spontaneous magnetization M_s. This means that the magnetization in the material can change only its direction throughout the magnetic body. Originally, this was an assumption by Pierre Weiss [Aha07, Section 1.2], but was justified through quantum mechanics (see [Aha07, Chapter 2]). This is temperature dependent, but the temperature is often assumed to be constant (see [Bro78a, Section 1.3] or [Aha07, Section 4.1]). This constant length constraint is only really true when speaking of an average of a suitably large volume of the material, and is a result of transferring from the quantum mechanical spin vectors $\boldsymbol{S}$ to the continuum approximation [Aha07, Section 7.1]

Within ferromagnetic materials, it is often enough to utilize the "magneto-quasi-static approximation". In essence, this sets $\partial \boldsymbol{D}/\partial t = \boldsymbol{0}$, yielding the magneto-quasi-static system of equations

$$\nabla \cdot \boldsymbol{B} = 0, \tag{2.4a}$$

$$\nabla \times \boldsymbol{E} = -\frac{\partial \boldsymbol{B}}{\partial t}, \tag{2.4b}$$

$$\nabla \times \boldsymbol{H} = \boldsymbol{0}. \tag{2.4c}$$

For a derivation and conditions of validity, see [Kno00, Section 1.2] or [RV10, Section 1.2]. Roughly stated, the validity of this approximation requires that the entire system receive any electromagnetic fields at the same time, i.e. the speed of light is infinite, and that the magnetic field dominates the electric field. Micromagnetics as described in the next section is sufficiently small scale that the speed of light is approximately infinite. We must exclude conductors to satisfy the second requirement, but this is non-restrictive as the field generated by currents in coils are dealt with separately as an applied field.

Reading the equations, we see that the magnetic flux density is solenoidal due to (2.4a). This is sometimes interpreted as meaning the magnetic flux density lines form closed loops or diverge to infinity, but this is not true in general [Kno00, Section 2.5 p.128]. On the other hand, taking the divergence of (2.4b) (noting the

divergence of a curl is zero) yields that (2.4a) holds throughout time, assuming any initial condition does. Lastly, (2.4c) yields that the magnetic field is irrotational, and can be written as the negative gradient of some scalar potential [Aha07, Section 6.1].

2.1.2 Ferri/antiferromagnetic materials

Ferrimagnetic (FiM) and antiferromagnetic (AFM) materials can be thought of as two overlapping ferromagnetic materials, with a coupling that encourages the magnetizations of each material to oppose each other at each point. Mathematically, an AFM material is modelled by two ferromagnetic sublattices with associated magnetizations $\boldsymbol{M}_1, \boldsymbol{M}_2$ with equal magnitude of magnetization $|\boldsymbol{M}_1|, |\boldsymbol{M}_2| = M_\mathrm{s}$, and a FiM material is an AFM material where the magnitudes differ. Therefore, FiM and AFM materials have a smaller total magnetization, and AFM materials have the potential to have zero total magnetization, where the total is the sum of the magnetization associated with each sublattice, i.e. $\boldsymbol{M} = \boldsymbol{M}_1 + \boldsymbol{M}_2$. This means that AFM materials have a very small magnetostatic field, which can be ignored in many circumstances, making them much simpler to work with numerically as the magnetostatic interaction can be ignored.

2.2 Micromagnetics

Micromagnetics is the study of magnetic materials between the regime of quantum theory, and the regime of domain theory [Bro78a, Preface]. This is a scale large enough to avoid details of individual atoms and their quantum mechanical spins, but small enough to resolve e.g. domain walls and vortices using a continuous magnetization vector field. It should be noted that the continuum approximation can fail if the walls between magnetic domains are too thin (on the order of a few atoms). As noted above, the magnetization has constant length, so we can define the normalized magnetization vector field $\boldsymbol{m} := \boldsymbol{M}/M_\mathrm{s}$, that satisfies $|\boldsymbol{m}| = 1$ within Ω, which we refer to as the unit length constraint of the magnetization.

The field of micromagnetics is phenomenological, and generally classical, despite ferromagnetic behaviour being necessarily quantum in nature. In the static case, a suitable sum of micromagnetic free energy terms are chosen, and then this energy is minimized to give an equilibrium state. In the dynamic case, a suitable derivative of the energy is used to determine the time evolution of the magnetization.

2.3 Micromagnetic free energy

The micromagnetic free energy is composed of several terms, which we shall include here for completeness. Not all terms are used in this work, due to the computational complexity involved, but most terms are well understood. For example, we shall ignore the magnetostatic energy (the energy associated with the magneto-quasi-static equations (2.4a–2.4c)), despite this being extremely important for realistic computation for FM/FiM materials. Similarly, many cited

works will ignore magnetostriction (Section 2.3.6), which will be the subject of Chapters 5 and 6.

2.3.1 Exchange energy

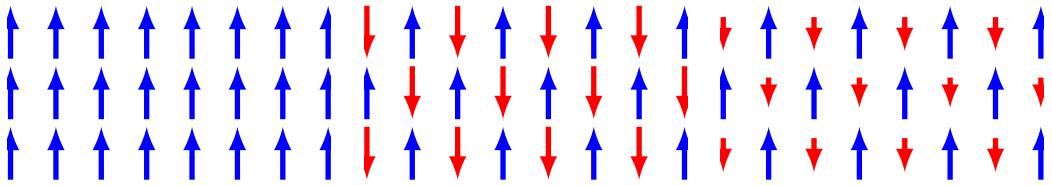

(a) FM (b) AFM (c) FiM

Figure 2.1: Classes of magnetic materials. Different colours correspond to different sublattices, and different sizes correspond to their contribution to the magnetic field generated by the magnet. In (a) we see all arrows mutually align, as in a ferromagnet (FM). In (b) we see two sublattices, which align with like colours, and anti-align with different colours, like in an antiferromagnet (AFM). In (c) we see a ferrimagnet (FiM), essentially an antiferromagnet where the two sublattices differ in their magnetic strength.

The (inhomogeneous intralattice) exchange energy comes from the quantum mechanical Heisenberg exchange Hamiltonian [Aha07, Chapter 3]

$$\mathcal{H}_{\text{ex}} = -J \sum_{\langle i,j \rangle} \boldsymbol{S}_i \cdot \boldsymbol{S}_j, \tag{2.5}$$

where the sum is over nearest neighbours, and the exchange integral constant J is positive, which encourages neighbouring spins $\boldsymbol{S}$ to point in the same direction. All ferromagnetic materials (see Figure 2.1a) are subject to this effect. This can be explained qualitatively with the Pauli Exclusion Principle and the Coulomb interaction [ESS20, Section 3.2]; as electrons cannot occupy the same position unless they point in opposite directions, the electrons move apart to lower their Coulomb repulsion, and orient themselves mutually. An important approximation made during the switch between quantum and classical is that the angles between the neighbouring spins are assumed to always be small. This is generally justified as the exchange forces are very strong on short length scales, which induces a qualitative level of continuity on the magnetization. In the micromagnetic form, we take the exchange energy as [Aha07, Section 7.1]

$$\mathcal{E}_{\text{ex}}[\boldsymbol{m}] = A \int_\Omega |\boldsymbol{\nabla m}|^2, \tag{2.6}$$

where A is the *exchange constant*, measured in $\mathrm{J\,m^{-1}}$. We note that sometimes the exchange constant is written as $A = C/2$, where a prefactor of $1/2$ is introduced [Aha07, Section 7.1].

When considering AFM/FiM materials (see Figures 2.1b and 2.1c), there are two additional exchange effects,

$$\mathcal{E}_{\text{ex}}[\boldsymbol{m}] = A_{11}\int_\Omega |\boldsymbol{\nabla}\boldsymbol{m}_1|^2 + A_{22}\int_\Omega |\boldsymbol{\nabla}\boldsymbol{m}_2|^2 + A_{12}\int_\Omega \boldsymbol{\nabla}\boldsymbol{m}_1 : \boldsymbol{\nabla}\boldsymbol{m}_2 - \frac{4A_0}{a^2}\int_\Omega \boldsymbol{m}_1\cdot\boldsymbol{m}_2.$$

Each field $\boldsymbol{m}_1, \boldsymbol{m}_2$ has its own inhomogeneous intralattice exchange energy with exchange constants $A_{11}, A_{22} > 0$, but also has contributions between the two lattices. The first is the inhomogeneous interlattice exchange with exchange constant A_{12}, and the other is the homogeneous interlattice exchange with exchange constant A_0, where a is the lattice constant (in meters). For AFM and FiM materials, $A_0 < 0$, but if $A_0 > 0$ we get a ferromagnetic material with two sublattices. The homogeneous interlattice exchange interaction enforces the constraint that $\boldsymbol{m}_1 + \boldsymbol{m}_2 \approx 0$ in AFM/FiM materials, because

$$\begin{aligned} 0 \le -\frac{2A_0}{a^2}|\boldsymbol{m}_1 + \boldsymbol{m}_2|^2 &= -\frac{2A_0}{a^2}|\boldsymbol{m}_1|^2 - \frac{2A_0}{a^2}|\boldsymbol{m}_2|^2 - \frac{4A_0}{a^2}\boldsymbol{m}_1\cdot\boldsymbol{m}_2 \\ &= -\frac{4A_0}{a^2} - \frac{4A_0}{a^2}\boldsymbol{m}_1\cdot\boldsymbol{m}_2 \end{aligned}$$

and as the magnitude of $\boldsymbol{m}_1, \boldsymbol{m}_2$ is constant, we see that $-A_0|\boldsymbol{m}_1 + \boldsymbol{m}_2|^2$ is minimized (remember that A_0 itself is negative) when $\boldsymbol{m}_1$ and $\boldsymbol{m}_2$ are anti-aligned, that is, $\boldsymbol{m}_1 \approx -\boldsymbol{m}_2$. Similarly, when $A_0 > 0$, $-A_0|\boldsymbol{m}_1 + \boldsymbol{m}_2|^2$ is minimized when $\boldsymbol{m}_1 \approx \boldsymbol{m}_2$. The inhomogeneous interlattice exchange interaction is less clearly interpreted, but is also significantly less important physically and is often ignored. When the inhomogeneous interlattice exchange is ignored, we set $A_{12} = 0$.

2.3.2 Magnetocrystalline anisotropy energy

The exchange interaction introduced above is isotropic. This means that if all magnetization vectors point in one direction, the exchange energy is minimized, but the direction chosen is irrelevant. As ferromagnetic materials are generally crystals, the crystal structure plays an important role. Certain directions are favourable for the magnetization, and other directions are more expensive energetically for the electronic spins to point towards. The directions that require less energy are known as "easy axes". The anisotropy term takes a general direction dependent form of

$$\mathcal{E}_{\text{anis}}[\boldsymbol{m}] = K\int_\Omega \phi(\boldsymbol{m}) \tag{2.7}$$

where $\phi : \mathbb{S}^2 \to \mathbb{R}$ is a generally non-negative even function, that only takes the value 0 when the input is along an easy axis, and $K > 0$ is a material constant measured in $\mathrm{J\,m^{-3}}$. We interpret ϕ as an energy density, resulting from the energy required to rotate the magnetization out of the easy axes.

We state two particular cases, considering only the lowest order contributions:

- *Uniaxial anisotropy*: There is only one preferred direction $\boldsymbol{a} \in \mathbb{S}^2$, modelled by
$$\phi(\boldsymbol{m}) = 1 - (\boldsymbol{a} \cdot \boldsymbol{m})^2, \tag{2.8}$$
shown in Figure 2.2a. This is typical of hexagonal crystals [Aha07, Section 5.1.1]. We note that the constant is arbitrarily added to make the term non-negative. It does not affect the energy minimization process.
- *Planar anisotropy*: There are infinitely many preferred directions, perpendicular to some vector $\boldsymbol{a} \in \mathbb{S}^2$, modelled by the energy density
$$\phi(\boldsymbol{m}) = (\boldsymbol{a} \cdot \boldsymbol{m})^2, \tag{2.9}$$
shown in Figure 2.2b. Clearly the planar anisotropy term is the negative of the uniaxial term.

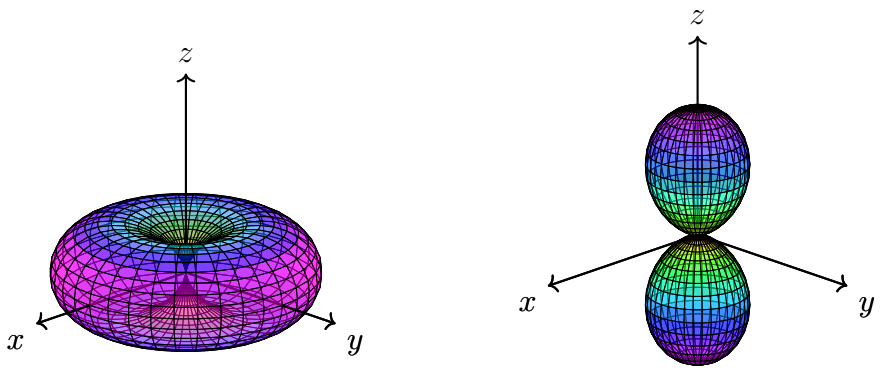

(a) Uniaxial anisotropy. (b) Planar anisotropy.

Figure 2.2: Magnetocrystalline anisotropy functions with $\boldsymbol{a} = (0, 0, 1)$. Directions where the surface is far from the origin are energetically unfavourable. The colour indicates the distance from zero, with purple indicating further, and red-green meaning closer to zero.

2.3.3 Magnetostatic energy

Roughly stated, the magnetostatic contribution to the energy forces the magnetization to satisfy the magneto-quasi-static equations (2.4a–2.4c). It is therefore one of the most important contributions to the energy, and due to the long range behaviour (see [Aha07, Section 6.2.2] for further details), it is also the hardest to compute numerically [Aha01, Section 2]. This is especially the case as errors may propagate throughout the solution.

As specified in (2.3), the magnetization is related to the magnetic flux density $\boldsymbol{B}$, which satisfies $\nabla \cdot \boldsymbol{B} = 0$. It follows that the magnetization, and its demagnetizing field $\boldsymbol{H}_s =: M_s \boldsymbol{h}_s$ (also known as the stray field), satisfy
$$\nabla \cdot \boldsymbol{h}_s = -\nabla \cdot (\chi_\Omega \boldsymbol{m}), \tag{2.10}$$
and using (2.4c) we can write [2] $\boldsymbol{h}_s = -\nabla V$ for some scalar potential V, as the full

[2] Usually the symbol u is used, but we reserve this for the displacement.

space $\mathbb{R}^3$ is simply connected. With appropriate regularity conditions at infinity, and well known continuity properties of $\boldsymbol{B}, \boldsymbol{H}$ (see [ESS20, Section 3.5.4]) the potential satisfies a Poisson problem,

$$\nabla^2 V^{(\text{in})} = \nabla \cdot \boldsymbol{m}, \qquad \text{in } \Omega, \tag{2.11a}$$

$$\nabla^2 V^{(\text{out})} = 0, \qquad \text{in } \mathbb{R}^3 \setminus \overline{\Omega}, \tag{2.11b}$$

$$V^{(\text{in})} = V^{(\text{out})}, \qquad \text{on } \partial\Omega, \tag{2.11c}$$

$$\left(V^{(\text{out})} - V^{(\text{in})}\right) \cdot \boldsymbol{n} = -\boldsymbol{m} \cdot \boldsymbol{n}, \qquad \text{on } \partial\Omega, \tag{2.11d}$$

$$V(\boldsymbol{x}) = O(1/|\boldsymbol{x}|), \qquad |\boldsymbol{x}| \to \infty. \tag{2.11e}$$

The magnetostatic energy is then given by

$$\mathcal{E}_{\text{s}}[\boldsymbol{m}] = \frac{\mu_0}{2} \int_{\mathbb{R}^3} |\boldsymbol{H}_{\text{s}}(\boldsymbol{m})|^2 = -\int_{\Omega} \boldsymbol{H}_{\text{s}}(\boldsymbol{m}) \cdot \boldsymbol{m} = \frac{\mu_0}{2} \int_{\mathbb{R}^3} |\nabla V(\boldsymbol{m})|^2. \tag{2.12}$$

The factor of $1/2$ is to avoid double counting during the integration. We will ignore this energy, due to the complexity involved in calculation. Our focus is not on producing physically correct models of reality, but to investigate the coupling between vector fields. The magnetostatic energy can be legitimately ignored when the magnetic body is very small, as the exchange energy is strong enough to override it [Aha07, Section 6.2.2].

The classical solution for the potential is well known, and can be written as

$$V(\boldsymbol{x}) = \frac{1}{4\pi} \left(-\int_{\Omega} \frac{\nabla \cdot \boldsymbol{m}(\boldsymbol{y})}{|\boldsymbol{x} - \boldsymbol{y}|} \mathrm{d}\boldsymbol{y} + \int_{\partial\Omega} \frac{\boldsymbol{n} \cdot \boldsymbol{m}(\boldsymbol{y}')}{|\boldsymbol{x} - \boldsymbol{y}|} \mathrm{d}\boldsymbol{y} \right), \tag{2.13}$$

although these are usually not particularly useful for computation. Even for the simple case for a uniformly magnetized sphere $\boldsymbol{m} = (0, 0, 1)$, it is difficult to show that the potential is simply $-z/3$. As such, if we were to require magnetostatic effects, we would utilize the NG-BEM module for PYTHON to implement [PRS18, Algorithm 12], which is based upon the Finite Element Method Boundary Element Method (FEM-BEM) method [FK90].

2.3.4 Antisymmetric exchange (DMI) energy

The antisymmetric exchange interaction, also known as the Dzyaloshinskii–Moriya Interaction (henceforth referred to as DMI) is described by the Hamiltonian

$$\mathcal{H}_{\text{DM}} = \sum_{\langle i,j \rangle} \boldsymbol{D}_{(i)(j)} \cdot (\boldsymbol{S}_i \times \boldsymbol{S}_j) \tag{2.14}$$

where $\boldsymbol{D}_{(i)(j)} \in \mathbb{R}^3$ are Dzyaloshinskii vectors. The form of these vectors depends upon the crystal symmetry in question, but in general DMI encourages the spins to align perpendicularly to their neighbours, in direct competition with the exchange energy of Section 2.3.1. If the crystal has inversion symmetry, then there can be no DMI effect, as interchanging i and j would via properties of the cross product,

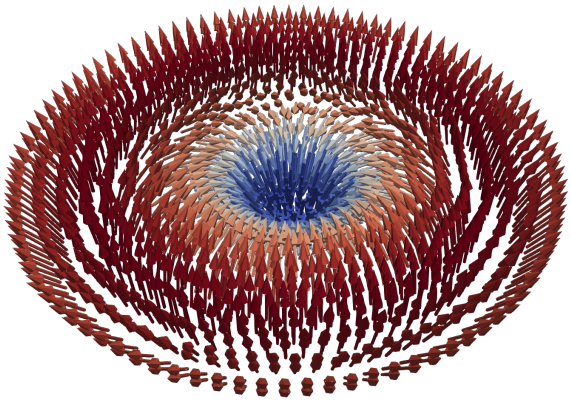

Figure 2.3: Example of a magnetic skyrmion in a disc. In the middle, the skyrmion is pointing down, and towards the edge the skyrmion points upwards.

imply that $\boldsymbol{D}_{(i)(j)} = \boldsymbol{0}$. At the continuum level, this is modelled with the energy contribution

$$\mathcal{E}_{\mathrm{DM}}[\boldsymbol{m}] = \int_\Omega \boldsymbol{D} : (\boldsymbol{\nabla m} \times \boldsymbol{m}) = \sum_{j=1}^{3} \int_\Omega \boldsymbol{d}_j \cdot (\partial_j \boldsymbol{m} \times \boldsymbol{m}), \tag{2.15}$$

where $\boldsymbol{D} \in \mathbb{R}^{3\times 3}$ is the spiralization tensor with columns $\boldsymbol{d}_j \in \mathbb{R}^3, j = 1, 2, 3$. DMI is typically characterized by a single constant D, and two typical forms of the DMI contribution are:

1. Bulk DMI has the form
$$\mathcal{E}_{\mathrm{DM}}[\boldsymbol{m}] = D \int_\Omega \boldsymbol{m} \cdot (\nabla \times \boldsymbol{m}).$$
2. If the body is a thin film in the xy plane, then interfacial DMI takes the form
$$\mathcal{E}_{\mathrm{DM}}[\boldsymbol{m}] = D \int_\Omega \boldsymbol{m} \nabla m_z - m_z \nabla \cdot \boldsymbol{m}.$$

DMI is a necessary ingredient in the stability of magnetic skyrmions. An example of a magnetic skyrmion is shown in Figure 2.3. Skyrmions are topologically protected and stable vortex configurations of the magnetization, and these conserve a topological charge

$$n = \frac{1}{4\pi} \int_\Omega \boldsymbol{m} \cdot \left(\frac{\partial \boldsymbol{m}}{\partial x} \times \frac{\partial \boldsymbol{m}}{\partial y} \right) \mathrm{d}x\mathrm{d}y,$$

where this integral is understood in a two-dimensional sense. For skyrmions, we have $n = 1$, which will appear in Chapter 7. There are other types of skyrmion such as an antiskyrmion, which has topological charge $n = -1$.

2.3.5 Zeeman energy

To model the interaction of the magnet with an external field, phenomenologically we take the energy

$$\mathcal{E}_{\text{ext}}[\boldsymbol{m}] = -\mu_0 M_{\text{s}} \int_\Omega \boldsymbol{H}_{\text{ext}} \cdot \boldsymbol{m}. \tag{2.16}$$

This encourages the magnetization to point in the same direction as the external field. This is the most easily controlled element of micromagnetics.

2.3.6 Magnetoelastic energy

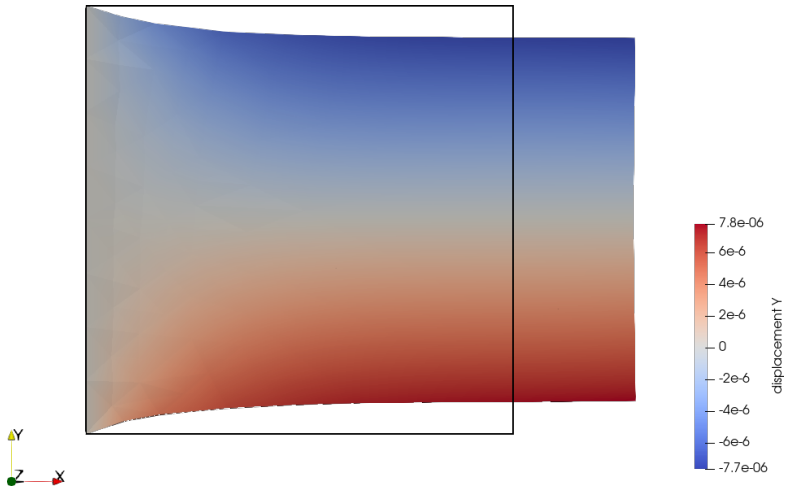

Figure 2.4: Illustration of isotropic, isochoric magnetostriction of a cube shaped ferromagnetic material. The ferromagnetic unit cube is initially uniformly magnetized along the x-direction in the undeformed state the edges of which are shown by the black square. The final state shows the body elongated in the x-direction, and contracted in the y and z directions. The colour indicates the strength of the displacement in the y coordinate. The mesh displacement has been scaled by a factor of 10^4.

Ferromagnetic bodies, like any other material, are sensitive to mechanical stresses, body forces (typically gravity), and deformation. If the magnetization changes, this results in distortion of the underlying crystal lattice, and similarly if a strain is induced in the lattice the magnetization changes [CG05, Section 14.1]. Magnetostriction was first discovered by J. Joule in 1842 (see, for example, [Lee55, Section 1.2], [Jil16, Section 5.3] or [CS13, Ch.6]), although C.G. Page had observed sounds produced by magnetostriction in 1837 [Kac14, Section 2]. Applications of magnetostriction date back to at least 1861, with telephonic receivers [DDCF16]. Other early uses include hydrophones, torque meters, and scanning sonar [DDCF16], such as those based upon nickel alloys that were built in World War 2 [CS13, TdL93], or delay lines built in the 1960s [TdL93].

For a detailed overview of the history of magnetostriction, from the 1600s onwards, see [Kac14], or for a lighter overview see [Ens09, Section 5.1]. The rigorous mathematical formulation of magnetoelastic materials was attempted in the book [Bro66], and a general overview of magnetostriction is available in [TdL93]. We utilize the "small deformation" regime [Bro66, Section 9], which is completely

Material	Magnetostriction ($\Delta\ell/\ell \cdot 10^6$)
Nickel	-40
Iron	-5
Iron 60%/ Nickel	-34
Terfenol-D	+1300
$SmFe_2$	-1560
Permendur (Fe 49%/Co 49%/V 2%)	+45

Table 2.1: Examples of magnetostriction constants, taken from [Ens09, Table 5.1].

justified for many materials as the associated strains are tiny, on the order of 10^{-6}. All ferromagnetic materials exhibit magnetostriction, but for most this effect is very small, so the small-strain regime covers many cases. For example, early transducers based on magnetostriction used nickel, nickel-iron alloys, or iron-cobalt-vanadium alloys [Ens09], which have relatively small magnetostriction as seen in Table 2.1. Some materials fall outside of the small-strain regime. For example, in the 1960s so-called "giant magnetostriction" was discovered in $YbFe_2$ [Ens09], Terbium and Dysprosium, but these suffered from restrictive temperature requirements [CS13, Ch.6]. In the 1970s, Terfenol-D was developed by the Naval Ordnance Laboratories (NOL)[3], which is a giant magnetostrictive material at room temperatures [CS13, Ch.6] becoming commercially available in the 1980s [DDCF16]. Most commercially available magnetostrictive actuators contain Terfenol-D [CS13, p.626]. More recently, magnetic shape-memory alloys (MSMAs), an example of a smart material with a shape-memory effect driven magnetically have been discovered, which can yield 10% strain (such as in Ni−Mn−Ga) [CS13, p.643]. Magnetostriction of other materials is described in [TdL93, Ch.4], including but not limited to FiM, AFM, and rare earth metals.

The magnetoelastic energy arises from the interaction between the magnetization and strains (length changes) within the crystal lattice [Bro78a, Section 8.1]. Suppose that the magnetization is not aligned with the easy axis, and that there is a strong external field preventing the magnetization from rotating into the easy axis. Then it is energetically beneficial to locally adjust the easy axis instead, and this is only possible by deforming the crystal lattice. Therefore, the magnetoelastic effect is closely related to the anisotropy introduced in Section 2.3.2, as the deformation of the crystal lattice is included during the anisotropy constant measurements (See [Kit49, Section 2.3], [Aha07, Section 5.1.3] or [MJ12, Section 6.1.3]). The magnetostrictive effect on the anisotropy constants is generally small [Bro63, p.125].

When working within the small-strain regime, this is composed of one primary term, but we consider two additional terms. For higher-order expansions of the

[3]Referred to as the Naval Research Laboratory (NRL) in [DDCF16].

magnetoelastic energy see [TdL93, Ch.2].

2.3.6.1 Nonmagnetic elastic energy

To clarify the upcoming magnetoelastic coupling, we first consider a material that is not ferromagnetic. Examples of references on standard elasticity are [AF05, Spe04, KR19, Sad14], or [MJ12, Section 6.1.2] for micromagnetically oriented essentials. As we work within the small-strain regime, we will avoid all discussion of reference frames. The deformation of the mesh from the initial configuration is measured by the displacement $\boldsymbol{U} : \Omega \to \mathbb{R}^3$, measured in m. Generally we impose a clamping condition on some portion of the boundary Γ_D, so that $\boldsymbol{U} = \boldsymbol{0}$, and apply some external traction (surface force density) $\boldsymbol{G} : \Gamma_N \to \mathbb{R}^3$ that is possibly zero, with units $\mathrm{N\,m^{-2}}$, and also consider a general body force density, typically gravity, $\boldsymbol{F}$ with units $\mathrm{N\,m^{-3}}$. We now immediately move to a nondimensionalised form with $\boldsymbol{u}$ measuring the dimensionless displacement, $\boldsymbol{f}$ the body force density, and $\boldsymbol{g}$ the surface force density. We remind the reader that the magnetization $\boldsymbol{m}$ is already dimensionless. For details, see Appendix C.

The (symmetric) strain tensor $\boldsymbol{\varepsilon}(\boldsymbol{u}) \in \mathbb{R}^{3\times3}$, measuring "stretching" within the body, is given by

$$\boldsymbol{\varepsilon}(\boldsymbol{u}) = \frac{1}{2}\left(\boldsymbol{\nabla u} + \boldsymbol{\nabla u}^\top\right), \tag{2.17}$$

and the (symmetric) stress tensor $\boldsymbol{\sigma}(\boldsymbol{u}) \in \mathbb{R}^{3\times3}$, describing internal forces, is related to the elastic strain through Hooke's law [KR19, Section 5.1]

$$\boldsymbol{\sigma} = \mathbb{C}\boldsymbol{\varepsilon}_{\mathrm{el}}(\boldsymbol{u}), \tag{2.18}$$

where the elastic tensor $\mathbb{C} \in \mathbb{R}^{3^4}$ is a positive definite fourth order tensor, with 81 entries of which 21 are independent due to major and minor symmetries (see Appendix B). The most general isotropic fourth order tensor is spanned by $\{\delta_{ij}\delta_{k\ell}, \delta_{ik}\delta_{j\ell}, \delta_{i\ell}\delta_{jk}\}$ (see for example [KF75]) and noting that the strain is symmetric yields

$$\mathbb{C}_{ijk\ell} = \lambda\delta_{ij}\delta_{k\ell} + 2\mu\delta_{ik}\delta_{j\ell}, \tag{2.19}$$

for Lamé parameters λ, μ (with $\mu > 0$) when the elastic tensor is assumed to be isotropic. For standard elasticity, we have $\boldsymbol{\varepsilon} \equiv \boldsymbol{\varepsilon}_{\mathrm{el}}$.

Equilibrium states correspond to minimizers of the energy

$$\mathcal{E}_{\mathrm{el}}[\boldsymbol{u}] = \frac{1}{2}\int_\Omega \boldsymbol{\varepsilon}_{\mathrm{el}}(\boldsymbol{u}) : \mathbb{C}\boldsymbol{\varepsilon}_{\mathrm{el}}(\boldsymbol{u}) - \int_\Omega \boldsymbol{f}\cdot\boldsymbol{u} - \int_{\Gamma_N} \boldsymbol{g}\cdot\boldsymbol{u}. \tag{2.20}$$

If the system is out of equilibrium, the time evolution is governed by the conservation of linear momentum equation [AF05, Section 4.3]

$$\partial_{tt}\boldsymbol{u} = \boldsymbol{\nabla}\cdot\boldsymbol{\sigma}(\boldsymbol{u}) + \boldsymbol{f} = -\frac{\delta\mathcal{E}_{\mathrm{el}}[\boldsymbol{u}]}{\delta\boldsymbol{u}} \tag{2.21}$$

subject to the boundary conditions $\boldsymbol{u} = \boldsymbol{0}$ on Γ_D and $\boldsymbol{\sigma n} = \boldsymbol{g}$ on Γ_N, and initial conditions $\boldsymbol{u}(0) = \boldsymbol{u}^0$, $\dot{\boldsymbol{u}}(0) = \dot{\boldsymbol{u}}^0$. Minimizers of the energy (2.20) can be

characterized by (2.21) with $\partial_{tt}\boldsymbol{u} = \mathbf{0}$. Multiplying the conservation of momentum law by $\partial_t \boldsymbol{u}$ leads to a conservation of energy law

$$\frac{\mathrm{d}}{\mathrm{d}t}\left(\frac{1}{2}|\partial_t \boldsymbol{u}|^2 + \mathcal{E}_{\mathrm{el}}(\boldsymbol{u})\right) = 0 \tag{2.22}$$

yielding that the total energy, the sum of the potential and kinetic energy, is constant.

2.3.6.2 Magnetoelastic energy

Following [Vis85] we decompose the total strain $\boldsymbol{\varepsilon}$ into a sum of the elastic strain $\boldsymbol{\varepsilon}_{\mathrm{el}}$ and magnetostrain $\boldsymbol{\varepsilon}_{\mathrm{m}}$, that is

$$\boldsymbol{\varepsilon}_{\mathrm{el}}(\boldsymbol{u}, \boldsymbol{m}) = \boldsymbol{\varepsilon}(\boldsymbol{u}) - \boldsymbol{\varepsilon}_{\mathrm{m}}(\boldsymbol{m}). \tag{2.23}$$

The magnetoelastic energy is then given by

$$\mathcal{E}_{\mathrm{el}}[\boldsymbol{u}, \boldsymbol{m}] = \frac{1}{2}\int_\Omega [\boldsymbol{\varepsilon}(\boldsymbol{u}) - \boldsymbol{\varepsilon}_{\mathrm{m}}(\boldsymbol{m})] : \{\mathbb{C}[\boldsymbol{\varepsilon}(\boldsymbol{u}) - \boldsymbol{\varepsilon}_{\mathrm{m}}(\boldsymbol{m})]\} - \int_\Omega \boldsymbol{f}\cdot\boldsymbol{u} - \int_{\Gamma_N} \boldsymbol{g}\cdot\boldsymbol{u}. \tag{2.24}$$

If $\boldsymbol{f} \equiv \boldsymbol{g} \equiv \mathbf{0}$, then the elastic energy is minimized by having $\boldsymbol{\varepsilon}(\boldsymbol{u}) = \boldsymbol{\varepsilon}_{\mathrm{m}}(\boldsymbol{m})$ everywhere within the material (ignoring boundary conditions). The magnetostrain has several forms in the literature, which are all covered by the minorly symmetric (see Appendix B) magnetostriction tensor $\mathbb{Z} \in \mathbb{R}^{3^4}$ [FCV19], yielding

$$\boldsymbol{\varepsilon}_{\mathrm{m}}(\boldsymbol{m}) = \mathbb{Z}(\boldsymbol{m} \otimes \boldsymbol{m}). \tag{2.25}$$

A less general but more common form is

$$\boldsymbol{\varepsilon}_{\mathrm{m}}(\boldsymbol{m}) = \boldsymbol{\lambda}^*(\boldsymbol{m} \otimes \boldsymbol{m}) = \boldsymbol{\lambda}\left(\boldsymbol{m} \otimes \boldsymbol{m} - \frac{1}{3}\mathbf{I}\right), \tag{2.26}$$

for some fully symmetric fourth order tensor $\boldsymbol{\lambda}^*$, $\boldsymbol{\lambda}$ [Vis85, BPPR14, PRS16]. Bearing in mind that $m_1^2 + m_2^2 + m_3^2 = 1$, we see that the two expressions in (2.26) are equivalent. Generally the magnetostrain is assumed to be isochoric [HS98, Section 3.2.6] (i.e. it has zero trace), meaning the magnetostrain does not affect volume. Importantly, $\mathbb{Z}$ covers the common cubic case, considered e.g. in [JW98, SLW04, MMHH$^+$14, RBJ21b, RBJ21a] and given by

$$\boldsymbol{\varepsilon}_{\mathrm{m}}(\boldsymbol{m}) = \frac{3}{2}\left\{\lambda_{100}\left(\boldsymbol{m} \otimes \boldsymbol{m} - \frac{1}{3}\mathbf{I}\right) + (\lambda_{111} - \lambda_{100})\sum_{\substack{i,j=1 \\ i\neq j}}^{3} (\boldsymbol{m}\cdot\boldsymbol{e}_i^{\mathrm{c}})(\boldsymbol{m}\cdot\boldsymbol{e}_j^{\mathrm{c}})(\boldsymbol{e}_i^{\mathrm{c}} \otimes \boldsymbol{e}_j^{\mathrm{c}})\right\},$$

where $\mathbf{I} \in \mathbb{R}^{3\times 3}$ denotes the 3-by-3 identity matrix, $\lambda_{100}, \lambda_{111} \in \mathbb{R}$ are material constants, and $\{\boldsymbol{e}_1^{\mathrm{c}}, \boldsymbol{e}_2^{\mathrm{c}}, \boldsymbol{e}_3^{\mathrm{c}}\}$ denotes an orthonormal set yielding the crystal basis. When $\lambda_{100} = \lambda_{111}$, this reduces to the isotropic case considered in [BHB$^+$14, PWH$^+$15, DW23a, TdL93], and we utilize the magnetostriction constant λ_{100}, writing

$$\boldsymbol{\varepsilon}_{\mathrm{m}}(\boldsymbol{m}) = \frac{3}{2}\lambda_{100}\left(\boldsymbol{m} \otimes \boldsymbol{m} - \frac{1}{3}\mathbf{I}\right).$$

The tensors $\boldsymbol{\lambda}^*, \boldsymbol{\lambda}$ are also sometimes assumed to be positive definite [Vis85, BPPR14, PRS16, Baň08, Baň05, BS05] or non-negative [CEF11]. This is overly restrictive physically as ferromagnetic materials such as nickel have $\lambda_{100} \approx -34 \cdot 10^{-6}$ (see [Lee55, p.197]). Positive definiteness is especially broken in the case of $SmFe_2$, with a negative giant magnetostriction of $-1560 \cdot 10^{-6}$ [CS13, Table 6.1], and in iron the magnetostriction changes from positive to negative as the external field strength is increased, called Villari reversal [DDCF16]. Despite this, we will always assume that the magnetostriction tensor is constant for simplicity. The restriction is also mathematically unnecessary; the elastic tensor $\mathbb{C}$ must be assumed to be positive definite to provide ellipticity. The magnetostriction tensor $\mathbb{Z}$ however plays no such role, and hence we do not impose positive definiteness upon it. When $\lambda_{100} > 0$ ($\lambda_{100} < 0$) the body elongates (contracts) in the direction of $\boldsymbol{m}$ and contracts (elongates) in the plane perpendicular to $\boldsymbol{m}$ [CS13, Ch.6].

2.3.7 Statics

For static micromagnetics, an energy for the system is prescribed. These will usually involve at least the exchange term (Section 2.3.1) and physically realistic simulations will also include anisotropy (Section 2.3.2) and magnetostatics (Section 2.3.3). Physical micromagnetic states correspond to minimizers of the total energy $\mathcal{E}[\boldsymbol{m}]$, i.e. those states $\boldsymbol{m}$ solving

$$\min_{|\boldsymbol{m}|=1} \mathcal{E}[\boldsymbol{m}], \tag{2.27}$$

with a necessary condition given by Brown's equations

$$-\boldsymbol{m} \times \boldsymbol{h}_{\text{eff}}[\boldsymbol{m}] = \boldsymbol{0}, \tag{2.28a}$$

$$\partial_n \boldsymbol{m} = \boldsymbol{0}. \tag{2.28b}$$

The "effective field" $\boldsymbol{h}_{\text{eff}}[\boldsymbol{m}]$ is given by the negative Gateaux derivative of the energy functional:

$$\boldsymbol{h}_{\text{eff}}[\boldsymbol{m}] = -\frac{\delta \mathcal{E}[\boldsymbol{m}]}{\delta \boldsymbol{m}} \tag{2.29}$$

and is interpreted as the local magnetic field affecting the magnetization. The condition (2.28a) means that the torque applied to the magnetization by the effective field is zero throughout the magnetic body. Observe that the component of the effective field that is parallel to the magnetization is irrelevant and does not participate in the equilibrium condition, which comes from the unit length constraint $|\boldsymbol{m}| = 1$. If there are multiple magnetization fields, such as in AFM or FiM materials, then we require that (2.28a) and (2.28b) hold for each magnetization field, where the effective field is defined per magnetization, i.e.

$$\boldsymbol{h}_{\text{eff},\ell}[\boldsymbol{m}_1, \boldsymbol{m}_2] = -\frac{\delta \mathcal{E}[\boldsymbol{m}_1, \boldsymbol{m}_2]}{\delta \boldsymbol{m}_\ell} \tag{2.30}$$

for $\ell = 1, 2$.

2.3.8 Dynamics

Dynamical micromagnetics is governed by the phenomenological Landau–Lifshitz–Gilbert (LLG) equation [Gil04]

$$\partial_t \boldsymbol{m} = -\boldsymbol{m} \times \boldsymbol{h}_{\text{eff}}[\boldsymbol{m}] + \alpha \boldsymbol{m} \times \partial_t \boldsymbol{m}, \tag{2.31a}$$

$$\boldsymbol{m}(0) = \boldsymbol{m}^0, \tag{2.31b}$$

$$\partial_{\boldsymbol{n}} \boldsymbol{m} = \boldsymbol{0}, \tag{2.31c}$$

where the initial condition satisfies $|\boldsymbol{m}^0| = 1$, and the boundary condition is supplemented from the stationary problem 2.28b. On the right-hand side of (2.31a), the first term models *precession* of the magnetization around the effective field (see Figure 2.5a), whilst the second term models energy loss (see Figure 2.5b), where the constant $\alpha \geq 0$ is the Gilbert damping parameter. If $\alpha = 0$, then the LLG equation is conservative, but otherwise $\alpha > 0$ models the fact that the dynamics of magnetic systems leads to stationary states. We show the dynamics of one component of a fictional[4] magnetization in Figure 2.5. The static case (2.28a) is clearly recovered upon setting $\partial_t \boldsymbol{m} = \boldsymbol{0}$. Furthermore, we see that the constraint $|\boldsymbol{m}| = 1$ is maintained by the LLG equation, as

$$\frac{\mathrm{d}}{\mathrm{d}t}|\boldsymbol{m}|^2 = \boldsymbol{m} \cdot \partial_t \boldsymbol{m} = 0. \tag{2.32}$$

The LLG equation is non-linear, being a sum of products of $\boldsymbol{m}$ and its derivatives, and non-convex due to the unit length constraint $|\boldsymbol{m}| = 1$. This makes it very difficult to work with numerically, and special attention must be paid to designing schemes that preserve this constraint. Taking the cross product of $\boldsymbol{m}$ with (2.31a) yields

$$\boldsymbol{m} \times \partial_t \boldsymbol{m} = -\boldsymbol{m} \times (\boldsymbol{m} \times \boldsymbol{h}_{\text{eff}}[\boldsymbol{m}]) + \alpha \boldsymbol{m} \times (\boldsymbol{m} \times \partial_t \boldsymbol{m})$$

and through the vector identity $\boldsymbol{a} \times (\boldsymbol{b} \times \boldsymbol{c}) = (\boldsymbol{a} \cdot \boldsymbol{c})\boldsymbol{b} - (\boldsymbol{a} \cdot \boldsymbol{b})\boldsymbol{c}$ for $\boldsymbol{a}, \boldsymbol{b}, \boldsymbol{c} \in \mathbb{R}^3$ and the orthogonality (2.32) we have

$$\boldsymbol{m} \times \partial_t \boldsymbol{m} = -(\boldsymbol{m} \cdot \boldsymbol{h}_{\text{eff}}[\boldsymbol{m}])\boldsymbol{m} + \boldsymbol{h}_{\text{eff}}[\boldsymbol{m}] - \alpha \partial_t \boldsymbol{m}. \tag{2.33}$$

If we take the scalar product of $\partial_t \boldsymbol{m}$ and (2.33) we have via (2.32) that

$$\boldsymbol{h}_{\text{eff}}[\boldsymbol{m}] \cdot \partial_t \boldsymbol{m} = -\alpha |\partial_t \boldsymbol{m}|^2. \tag{2.34}$$

The LLG equation, in the absence of changing external fields, satisfies a dissipative energy law. Integrating (2.34) in space yields

$$\frac{\mathrm{d}}{\mathrm{d}t}(\mathcal{E}[\boldsymbol{m}]) = -\alpha \int_\Omega |\partial_t \boldsymbol{m}|^2 \leq 0, \tag{2.35}$$

which is known as a Lyapunov structure. Thus, the LLG equation can also be used as a method for minimizing energy in the static case, although this is not ideal, due to the precession term, which restricts the magnetization from moving in the most energy decreasing direction. LLG minimization schemes can easily be changed into a minimization scheme by setting the left-hand side of (2.33) to the zero vector, that is setting $\boldsymbol{m} \times \partial_t \boldsymbol{m} = \boldsymbol{0}$.

[4] In the sense that the graph is not a simulation, nor an exact solution to the LLG equation, merely a useful representation of the behaviour we wish to describe.

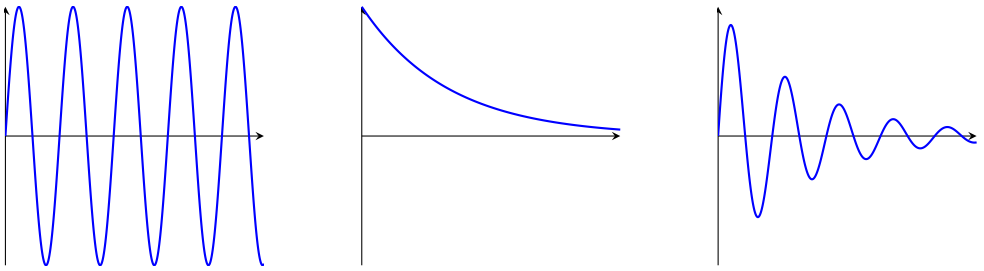

(a) Precession. (b) Damping. (c) Damped precession.

Figure 2.5: LLG dynamics. Precession, damping, and damped precession for one component of the magnetization.

2.3.8.1 Inertial dynamics

The LLG equation is not capable of describing the motion of the magnetization when the timescales are extremely small, e.g. at subpicosecond timescales. In this case, we require the inertial LLG (iLLG) equation

$$\partial_t \boldsymbol{m} = -\boldsymbol{m} \times \boldsymbol{h}_{\text{eff}}[\boldsymbol{m}] + \alpha \boldsymbol{m} \times \partial_t \boldsymbol{m} + \tau \boldsymbol{m} \times \partial_{tt} \boldsymbol{m} \tag{2.36a}$$

$$\partial_{\boldsymbol{n}} \boldsymbol{m} = \boldsymbol{0}, \tag{2.36b}$$

$$\boldsymbol{m}(0) = \boldsymbol{m}^0, \tag{2.36c}$$

$$\partial_t \boldsymbol{m}(0) = \boldsymbol{v}^0. \tag{2.36d}$$

The numerical approximation of this is the subject of Chapter 8. In (2.36a) we include a third term including the second time derivative, but the magnetization clearly still satisfies the unit length constraint $|\boldsymbol{m}| = 1$. We have an additional initial condition (2.36d) that satisfies the compatibility condition $\boldsymbol{m}^0 \cdot \boldsymbol{v}^0 = 0$. The parameter $\tau > 0$ denotes an angular momentum relaxation time measured in seconds, and if $\tau = 0$ we retrieve (2.31a) if the initial conditions satisfy

$$\boldsymbol{v}^0 = -\boldsymbol{m}^0 \times \boldsymbol{h}_{\text{eff}}[\boldsymbol{m}^0] + \alpha \boldsymbol{m}^0 \times \boldsymbol{v}^0.$$

The iLLG equation also satisfies an energy law,

$$\frac{\mathrm{d}}{\mathrm{d}t}\left(\mathcal{E}[\boldsymbol{m}] + \frac{\tau}{2}\int_\Omega |\partial_t \boldsymbol{m}|^2\right) = -\alpha \int_\Omega |\partial_t \boldsymbol{m}|^2 \leq 0, \tag{2.37}$$

where the term $\mathcal{E}[\boldsymbol{m}] + \int_\Omega \tau |\partial_t \boldsymbol{m}|^2/2$ is understood as a total energy, $\mathcal{E}[\boldsymbol{m}]$ denotes a potential energy, and $\int_\Omega \tau |\partial_t \boldsymbol{m}|^2/2$ denotes a type of "kinetic energy". The most notable difference between the standard LLG dynamics and the iLLG dynamics is nutation. Nutation is a small amplitude and high frequency oscillation imposed upon the larger LLG oscillations. These oscillations only remain for timescales on the order of τ, with long term behaviour being that of the LLG equation's damped precession. We provide a suggestive diagram in Figure 2.6 for one component of the magnetization for a fictional iLLG system.

2.3.8.2 Antiferromagnetic dynamics

When we consider antiferromagnetic (AFM) and ferrimagnetic (FiM) materials (see Chapter 7), we have two sublattices to consider. Mathematically, we then have

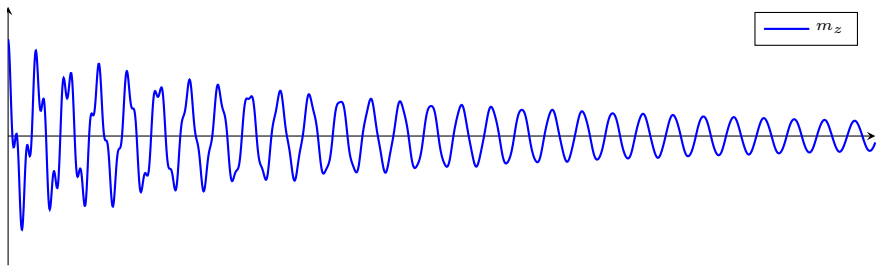

Figure 2.6: Nutation imposed upon damped precessive dynamics. The nutation dynamics decay after a short period of time, leaving just the damped precession.

two magnetization vector fields $\boldsymbol{m}_1, \boldsymbol{m}_2$ satisfying $|\boldsymbol{m}_1| = |\boldsymbol{m}_2| = 1$, corresponding to each sublattice, and to each of these fields we have an LLG equation that is coupled through the effective field, i.e.

$$\partial_t \boldsymbol{m}_1 = -\boldsymbol{m}_1 \times \boldsymbol{h}_{\text{eff},1}[\boldsymbol{m}_1, \boldsymbol{m}_2] + \alpha_1 \boldsymbol{m}_1 \times \partial_t \boldsymbol{m}_1, \tag{2.38a}$$
$$\partial_t \boldsymbol{m}_2 = -\boldsymbol{m}_2 \times \boldsymbol{h}_{\text{eff},2}[\boldsymbol{m}_1, \boldsymbol{m}_2] + \alpha_2 \boldsymbol{m}_2 \times \partial_t \boldsymbol{m}_2, \tag{2.38b}$$
$$\partial_{\boldsymbol{n}} \boldsymbol{m}_1 = \partial_{\boldsymbol{n}} \boldsymbol{m}_2 = \boldsymbol{0}, \tag{2.38c}$$
$$\boldsymbol{m}_1(0) = \boldsymbol{m}_1^0, \tag{2.38d}$$
$$\boldsymbol{m}_2(0) = \boldsymbol{m}_2^0. \tag{2.38e}$$

The system (2.38) has two Gilbert damping parameters $\alpha_1, \alpha_2 > 0$ associated with each lattice, but these are typically identical for AFM systems. AFM and FiM systems satisfy a similar energy law to that of (2.35),

$$\frac{\mathrm{d}}{\mathrm{d}t}(\mathcal{E}[\boldsymbol{m}_1, \boldsymbol{m}_2]) = -\alpha_1 \int_\Omega |\partial_t \boldsymbol{m}_1|^2 - \alpha_2 \int_\Omega |\partial_t \boldsymbol{m}_2|^2 \leq 0, \tag{2.39}$$

where both magnetization fields contribute to the energy decay. A suggestive diagram for a fictional AFM system is shown in Figure 2.7 for one component of each magnetization.

The static configuration corresponds to setting $\partial_t \boldsymbol{m}_1 = \partial_t \boldsymbol{m}_2 = \boldsymbol{0}$ in (2.38), yielding Brown's equations

$$-\boldsymbol{m}_1 \times \boldsymbol{h}_{\text{eff},1}[\boldsymbol{m}_1, \boldsymbol{m}_2] = \boldsymbol{0}$$
$$-\boldsymbol{m}_2 \times \boldsymbol{h}_{\text{eff},2}[\boldsymbol{m}_1, \boldsymbol{m}_2] = \boldsymbol{0}.$$

2.4 Magnetostrictive dynamics

For a magnetostrictive material, the governing equations are given by coupling the LLG equation and the conservation of momentum equation,

$$\partial_t \boldsymbol{m} = -\boldsymbol{m} \times \boldsymbol{h}_{\text{eff}}[\boldsymbol{u}, \boldsymbol{m}] + \alpha\, \boldsymbol{m} \times \partial_t \boldsymbol{m}, \tag{2.40}$$
$$\partial_{tt} \boldsymbol{u} = \boldsymbol{\nabla} \cdot (\mathbb{C}[\boldsymbol{\varepsilon}(\boldsymbol{u}) - \boldsymbol{\varepsilon}_{\text{m}}(\boldsymbol{m})]) + \boldsymbol{f}. \tag{2.41}$$

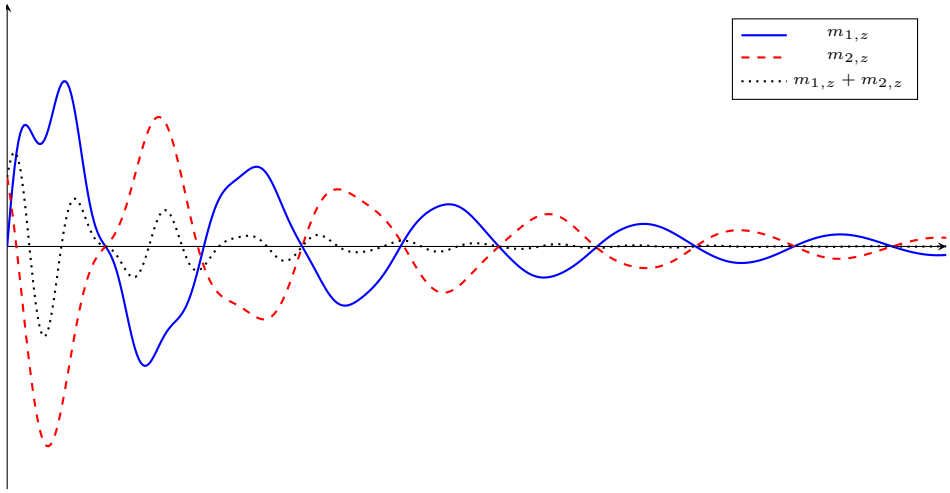

Figure 2.7: Antiferromagnetic dynamics. The two magnetization fields undergo damped precession and align away from the other field simultaneously. The total magnetization approaches zero over time.

To use these equations, the effective field $\boldsymbol{h}_{\text{eff}}[\boldsymbol{u}, \boldsymbol{m}]$ corresponding to the magnetoelastic energy $\mathcal{E}_{\text{el}}[\boldsymbol{u}, \boldsymbol{m}]$ must be calculated. We define the stress as $\boldsymbol{\sigma}(\boldsymbol{u}, \boldsymbol{m}) = \mathbb{C}[\boldsymbol{\varepsilon}(\boldsymbol{u}) - \boldsymbol{\varepsilon}_{\text{m}}(\boldsymbol{m})]$, and derive a useful lemma for manipulation of the various tensors involved.

Lemma 2.4.1. *Let $\mathbb{Z}$ be a minorly symmetric 4-tensor, let $\boldsymbol{\sigma}$ be a symmetric 2-tensor, and let $\boldsymbol{m}, \boldsymbol{w} \in \mathbb{R}^3$. We have*

$$(\mathbb{Z}^\top \boldsymbol{\sigma})\boldsymbol{w} \cdot \boldsymbol{m} = (\mathbb{Z}^\top \boldsymbol{\sigma})\boldsymbol{m} \cdot \boldsymbol{w} = \boldsymbol{\sigma} : \mathbb{Z}(\boldsymbol{m} \otimes \boldsymbol{w}). \tag{2.42}$$

Proof. We have by the minor symmetry of $\mathbb{Z}$ that (using Einstein summation notation)

$$\begin{aligned}
(\mathbb{Z}^\top \boldsymbol{\sigma})\boldsymbol{m} \cdot \boldsymbol{w} &= \mathbb{Z}^\top_{ijkl} \boldsymbol{\sigma}_{kl} m_j w_i && (2.43)\\
&= \mathbb{Z}^\top_{jikl} \boldsymbol{\sigma}_{kl} m_i w_j && (2.44)\\
&= \mathbb{Z}^\top_{ijkl} \boldsymbol{\sigma}_{kl} w_j m_i && (2.45)\\
&= (\mathbb{Z}^\top \boldsymbol{\sigma})\boldsymbol{w} \cdot \boldsymbol{m}. && (2.46)
\end{aligned}$$

Furthermore, we have

$$\begin{aligned}
(\mathbb{Z}^\top \boldsymbol{\sigma})\boldsymbol{m} \cdot \boldsymbol{w} &= \mathbb{Z}^\top_{ijkl} \boldsymbol{\sigma}_{kl} m_j w_i && (2.47)\\
&= \boldsymbol{\sigma}_{kl} \mathbb{Z}^\top_{ijkl} m_j w_i && (2.48)\\
&= \boldsymbol{\sigma}_{kl} \mathbb{Z}_{klij} m_j w_i && (2.49)\\
&= \boldsymbol{\sigma}_{kl} (\mathbb{Z}(\boldsymbol{m} \otimes \boldsymbol{w}))_{kl} && (2.50)\\
&= \boldsymbol{\sigma} : \mathbb{Z}(\boldsymbol{m} \otimes \boldsymbol{w}). && (2.51)
\end{aligned}$$

□

Remark 2.4.2. *The stress tensor $\boldsymbol{\sigma}$ is assumed to be symmetric in line with, what Brown [Bro78a, Chapter 8] calls, the Voigt approximation of magnetostriction.*

This is generally true in elasticity theory, but due to couplings of the form $\boldsymbol{m} \times \boldsymbol{h}$ that are present in ferromagnetic materials, this may not be the case.

We now derive the variational derivative of the magnetoelastic energy.

Lemma 2.4.3. *Let the magnetoelastic energy be given by*

$$\mathcal{E}[\boldsymbol{u}, \boldsymbol{m}] = \frac{1}{2} \int_\Omega \mathbb{C}[\boldsymbol{\varepsilon}(\boldsymbol{u}) - \boldsymbol{\varepsilon}_\mathrm{m}(\boldsymbol{m})] : [\boldsymbol{\varepsilon}(\boldsymbol{u}) - \boldsymbol{\varepsilon}_\mathrm{m}(\boldsymbol{m})].$$

Then the variational derivative of the magnetoelastic energy is

$$\frac{\delta \mathcal{E}[\boldsymbol{u}, \boldsymbol{m}]}{\delta \boldsymbol{m}} = -2\mathbb{Z}^\top \boldsymbol{\sigma} \boldsymbol{m}.$$

Proof. We prove this using the definition of the Fréchet derivative, that is, we search for a function $\delta\mathcal{E}[\boldsymbol{u}, \boldsymbol{m}]/\delta\boldsymbol{m}$ such that as $s \to 0$

$$\mathcal{E}[\boldsymbol{u}, \boldsymbol{m} + s\boldsymbol{w}] - \mathcal{E}[\boldsymbol{u}, \boldsymbol{m}] = s \int_\Omega \left(\frac{\delta \mathcal{E}[\boldsymbol{u}, \boldsymbol{m}]}{\delta \boldsymbol{m}} \right) \cdot \boldsymbol{w} \, \mathrm{d}x + O(s^2)$$

Let $s \in \mathbb{R}$. Now, for some $\boldsymbol{w}$ we have

$$\begin{aligned}
\boldsymbol{\varepsilon}_\mathrm{m}(\boldsymbol{m} + s\boldsymbol{w}) &= \mathbb{Z}\left((\boldsymbol{m} + s\boldsymbol{w}) \otimes (\boldsymbol{m} + s\boldsymbol{w})\right) && (2.52)\\
&= \mathbb{Z}\left(\boldsymbol{m} \otimes \boldsymbol{m} + s\boldsymbol{w} \otimes \boldsymbol{m} + \boldsymbol{m} \otimes s\boldsymbol{w} + s\boldsymbol{w} \otimes s\boldsymbol{w}\right) && (2.53)\\
&= \boldsymbol{\varepsilon}_\mathrm{m}(\boldsymbol{m}) + s\mathbb{Z}\left(\boldsymbol{w} \otimes \boldsymbol{m} + \boldsymbol{m} \otimes \boldsymbol{w}\right) + O(s^2). && (2.54)
\end{aligned}$$

Dropping terms of order s^2 or higher

$$\begin{aligned}
&\mathcal{E}[\boldsymbol{u}, \boldsymbol{m} + s\boldsymbol{w}] - \mathcal{E}(\boldsymbol{u}, \boldsymbol{m})\\
&\qquad = -\int_\Omega [\boldsymbol{\varepsilon}(\boldsymbol{u})] : (\mathbb{C}[\boldsymbol{\varepsilon}_\mathrm{m}(\boldsymbol{m} + s\boldsymbol{w})]) \, \mathrm{d}x\\
&\qquad + \frac{1}{2} \int_\Omega [\boldsymbol{\varepsilon}_\mathrm{m}(\boldsymbol{m} + s\boldsymbol{w})] : (\mathbb{C}[\boldsymbol{\varepsilon}_\mathrm{m}(\boldsymbol{m} + s\boldsymbol{w})]) \, \mathrm{d}x\\
&\qquad + \int_\Omega [\boldsymbol{\varepsilon}(\boldsymbol{u})] : (\mathbb{C}[\boldsymbol{\varepsilon}_\mathrm{m}(\boldsymbol{m})]) \, \mathrm{d}x\\
&\qquad - \frac{1}{2} \int_\Omega [\boldsymbol{\varepsilon}_\mathrm{m}(\boldsymbol{m})] : (\mathbb{C}[\boldsymbol{\varepsilon}_\mathrm{m}(\boldsymbol{m})]) \, \mathrm{d}x\\
&\qquad = -\int_\Omega [\boldsymbol{\varepsilon}(\boldsymbol{u})] : (\mathbb{C}[\boldsymbol{\varepsilon}_\mathrm{m}(\boldsymbol{m} + s\boldsymbol{w}) - \boldsymbol{\varepsilon}_\mathrm{m}(\boldsymbol{m})]) \, \mathrm{d}x\\
&\qquad + \frac{1}{2} \int_\Omega [\boldsymbol{\varepsilon}_\mathrm{m}(\boldsymbol{m} + s\boldsymbol{w})] : (\mathbb{C}[\boldsymbol{\varepsilon}_\mathrm{m}(\boldsymbol{m} + s\boldsymbol{w})]) \, \mathrm{d}x\\
&\qquad - \frac{1}{2} \int_\Omega [\boldsymbol{\varepsilon}_\mathrm{m}(\boldsymbol{m})] : (\mathbb{C}[\boldsymbol{\varepsilon}_\mathrm{m}(\boldsymbol{m})]) \, \mathrm{d}x\\
&\qquad = -\int_\Omega [\boldsymbol{\varepsilon}(\boldsymbol{u})] : (\mathbb{C}[s\mathbb{Z}\left(\boldsymbol{w} \otimes \boldsymbol{m} + \boldsymbol{m} \otimes \boldsymbol{w}\right)]) \, \mathrm{d}x\\
&\qquad + \frac{1}{2} \int_\Omega [\boldsymbol{\varepsilon}_\mathrm{m}(\boldsymbol{m} + s\boldsymbol{w})] : (\mathbb{C}[\boldsymbol{\varepsilon}_\mathrm{m}(\boldsymbol{m} + s\boldsymbol{w})]) \, \mathrm{d}x\\
&\qquad - \frac{1}{2} \int_\Omega [\boldsymbol{\varepsilon}_\mathrm{m}(\boldsymbol{m})] : (\mathbb{C}[\boldsymbol{\varepsilon}_\mathrm{m}(\boldsymbol{m})]) \, \mathrm{d}x.
\end{aligned}$$

Furthermore,

$$\begin{aligned}
&\frac{1}{2}\int_\Omega [\boldsymbol{\varepsilon}_{\mathrm{m}}(\boldsymbol{m}+s\boldsymbol{w})] : (\mathbb{C}[\boldsymbol{\varepsilon}_{\mathrm{m}}(\boldsymbol{m}+s\boldsymbol{w})])\,\mathrm{d}x \\
&= \frac{1}{2}\int_\Omega [\boldsymbol{\varepsilon}_{\mathrm{m}}(\boldsymbol{m})] : (\mathbb{C}[\boldsymbol{\varepsilon}_{\mathrm{m}}(\boldsymbol{m})])\,\mathrm{d}x + \int_\Omega [\boldsymbol{\varepsilon}_{\mathrm{m}}(\boldsymbol{m})] : (\mathbb{C}[s\mathbb{Z}\,(\boldsymbol{w}\otimes\boldsymbol{m}+\boldsymbol{m}\otimes\boldsymbol{w})])\,\mathrm{d}x.
\end{aligned}$$

Combining the above, we get with the symmetry of $\mathbb{C}$ that

$$\begin{aligned}
&\mathcal{E}[\boldsymbol{u},\boldsymbol{m}+s\boldsymbol{w}] - \mathcal{E}[\boldsymbol{u},\boldsymbol{m}] \\
&\qquad = -\int_\Omega [\boldsymbol{\varepsilon}(\boldsymbol{u})] : (\mathbb{C}[s\mathbb{Z}\,(\boldsymbol{w}\otimes\boldsymbol{m}+\boldsymbol{m}\otimes\boldsymbol{w})])\,\mathrm{d}x \\
&\qquad + \int_\Omega [\boldsymbol{\varepsilon}_{\mathrm{m}}(\boldsymbol{m})] : (\mathbb{C}[s\mathbb{Z}\,(\boldsymbol{w}\otimes\boldsymbol{m}+\boldsymbol{m}\otimes\boldsymbol{w})])\,\mathrm{d}x \\
&\qquad = -s\int_\Omega [\boldsymbol{\varepsilon}(\boldsymbol{u}) - \boldsymbol{\varepsilon}_{\mathrm{m}}(\boldsymbol{m})] : (\mathbb{C}[\mathbb{Z}\,(\boldsymbol{w}\otimes\boldsymbol{m}+\boldsymbol{m}\otimes\boldsymbol{w})])\,\mathrm{d}x \\
&\qquad = -s\int_\Omega [\mathbb{Z}\,(\boldsymbol{w}\otimes\boldsymbol{m}+\boldsymbol{m}\otimes\boldsymbol{w})] : (\mathbb{C}[\boldsymbol{\varepsilon}(\boldsymbol{u}) - \boldsymbol{\varepsilon}_{\mathrm{m}}(\boldsymbol{m})])\,\mathrm{d}x \\
&\qquad = -s\int_\Omega [\mathbb{Z}\,(\boldsymbol{w}\otimes\boldsymbol{m}+\boldsymbol{m}\otimes\boldsymbol{w})] : \boldsymbol{\sigma}\mathrm{d}x.
\end{aligned}$$

Now, we can flip the inside and then use the previous Lemma, yielding

$$\begin{aligned}
&\mathcal{E}[\boldsymbol{u},\boldsymbol{m}+s\boldsymbol{w}] - \mathcal{E}[\boldsymbol{u},\boldsymbol{m}] \\
&\qquad = -s\int_\Omega \boldsymbol{\sigma} : [\mathbb{Z}\,(\boldsymbol{w}\otimes\boldsymbol{m})]\mathrm{d}x - s\int_\Omega \boldsymbol{\sigma} : [\mathbb{Z}\,(\boldsymbol{m}\otimes\boldsymbol{w})]\mathrm{d}x \\
&\qquad = -s\int_\Omega (\mathbb{Z}^\top\boldsymbol{\sigma})\boldsymbol{w}\cdot\boldsymbol{m}\mathrm{d}x - s\int_\Omega (\mathbb{Z}^\top\boldsymbol{\sigma})\boldsymbol{m}\cdot\boldsymbol{w}\mathrm{d}x \\
&\qquad = s\int_\Omega (-2\mathbb{Z}^\top\boldsymbol{\sigma}\boldsymbol{m})\cdot\boldsymbol{w}\mathrm{d}x.
\end{aligned}$$

It follows that the variational derivative of the magnetoelastic contribution is $-2\mathbb{Z}^\top\boldsymbol{\sigma}\boldsymbol{m}$. □

We can then see that if the stress $\boldsymbol{\sigma}$ is zero, there are no effects from magnetostriction in either the LLG equation or the conservation of momentum equation, which in general occurs only when $\boldsymbol{\varepsilon}(\boldsymbol{u}) = \boldsymbol{\varepsilon}_{\mathrm{m}}(\boldsymbol{m})$.

The magnetostrictive system also satisfies an energy law for the total energy, where the total energy is the sum of the kinetic energy (only involving the displacement) and the potential energy from both magnetic and elastic sources,

$$\frac{\mathrm{d}}{\mathrm{d}t}\left(\mathcal{E}[\boldsymbol{u},\boldsymbol{m}] + \frac{1}{2}|\partial_t\boldsymbol{u}|^2\right) = -\alpha|\partial_t\boldsymbol{m}|^2 \leq 0 \tag{2.55}$$

with minima being characterized by

$$\frac{\delta\mathcal{E}[\boldsymbol{u},\boldsymbol{m}]}{\delta\boldsymbol{m}} = \boldsymbol{0}, \qquad \frac{\delta\mathcal{E}[\boldsymbol{u},\boldsymbol{m}]}{\delta\boldsymbol{u}} = \boldsymbol{0},$$

holding simultaneously.

Remark 2.4.4. *It is useful to compare the coupled system (with LLG and elasticity linked together) with the decoupled systems (where we consider only the LLG equation or elasticity in isolation) which we show in Figure 2.8. For the decoupled systems, the LLG equation does not have a concept of momentum. The first time that the effective field is zero everywhere, the dynamics in the system is completed. In the conservation of momentum equation there is no dissipation, and the dynamics continue indefinitely. When we couple the systems together however, the LLG equation inherits a momentum that is stored by the displacement, and the conservation of momentum equation inherits a dissipation mechanism. Therefore, the coupled system exhibits phenomena that are unavailable in the individual systems. Qualitatively, we imagine a quadratic valley with a ball on one side, a height H from the lowest point. The uncoupled LLG equation describes the ball rolling down the valley, slowing until it stops at the bottom without reaching the other side of the valley as seen in Figure 2.8a. The uncoupled conservation of momentum equation on the other hand describes a ball that rolls down one side, and rolls up the opposite side, reaching the same height as seen in Figure 2.8b. The coupled system describes a ball that rolls down, oscillates around the bottom of the valley decaying, and, eventually stopping as seen in Figure 2.8c.*

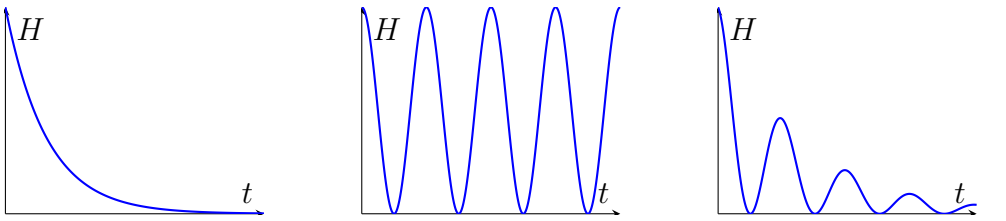

(a) LLG. (b) Elastic. (c) Magnetoelastic.

Figure 2.8: Different types of "ball rolling down a hill" dynamics for each type of system. The height H is plotted against the time t. The LLG system approaches the minima without ever approaching the starting point. The elastic system returns to the starting point every iteration. The magnetoelastic system attempts to return to the starting point, but energy loss prevents this.

2.5 Summary of models

To summarise which portions of the above physical background will appear in later portions of the this, we state them in Table 2.2. The exchange effect is the most important effect mathematically and, along with ferromagnetic materials, is present in all chapters. It should also be noted that the magnetostatic contribution is not considered any further within this thesis.

Background	Chapter				
	4	5	6	7	8
FM	✓	✓	✓	✓	✓
AFM/FiM				✓	
Exchange	✓	✓	✓	✓	✓
Anisotropy				✓	
Magnetostatics					
DMI				✓	
Zeeman		✓	✓	✓	✓
Magnetoelastics		✓	✓		
Statics	✓			✓	
LLG		✓	✓	✓	
iLLG					✓

Table 2.2: The subsections in Chapter 2 that are relevant in the later chapters are marked with a tick, and are left empty otherwise.

Chapter 3

Preliminaries

In this chapter, we introduce the notation and definitions required for stating the numerical schemes.

3.1 Functional analysis spaces

For denoting Lebesgue, Sobolev, and Bochner spaces we use standard notation (see e.g. [Bar15b]). Let $\Omega \subset \mathbb{R}^3$ be a bounded Lipschitz domain. The set $C^0(\overline{\Omega})$ denotes the set of continuous functions on $\overline{\Omega}$. For $p \in [1, \infty]$ we consider the Lebesgue space L^p

$$L^p(\Omega) = \{y : \Omega \to \mathbb{R} \text{ measureable: } \|y\|_{L^p(\Omega)} < \infty\},$$

where we define the norm as

$$\|y\|_{L^p(\Omega)} = \begin{cases} \left(\int_\Omega |y(\boldsymbol{x})|^p \, \mathrm{d}\boldsymbol{x} \right)^{1/p}, & \text{if } p \in [1, \infty), \\ \operatorname*{ess\,sup}_{\boldsymbol{x} \in \Omega} |y(\boldsymbol{x})|, & \text{if } p = \infty. \end{cases}$$

Further, for an integer $k \geq 0$ we have the Sobolev space

$$W^{k,p}(\Omega) = \{y \in L^p(\Omega) : D^{\boldsymbol{\alpha}} y \in L^p(\Omega) \text{ for all } |\boldsymbol{\alpha}| \leq k\}$$

with norm defined by

$$\|y\|_{W^{k,p}(\Omega)} = \begin{cases} \left(\sum_{0 \leq |\boldsymbol{\alpha}| \leq k} \|D^{\boldsymbol{\alpha}} y\|^p_{L^p(\Omega)} \right)^{1/p}, & \text{if } p \in [1, \infty), \\ \max_{0 \leq |\boldsymbol{\alpha}| \leq k} \|D^{\boldsymbol{\alpha}} y\|_{L^\infty(\Omega)}, & \text{if } p = \infty. \end{cases}$$

Setting $k = 0$ yields $W^{0,p}(\Omega) = L^p(\Omega)$. We note that these are all Banach spaces, and in the case $p = 2$ we also have the Hilbert spaces $L^2(\Omega) = W^{0,2}(\Omega), H^k(\Omega) = W^{k,2}$, with inner products

$$\langle y, v \rangle_\Omega = \int_\Omega y(\boldsymbol{x}) v(\boldsymbol{x}) \, \mathrm{d}\boldsymbol{x}, \qquad \langle y, v \rangle_{H^k(\Omega)} = \sum_{0 \leq |\boldsymbol{\alpha}| \leq k} \langle D^{\boldsymbol{\alpha}} y, D^{\boldsymbol{\alpha}} v \rangle_\Omega,$$

respectively. In the special case $k = 1, p = 2$, we have

$$\langle y, v \rangle_{H^1(\Omega)} = \langle y, v \rangle_\Omega + \langle \boldsymbol{\nabla} y, \boldsymbol{\nabla} v \rangle_\Omega \,.$$

For time-dependent functions defined on a time interval $(0, T)$ for some $T > 0$, we must consider mappings $y : (0, T) \to B$ for a Banach space B. For $p \in [1, \infty]$ we consider the Bochner space

$$L^p(0, T; B) = \{y : (0, T) \to B \text{ measurable: } \|y\|_{L^p(0,T;B)} < \infty\}$$

with norm

$$\|y\|_{L^p(0,T;B)} = \begin{cases} \left(\displaystyle\int_0^T \|y(t)\|_B^p \,\mathrm{d}t \right)^{1/p}, & \text{if } p \in [1, \infty), \\ \displaystyle\operatorname*{ess\,sup}_{t \in (0,T)} \|y(t)\|_B \,, & \text{if } p = \infty. \end{cases}$$

We also consider for $p \in [1, \infty]$ the space

$$W^{1,p}(0, T; B) = \{y \in L^p(0, T; B) : \partial_t y \in L^p(0, T; B)\}$$

with norm

$$\|y\|_{W^{1,p}(0,T;B)} = \begin{cases} \left(\|y\|_{L^p(0,T;B)}^p + \|\partial_t y\|_{L^p(0,T;B)}^p \right)^{1/p}, & \text{if } p \in [1, \infty), \\ \displaystyle\operatorname*{ess\,sup}_{t \in (0,T)} \left(\|y(t)\|_B + \|\partial_t y(t)\|_B \right), & \text{if } p = \infty. \end{cases}$$

We set $H^1(0, T; B) = W^{1,2}(0, T; B)$. For vector-valued and matrix-valued functions $\boldsymbol{y}, \boldsymbol{v} : \Omega \to \mathbb{R}^3$, $\boldsymbol{A}, \boldsymbol{B} : \Omega \to \mathbb{R}^{3\times3}$, the extensions of the above spaces are natural. Via an abuse of notation, we write $L^2(\Omega, \mathbb{R}^3)$ and $L^2(\Omega, \mathbb{R}^{3\times3})$ as $\boldsymbol{L}^2(\Omega)$ with inner products

$$\begin{aligned} \langle \boldsymbol{y}, \boldsymbol{v} \rangle_\Omega &= \int_\Omega \boldsymbol{y}(\boldsymbol{x}) \cdot \boldsymbol{v}(\boldsymbol{x}) \,\mathrm{d}\boldsymbol{x} \qquad \text{for all } \boldsymbol{y}, \boldsymbol{v} \in L^2(\Omega, \mathbb{R}^3), \\ \langle \boldsymbol{A}, \boldsymbol{B} \rangle_\Omega &= \int_\Omega \boldsymbol{A}(\boldsymbol{x}) : \boldsymbol{B}(\boldsymbol{x}) \,\mathrm{d}\boldsymbol{x} \qquad \text{for all } \boldsymbol{A}, \boldsymbol{B} \in L^2(\Omega, \mathbb{R}^{3\times3}), \end{aligned}$$

and $H^1(\Omega, \mathbb{R}^3)$ as $\boldsymbol{H}^1(\Omega)$. The abuse of notation is resolved by the dimension of the argument. We write

$$\langle y, v \rangle_\Omega := \langle y, v \rangle \,, \qquad \|y\|_{L^2(\Omega)} := \|y\| \,,$$

omitting the domain (any other inner product or norm will be denoted by the same notation, but supplemented with a suitable subscript). We will denote by $\langle \cdot, \cdot \rangle$ also the duality pairing between $\boldsymbol{H}^1(\Omega)$ and its dual, and note that it coincides with the inner product of $\boldsymbol{L}^2(\Omega)$ if the arguments are in $\boldsymbol{L}^2(\Omega)$.

3.2 Time discretization

For the time discretization, we consider a uniform partition $t_0 < t_1 < \cdots < t_N = T$ of $[0, T]$ into N uniform intervals with a constant time-step size $k = T/N$, that is, $t_i = ik$ for each $i = 0, \ldots, N$. Given a sequence $\{\phi^i\}_{0 \le i \le N}$ and $\dot{\phi}^0$ we define the discrete time derivatives

$$\mathrm{d}_t \phi^i := \begin{cases} \dot{\phi}^0, & \text{if } i = 0, \\ \dfrac{\phi^i - \phi^{i-1}}{k}, & \text{if } 1 \le i \le N, \end{cases} \tag{3.1}$$

$$\mathrm{d}_t^2 \phi^{i+1} := \frac{\mathrm{d}_t \phi^{i+1} - \mathrm{d}_t \phi^i}{k} = \begin{cases} \dfrac{\phi^1 - \phi^0 - k\dot{\phi}^0}{k^2}, & \text{if } i = 0, \\ \dfrac{\phi^{i+1} - 2\phi^i + \phi^{i-1}}{k^2}, & \text{if } 1 \le i \le N-1, \end{cases} \tag{3.2}$$

and consider the time reconstructions $\phi_k, \phi_k^-, \phi_k^+$ defined for all $0 \le i \le N-1$ and $t \in [t_i, t_{i+1})$ via

$$\phi_k(t) := \frac{t - t_i}{k}\phi^{i+1} + \frac{t_{i+1} - t}{k}\phi^i, \quad \phi_k^-(t) := \phi^i, \quad \phi_k^+(t) := \phi^{i+1}, \tag{3.3a}$$

$$\dot{\phi}_k(t) := \mathrm{d}_t \phi^i + (t - t_i)\mathrm{d}_t^2 \phi^{i+1}, \quad \dot{\phi}_k^-(t) := \mathrm{d}_t \phi^i, \quad \dot{\phi}_k^+(t) := \mathrm{d}_t \phi^{i+1}. \tag{3.3b}$$

We see that $\partial_t \phi_k(t) = \dot{\phi}_k^+(t) = \mathrm{d}_t \phi^{i+1}$ for all $i \in \mathbb{N}_0$ and $t \in [t_i, t_{i+1})$. When working with higher order time discretizations, we may sometimes need an approximation to a function at some point in the future. We can do this in a simple way using only known information, with the following extrapolations. We define the following extrapolations for a sequence of functions via

$$\widehat{\boldsymbol{\phi}}^i = \begin{cases} \boldsymbol{\phi}^0, \text{ if } i = 0 \\ \boldsymbol{\phi}^1, \text{ if } i = 1 \\ 2\boldsymbol{\phi}^{i-1} - \boldsymbol{\phi}^{i-2}, \text{ if } i \ge 2, \end{cases}$$

for the extrapolation to the next time-step and

$$\widehat{\boldsymbol{\phi}}^{i+1/2} = \begin{cases} \boldsymbol{\phi}^0, \text{ if } i = 0 \\ \frac{3}{2}\boldsymbol{\phi}^i - \frac{1}{2}\boldsymbol{\phi}^{i-1}, \text{ if } i \ge 1, \end{cases}$$

for the extrapolation to the midpoint of the current and next time-steps.

3.3 Spatial discretization

For the spatial discretization, we use first-order finite elements. Assuming the domain of interest Ω to be a polyhedral domain, consider a family $\{\mathcal{T}_h\}_{h>0}$ of shape-regular tetrahedral meshes of Ω, which are parameterized by the mesh size $h = \max_{K \in \mathcal{T}_h} \operatorname{diam}(K)$, where K is a tetrahedron. The set of nodes in $\mathcal{T}_h$ is denoted by $\mathcal{N}_h$. For any $K \in \mathcal{T}_h$, we let $\mathcal{P}^1(K)$ be the space of polynomials of

degree at most 1 on K. We then denote by $\mathcal{S}^1(\mathcal{T}_h)$ the space of piecewise affine and globally continuous functions from $\Omega \to \mathbb{R}$, that is,

$$\mathcal{S}^1(\mathcal{T}_h) = \{v_h \in C^0(\overline{\Omega}) : v_h|_K \in \mathcal{P}^1(K) \text{ for all } K \in \mathcal{T}_h\}.$$

It is known that $\mathcal{S}^1(\mathcal{T}_h)$ is a finite-dimensional subspace of $H^1(\Omega)$, satisfying $\dim \mathcal{S}^1(\mathcal{T}_h) = N = \#\mathcal{N}_h$. We let $\mathcal{I}_h : C^0(\overline{\Omega}) \to \mathcal{S}^1(\mathcal{T}_h)$ denote the nodal interpolation operator, where for all $v \in C^0(\overline{\Omega})$, $\mathcal{I}_h[v]$ is the unique element of $\mathcal{S}^1(\mathcal{T}_h)$ such that $\mathcal{I}_h[v](z) = v(z)$ for all $z \in \mathcal{N}_h$. If $\boldsymbol{v} \in \boldsymbol{C}^0(\overline{\Omega})$, then we apply the interpolation operator to each component, and use the same notation for the vector-valued interpolation operator $\mathcal{I}_h[\boldsymbol{v}] \in \mathcal{S}^1(\mathcal{T}_h)^3$.

We can then define the mass-lumped L^2 product $\langle \cdot, \cdot \rangle_h$ defined by

$$\langle \boldsymbol{\phi}, \boldsymbol{\psi} \rangle_h = \int_\Omega \mathcal{I}_h[\boldsymbol{\phi} \cdot \boldsymbol{\psi}] \text{ for all } \boldsymbol{\phi}, \boldsymbol{\psi} \in \boldsymbol{C}^0(\overline{\Omega}). \tag{3.4}$$

This defines an inner product on $\mathcal{S}^1(\mathcal{T}_h)^3$, and the induced norm satisfies the equivalence

$$\|\boldsymbol{\phi}_h\| \le \|\boldsymbol{\phi}_h\|_h \le \sqrt{5}\, \|\boldsymbol{\phi}_h\| \text{ for all } \boldsymbol{\phi}_h \in \mathcal{S}^1(\mathcal{T}_h)^3, \tag{3.5}$$

and the approximation property

$$|\, \langle \boldsymbol{\phi}_h, \boldsymbol{\psi}_h \rangle - \langle \boldsymbol{\phi}_h, \boldsymbol{\psi}_h \rangle_h \,| \le C h^2 \, \|\boldsymbol{\nabla} \boldsymbol{\phi}_h\| \, \|\boldsymbol{\nabla} \boldsymbol{\psi}_h\| \,, \tag{3.6}$$

where the constant $C > 0$ depends only upon the shape-regularity of $\mathcal{T}_h$, as shown in [Bar15b, Lemma 3.9]. For all $K \in \mathcal{T}_h$ and $1 \le r, p \le \infty$, we have the local inverse estimate

$$\|\boldsymbol{\phi}_h\|_{\boldsymbol{L}^p(K)} \le C h_K^{3(r-p)/(pr)} \, \|\boldsymbol{\phi}_h\|_{\boldsymbol{L}^r(K)} \quad \text{for all } \boldsymbol{\phi}_h \in \mathcal{S}^1(\mathcal{T}_h)^3 \tag{3.7}$$

(see, e.g. [Bar15b, Lemma 3.5]). For all $1 \le p < \infty$, the L^p-norm of functions in $\mathcal{S}^1(\mathcal{T}_h)^3$ is equivalent with the ℓ^p-norm of the vector collecting their nodal values, weighted by the local mesh size, i.e.

$$C^{-1} \, \|\boldsymbol{\phi}_h\|_{\boldsymbol{L}^p(\Omega)} \le \left(\sum_{z \in \mathcal{N}_h} h_z^3 \, |\boldsymbol{\phi}_h(z)|^p \right)^{1/p} \le C \, \|\boldsymbol{\phi}_h\|_{\boldsymbol{L}^p(\Omega)} \quad \text{for all } \boldsymbol{\phi}_h \in \mathcal{S}^1(\mathcal{T}_h)^3, \tag{3.8}$$

where $h_z > 0$ denotes the diameter of the node patch of $z \in \mathcal{N}_h$ (cf. [Bar15b, Lemma 3.4]). If $p = \infty$, we have that

$$\|\boldsymbol{\phi}_h\|_{\boldsymbol{L}^\infty(\Omega)} = \max_{z \in \mathcal{N}_h} |\boldsymbol{\phi}_h(z)| \quad \text{for all } \boldsymbol{\phi}_h \in \mathcal{S}^1(\mathcal{T}_h)^3.$$

We define the admissible set for the magnetization as

$$\boldsymbol{\mathcal{M}} = \{\boldsymbol{m} \in \boldsymbol{H}^1(\Omega) : |\boldsymbol{m}|^2 = 1 \text{ a.e. in } \Omega\}. \tag{3.9}$$

We also define the discrete admissible set for the magnetization as

$$\boldsymbol{\mathcal{M}}_{h,\delta} = \{\boldsymbol{\phi}_h \in \mathcal{S}^1(\mathcal{T}_h)^3 : |\boldsymbol{\phi}_h(z)| \ge 1 \text{ for all } z \in \mathcal{N}_h, \text{ and } \left\| \mathcal{I}_h[|\boldsymbol{\phi}_h|^2] - 1 \right\|_{L^1(\Omega)} \le \delta\} \tag{3.10}$$

for some $\delta > 0$. Note that elements of $\boldsymbol{\mathcal{M}}_{h,\delta}$ do not generally satisfy the unit length constraint, not even at the vertices of the mesh, but the unit length constraint error is controlled in L^1-sense by the parameter δ. In the case where $\delta = 0$ we obtain

$$\boldsymbol{\mathcal{M}}_{h,0} = \{\boldsymbol{\phi}_h \in \mathcal{S}^1(\mathcal{T}_h)^3 : |\boldsymbol{\phi}_h(z)| = 1 \text{ for all } z \in \mathcal{N}_h\}$$

where the constraint holds exactly at each vertex of the mesh. Again, there is no expectation that the constraint holds exactly at any other points than the vertices. Elements of the sets $\boldsymbol{\mathcal{M}}_{h,\delta}, \boldsymbol{\mathcal{M}}_{h,0}$ have $3N$ free parameters, although for $\boldsymbol{\mathcal{M}}_{h,0}$ the third component is restricted by the other two components by $(\boldsymbol{\phi}(z) \cdot \boldsymbol{e}_1)^2 = 1 - (\boldsymbol{\phi}(z) \cdot \boldsymbol{e}_2)^2 - (\boldsymbol{\phi}(z) \cdot \boldsymbol{e}_3)^2$, where $\boldsymbol{e}_1, \boldsymbol{e}_2, \boldsymbol{e}_3$ denotes the standard basis of $\mathbb{R}^3$. Elements of $\boldsymbol{\mathcal{M}}_{h,0}$ satisfy a useful maximum property.

Proposition 3.3.1. *For all $\boldsymbol{\phi}_h \in \boldsymbol{\mathcal{M}}_{h,0}$ it holds that $\|\boldsymbol{\phi}_h\|_{\boldsymbol{L}^\infty(\Omega)} = 1$.*

We define the nodal projection operator $\Pi_h : \boldsymbol{\mathcal{M}}_{h,\delta} \to \boldsymbol{\mathcal{M}}_{h,0}$ by $\Pi_h \boldsymbol{\phi}_h(z) = \boldsymbol{\phi}_h(z)/|\boldsymbol{\phi}_h(z)|$ for all $z \in \mathcal{N}_h$ and $\boldsymbol{\phi}_h \in \boldsymbol{\mathcal{M}}_{h,\delta}$. The following energy decreasing property for the continuous analogue of the nodal projection operator holds (cf. [Alo97]).

Proposition 3.3.2. *Let $\boldsymbol{\phi} \in \boldsymbol{H}^1(\Omega)$ be such that $|\boldsymbol{\phi}| \geq 1$ a.e. in Ω. Then $\boldsymbol{\phi}/|\boldsymbol{\phi}| \in \boldsymbol{H}^1(\Omega)$ and*

$$\|\boldsymbol{\nabla}(\boldsymbol{\phi}/|\boldsymbol{\phi}|)\| \leq \|\boldsymbol{\nabla}\boldsymbol{\phi}\| .$$

The discrete nodal projection operator satisfies a weaker stability property than Proposition 3.3.2, which does not discount the possibility of an energy increase (see [Bar16, Lemma 2.2]).

Proposition 3.3.3. *Let $\{\mathcal{T}_h\}$ be a shape-regular family of meshes. Then*

$$\|\boldsymbol{\nabla}\Pi_h\boldsymbol{\phi}_h\| \leq C \|\boldsymbol{\nabla}\boldsymbol{\phi}_h\| , \text{ for all } \boldsymbol{\phi}_h \in \boldsymbol{\mathcal{M}}_{h,\delta} \tag{3.11}$$

for $\delta > 0$ where $C \geq 1$ depends only upon the shape-regularity of the meshes.

Although not necessary for our algorithms, we recall the following about weakly acute meshes. We call the angle between two faces of a tetrahedron K a *dihedral angle*. If each of the six dihedral angles of K are less than $\pi/2$, we say that K is weakly acute. If all $K \in \mathcal{T}_h$ are weakly acute, we say that $\mathcal{T}_h$ is weakly acute. A true analogue for Proposition 3.3.2 in the sense that (3.11) holds with $C = 1$ is demonstrated in the following (see [Bar15b]).

Proposition 3.3.4. *Let $\{\mathcal{T}_h\}_{h>0}$ be a family of regular triangulations of Ω satisfying the angle condition*

$$\left\langle \boldsymbol{\nabla}\boldsymbol{\varphi}_{z_1}, \boldsymbol{\nabla}\boldsymbol{\varphi}_{z_2} \right\rangle \leq 0 \text{ for every } z_1, z_2 \in \mathcal{N}_h. \tag{3.12}$$

Then

$$\|\boldsymbol{\nabla}\Pi_h\boldsymbol{\phi}_h\| \leq \|\boldsymbol{\nabla}\boldsymbol{\phi}_h\| \text{ for all } \boldsymbol{\phi}_h \in \boldsymbol{\mathcal{M}}_{h,\delta} \tag{3.13}$$

for every $\delta > 0$.

If $\mathcal{T}_h$ is weakly acute, then (3.12) holds, so for $\boldsymbol{\phi}_h \in \boldsymbol{\mathcal{M}}_{h,\delta}$ we have that the nodal projection operator is energy decreasing. If $\mathcal{T}_h$ is not weakly acute, there

exists $\boldsymbol{\phi}_h$ such that (3.13) does not hold (see [Bar15b]). In three dimensions this is a very restrictive property, but this is less of an issue in two dimensions. In this thesis, we work exclusively with the full three-dimensional problem, and so the assumption of weak acuteness would be far too restrictive.

To realize the orthogonality constraint $\boldsymbol{m} \cdot \partial_t \boldsymbol{m} = 0$ in the discrete setting, given $\boldsymbol{\phi}_h \in \boldsymbol{\mathcal{M}}_{h,\delta}$ we define the discrete tangent space

$$\boldsymbol{\mathcal{K}}_h[\boldsymbol{\phi}_h] = \{\boldsymbol{\psi}_h \in \mathcal{S}^1(\mathcal{T}_h)^3 : \boldsymbol{\phi}_h(z) \cdot \boldsymbol{\psi}_h(z) = 0 \text{ for all } z \in \mathcal{N}_h\}. \tag{3.14}$$

The discrete tangent space enforces the orthogonality at the nodes only, and has dimension $\dim \boldsymbol{\mathcal{K}}_h[\boldsymbol{\phi}_h] = 2N$. For use in energy minimization, let $(\boldsymbol{\mathcal{H}}, \langle \cdot, \cdot \rangle_{\boldsymbol{\mathcal{H}}})$ be a Hilbert space such that $\boldsymbol{\mathcal{M}}$ is continuously embedded within $\mathcal{H}$, and suppose that there exists some constant $c_{\boldsymbol{\mathcal{H}}} \geq 1$ such that

$$c_{\boldsymbol{\mathcal{H}}}^{-1} \|\boldsymbol{\phi}\| \leq \|\boldsymbol{\phi}\|_{\boldsymbol{\mathcal{H}}} \leq c_{\boldsymbol{\mathcal{H}}} \|\boldsymbol{\phi}\|_{\boldsymbol{H}^1(\Omega)} \quad \text{for all } \boldsymbol{\phi} \in \boldsymbol{H}^1(\Omega). \tag{3.15}$$

Two examples of such spaces are

$$\langle \cdot, \cdot \rangle_{\boldsymbol{\mathcal{H}}} = \begin{cases} \langle \cdot, \cdot \rangle & \text{if } \boldsymbol{\mathcal{H}} = \boldsymbol{L}^2, \\ \langle \cdot, \cdot \rangle + \langle \boldsymbol{\nabla} \cdot, \boldsymbol{\nabla} \cdot \rangle & \text{if } \boldsymbol{\mathcal{H}} = \boldsymbol{H}^1. \end{cases}$$

Finally, in the following chapters, we may denote by $C > 0$ a generic constant that is independent of the discretization parameters h, k, and is not necessarily the same at each occurrence. The constant may also be ignored, so that the inequality $a \leq Cb$, for $C > 0$, may simply be written as $a \lesssim b$.

Chapter 4

Tangent Plane Schemes

4.1 Harmonic maps

To discuss the basics of the tangent plane scheme we consider a heavily simplified micromagnetic model, including only the highest order energy term

$$\mathcal{E}[\boldsymbol{m}] = \frac{1}{2}\int_\Omega |\boldsymbol{\nabla m}|^2. \tag{4.1}$$

Subject to the constraint that $|\boldsymbol{m}| = 1$, this aligns with the study of so-called *harmonic maps* with Neumann boundary conditions $\partial_{\boldsymbol{n}}\boldsymbol{m} = \boldsymbol{0}$ (see [Bar15b, Chapter 7]). A harmonic map is a stationary point of the exchange energy with a unit length constraint, but usually has Dirichlet boundary conditions, which discourage constant minimizers. We choose Neumann boundary conditions to make the transition to the micromagnetic formulation more natural, but this means that the minimizer states will be constant, and uniqueness should not be expected. In fact, any minimizer of (4.1) can be freely rotated, yielding another minimizer. Taking the first variation of the energy (4.1) leads to the Euler–Lagrange equation

$$-\boldsymbol{\Delta m} = |\boldsymbol{\nabla m}|^2\boldsymbol{m}, \tag{4.2}$$

which yields the following variational formulation.

Definition 4.1.1. *We say that $\boldsymbol{m} \in \boldsymbol{\mathcal{M}}$ such that*

$$\langle \boldsymbol{\nabla m}, \boldsymbol{\nabla \phi}\rangle = \left\langle |\boldsymbol{\nabla m}|^2\boldsymbol{m}, \boldsymbol{\phi}\right\rangle, \tag{4.3}$$

for all $\boldsymbol{\phi} \in \boldsymbol{H}^1(\Omega) \cap \boldsymbol{L}^\infty(\Omega)$ is a harmonic map.

Note that we require $\boldsymbol{\phi} \in \boldsymbol{L}^\infty(\Omega)$ to ensure the right-hand side is well-defined. The non-linear term $|\boldsymbol{\nabla m}|^2$ should be understood as a Lagrange multiplier corresponding to the unit length constraint. The Neumann conditions are natural boundary conditions. This formulation is however, quite non-linear, and if we restrict the test function $\boldsymbol{\phi}$ to be such that $\boldsymbol{m}\cdot\boldsymbol{\phi} = 0$, then the non-linear term $\langle|\boldsymbol{\nabla m}|^2\boldsymbol{m}, \boldsymbol{\phi}\rangle$ disappears, leaving spiritually the weak formulation of the Laplace equation

$$\langle \boldsymbol{\nabla m}, \boldsymbol{\nabla \phi}\rangle = 0. \tag{4.4}$$

These two forms of the problem are in fact equivalent, and are stationary points of the energy (4.1), as shown in [Bar15b, Lemma 7.1]. Note that stationary points may not be minimizers themselves, so this condition is necessary but not sufficient.

Lemma 4.1.2. *A function $\boldsymbol{m} \in \boldsymbol{\mathcal{M}}$ is a harmonic map if and only if*

$$\langle \boldsymbol{\nabla m}, \boldsymbol{\nabla}[\boldsymbol{m} \times \boldsymbol{\phi}] \rangle = \sum_{\ell=1}^{3} \langle \partial_\ell \boldsymbol{m}, \boldsymbol{m} \times \partial_\ell \boldsymbol{\phi} \rangle = 0$$

for all $\boldsymbol{\phi} \in \boldsymbol{H}^1(\Omega) \cap \boldsymbol{L}^\infty(\Omega)$, which is the case if and only if

$$\langle \boldsymbol{\nabla m}, \boldsymbol{\nabla \phi} \rangle = 0$$

for all $\boldsymbol{\phi} \in \boldsymbol{\mathcal{K}}(\boldsymbol{m})$ where

$$\boldsymbol{\mathcal{K}}(\boldsymbol{m}) = \{\boldsymbol{\phi} \in \boldsymbol{H}^1(\Omega) : \boldsymbol{m} \cdot \boldsymbol{\phi} = 0 \text{ a.e. in } \Omega\}.$$

To seek minimizers, we employ the method of $\boldsymbol{\mathcal{H}}$-gradient flow through

$$\langle \partial_t \boldsymbol{m}, \boldsymbol{\phi} \rangle_{\boldsymbol{\mathcal{H}}} = - \langle \boldsymbol{\nabla m}, \boldsymbol{\nabla \phi} \rangle , \tag{4.5}$$

for all $\boldsymbol{\phi} \in \boldsymbol{H}^1(\Omega)$ with $\boldsymbol{m} \cdot \boldsymbol{\phi} = 0$, with the initial condition $\boldsymbol{m}^0 \in \boldsymbol{\mathcal{M}}$. The idea of gradient flow is that the time derivative $\partial_t \boldsymbol{m}$ is an approximation of the negative derivative of the energy with respect to $\boldsymbol{m}$, that is in some sense we have

$$\partial_t \boldsymbol{m} = -\frac{\delta \mathcal{E}[\boldsymbol{m}]}{\delta \boldsymbol{m}},$$

so that advancing forward in "time" via the formula

$$\boldsymbol{m}(t + \Delta t) = \boldsymbol{m}(t) - \frac{\Delta \mathcal{E}[\boldsymbol{m}]}{\delta \boldsymbol{m}} \Delta t$$

decreases the energy $\mathcal{E}[\boldsymbol{m}(t + \Delta t)] < \mathcal{E}[\boldsymbol{m}(t)]$ and approaches a minimum. The metric $\boldsymbol{\mathcal{H}}$ is called the metric of gradient flow, and we are free to choose this metric provided certain conditions are met (see (3.15)).

4.2 Conditional algorithm

The tangent plane scheme for harmonic maps requires some approximation $\boldsymbol{m}_h^0 \in \boldsymbol{\mathcal{M}}_{h,0}$ to the initial guess $\boldsymbol{m}^0$, and takes the time derivative $\partial_t \boldsymbol{m} = \boldsymbol{v}$ as a new variable, and applies a predictor-corrector scheme to advance. The update $\partial_t \boldsymbol{m}(t_i) \approx \boldsymbol{v}_h^i \in \boldsymbol{\mathcal{K}}_h[\boldsymbol{m}_h^i]$ is found in the tangent space of the current approximation $\boldsymbol{m}(t_i) \approx \boldsymbol{m}_h^i$. For this presentation, we include a combination of the projection and projection-free schemes shown in [Bar15b, Chapter 7].

Algorithm 4.2.1 (Conditional Energy Minimisation)**.** *Parameters: Mesh size $h > 0$, time-step size $k > 0$, $\theta \in (1/2, 1]$, tolerance $\varepsilon > 0$.*
Input: Approximate initial condition $\boldsymbol{m}_h^0 \in \boldsymbol{\mathcal{M}}_{h,0}$.
Loop: While $\max\{\|\boldsymbol{v}_h^i\|_{\boldsymbol{\mathcal{H}}}, k \|\boldsymbol{\nabla v}_h^i\|\} > \varepsilon$*, iterate* (i)–(ii)*:*

(i) Compute $\boldsymbol{v}_h^i \in \boldsymbol{\mathcal{K}}_h[\boldsymbol{m}_h^i]$ *such that, for all* $\boldsymbol{\phi}_h \in \boldsymbol{\mathcal{K}}_h[\boldsymbol{m}_h^i]$*, it holds that*

$$\left\langle \boldsymbol{v}_h^i, \boldsymbol{\phi}_h \right\rangle_{\boldsymbol{\mathcal{H}}} + \theta k \left\langle \boldsymbol{\nabla} \boldsymbol{v}_h^i, \boldsymbol{\nabla} \boldsymbol{\phi}_h \right\rangle = - \left\langle \boldsymbol{\nabla} \boldsymbol{m}_h^i, \boldsymbol{\nabla} \boldsymbol{\phi}_h \right\rangle . \tag{4.6}$$

(ii) If $\|\boldsymbol{\nabla} \Pi_h(\boldsymbol{m}_h^i + k\boldsymbol{v}_h^i)\| < \|\boldsymbol{\nabla}(\boldsymbol{m}_h^i + k\boldsymbol{v}_h^i)\|$ *define*

$$\boldsymbol{m}_h^{i+1} := \Pi_h(\boldsymbol{m}_h^i + k\boldsymbol{v}_h^i) \in \boldsymbol{\mathcal{M}}_{h,0}, \tag{4.7}$$

else define

$$\boldsymbol{m}_h^{i+1} := \boldsymbol{m}_h^i + k\boldsymbol{v}_h^i \in \mathcal{S}^1(\mathcal{T}_h)^3. \tag{4.8}$$

Output: If N^* *denotes the smallest integer satisfying the stopping condition, define the approximate stationary point* $\boldsymbol{m}_h := \boldsymbol{m}_h^{N^*}$.

This method treats the exchange term implicitly, where the parameter θ controls the "degree of implicitness". We also see that despite the harmonic map problem being non-linear, we only have to solve a linear system to get the next approximation. We observe that if the mesh is weakly acute, then (ii) will always apply a projection, yielding a scheme like that in Figure 4.1a. The conditional use of the nodal projection, as in Figure 4.1c, allows for the benefits to the unit length constraint, without the requirement of weakly acute meshes for stability. A simple case where the projection step will apply is shown in Figure 4.2, where in Figure 4.2a the discrete magnetization at each node points in the same direction but has different magnitudes at each node. It follows that exchange energy only arises from differences in magnitude, which will prevent the discrete magnetization from satisfying $\|\boldsymbol{\nabla} \boldsymbol{m}_h\|^2 = 0$. However, when a projection is applied, as in Figure 4.2b the gradient of the discrete magnetization will be precisely zero, and the energy decreasing inequality $\|\boldsymbol{\nabla} \Pi_h \boldsymbol{m}_h\| \leq \|\boldsymbol{\nabla} \boldsymbol{m}_h\|$ will necessarily hold, independent of the underlying mesh being weakly acute. To restate this, it is true (shown in [Bar15b, Proposition 7.3]) that if the mesh $\mathcal{T}_h$ is not weakly acute, there exists some function $\boldsymbol{\phi}_h \in \mathcal{T}_h$ with $\|\boldsymbol{\nabla} \Pi_h \boldsymbol{\phi}_h\| > \|\boldsymbol{\nabla} \boldsymbol{\phi}_h\|$, but for any mesh there also exist functions satisfying the energy decreasing property. In Algorithm 4.2.1, the stopping condition is chosen such that the operator norm of the residual in the variational formulation of the discrete function is proportional to ε, which is important in the upcoming convergence analysis.

Remark 4.2.2. *Algorithm 4.2.1 allows for the possibility that no projection occurs at any iteration. This then yields a projection-free scheme as shown in Figure 4.1b. We believe that the potential for at least one projection is worth the expense of checking at each time step.*

The typical method for showing convergence of a finite element method involves the following steps:

1. Showing well-posedness of the method.
2. Proving boundedness from stability estimates.
3. Deducing (weakly)-convergent subsequences from boundedness.
4. Showing that these subsequences satisfy the Euler–Lagrange equation.

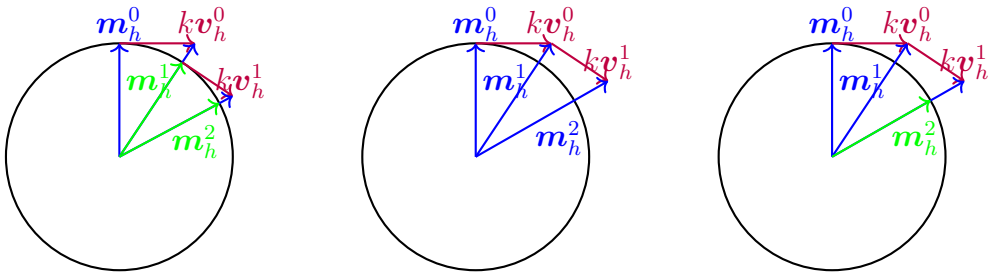

Figure 4.1: Illustration of (a) fully projected scheme (b) projection-free scheme (c) conditional projection scheme used in Algorithm 4.2.1 with no projection on $\boldsymbol{m}_h^1$ followed by a projection on $\boldsymbol{m}_h^2$. Here we denote projection-free updates as blue, tangent space vectors in red, and updates that are projected in green. In (a), we see a projection at every step, pulling the blue arrow back to the green arrow on the sphere. In (b), we see no projections, resulting in successive green arrows increasing in length. In (c), we first see a projection-free step (in blue), followed by a step that is projected back onto the sphere (in green).

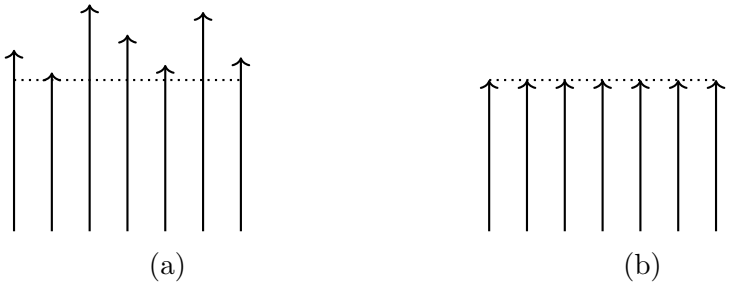

Figure 4.2: Uniformly magnetized magnetization (a) before projection with varying magnitudes (b) after projection step with $|\boldsymbol{m}_h(z)| = 1$ for each $z \in \mathcal{N}_h$.

We now show that Algorithm 4.2.1 is well-posed and stable using standard techniques associated with the energy method for elliptic PDEs.

Proposition 4.2.3. *Algorithm 4.2.1 is well-posed, and satisfies the stability estimate for each* $0 \leq i \leq N-1$

$$\mathcal{E}[\boldsymbol{m}_h^{i+1}] + k\left\|\boldsymbol{v}_h^i\right\|_{\boldsymbol{\mathcal{H}}}^2 + \left(\theta - \frac{1}{2}\right) k^2 \left\|\boldsymbol{\nabla} \boldsymbol{v}_h^i\right\|^2 \leq \mathcal{E}[\boldsymbol{m}_h^i], \tag{4.9}$$

with equality if and only if the step is projection-free. Additionally, the following discrete energy law holds for every $N \in \mathbb{N}$

$$\mathcal{E}[\boldsymbol{m}_h^N] + k\sum_{i=0}^{N-1}\left\|\boldsymbol{v}_h^i\right\|_{\boldsymbol{\mathcal{H}}}^2 + \left(\theta - \frac{1}{2}\right) k^2 \sum_{i=0}^{N-1}\left\|\boldsymbol{\nabla} \boldsymbol{v}_h^i\right\|^2 \leq \mathcal{E}[\boldsymbol{m}_h^0]. \tag{4.10}$$

Proof. The Lax–Milgram lemma implies that there is a unique solution $\boldsymbol{v}_h^i$ to (4.6). As $\boldsymbol{v}_h^i \in \boldsymbol{\mathcal{K}}_h[\boldsymbol{m}_h^i]$, we have that for each $z \in \mathcal{N}_h$ that

$$|\boldsymbol{m}_h^i(z) + k\boldsymbol{v}_h^i(z)|^2 = |\boldsymbol{m}_h^i(z)|^2 + k|\boldsymbol{v}_h^i(z)|^2 \geq 1$$

thus the projection step (4.7) is always well-defined. Now choosing $\boldsymbol{\phi}_h = k\boldsymbol{v}_h^i$ in (4.6) yields

$$k\left\|\boldsymbol{v}_h^i\right\|_{\boldsymbol{\mathcal{H}}}^2 + \theta k^2\left\|\boldsymbol{\nabla}\boldsymbol{v}_h^i\right\|^2 = -k\left\langle\boldsymbol{\nabla}\boldsymbol{m}_h^i, \boldsymbol{\nabla}\boldsymbol{v}_h\right\rangle. \tag{4.11}$$

From (4.7) and (4.8) respectively we have by construction

$$\frac{1}{2}\left\|\boldsymbol{\nabla}\boldsymbol{m}_h^{i+1}\right\|^2 < \frac{1}{2}\left\|\boldsymbol{\nabla}(\boldsymbol{m}_h^i + k\boldsymbol{v}_h^i)\right\|^2,$$
$$\frac{1}{2}\left\|\boldsymbol{\nabla}\boldsymbol{m}_h^{i+1}\right\|^2 = \frac{1}{2}\left\|\boldsymbol{\nabla}(\boldsymbol{m}_h^i + k\boldsymbol{v}_h^i)\right\|^2,$$

so that all iterates satisfy

$$\frac{1}{2}\left\|\boldsymbol{\nabla}\boldsymbol{m}_h^{i+1}\right\|^2 \leq \frac{1}{2}\left\|\boldsymbol{\nabla}(\boldsymbol{m}_h^i + k\boldsymbol{v}_h^i)\right\|^2 = \frac{1}{2}\left\|\boldsymbol{\nabla}\boldsymbol{m}_h^i\right\|^2 + k\left\langle\boldsymbol{\nabla}\boldsymbol{m}_h^i, \boldsymbol{\nabla}\boldsymbol{v}_h^i\right\rangle + \frac{k^2}{2}\left\|\boldsymbol{\nabla}\boldsymbol{v}_h^i\right\|^2.$$

Combining the above yields (4.9), and summing over $0 \leq i \leq N-1$ yields (4.10). From the energy law and noting $\theta \in (1/2, 1]$, we deduce that the sums

$$k\sum_{i=0}^{\infty}\left\|\boldsymbol{v}_h^i\right\|_{\boldsymbol{\mathcal{H}}}^2, \quad k^2\sum_{i=0}^{\infty}\left\|\boldsymbol{\nabla}\boldsymbol{v}_h^i\right\|^2$$

are convergent, hence $\left\|\boldsymbol{v}_h^i\right\|_{\boldsymbol{\mathcal{H}}}, k\left\|\boldsymbol{\nabla}\boldsymbol{v}_h^i\right\| \to 0$ as $i \to \infty$. We conclude that there exists some $N^* \in \mathbb{N}$ such that the stopping condition is met. □

Algorithm 4.2.1 then satisfies the local energy decreasing property $\left\|\boldsymbol{\nabla}\boldsymbol{m}_h^{i+1}\right\| \leq \left\|\boldsymbol{\nabla}\boldsymbol{m}_h^i\right\|$ for all iterations i. Additionally, we know that Algorithm 4.2.1 stops in a finite number of iterations. To get a *very* crude overestimate for the number of iterations, suppose that the stopping condition is almost met every iteration, with either

$$\left\|\boldsymbol{v}_h^i\right\|_{\boldsymbol{\mathcal{H}}} = \varepsilon \text{ or } k\left\|\boldsymbol{\nabla}\boldsymbol{v}_h^i\right\| = \varepsilon.$$

Then, inserting this into (4.10) we have

$$k\sum_{i=0}^{N-1}\boldsymbol{\varepsilon}^2 \leq \mathcal{E}[\boldsymbol{m}_h^0], \quad \left(\theta - \frac{1}{2}\right)\sum_{i=0}^{N-1}\boldsymbol{\varepsilon}^2 \leq \mathcal{E}[\boldsymbol{m}_h^0].$$

We can simplify this to say that the stopping iteration N^* is bounded by

$$N^* \leq \frac{\mathcal{E}[\boldsymbol{m}_h^0]}{\varepsilon^2}\max\left\{\frac{1}{k}, \frac{1}{\theta - 1/2}\right\}.$$

This is an extremely huge overestimate, not least because for early iterations $\left\|\boldsymbol{v}_h^i\right\|_{\boldsymbol{\mathcal{H}}}$ and $k\left\|\boldsymbol{\nabla}\boldsymbol{v}_h^i\right\|$ are significantly larger than ε. However, this inequality makes obvious the following behaviours. For smaller tolerances ε and smaller time-step sizes k, Algorithm 4.2.1 will generally require more iterations. Additionally, if the initial state is "hot", in that $\mathcal{E}[\boldsymbol{m}_h^0]$ is large, then more iterations are required to stop. Lastly, when the implicitness parameter θ is close to $1/2$, then more iterations may be required as less artificial dissipation is introduced. We can now state the boundedness properties of the iterates.

Proposition 4.2.4. *Suppose that there exists $c_0 > 0$ independent of the discretization parameters such that $\sup_{h>0}(\|\boldsymbol{m}_h^0\|^2_{\boldsymbol{H}^1(\Omega)}) \leq c_0$, and assume that $\theta \in (1/2, 1]$. Then iterates from 4.2.1 satisfy for $i \in \mathbb{N}$*

$$\left\|\boldsymbol{m}_h^i\right\|^2_{\boldsymbol{H}^1(\Omega)} + k\sum_{i=0}^{N-1}\left\|\boldsymbol{v}_h^i\right\|^2_{\boldsymbol{\mathcal{H}}} + k^2\sum_{i=0}^{N-1}\left\|\boldsymbol{\nabla}\boldsymbol{v}_h^i\right\|^2 \leq C, \tag{4.12}$$

and

$$\left\|\mathcal{I}_h[|\boldsymbol{m}_h^i|^2] - 1\right\|_{L^1(\Omega)} \leq Ck \tag{4.13}$$

where the constant $C > 0$ in each inequality depends only upon the shape-regularity of the mesh, and c_0.

Proof. Suppose that in iteration i, a nodal projection is applied so that we have $|\boldsymbol{m}_h^{i+1}(z)|^2 = 1$ for each $z \in \mathcal{N}_h$. Now suppose that iteration i is projection-free, and iteration j is when the last projection was applied. As $\boldsymbol{v}_h^i \in \boldsymbol{\mathcal{K}}_h[\boldsymbol{m}_h^i]$ we have for each $z \in \mathcal{N}_h$ that

$$\begin{aligned}
|\boldsymbol{m}_h^{i+1}(z)|^2 &= |\boldsymbol{m}_h^i(z)|^2 + k^2|\boldsymbol{v}_h^i(z)|^2 \\
&= |\boldsymbol{m}_h^{j+1}(z)|^2 + k^2\sum_{\ell=j+1}^{i}|\boldsymbol{v}_h^\ell(z)|^2 \\
&= 1 + k^2\sum_{\ell=j+1}^{i}|\boldsymbol{v}_h^\ell(z)|^2.
\end{aligned}$$

In either the projection or projection-free case, we have that

$$|\boldsymbol{m}_h^{i+1}(z)|^2 \leq 1 + k^2\sum_{\ell=0}^{i}|\boldsymbol{v}_h^\ell(z)|^2.$$

Then from the equivalence of the L^p norm of a discrete function with the weighted ℓ^p norm of the vector containing their nodal values (see for example [Bar15b, Lemma 3.4]), we have that

$$\begin{aligned}
\left\|\mathcal{I}_h[|\boldsymbol{m}_h^i|^2] - 1\right\|_{L^1(\Omega)} &\leq Ck^2\sum_{j=0}^{i-1}\left\|\boldsymbol{v}_h^j\right\|^2, \\
\left\|\boldsymbol{m}_h^i\right\|^2 &\leq |\Omega| + Ck^2\sum_{j=0}^{i-1}\left\|\boldsymbol{v}_h^j\right\|^2.
\end{aligned}$$

Now, combining this with (4.10) yields for each $i \in \mathbb{N}$

$$\begin{aligned}
\left\|\mathcal{I}_h[|\boldsymbol{m}_h^i|^2] - 1\right\|_{L^1(\Omega)} &\leq Ck\left\|\boldsymbol{\nabla}\boldsymbol{m}_h^0\right\|^2, \\
\left\|\boldsymbol{m}_h^i\right\|^2 &\leq |\Omega| + Ck\left\|\boldsymbol{\nabla}\boldsymbol{m}_h^0\right\|^2.
\end{aligned}$$

Applying the assumption of the proposition and the equivalence of norms (3.15) to (4.10) and the above completes the proof. □

The unit length constraint error measure is controlled suitably by both the projection and projection-free time-stepping, along with the L^2-norm of $\boldsymbol{m}_h^i$. In particular iterates from Algorithm 4.2.1 satisfy $\boldsymbol{m}_h^i \in \boldsymbol{\mathcal{M}}_{h,\delta}$ with $\delta = Ck$.

To show that Algorithm 4.2.1 produces sequences converging to weak solutions of (4.4), we state the following lemma from [Bar15b, Lemma 7.2] showing that the projection-free step is sufficient for the unit length constraint in the limit.

Lemma 4.2.5 (Constraint violation)**.** *Let $\{\boldsymbol{m}_h\}_{h>0} \subset \boldsymbol{H}^1(\Omega)$ be a bounded sequence such that $\boldsymbol{m}_h \in \mathcal{S}^1(\mathcal{T}_h)^3$ for all $h > 0$, $\boldsymbol{m}_h \to \boldsymbol{m}$ in $\boldsymbol{L}^2(\Omega)$ for some $\boldsymbol{m} \in \boldsymbol{H}^1(\Omega)$ as $h \to 0$, and*

$$\left\|\mathcal{I}_h[|\boldsymbol{m}_h|^2] - 1\right\|_{L^1(\Omega)} \to 0, \qquad \text{as } h \to 0.$$

Then we have $|\boldsymbol{m}|^2 = 1$ almost everywhere in Ω.

Proof. Applying the triangle inequality twice yields

$$\begin{aligned}&\left\||\boldsymbol{m}_h|^2 - 1\right\|_{L^1(\Omega)}\\ &\quad\le \left\||\boldsymbol{m}|^2 - |\boldsymbol{m}_h|^2\right\|_{L^1(\Omega)} + \left\||\boldsymbol{m}_h|^2 - \mathcal{I}_h[|\boldsymbol{m}_h|^2]\right\|_{L^1(\Omega)} + \left\|\mathcal{I}_h[|\boldsymbol{m}_h|^2] - 1\right\|_{L^1(\Omega)}.\end{aligned}$$

The third term tends to zero as $h \to 0$ as a result of the assumptions of the lemma. The first term also vanishes as $h \to 0$ because

$$\left\||\boldsymbol{m}|^2 - |\boldsymbol{m}_h|^2\right\|_{L^1(\Omega)} \le \|\boldsymbol{m} + \boldsymbol{m}_h\|\,\|\boldsymbol{m} - \boldsymbol{m}_h\| \lesssim \|\boldsymbol{m} - \boldsymbol{m}_h\| \to 0.$$

The remaining term vanishes in the limit upon usage of Hölder's inequality and a nodal interpolation estimate. □

We can now show that Algorithm 4.2.1 produces weak solutions.

Theorem 4.2.6. *Replicate the assumptions of Proposition 4.2.4 and further suppose that $k \to 0$ and $\varepsilon \to 0$ as $h \to 0$. Then as $h \to 0$, the sequence of approximate stationary points $\{\boldsymbol{m}_h\}_{h>0}$ generated by Algorithm 4.2.1, upon extraction of a subsequence, converges weakly in $\boldsymbol{H}^1(\Omega)$ toward a harmonic map $\boldsymbol{m} \in \boldsymbol{\mathcal{M}}$.*

The following proof uses ideas from [Bar15b, Chapter 7].

Proof. We have by Proposition 4.2.4 that the sequence $\{\boldsymbol{m}_h\}_{h>0}$ is bounded in $\boldsymbol{H}^1(\Omega)$, and so there exists a (nonrelabeled) weakly convergent subsequence of $\{\boldsymbol{m}_h\}_{h>0}$ such that $\boldsymbol{m}_h \rightharpoonup \boldsymbol{m}$ in $\in \boldsymbol{H}^1(\Omega)$ and $\boldsymbol{m}_h \to \boldsymbol{m}$ in $\in \boldsymbol{L}^2(\Omega)$. By (4.13) we have that $\|\mathcal{I}_h[|\boldsymbol{m}_h|^2] - 1\|_{L^1(\Omega)} \to 0$ as $h \to 0$, so applying Lemma 4.2.5 yields that $\boldsymbol{m} \in \boldsymbol{\mathcal{M}}$. Using (4.6) we see that each approximate stationary point $\boldsymbol{m}_h$ satisfies the variational formulation

$$-\langle \boldsymbol{\nabla}\boldsymbol{m}_h, \boldsymbol{\nabla}\boldsymbol{\phi}_h\rangle = \mathcal{R}_h(\boldsymbol{\phi}_h)$$

for all $\boldsymbol{\phi}_h \in \boldsymbol{\mathcal{K}}_h[\boldsymbol{m}_h]$ where the remainder term on the right-hand side is given by

$$\mathcal{R}_h(\boldsymbol{\phi}_h) = \left\langle \boldsymbol{v}_h^{N^*}, \boldsymbol{\phi}_h\right\rangle_{\boldsymbol{\mathcal{H}}} + \theta k \left\langle \boldsymbol{\nabla}\boldsymbol{v}_h^{N^*}, \boldsymbol{\nabla}\boldsymbol{\phi}_h\right\rangle$$

and hence satisfies $|\mathcal{R}_h(\boldsymbol{\phi})| \leq C\varepsilon \|\boldsymbol{\phi}\|_{\boldsymbol{H}^1(\Omega)}$ for all $\boldsymbol{\phi} \in \boldsymbol{H}^1(\Omega)$ by the stopping condition of Algorithm 4.2.1. It follows that $\mathcal{R}_h \to 0$ in $\boldsymbol{H}^1(\Omega)^*$ as $h \to 0$. Now let $\boldsymbol{\psi} \in \boldsymbol{C}^\infty(\overline{\Omega})$, and choose $\boldsymbol{\phi}_h = \mathcal{I}_h[\boldsymbol{m}_h \times \boldsymbol{\psi}] \in \boldsymbol{\mathcal{K}}_h[\boldsymbol{m}_h]$. Noting that $D^2\boldsymbol{m}_h|_K = 0$ for every $K \in \mathcal{T}_h$, we have via nodal interpolation estimates that

$$\begin{aligned}\|\boldsymbol{\nabla}(\boldsymbol{\phi}_h - \boldsymbol{m}_h \times \boldsymbol{\psi})\|_{\boldsymbol{L}^2(K)} \leq& ch_K \left\|D^2(\boldsymbol{m}_h \times \boldsymbol{\psi})\right\|_{\boldsymbol{L}^2(K)} \\ \leq& ch_K \Big(\|\boldsymbol{\nabla}\boldsymbol{m}_h\|_{\boldsymbol{L}^2(K)} \|\boldsymbol{\nabla}\boldsymbol{\psi}\|_{\boldsymbol{L}^\infty(K)} \\ &+ \|\boldsymbol{m}_h\|_{\boldsymbol{L}^\infty(K)} \left\|D^2\boldsymbol{\psi}\right\|_{\boldsymbol{L}^2(K)}\Big)\end{aligned}$$

yielding $\|\boldsymbol{\nabla}\boldsymbol{\phi}_h\|$ is bounded, and that $\boldsymbol{\phi}_h - \boldsymbol{m}_h \times \boldsymbol{\psi} \to 0$ in $\boldsymbol{H}^1(\Omega)$ as $h \to 0$. Therefore, we have

$$\langle \boldsymbol{\nabla}\boldsymbol{m}_h, \boldsymbol{\nabla}\boldsymbol{\phi}_h \rangle = \langle \boldsymbol{\nabla}\boldsymbol{m}_h, \boldsymbol{\nabla}(\boldsymbol{m}_h \times \boldsymbol{\psi}) \rangle + \langle \boldsymbol{\nabla}\boldsymbol{m}_h, \boldsymbol{\nabla}(\boldsymbol{\phi}_h - \boldsymbol{m}_h \times \boldsymbol{\psi}) \rangle$$

and as $\boldsymbol{\nabla}\boldsymbol{m}_h \rightharpoonup \boldsymbol{\nabla}\boldsymbol{m}$ and $\boldsymbol{m}_h \to \boldsymbol{m}$ as $h \to 0$, taking limits yields that

$$\begin{aligned}\langle \boldsymbol{\nabla}\boldsymbol{m}, \boldsymbol{\nabla}(\boldsymbol{m} \times \boldsymbol{\psi}) \rangle &= \langle \boldsymbol{\nabla}\boldsymbol{m}, \boldsymbol{m} \times \boldsymbol{\nabla}\boldsymbol{\psi} \rangle \\ &= \lim_{h \to 0} \langle \boldsymbol{\nabla}\boldsymbol{m}_h, \boldsymbol{m}_h \times \boldsymbol{\nabla}\boldsymbol{\psi} \rangle \\ &= \lim_{h \to 0} \mathcal{R}_h(\boldsymbol{m}_h \times \boldsymbol{\psi}) = 0.\end{aligned}$$

Applying Lemma 4.1.2 completes the proof. □

4.3 Post-processing

As an alternative/addition to Algorithm 4.2.1, we also consider a very weak version of the fully projected algorithm. As we know, for the fully projected algorithm to be stable in the sense that

$$\mathcal{E}[\Pi_h \boldsymbol{m}_h] \leq \mathcal{E}[\boldsymbol{m}_h]$$

we require that the mesh $\mathcal{T}_h$ is weakly acute. Let $a \geq 1$ be a parameter. Then we have the observation

$$\mathcal{E}[\boldsymbol{m}/a] = \frac{1}{a^2}\mathcal{E}[\boldsymbol{m}] \leq \mathcal{E}[\boldsymbol{m}],$$

which holds in the continuous and discrete case. In particular, for a projection-free algorithm, we get $\min_{z \in \mathcal{N}_h} |\boldsymbol{m}_h(z)| \geq 1$. Therefore, if we choose $a = \min_{z \in \mathcal{N}_h} |\boldsymbol{m}_h(z)|$, we will have the constraint violation reducing property

$$1 \leq |\boldsymbol{m}_h(z)/a|^2 = \frac{1}{a^2}|\boldsymbol{m}_h(z)|^2 \leq |\boldsymbol{m}_h(z)|^2,$$

and also know that for at least one $z \in \mathcal{N}_h$, $|\boldsymbol{m}_h(z)| = 1$. We can then write the algorithm as follows.

Algorithm 4.3.1 (Compensated Energy Minimisation)**.** *Parameters: Mesh size $h > 0$, time-step size $k > 0$, $\theta \in (1/2, 1]$, tolerance $\varepsilon > 0$.*
Input: Approximate initial condition $\boldsymbol{m}_h^0 \in \boldsymbol{\mathcal{M}}_{h,0}$.
Loop: While $\max\{\|\boldsymbol{v}_h^i\|_{\boldsymbol{\mathcal{H}}}, k\|\boldsymbol{\nabla}\boldsymbol{v}_h^i\|\} > \varepsilon$, iterate (i)–(ii)*:*

(i) Compute $\boldsymbol{v}_h^i \in \boldsymbol{\mathcal{K}}_h[\boldsymbol{m}_h^i]$ *such that, for all* $\boldsymbol{\phi}_h \in \boldsymbol{\mathcal{K}}_h[\boldsymbol{m}_h^i]$*, it holds that*

$$\left\langle \boldsymbol{v}_h^i, \boldsymbol{\phi}_h \right\rangle_{\boldsymbol{\mathcal{H}}} + \theta k \left\langle \boldsymbol{\nabla} \boldsymbol{v}_h^i, \boldsymbol{\nabla} \boldsymbol{\phi}_h \right\rangle = - \left\langle \boldsymbol{\nabla} \boldsymbol{m}_h^i, \boldsymbol{\nabla} \boldsymbol{\phi}_h \right\rangle . \tag{4.14}$$

(ii) Define

$$\boldsymbol{m}_h^{i+1} := \frac{\boldsymbol{m}_h^i + k\boldsymbol{v}_h^i}{\min_{z \in \mathcal{N}_h} |\boldsymbol{m}_h^i(z) + k\boldsymbol{v}_h^i(z)|} \in \mathcal{S}^1(\mathcal{T}_h)^3. \tag{4.15}$$

Output: If N^* *denotes the smallest integer satisfying the stopping condition, define the approximate stationary point* $\boldsymbol{m}_h := \boldsymbol{m}_h^{N^*}$.

The proof that as $h, k \to 0$, Algorithm 4.3.1 yields harmonic maps is similar to the proof for Algorithm 4.2.1. The only parts that require modification are Proposition 4.2.4, where we use the observation

$$1 \leq |\boldsymbol{m}_h^{i+1}(z)|^2 \leq |\boldsymbol{m}_h^i(z) + k\boldsymbol{v}_h^i(z)|^2$$

to show boundedness and prove that the constraint violation is bounded by the time-step, and Proposition 4.2.3 where (4.9) uses

$$\mathcal{E}[\boldsymbol{m}_h^{i+1}] \leq \mathcal{E}[\boldsymbol{m}_h^i + k\boldsymbol{v}_h^i].$$

This method of post-processing can be used for any micromagnetic energy where the energy is quadratic in $\boldsymbol{m}$ and strictly non-negative.

4.4 LLG dynamics

It is useful to see how the LLG equation is related to the gradient flow schemes for harmonic maps. For dynamical micromagnetic systems, we must turn to the LLG equation (2.31a). For simplicity, we again only consider the exchange energy

$$\mathcal{E}[\boldsymbol{m}] = \frac{1}{2} \|\boldsymbol{\nabla} \boldsymbol{m}\|^2$$

as in the harmonic map case. Then the initial value problem (2.31a)–(2.31c) becomes

$$\partial_t \boldsymbol{m} = -\boldsymbol{m} \times \boldsymbol{\Delta} \boldsymbol{m} + \alpha \boldsymbol{m} \times \partial_t \boldsymbol{m}, \tag{4.16a}$$

$$\boldsymbol{m}(0) = \boldsymbol{m}^0, \tag{4.16b}$$

$$\partial_{\boldsymbol{n}} \boldsymbol{m} = \boldsymbol{0}. \tag{4.16c}$$

We use the alternative form of the LLG equation suggested by Alouges [Alo08]. Using (B.1), we get

$$\begin{aligned} -\boldsymbol{m} \times (\boldsymbol{m} \times \boldsymbol{\Delta} \boldsymbol{m}) &= (\boldsymbol{m} \cdot \boldsymbol{m}) \boldsymbol{\Delta} \boldsymbol{m} - (\boldsymbol{m} \cdot \boldsymbol{\Delta} \boldsymbol{m}) \boldsymbol{m}, \\ \boldsymbol{m} \times (\boldsymbol{m} \times \partial_t \boldsymbol{m}) &= (\boldsymbol{m} \cdot \partial_t \boldsymbol{m}) \boldsymbol{m} - (\boldsymbol{m} \cdot \boldsymbol{m}) \partial_t \boldsymbol{m}. \end{aligned}$$

We can now apply the orthogonality $\boldsymbol{m} \cdot \partial_t \boldsymbol{m} = 0$ and unit length constraint $\boldsymbol{m} \cdot \boldsymbol{m} = 1$, resulting in

$$\begin{aligned} \boldsymbol{m} \times (\boldsymbol{m} \times \boldsymbol{\Delta} \boldsymbol{m}) &= (\boldsymbol{m} \cdot \boldsymbol{\Delta} \boldsymbol{m}) \boldsymbol{m} - \boldsymbol{\Delta} \boldsymbol{m}, \\ \boldsymbol{m} \times (\boldsymbol{m} \times \partial_t \boldsymbol{m}) &= -\partial_t \boldsymbol{m}. \end{aligned}$$

Lastly, differentiating the constraint $|\boldsymbol{m}|^2 = 1$ with respect to each spatial variable we have

$$\boldsymbol{m} \cdot \partial_i \boldsymbol{m} = 0, \text{ for } i = 1, 2, 3,$$

and differentiating once again,

$$\partial_i(\boldsymbol{m} \cdot \partial_i \boldsymbol{m}) = |\partial_i \boldsymbol{m}|^2 + \boldsymbol{m} \cdot \partial_{ii} \boldsymbol{m} = 0, \text{ for } i = 1, 2, 3,$$

which can be rewritten with the gradient and Laplace operators as the relation

$$-\boldsymbol{m} \cdot \boldsymbol{\Delta} \boldsymbol{m} = |\boldsymbol{\nabla} \boldsymbol{m}|^2.$$

By applying $\boldsymbol{m}\times$ to both sides of (4.16a) and combining the above, we get

$$\alpha \partial_t \boldsymbol{m} + \boldsymbol{m} \times \partial_t \boldsymbol{m} = \boldsymbol{\Delta} \boldsymbol{m} + |\boldsymbol{\nabla} \boldsymbol{m}|^2 \boldsymbol{m}. \tag{4.17}$$

We can then see that setting $\partial_t \boldsymbol{m} = \boldsymbol{0}$ yields the harmonic map Euler–Lagrange equation (4.2). Importantly, (4.17) is linear with respect to the velocity $\partial_t \boldsymbol{m}$, which inspires the choice of free variable $\boldsymbol{v} = \partial_t \boldsymbol{m}$, so that (4.17) becomes

$$\alpha \boldsymbol{v} + \boldsymbol{m} \times \boldsymbol{v} = \boldsymbol{\Delta} \boldsymbol{m} + |\boldsymbol{\nabla} \boldsymbol{m}|^2 \boldsymbol{m}, \tag{4.18}$$

subject to the orthogonality condition $\boldsymbol{m} \cdot \boldsymbol{v} = 0$. As for the harmonic map case, the last term is very non-linear, but can be eliminated once more by testing with functions $\boldsymbol{\phi}$ satisfying $\boldsymbol{m} \cdot \boldsymbol{\phi} = 0$. Therefore, the variational form of (4.18) is as follows: Find $\boldsymbol{v}(t) \in \boldsymbol{L}^2(\Omega)$ with $\boldsymbol{m}(t) \cdot \boldsymbol{v}(t) = 0$ a.e. in Ω such that

$$\alpha \left\langle \boldsymbol{v}, \boldsymbol{\phi} \right\rangle + \left\langle \boldsymbol{m} \times \boldsymbol{v}, \boldsymbol{\phi} \right\rangle = - \left\langle \boldsymbol{\nabla} \boldsymbol{m}, \boldsymbol{\nabla} \boldsymbol{\phi} \right\rangle, \tag{4.19}$$

for all $\boldsymbol{\phi} \in \boldsymbol{H}^1(\Omega)$ satisfying $\boldsymbol{m}(t) \cdot \boldsymbol{\phi} = 0$ a.e. in Ω. Comparing (4.5) to (4.19), we see that the metric of gradient flow is $\boldsymbol{L}^2$ multiplied by the damping parameter α, and on the left-hand side of (4.19) there is an additional precession term $\boldsymbol{m} \times \boldsymbol{v}$, but otherwise identical. The conditional projection scheme used in Algorithm 4.2.1 is less appropriate for dynamics. This is because the non-linearity of the projection can yield large time derivatives $\mathrm{d}_t \boldsymbol{m}_h^{i+1}$.

It is worth noting that equation (4.19) is the template for the fully discrete tangent plane schemes that will be applied later for the LLG equation. The first implementation of this will be seen in Algorithm 5.4.1.

4.5 Numerical experiments

To demonstrate the effectiveness of Algorithm 4.2.1 and Algorithm 4.3.1 at approximating harmonic maps, we consider two experiments. For the first experiment, we will use a very coarse mesh consisting of just two tetrahedra that are not weakly acute to demonstrate the behaviour when nodal-projections are not regularly made. The second experiment will use a much more refined mesh, suggesting that the nodal-projection step will normally occur. We consider three measures of quality:

- The energy at the final iteration $\mathcal{E}(\boldsymbol{m}_h^N)$.
- The unit length constraint violation $\left\|\mathcal{I}_h[|\boldsymbol{m}_h^N|^2] - 1\right\|_{L^1(\Omega)}$ at the final iteration.
- The nodal maximum error $\left\|\boldsymbol{m}_h^N\right\|_{\boldsymbol{L}^\infty(\Omega)} - 1$ at the final iteration.

4.5.1 Implementation

For the implementation of Algorithm 4.2.1 (and later algorithms), we use the PYTHON library Netgen/NGSolve [Sch25] for the general finite element implementation. For the tangent plane scheme we use the null-space method described in [RGJ13, KPP+19], but an alternative to the null-space method is a classical saddle-point scheme as described in [Bar15b, Section 7.2.5]. We shall discuss both methods here, but we stress that we do not apply the saddle-point scheme. We note here that the ordering in our description of the method is different to the references, as Netgen/NGSolve orders vector values in the form

$$[\phi_x(z_1), \phi_x(z_2), \ldots, \phi_x(z_N), \phi_y(z_1), \phi_y(z_2), \ldots, \phi_y(z_N), \phi_z(z_1), \ldots, \phi_z(z_N)]$$

where all x values are collected, followed by all y values, and then all z values as opposed to the ordering

$$[\phi_x(z_1), \phi_y(z_1), \phi_z(z_1), \phi_x(z_2), \phi_y(z_2), \phi_z(z_3), \ldots, \phi_x(z_N), \phi_y(z_N), \phi_z(z_N)].$$

For the purposes of this section, we will ignore the superscript i related to the iteration number. We denote by $\boldsymbol{e}_1, \boldsymbol{e}_2, \boldsymbol{e}_3$ the standard basis of $\mathbb{R}^3$, and enumerate the set of nodes $\mathcal{N}_h = \{z_n\}_{1\leq n\leq N}$ of $\mathcal{T}_h$. Belonging to $\mathcal{T}_h$ is the set of hat functions $\varphi_n = \varphi_{z_n}$, and we note that the set $\{\boldsymbol{\varphi}_i\}_{1\leq i\leq 3N}$ defined by

$$\boldsymbol{\varphi}_{n+N(p-1)} := \varphi_n \boldsymbol{e}_p, \qquad 1 \leq n \leq N, \quad 1 \leq p \leq 3,$$

is a basis of $\mathcal{S}^1(\mathcal{T}_h)^3$. The discretization of Algorithm 4.2.1 yields a system of equations

$$A\boldsymbol{v} = \boldsymbol{b}$$

where $A \in \mathbb{R}^{3N\times 3N}$ is the positive definite finite element matrix associated with the left-hand side of (4.6), i.e.

$$A_{ij} = \left\langle \boldsymbol{\varphi}_i, \boldsymbol{\varphi}_j \right\rangle_{\boldsymbol{\mathcal{H}}} + \theta k \left\langle \boldsymbol{\nabla}\boldsymbol{\varphi}_i, \boldsymbol{\nabla}\boldsymbol{\varphi}_j \right\rangle$$

and $\boldsymbol{v} \in \mathbb{R}^{3N}$ is the vector of nodal values of $\boldsymbol{v}_h$, in that

$$\boldsymbol{v}_h = \sum_{i=1}^{3N} v_i \boldsymbol{\varphi}_i.$$

The vector $\boldsymbol{b} \in \mathbb{R}^{3N}$ is the right-hand side of (4.6), i.e.

$$\boldsymbol{b}_i = -\left\langle \boldsymbol{\nabla}\boldsymbol{m}_h, \boldsymbol{\nabla}\boldsymbol{\varphi}_i \right\rangle,$$

where the magnetization function $\boldsymbol{m}_h$ is

$$\boldsymbol{m}_h = \sum_{i=1}^{3N} m_i \boldsymbol{\varphi}_i.$$

It is important to realize that without further modification, the unit length constraint is not realized. The saddle-point approach , the easier method of the two mentioned above, uses a matrix $B \in \mathbb{R}^{N\times 3N}$ satisfying $B\boldsymbol{v} = \mathbf{0}$, and we modify the system of equations to

$$\begin{bmatrix} A & B^T \\ B & 0 \end{bmatrix} \begin{bmatrix} \boldsymbol{v} \\ \boldsymbol{\lambda} \end{bmatrix} = \begin{bmatrix} \boldsymbol{b} \\ \mathbf{0} \end{bmatrix}$$

where $\boldsymbol{\lambda} \in \mathbb{R}^N$ is a Lagrange multiplier corresponding to the tangent space constraint. The matrix $B = [B_1, B_2, B_3]$ is simple to build, where for each $p = 1, 2, 3$

$$B_p = \begin{pmatrix} \frac{m_{1+N(p-1)}}{|\boldsymbol{m}_h(z_1)|} & 0 & \cdots & 0 \\ 0 & \frac{m_{2+N(p-1)}}{|\boldsymbol{m}_h(z_2)|} & \ddots & 0 \\ 0 & \ddots & \ddots & 0 \\ 0 & \cdots & 0 & \frac{m_{Np}}{|\boldsymbol{m}_h(z_N)|} \end{pmatrix} \in \mathbb{R}^{N\times N}.$$

Each block of B corresponds to one direction of $\boldsymbol{e}_1, \boldsymbol{e}_2, \boldsymbol{e}_3$, and a routine calculation shows that $\boldsymbol{v}_h \in \boldsymbol{\mathcal{K}}_h[\boldsymbol{m}_h]$ if and only if the vector of values $\boldsymbol{v}$ satisfies $B\boldsymbol{v} = \mathbf{0}$. We also have the identity

$$BB^\top = \sum_{i=1}^{3} B_i B_i^\top = I_{N\times N},$$

which follows from

$$B_p B_p^\top = \begin{pmatrix} \frac{m_{1+N(p-1)}^2}{|\boldsymbol{m}_h(z_1)|^2} & 0 & \cdots & 0 \\ 0 & \frac{m_{2+N(p-1)}^2}{|\boldsymbol{m}_h(z_2)|^2} & \ddots & 0 \\ 0 & \ddots & \ddots & 0 \\ 0 & \cdots & 0 & \frac{m_{Np}^2}{|\boldsymbol{m}_h(z_N)|^2} \end{pmatrix}$$

and the normalization condition for $i = 1, \ldots, N$

$$\sum_{p=1}^{3} \frac{m_{i+N(p-1)}^2}{|\boldsymbol{m}_h(z_i)|^2} = 1.$$

This modification has expanded the original $2N \times 2N$ problem of (4.6) to a $4N \times 4N$ system, so it will be more costly to solve, and the block matrix equation is not positive definite, despite the linear system being positive definite as seen in Proposition 4.2.3.

The null-space method is designed to avoid these deficits however, by introducing a matrix $Q \in \mathbb{R}^{2N\times 3N}$ which is called the "null-basis". We recall the construction as designed in [RGJ13], although an alternative construction based upon Householder reflections is given in [PRS16, Section 6.1.2]. To build Q, we write for each $j = 1 \dots N$, $\widehat{\boldsymbol{m}}_j = \frac{\boldsymbol{m}_h(z_j)}{|\boldsymbol{m}_h(z_j)|} = (u_j, v_j, w_j)$, and then define two orthonormal vectors $\boldsymbol{l}_j, \boldsymbol{n}_j$ via

$$\boldsymbol{l}_j = \frac{1}{\sqrt{v^2+w^2}} \begin{bmatrix} 0 \\ -w \\ v \end{bmatrix}, \qquad \boldsymbol{n}_j = \frac{1}{\sqrt{v^2+w^2}} \begin{bmatrix} v^2+w^2 \\ -uv \\ -uw \end{bmatrix};$$
$$\boldsymbol{l}_j = \frac{1}{\sqrt{u^2+w^2}} \begin{bmatrix} w \\ 0 \\ -u \end{bmatrix}, \qquad \boldsymbol{n}_j = \frac{1}{\sqrt{u^2+w^2}} \begin{bmatrix} -vu \\ u^2+w^2 \\ -vw \end{bmatrix};$$
$$\boldsymbol{l}_j = \frac{1}{\sqrt{u^2+v^2}} \begin{bmatrix} -v \\ u \\ 0 \end{bmatrix}, \qquad \boldsymbol{n}_j = \frac{1}{\sqrt{u^2+v^2}} \begin{bmatrix} -wu \\ -wv \\ u^2+v^2 \end{bmatrix},$$

where the first, second, and third options are chosen to depend upon which of $|u_j|, |v_j|, |w_j|$ is smallest respectively. The divisions are well-defined as $u_j^2 + v_j^2 + w_j^2 = 1$, and the triplet $(\widehat{\boldsymbol{m}}_j, \boldsymbol{n}_j, \boldsymbol{l}_j)$ forms an orthonormal basis. The null-basis $Q = [Q_1, Q_2, Q_3]$ is then defined by

$$Q_i = \begin{pmatrix} \boldsymbol{l}_1 \cdot \boldsymbol{e}_i & 0 & \cdots & 0 \\ \boldsymbol{n}_1 \cdot \boldsymbol{e}_i & 0 & \cdots & 0 \\ 0 & \boldsymbol{l}_2 \cdot \boldsymbol{e}_i & \cdots & 0 \\ 0 & \boldsymbol{n}_2 \cdot \boldsymbol{e}_i & \cdots & 0 \\ 0 & \ddots & \ddots & 0 \\ 0 & 0 & \cdots & \boldsymbol{l}_N \cdot \boldsymbol{e}_i \\ 0 & 0 & \cdots & \boldsymbol{n}_N \cdot \boldsymbol{e}_i \end{pmatrix} \in \mathbb{R}^{2N\times N}.$$

We again have that $QQ^\top = I_{2N\times 2N}$ because $\boldsymbol{n}_j, \boldsymbol{l}_j$ are orthonormal with respect to each other and the repeated block multiplication

$$\begin{pmatrix} \boldsymbol{l}_1 \cdot \boldsymbol{e}_i \\ \boldsymbol{n}_1 \cdot \boldsymbol{e}_i \end{pmatrix} \begin{pmatrix} \boldsymbol{l}_1 \cdot \boldsymbol{e}_i & \boldsymbol{n}_1 \cdot \boldsymbol{e}_i \end{pmatrix} = \begin{pmatrix} (\boldsymbol{l}_1 \cdot \boldsymbol{e}_i)^2 & (\boldsymbol{l}_1 \cdot \boldsymbol{e}_i)(\boldsymbol{n}_1 \cdot \boldsymbol{e}_i) \\ (\boldsymbol{l}_1 \cdot \boldsymbol{e}_i)(\boldsymbol{n}_1 \cdot \boldsymbol{e}_i) & (\boldsymbol{n}_1 \cdot \boldsymbol{e}_i)^2 \end{pmatrix}.$$

It is also true that Q is related to B by

$$B^\top B + Q^\top Q = I_{3N\times 3N}.$$

The resulting linear system is

$$(QAQ^\top)\boldsymbol{z} = Q\boldsymbol{b}$$

where $QAQ^\top \in \mathbb{R}^{2N\times 2N}$ is positive definite as

$$(QAQ^\top)\boldsymbol{z} \cdot \boldsymbol{z} = A(Q^\top \boldsymbol{z}) \cdot (Q^\top \boldsymbol{z}) \geq 0,$$

and $\boldsymbol{z}, (Q\boldsymbol{b}) \in \mathbb{R}^{2N}$. The desired vector $\boldsymbol{v}$ is retrieved via the relation $Q^T\boldsymbol{z} = \boldsymbol{v}$. Moreover, it is shown in [RGJ13, PRS16] that these formulations are identical to each other and the formulation (4.6), with a unique solution $\boldsymbol{v}$ or $\boldsymbol{z}$, depending upon the scheme chosen.

The resulting linear systems from either the saddle-point scheme or null-space method can be solved using GMRES, although we note that the conjugate gradient (CG) method is possible here for the null-space method as the linear systems are indeed symmetric. We do not use the CG method to make comparisons with the non-symmetric linear system that results from the discretization of the LLG equations. The GMRES settings chosen were the defaults given in SciPy, with a relative tolerance of $1 \cdot 10^{-8}$. The solver restarts when the number of iterations exceeds $\max(20, n)$ where n refers to the length of the right-hand side vector. The preconditioner used is a sparse incomplete LU decomposition preconditioner provided by the SciPy library. We used the default settings, which has a drop tolerance of $1 \cdot 10^{-4}$ and a fill factor of 10.

Lastly, in terms of actual real implementation in code we have the following recommendations for testing. The dot product between $\boldsymbol{m}_h^{i+1}(z)$ and $\boldsymbol{v}_h^i$ should be computed nodewise at each iteration. If this value is not close to zero, then the solver is failing. The computed value we used was

$$\max |Bv_h^i|.$$

When it comes to the actual writing of the code, for the saddle-point scheme we recommend checking that

$$BB^\top = I_{N\times N}$$

for various normalised magnetisation vectors and for the null-space method we recommend checking that

$$B^\top B + Q^\top Q = I_{3N\times 3N}.$$

4.5.2 Coarse mesh

For this experiment, we use the coarse mesh defined via the vertices listed in Table 4.1. The discrete initial condition is also defined in Table 4.1, yielding an initial energy of $\mathcal{E}[\boldsymbol{m}_h^0] \approx 1.5$ and mesh size $h \approx 4.6$. This mesh is not weakly acute, hence methods that rely fully on projection are not stable. We choose the parameters $k = 0.01$, $\varepsilon = 1 \cdot 10^{-7}$, $\theta = 0.50000005$ with the mass-lumped L^2-gradient metric. The algorithm runs for 3061 iterations, of which 764 involved a nodal-projection step. The energy decreases as expected, as shown in Figure 4.3a. Algorithm 4.2.1 applies only nodal-projections from iteration 0 until iteration 247. After this, it is fully projection-free until iteration 833, where a single projection is made, followed by fully projection-free until iteration 1385 where another single projection is made, followed by projection-free iterations. There are no further projections until iteration 1935, after which the choice of projection vs. projection-free appears to be random.

For reference, we run Algorithm 4.2.1 with the conditional component disabled, yielding a fully projection-free algorithm as in [Bar15b, Algorithm 7.2] that ran

x	y	z	$\boldsymbol{m}_h^0(x,y,z)$
2.00	0.00	0.00	$(1,0,0)$
0.00	2.00	0.00	$(0,1,0)$
-0.782	0.177	0.934	$(0,0,1)$
-1.675	-1.904	2.00	$(1/\sqrt{2},1/\sqrt{2},0)$
0.00	0.00	0.00	$(0,1/\sqrt{2},1/\sqrt{2})$

Table 4.1: Vertices used in the coarse mesh of Experiment 4.5.2.

for 3036 iterations. The energetic behaviour is roughly the same as the conditional variant as seen in Figure 4.3b, and both algorithms take almost the same number of iterations. However, the unit length constraint violation is considerably worse as is obvious in Figure 4.3d, being around 3 orders of magnitude larger than the maximum constraint error of Algorithm 4.2.1. Similarly, in Figures 4.3e and 4.3f we see that the projection-free algorithm has a much larger error in the nodal maximum norm than the conditional projection algorithm.

We note that for each algorithm, the number of GMRES iterations was 1.

Figure 4.3c indicates the non-linear nature of the nodal-projection operator Π_h, where first isolated projection results in a very sharp decrease in the unit length constraint. The non-linearity of Π_h is the reason for the requirement of highly structured meshes with restrictive angle conditions.

4.5.3 Refined mesh

For this experiment, we consider the unit cube $[-1/2,1/2]^3$, discretized into 891 vertices and 3831 elements, with $h \approx 0.24$. As this mesh is generated in an unstructured way, it is not weakly acute. For the initial condition, we assign each node three random numbers from $(-1,1)$ for m_x, m_y, m_z respectively and normalize so that $\boldsymbol{m}_h^0 \in \boldsymbol{\mathcal{M}}_{h,0}$. For the resulting initial condition, we have $\mathcal{E}[\boldsymbol{m}_h^0] \approx 199.4$. We then use the same parameters as in Section 4.5.2. Algorithm 4.2.1 ran for 196 iterations, of which 171 involved a nodal-projection. The first projection-free iteration occurs at iteration 136, after which Algorithm 4.2.1 alternates between applying a projection or not. We then ran the projection-free scheme as a reference, which lasted for 972 iterations, and also Algorithm 4.3.1 which needed 968 iterations to reach the stopping condition. We see once again that the energetic behaviour is roughly the same for all three algorithms at the beginning, but in Figure 4.3b the final energy is $\mathcal{E}[\boldsymbol{m}_h^{972}] \approx 24$, which is much greater than the expected energy of zero approached by Algorithm 4.2.1 in Figure 4.4a. This is directly due to the failure to maintain the unit length constraint. The final energy achieved by Algorithm 4.3.1 was $\mathcal{E}(\boldsymbol{m}_h^{968}) \approx 22$, a small improvement. In Figures 4.4d and 4.4g the violation is on the order of 10^{-13}, which is essentially zero. In Figures 4.4e and 4.4h on the other hand, the violation is around 1.75 and 2.5 respectively. Between Figures 4.4e and 4.4f, the post-processing has reduced the final constraint violation from 1.75 for the projection-free algorithm to 1.5 for Algorithm 4.3.1. Similarly, the nodal maximum error from Algorithm 4.3.1 shown

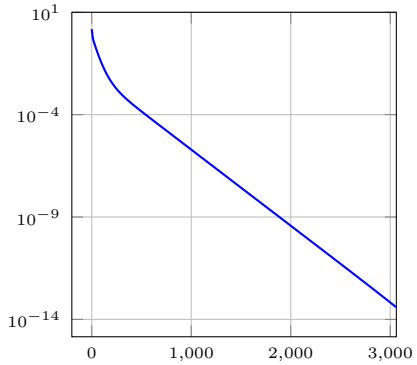

(a) Energy.

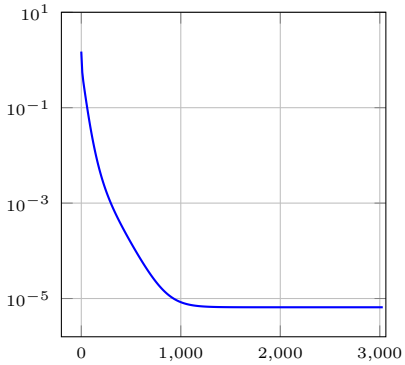

(b) Energy.

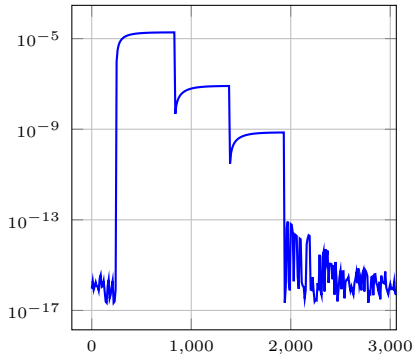

(c) Unit length constraint violation.

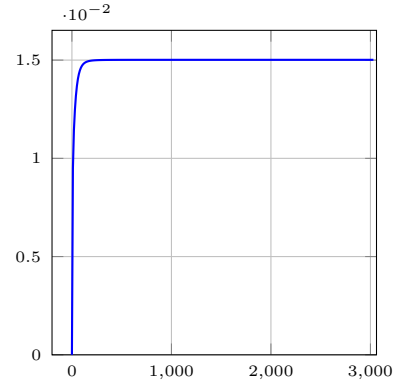

(d) Unit length constraint violation.

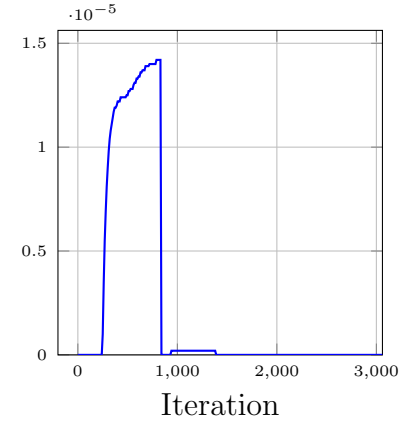

(e) Nodal max error.

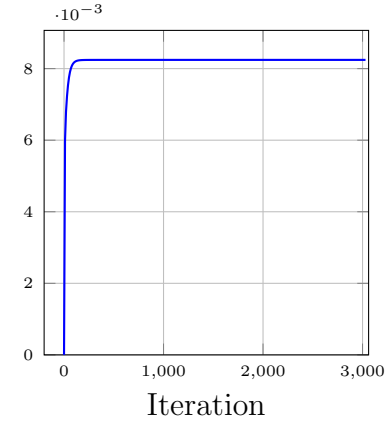

(f) Nodal max error.

Figure 4.3: Experiment of Section 4.5.2. (a), (b) Energy $\mathcal{E}[\boldsymbol{m}_h^i]$, (c), (d) unit length constraint violation $\|\mathcal{I}_h[|\boldsymbol{m}_h^i|^2] - 1\|_{L^1(\Omega)}$ (e), (f) nodal maximum error $\|\boldsymbol{m}_h^i\|_{\boldsymbol{L}^\infty(\Omega)} - 1$, computed with Algorithm 4.2.1 (left) and the projection-free variant (right).

in Figure 4.4i is around 2.4 as opposed to 2.6 for the projection-free algorithm, as seen in Figure 4.4h. It follows that the post-processing step improves the energy minimization and the unit length constraints, but this effect will be weaker for

smaller time-steps.

We note that the average number of GMRES iterations for each algorithm was 2.

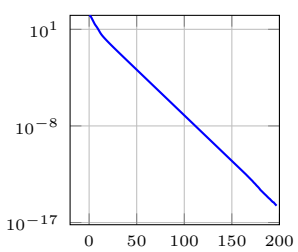

(a) Energy.

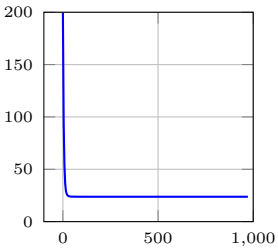

(b) Energy.

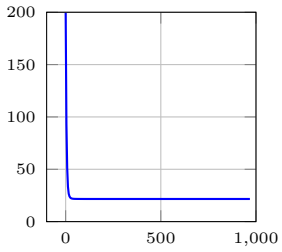

(c) Energy.

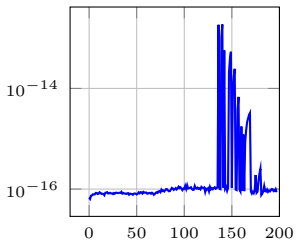

(d) Constraint violation.

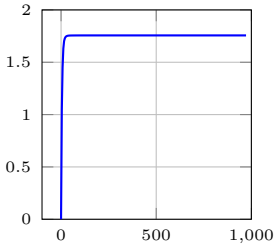

(e) Constraint violation.

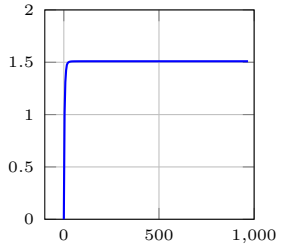

(f) Constraint violation.

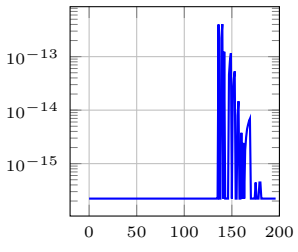

(g) Nod.max error.

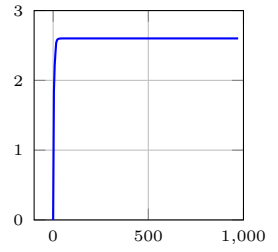

(h) Nod.max error.

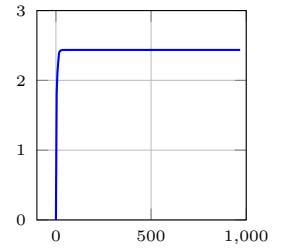

(i) Nod.max error.

Figure 4.4: Experiment of Section 4.5.3. (a), (b), (c) Energy $\mathcal{E}[\boldsymbol{m}_h^i]$, (d), (e), (f) unit length constraint violation $\|\mathcal{I}_h[|\boldsymbol{m}_h^i|^2] - 1\|_{L^1(\Omega)}$ (g), (h), (i) nodal maximum error $\|\boldsymbol{m}_h^i\|_{\boldsymbol{L}^\infty(\Omega)} - 1$, computed with Algorithm 4.2.1 (left), the projection-free variant (middle), and Algorithm 4.3.1 (right) respectively.

0

Chapter 5

Magnetostriction I

For the paper that this chapter is based on, see [NR25c].

5.1 Introduction

In this chapter, we design and analyse a fully discrete numerical scheme for the coupled nonlinear system of partial differential equations (PDEs) modelling the dynamics of magnetization and displacement in magnetoelastic materials in the small-strain regime (see Section 2.4). The proposed system consists of the LLG equation for the magnetization and the conservation of linear momentum law for the displacement (see (5.4)–(5.5) below). The two equations are non-linearly coupled to each other: one of the contributions to the effective field appearing in the LLG equation depends on the mechanical stress in the body (and thus on the displacement) and there is a magnetization-dependent contribution to the strain (usually referred to as the magnetostrain) in the conservation of momentum law. One additional difficulty is represented by a nonconvex pointwise constraint on the magnetization, which is a vector field of constant unit length.

Summarizing, the contribution of the present chapter over the existing literature (and, in particular, over [Vis85, CEF11, BPPR14]) is threefold:

- We consider a more general setting than in [Vis85, CEF11, BPPR14] including volume/surface forces and a more general magnetoelastic contribution based upon the magnetostriction tensor $\mathbb{Z}$ (see equation (5.1) below), which allows for more general crystal classes to be considered. In particular, previous papers have described this tensor as fully symmetric and positive definite, e.g. [Vis85, BPPR14, Baň05, Baň08, CEF11], which is not true in general (such as in nickel, which has negative magnetostriction). Since our convergence proof is constructive, a byproduct of our analysis is a proof of existence of weak solutions for a more general model of magnetoelastic materials in the small-strain regime.
- Our integrator is energetically "mindful", in the sense that our approximations satisfy a discrete energy law which resembles the one satisfied by solutions of the continuous problem (cf. Proposition 5.4.4 below). Under a

restrictive CFL-like condition on the discretization parameters, specifically $k = o(h^9)$, we can pass the result to the limit and obtain an energy inequality for weak solutions. This aspect was not considered in [BPPR14], where only boundedness of energy was proven. Numerical experiments show robustness of the energetic behaviour of the integrator, which seems to indicate that the restrictive CFL-like condition might be an artifact of the proof.

- The spatial meshes used by our integrator are assumed to be only shape-regular (and do not need to be weakly acute as in [BPPR14]). This allows for the use of general mesh generators. This is especially useful in three dimensions, as weakly acute meshes are difficult to generate for arbitrary shapes [BKK+20]. Following [Bar16, AHP+14], the assumption on the meshes is removed by omitting the nodal projection from the magnetization update. However, the nodal projection is kept for the magnetization appearing in the magnetoelastic terms for the sake of unconditional stability. These modifications of the original algorithm of [BPPR14] give rise to additional errors that need to be controlled, which makes the analysis more involved (e.g. a more accurate estimate of the projection error is needed; see Lemma 5.6.6 below). Finally, the discrete variational problems appearing in our integrator are standard and therefore easy to implement in standard finite element packages. For example, like in the rest of the thesis, we use Netgen/NGSolve [Sch25].

5.2 Model problem

Let $\Omega \subset \mathbb{R}^3$ be a bounded Lipschitz domain representing the volume occupied by a ferromagnetic body. We assume the boundary $\partial\Omega$ is split into two disjoint relatively open parts Γ_D (of positive surface measure) and Γ_N, i.e. $\partial\Omega = \overline{\Gamma}_D \cup \overline{\Gamma}_N$ and $\Gamma_D \cap \Gamma_N = \emptyset$. Let $T > 0$ denote some final time.

The magnetomechanical state of the material is described by two vector fields: the displacement $\boldsymbol{u} : \Omega \times (0,T) \to \mathbb{R}^3$ and the magnetization $\boldsymbol{m} : \Omega \times (0,T) \to \mathbb{S}^2$. The total strain $\boldsymbol{\varepsilon}$ is made up of the elastic strain $\boldsymbol{\varepsilon}_{\mathrm{el}}$ and the magnetization-dependent generally incompatible (in the sense that it does not satisfy the Saint–Venant compatibility conditions [ACGK06, MMHH+14]) magnetostrain $\boldsymbol{\varepsilon}_{\mathrm{m}}$, i.e. $\boldsymbol{\varepsilon} = \boldsymbol{\varepsilon}_{\mathrm{el}} + \boldsymbol{\varepsilon}_{\mathrm{m}}$. The total strain is given by

$$\boldsymbol{\varepsilon}(\boldsymbol{u}) = \frac{1}{2}\left(\boldsymbol{\nabla}\boldsymbol{u} + \boldsymbol{\nabla}\boldsymbol{u}^{\top}\right)$$

(strain-displacement relation). Following [FCV19], we consider the expression

$$\boldsymbol{\varepsilon}_{\mathrm{m}}(\boldsymbol{m}) = \mathbb{Z} : (\boldsymbol{m} \otimes \boldsymbol{m}), \tag{5.1}$$

where $\mathbb{Z} \in \mathbb{R}^{3^4}$ is a fourth-order tensor, which we assume to be minorly symmetric (i.e. $\mathbb{Z}_{ij\ell m} = \mathbb{Z}_{ji\ell m} = \mathbb{Z}_{ijm\ell}$ for all $i,j,\ell,m = 1,2,3$, cf. Appendix B.2). It follows that

$$\boldsymbol{\varepsilon}_{\mathrm{el}}(\boldsymbol{u},\boldsymbol{m}) = \boldsymbol{\varepsilon}(\boldsymbol{u}) - \boldsymbol{\varepsilon}_{\mathrm{m}}(\boldsymbol{m}).$$

The elastic part of the strain compensates for the magnetic part to make the total strain compatible [MMHH+14]. The elastic strain is related to the stress tensor $\boldsymbol{\sigma}$ by Hooke's law

$$\boldsymbol{\sigma}(\boldsymbol{u}, \boldsymbol{m}) = \mathbb{C} : \boldsymbol{\varepsilon}_{\mathrm{el}}(\boldsymbol{u}, \boldsymbol{m}),$$

where $\mathbb{C} \in \mathbb{R}^{3^4}$ is the fourth-order, fully symmetric (i.e. $\mathbb{C}_{ij\ell m} = \mathbb{C}_{\ell mij} = \mathbb{C}_{ji\ell m} = \mathbb{C}_{ijm\ell}$ for all $i, j, \ell, m = 1, 2, 3$, cf. Appendix B.2), positive definite stiffness tensor. The elastic energy reads as

$$\mathcal{E}_{\mathrm{el}}[\boldsymbol{u}, \boldsymbol{m}] = \frac{1}{2} \int_\Omega [\boldsymbol{\varepsilon}(\boldsymbol{u}) - \boldsymbol{\varepsilon}_{\mathrm{m}}(\boldsymbol{m})] : \{\mathbb{C} : [\boldsymbol{\varepsilon}(\boldsymbol{u}) - \boldsymbol{\varepsilon}_{\mathrm{m}}(\boldsymbol{m})]\} - \int_\Omega \boldsymbol{f} \cdot \boldsymbol{u} - \int_{\Gamma_N} \boldsymbol{g} \cdot \boldsymbol{u},$$

where the last two terms model the work done by a volume force $\boldsymbol{f} : \Omega \to \mathbb{R}^3$ and a surface force $\boldsymbol{g} : \Gamma_N \to \mathbb{R}^3$ (traction), both assumed to be constant in time. The magnetic energy, for simplicity assumed to comprise only the Heisenberg exchange contribution, is given by

$$\mathcal{E}_{\mathrm{m}}[\boldsymbol{m}] = \frac{1}{2} \int_\Omega |\boldsymbol{\nabla} \boldsymbol{m}|^2. \tag{5.2}$$

The total free energy of the system is defined as the sum of the magnetic and elastic energies, i.e.

$$\begin{aligned} \mathcal{E}[\boldsymbol{u}, \boldsymbol{m}] &= \mathcal{E}_{\mathrm{m}}[\boldsymbol{m}] + \mathcal{E}_{\mathrm{el}}[\boldsymbol{u}, \boldsymbol{m}] \\ &= \frac{1}{2} \int_\Omega |\boldsymbol{\nabla} \boldsymbol{m}|^2 + \frac{1}{2} \int_\Omega [\boldsymbol{\varepsilon}(\boldsymbol{u}) - \boldsymbol{\varepsilon}_{\mathrm{m}}(\boldsymbol{m})] : \{\mathbb{C} : [\boldsymbol{\varepsilon}(\boldsymbol{u}) - \boldsymbol{\varepsilon}_{\mathrm{m}}(\boldsymbol{m})]\} \\ &\qquad - \int_\Omega \boldsymbol{f} \cdot \boldsymbol{u} - \int_{\Gamma_N} \boldsymbol{g} \cdot \boldsymbol{u}. \end{aligned} \tag{5.3}$$

The dynamics of $\boldsymbol{u}$ and $\boldsymbol{m}$ is governed by the coupled system of the conservation of (linear) momentum law and the LLG equation

$$\partial_{tt} \boldsymbol{u} = \nabla \cdot \boldsymbol{\sigma}(\boldsymbol{u}, \boldsymbol{m}) + \boldsymbol{f} \qquad \text{in } \Omega \times (0, T), \tag{5.4}$$

$$\partial_t \boldsymbol{m} = -\boldsymbol{m} \times \boldsymbol{h}_{\mathrm{eff}}[\boldsymbol{u}, \boldsymbol{m}] + \alpha\, \boldsymbol{m} \times \partial_t \boldsymbol{m} \qquad \text{in } \Omega \times (0, T), \tag{5.5}$$

supplemented with the initial and boundary conditions

$$\boldsymbol{u}(0) = \boldsymbol{u}^0 \qquad \text{in } \Omega, \tag{5.6a}$$

$$\partial_t \boldsymbol{u}(0) = \dot{\boldsymbol{u}}^0 \qquad \text{in } \Omega, \tag{5.6b}$$

$$\boldsymbol{m}(0) = \boldsymbol{m}^0 \qquad \text{in } \Omega, \tag{5.6c}$$

$$\boldsymbol{u} = \boldsymbol{0} \qquad \text{on } \Gamma_D \times (0, T), \tag{5.6d}$$

$$\boldsymbol{\sigma} \boldsymbol{n} = \boldsymbol{g} \qquad \text{on } \Gamma_N \times (0, T), \tag{5.6e}$$

$$\partial_{\boldsymbol{n}} \boldsymbol{m} = \boldsymbol{0} \qquad \text{on } \partial\Omega \times (0, T), \tag{5.6f}$$

where $\boldsymbol{u}^0, \dot{\boldsymbol{u}}^0 : \Omega \to \mathbb{R}^3$ and $\boldsymbol{m}^0 : \Omega \to \mathbb{S}^2$ are suitable initial data, while $\boldsymbol{n} : \partial\Omega \to \mathbb{S}^2$ denotes the outward-pointing unit normal vector to $\partial\Omega$. In (5.5), $\alpha > 0$ denotes the Gilbert damping parameter, whereas the effective field $\boldsymbol{h}_{\mathrm{eff}}[\boldsymbol{u}, \boldsymbol{m}]$ is the variational derivative of the free energy with respect to the magnetization, i.e.

$$\boldsymbol{h}_{\mathrm{eff}}[\boldsymbol{u}, \boldsymbol{m}] = -\frac{\delta \mathcal{E}[\boldsymbol{u}, \boldsymbol{m}]}{\delta \boldsymbol{m}} = \boldsymbol{\Delta} \boldsymbol{m} + \boldsymbol{h}_{\mathrm{m}}[\boldsymbol{u}, \boldsymbol{m}],$$

where the elastic field reads as

$$\boldsymbol{h}_{\mathrm{m}}[\boldsymbol{u},\boldsymbol{m}] = 2\,[\mathbb{Z}^{\top} : \boldsymbol{\sigma}(\boldsymbol{u},\boldsymbol{m})]\boldsymbol{m} = 2\,(\mathbb{Z}^{\top} : \{\mathbb{C} : [\boldsymbol{\varepsilon}(\boldsymbol{u}) - \boldsymbol{\varepsilon}_{\mathrm{m}}(\boldsymbol{m})]\})\boldsymbol{m}, \tag{5.7}$$

with $\mathbb{Z}^{\top}$ being the transpose of $\mathbb{Z}$ (cf. Appendix B.2). Note that (5.4) can be rewritten as

$$\partial_{tt}\boldsymbol{u} = -\frac{\delta\mathcal{E}[\boldsymbol{u},\boldsymbol{m}]}{\delta\boldsymbol{u}}.$$

A simple formal calculation reveals that sufficiently smooth solutions to (5.4)–(5.6) satisfy the energy law

$$\frac{\mathrm{d}}{\mathrm{d}t}\left(\mathcal{E}[\boldsymbol{u}(t),\boldsymbol{m}(t)] + \frac{1}{2}\left\|\partial_t\boldsymbol{u}(t)\right\|^2\right) = -\alpha\left\|\partial_t\boldsymbol{m}(t)\right\|^2 \leq 0, \tag{5.8}$$

i.e., the sum of the total energy (5.3) (which can be understood as a potential energy) and the kinetic energy $\|\partial_t\boldsymbol{u}\|^2/2$ decays over time, with the decay being modulated by α.

For the data of the problem, we assume that $\mathbb{C} \in \boldsymbol{L}^{\infty}(\Omega)$ is uniformly positive definite, i.e., there exists $C_0 > 0$ such that

$$\boldsymbol{A} : (\mathbb{C} : \boldsymbol{A}) \geq C_0\left\|\boldsymbol{A}\right\|^2 \quad \text{for all } \boldsymbol{A} \in \mathbb{R}^{3\times 3}, \tag{5.9}$$

$\mathbb{Z} \in \boldsymbol{L}^{\infty}(\Omega)$, $\boldsymbol{f} \in \boldsymbol{L}^2(\Omega)$, $\boldsymbol{g} \in \boldsymbol{L}^2(\Gamma_N)$, $\boldsymbol{u}^0 \in \boldsymbol{H}^1(\Omega)$, $\dot{\boldsymbol{u}}^0 \in \boldsymbol{L}^2(\Omega)$, and $\boldsymbol{m}^0 \in \boldsymbol{H}^1(\Omega;\mathbb{S}^2)$. In the following definition, we state the notion of a weak solution of the initial boundary value problem (5.4)–(5.6); see [CEF11]. Hereafter, we shall denote L^2-integrals in space over some domain D with $\langle\cdot,\cdot\rangle_D$, omitting the subscript if $D = \Omega$. Moreover, we denote by Ω_T the space-time cylinder $\Omega \times (0,T)$.

Definition 5.2.1. *We say that a pair $(\boldsymbol{u},\boldsymbol{m}) : \Omega_T \to \mathbb{R}^3 \times \mathbb{R}^3$ is a weak solution to the initial boundary value problem (5.4)–(5.6) if the following conditions hold:*

(i) *It is the case that both $\boldsymbol{u} \in L^{\infty}(0,T;\boldsymbol{H}^1_D(\Omega))$ with $\partial_t\boldsymbol{u} \in L^{\infty}(0,T;\boldsymbol{L}^2(\Omega))$ and $\boldsymbol{m} \in L^{\infty}(0,T;\boldsymbol{H}^1(\Omega;\mathbb{S}^2))$ with $\partial_t\boldsymbol{m} \in L^2(0,T;\boldsymbol{L}^2(\Omega))$;*

(ii) *for all $\boldsymbol{\xi} \in \boldsymbol{C}^{\infty}_c([0,T);\boldsymbol{C}^{\infty}(\overline{\Omega}))$ and $\boldsymbol{\varphi} \in \boldsymbol{C}^{\infty}(\overline{\Omega_T})$, we have*

$$\begin{aligned}
&-\int_0^T \langle\partial_t\boldsymbol{u}(t),\partial_t\boldsymbol{\xi}(t)\rangle\,\mathrm{d}t + \int_0^T \langle\mathbb{C} : [\boldsymbol{\varepsilon}(\boldsymbol{u}(t)) - \boldsymbol{\varepsilon}_{\mathrm{m}}(\boldsymbol{m}(t))],\boldsymbol{\varepsilon}(\boldsymbol{\xi}(t))\rangle\,\mathrm{d}t \\
&\qquad = \int_0^T \langle\boldsymbol{f},\boldsymbol{\xi}(t)\rangle\,\mathrm{d}t + \int_0^T \langle\boldsymbol{g},\boldsymbol{\xi}(t)\rangle_{\Gamma_N}\,\mathrm{d}t + \left\langle\dot{\boldsymbol{u}}^0,\boldsymbol{\xi}(0)\right\rangle,
\end{aligned} \tag{5.10}$$

$$\begin{aligned}
&\int_0^T \langle\partial_t\boldsymbol{m}(t),\boldsymbol{\varphi}(t)\rangle\,\mathrm{d}t - \alpha\int_0^T \langle\boldsymbol{m}(t)\times\partial_t\boldsymbol{m}(t),\boldsymbol{\varphi}(t)\rangle\,\mathrm{d}t \\
&\qquad = \int_0^T \langle\boldsymbol{m}(t)\times\boldsymbol{\nabla}\boldsymbol{m}(t),\boldsymbol{\nabla}\boldsymbol{\varphi}(t)\rangle\,\mathrm{d}t \\
&\qquad\quad - \int_0^T \langle\boldsymbol{m}(t)\times\boldsymbol{h}_{\mathrm{m}}[\boldsymbol{u}(t),\boldsymbol{m}(t)],\boldsymbol{\varphi}(t)\rangle\,\mathrm{d}t;
\end{aligned} \tag{5.11}$$

(iii) *the initial conditions* $\boldsymbol{u}(0) = \boldsymbol{u}^0$ *and* $\boldsymbol{m}(0) = \boldsymbol{m}^0$ *hold in the sense of traces;*

(iv) *for almost all* $t' \in (0, T)$*, it holds that*

$$\mathcal{E}[\boldsymbol{u}(t'), \boldsymbol{m}(t')] + \frac{1}{2} \|\partial_t \boldsymbol{u}(t')\|^2 + \alpha \int_0^{t'} \|\partial_t \boldsymbol{m}(t)\|^2 \, \mathrm{d}t \leq \mathcal{E}[\boldsymbol{u}^0, \boldsymbol{m}^0] + \frac{1}{2} \left\|\dot{\boldsymbol{u}}^0\right\|^2. \quad (5.12)$$

Equations (5.10) and (5.11) are space-time variational formulations of (5.4) and (5.5), respectively. the initial condition (5.6b) and the boundary conditions (5.6e) and (5.6f) are imposed as natural boundary conditions in the variational formulations; the initial conditions (5.6a) and (5.6c) are imposed in the sense of traces in (iii); The Dirichlet boundary condition (5.6d) is imposed as an essential boundary condition. Equation (5.12) is the weak counterpart of the energy law (5.8) satisfied by strong solutions.

Remark 5.2.2. *Formula* (5.1) *is the general expression of the magnetostrain for anisotropic ferromagnets [FCV19] and covers the typical forms of the magnetostrain found in literature. These usually assume that the magnetostrain is* isochoric *[HS98, Section 3.2.6] (i.e. it has zero trace). In an isochoric material, the magnetic body elongates (contracts) in the magnetization direction, and contracts (elongates) in the other two for positive (negative) magnetostriction. An example of positive magnetostriction is shown in Figure 2.4. Importantly, formula* (5.1) *covers the common* cubic *case, considered in e.g., [JW98, SLW04, MMHH+14, RBJ21b, RBJ21a] and given by*

$$\boldsymbol{\varepsilon}_{\mathrm{m}}(\boldsymbol{m}) = \frac{3}{2} \left\{ \lambda_{100} \left(\boldsymbol{m} \otimes \boldsymbol{m} - \frac{I}{3} \right) + (\lambda_{111} - \lambda_{100}) \sum_{\substack{i,j=1 \\ i \neq j}}^{3} (\boldsymbol{m} \cdot \boldsymbol{e}_i^{\mathrm{c}})(\boldsymbol{m} \cdot \boldsymbol{e}_j^{\mathrm{c}})(\boldsymbol{e}_i^{\mathrm{c}} \otimes \boldsymbol{e}_j^{\mathrm{c}}) \right\},$$

where $I \in \mathbb{R}^{3\times 3}$ *denotes the* 3*-by-*3 *identity matrix,* $\lambda_{100}, \lambda_{111} \in \mathbb{R}$ *are material constants, and* $\{\boldsymbol{e}_1^{\mathrm{c}}, \boldsymbol{e}_2^{\mathrm{c}}, \boldsymbol{e}_3^{\mathrm{c}}\}$ *denotes an orthonormal set yielding the crystal basis. When* $\lambda_{100} = \lambda_{111}$*, the latter reduces to the so-called* isotropic *case*

$$\boldsymbol{\varepsilon}_{\mathrm{m}}(\boldsymbol{m}) = \frac{3}{2} \lambda_{100} \left(\boldsymbol{m} \otimes \boldsymbol{m} - \frac{I}{3} \right), \quad (5.13)$$

considered in e.g., [BHB+14, PWH+15, DW23a]. For further details regarding specific crystal classes and their magnetostrain representation, we refer to [FCV19].

Remark 5.2.3. *For the sake of simplicity (and since the focus of this work is on the design of a numerical method for the coupled system* (5.4)–(5.5)*), we neglect from the magnetic energy* (5.2) *all lower-order contributions (magnetocrystalline anisotropy, Zeeman energy, magnetostatic energy, Dzyaloshinskii–Moriya interaction). However, we note that their numerical integration is well understood; see e.g. [BFF+14, DFPP+20, HPP+19].*

5.3 Preliminaries

For general preliminaries, see Chapter 3. In this section, we only include the additional preliminaries not otherwise mentioned previously.

5.3.1 Space discretization

We consider the space $\mathcal{S}^1_D(\mathcal{T}_h) = \mathcal{S}^1(\mathcal{T}_h) \cap H^1_D(\Omega)$, where homogeneous Dirichlet boundary conditions on Γ_D are imposed explicitly. For all $0 \leq i \leq N$, the approximate displacement at time t_i, $\boldsymbol{u}_h^i \approx \boldsymbol{u}(t_i)$, will be sought in the finite element space $\mathcal{S}^1_D(\mathcal{T}_h)^3$.

5.4 Algorithm and main results

In the following algorithm, we state the fully discrete numerical scheme we propose to approximate solutions to the initial boundary value problem (5.4)–(5.6). We recall that the nodal projection operator is denoted by $\Pi_h : \boldsymbol{\mathcal{M}}_{h,\delta} \to \boldsymbol{\mathcal{M}}_{h,0}$, and acts on a function $\boldsymbol{\phi} \in \boldsymbol{\mathcal{M}}_{h,\delta}$ via $\Pi_h \boldsymbol{\phi}_h(z) = \boldsymbol{\phi}(z)/|\boldsymbol{\phi}(z)|$ for each node $z \in \mathcal{N}_h$.

Algorithm 5.4.1 (decoupled algorithm for the LLG equation with magnetostriction)**.** *Discretization parameters: Mesh size $h > 0$, time-step size $k > 0$, $\theta \in (1/2, 1]$.*
Input: Approximate initial conditions $\boldsymbol{m}_h^0 \in \boldsymbol{\mathcal{M}}_{h,0}$, $\boldsymbol{u}_h^0 \in \mathcal{S}^1_D(\mathcal{T}_h)^3$, $\dot{\boldsymbol{u}}_h^0 \in \mathcal{S}^1(\mathcal{T}_h)^3$.
Loop: For all integers $0 \leq i \leq N-1$, iterate (i)–(iii)*:*

(i) *Compute $\boldsymbol{v}_h^i \in \boldsymbol{\mathcal{K}}_h[\boldsymbol{m}_h^i]$ such that, for all $\boldsymbol{\phi}_h \in \boldsymbol{\mathcal{K}}_h[\boldsymbol{m}_h^i]$, it holds that*

$$\alpha \left\langle \boldsymbol{v}_h^i, \boldsymbol{\phi}_h \right\rangle_h + \left\langle \boldsymbol{m}_h^i \times \boldsymbol{v}_h^i, \boldsymbol{\phi}_h \right\rangle_h + \theta k \left\langle \boldsymbol{\nabla} \boldsymbol{v}_h^i, \boldsymbol{\nabla} \boldsymbol{\phi}_h \right\rangle = -\left\langle \boldsymbol{\nabla} \boldsymbol{m}_h^i, \boldsymbol{\nabla} \boldsymbol{\phi}_h \right\rangle + \left\langle \boldsymbol{h}_{\mathrm{m}}[\boldsymbol{u}_h^i, \Pi_h \boldsymbol{m}_h^i], \boldsymbol{\phi}_h \right\rangle . \quad (5.14)$$

(ii) *Define*

$$\boldsymbol{m}_h^{i+1} := \boldsymbol{m}_h^i + k \boldsymbol{v}_h^i \in \mathcal{S}^1(\mathcal{T}_h)^3. \quad (5.15)$$

(iii) *Compute $\boldsymbol{u}_h^{i+1} \in \mathcal{S}^1_D(\mathcal{T}_h)^3$ such that, for all $\boldsymbol{\psi}_h \in \mathcal{S}^1_D(\mathcal{T}_h)^3$, it holds that*

$$\left\langle \mathrm{d}_t^2 \boldsymbol{u}_h^{i+1}, \boldsymbol{\psi}_h \right\rangle + \left\langle \mathbb{C} : \boldsymbol{\varepsilon}(\boldsymbol{u}_h^{i+1}), \boldsymbol{\varepsilon}(\boldsymbol{\psi}_h) \right\rangle = \left\langle \mathbb{C} : \boldsymbol{\varepsilon}_{\mathrm{m}}(\Pi_h \boldsymbol{m}_h^{i+1}), \boldsymbol{\varepsilon}(\boldsymbol{\psi}_h) \right\rangle + \langle \boldsymbol{f}, \boldsymbol{\psi}_h \rangle + \langle \boldsymbol{g}, \boldsymbol{\psi}_h \rangle_{\Gamma_N} . \quad (5.16)$$

Output: Approximations $\{(\boldsymbol{u}_h^i, \boldsymbol{m}_h^i)\}_{0 \leq i \leq N}$.

Algorithm 5.4.1 resembles the decoupled algorithm proposed in [BPPR14]. The discrete initial data $\boldsymbol{m}_h^0 \in \boldsymbol{\mathcal{M}}_{h,0}$, $\boldsymbol{u}_h^0 \in \mathcal{S}^1_D(\mathcal{T}_h)^3$ and $\dot{\boldsymbol{u}}_h^0 \in \mathcal{S}^1(\mathcal{T}_h)^3$ denote suitable approximations of the initial conditions $\boldsymbol{m}^0$, $\boldsymbol{u}^0$ and $\dot{\boldsymbol{u}}^0$, respectively. For every time-step, given current approximations of the magnetization and the displacement, we compute the new magnetization first, and then the updated displacement using this.

Specifically, to compute the new magnetization, we use the tangent plane scheme [AJ06, BKP08, Alo08]: In step (i), given $\boldsymbol{u}_h^i$ and $\boldsymbol{m}_h^i$, we compute an

approximation $\boldsymbol{v}_h^i \approx \partial_t \boldsymbol{m}(t_i)$ residing in the discrete tangent space $\boldsymbol{\mathcal{K}}_h[\boldsymbol{m}_h^i]$. The variational problem (5.14) solved by $\boldsymbol{v}_h^i$ is a discretization of the equivalent formulation of the LLG equation

$$\alpha\, \partial_t \boldsymbol{m} + \boldsymbol{m} \times \partial_t \boldsymbol{m} = \boldsymbol{h}_{\text{eff}}[\boldsymbol{u}, \boldsymbol{m}] - (\boldsymbol{h}_{\text{eff}}[\boldsymbol{u}, \boldsymbol{m}] \cdot \boldsymbol{m})\boldsymbol{m}, \tag{5.17}$$

which can be obtained from (5.5) via simple algebraic manipulations; cf. [AJ06]. Looking at (5.14), we note that the discrete variational formulation of the left-hand side of (5.17) makes use of the mass-lumped L^2-product (3.4). The two terms constituting the effective field $\boldsymbol{h}_{\text{eff}}[\boldsymbol{u}, \boldsymbol{m}]$ are treated differently: The exchange contribution is treated implicitly and therefore contributes to the left-hand side of (5.14). The 'degree of implicitness' is modulated by the parameter $\theta \in (1/2, 1]$. The elastic field is treated explicitly. In step (ii), with $\boldsymbol{v}_h^i$ at hand, we compute the new magnetization $\boldsymbol{m}_h^{i+1}$ using a first-order time-stepping; cf. (5.15). Differently from the seminal papers on the tangent plane schemes [AJ06, BKP08, Alo08] and from [BPPR14], we follow the approach of [Bar16, AHP$^+$14] and in our update we do not use the nodal projection. In particular, it holds that $\mathrm{d}_t \boldsymbol{m}_h^{i+1} = \boldsymbol{v}_h^i$. Finally, in step (iii), we compute the new displacement $\boldsymbol{u}_h^{i+1}$ using a standard finite element discretization of (5.4). We use the backward Euler method in time (the second time derivative in (5.4) is approximated using the different quotient (3.2)).

In Algorithm 5.4.1, we apply the nodal projection to all approximate magnetizations arising from the elastic energy, i.e., in the elastic field on the right-hand side of (5.14) and in the magnetostrain term on the right-hand side of (5.16), whereas the nodal projection is omitted from the magnetization in the exchange field on the right-hand side of (5.14), the cross product on the left-hand side of (5.14), and from the update (5.15).

Notably, despite the nonlinearity of the LLG equation and its nonlinear coupling with the conservation of momentum law, Algorithm 5.4.1 is *fully linear* and only requires the solution of two linear systems per time-step. The linear system for the magnetization is solved using GMRES with a spILU decomposition preconditioner. The relative tolerance of the GMRES solver was set to $1 \cdot 10^{-8}$.The spILU preconditioner used a fill-in ratio of 10, and a drop tolerance of $1 \cdot 10^{-4}$. For the elastic system, the Conjugate Gradient solver was used with a relative tolerance of $1 \cdot 10^{-8}$ and a Jacobi preconditioner.

Remark 5.4.2. *In Algorithm 5.4.1, the magnetization update is based on the projection-free tangent plane scheme [Bar16, AHP$^+$14]. As our analysis below will show, the unit length constraint is imposed inexactly, but the constraint violation error can be controlled by the time-step size. Moreover, passing the estimate to the limit, we can show that the constraint is satisfied by the weak solution towards which the finite element approximations are converging. Other approaches in the literature aim to impose the constraint exactly (at least at the vertices of the underlying finite element mesh). This can be achieved by projecting the magnetization onto the sphere after each update [AJ06, BKP08, Alo08], using constraint-preserving variational formulation [BP06] or designing magnetization updates based on exponential map [LN03]. In Algorithm 5.4.1, we refrain from these approaches as they lead to geometric restrictions on the finite element*

meshes [AJ06, BKP08, Alo08] or lead to the solution of nonlinear systems of equations at each time-step [LN03, BP06].

In the following proposition, we show the well-posedness of Algorithm 5.4.1. The proof, based on standard arguments, is postponed to Section 5.6.1.

Proposition 5.4.3. *Algorithm 5.4.1 is well-defined for every $\theta \in (1/2, 1]$, i.e. for every integer $0 \leq i \leq N-1$, there exists a unique $(\boldsymbol{v}_h^i, \boldsymbol{m}_h^{i+1}, \boldsymbol{u}_h^{i+1}) \in \boldsymbol{\mathcal{K}}_h[\boldsymbol{m}_h^i] \times \mathcal{S}^1(\mathcal{T}_h)^3 \times \mathcal{S}_D^1(\mathcal{T}_h)^3$ satisfying* (5.14)–(5.16).

In the following proposition, we establish a discrete counterpart of the energy law (5.8) satisfied by smooth solutions of the continuous problem (see also (5.12) for the corresponding property for weak solutions). Its proof is postponed to Section 5.6.2.

Proposition 5.4.4. *For every integer $0 \leq i \leq N-1$, the iterates of Algorithm 5.4.1 satisfy the discrete energy law*

$$\mathcal{E}[\boldsymbol{u}_h^{i+1}, \boldsymbol{m}_h^{i+1}] + \frac{1}{2}\left\|\mathrm{d}_t \boldsymbol{u}_h^{i+1}\right\|^2 - \mathcal{E}[\boldsymbol{u}_h^i, \boldsymbol{m}_h^i] - \frac{1}{2}\left\|\mathrm{d}_t \boldsymbol{u}_h^i\right\|^2 = -\alpha k \left\|\boldsymbol{v}_h^i\right\|_h^2 - D_{h,k}^i - E_{h,k}^i, \tag{5.18}$$

where $D_{h,k}^i$ and $E_{h,k}^i$ are given by

$$\begin{aligned} D_{h,k}^i = {} & k^2(\theta - 1/2)\left\|\boldsymbol{\nabla} \boldsymbol{v}_h^i\right\|^2 + \frac{1}{2}\left\|\mathrm{d}_t \boldsymbol{u}_h^{i+1} - \mathrm{d}_t \boldsymbol{u}_h^i\right\|^2 \\ & + \frac{1}{2}\left\|[\boldsymbol{\varepsilon}(\boldsymbol{u}_h^{i+1}) - \boldsymbol{\varepsilon}_{\mathrm{m}}(\boldsymbol{m}_h^{i+1})] - [\boldsymbol{\varepsilon}(\boldsymbol{u}_h^i) - \boldsymbol{\varepsilon}_{\mathrm{m}}(\boldsymbol{m}_h^i)]\right\|_{\mathbb{C}}^2 \geq 0 \end{aligned} \tag{5.19}$$

and

$$\begin{aligned} E_{h,k}^i = {} & k^2 \left\langle \mathbb{C} : [\boldsymbol{\varepsilon}(\boldsymbol{u}_h^{i+1}) - \boldsymbol{\varepsilon}_{\mathrm{m}}(\boldsymbol{m}_h^{i+1})], \boldsymbol{\varepsilon}_{\mathrm{m}}(\boldsymbol{v}_h^i) \right\rangle \\ & + 2k \left\langle \mathbb{C} : \{[\boldsymbol{\varepsilon}(\boldsymbol{u}_h^{i+1}) - \boldsymbol{\varepsilon}_{\mathrm{m}}(\boldsymbol{m}_h^{i+1})] - [\boldsymbol{\varepsilon}(\boldsymbol{u}_h^i) - \boldsymbol{\varepsilon}_{\mathrm{m}}(\boldsymbol{m}_h^i)]\}, \mathbb{Z}(\boldsymbol{m}_h^i \otimes \boldsymbol{v}_h^i) \right\rangle \\ & + 2k \left\langle \mathbb{C} : [\boldsymbol{\varepsilon}(\boldsymbol{u}_h^i) - \boldsymbol{\varepsilon}_{\mathrm{m}}(\boldsymbol{m}_h^i)], \mathbb{Z}[(\boldsymbol{m}_h^i - \Pi_h \boldsymbol{m}_h^i) \otimes \boldsymbol{v}_h^i] \right\rangle \\ & + \left\langle \mathbb{C} : [\boldsymbol{\varepsilon}_{\mathrm{m}}(\boldsymbol{m}_h^{i+1}) - \boldsymbol{\varepsilon}_{\mathrm{m}}(\Pi_h \boldsymbol{m}_h^{i+1})], \boldsymbol{\varepsilon}(\boldsymbol{u}_h^{i+1}) - \boldsymbol{\varepsilon}(\boldsymbol{u}_h^i) \right\rangle, \end{aligned} \tag{5.20}$$

respectively.

In (5.19), we use the norm $\|\cdot\|_{\mathbb{C}}^2 = \langle \mathbb{C} : (\cdot), \cdot \rangle$ for matrix-valued functions in $L^2(\Omega)^{3\times 3}$. Thanks to our assumptions on $\mathbb{C}$ (cf. (5.9)), this norm is equivalent to the standard L^2-norm.

Looking at the right-hand side of (5.18), we see that the inherent α-modulated energy dissipation of the model (cf. (5.8)) is spoiled by two terms:

- the artificial damping $D_{h,k}^i$, arising from the implicit treatment of the exchange contribution of the effective field in (5.14) (the first term) and the use of the backward Euler method in (5.16) (the last two terms),
- the error $E_{h,k}^i$ due to linearization (the first term) decoupling (the second term), and use of the nodal projection to impose the unit length constraint on the magnetizations appearing in the elasticity terms (the third and fourth terms).

Remark 5.4.5. *Our argument to show Proposition 5.4.4 for Algorithm 5.4.1 can be transferred to the algorithm of [BPPR14], hence a by-product of our analysis is a discrete energy law for that algorithm. Due to the use of the nodal projection in [BPPR14], the counterpart of* (5.18) *is only an inequality (not an identity), its proof requires assuming that the mesh is weakly acute, and the error term* $E_{h,k}^i$ *does not include the last two terms in* (5.20).

Now, we discuss the stability and the convergence of Algorithm 5.4.1. To this end, we consider the following convergence assumption on the approximate initial conditions:

$$\boldsymbol{u}_h^0 \to \boldsymbol{u}^0 \text{ in } \boldsymbol{H}^1(\Omega), \quad \dot{\boldsymbol{u}}_h^0 \to \dot{\boldsymbol{u}}^0 \text{ in } \boldsymbol{L}^2(\Omega), \quad \text{and} \quad \boldsymbol{m}_h^0 \to \boldsymbol{m}^0 \text{ in } \boldsymbol{H}^1(\Omega), \quad \text{as } h \to 0. \tag{5.21}$$

Firstly, we can show that Algorithm 5.4.1 is unconditionally stable and that the error in the unit length constraint can be controlled by the time-step size.

Proposition 5.4.6. *Suppose that assumption* (5.21) *is satisfied. There exists a threshold* $k_0 > 0$ *such that, if* $k < k_0$*, for every integer* $1 \le j \le N$*, the iterates of Algorithm 5.4.1 satisfy*

$$\begin{aligned} &\left\|\mathrm{d}_t \boldsymbol{u}_h^j\right\|^2 + \left\|\boldsymbol{\varepsilon}(\boldsymbol{u}_h^j)\right\|^2 + \sum_{i=0}^{j-1} \left\|\mathrm{d}_t \boldsymbol{u}_h^{i+1} - \mathrm{d}_t \boldsymbol{u}_h^i\right\|^2 + \sum_{i=0}^{j-1} \left\|\boldsymbol{\varepsilon}(\boldsymbol{u}_h^{i+1}) - \boldsymbol{\varepsilon}(\boldsymbol{u}_h^i)\right\|^2 \\ &\qquad + \left\|\boldsymbol{m}_h^j\right\|_{\boldsymbol{H}^1(\Omega)}^2 + k \sum_{i=0}^{j-1} \left\|\boldsymbol{v}_h^i\right\|^2 + \left(\theta - \frac{1}{2}\right) k^2 \sum_{i=0}^{j-1} \left\|\boldsymbol{\nabla} \boldsymbol{v}_h^i\right\|^2 \le C \end{aligned} \tag{5.22}$$

and

$$\left\|\mathcal{I}_h\left[\left|\boldsymbol{m}_h^j\right|^2\right] - 1\right\|_{L^1(\Omega)} \le Ck. \tag{5.23}$$

The threshold $k_0 > 0$ *and the constant* $C > 0$ *depend only on the shape-regularity parameter of* $\mathcal{T}_h$*, the problem data* α*,* T*,* Ω*,* $\mathbb{C}$*,* $\mathbb{Z}$*,* $\boldsymbol{f}$ *and* $\boldsymbol{g}$*, and the uniform bounds of the energy of the approximate initial data guaranteed by* (5.21).

For the proof of the result, we refer to Section 5.6.3. Note that (5.23) implies that, if the time-step size is sufficiently small, the approximate magnetizations generated by the algorithm belong to the set $\boldsymbol{\mathcal{M}}_{h,\delta}$ from (3.10) with $\delta = Ck$.

With the approximations generated by Algorithm 5.4.1, we can construct the piecewise affine time reconstructions $\boldsymbol{u}_{hk} : (0,T) \to \mathcal{S}^1(\mathcal{T}_h)^3$ and $\boldsymbol{m}_{hk} : (0,T) \to \mathcal{S}^1(\mathcal{T}_h)^3$; see (3.3). In the following theorem, we show that the sequences $\{\boldsymbol{u}_{hk}\}$ and $\{\boldsymbol{m}_{hk}\}$ converge in a suitable sense towards a weak solution of the initial boundary value problem (5.4)–(5.6) as h, k go to 0. Its proof is postponed to Sections 5.6.4–5.6.5.

Theorem 5.4.7. *Suppose that assumption* (5.21) *is satisfied.*

(i) *There exist a weak solution* $(\boldsymbol{u}, \boldsymbol{m})$ *of* (5.4)–(5.6) *in the sense of Definition 5.2.1(i)–(iii) and a (nonrelabeled) subsequence of* $\{(\boldsymbol{u}_{hk}, \boldsymbol{m}_{hk})\}$ *which converges towards* $(\boldsymbol{u}, \boldsymbol{m})$ *as* $h, k \to 0$*. In particular, as* $h, k \to 0$*, it holds that* $\boldsymbol{u}_{hk} \overset{*}{\rightharpoonup} \boldsymbol{u}$ *in* $L^\infty(0,T;\boldsymbol{H}_D^1(\Omega))$*,* $\partial_t \boldsymbol{u}_{hk} \overset{*}{\rightharpoonup} \partial_t \boldsymbol{u}$ *in* $L^\infty(0,T;\boldsymbol{L}^2(\Omega))$*,* $\boldsymbol{m}_{hk} \overset{*}{\rightharpoonup} \boldsymbol{m}$ *in* $L^\infty(0,T;\boldsymbol{H}^1(\Omega;\mathbb{S}^2))$*, and* $\partial_t \boldsymbol{m}_{hk} \rightharpoonup \partial_t \boldsymbol{m}$ *in* $\boldsymbol{L}^2(\Omega_T)$.

(ii) *If the discretization parameters additionally satisfy the CFL-like condition* $k = o(h^9)$*, the weak solution from part (i) satisfies the energy inequality* (5.12) *from Definition 5.2.1(iv).*

The proof of Theorem 5.4.7 is constructive and provides also a proof of existence of weak solutions. We recall that, due to the non-convex nature of the problem, uniqueness of weak solutions cannot be expected (cf. the explicit proof of non-uniqueness of weak solutions to the pure LLG equation in [AS92]). Moreover, if $\theta \in [0, 1/2]$, then Theorem 5.4.7 still holds, but with an additional CFL condition for part (i), i.e. $k = o(h^2)$ if $\theta \in [0, 1/2)$ and $k = o(h)$ if $\theta = 1/2$; see [Alo08].

Remark 5.4.8. *The application of the nodal projection to all approximate magnetizations arising from the elastic energy is responsible for two of the error terms in* (5.20) *and for the severe CFL-like condition in Theorem 5.4.7(ii) (cf. the analysis in Section 5.6.5 below), so one would be tempted to completely remove it. However, we believe that a fully projection-free approach would not lead to an unconditionally stable method. In particular, the use of the nodal projection on the outermost magnetization in the elastic field (cf.* (5.7)*) is non-negotiable as the total strain* $\boldsymbol{\varepsilon}(\boldsymbol{u})$ *is only in* $\boldsymbol{L}^2(\Omega)$*. For a stable method, it would be sufficient to take only one projection, not two, within the magnetostrain as this would yield the estimate* $\|\mathbb{Z} : (\Pi_h \boldsymbol{m}_h \otimes \boldsymbol{m}_h)\| \lesssim \|\boldsymbol{m}_h\|$*, which would allow for the stability estimate of Proposition 5.4.6. However, we prefer not to use this approach as it would introduce some 'unnatural' non-symmetry.*

Remark 5.4.9. *The proof of the energy inequality typically requires extra assumptions to be proven. In [BFF+14, Appendix A], in the case of the LLG equation (with full effective field), its proof requires higher regularity and stronger convergence assumptions on the applied field and general contribution terms. In [DFPP+20, Theorem 3.2], in the case of the coupled system of the LLG equation and the eddy current equation, a similar situation arises with a CFL-like condition* $k = o(h^{3/2})$*. The very severe CFL-like condition in Theorem 5.4.7(ii) is an artifact of the analysis and is due to the nonlinearity of the coupling and the fact that our proof requires explicit estimates of the error associated with the use of the nodal projection in the elastic terms. In particular, we need to estimate this error in a norm that is stronger than the* L^1*-norm, which leads to a reduced convergence rate with respect to the time-step size* k *(see Lemma 5.6.6 below). This, combined with the fact that we need inverse estimates to obtain quantities we are able to control, leads to the CFL-like condition. For more details, we refer to the proof of the result in Section 5.6.5 below. However, we stress that this restriction does not show up within the numerics (see, in particular, the experiment Section 5.5.3.3 and furthermore this CFL-like condition does not affect the stability of the method. In fact, this CFL-like condition allows us to ask for more of the solution in terms of uniqueness, eliminating solutions that do not obey the energy law as they are "unnatural".*

5.5 Numerical experiments

In this section, to show the applicability of our algorithm, we present a collection of numerical experiments. The meshes were generated using Netgen, by producing a rough mesh and then successively refining the mesh until the maximum mesh size was below a desired tolerance.

5.5.1 Material parameters

In the upcoming numerical experiments, we use material parameters estimated for $(Fe_{90}Co_{10})_{78}Si_{12}B_{10}$ (which we shall call FeCoSiB) from [DW23b]. For the mass density and the Gilbert damping parameter (needed in our model, but not in [DW23b]), we take the values used in [KO85] and [HZJB23], respectively. The resulting exchange length is $\ell_{\text{ex}} = \sqrt{2A/(\mu_0 M_s^2)} \approx 3 \cdot 10^{-9}$ m. The stiffness tensor $\mathbb{C}$ is assumed to be isotropic and acts on symmetric matrices $\boldsymbol{\varepsilon}$ (the only type required) as

$$\mathbb{C} : \boldsymbol{\varepsilon} = 2\mu\, \boldsymbol{\varepsilon} + \lambda \operatorname{tr}(\boldsymbol{\varepsilon})\, I,$$

where μ and λ are the Lamé constants (for FeCoSiB after nondimensionalization we have $\mu \approx 6.89$ and $\lambda \approx 21.96$). For the magnetostrain, we consider the expression in (5.13). In some experiments, the magnetic energy (5.2) will be supplemented with the term $-\langle \boldsymbol{h}_{\text{ext}}, \boldsymbol{m} \rangle$ (Zeeman energy), modelling the interaction of the magnetization with an applied external field $\boldsymbol{h}_{\text{ext}}$. For the sake of reproducibility, the values used are reported in Table 5.1 (we refer to Appendix C.1 for the relationship between the fully dimensional model and the dimensionless setting of this thesis).

Symbol	Name	Value
A	Exchange constant	$1.5 \cdot 10^{-11}$ J m^{-1}
α	Gilbert damping parameter	0.005
γ	Gyromagnetic ratio	$1.761 \cdot 10^{11}$ rad s^{-1} T^{-1}
μ_0	Permeability of free space	$1.25663706 \cdot 10^{-6}$
M_s	Saturation magnetization	$1.5 \cdot 10^{6}$ A m^{-1}
λ_{100}	Saturation magnetostrain	$30 \cdot 10^{-6}$
ρ	Density	7900 kg m^{-3}
g	Gravitational acceleration	9.81 m s^{-2}
μ	First Lamé constant	172 GPa
λ	Second Lamé constant	54 GPa

Table 5.1: Estimated material parameters for FeCoSiB taken from [DW23b, KO85, HZJB23].

5.5.2 Magnetoelastic coupling

In this section, we present two numerical experiments aimed at showcasing the capability of Algorithm 5.4.1 to simulate physical processes involving magnetoelastic materials.

The simulation object is a bar of FeCoSiB, clamped at one end ($y = 0$ plane), shown in Figure 5.1. The bar has a physical length of $20\ell_{\text{ex}}$ and width/height of $6\ell_{\text{ex}}$. The maximum mesh size is $h_{\max} \approx 0.9\ell_{\text{ex}}$ (thereby being below the exchange length). The initial magnetization is uniformly in the x-direction $\boldsymbol{m}_h^0 = (1, 0, 0)$, whereas we set zero initial displacement $\boldsymbol{u}_h^0 = \boldsymbol{0}$ with zero initial velocity $\dot{\boldsymbol{u}}_h^0 = \boldsymbol{0}$. Gravity is enabled and implemented as a volume force $\boldsymbol{f} = (0, 0, -g)$, with a value of $-g = -2.97 \cdot 10^{-14}$ after nondimensionalisation. If enabled, tractions (represented by a surface force $\boldsymbol{g}$ applied on Γ_N) and applied external fields $\boldsymbol{h}_{\text{ext}}$ are applied along the $+y$ direction. Simulations are run for 1 ns, using time-steps of size $2 \cdot 10^{-12}$ s. This corresponds to a non-dimensional time length of $T \approx 330$ and time-step $k \approx 0.66$.

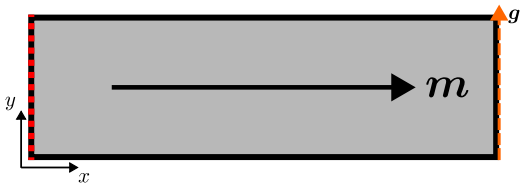

Figure 5.1: Experiments of Section 5.5.2: View from above of the FeCoSiB bar of dimensions $(20\ell_{\text{ex}}, 6\ell_{\text{ex}}, 6\ell_{\text{ex}})$.

5.5.2.1 Direct magnetostrictive effect

In this experiment, we show that changes in the magnetization yield changes in the mechanical state of the body. To this end, we neglect traction and apply a uniform applied external field $\boldsymbol{h}_{\text{ext}}$ along the $+y$ direction with low values of $0, 1 \cdot 10^{-4}, 3 \cdot 10^{-4}, 5 \cdot 10^{-4}, 7 \cdot 10^{-4}$, which corresponds to fields of strength 0, 0.2, 0.6, 0.9, 1.3 mT. The fields are weak so that the dynamics is not too fast.

We observe the magnetization aligning with the applied external field as expected through a precession, yielding an effect on the displacement. The coupling is clearly visible in Figure 5.2, where we plot the time evolution of the average magnetization and displacement components, e.g. $\langle u_x \rangle = (1/|\Omega|) \int_\Omega u_x$. The applied field is pointing in the y-direction, so the y and z components begin to increase in magnitude as seen in Figures 5.2b and 5.2c, taking from the x component. The displacement on the other hand mirrors the magnetization in the y and z components, with the x component increasing due to magnetostriction, and then changing slowly as the magnetization changes. Moreover, we see that, with stronger applied magnetic fields, the average magnetization in the y direction increases, displacing the body in the same direction.

In Figure 5.3, we plot the time evolution of the energy for all considered applied external fields. For stronger applied fields, the energy reaches a lower value at later times. Importantly, we always see the energy decreasing.

The average number of GMRES iterations for this experiment was about 33 iterations.

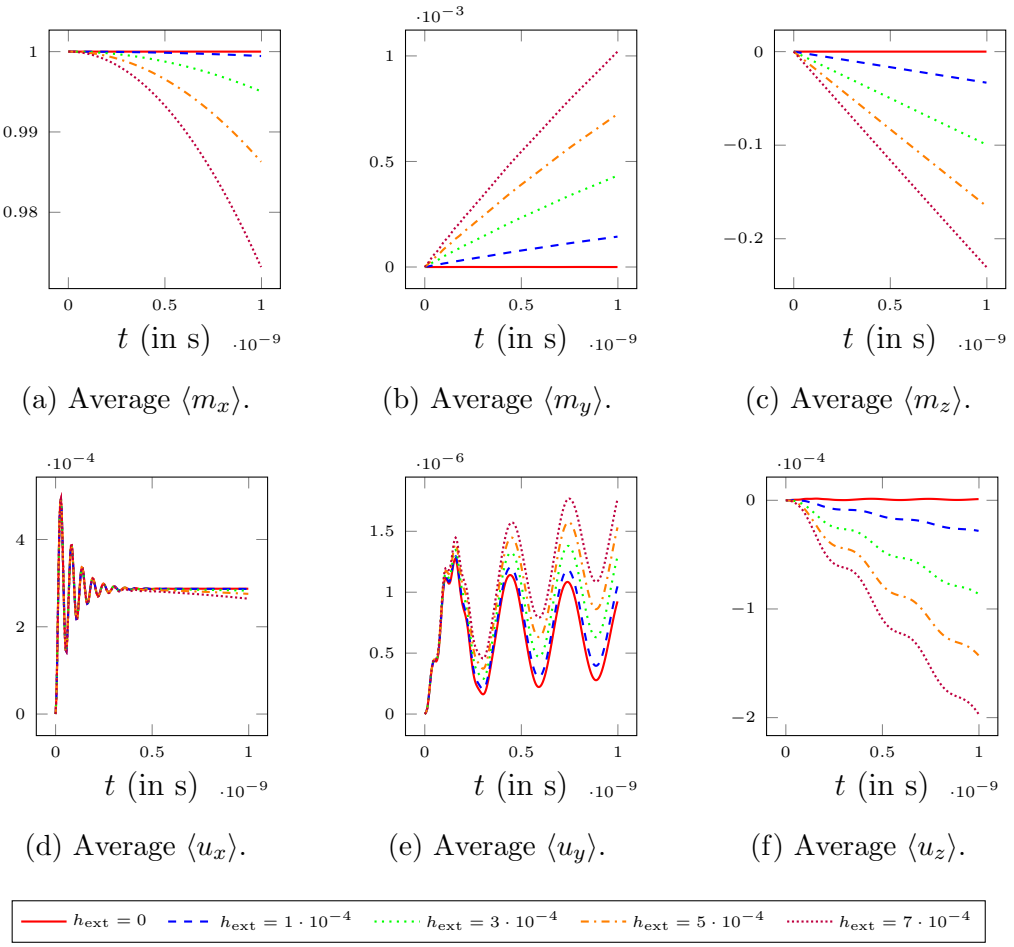

(a) Average $\langle m_x \rangle$. (b) Average $\langle m_y \rangle$. (c) Average $\langle m_z \rangle$.

(d) Average $\langle u_x \rangle$. (e) Average $\langle u_y \rangle$. (f) Average $\langle u_z \rangle$.

Figure 5.2: Experiment of Section 5.5.2.1: Time evolution of the average magnetization and displacement components for varied applied magnetic fields.

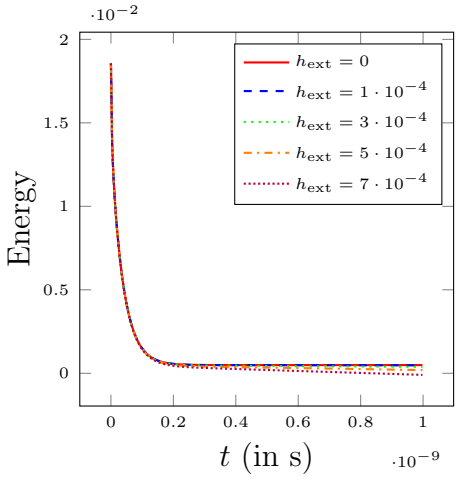

Figure 5.3: Experiment of Section 5.5.2.1: Total energy over time for varied applied magnetic fields.

5.5.2.2 Inverse magnetostrictive effect

In this experiment, we show that changes in the mechanical state of the body yield changes in the magnetization. To this end, we disable the Zeeman field and apply a traction on the $x = 20\ell_{\text{ex}}$ plane in the $+y$ direction. Specifically, we consider a surface force of the form $\boldsymbol{g} = (0, b, 0)$ for $b \in \{0, 1.28 \cdot 10^{-9}, 3.19 \cdot 10^{-9}, 6.38 \cdot 10^{-9}, 1.28 \cdot 10^{-8}\}$, which corresponds to forces of strength 0, 10, 25, 50, 100 $\mathrm{N\,m^{-2}}$.

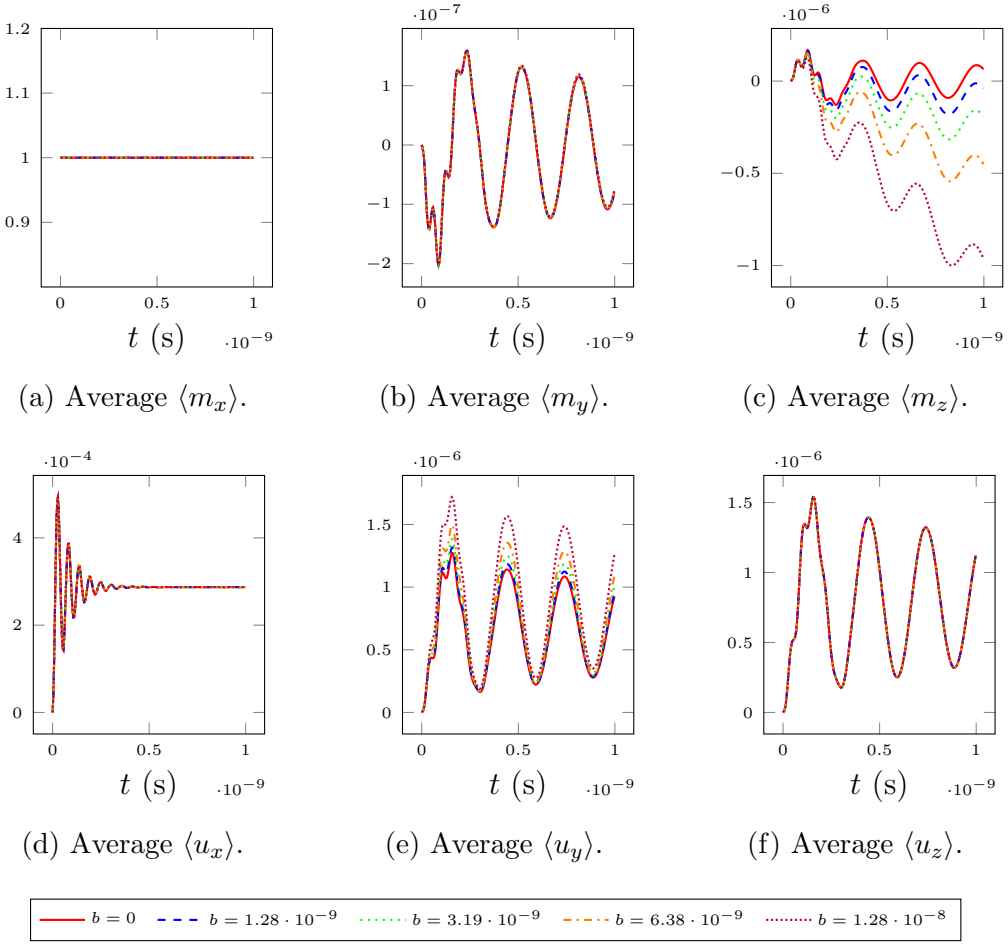

(a) Average $\langle m_x \rangle$. (b) Average $\langle m_y \rangle$. (c) Average $\langle m_z \rangle$.

(d) Average $\langle u_x \rangle$. (e) Average $\langle u_y \rangle$. (f) Average $\langle u_z \rangle$.

Figure 5.4: Experiment of Section 5.5.2.2: Time evolution of the average magnetization and displacement components for varied traction strengths.

The time evolution of the average displacement and magnetization components is shown in Figure 5.4. When more traction is applied, the average displacement in the y direction increases. The z component of the magnetization in Figure 5.4c is the most interesting, as it decreases more strongly due to stronger tractions. The average number of GMRES iterations for this experiment was 40.

5.5.2.3 Nutation dynamics

It has been shown that at extremely short timescales, the LLG equation is inadequate for the ultrafast dynamics that occur [CRW11, WC12], as will be discussed in Chapter 8. At these timescales, the LLG equation (5.5) should then

be replaced by the iLLG equation, given by

$$\partial_t \boldsymbol{m} = -\boldsymbol{m} \times \boldsymbol{h}_{\text{eff}}[\boldsymbol{m}] + \alpha\, \boldsymbol{m} \times \partial_t \boldsymbol{m} + \tau\, \boldsymbol{m} \times \partial_{tt} \boldsymbol{m}, \tag{5.24}$$

where the additional parameter $\tau > 0$ is a relaxation time (see Section 2.3.8.1). The main difference between iLLG and LLG dynamics is the inclusion of nutation, where the LLG path is not instantly followed due to the inertia of the magnetization [NAK+21]. A preliminary form of the iLLG equation was initially derived using an expansion coming from the magnetoelastic coupling [Suh98, Suh07]. Here the momentum is stored by the displacement instead of the magnetization. With the experiment in this section, we aim to demonstrate this effect.

We consider the same material parameters as in the previous experiments, except for the Gilbert damping parameter (for which we choose $\alpha = 0.1$). Moreover, as the nutation effects are small, we increase the magnetostriction constant λ_{100} in Table 5.1. For the ferromagnetic body, we consider a hemisphere of radius ℓ_{ex} with a clamped planar face with outer normal $(-1, 0, 0)$. We use the values $\{20\lambda_{100}, 50\lambda_{100}, 100\lambda_{100}\}$, and compare this to a reference LLG simulation with no magnetoelastic coupling (computed by the same algorithm with $0\lambda_{100}$). The initial magnetization is slightly perturbed from the x-direction, specifically $\boldsymbol{m}^0 = (0.9, 0.2, 0)$ (normalized), and subject to a strong Zeeman field $\boldsymbol{h}_{\text{ext}} = (1, 0, 0) = (3\pi/5, 0, 0)\text{T}$. The initial displacement and velocity are zero. We set $\theta = 0.50000005$, and consider a non-dimensional time-step $k = 0.001 \approx 3 \cdot 10^{-15}\text{s}$, for time $T = 1 \cdot 10^{-10}\text{s}$. The mesh is made of 210 nodes, 672 elements, and satisfies $h_{\max} \approx 0.6\ell_{\text{ex}}$. The average number of GMRES iterations for this experiment was 2.

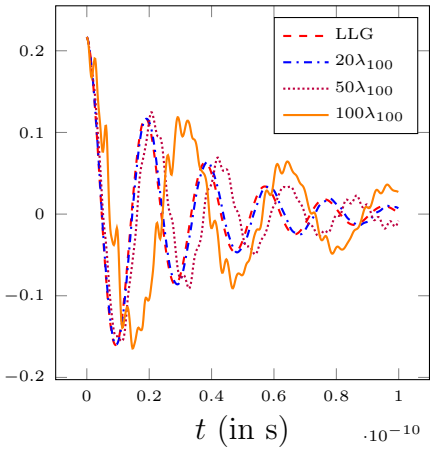

Figure 5.5: Experiment of Section 5.5.2.3: Time evolution of the average $\langle \boldsymbol{m}_y \rangle$ for varying magnetostrain values λ_{100}, compared with purely LLG without magnetoelastic effects.

The results can be seen in Figure 5.5. It is easily seen that as the magnetostrain parameter is increased, the dissipative effects decrease, seen as a stretching effect to the right. As expected, we see nutation effects perturbing the natural LLG precession behaviour, especially for $50\lambda_{100}$ and $100\lambda_{100}$.

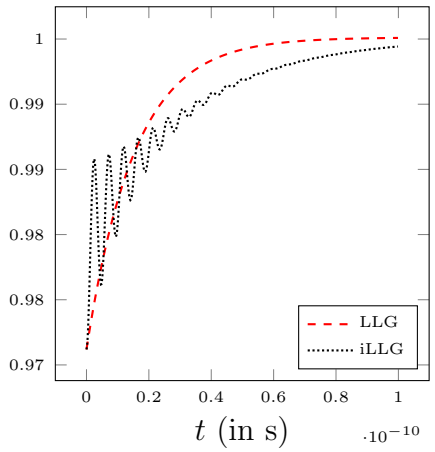

(a) Average $\langle m_x \rangle$ for reference iLLG and LLG.

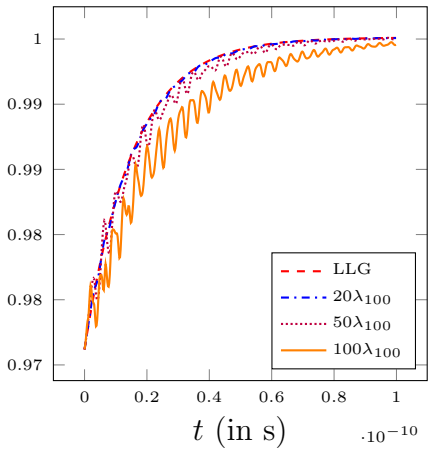

(b) Average $\langle m_x \rangle$ for magnetoelastic LLG.

Figure 5.6: Experiment of Section 5.5.2.3. Average magnetization $\langle m_x \rangle$ of (a) reference LLG and iLLG, (b) magnetoelastic LLG with varying magnetostrain.

For reference, we also consider this same system without magnetoelastic coupling for the iLLG equation. The modifications required to extend the tangent plane scheme presented in [Alo08] to the iLLG equation are described and analysed in [Rug22]. For consistency, we apply the first-order tangent plane scheme here with the nodal projection step removed, similar to the projection-free method applied in Chapter 8. We choose the relaxation time arbitrarily to be $\tau = 0.4 \approx 1.21$ps. The average x component of the magnetization for iLLG is shown in Figure 5.6a, and the average x components of the magnetization for the magnetoelastic LLG simulations is shown in Figure 5.6b. The qualitative similarities are obvious, with additional oscillations not seen in the pure LLG case, along with lessened damping.

5.5.3 Properties of Algorithm 5.4.1

In this section, we present three experiments to numerically investigate the properties of Algorithm 5.4.1. For all of them, the computational domain will be a cube with edge length equal to $6\ell_{\text{ex}}$.

5.5.3.1 θ-dependence

In this experiment, we investigate the effect on numerical simulations of the parameter $\theta \in (1/2, 1]$, which controls the 'degree of implicitness' in the treatment of the exchange contribution in (5.14). We use material parameters for FeCoSiB (cf. Table 5.1) except for the Gilbert damping parameter, for which we use the smaller value $\alpha = 0.001$. The initial condition for the magnetization is a 'hot' magnetic state, i.e. the values at the vertices of the mesh (which in this experiment has mesh size $h_{\max} \approx 3\ell_{\text{ex}}$) are assigned randomly to the magnetization before being normalized. The displacement and its time derivative are initialized by zero.

We run the simulation for $1 \cdot 10^{-11}$ s using a time step size of $1 \cdot 10^{-15}$ s and different values of $\theta \in \{0.50000005, 0.505, 0.6, 0.7, 0.8, 0.9, 1\}$. The average number of GMRES iterations for this experiment was 2.

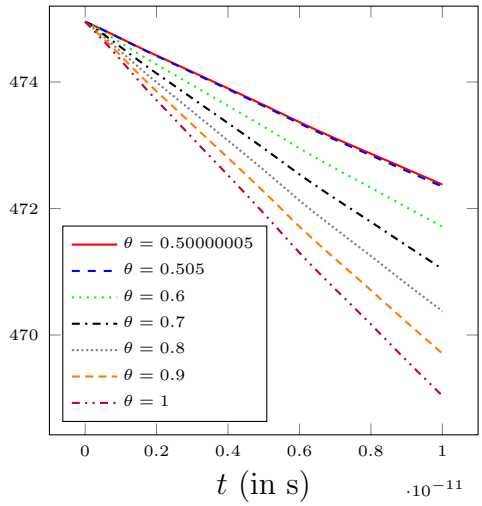

Figure 5.7: Experiment of Section 5.5.3.1: Time evolution of the total energy for different values of θ.

The energy-decreasing behaviour can be seen in Figure 5.7, with considerably more energy loss associated with greater θ values. So changing the θ-implicitness parameter away from $1/2$ can yield considerable amounts of artificial numerical damping, which can be particularly bad in certain situations (e.g., in the case of long-time simulations).

5.5.3.2 Unit length constraint violation

An essential property of the LLG equation at constant temperature is the unit length constraint on the magnetization. Hence, an essential feature of any approximation algorithm must be the capability to achieve the unit length constraint. For Algorithm 5.4.1, this property is the subject of Proposition 5.4.6, particularly (5.23), i.e.

$$\left\| \mathcal{I}_h\left[\left| \boldsymbol{m}_h^j \right|^2 \right] - 1 \right\|_{L^1(\Omega)} \leq Ck,$$

which shows that the unit length constraint is violated at most linearly in time (if measured in the L^1-norm).

To see this numerically, we again consider a hot magnet as in Section 5.5.3.1, a particularly bad case with plenty of rotation by the magnetization (note that the constant $C > 0$ in (5.23) depends, among other things, upon the energy of the initial magnetization and is large for a random configuration), and use various time-steps with $\theta = 0.50000005$. The average number of GMRES iterations for this experiment was 2.

In Figure 5.8a, we plot the constraint violation (measured as the left-hand side of (5.23)) at the final iterate $\boldsymbol{m}_h^N$ of Algorithm 5.4.1 against the time-step size

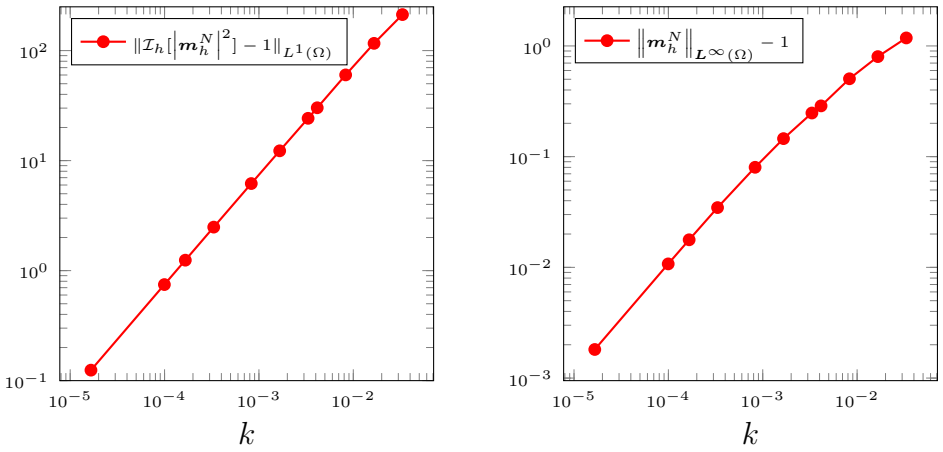

(a) Constraint violation. (b) Nodal maximum.

Figure 5.8: Experiment of Section 5.5.3.2: (a) Constraint violation at the final iterate against the time-step size. (b) L^∞-norm error of the magnetization at the final iterate against the time-step size.

k. We observe that the error decays linearly in k as predicted by (5.23). The constraint violation is of the order 10^2 for k on the order of $10^{-3/2}$ due to the hot initial state, as the magnetization at a node may need to rotate several times. Note that these simulations are run for only 0.01 ns as we are only interested in verifying the constraint violation inequalities.

In Figure 5.8b, we plot the L^∞-norm error of the magnetization at the final iterate against the time-step size k. We note that while we can control the integral violation with (5.23), in our projection-free algorithm we cannot directly control the maximum norm $\|\boldsymbol{m}_h^j\|_{\boldsymbol{L}^\infty(\Omega)}$, which with a projection would be 1 for each j. We see that the nodal maximum error numerically tends to 0 as desired, in an almost linear fashion, as we shall show. Using similar methods to those to prove (5.23) (see Lemma 5.6.2 below) and classical inverse estimates [Bar15b, Lemma 3.5], one can show that

$$\begin{aligned}\|\boldsymbol{m}_h^j\|_{\boldsymbol{L}^\infty}^2 - 1 &= \max_{z\in\mathcal{N}_h} |\boldsymbol{m}_h^j(z)|^2 - 1 \le k^2 \sum_{i=0}^{j-1} \max_{z\in\mathcal{N}_h} |\boldsymbol{v}_h^i(z)|^2 \\ &= k^2 \sum_{i=0}^{j-1} \|\boldsymbol{v}_h^i\|_{\boldsymbol{L}^\infty(\Omega)}^2 \lesssim h_{\min}^{-3} k^2 \sum_{i=0}^{j-1} \|\boldsymbol{v}_h^i\|_{\boldsymbol{L}^2(\Omega)}^2 \lesssim h_{\min}^{-3} k,\end{aligned}$$

thus the desired convergence $\|\boldsymbol{m}_h^j\|_{\boldsymbol{L}^\infty(\Omega)} - 1 \to 0$ as $h, k \to 0$ can be obtained assuming the CFL condition $k = o(h^3)$. We see this linear behaviour in Figure 5.8b because the mesh size is fixed.

5.5.3.3 Energy law robustness

In this experiment, we investigate the robustness of the evolution of the energy of the approximations generated by Algorithm 5.4.1 with respect to the discretization parameters.

We consider a similar setup to the one used in Section 5.5.3.1. Specifically, we keep $\theta = 0.50000005$ and $\alpha = 0.001$, but we add a Zeeman field $\boldsymbol{h}_{\text{ext}} = (0.001, 0, 0) \approx (1.9, 0, 0)\text{mT}$ to encourage the system to approach the same final state. To give consistency between mesh refinements we change from a purely random initial state to the following initial condition for the magnetization,

$$\boldsymbol{m}^0(x, y, z) = \frac{1}{\sqrt{5}}(2, \sin(x + y + z), \cos(x + y + z)) \quad \text{for all } (x, y, z) \in \Omega.$$

It is easily shown that the initial condition satisfies $\|\boldsymbol{\nabla} \boldsymbol{m}^0\|^2 / 2 = 64.8$ and $|\boldsymbol{m}^0| = 1$ in Ω. NGSolve interpolates the initial condition onto the mesh via an Oswald-type interpolation [Osw93], applying an L^2-projection and then averaging for conformity, thus to enforce the condition $\boldsymbol{m}_h^0 \in \boldsymbol{\mathcal{M}}_{h,0}$ we apply the nodal projection to the result of this interpolation. We then ran the simulation for $T \approx 3.32$ with combinations of $k = 0.01,\ 0.005,\ 0.0025,\ 0.00125,\ 0.000625$ as time-step size and $h = 1.59,\ 1.09,\ 0.84,\ 0.45$ as mesh size. The average number of GMRES iterations for each experiment was 3, except for $h = 0.45$ which had 30.

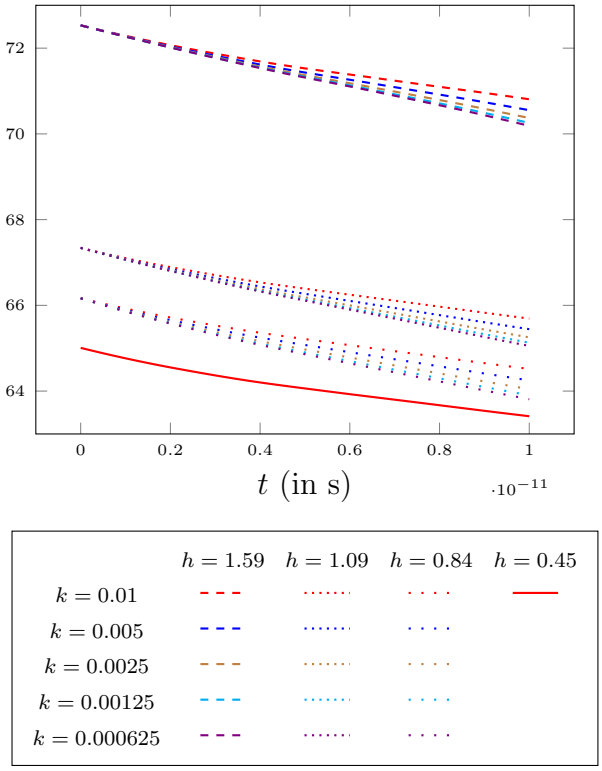

Figure 5.9: Experiment of Section 5.5.3.3. Time evolution of the total energy for different values of h and k.

As can be observed in Figure 5.9, the energy decay (and thus stability of the algorithm) occurs for all mesh sizes and time-steps. The initial energy is different for each due to the differing underlying mesh, and the interpolation process mentioned above (which is also different for each mesh), however the

initial energies approach the actual energy. The different energy progressions are clustered into the four groups with similar energy decay when the time-step is the same. When the time-step size is smaller, the energy decay is slower, likely due to the error term in the discrete energy law (cf. the term $E^i_{h,k}$ in (5.18)). With no error term present, the dissipation would always reduce with lower time-step sizes.

These results show that the algorithm behaves energetically well for all combinations of mesh and time-step size considered, including the worst case scenario for a CFL-like condition (when the finest mesh with $h = 0.45$ and the largest time-step size $k = 0.01$ are used). Clearly, this is not a mathematical proof that the restrictive CFL-like condition we need to show Theorem 5.4.7(ii) is not needed, however our numerical experiments seem to corroborate this claim.

5.6 Proofs

In this section, we collect the proofs of the results presented in Section 5.4.

5.6.1 Well-posedness

We start by showing an estimate of the L^2-norm of the discrete elastic field.

Lemma 5.6.1. *For all $\boldsymbol{u}_h, \boldsymbol{m}_h \in \mathcal{S}^1(\mathcal{T}_h)^3$ with $|\boldsymbol{m}_h(z)| \geq 1$ for all $z \in \mathcal{N}_h$, it holds that*

$$\|\boldsymbol{h}_{\mathrm{m}}[\boldsymbol{u}_h, \Pi_h \boldsymbol{m}_h]\|^2 \leq 8 \|\mathbb{Z}\|^2_{\boldsymbol{L}^\infty(\Omega)} \|\mathbb{C}\|^2_{\boldsymbol{L}^\infty(\Omega)} \left(\|\boldsymbol{\varepsilon}(\boldsymbol{u}_h)\|^2 + \|\mathbb{Z}\|^2_{\boldsymbol{L}^\infty(\Omega)} |\Omega| \right). \quad (5.25)$$

Proof. Using the expression of the discrete elastic field, we have

$$\begin{aligned}
&\|\boldsymbol{h}_{\mathrm{m}}[\boldsymbol{u}_h, \Pi_h \boldsymbol{m}_h]\|^2 \\
&\overset{(5.7)}{=} \left\| 2(\mathbb{Z}^\top : \{\mathbb{C} : [\boldsymbol{\varepsilon}(\boldsymbol{u}_h) - \boldsymbol{\varepsilon}_{\mathrm{m}}(\Pi_h \boldsymbol{m}_h)]\}) \Pi_h \boldsymbol{m}_h \right\|^2 \\
&\leq 4 \|\mathbb{Z}\|^2_{\boldsymbol{L}^\infty(\Omega)} \|\mathbb{C}\|^2_{\boldsymbol{L}^\infty(\Omega)} \|\boldsymbol{\varepsilon}(\boldsymbol{u}_h) - \mathbb{Z} : (\Pi_h \boldsymbol{m}_h \otimes \Pi_h \boldsymbol{m}_h)\|^2 \|\Pi_h \boldsymbol{m}_h\|^2_{\boldsymbol{L}^\infty(\Omega)} \\
&\leq 8 \|\mathbb{Z}\|^2_{\boldsymbol{L}^\infty(\Omega)} \|\mathbb{C}\|^2_{\boldsymbol{L}^\infty(\Omega)} \left(\|\boldsymbol{\varepsilon}(\boldsymbol{u}_h)\|^2 + \|\mathbb{Z}\|^2_{\boldsymbol{L}^\infty(\Omega)} |\Omega| \right),
\end{aligned}$$

where we have used the boundedness of the fourth-order tensors and $\Pi_h \boldsymbol{m}_h$. □

We can now show the well-posedness of Algorithm 5.4.1.

Proof of Proposition 5.4.3. The proof of well-posedness is essentially identical to the one given in [BPPR14] for the algorithm proposed therein. We restate it here including other terms.

For the magnetization term, define the family of bilinear form $a^i_1(\cdot,\cdot) : \boldsymbol{\mathcal{K}}_h[\boldsymbol{m}^i_h] \times \boldsymbol{\mathcal{K}}_h[\boldsymbol{m}^i_h] \to \mathbb{R}$ for $i = 0, \ldots, N-1$, by

$$a^i_1(\boldsymbol{\phi}_h, \boldsymbol{\psi}_h) := \alpha \langle \boldsymbol{\phi}_h, \boldsymbol{\psi}_h \rangle_h + \theta k \langle \boldsymbol{\nabla} \boldsymbol{\phi}_h, \boldsymbol{\nabla} \boldsymbol{\psi}_h \rangle + \langle \boldsymbol{m}^i_h \times \boldsymbol{\phi}_h, \boldsymbol{\psi}_h \rangle$$

and the family of linear (and bounded by Lemma 5.6.1) functionals L_1^i for $i = 0, \dots, N-1$ by

$$L_1^i(\boldsymbol{\phi}_h) := -\left\langle \boldsymbol{\nabla} \boldsymbol{m}_h^i, \boldsymbol{\nabla} \boldsymbol{\phi}_h \right\rangle + \left\langle \boldsymbol{h}_{\mathrm{m}}[\boldsymbol{u}_h^i, \Pi_h \boldsymbol{m}_h^i], \boldsymbol{\phi}_h \right\rangle .$$

Then (5.14) can be rewritten as $a_1^i(\boldsymbol{v}_h^i, \boldsymbol{\psi}_h) = L_1^i(\boldsymbol{\psi}_h)$ for all $\boldsymbol{\psi}_h \in \boldsymbol{\mathcal{K}}_h[\boldsymbol{m}_h^i]$. We can see that $a_1^i(\cdot, \cdot)$ is positive definite (in $\boldsymbol{L}^2(\Omega)$ and $\boldsymbol{H}^1(\Omega)$), as letting $\boldsymbol{\phi}_h = \boldsymbol{\psi}_h$ eliminates the final term, leaving a combination of the L^2-norm and H^1-seminorm. It follows by the finite dimensionality that (5.14) has a unique solution $\boldsymbol{v}_h^i \in \boldsymbol{\mathcal{K}}_h[\boldsymbol{m}_h^i]$.

For the displacement term, define the bilinear form $a_2 : \mathcal{S}_D^1(\mathcal{T}_h)^3 \times \mathcal{S}_D^1(\mathcal{T}_h)^3 \to \mathbb{R}$ by

$$a_2(\boldsymbol{\phi}_h, \boldsymbol{\psi}_h) := \langle \boldsymbol{\phi}_h, \boldsymbol{\psi}_h \rangle + k^2 \left\langle \mathbb{C} : \boldsymbol{\varepsilon}(\boldsymbol{\phi}_h), \boldsymbol{\varepsilon}(\boldsymbol{\psi}_h) \right\rangle .$$

As $\mathbb{C}$ is positive definite by assumption, applying Korn's inequality (see, e.g. [BS08, Theorem 11.2.6]) yields positive definiteness of $a_2(\cdot, \cdot)$ in $\boldsymbol{H}^1(\Omega)$. Furthermore, defining the family of linear functionals

$$\begin{aligned} L_2^i(\boldsymbol{\psi}_h) := k^2 \left\langle \mathbb{C} : \boldsymbol{\varepsilon}_{\mathrm{m}}(\Pi_h \boldsymbol{m}_h^{i+1}), \boldsymbol{\varepsilon}(\boldsymbol{\psi}_h) \right\rangle + k \left\langle \mathrm{d}_t \boldsymbol{u}_h^i, \boldsymbol{\psi}_h \right\rangle \\ + \left\langle \boldsymbol{u}_h^i, \boldsymbol{\psi}_h \right\rangle + k^2 \left\langle \boldsymbol{f}, \boldsymbol{\psi}_h \right\rangle + k^2 \left\langle \boldsymbol{g}, \boldsymbol{\psi}_h \right\rangle_{\Gamma_N} , \end{aligned}$$

we have that (5.16) is equivalent to $a_2(\boldsymbol{u}_h^{i+1}, \boldsymbol{\psi}_h) = L_2^i(\boldsymbol{\psi}_h)$ for all $\boldsymbol{\psi}_h \in \mathcal{S}_D^1(\mathcal{T}_h)^3$, for each $i = 0, \dots, N-1$. Again exploiting the finite dimension, we have existence and uniqueness of a solution $\boldsymbol{u}_h^{i+1} \in \mathcal{S}_D^1(\mathcal{T}_h)^3$ to (5.16). □

5.6.2 Discrete energy law

We now prove the discrete energy law satisfied by the iterates of Algorithm 5.4.1.

Proof of Proposition 5.4.4. Let $0 \leq i \leq N-1$ be an arbitrary integer. Choosing the test function $\boldsymbol{\phi}_h = \boldsymbol{v}_h^i \in \boldsymbol{\mathcal{K}}_h[\boldsymbol{m}_h^i]$ in (5.14), we obtain

$$\alpha \left\| \boldsymbol{v}_h^i \right\|_h^2 + \theta k \left\| \boldsymbol{\nabla} \boldsymbol{v}_h^i \right\|^2 = -\left\langle \boldsymbol{\nabla} \boldsymbol{m}_h^i, \boldsymbol{\nabla} \boldsymbol{v}_h^i \right\rangle + \left\langle \boldsymbol{h}_{\mathrm{m}}[\boldsymbol{u}_h^i, \Pi_h \boldsymbol{m}_h^i], \boldsymbol{v}_h^i \right\rangle .$$

Moreover, we have

$$\frac{1}{2} \left\| \boldsymbol{\nabla} \boldsymbol{m}_h^{i+1} \right\|^2 = \frac{1}{2} \left\| \boldsymbol{\nabla} \boldsymbol{m}_h^i \right\|^2 + k \left\langle \boldsymbol{\nabla} \boldsymbol{m}_h^i, \boldsymbol{\nabla} \boldsymbol{v}_h^i \right\rangle + \frac{k^2}{2} \left\| \boldsymbol{\nabla} \boldsymbol{v}_h^i \right\|^2 .$$

Combining the two above equations, we obtain

$$\mathcal{E}_{\mathrm{m}}[\boldsymbol{m}_h^{i+1}] - \mathcal{E}_{\mathrm{m}}[\boldsymbol{m}_h^i] = -\alpha k \left\| \boldsymbol{v}_h^i \right\|_h^2 - k^2(\theta - 1/2) \left\| \boldsymbol{\nabla} \boldsymbol{v}_h^i \right\|^2 + k \left\langle \boldsymbol{h}_{\mathrm{m}}[\boldsymbol{u}_h^i, \Pi_h \boldsymbol{m}_h^i], \boldsymbol{v}_h^i \right\rangle . \tag{5.26}$$

Choosing the test function $\boldsymbol{\psi}_h = \boldsymbol{u}_h^{i+1} - \boldsymbol{u}_h^i = k \, \mathrm{d}_t \boldsymbol{u}_h^{i+1}$ in (5.16) yields

$$\begin{aligned} \left\langle \mathrm{d}_t \boldsymbol{u}_h^{i+1} - \mathrm{d}_t \boldsymbol{u}_h^i, \mathrm{d}_t \boldsymbol{u}_h^{i+1} \right\rangle + \left\langle \mathbb{C}[\boldsymbol{\varepsilon}(\boldsymbol{u}_h^{i+1}) - \boldsymbol{\varepsilon}_{\mathrm{m}}(\Pi_h \boldsymbol{m}_h^{i+1})], \boldsymbol{\varepsilon}(\boldsymbol{u}_h^{i+1}) - \boldsymbol{\varepsilon}(\boldsymbol{u}_h^i) \right\rangle \\ = \left\langle \boldsymbol{f}, \boldsymbol{u}_h^{i+1} - \boldsymbol{u}_h^i \right\rangle + \left\langle \boldsymbol{g}, \boldsymbol{u}_h^{i+1} - \boldsymbol{u}_h^i \right\rangle_{\Gamma_N} . \end{aligned}$$

Using Lemma B.2.5, the first term on the left-hand side can be reformulated as

$$\left\langle \mathrm{d}_t \boldsymbol{u}_h^{i+1} - \mathrm{d}_t \boldsymbol{u}_h^i, \mathrm{d}_t \boldsymbol{u}_h^{i+1} \right\rangle = \frac{1}{2} \left\| \mathrm{d}_t \boldsymbol{u}_h^{i+1} \right\|^2 - \frac{1}{2} \left\| \mathrm{d}_t \boldsymbol{u}_h^i \right\|^2 + \frac{1}{2} \left\| \mathrm{d}_t \boldsymbol{u}_h^{i+1} - \mathrm{d}_t \boldsymbol{u}_h^i \right\|^2$$

which yields

$$\begin{aligned} &\frac{1}{2} \left\| \mathrm{d}_t \boldsymbol{u}_h^{i+1} \right\|^2 - \frac{1}{2} \left\| \mathrm{d}_t \boldsymbol{u}_h^i \right\|^2 + \frac{1}{2} \left\| \mathrm{d}_t \boldsymbol{u}_h^{i+1} - \mathrm{d}_t \boldsymbol{u}_h^i \right\|^2 \\ &\qquad + \left\langle \mathbb{C}[\boldsymbol{\varepsilon}(\boldsymbol{u}_h^{i+1}) - \boldsymbol{\varepsilon}_{\mathrm{m}}(\Pi_h \boldsymbol{m}_h^{i+1})], \boldsymbol{\varepsilon}(\boldsymbol{u}_h^{i+1}) - \boldsymbol{\varepsilon}(\boldsymbol{u}_h^i) \right\rangle \\ &\qquad\qquad = \left\langle \boldsymbol{f}, \boldsymbol{u}_h^{i+1} - \boldsymbol{u}_h^i \right\rangle + \left\langle \boldsymbol{g}, \boldsymbol{u}_h^{i+1} - \boldsymbol{u}_h^i \right\rangle_{\Gamma_N}. \end{aligned} \tag{5.27}$$

Similarly, we have

$$\begin{aligned} &\left\langle \mathbb{C} : [\boldsymbol{\varepsilon}(\boldsymbol{u}_h^{i+1}) - \boldsymbol{\varepsilon}_{\mathrm{m}}(\Pi_h \boldsymbol{m}_h^{i+1})], \boldsymbol{\varepsilon}(\boldsymbol{u}_h^{i+1}) - \boldsymbol{\varepsilon}(\boldsymbol{u}_h^i) \right\rangle \\ &\quad = \left\langle \mathbb{C} : [\boldsymbol{\varepsilon}(\boldsymbol{u}_h^{i+1}) - \boldsymbol{\varepsilon}_{\mathrm{m}}(\boldsymbol{m}_h^{i+1})], \boldsymbol{\varepsilon}(\boldsymbol{u}_h^{i+1}) - \boldsymbol{\varepsilon}(\boldsymbol{u}_h^i) \right\rangle \\ &\qquad + \left\langle \mathbb{C} : [\boldsymbol{\varepsilon}_{\mathrm{m}}(\boldsymbol{m}_h^{i+1}) - \boldsymbol{\varepsilon}_{\mathrm{m}}(\Pi_h \boldsymbol{m}_h^{i+1})], \boldsymbol{\varepsilon}(\boldsymbol{u}_h^{i+1}) - \boldsymbol{\varepsilon}(\boldsymbol{u}_h^i) \right\rangle \\ &\quad = \left\langle \mathbb{C} : [\boldsymbol{\varepsilon}(\boldsymbol{u}_h^{i+1}) - \boldsymbol{\varepsilon}_{\mathrm{m}}(\boldsymbol{m}_h^{i+1})], [\boldsymbol{\varepsilon}(\boldsymbol{u}_h^{i+1}) - \boldsymbol{\varepsilon}_{\mathrm{m}}(\boldsymbol{m}_h^{i+1})] - [\boldsymbol{\varepsilon}(\boldsymbol{u}_h^i) - \boldsymbol{\varepsilon}_{\mathrm{m}}(\boldsymbol{m}_h^i)] \right\rangle \\ &\qquad + \left\langle \mathbb{C} : [\boldsymbol{\varepsilon}(\boldsymbol{u}_h^{i+1}) - \boldsymbol{\varepsilon}_{\mathrm{m}}(\boldsymbol{m}_h^{i+1})], \boldsymbol{\varepsilon}_{\mathrm{m}}(\boldsymbol{m}_h^{i+1}) - \boldsymbol{\varepsilon}_{\mathrm{m}}(\boldsymbol{m}_h^i) \right\rangle \\ &\qquad + \left\langle \mathbb{C} : [\boldsymbol{\varepsilon}_{\mathrm{m}}(\boldsymbol{m}_h^{i+1}) - \boldsymbol{\varepsilon}_{\mathrm{m}}(\Pi_h \boldsymbol{m}_h^{i+1})], \boldsymbol{\varepsilon}(\boldsymbol{u}_h^{i+1}) - \boldsymbol{\varepsilon}(\boldsymbol{u}_h^i) \right\rangle \\ &\quad \overset{(B.7)}{=} \frac{1}{2} \left\| \boldsymbol{\varepsilon}(\boldsymbol{u}_h^{i+1}) - \boldsymbol{\varepsilon}_{\mathrm{m}}(\boldsymbol{m}_h^{i+1}) \right\|_{\mathbb{C}}^2 - \frac{1}{2} \left\| \boldsymbol{\varepsilon}(\boldsymbol{u}_h^i) - \boldsymbol{\varepsilon}_{\mathrm{m}}(\boldsymbol{m}_h^i) \right\|_{\mathbb{C}}^2 \\ &\qquad + \frac{1}{2} \left\| [\boldsymbol{\varepsilon}(\boldsymbol{u}_h^{i+1}) - \boldsymbol{\varepsilon}_{\mathrm{m}}(\boldsymbol{m}_h^{i+1})] - [\boldsymbol{\varepsilon}(\boldsymbol{u}_h^i) - \boldsymbol{\varepsilon}_{\mathrm{m}}(\boldsymbol{m}_h^i)] \right\|_{\mathbb{C}}^2 \\ &\qquad + \left\langle \mathbb{C} : [\boldsymbol{\varepsilon}(\boldsymbol{u}_h^{i+1}) - \boldsymbol{\varepsilon}_{\mathrm{m}}(\boldsymbol{m}_h^{i+1})], \boldsymbol{\varepsilon}_{\mathrm{m}}(\boldsymbol{m}_h^{i+1}) - \boldsymbol{\varepsilon}_{\mathrm{m}}(\boldsymbol{m}_h^i) \right\rangle \\ &\qquad + \left\langle \mathbb{C} : [\boldsymbol{\varepsilon}_{\mathrm{m}}(\boldsymbol{m}_h^{i+1}) - \boldsymbol{\varepsilon}_{\mathrm{m}}(\Pi_h \boldsymbol{m}_h^{i+1})], \boldsymbol{\varepsilon}(\boldsymbol{u}_h^{i+1}) - \boldsymbol{\varepsilon}(\boldsymbol{u}_h^i) \right\rangle, \end{aligned}$$

respectively. Altogether, we thus obtain

$$\begin{aligned} &\mathcal{E}_{\mathrm{el}}[\boldsymbol{u}_h^{i+1}, \boldsymbol{m}_h^{i+1}] + \frac{1}{2} \left\| \mathrm{d}_t \boldsymbol{u}_h^{i+1} \right\|^2 - \mathcal{E}_{\mathrm{el}}[\boldsymbol{u}_h^i, \boldsymbol{m}_h^i] - \frac{1}{2} \left\| \mathrm{d}_t \boldsymbol{u}_h^i \right\|^2 \\ &\quad = -\frac{1}{2} \left\| \mathrm{d}_t \boldsymbol{u}_h^{i+1} - \mathrm{d}_t \boldsymbol{u}_h^i \right\|^2 - \frac{1}{2} \left\| [\boldsymbol{\varepsilon}(\boldsymbol{u}_h^{i+1}) - \boldsymbol{\varepsilon}_{\mathrm{m}}(\boldsymbol{m}_h^{i+1})] - [\boldsymbol{\varepsilon}(\boldsymbol{u}_h^i) - \boldsymbol{\varepsilon}_{\mathrm{m}}(\boldsymbol{m}_h^i)] \right\|_{\mathbb{C}}^2 \\ &\qquad - \left\langle \mathbb{C} : [\boldsymbol{\varepsilon}(\boldsymbol{u}_h^{i+1}) - \boldsymbol{\varepsilon}_{\mathrm{m}}(\boldsymbol{m}_h^{i+1})], \boldsymbol{\varepsilon}_{\mathrm{m}}(\boldsymbol{m}_h^{i+1}) - \boldsymbol{\varepsilon}_{\mathrm{m}}(\boldsymbol{m}_h^i) \right\rangle \\ &\qquad - \left\langle \mathbb{C} : [\boldsymbol{\varepsilon}_{\mathrm{m}}(\boldsymbol{m}_h^{i+1}) - \boldsymbol{\varepsilon}_{\mathrm{m}}(\Pi_h \boldsymbol{m}_h^{i+1})], \boldsymbol{\varepsilon}(\boldsymbol{u}_h^{i+1}) - \boldsymbol{\varepsilon}(\boldsymbol{u}_h^i) \right\rangle. \end{aligned} \tag{5.28}$$

Combining (5.26) and (5.28) yields

$$\begin{aligned} &\mathcal{E}[\boldsymbol{u}_h^{i+1}, \boldsymbol{m}_h^{i+1}] + \frac{1}{2} \left\| \mathrm{d}_t \boldsymbol{u}_h^{i+1} \right\|^2 - \mathcal{E}[\boldsymbol{u}_h^i, \boldsymbol{m}_h^i] - \frac{1}{2} \left\| \mathrm{d}_t \boldsymbol{u}_h^i \right\|^2 \\ &\quad = -\alpha k \left\| \boldsymbol{v}_h^i \right\|_h^2 - k^2(\theta - 1/2) \left\| \boldsymbol{\nabla} \boldsymbol{v}_h^i \right\|^2 + k \left\langle \boldsymbol{h}_{\mathrm{m}}[\boldsymbol{u}_h^i, \Pi_h \boldsymbol{m}_h^i], \boldsymbol{v}_h^i \right\rangle \\ &\qquad - \frac{1}{2} \left\| \mathrm{d}_t \boldsymbol{u}_h^{i+1} - \mathrm{d}_t \boldsymbol{u}_h^i \right\|^2 - \frac{1}{2} \left\| [\boldsymbol{\varepsilon}(\boldsymbol{u}_h^{i+1}) - \boldsymbol{\varepsilon}_{\mathrm{m}}(\boldsymbol{m}_h^{i+1})] - [\boldsymbol{\varepsilon}(\boldsymbol{u}_h^i) - \boldsymbol{\varepsilon}_{\mathrm{m}}(\boldsymbol{m}_h^i)] \right\|_{\mathbb{C}}^2 \\ &\qquad - \left\langle \mathbb{C} : [\boldsymbol{\varepsilon}(\boldsymbol{u}_h^{i+1}) - \boldsymbol{\varepsilon}_{\mathrm{m}}(\boldsymbol{m}_h^{i+1})], \boldsymbol{\varepsilon}_{\mathrm{m}}(\boldsymbol{m}_h^{i+1}) - \boldsymbol{\varepsilon}_{\mathrm{m}}(\boldsymbol{m}_h^i) \right\rangle \\ &\qquad - \left\langle \mathbb{C} : [\boldsymbol{\varepsilon}(\boldsymbol{m}_h^{i+1}) - \boldsymbol{\varepsilon}_{\mathrm{m}}(\Pi_h \boldsymbol{m}_h^{i+1})], \boldsymbol{\varepsilon}_{\mathrm{m}}(\boldsymbol{u}_h^{i+1}) - \boldsymbol{\varepsilon}(\boldsymbol{u}_h^i) \right\rangle \\ &\quad = -\alpha k \left\| \boldsymbol{v}_h^i \right\|_h^2 - D_{h,k}^i - E_{h,k}^i, \end{aligned}$$

where, in the last identity, we have used the expression of $D^i_{h,k}$ in (5.19), and we have defined

$$\begin{aligned} E^i_{h,k} := &\left\langle \mathbb{C} : [\boldsymbol{\varepsilon}(\boldsymbol{u}_h^{i+1}) - \boldsymbol{\varepsilon}_{\mathrm{m}}(\boldsymbol{m}_h^{i+1})], \boldsymbol{\varepsilon}_{\mathrm{m}}(\boldsymbol{m}_h^{i+1}) - \boldsymbol{\varepsilon}_{\mathrm{m}}(\boldsymbol{m}_h^{i}) \right\rangle \\ &- k \left\langle \boldsymbol{h}_{\mathrm{m}}[\boldsymbol{u}_h^i, \Pi_h \boldsymbol{m}_h^i], \boldsymbol{v}_h^i \right\rangle \\ &+ \left\langle \mathbb{C} : [\boldsymbol{\varepsilon}_{\mathrm{m}}(\boldsymbol{m}_h^{i+1}) - \boldsymbol{\varepsilon}_{\mathrm{m}}(\Pi_h \boldsymbol{m}_h^{i+1})], \boldsymbol{\varepsilon}(\boldsymbol{u}_h^{i+1}) - \boldsymbol{\varepsilon}(\boldsymbol{u}_h^i) \right\rangle \end{aligned}$$

To conclude the proof of (5.18), it remains to show that the latter coincides with (5.20). To this end, using the expression of the elastic field and Lemma B.2.4, we obtain

$$\begin{aligned} k \left\langle \boldsymbol{h}_{\mathrm{m}}[\boldsymbol{u}_h^i, \Pi_h \boldsymbol{m}_h^i], \boldsymbol{v}_h^i \right\rangle &\overset{(5.7)}{=} 2k \left\langle \mathbb{Z}^\top \mathbb{C} : [\boldsymbol{\varepsilon}(\boldsymbol{u}_h^i) - \boldsymbol{\varepsilon}_{\mathrm{m}}(\Pi_h \boldsymbol{m}_h^i)] \Pi_h \boldsymbol{m}_h^i, \boldsymbol{v}_h^i \right\rangle \\ &\overset{(B.6)}{=} 2k \left\langle \mathbb{C} : [\boldsymbol{\varepsilon}(\boldsymbol{u}_h^i) - \boldsymbol{\varepsilon}_{\mathrm{m}}(\Pi_h \boldsymbol{m}_h^i)], \mathbb{Z}(\Pi_h \boldsymbol{m}_h^i \otimes \boldsymbol{v}_h^i) \right\rangle . \end{aligned}$$

Moreover, from (5.15) and the minor symmetry of $\mathbb{Z}$, we get the expansion

$$\boldsymbol{\varepsilon}_{\mathrm{m}}(\boldsymbol{m}_h^{i+1}) = \boldsymbol{\varepsilon}_{\mathrm{m}}(\boldsymbol{m}_h^i) + 2k\, \mathbb{Z}(\boldsymbol{m}_h^i \otimes \boldsymbol{v}_h^i) + k^2 \boldsymbol{\varepsilon}_{\mathrm{m}}(\boldsymbol{v}_h^i). \tag{5.29}$$

Altogether, it follows that

$$\begin{aligned} E^i_{h,k} &= k^2 \left\langle \mathbb{C} : [\boldsymbol{\varepsilon}(\boldsymbol{u}_h^{i+1}) - \boldsymbol{\varepsilon}_{\mathrm{m}}(\boldsymbol{m}_h^{i+1})], \boldsymbol{\varepsilon}_{\mathrm{m}}(\boldsymbol{v}_h^i) \right\rangle \\ &\quad + 2k \left\langle \mathbb{C} : [\boldsymbol{\varepsilon}(\boldsymbol{u}_h^{i+1}) - \boldsymbol{\varepsilon}_{\mathrm{m}}(\boldsymbol{m}_h^{i+1})], \mathbb{Z}(\boldsymbol{m}_h^i \otimes \boldsymbol{v}_h^i) \right\rangle \\ &\quad - 2k \left\langle \mathbb{C} : [\boldsymbol{\varepsilon}(\boldsymbol{u}_h^{i}) - \boldsymbol{\varepsilon}_{\mathrm{m}}(\boldsymbol{m}_h^{i})], \mathbb{Z}(\Pi_h \boldsymbol{m}_h^i \otimes \boldsymbol{v}_h^i) \right\rangle \\ &\quad + \left\langle \mathbb{C} : [\boldsymbol{\varepsilon}_{\mathrm{m}}(\boldsymbol{m}_h^{i+1}) - \boldsymbol{\varepsilon}_{\mathrm{m}}(\Pi_h \boldsymbol{m}_h^{i+1})], \boldsymbol{\varepsilon}(\boldsymbol{u}_h^{i+1}) - \boldsymbol{\varepsilon}(\boldsymbol{u}_h^i) \right\rangle \\ &= k^2 \left\langle \mathbb{C} : [\boldsymbol{\varepsilon}(\boldsymbol{u}_h^{i+1}) - \boldsymbol{\varepsilon}_{\mathrm{m}}(\boldsymbol{m}_h^{i+1})], \boldsymbol{\varepsilon}_{\mathrm{m}}(\boldsymbol{v}_h^i) \right\rangle \\ &\quad + 2k \left\langle \mathbb{C} : \{[\boldsymbol{\varepsilon}(\boldsymbol{u}_h^{i+1}) - \boldsymbol{\varepsilon}_{\mathrm{m}}(\boldsymbol{m}_h^{i+1})] - [\boldsymbol{\varepsilon}(\boldsymbol{u}_h^{i}) - \boldsymbol{\varepsilon}_{\mathrm{m}}(\boldsymbol{m}_h^{i})]\}, \mathbb{Z}(\boldsymbol{m}_h^i \otimes \boldsymbol{v}_h^i) \right\rangle \\ &\quad + 2k \left\langle \mathbb{C} : [\boldsymbol{\varepsilon}(\boldsymbol{u}_h^{i}) - \boldsymbol{\varepsilon}_{\mathrm{m}}(\boldsymbol{m}_h^{i})], \mathbb{Z}[(\boldsymbol{m}_h^i - \Pi_h \boldsymbol{m}_h^i) \otimes \boldsymbol{v}_h^i] \right\rangle \\ &\quad + \left\langle \mathbb{C} : [\boldsymbol{\varepsilon}_{\mathrm{m}}(\boldsymbol{m}_h^{i+1}) - \boldsymbol{\varepsilon}_{\mathrm{m}}(\Pi_h \boldsymbol{m}_h^{i+1})], \boldsymbol{\varepsilon}(\boldsymbol{u}_h^{i+1}) - \boldsymbol{\varepsilon}(\boldsymbol{u}_h^i) \right\rangle . \end{aligned}$$

This shows (5.20) and concludes the proof. □

5.6.3 Stability

We now prove Proposition 5.4.6 showing unconditional stability of Algorithm 5.4.1 and an estimate of the violation of the unit length constraint. For the sake of clarity, we split the proof into several lemmas.

An immediate consequence of the projection-free update (5.14) is the following L^2-bound for the approximate magnetizations.

Lemma 5.6.2. *For every integer $1 \le j \le N$, it holds that*

$$\left\| \boldsymbol{m}_h^j \right\|^2 \le C_1 \left(1 + k^2 \sum_{i=0}^{j-1} \left\| \boldsymbol{v}_h^i \right\|^2 \right), \tag{5.30}$$

$$\left\| \mathcal{I}_h \big[\left| \boldsymbol{m}_h^j \right|^2 \big] - 1 \right\|_{L^1(\Omega)} \le C_2 k^2 \sum_{i=0}^{j-1} \left\| \boldsymbol{v}_h^i \right\|^2, \tag{5.31}$$

where $C_1, C_2 > 0$ are constants depending the shape-regularity parameter of $\mathcal{T}_h$ (C_1 depends also on $|\Omega|$).

Proof. We follow [Bar16]. Starting from (5.15) and noting that $\boldsymbol{v}_h^i \in \boldsymbol{\mathcal{K}}_h[\boldsymbol{m}_h^i]$, we have for each $z \in \mathcal{N}_h$ that for every $0 \leq i \leq j-1$

$$\left|\boldsymbol{m}_h^{i+1}(z)\right|^2 = \left|\boldsymbol{m}_h^i(z)\right|^2 + k^2 \left|\boldsymbol{v}_h^i(z)\right|^2.$$

Inductively, starting with $|\boldsymbol{m}_h^0(z)| = 1$, we deduce that

$$|\boldsymbol{m}_h^j(z)|^2 = 1 + k^2 \sum_{i=0}^{j-1} |\boldsymbol{v}_h^i(z)|^2.$$

Then, noting that $\|1\| = |\Omega|^{1/2}$ and using (3.8) yields (5.30) (for a suitable constant $C_1 > 0$ we do not explicitly compute). The same argument shows (5.31). □

We also have the following estimate of all quantities involving the magnetization.

Lemma 5.6.3. *For every integer $1 \leq j \leq N$, it holds that*

$$\left\|\boldsymbol{\nabla} \boldsymbol{m}_h^j\right\|^2 + k \sum_{i=0}^{j-1} \left\|\boldsymbol{v}_h^i\right\|^2 + \left(\theta - \frac{1}{2}\right) k^2 \sum_{i=0}^{j-1} \left\|\boldsymbol{\nabla} \boldsymbol{v}_h^i\right\|^2 \leq C_3 \left[\left\|\boldsymbol{\nabla} \boldsymbol{m}_h^0\right\|^2 + k \sum_{i=0}^{j-1} \left(1 + \left\|\boldsymbol{\varepsilon}(\boldsymbol{u}_h^i)\right\|^2\right)\right], \quad (5.32)$$

where $C_3 > 0$ depends only on α, $|\Omega|$, $\|\mathbb{Z}\|_{\boldsymbol{L}^\infty(\Omega)}$, and $\|\mathbb{C}\|_{\boldsymbol{L}^\infty(\Omega)}$.

Proof. Let $1 \leq j \leq N$ be an integer. Starting from (5.26) (cf. the proof of Proposition 5.4.4), we sum up from 0 to $j-1$ to obtain

$$\frac{1}{2}\left\|\boldsymbol{\nabla} \boldsymbol{m}_h^j\right\|^2 + \alpha k \sum_{i=0}^{j-1} \left\|\boldsymbol{v}_h^i\right\|_h^2 + \left(\theta - \frac{1}{2}\right) k^2 \sum_{i=0}^{j-1} \left\|\boldsymbol{\nabla} \boldsymbol{v}_h^i\right\|^2 = \frac{1}{2}\left\|\boldsymbol{\nabla} \boldsymbol{m}_h^0\right\|^2 + k \sum_{i=0}^{j-1} \left\langle \boldsymbol{h}_{\mathrm{m}}[\boldsymbol{u}_h^i, \Pi_h \boldsymbol{m}_h^i], \boldsymbol{v}_h^i \right\rangle.$$

Using Lemma 5.6.1, we can estimate the term involving the elastic field for some $\nu > 0$ by

$$\begin{aligned} \left|\left\langle \boldsymbol{h}_{\mathrm{m}}[\boldsymbol{u}_h^i, \Pi_h \boldsymbol{m}_h^i], \boldsymbol{v}_h^i \right\rangle\right| &\leq \frac{1}{4\nu}\left\|\boldsymbol{h}_{\mathrm{m}}[\boldsymbol{u}_h^i, \Pi_h \boldsymbol{m}_h^i]\right\|^2 + \nu \left\|\boldsymbol{v}_h^i\right\|^2 \\ &\overset{(5.25)}{\leq} \frac{2}{\nu} \|\mathbb{Z}\|_{\boldsymbol{L}^\infty(\Omega)}^2 \|\mathbb{C}\|_{\boldsymbol{L}^\infty(\Omega)}^2 \left(\left\|\boldsymbol{\varepsilon}(\boldsymbol{u}_h^i)\right\|^2 + \|\mathbb{Z}\|_{\boldsymbol{L}^\infty(\Omega)}^2 |\Omega|\right) \\ &\quad + \nu \left\|\boldsymbol{v}_h^i\right\|^2. \end{aligned}$$

Then we get

$$\begin{aligned} \frac{1}{2}\left\|\boldsymbol{\nabla} \boldsymbol{m}_h^j\right\|^2 + \alpha k \sum_{i=0}^{j-1} \left\|\boldsymbol{v}_h^i\right\|_h^2 + \left(\theta - \frac{1}{2}\right) k^2 \sum_{i=0}^{j-1} \left\|\boldsymbol{\nabla} \boldsymbol{v}_h^i\right\|^2 &\leq \frac{1}{2}\left\|\boldsymbol{\nabla} \boldsymbol{m}_h^0\right\|^2 \\ + \frac{2k}{\nu} \sum_{i=0}^{j-1} \|\mathbb{Z}\|_{\boldsymbol{L}^\infty(\Omega)}^2 \|\mathbb{C}\|_{\boldsymbol{L}^\infty(\Omega)}^2 \left(\left\|\boldsymbol{\varepsilon}(\boldsymbol{u}_h^i)\right\|^2 + \|\mathbb{Z}\|_{\boldsymbol{L}^\infty(\Omega)}^2 |\Omega|\right) + \nu k \sum_{i=0}^{j-1} \left\|\boldsymbol{v}_h^i\right\|^2. \end{aligned}$$

Using (3.5) and choosing $\nu = \alpha/2$ yields (5.32) (for a suitable constant $C_3 > 0$ which we do not compute explicitly). □

In the following lemma, we show that the magnetostrain is Lipschitz continuous with respect to the magnetization (the use of the nodal projection is exploited here).

Lemma 5.6.4. *For all $\boldsymbol{m}_{h,1}, \boldsymbol{m}_{h,2} \in \mathcal{S}^1(\mathcal{T}_h)^3$ satisfying $|\boldsymbol{m}_{h,\ell}(z)| \geq 1$ for all $\ell = 1, 2$ and $z \in \mathcal{N}_h$, it holds that*

$$\|\boldsymbol{\varepsilon}_{\mathrm{m}}(\Pi_h \boldsymbol{m}_{h,1}) - \boldsymbol{\varepsilon}_{\mathrm{m}}(\Pi_h \boldsymbol{m}_{h,2})\| \leq C_{\mathrm{m}} \|\boldsymbol{m}_{h,1} - \boldsymbol{m}_{h,2}\|, \tag{5.33}$$

where $C_{\mathrm{m}} > 0$ depends only on $\|\mathbb{Z}\|_{\boldsymbol{L}^\infty(\Omega)}$ and the shape-regularity parameter of $\mathcal{T}_h$.

Proof. Straightforward calculations exploiting the boundedness guaranteed by the nodal projection, i.e. $\|\Pi_h \boldsymbol{m}_{h,1}\|_{\boldsymbol{L}^\infty(\Omega)} = \|\Pi_h \boldsymbol{m}_{h,2}\|_{\boldsymbol{L}^\infty(\Omega)} = 1$, show that

$$\|\boldsymbol{\varepsilon}_{\mathrm{m}}(\Pi_h \boldsymbol{m}_{h,1}) - \boldsymbol{\varepsilon}_{\mathrm{m}}(\Pi_h \boldsymbol{m}_{h,2})\| \lesssim \|\Pi_h \boldsymbol{m}_{h,1} - \Pi_h \boldsymbol{m}_{h,2}\|,$$

where the hidden constant depends on $\|\mathbb{Z}\|_{\boldsymbol{L}^\infty(\Omega)}$. From the norm equivalence in [Bar15b, Lemma 3.4] and the fact that the projection onto the sphere is non-expanding (i.e. Lipschitz continuous with constant 1), it follows that

$$\|\Pi_h \boldsymbol{m}_{h,1} - \Pi_h \boldsymbol{m}_{h,2}\| \lesssim \|\boldsymbol{m}_{h,1} - \boldsymbol{m}_{h,2}\|,$$

where the hidden constant depends on the shape-regularity of the mesh. Combining the above two estimates yields the desired result, where $C_{\mathrm{m}} > 0$ is the product of the two constants hidden above. □

Lemma 5.6.5. *For every integer $1 \leq j \leq N$, the following estimate holds*

$$\begin{aligned}
&\left\|\mathrm{d}_t \boldsymbol{u}_h^j\right\|^2 + \left\|\boldsymbol{\varepsilon}(\boldsymbol{u}_h^j)\right\|^2 + \sum_{i=0}^{j-1} \left\|\mathrm{d}_t \boldsymbol{u}_h^{i+1} - \mathrm{d}_t \boldsymbol{u}_h^i\right\|^2 + \sum_{i=0}^{j-1} \left\|\boldsymbol{\varepsilon}(\boldsymbol{u}_h^{i+1}) - \boldsymbol{\varepsilon}(\boldsymbol{u}_h^i)\right\|^2 \\
&\qquad \leq C_4 \left[1 + \left\|\dot{\boldsymbol{u}}_h^0\right\|^2 + \left\|\boldsymbol{\varepsilon}(\boldsymbol{u}_h^0)\right\|^2 + \left\|\boldsymbol{\nabla} \boldsymbol{m}_h^0\right\|^2 + k \sum_{i=0}^{j-1} \left(1 + \left\|\boldsymbol{\varepsilon}(\boldsymbol{u}_h^i)\right\|^2\right)\right],
\end{aligned} \tag{5.34}$$

where $C_4 > 0$ depends only on the shape-regularity parameter of $\mathcal{T}_h$ and the problem data α, Ω, $\mathbb{C}$, $\mathbb{Z}$, $\boldsymbol{f}$ and $\boldsymbol{g}$.

Proof. Let $1 \leq j \leq N$ be an integer. Starting from (5.27) (cf. the proof of Proposition 5.4.4), summing up from 0 to $j-1$, we have

$$\begin{aligned}
&\frac{1}{2}\left\|\mathrm{d}_t \boldsymbol{u}_h^j\right\|^2 - \frac{1}{2}\left\|\mathrm{d}_t \boldsymbol{u}_h^0\right\|^2 \\
&\qquad + \frac{1}{2}\sum_{i=0}^{j-1} \left\|\mathrm{d}_t \boldsymbol{u}_h^{i+1} - \mathrm{d}_t \boldsymbol{u}_h^i\right\|^2 + \sum_{i=0}^{j-1} \left\langle \mathbb{C} : \boldsymbol{\varepsilon}(\boldsymbol{u}_h^{i+1}), \boldsymbol{\varepsilon}(\boldsymbol{u}_h^{i+1}) - \boldsymbol{\varepsilon}(\boldsymbol{u}_h^i)\right\rangle \\
&\qquad\qquad = \sum_{i=0}^{j-1} \left\langle \mathbb{C} : \boldsymbol{\varepsilon}_{\mathrm{m}}(\Pi_h \boldsymbol{m}_h^{i+1}), \boldsymbol{\varepsilon}(\boldsymbol{u}_h^{i+1}) - \boldsymbol{\varepsilon}(\boldsymbol{u}_h^i)\right\rangle \\
&\qquad\qquad\qquad + \left\langle \boldsymbol{f}, \boldsymbol{u}_h^j\right\rangle - \left\langle \boldsymbol{f}, \boldsymbol{u}_h^0\right\rangle + \left\langle \boldsymbol{g}, \boldsymbol{u}_h^j\right\rangle_{\Gamma_N} - \left\langle \boldsymbol{g}, \boldsymbol{u}_h^0\right\rangle_{\Gamma_N}.
\end{aligned}$$

Applying Lemma B.2.5 to the last term on the left-hand side and rearranging we have

$$\begin{aligned}
&\frac{1}{2}\left\|\mathrm{d}_t \boldsymbol{u}_h^j\right\|^2 + \frac{1}{2}\left\|\boldsymbol{\varepsilon}(\boldsymbol{u}_h^j)\right\|_{\mathbb{C}}^2 + \frac{1}{2}\sum_{i=0}^{j-1}\left\|\mathrm{d}_t \boldsymbol{u}_h^{i+1} - \mathrm{d}_t \boldsymbol{u}_h^i\right\|^2 + \frac{1}{2}\sum_{i=0}^{j-1}\left\|\boldsymbol{\varepsilon}(\boldsymbol{u}_h^{i+1}) - \boldsymbol{\varepsilon}(\boldsymbol{u}_h^i)\right\|_{\mathbb{C}}^2 \\
&\quad = \frac{1}{2}\left\|\mathrm{d}_t \boldsymbol{u}_h^0\right\|^2 + \frac{1}{2}\left\|\boldsymbol{\varepsilon}(\boldsymbol{u}_h^0)\right\|_{\mathbb{C}}^2 + \sum_{i=0}^{j-1}\left\langle \mathbb{C} : \boldsymbol{\varepsilon}_{\mathrm{m}}(\Pi_h \boldsymbol{m}_h^{i+1}), \boldsymbol{\varepsilon}(\boldsymbol{u}_h^{i+1}) - \boldsymbol{\varepsilon}(\boldsymbol{u}_h^i)\right\rangle \\
&\qquad\qquad + \left\langle \boldsymbol{f}, \boldsymbol{u}_h^j\right\rangle - \left\langle \boldsymbol{f}, \boldsymbol{u}_h^0\right\rangle + \left\langle \boldsymbol{g}, \boldsymbol{u}_h^j\right\rangle_{\Gamma_N} - \left\langle \boldsymbol{g}, \boldsymbol{u}_h^0\right\rangle_{\Gamma_N}.
\end{aligned}$$

The term involving the magnetostrain can be estimated as

$$\begin{aligned}
&\sum_{i=0}^{j-1}\left\langle \mathbb{C} : \boldsymbol{\varepsilon}_{\mathrm{m}}(\Pi_h \boldsymbol{m}_h^{i+1}), \boldsymbol{\varepsilon}(\boldsymbol{u}_h^{i+1}) - \boldsymbol{\varepsilon}(\boldsymbol{u}_h^i)\right\rangle \\
&\quad = \left\langle \boldsymbol{\varepsilon}_{\mathrm{m}}(\Pi_h \boldsymbol{m}_h^j), \mathbb{C} : \boldsymbol{\varepsilon}(\boldsymbol{u}_h^j)\right\rangle - \left\langle \boldsymbol{\varepsilon}_{\mathrm{m}}(\Pi_h \boldsymbol{m}_h^1), \mathbb{C} : \boldsymbol{\varepsilon}(\boldsymbol{u}_h^0)\right\rangle \\
&\qquad\qquad - k\sum_{i=1}^{j-1}\left\langle \mathrm{d}_t \boldsymbol{\varepsilon}_{\mathrm{m}}(\Pi_h \boldsymbol{m}_h^{i+1}), \mathbb{C} : \boldsymbol{\varepsilon}(\boldsymbol{u}_h^i)\right\rangle \\
&\quad \le \left\|\boldsymbol{\varepsilon}_{\mathrm{m}}(\Pi_h \boldsymbol{m}_h^j)\right\|^2 + \frac{1}{4}\left\|\boldsymbol{\varepsilon}(\boldsymbol{u}_h^j)\right\|_{\mathbb{C}}^2 + \frac{1}{2}\left\|\boldsymbol{\varepsilon}_{\mathrm{m}}(\Pi_h \boldsymbol{m}_h^1)\right\|_{\mathbb{C}}^2 + \frac{1}{2}\left\|\boldsymbol{\varepsilon}(\boldsymbol{u}_h^0)\right\|_{\mathbb{C}}^2 \\
&\qquad + \frac{k}{2}\sum_{i=1}^{j-1}\left\|\mathrm{d}_t \boldsymbol{\varepsilon}_{\mathrm{m}}(\Pi_h \boldsymbol{m}_h^{i+1})\right\|^2 + \frac{k}{2}\sum_{i=1}^{j-1}\left\|\boldsymbol{\varepsilon}(\boldsymbol{u}_h^i)\right\|_{\mathbb{C}}^2 \\
&\quad \le \frac{3}{2}\left\|\mathbb{Z}\right\|_{\boldsymbol{L}^\infty(\Omega)}^2 |\Omega| + \frac{1}{4}\left\|\boldsymbol{\varepsilon}(\boldsymbol{u}_h^j)\right\|_{\mathbb{C}}^2 + \frac{1}{2}\left\|\boldsymbol{\varepsilon}(\boldsymbol{u}_h^0)\right\|_{\mathbb{C}}^2 \\
&\qquad + \frac{k}{2}\sum_{i=1}^{j-1}\left\|\mathrm{d}_t \boldsymbol{\varepsilon}_{\mathrm{m}}(\Pi_h \boldsymbol{m}_h^{i+1})\right\|^2 + \frac{k}{2}\sum_{i=1}^{j-1}\left\|\boldsymbol{\varepsilon}(\boldsymbol{u}_h^i)\right\|_{\mathbb{C}}^2.
\end{aligned}$$

Using Lemma 5.6.4, we get

$$\begin{aligned}
\left\|\mathrm{d}_t \boldsymbol{\varepsilon}_{\mathrm{m}}(\Pi_h \boldsymbol{m}_h^{i+1})\right\| &= \frac{1}{k}\left\|\boldsymbol{\varepsilon}_{\mathrm{m}}(\Pi_h \boldsymbol{m}_h^{i+1}) - \boldsymbol{\varepsilon}_{\mathrm{m}}(\Pi_h \boldsymbol{m}_h^i)\right\| \\
&\overset{(5.33)}{\le} \frac{1}{k} C_{\mathrm{m}}\left\|\boldsymbol{m}_h^{i+1} - \boldsymbol{m}_h^i\right\| = C_{\mathrm{m}}\left\|\boldsymbol{v}_h^i\right\|.
\end{aligned}$$

It follows that

$$\frac{k}{2}\sum_{i=1}^{j-1}\left\|\mathrm{d}_t \boldsymbol{\varepsilon}_{\mathrm{m}}(\Pi_h \boldsymbol{m}_h^{i+1})\right\|^2 \le \frac{C_{\mathrm{m}}^2\, k}{2}\sum_{i=1}^{j-1}\left\|\boldsymbol{v}_h^i\right\|^2.$$

Moreover, for every $\delta > 0$ we have that

$$\begin{aligned}
\left|\left\langle \boldsymbol{f}, \boldsymbol{u}_h^j\right\rangle + \left\langle \boldsymbol{g}, \boldsymbol{u}_h^j\right\rangle_{\Gamma_N}\right| &\le C_{\mathrm{KPC}}(\|\boldsymbol{f}\| + \|\boldsymbol{g}\|_{\Gamma_N})\left\|\boldsymbol{\varepsilon}(\boldsymbol{u}_h^j)\right\|_{\mathbb{C}} \\
&\le \frac{C_{\mathrm{KPC}}^2}{4\delta}(\|\boldsymbol{f}\| + \|\boldsymbol{g}\|_{\Gamma_N})^2 + \delta\left\|\boldsymbol{\varepsilon}(\boldsymbol{u}_h^j)\right\|_{\mathbb{C}}^2,
\end{aligned}$$

where $C_{\mathrm{KPC}} > 0$ is a constant depending only on $|\Omega|$ and $\mathbb{C}$ (a combination of the continuity constant of the trace operator $\boldsymbol{H}^1(\Omega) \to \boldsymbol{L}^2(\Gamma_N)$, the constants

appearing in Poincaré's and Korn's inequalities, and the equivalence constant in the norm equivalence $\|\cdot\| \simeq \|\cdot\|_{\mathbb{C}}$). Overall, choosing $\delta = 1/8$ and recalling that $\mathrm{d}_t \boldsymbol{u}_h^0 = \dot{\boldsymbol{u}}_h^0$, we obtain

$$\begin{aligned}
&\frac{1}{2}\left\|\mathrm{d}_t \boldsymbol{u}_h^j\right\|^2 + \frac{1}{8}\left\|\boldsymbol{\varepsilon}(\boldsymbol{u}_h^j)\right\|_{\mathbb{C}}^2 \\
&\qquad + \frac{1}{2}\sum_{i=0}^{j-1}\left\|\mathrm{d}_t \boldsymbol{u}_h^{i+1} - \mathrm{d}_t \boldsymbol{u}_h^i\right\|^2 + \frac{1}{2}\sum_{i=0}^{j-1}\left\|\boldsymbol{\varepsilon}(\boldsymbol{u}_h^{i+1}) - \boldsymbol{\varepsilon}(\boldsymbol{u}_h^i)\right\|_{\mathbb{C}}^2 \\
&\quad \leq \frac{3}{2}\|\mathbb{Z}\|_{\boldsymbol{L}^\infty(\Omega)}^2 |\Omega| + 2C_{\mathrm{KPC}}^2(\|\boldsymbol{f}\| + \|\boldsymbol{g}\|_{\Gamma_N})^2 + \frac{1}{2}\left\|\dot{\boldsymbol{u}}_h^0\right\|^2 \\
&\qquad + \left[1 + C_{\mathrm{KPC}}\left(\|\boldsymbol{f}\| + \|\boldsymbol{g}\|_{\Gamma_N}\right)\right]\left\|\boldsymbol{\varepsilon}(\boldsymbol{u}_h^0)\right\|_{\mathbb{C}}^2 \\
&\qquad\quad + \frac{k}{2}\sum_{i=1}^{j-1}\left\|\boldsymbol{\varepsilon}(\boldsymbol{u}_h^i)\right\|_{\mathbb{C}}^2 + \frac{C_{\mathrm{m}}^2\, k}{2}\sum_{i=1}^{j-1}\left\|\boldsymbol{v}_h^i\right\|^2.
\end{aligned}$$

Applying Lemma 5.6.3 to estimate the last term on the right-hand side, we obtain (5.34) (for a suitable constant $C_4 > 0$ which we do not compute explicitly). □

We are now in a position to prove Proposition 5.4.6.

Proof of Proposition 5.4.6. We apply Lemmas 5.6.2, 5.6.3 and 5.6.5. Combining (5.30), (5.32) and (5.34), we obtain

$$\begin{aligned}
&\left\|\mathrm{d}_t \boldsymbol{u}_h^j\right\|^2 + \left\|\boldsymbol{\varepsilon}(\boldsymbol{u}_h^j)\right\|^2 + \sum_{i=0}^{j-1}\left\|\mathrm{d}_t \boldsymbol{u}_h^{i+1} - \mathrm{d}_t \boldsymbol{u}_h^i\right\|^2 + \sum_{i=0}^{j-1}\left\|\boldsymbol{\varepsilon}(\boldsymbol{u}_h^{i+1}) - \boldsymbol{\varepsilon}(\boldsymbol{u}_h^i)\right\|^2 \\
&\qquad + \left\|\boldsymbol{m}_h^j\right\|_{\boldsymbol{H}^1(\Omega)}^2 + (1 - C_1 k)k\sum_{i=0}^{j-1}\left\|\boldsymbol{v}_h^i\right\|^2 + \left(\theta - \frac{1}{2}\right)k^2\sum_{i=0}^{j-1}\left\|\boldsymbol{\nabla}\boldsymbol{v}_h^i\right\|^2 \\
&\qquad\quad \leq C_1 + C_4 + (C_3 + C_4)\left\|\boldsymbol{\nabla}\boldsymbol{m}_h^0\right\|^2 + C_4\left\|\dot{\boldsymbol{u}}_h^0\right\|^2 + C_4\left\|\boldsymbol{\varepsilon}(\boldsymbol{u}_h^0)\right\|^2 \\
&\qquad\qquad + (C_3 + C_4)k\sum_{i=0}^{j-1}\left(1 + \left\|\boldsymbol{\varepsilon}(\boldsymbol{u}_h^i)\right\|^2\right) \\
&\qquad\quad \leq C_1 + C_4 + (C_3 + C_4)\left\|\boldsymbol{\nabla}\boldsymbol{m}_h^0\right\|^2 + C_4\left\|\dot{\boldsymbol{u}}_h^0\right\|^2 + C_4\left\|\boldsymbol{\varepsilon}(\boldsymbol{u}_h^0)\right\|^2 \\
&\qquad\qquad + (C_3 + C_4)T + (C_3 + C_4)k\sum_{i=0}^{j-1}\left\|\boldsymbol{\varepsilon}(\boldsymbol{u}_h^i)\right\|^2,
\end{aligned}$$

where in the last estimate we have used that $kj \leq T$. If the time-step size k is sufficiently small, the coefficients in front of all terms on the left-hand side are strictly positive. Given the boundedness of the approximate initial data guaranteed by assumption (5.21), the desired stability estimate (5.22) then follows from the discrete Grönwall lemma; see e.g. [Tho06, Lemma 10.5]. Finally, (5.23) follows from (5.22) and (5.31). This concludes the proof. □

5.6.4 Convergence

The proof of convergence of Algorithm 5.4.1 (Theorem 5.4.7(i)) follows the standard argument to prove existence of weak solutions for parabolic equations (uniform boundedness of Galerkin approximations, extraction of subsequences with suitable convergence properties, identification of the limit with a weak solution of the problem; see, e.g., [Eva10, Section 7.1]) and thus has the same structure as the one which proves the convergence of [BPPR14, Algorithm 4.1]. Therefore, in the upcoming analysis, we will provide only a sketch of the steps of the proof that can be found in [BPPR14]. However, we will present in detail the (non-obvious) steps that we have to perform to cope with the partial omission of the nodal projection (for which we borrow ideas from [AHP+14, Bar16]) and to prove our novel energy estimate.

We start the proof with showing the following lemma, which provides an estimate of the L^p-norm ($p \geq 1$) of the difference between the approximate magnetizations generated by Algorithm 5.4.1 and their nodal projections.

Lemma 5.6.6. *Let $p \in [1, \infty)$. For all integers $1 \leq j \leq N$, it holds that*

$$\left\|\boldsymbol{m}_h^j - \Pi_h \boldsymbol{m}_h^j\right\|_{\boldsymbol{L}^p(\Omega)} \leq C \frac{T^{1-1/p}}{2} k^{1+1/p} \sum_{i=0}^{j-1} \left\|\boldsymbol{v}_h^i\right\|_{\boldsymbol{L}^{2p}(\Omega)}^2, \tag{5.35}$$

where $C > 0$ depends only on the shape-regularity of $\mathcal{T}_h$.

Proof. Let $1 \leq j \leq N$ be an integer. For all $z \in \mathcal{N}_h$, we have that

$$\begin{aligned}\left|\boldsymbol{m}_h^j(z) - \Pi_h \boldsymbol{m}_h^j(z)\right| &= \left|\boldsymbol{m}_h^j(z) - \frac{\boldsymbol{m}_h^j(z)}{\left|\boldsymbol{m}_h^j(z)\right|}\right| = \left|\boldsymbol{m}_h^j(z)\right| - 1 \\ &= \frac{\left|\boldsymbol{m}_h^j(z)\right|^2 - 1}{\left|\boldsymbol{m}_h^j(z)\right| + 1} \leq \frac{1}{2}\left(\left|\boldsymbol{m}_h^j(z)\right|^2 - 1\right) = \frac{k^2}{2} \sum_{i=0}^{j-1} \left|\boldsymbol{v}_h^i(z)\right|^2.\end{aligned}$$

If $p = 1$, the norm equivalence (3.8) immediately yields (5.35). If $p > 1$, applying (3.8) twice and using the convexity of x^p for $x > 0$ as well as $jk \leq T$, we obtain

$$\begin{aligned}\left\|\boldsymbol{m}_h^j - \Pi_h \boldsymbol{m}_h^j\right\|_{\boldsymbol{L}^p(\Omega)}^p &\lesssim \sum_{z \in \mathcal{N}_h} h_z^3 \left|\boldsymbol{m}_h^j(z) - \Pi_h \boldsymbol{m}_h^j(z)\right|^p \\ &\leq \sum_{z \in \mathcal{N}_h} h_z^3 \left(\frac{k^2}{2} \sum_{i=0}^{j-1} \left|\boldsymbol{v}_h^i(z)\right|^2\right)^p \\ &\leq \sum_{z \in \mathcal{N}_h} h_z^3 \frac{k^{2p}}{2^p} j^{p-1} \sum_{i=0}^{j-1} \left|\boldsymbol{v}_h^i(z)\right|^{2p} \\ &\leq \sum_{z \in \mathcal{N}_h} h_z^3 \frac{k^{p+1}}{2^p} T^{p-1} \sum_{i=0}^{j-1} \left|\boldsymbol{v}_h^i(z)\right|^{2p} \\ &\lesssim \frac{k^{p+1}}{2^p} T^{p-1} \sum_{i=0}^{j-1} \left\|\boldsymbol{v}_h^i\right\|_{\boldsymbol{L}^{2p}(\Omega)}^{2p},\end{aligned}$$

where the hidden constants depend only on the shape-regularity of $\mathcal{T}_h$. Then, (5.35) for $p > 1$ follows from the inequality $\|\cdot\|_{\ell^p} \le \|\cdot\|_{\ell^1}$ satisfied by the p-norms in finite dimensions. This concludes the proof. □

Now, let $\{\boldsymbol{m}_{hk}\}$, $\{\boldsymbol{m}_{hk}^{\pm}\}$, $\{\boldsymbol{v}_{hk}^{-}\}$, $\{\boldsymbol{u}_{hk}\}$, $\{\boldsymbol{u}_{hk}^{\pm}\}$, $\{\dot{\boldsymbol{u}}_{hk}\}$, $\{\dot{\boldsymbol{u}}_{hk}^{\pm}\}$ be the time reconstructions defined according to (3.3) using the approximations $\{(\boldsymbol{u}_h^i, \boldsymbol{m}_h^i)\}_{0\le i\le N}$ generated by Algorithm 5.4.1. In the following lemma, we show that the uniform stability established in Proposition 5.4.6 allows us to extract convergent subsequences from the sequences of time reconstructions.

Lemma 5.6.7. *Under the assumptions of Theorem 5.4.7(i), there exist* $\boldsymbol{u} \in L^\infty(0,T;\boldsymbol{H}^1_D(\Omega))$ *with* $\partial_t\boldsymbol{u} \in L^\infty(0,T;\boldsymbol{L}^2(\Omega))$ *and* $\boldsymbol{m} \in L^\infty(0,T;\boldsymbol{H}^1(\Omega;\mathbb{S}^2))$ *with* $\partial_t\boldsymbol{m} \in L^2(0,T;\boldsymbol{L}^2(\Omega))$ *such that, upon extraction of (nonrelabeled) subsequences, we have the following convergence results:*

$$\boldsymbol{u}_{hk} \rightharpoonup \boldsymbol{u} \quad \text{in } \boldsymbol{H}^1(\Omega_T), \tag{5.36a}$$
$$\boldsymbol{u}_{hk}, \boldsymbol{u}_{hk}^{\pm} \overset{*}{\rightharpoonup} \boldsymbol{u} \quad \text{in } L^\infty(0,T;\boldsymbol{H}^1(\Omega)), \tag{5.36b}$$
$$\boldsymbol{u}_{hk}, \boldsymbol{u}_{hk}^{\pm} \rightharpoonup \boldsymbol{u} \quad \text{in } L^2(0,T;\boldsymbol{H}^1(\Omega)), \tag{5.36c}$$
$$\boldsymbol{u}_{hk}, \boldsymbol{u}_{hk}^{\pm} \to \boldsymbol{u} \quad \text{in } \boldsymbol{L}^2(\Omega_T), \tag{5.36d}$$
$$\dot{\boldsymbol{u}}_{hk}, \dot{\boldsymbol{u}}_{hk}^{\pm} \overset{*}{\rightharpoonup} \partial_t\boldsymbol{u} \quad \text{in } L^\infty(0,T;\boldsymbol{L}^2(\Omega)), \tag{5.36e}$$
$$\dot{\boldsymbol{u}}_{hk}, \dot{\boldsymbol{u}}_{hk}^{\pm} \rightharpoonup \partial_t\boldsymbol{u} \quad \text{in } \boldsymbol{L}^2(\Omega_T), \tag{5.36f}$$
$$\boldsymbol{m}_{hk} \rightharpoonup \boldsymbol{m} \quad \text{in } \boldsymbol{H}^1(\Omega_T), \tag{5.36g}$$
$$\boldsymbol{m}_{hk} \to \boldsymbol{m} \quad \text{in } \boldsymbol{H}^s(\Omega_T) \text{ for all } s \in (0,1), \tag{5.36h}$$
$$\boldsymbol{m}_{hk}, \boldsymbol{m}_{hk}^{\pm} \overset{*}{\rightharpoonup} \boldsymbol{m} \quad \text{in } L^\infty(0,T;\boldsymbol{H}^1(\Omega)), \tag{5.36i}$$
$$\boldsymbol{m}_{hk}, \boldsymbol{m}_{hk}^{\pm} \rightharpoonup \boldsymbol{m} \quad \text{in } L^2(0,T;\boldsymbol{H}^1(\Omega)), \tag{5.36j}$$
$$\boldsymbol{m}_{hk}, \boldsymbol{m}_{hk}^{\pm} \to \boldsymbol{m} \quad \text{in } L^2(0,T;\boldsymbol{H}^s(\Omega)) \text{ for all } s \in (0,1), \tag{5.36k}$$
$$\boldsymbol{m}_{hk}, \boldsymbol{m}_{hk}^{\pm} \to \boldsymbol{m} \quad \text{in } \boldsymbol{L}^2(\Omega_T), \tag{5.36l}$$
$$\boldsymbol{m}_{hk}, \boldsymbol{m}_{hk}^{\pm} \to \boldsymbol{m} \quad \text{pointwise a.e. in } \Omega_T, \tag{5.36m}$$
$$\boldsymbol{v}_{hk}^{-} \rightharpoonup \partial_t\boldsymbol{m} \quad \text{in } \boldsymbol{L}^2(\Omega_T), \tag{5.36n}$$

as $h, k \to 0$.

Proof. Using the boundedness expressed in Proposition 5.4.6, we can successively extract weakly(-star) convergent subsequences (nonrelabeled, with possibly different limits) from $\{\boldsymbol{u}_{hk}\}$ and $\{\boldsymbol{u}_{hk}^{\pm}\}$, from $\{\dot{\boldsymbol{u}}_{hk}\}$ and $\{\dot{\boldsymbol{u}}_{hk}^{\pm}\}$, from $\{\boldsymbol{m}_{hk}\}$ and $\{\boldsymbol{m}_{hk}^{\pm}\}$, and from $\{\boldsymbol{v}_{hk}^{-}\}$.

Let $\boldsymbol{u} \in \boldsymbol{H}^1(\Omega_T)$ satisfy the weak convergence (5.36a). Owing to the continuous inclusions $\boldsymbol{H}^1(\Omega_T) \subset L^2(0,T;\boldsymbol{H}^1(\Omega)) \subset \boldsymbol{L}^2(\Omega_T)$ and the compact inclusion $\boldsymbol{H}^1(\Omega_T) \Subset \boldsymbol{L}^2(\Omega_T)$, we obtain convergences (5.36c) and (5.36d). Moreover, from the continuous inclusion $L^\infty(0,T;\boldsymbol{H}^1(\Omega)) \subset L^2(0,T;\boldsymbol{H}^1(\Omega))$, we can identify the weak-star limit of $\{\boldsymbol{u}_{hk}\}$ in $L^\infty(0,T;\boldsymbol{H}^1(\Omega))$ with the weak limit in $L^2(0,T;\boldsymbol{H}^1(\Omega))$, which shows (5.36b) for $\{\boldsymbol{u}_{hk}\}$.

Let $\boldsymbol{m} \in \boldsymbol{H}^1(\Omega_T)$ satisfy the weak convergence as in (5.36g). Arguing as above and using a well-known result for convergence in L^p-spaces, we obtain conver-

gences (5.36j), (5.36l) and (upon extraction of a further subsequence) (5.36m) for $\{\boldsymbol{m}_{hk}\}$. Using the continuous inclusion

$$L^\infty(0,T;\boldsymbol{H}^1(\Omega)) \subset L^2(0,T;\boldsymbol{H}^1(\Omega)),$$

shows (5.36i) for $\{\boldsymbol{m}_{hk}\}$.

Let $0 < s < 1$ be arbitrary. Since $\boldsymbol{H}^s(\Omega_T) = [\boldsymbol{L}^2(\Omega_T), \boldsymbol{H}^1(\Omega_T)]_s$ and

$$L^2(0,T;\boldsymbol{H}^s(\Omega)) = [\boldsymbol{L}^2(\Omega_T), L^2(0,T;\boldsymbol{H}^1(\Omega))]_s,$$

well-known results from interpolation theory (see, e.g., [BL76, Theorem 6.4.5 and Theorem 3.8.1] and [BL76, Theorem 5.1.2]) yield the compact embedding $\boldsymbol{H}^1(\Omega_T) \Subset \boldsymbol{H}^s(\Omega_T)$ and the continuous inclusion $\boldsymbol{H}^s(\Omega_T) \subset L^2(0,T;\boldsymbol{H}^s(\Omega))$. These in turn show convergences (5.36h) and (5.36k) for $\{\boldsymbol{m}_{hk}\}$. Furthermore, we have that (5.36n) follows directly from $\partial_t \boldsymbol{m}_{hk} = \boldsymbol{v}_{hk}^-$.

Overall, this shows the convergence results (5.36a)–(5.36d) and (5.36g)–(5.36n) for the sequences $\{\boldsymbol{u}_{hk}\}$, $\{\boldsymbol{m}_{hk}\}$ and $\{\boldsymbol{v}_{hk}^-\}$. Using the same argument, one can obtain the same results for $\{\boldsymbol{u}_{hk}^\pm\}$ and $\{\boldsymbol{m}_{hk}^\pm\}$. Since the quantity

$$\sum_{i=0}^{j-1} \left\|\boldsymbol{m}_h^{i+1} - \boldsymbol{m}_h^i\right\|^2 + \sum_{i=0}^{j-1} \left\|\boldsymbol{u}_h^{i+1} - \boldsymbol{u}_h^i\right\|^2 + \sum_{i=0}^{j-1} \left\|\mathrm{d}_t \boldsymbol{u}_h^{i+1} - \mathrm{d}_t \boldsymbol{u}_h^i\right\| \tag{5.37}$$

is uniformly bounded, arguing as in [BPPR14, Lemma 5.7] we can show that the limits of $\{\boldsymbol{u}_{hk}\}$ and $\{\boldsymbol{u}_{hk}^\pm\}$ (resp. $\{\boldsymbol{m}_{hk}\}$ and $\{\boldsymbol{m}_{hk}^\pm\}$) coincide. The continuous inclusion $L^\infty(0,T;\boldsymbol{L}^2(\Omega)) \subset L^2(0,T;\boldsymbol{L}^2(\Omega)) = \boldsymbol{L}^2(\Omega_T)$, the boundedness of the third term in (5.37) and the identity $\partial_t \boldsymbol{u}_{hk} = \dot{\boldsymbol{u}}_{hk}^+$ imply (5.36e)–(5.36f). Finally, the fact that $\boldsymbol{m}$ satisfies $|\boldsymbol{m}| = 1$ a.e. in Ω follows from the available convergence results and (5.23). For the details, we refer to Step 3 of the proof of [HPP+19, Proposition 6]. This concludes the proof. □

Let $\{\widehat{\boldsymbol{m}}_{hk}^\pm\}$ be the piecewise constant time reconstructions defined using the projection of the approximate magnetizations, i.e, $\widehat{\boldsymbol{m}}_{hk}^-(t) := \Pi_h \boldsymbol{m}_h^i$ and $\widehat{\boldsymbol{m}}_{hk}^+(t) := \Pi_h \boldsymbol{m}_h^{i+1}$ for all $i = 0, \dots, N_1$ and $t \in [t_i, t_{i+1})$ (cf. (3.3)).

In the following lemma, we establish further convergence results that will be needed to identify the limit $(\boldsymbol{u}, \boldsymbol{m})$ constructed in Lemma 5.6.7 with a weak solution of (5.4)–(5.6).

Lemma 5.6.8 (auxiliary convergences)**.** *With the assumptions of Theorem 5.4.7(i), upon extraction of a further (nonrelabeled) subsequence, we have the following convergence results:*

$$\widehat{\boldsymbol{m}}_{hk}^\pm \overset{*}{\rightharpoonup} \boldsymbol{m} \quad \text{in } L^\infty(0,T;\boldsymbol{H}^1(\Omega)), \tag{5.38a}$$

$$\widehat{\boldsymbol{m}}_{hk}^\pm \rightharpoonup \boldsymbol{m} \quad \text{in } L^2(0,T;\boldsymbol{H}^1(\Omega)), \tag{5.38b}$$

$$\widehat{\boldsymbol{m}}_{hk}^\pm \to \boldsymbol{m} \quad \text{in } \boldsymbol{L}^2(\Omega_T), \tag{5.38c}$$

$$\boldsymbol{m}_{hk}^\pm \otimes \boldsymbol{m}_{hk}^\pm \to \boldsymbol{m} \otimes \boldsymbol{m} \quad \text{in } \boldsymbol{L}^2(\Omega_T), \tag{5.38d}$$

$$\widehat{\boldsymbol{m}}_{hk}^\pm \otimes \widehat{\boldsymbol{m}}_{hk}^\pm \to \boldsymbol{m} \otimes \boldsymbol{m} \quad \text{in } \boldsymbol{L}^2(\Omega_T), \tag{5.38e}$$

as $h, k \to 0$.

Proof. Firstly, we note that $\|\Pi_h \boldsymbol{m}_h^i\|_{\boldsymbol{L}^\infty(\Omega)} = 1$ and $\|\boldsymbol{\nabla}\Pi_h \boldsymbol{m}_h^i\| \lesssim \|\boldsymbol{\nabla}\boldsymbol{m}_h^i\| \lesssim 1$ for all $i = 0, \dots, N$ (the estimate of the gradient follows from (5.22) and (3.11)). We infer that the sequences $\{\widehat{\boldsymbol{m}}_{hk}^{\pm}\}$ are uniformly bounded in $L^\infty(0,T;\boldsymbol{H}^1(\Omega))$ and arguing as in the proof of Lemma 5.6.7, we can extract subsequences satisfying the convergence properties in (5.38a)–(5.38c). The fact that the limit is exactly the function $\boldsymbol{m} \in L^\infty(0,T;\boldsymbol{H}^1(\Omega;\mathbb{S}^2))$ constructed in Lemma 5.6.7 follows from Lemma 5.6.6 (applied $p = 1$), which guarantee that $\widehat{\boldsymbol{m}}_{hk}^{\pm} \to \boldsymbol{m}$ in $\boldsymbol{L}^1(\Omega_T)$, which in turn implies that the limit functions in $\boldsymbol{L}^2(\Omega_T)$, $L^2(0,T;\boldsymbol{H}^1(\Omega))$ and $L^\infty(0,T;\boldsymbol{H}^1(\Omega))$ must necessarily be the same.

To show (5.38d)–(5.38e), we note that for $\boldsymbol{x}, \boldsymbol{y} \in \mathbb{R}^3$ we have

$$\boldsymbol{x}\otimes\boldsymbol{x} - \boldsymbol{y}\otimes\boldsymbol{y} = \frac{1}{2}[(\boldsymbol{x}+\boldsymbol{y})\otimes(\boldsymbol{x}-\boldsymbol{y}) + (\boldsymbol{x}-\boldsymbol{y})\otimes(\boldsymbol{x}+\boldsymbol{y})].$$

Let $3/4 \le s < 1$. Using the above identity and the continuous inclusion $\boldsymbol{H}^s(\Omega) \subset \boldsymbol{L}^4(\Omega)$ for all $s \ge 3/4$, for arbitrary $t \in (0,T)$, we have

$$\begin{aligned}
&\big\|\boldsymbol{m}_{hk}^{\pm}(t)\otimes\boldsymbol{m}_{hk}^{\pm}(t) - \boldsymbol{m}(t)\otimes\boldsymbol{m}(t)\big\| \\
&\qquad\le \big\|\boldsymbol{m}_{hk}^{\pm}(t) + \boldsymbol{m}(t)\big\|_{\boldsymbol{L}^4(\Omega)} \big\|\boldsymbol{m}(t) - \boldsymbol{m}_{hk}^{\pm}(t)\big\|_{\boldsymbol{L}^4(\Omega)} \\
&\qquad\lesssim \big\|\boldsymbol{m}_{hk}^{\pm}(t) + \boldsymbol{m}(t)\big\|_{\boldsymbol{H}^1(\Omega)} \big\|\boldsymbol{m}(t) - \boldsymbol{m}_{hk}^{\pm}(t)\big\|_{\boldsymbol{H}^s(\Omega)}.
\end{aligned}$$

It follows that

$$\begin{aligned}
&\big\|\boldsymbol{m}_{hk}^{\pm}\otimes\boldsymbol{m}_{hk}^{\pm} - \boldsymbol{m}\otimes\boldsymbol{m}\big\|_{\boldsymbol{L}^2(\Omega_T)} \\
&\qquad\lesssim \big\|\boldsymbol{m}_{hk}^{\pm} + \boldsymbol{m}\big\|_{L^\infty(0,T;\boldsymbol{H}^1(\Omega))} \big\|\boldsymbol{m} - \boldsymbol{m}_{hk}^{\pm}\big\|_{L^2(0,T;\boldsymbol{H}^s(\Omega))}.
\end{aligned}$$

Convergence (5.38d) then follows from the uniform boundedness of both $\boldsymbol{m}_{hk}^{\pm}$ and $\boldsymbol{m}$ in $L^\infty(0,T;\boldsymbol{H}^1(\Omega))$ and the strong convergence (5.36k) from Lemma 5.6.7. The proof of (5.38e) is identical (due to the use of the nodal projection, one can use the Hölder inequality $\|\cdot\|_{L^2} \le \|\cdot\|_{L^\infty}\|\cdot\|_{L^2}$). This concludes the proof. □

Now, we are in a position to prove Theorem 5.4.7(i).

Proof of Theorem 5.4.7(i). We apply Lemma 5.6.7, which immediately yields that $\boldsymbol{u} \in L^\infty(0,T;\boldsymbol{H}^1_D(\Omega))$ with $\partial_t\boldsymbol{u} \in L^\infty(0,T;\boldsymbol{L}^2(\Omega))$ and $\boldsymbol{m} \in L^\infty(0,T;\boldsymbol{H}^1(\Omega;\mathbb{S}^2))$ with $\partial_t\boldsymbol{m} \in L^2(0,T;\boldsymbol{L}^2(\Omega))$ as well as subsequences of $\{\boldsymbol{u}_{hk}\}$ and $\{\boldsymbol{m}_{hk}\}$ satisfying the desired convergence properties. This already shows that $\boldsymbol{u}$ and $\boldsymbol{m}$ satisfy property (i) of Definition 5.2.1. Property (iii) follows from the available convergence results, the continuity of the trace operator $\boldsymbol{H}^1(\Omega_T) \to \boldsymbol{H}^{1/2}(\Omega)$, and assumption (5.21) on the discrete initial data. To conclude the proof, it remains to show that property (ii) holds, i.e., that $\boldsymbol{u}$ and $\boldsymbol{m}$ satisfy the variational formulations (5.10) and (5.11), respectively. The result follows from the convergence properties established in Lemmas 5.6.7–5.6.8. We omit the details, because

- the proof that $\boldsymbol{u}$ satisfies (5.10) is identical to the one presented in [BPPR14, page 1378], which is a consequence of the fact that in the displacement update (5.16) we employ the nodal projection for the magnetization appearing

on the right-hand side (our generalized setting involving a more general expression for the magnetostrain, body forces and traction does not pose further mathematical challenges here).

- The proof that $\boldsymbol{m}$ satisfies (5.11) can be obtained combining the argument of [BPPR14, pages 1376–1378] (which show convergence of the method with nodal projection towards a variational formulation of the LLG equation with magnetoelastic term) with the one of [HPP+19, page 1363] (where the modifications due to the omission of the nodal projection are presented).

This concludes the proof. □

5.6.5 Energy inequality

In this section, we use the compact notation $\widehat{\boldsymbol{m}}_h = \Pi_h \boldsymbol{m}_h$ to denote the nodal projection of a general magnetization approximation $\boldsymbol{m}_h$.

To start with, in the following proposition, we state a variant of Proposition 5.4.4 for the discrete energy

$$\widehat{\mathcal{E}}_h[\boldsymbol{u}_h, \boldsymbol{m}_h] = \frac{1}{2} \|\boldsymbol{\nabla} \boldsymbol{m}_h\|^2 + \frac{1}{2} \|\boldsymbol{\varepsilon}(\boldsymbol{u}_h) - \boldsymbol{\varepsilon}_{\mathrm{m}}(\widehat{\boldsymbol{m}}_h)\|_{\mathbb{C}}^2 - \langle \boldsymbol{f}, \boldsymbol{u}_h \rangle - \langle \boldsymbol{g}, \boldsymbol{u}_h \rangle_{\Gamma_N},$$

which is obtained from (5.3) by applying the nodal projection to the discrete magnetization appearing in the elastic energy. We omit the proof since it is very similar to the one of Proposition 5.4.4.

Proposition 5.6.9. *For every integer $0 \leq i \leq N-1$, the iterates of Algorithm 5.4.1 satisfy the discrete energy law*

$$\widehat{\mathcal{E}}_h[\boldsymbol{u}_h^{i+1}, \boldsymbol{m}_h^{i+1}] + \frac{1}{2} \left\|\mathrm{d}_t \boldsymbol{u}_h^{i+1}\right\|^2 - \widehat{\mathcal{E}}_h[\boldsymbol{u}_h^{i}, \boldsymbol{m}_h^{i}] - \frac{1}{2} \left\|\mathrm{d}_t \boldsymbol{u}_h^{i}\right\|^2 = -\alpha k \left\|\boldsymbol{v}_h^i\right\|_h^2 - \widehat{D}_{h,k}^i - \widehat{E}_{h,k}^i, \tag{5.39}$$

where $\widehat{D}_{h,k}^i$ and $\widehat{E}_{h,k}^i$ are given by

$$\begin{aligned}\widehat{D}_{h,k}^i &:= k^2(\theta - 1/2) \left\|\boldsymbol{\nabla} \boldsymbol{v}_h^i\right\|^2 + \frac{1}{2} \left\|\mathrm{d}_t \boldsymbol{u}_h^{i+1} - \mathrm{d}_t \boldsymbol{u}_h^i\right\|^2 \\ &\qquad + \frac{1}{2} \left\|[\boldsymbol{\varepsilon}(\boldsymbol{u}_h^{i+1}) - \boldsymbol{\varepsilon}_{\mathrm{m}}(\widehat{\boldsymbol{m}}_h^{i+1})] - [\boldsymbol{\varepsilon}(\boldsymbol{u}_h^{i}) - \boldsymbol{\varepsilon}_{\mathrm{m}}(\widehat{\boldsymbol{m}}_h^{i})]\right\|_{\mathbb{C}}^2 \geq 0\end{aligned}$$

and

$$\begin{aligned}\widehat{E}_{h,k}^i &:= \sum_{\ell=1}^{5} \widehat{E}_{h,k,\ell}^i \\ &:= \left\langle \boldsymbol{\sigma}(\boldsymbol{u}_h^{i+1}, \widehat{\boldsymbol{m}}_h^{i+1}) - \boldsymbol{\sigma}(\boldsymbol{u}_h^{i}, \widehat{\boldsymbol{m}}_h^{i}), \boldsymbol{\varepsilon}_{\mathrm{m}}(\widehat{\boldsymbol{m}}_h^{i+1}) - \boldsymbol{\varepsilon}_{\mathrm{m}}(\widehat{\boldsymbol{m}}_h^{i}) \right\rangle \\ &\quad + \left\langle \boldsymbol{\sigma}(\boldsymbol{u}_h^{i}, \widehat{\boldsymbol{m}}_h^{i}), \boldsymbol{\varepsilon}_{\mathrm{m}}(\widehat{\boldsymbol{m}}_h^{i+1}) - \boldsymbol{\varepsilon}_{\mathrm{m}}(\boldsymbol{m}_h^{i+1}) \right\rangle \\ &\quad + \left\langle \boldsymbol{\sigma}(\boldsymbol{u}_h^{i}, \widehat{\boldsymbol{m}}_h^{i}), \boldsymbol{\varepsilon}_{\mathrm{m}}(\boldsymbol{m}_h^{i}) - \boldsymbol{\varepsilon}_{\mathrm{m}}(\widehat{\boldsymbol{m}}_h^{i}) \right\rangle \\ &\quad + 2k \left\langle \boldsymbol{\sigma}(\boldsymbol{u}_h^{i}, \widehat{\boldsymbol{m}}_h^{i}), \mathbb{Z} : [(\widehat{\boldsymbol{m}}_h^{i} - \boldsymbol{m}_h^{i}) \otimes \boldsymbol{v}_h^i] \right\rangle + k^2 \left\langle \boldsymbol{\sigma}(\boldsymbol{u}_h^{i}, \widehat{\boldsymbol{m}}_h^{i}), \boldsymbol{\varepsilon}_{\mathrm{m}}(\boldsymbol{v}_h^i) \right\rangle,\end{aligned}$$

respectively.

Now, we are in a position to prove Theorem 5.4.7(ii).

Proof of Theorem 5.4.7(ii). Let $t' \in (0,T)$. Let $1 \leq j \leq N$ such that $t' \in (t_{j-1}, t_j)$. Summing (5.39) for $i = 0, \ldots, j-1$ yields

$$\begin{aligned}\widehat{\mathcal{E}}_h[\boldsymbol{u}_h^j, \boldsymbol{m}_h^j] + \frac{1}{2}\left\|\mathrm{d}_t \boldsymbol{u}_h^j\right\|^2 \\ - \widehat{\mathcal{E}}_h[\boldsymbol{u}_h^0, \boldsymbol{m}_h^0] - \frac{1}{2}\left\|\mathrm{d}_t \boldsymbol{u}_h^0\right\|^2 \\ + \alpha k \sum_{i=0}^{j-1} \left\|\boldsymbol{v}_h^i\right\|_h^2 + \sum_{i=0}^{j-1} \widehat{D}_{h,k}^i = -\sum_{i=0}^{j-1} \widehat{E}_{h,k}^i.\end{aligned}$$

We can combine the Cauchy–Schwarz inequality and weighted Young inequality, with Lemma 5.6.4, to obtain the estimate

$$\begin{aligned}|E_{h,k,1}^i| &= |\Big\langle \boldsymbol{\sigma}(\boldsymbol{u}_h^{i+1}, \widehat{\boldsymbol{m}}_h^{i+1}) - \boldsymbol{\sigma}(\boldsymbol{u}_h^i, \widehat{\boldsymbol{m}}_h^i), \boldsymbol{\varepsilon}_{\mathrm{m}}(\widehat{\boldsymbol{m}}_h^{i+1}) - \boldsymbol{\varepsilon}_{\mathrm{m}}(\widehat{\boldsymbol{m}}_h^i)\Big\rangle| \\ &\leq \left\|[\boldsymbol{\varepsilon}(\boldsymbol{u}_h^{i+1}) - \boldsymbol{\varepsilon}_{\mathrm{m}}(\widehat{\boldsymbol{m}}_h^{i+1})] - [\boldsymbol{\varepsilon}(\boldsymbol{u}_h^i) - \boldsymbol{\varepsilon}_{\mathrm{m}}(\widehat{\boldsymbol{m}}_h^i)]\right\|_{\mathbb{C}} \left\|\boldsymbol{\varepsilon}_{\mathrm{m}}(\widehat{\boldsymbol{m}}_h^{i+1}) - \boldsymbol{\varepsilon}_{\mathrm{m}}(\widehat{\boldsymbol{m}}_h^i)\right\|_{\mathbb{C}} \\ &\leq \frac{1}{4}\left\|[\boldsymbol{\varepsilon}(\boldsymbol{u}_h^{i+1}) - \boldsymbol{\varepsilon}_{\mathrm{m}}(\widehat{\boldsymbol{m}}_h^{i+1})] - [\boldsymbol{\varepsilon}(\boldsymbol{u}_h^i) - \boldsymbol{\varepsilon}_{\mathrm{m}}(\widehat{\boldsymbol{m}}_h^i)]\right\|_{\mathbb{C}}^2 \\ &\quad + C_{\mathrm{m}}^2 \left\|\mathbb{C}\right\|_{\boldsymbol{L}^\infty(\Omega)} k^2 \left\|\boldsymbol{v}_h^i\right\|^2.\end{aligned}$$

We now estimate $E_{h,k,4}^i$ (assuming $i \geq 1$, because $E_{h,k,4}^0 = 0$ as $\widehat{\boldsymbol{m}}_h^0 = \boldsymbol{m}_h^0$ by assumption). Using the Cauchy–Schwarz inequality, the Hölder inequality (for $p = 2/(1-2\varepsilon)$ and $p' = 2p/(p-2)$ with $0 < \varepsilon \ll 1/2$ arbitrary), Lemma 5.6.6, and classical inverse estimates (see, e.g. [Bar15b, Lemma 3.5]), we obtain

$$\begin{aligned}|E_{h,k,4}^i| &= 2k|\Big\langle \boldsymbol{\sigma}(\boldsymbol{u}_h^i, \widehat{\boldsymbol{m}}_h^i), \mathbb{Z} : [(\widehat{\boldsymbol{m}}_h^i - \boldsymbol{m}_h^i) \otimes \boldsymbol{v}_h^i]\Big\rangle| \\ &\leq 2\left\|\mathbb{Z}\right\|_{\boldsymbol{L}^\infty(\Omega)} k \left\|\boldsymbol{\sigma}(\boldsymbol{u}_h^i, \widehat{\boldsymbol{m}}_h^i)\right\| \left\|\widehat{\boldsymbol{m}}_h^i - \boldsymbol{m}_h^i\right\|_{\boldsymbol{L}^p(\Omega)} \left\|\boldsymbol{v}_h^i\right\|_{\boldsymbol{L}^{p'}(\Omega)} \\ &\lesssim k \left\|\boldsymbol{\sigma}(\boldsymbol{u}_h^i, \widehat{\boldsymbol{m}}_h^i)\right\| k^{(p+1)/p} \left(\sum_{\ell=0}^{i-1} \left\|\boldsymbol{v}_h^\ell\right\|_{\boldsymbol{L}^{2p}(\Omega)}^2\right) \left\|\boldsymbol{v}_h^i\right\|_{\boldsymbol{L}^{p'}(\Omega)} \\ &\lesssim k^{2+1/p} \left\|\boldsymbol{\sigma}(\boldsymbol{u}_h^i, \widehat{\boldsymbol{m}}_h^i)\right\| h_{\min}^{3(1-p)/p} \left(\sum_{\ell=0}^{i-1} \left\|\boldsymbol{v}_h^\ell\right\|^2\right) h_{\min}^{3(2-p')/(2p')} \left\|\boldsymbol{v}_h^i\right\| \\ &\lesssim h_{\min}^{-3} k^{5/2-\varepsilon} \left\|\boldsymbol{\sigma}(\boldsymbol{u}_h^i, \widehat{\boldsymbol{m}}_h^i)\right\| \left(\sum_{\ell=0}^{i-1} \left\|\boldsymbol{v}_h^\ell\right\|^2\right) \left\|\boldsymbol{v}_h^i\right\|.\end{aligned}$$

Similarly, we obtain

$$|E_{h,k,5}^i| = |k^2 \left\langle \boldsymbol{\sigma}(\boldsymbol{u}_h^i, \widehat{\boldsymbol{m}}_h^i), \boldsymbol{\varepsilon}_{\mathrm{m}}(\boldsymbol{v}_h^i)\right\rangle| \lesssim h_{\min}^{-3/2} k^2 \left\|\boldsymbol{\sigma}(\boldsymbol{u}_h^i, \widehat{\boldsymbol{m}}_h^i)\right\| \left\|\boldsymbol{v}_h^i\right\|^2.$$

Moreover, noting $\boldsymbol{m}_h^0 = \widehat{\boldsymbol{m}}_h^0$ we have that

$$
\begin{aligned}
&\sum_{i=0}^{j-1} \left(\widehat{E}_{h,k,2}^i + \widehat{E}_{h,k,3}^i \right) \\
&\quad = \sum_{i=0}^{j-1} \left\langle \boldsymbol{\sigma}(\boldsymbol{u}_h^i, \widehat{\boldsymbol{m}}_h^i), \boldsymbol{\varepsilon}_{\mathrm{m}}(\widehat{\boldsymbol{m}}_h^{i+1}) - \boldsymbol{\varepsilon}_{\mathrm{m}}(\boldsymbol{m}_h^{i+1}) \right\rangle \\
&\qquad + \sum_{i=0}^{j-1} \left\langle \boldsymbol{\sigma}(\boldsymbol{u}_h^i, \widehat{\boldsymbol{m}}_h^i), \boldsymbol{\varepsilon}_{\mathrm{m}}(\boldsymbol{m}_h^i) - \boldsymbol{\varepsilon}_{\mathrm{m}}(\widehat{\boldsymbol{m}}_h^i) \right\rangle \\
&\quad = \left\langle \boldsymbol{\sigma}(\boldsymbol{u}_h^0, \widehat{\boldsymbol{m}}_h^0), \boldsymbol{\varepsilon}_{\mathrm{m}}(\boldsymbol{m}_h^0) - \boldsymbol{\varepsilon}_{\mathrm{m}}(\widehat{\boldsymbol{m}}_h^0) \right\rangle - \left\langle \boldsymbol{\sigma}(\boldsymbol{u}_h^{j-1}, \widehat{\boldsymbol{m}}_h^{j-1}), \boldsymbol{\varepsilon}_{\mathrm{m}}(\boldsymbol{m}_h^j) - \boldsymbol{\varepsilon}_{\mathrm{m}}(\widehat{\boldsymbol{m}}_h^j) \right\rangle \\
&\qquad + \sum_{i=0}^{j-2} \left\langle \boldsymbol{\sigma}(\boldsymbol{u}_h^{i+1}, \widehat{\boldsymbol{m}}_h^{i+1}) - \boldsymbol{\sigma}(\boldsymbol{u}_h^i, \widehat{\boldsymbol{m}}_h^i), \boldsymbol{\varepsilon}_{\mathrm{m}}(\boldsymbol{m}_h^i) - \boldsymbol{\varepsilon}_{\mathrm{m}}(\widehat{\boldsymbol{m}}_h^i) \right\rangle . \\
&\quad = - \left\langle \boldsymbol{\sigma}(\boldsymbol{u}_h^{j-1}, \widehat{\boldsymbol{m}}_h^{j-1}), \boldsymbol{\varepsilon}_{\mathrm{m}}(\boldsymbol{m}_h^j) - \boldsymbol{\varepsilon}_{\mathrm{m}}(\widehat{\boldsymbol{m}}_h^j) \right\rangle \\
&\qquad + \sum_{i=0}^{j-2} \left\langle \boldsymbol{\sigma}(\boldsymbol{u}_h^{i+1}, \widehat{\boldsymbol{m}}_h^{i+1}) - \boldsymbol{\sigma}(\boldsymbol{u}_h^i, \widehat{\boldsymbol{m}}_h^i), \boldsymbol{\varepsilon}_{\mathrm{m}}(\boldsymbol{m}_h^i) - \boldsymbol{\varepsilon}_{\mathrm{m}}(\widehat{\boldsymbol{m}}_h^i) \right\rangle
\end{aligned}
$$

Using inverse estimates, Lemma 5.6.4 and Lemma 5.6.6, we obtain the estimate

$$
\begin{aligned}
&\left| \left\langle \boldsymbol{\sigma}(\boldsymbol{u}_h^{i+1}, \widehat{\boldsymbol{m}}_h^{i+1}) - \boldsymbol{\sigma}(\boldsymbol{u}_h^i, \widehat{\boldsymbol{m}}_h^i), \boldsymbol{\varepsilon}_{\mathrm{m}}(\boldsymbol{m}_h^i) - \boldsymbol{\varepsilon}_{\mathrm{m}}(\widehat{\boldsymbol{m}}_h^i) \right\rangle \right| \\
&\quad \lesssim \left(\left\| \boldsymbol{\varepsilon}(\boldsymbol{u}_h^{i+1}) - \boldsymbol{\varepsilon}(\boldsymbol{u}_h^i) \right\| + \left\| \boldsymbol{\varepsilon}_{\mathrm{m}}(\widehat{\boldsymbol{m}}_h^{i+1}) - \boldsymbol{\varepsilon}_{\mathrm{m}}(\widehat{\boldsymbol{m}}_h^i) \right\| \right) \left\| \boldsymbol{\varepsilon}_{\mathrm{m}}(\boldsymbol{m}_h^i) - \boldsymbol{\varepsilon}_{\mathrm{m}}(\widehat{\boldsymbol{m}}_h^i) \right\| \\
&\quad \lesssim \left(h_{\min}^{-1} k \left\| \mathrm{d}_t \boldsymbol{u}_h^{i+1} \right\| + k^2 \left\| \boldsymbol{v}_h^i \right\|^2 \right) \left\| \boldsymbol{m}_h^i + \widehat{\boldsymbol{m}}_h^i \right\|_{\boldsymbol{H}^1(\Omega)} k^{4/3} h_{\min}^{-2} \sum_{\ell=0}^{i-1} \left\| \boldsymbol{v}_h^\ell \right\|^2 .
\end{aligned}
$$

Altogether, omitting all non-negative dissipative terms and using the stability from Proposition 5.4.6, we thus obtain

$$
\begin{aligned}
&\widehat{\mathcal{E}}_h[\boldsymbol{u}_h^j, \boldsymbol{m}_h^j] + \frac{1}{2} \left\| \mathrm{d}_t \boldsymbol{u}_h^j \right\|^2 - \widehat{\mathcal{E}}_h[\boldsymbol{u}_h^0, \boldsymbol{m}_h^0] - \frac{1}{2} \left\| \mathrm{d}_t \boldsymbol{u}_h^0 \right\|^2 + \alpha k \sum_{i=0}^{j-1} \left\| \boldsymbol{v}_h^i \right\|_h^2 \\
&\qquad\qquad - \left\langle \boldsymbol{\sigma}(\boldsymbol{u}_h^{j-1}, \widehat{\boldsymbol{m}}_h^{j-1}), \boldsymbol{\varepsilon}_{\mathrm{m}}(\boldsymbol{m}_h^j) - \boldsymbol{\varepsilon}_{\mathrm{m}}(\widehat{\boldsymbol{m}}_h^j) \right\rangle \\
&\quad \lesssim \sum_{i=0}^{j-1} \Big(k^2 \left\| \boldsymbol{v}_h^i \right\|^2 + h_{\min}^{-3} k^{4/3} \left\| \mathrm{d}_t \boldsymbol{u}_h^{i+1} \right\| \left\| \boldsymbol{m}_h^i + \widehat{\boldsymbol{m}}_h^i \right\|_{\boldsymbol{H}^1(\Omega)} + h_{\min}^{-2} k^{7/3} \left\| \boldsymbol{v}_h^i \right\|^2 \\
&\qquad\qquad + h_{\min}^{-3} k^{3/2-\varepsilon} \left\| \boldsymbol{\sigma}(\boldsymbol{u}_h^i, \widehat{\boldsymbol{m}}_h^i) \right\| \left\| \boldsymbol{v}_h^i \right\| + h_{\min}^{-3/2} k^2 \left\| \boldsymbol{v}_h^i \right\|^2 \Big) \\
&\quad \lesssim k + h_{\min}^{-3} k^{1/3} + h_{\min}^{-2} k^{4/3} + h_{\min}^{-3} k^{1/2-\varepsilon} + h_{\min}^{-3/2} k.
\end{aligned}
$$

Using (3.5), rewriting the above using the time reconstructions (3.3) and integrat-

ing in time over an arbitrary measurable set $\mathfrak{T} \subset [0,T]$, we obtain

$$\begin{aligned}
&\int_{\mathfrak{T}} \left(\mathcal{E}[\boldsymbol{u}_{hk}^+(t'), \boldsymbol{m}_{hk}^+(t')] + \frac{1}{2} \left\| \dot{\boldsymbol{u}}_{hk}^+(t') \right\|^2 - \widehat{\mathcal{E}}_h[\boldsymbol{u}_{hk}^-(0), \boldsymbol{m}_{hk}^-(0)] - \frac{1}{2} \left\| \dot{\boldsymbol{u}}_{hk}^-(0) \right\|^2 \right) \mathrm{d}t' \\
&\quad + \int_{\mathfrak{T}} \left(\alpha \int_0^{t'} \left\| \boldsymbol{v}_{hk}^-(t) \right\|^2 \mathrm{d}t \right) \mathrm{d}t' + \int_{\mathfrak{T}} \left(\alpha \int_{t'}^{t_j} \left\| \boldsymbol{v}_{hk}^-(t) \right\|^2 \mathrm{d}t \right) \mathrm{d}t' \\
&\quad - \int_{\mathfrak{T}} \left\langle \boldsymbol{\sigma}(\boldsymbol{u}_{hk}^-(t'), \widehat{\boldsymbol{m}}_{hk}^-(t')), \boldsymbol{\varepsilon}_{\mathrm{m}}(\boldsymbol{m}_{hk}^+(t')) - \boldsymbol{\varepsilon}_{\mathrm{m}}(\widehat{\boldsymbol{m}}_{hk}^+(t')) \right\rangle \mathrm{d}t' \\
&\lesssim k + h_{\min}^{-3} k^{1/3} + h_{\min}^{-2} k^{4/3} + h_{\min}^{-3} k^{1/2-\varepsilon} + h_{\min}^{-3/2} k.
\end{aligned}$$

We now consider the limit of this inequality as $h, k \to 0$. The assumed CFL-like condition $k = o(h^9)$ implies that the right-hand side converges to 0 in the limit as $h, k \to 0$. The last two terms on the left-hand side converge to 0: the first one by no concentration of Lebesgue functions, the other thanks to the available convergence results (cf. the convergences guaranteed by Lemmas 5.6.7–5.6.8). Weak lower semicontinuity guarantees

$$\begin{aligned}
&\int_{\mathfrak{T}} \left(\mathcal{E}[\boldsymbol{u}(t'), \boldsymbol{m}(t')] + \frac{1}{2} \left\| \partial_t \boldsymbol{u}(t') \right\|^2 + \alpha \int_0^{t'} \left\| \partial_t \boldsymbol{m}(t) \right\|^2 \mathrm{d}t \right) \mathrm{d}t' \\
&\quad \leq \liminf_{h,k \to 0} \int_{\mathfrak{T}} \left(\widehat{\mathcal{E}}_h[\boldsymbol{u}_{hk}^+(t'), \boldsymbol{m}_{hk}^+(t')] + \frac{1}{2} \left\| \dot{\boldsymbol{u}}_{hk}^+(t') \right\|^2 + \alpha \int_0^{t'} \left\| \boldsymbol{v}_{hk}^-(t) \right\|^2 \mathrm{d}t \right) \mathrm{d}t'.
\end{aligned}$$

Assumption (5.21) yields

$$\lim_{h,k \to 0} \left(\widehat{\mathcal{E}}_h[\boldsymbol{u}_{hk}^-(0), \boldsymbol{m}_{hk}^-(0)] + \frac{1}{2} \left\| \dot{\boldsymbol{u}}_{hk}^-(0) \right\|^2 \right) = \mathcal{E}[\boldsymbol{u}^0, \boldsymbol{m}^0] + \frac{1}{2} \left\| \dot{\boldsymbol{u}}^0 \right\|^2.$$

Since $\mathfrak{T} \subset [0,T]$ was arbitrary, this shows that the energy inequality (5.12) holds a.e. in $(0,T)$ and concludes the proof. □

Chapter 6

Magnetostriction II

6.1 Introduction

In this chapter, like in the previous one, we consider the coupled system of PDE's modelling magnetostriction consisting of the conservation of linear momentum equation and the LLG equation. However, we consider a new approach for the time discretization that is based upon the Newmark-β scheme for the conservation of momentum equation, and a midpoint scheme for the LLG equation.

This still yields for the LLG equation with magnetostriction an integrator that is decoupled, fully linear, and unconditionally stable. Moreover, we obtain a scheme that is formally of second-order in time (thereby improving the first-order scheme discussed in Chapter 5) and is characterized by a favourable energetic behaviour.

To understand the model problem see Section 5.2. In this chapter, for simplicity, we ignore any traction and external forces, and only consider the exchange and magnetoelastic energies. Summarizing the contribution of the present chapter over the existing literature, namely [BPPR14, NR25c], the novel components are

- Where the works of [BPPR14, NR25c] are of first-order in time, the fully discrete scheme we present in this chapter is formally of second-order in time. To the author's knowledge, this is the first such second-order time discretization for the coupled LLG and linear elasticity equations. Moreover, despite the non-linearity of the equations, the solver is still decoupled and fully linear.
- We extend the stability analysis of [BPPR14, NR25c] to this second-order scheme, and under relaxed assumptions on the initial data and parameters, we show unconditional stability.
- As a result of the improved time discretization, we achieve better energetic behaviour. The methods of [BPPR14, NR25c] relied on a fully implicit solver for the displacement and magnetization, resulting in excessive energy dissipation. The scheme presented here remedies this via a Newmark-β approach for the elasticity, and a projection-free midpoint scheme for the magnetization.

6.2 Preliminaries

For general preliminaries, see Chapter 3.

6.2.1 Time Discretization

For the time discretization, we utilize a midpoint scheme for the magnetization resembling [ABRW25], and a Newmark-β scheme based upon [New59] for the displacement. For the Newmark-β scheme, we approximate the displacement with a second-order truncated Taylor series

$$\boldsymbol{u}(t+k) \approx \boldsymbol{u}(t) + k\partial_t \boldsymbol{u}(t) + \frac{k^2}{2}\partial_{tt}\boldsymbol{u}(t)$$

and approximate the velocity with a first-order Taylor expansion

$$\dot{\boldsymbol{u}}(t+k) \approx \dot{\boldsymbol{u}}(t) + k\partial_{tt}\boldsymbol{u}(t).$$

We now approximate the acceleration terms as a combination of the current and future time-steps, i.e. weighted by parameters β, γ, inserting $\partial_t \boldsymbol{u} = \dot{\boldsymbol{u}}$

$$\begin{aligned}
\boldsymbol{u}(t+k) &\approx \boldsymbol{u}(t) + k\dot{\boldsymbol{u}}(t) + \frac{k^2}{2}\left[(1-2\beta)\,\partial_{tt}\boldsymbol{u}(t) + 2\beta\partial_{tt}\boldsymbol{u}(t+k)\right] \\
\dot{\boldsymbol{u}}(t+k) &\approx \dot{\boldsymbol{u}}(t) + k\left[(1-\gamma)\partial_{tt}\boldsymbol{u}(t) + \gamma\partial_{tt}\boldsymbol{u}(t+k)\right].
\end{aligned}$$

Lastly, we can insert the definition of the acceleration from (5.4) yielding the system of equations

$$\begin{aligned}
\boldsymbol{u}(t+k) &\approx \boldsymbol{u}(t) + k\dot{\boldsymbol{u}}(t) \\
&\qquad + \frac{k^2}{2}\nabla\cdot\left[(1-2\beta)\,\boldsymbol{\sigma}(\boldsymbol{u}(t),\boldsymbol{m}(t)) + 2\beta\boldsymbol{\sigma}(\boldsymbol{u}(t+k),\boldsymbol{m}(t+k))\right] \quad (6.1) \\
\dot{\boldsymbol{u}}(t+k) &\approx \dot{\boldsymbol{u}}(t) + k\nabla\cdot\left[(1-\gamma)\boldsymbol{\sigma}(\boldsymbol{u}(t),\boldsymbol{m}(t)) + \gamma\boldsymbol{\sigma}(\boldsymbol{u}(t+k),\boldsymbol{m}(t+k))\right]. \quad (6.2)
\end{aligned}$$

As the acceleration is independent of the velocity, we observe that for $\beta > 0$ (6.1) is implicitly defined but independent of the future velocity, and (6.2) is explicit. This means that the displacement equation can be solved first, and the velocity can be updated after the displacement. We can eliminate the velocity entirely by rearranging (6.1) for the velocity $\dot{\boldsymbol{u}}(t)$, evaluating at t and $t+k$, and then eliminating $\dot{\boldsymbol{u}}(t+k)$ and $\dot{\boldsymbol{u}}(t)$ from (6.2). This gives

$$\begin{aligned}
\boldsymbol{u}(t+2k) \approx\ & 2\boldsymbol{u}(t+k) - \boldsymbol{u}(t) \\
&+ k^2\nabla\cdot\Bigg[\beta\boldsymbol{\sigma}[\boldsymbol{u}(t+2k),\boldsymbol{m}(t+2k)] \\
&+ \left(\frac{1}{2}+\gamma-2\beta\right)\boldsymbol{\sigma}[\boldsymbol{u}(t+k),\boldsymbol{m}(t+k)] \\
&+ \left(\frac{1}{2}-\gamma+\beta\right)\boldsymbol{\sigma}[\boldsymbol{u}(t),\boldsymbol{m}(t)]\Bigg]. \quad (6.3)
\end{aligned}$$

This multistep formulation is much more useful for purposes of analysis, and can be compared to the formulation applied in either of [BPPR14] or Algorithm 5.4.1. To more clearly understand the effects of γ and β we can instead write (6.1) and (6.2) as a sum of averages and differences following [Kre06]. We can rearrange (6.2) for $\dot{\boldsymbol{u}}(t)$, i.e.,

$$\dot{\boldsymbol{u}}(t+k) - k\left[(1-\gamma)\partial_{tt}\boldsymbol{u}(t) + \gamma\partial_{tt}\boldsymbol{u}(t+k)\right] \approx \dot{\boldsymbol{u}}(t)$$

and inserting this into (6.1) yields

$$\begin{aligned}\boldsymbol{u}(t+k) - \boldsymbol{u}(t) \approx \frac{k}{2}(\dot{\boldsymbol{u}}(t+k) + \dot{\boldsymbol{u}}(t)) \\ + k^2\left(\beta - \frac{\gamma}{2}\right)\nabla\cdot\left[\boldsymbol{\sigma}(\boldsymbol{u}(t+k),\boldsymbol{m}(t+k)) - \boldsymbol{\sigma}(\boldsymbol{u}(t),\boldsymbol{m}(t))\right].\end{aligned}$$

To get the velocity in a similar form, we add and subtract $(k/2)\partial_{tt}u(t+k)$ to the right-hand side of (6.2) and rearranging to get

$$\begin{aligned}\dot{\boldsymbol{u}}(t+k) - \dot{\boldsymbol{u}}(t) \approx \frac{k}{2}\nabla\cdot\left[\boldsymbol{\sigma}(\boldsymbol{u}(t+k),\boldsymbol{m}(t+k)) + \boldsymbol{\sigma}(\boldsymbol{u}(t),\boldsymbol{m}(t))\right] \\ + k\left(\gamma - \frac{1}{2}\right)\nabla\cdot\left[\boldsymbol{\sigma}(\boldsymbol{u}(t+k),\boldsymbol{m}(t+k)) - \boldsymbol{\sigma}(\boldsymbol{u}(t),\boldsymbol{m}(t))\right].\end{aligned}$$

It follows that we get a symmetric scheme when $\gamma = 1/2, \beta = \gamma/2 = 1/4$.

6.3 Algorithm and Main Results

In this section, we present two formulations of the scheme, with the midpoint scheme for the magnetization and multi-step Newmark-β method for the displacement.

Algorithm 6.3.1 (Midpoint-Newmark-β LLG-M)**.** *Discretization parameters: Mesh size $h > 0$, time-step size $k > 0$, $\theta \in (1/2, 1]$, $\beta \in [0,1]$, $\gamma \in [1/2, 3/2]$.*
Input: Approximate initial conditions $\boldsymbol{m}_h^0 \in \boldsymbol{\mathcal{M}}_{h,0}$, $\boldsymbol{u}_h^0 \in \mathcal{S}_D^1(\mathcal{T}_h)^3$, $\dot{\boldsymbol{u}}_h^0 \in \mathcal{S}^1(\mathcal{T}_h)^3$.
Initialization:

1. *Compute $\boldsymbol{v}_h^1 \in \boldsymbol{\mathcal{K}}_h[\boldsymbol{m}_h^0]$ such that for all $\boldsymbol{\phi}_h \in \boldsymbol{\mathcal{K}}_h[\boldsymbol{m}_h^0]$ we have*

$$\begin{aligned}\alpha\left\langle \boldsymbol{v}_h^1, \boldsymbol{\phi}_h\right\rangle + \left\langle \boldsymbol{m}_h^0 \times \boldsymbol{v}_h^1, \boldsymbol{\phi}_h\right\rangle + \theta k\left\langle \boldsymbol{\nabla}\boldsymbol{v}_h^1, \boldsymbol{\nabla}\boldsymbol{\phi}_h\right\rangle \\ = -\left\langle \boldsymbol{\nabla}\boldsymbol{m}_h^0, \boldsymbol{\nabla}\boldsymbol{\phi}_h\right\rangle + \left\langle \boldsymbol{h}_{\mathrm{m}}[\boldsymbol{u}_h^0, \boldsymbol{m}_h^0], \boldsymbol{\phi}_h\right\rangle, \quad (6.4)\end{aligned}$$

   and define

$$\boldsymbol{m}_h^1 = \boldsymbol{m}_h^0 + k\boldsymbol{v}_h^1. \quad (6.5)$$

2. *Compute $\boldsymbol{u}_h^1 \in \mathcal{S}_D^1(\mathcal{T}_h)^3$ such that for all $\boldsymbol{\psi}_h \in \mathcal{S}_D^1(\mathcal{T}_h)^3$ we have*

$$\begin{aligned}\left\langle \boldsymbol{u}_h^1, \boldsymbol{\psi}_h\right\rangle + \beta k^2\left\langle \mathbb{C}\boldsymbol{\varepsilon}(\boldsymbol{u}_h^1), \boldsymbol{\varepsilon}(\boldsymbol{\psi}_h)\right\rangle = \left\langle \boldsymbol{u}_h^0, \boldsymbol{\psi}_h\right\rangle + k\left\langle \dot{\boldsymbol{u}}_h^0, \boldsymbol{\psi}_h\right\rangle \\ - k^2\left(\frac{1}{2} - \beta\right)\left\langle \boldsymbol{\sigma}[\boldsymbol{u}_h^0, \boldsymbol{m}_h^0], \boldsymbol{\varepsilon}(\boldsymbol{\psi}_h)\right\rangle + \beta k^2\left\langle \mathbb{C}\boldsymbol{\varepsilon}_{\mathrm{m}}(\Pi_h\boldsymbol{m}_h^1), \boldsymbol{\varepsilon}(\boldsymbol{\psi}_h)\right\rangle. \quad (6.6)\end{aligned}$$

Loop: For all integers $1 \leq i \leq N-1$, iterate (i)–(iii)*:*

(i) Compute $\boldsymbol{v}_h^{i+1} \in \boldsymbol{\mathcal{K}}_h[\widehat{\boldsymbol{m}}_h^{i+1/2}]$ such that for all $\boldsymbol{\phi}_h \in \boldsymbol{\mathcal{K}}_h[\widehat{\boldsymbol{m}}_h^{i+1/2}]$ we have

$$\begin{aligned}\alpha \left\langle \boldsymbol{v}_h^{i+1}, \boldsymbol{\phi}_h \right\rangle + \left\langle \widehat{\boldsymbol{m}}_h^{i+1/2} \times \boldsymbol{v}_h^{i+1}, \boldsymbol{\phi}_h \right\rangle + \frac{k}{2} \left\langle \boldsymbol{\nabla} \boldsymbol{v}_h^{i+1}, \boldsymbol{\nabla} \boldsymbol{\phi}_h \right\rangle \\ = - \left\langle \boldsymbol{\nabla} \boldsymbol{m}_h^i, \boldsymbol{\nabla} \boldsymbol{\phi}_h \right\rangle + \left\langle \boldsymbol{h}_{\mathrm{m}}[\widehat{\boldsymbol{u}}_h^{i+1/2}, \Pi_h \widehat{\boldsymbol{m}}_h^{i+1/2}], \boldsymbol{\phi}_h \right\rangle, \quad (6.7)\end{aligned}$$

and define

$$\boldsymbol{m}_h^{i+1} = \boldsymbol{m}_h^i + k \boldsymbol{v}_h^{i+1}. \quad (6.8)$$

(ii) Compute $\boldsymbol{u}_h^{i+1} \in \mathcal{S}_D^1(\mathcal{T}_h)^3$ such that for all $\boldsymbol{\psi}_h \in \mathcal{S}_D^1(\mathcal{T}_h)^3$ we have

$$\begin{aligned}\left\langle \boldsymbol{u}_h^{i+1}, \boldsymbol{\psi}_h \right\rangle + \beta k^2 \left\langle \mathbb{C} \boldsymbol{\varepsilon}(\boldsymbol{u}_h^{i+1}), \boldsymbol{\varepsilon}(\boldsymbol{\psi}_h) \right\rangle \\ = 2 \left\langle \boldsymbol{u}_h^i, \boldsymbol{\psi}_h \right\rangle - \left\langle \boldsymbol{u}_h^{i-1}, \boldsymbol{\psi}_h \right\rangle \\ - k^2 \left(\frac{1}{2} + \gamma - 2\beta \right) \left\langle \boldsymbol{\sigma}[\boldsymbol{u}_h^i, \Pi_h \boldsymbol{m}_h^i], \boldsymbol{\varepsilon}(\boldsymbol{\psi}_h) \right\rangle \\ - k^2 \left(\frac{1}{2} - \gamma + \beta \right) \left\langle \boldsymbol{\sigma}[\boldsymbol{u}_h^{i-1}, \Pi_h \boldsymbol{m}_h^{i-1}], \boldsymbol{\varepsilon}(\boldsymbol{\psi}_h) \right\rangle \\ + \beta k^2 \left\langle \mathbb{C} \boldsymbol{\varepsilon}_{\mathrm{m}}(\Pi_h \boldsymbol{m}_h^{i+1}), \boldsymbol{\varepsilon}(\boldsymbol{\psi}_h) \right\rangle. \quad (6.9)\end{aligned}$$

Output: Approximations $\{(\boldsymbol{u}_h^i, \boldsymbol{m}_h^i)\}_{0 \leq i \leq N}$.

We note that in the initialization step, there is no nodal projection applied to the initial condition. This is because the nodal projection operator is idempotent, and the initial condition is assumed to satisfy $\boldsymbol{m}_h^0 \in \boldsymbol{\mathcal{M}}_{h,0}$.

Remark 6.3.2. *When $\gamma = 3/2, \beta = 1$ in* (6.9)*, we recover a similar discretization to that used in Algorithm 5.4.1 and [BPPR14], albeit with a different initialization step, and a more precise discretization for the magnetization. This choice is the unique pair of γ and β such that the coefficients $1/2 + \gamma - 2\beta, 1/2 - \gamma + \beta$ are zero.*

Remark 6.3.3. *To formally have second-order convergence in time, we require $\gamma = 1/2$. If $\gamma > 1/2$ then the numerical scheme has additional numerical dissipation, modulated by $(\gamma - 1/2)$, so choosing $\gamma < 1/2$ therefore requires a suitable CFL condition for stability. For elastic systems it is sometimes desirable to include numerical dissipation to eliminate spurious higher order modes of oscillation that remain indefinitely. This is not as relevant for the magnetomechanical system here, as the LLG equation already includes a physical mechanism for energy dissipation. The β parameter is associated with the stability of the system, with a typical value of $\beta \geq 1/4$ yielding unconditional convergence. See [Kre06] for further details on the stability analysis for the standard Newmark-β scheme. For our system, $\beta = 1/4$ is out of reach as the analysis will reveal. The explicit Verlet scheme [HLW03] is retrieved with $\beta = 0, \gamma = 1/2$.*

Remark 6.3.4. *The effective field derived from the magnetoelastic energy,*

$$2\mathbb{Z}^\top \boldsymbol{\sigma}[\boldsymbol{u}, \boldsymbol{m}] \boldsymbol{m},$$

is handled explicitly. For the approximation of this term to be formally second-order in time, we insert extrapolations for both the displacement and magnetization, giving

$$2\mathbb{Z}^\top \boldsymbol{\sigma}[\widehat{\boldsymbol{u}}^{i+1/2}, \widehat{\boldsymbol{m}}^{i+1/2}]\widehat{\boldsymbol{m}}^{i+1/2}.$$

An alternative to this would be to apply an extrapolation procedure to the entire term, i.e. to use

$$3\mathbb{Z}^\top \boldsymbol{\sigma}[\boldsymbol{u}^{i+1}, \boldsymbol{m}^{i+1}]\boldsymbol{m}^{i+1} - \mathbb{Z}^\top \boldsymbol{\sigma}[\boldsymbol{u}^{i}, \boldsymbol{m}^{i}]\boldsymbol{m}^{i}.$$

We do not use this for simplicity in the analysis.

Remark 6.3.5. *If the order of* (6.9) *and* (6.7) *was reversed, then the displacement term could be formed without an extrapolation, at the cost of inserting an extrapolation for the magnetization into* (6.9)*. If a parallel solver was desired, then extrapolations could be inserted into both equations.*

6.4 Analysis

In this section, we present the stability analysis of Algorithm 6.3.1. First, we shall state some assumptions on the initial data and the extrapolation for the midpoint scheme.

(A1) We have $\boldsymbol{m}_h^0, \boldsymbol{u}_h^0 \to \boldsymbol{m}^0, \boldsymbol{u}^0$ in $\boldsymbol{H}^1(\Omega)$ and $\dot{\boldsymbol{u}}_h^0 \to \dot{\boldsymbol{u}}^0$ in $\boldsymbol{L}^2(\Omega)$, as $h \to 0$.

(A2) For the midpoint scheme (6.7) we require that the extrapolation $\widehat{\boldsymbol{m}}_h^{i+1/2}$ is non-zero at all nodes $z \in \mathcal{N}_h$. This is so that the tangent space at each node is non-trivial, and that the nodal projection $\Pi_h \widehat{\boldsymbol{m}}_h^{i+1/2}$ is well-defined.

Assumption (A2) is needed because unlike what we can prove for the BDF2 method (see Proposition 8.4.2), where this property can be established for the extrapolation, we cannot prove this here as the midpoint scheme is not monotonically increasing in the unit length constraint. This assumption is plausible, and could be proven if given additional convergence (with rates) towards a strong solution (see for example [AFKL21, Remark 3.2]). Furthermore, the assumption was valid for all numerical experiments. We now show that the initialization steps are well-defined and satisfy a boundedness in terms of the initial data.

Proposition 6.4.1. *Let $\beta > 1/4$. For the initialization steps* (6.4) *and* (6.6) *we have the stability*

$$\begin{aligned}\left\|\boldsymbol{\nabla} \boldsymbol{m}_h^1\right\|^2 + k\left\|\boldsymbol{v}_h^1\right\|^2 + (\theta - 1/2)k^2\left\|\boldsymbol{\nabla} \boldsymbol{v}_h^1\right\|^2 \\ + \left\|\mathrm{d}_t \boldsymbol{u}_h^1\right\|^2 + \left\|\boldsymbol{\varepsilon}(\boldsymbol{u}_h^1)\right\|_{\mathbb{C}}^2 + k^2(\beta - 1/4)\left\|\boldsymbol{\varepsilon}(\mathrm{d}_t \boldsymbol{u}_h^1)\right\|_{\mathbb{C}}^2 \\ \lesssim 1 + \left\|\boldsymbol{\nabla} \boldsymbol{m}_h^0\right\|^2 + \left\|\dot{\boldsymbol{u}}_h^0\right\|^2 + (1+k)\left\|\boldsymbol{\varepsilon}(\boldsymbol{u}_h^0)\right\|^2, \quad (6.10)\end{aligned}$$

where the hidden constant depends upon the problem data and $|\Omega|$.

Remark 6.4.2. *We must have $\beta > 1/4$ in a strict sense so that terms coming from the right-hand side of* (6.6) *can be suppressed by terms that occur naturally from the Newmark-β scheme. If $\beta = 1/4$ then the term $\|\boldsymbol{\varepsilon}(\mathrm{d}_t \boldsymbol{u}_h^1)\|_{\mathbb{C}}^2$ cannot be*

suitably controlled. In the case where $0 \leq \beta < 1/4$ we would require a weak CFL condition of the form $k = O(h)$ for stability, and this would introduce further technical problems in later propositions.

Proof. We immediately see by the Lax-Milgram theorem that there exists $\boldsymbol{u}_h^1 \in \mathcal{S}_D^1(\mathcal{T}_h)$, $\boldsymbol{v}_h^1 \in \boldsymbol{\mathcal{K}}_h[\boldsymbol{m}_h^0]$ such that (6.4) and (6.6) hold respectively. In (6.4), we choose $\boldsymbol{\phi}_h = k\boldsymbol{v}_h^1$, yielding

$$\alpha k \left\|\boldsymbol{v}_h^1\right\|^2 + \theta k^2 \left\|\boldsymbol{\nabla} \boldsymbol{v}_h^1\right\|^2 = -k \left\langle \boldsymbol{\nabla} \boldsymbol{m}_h^0, \boldsymbol{\nabla} \boldsymbol{v}_h^1 \right\rangle + k \left\langle \boldsymbol{h}_{\mathrm{m}}[\boldsymbol{u}_h^0, \boldsymbol{m}_h^0], \boldsymbol{v}_h^1 \right\rangle .$$

Using the time-stepping (6.5) we have

$$-k \left\langle \boldsymbol{\nabla} \boldsymbol{m}_h^0, \boldsymbol{\nabla} \boldsymbol{v}_h^1 \right\rangle = -\frac{1}{2} \left\|\boldsymbol{\nabla} \boldsymbol{m}_h^1\right\|^2 + \frac{1}{2} \left\|\boldsymbol{\nabla} \boldsymbol{m}_h^0\right\|^2 + \frac{k^2}{2} \left\|\boldsymbol{\nabla} \boldsymbol{v}_h^1\right\|^2$$

and combining the above we have

$$\frac{1}{2} \left\|\boldsymbol{\nabla} \boldsymbol{m}_h^1\right\|^2 + \alpha k \left\|\boldsymbol{v}_h^1\right\|^2 + (\theta - 1/2) k^2 \left\|\boldsymbol{\nabla} \boldsymbol{v}_h^1\right\|^2 = \frac{1}{2} \left\|\boldsymbol{\nabla} \boldsymbol{m}_h^0\right\|^2 + k \left\langle \boldsymbol{h}_{\mathrm{m}}[\boldsymbol{u}_h^0, \boldsymbol{m}_h^0], \boldsymbol{v}_h^1 \right\rangle .$$

Using Lemma 5.6.1, the last term on the right-hand side can be overestimated as

$$\begin{aligned}
&\frac{1}{2} \left\|\boldsymbol{\nabla} \boldsymbol{m}_h^1\right\|^2 + \alpha k \left\|\boldsymbol{v}_h^1\right\|^2 + (\theta - 1/2) k^2 \left\|\boldsymbol{\nabla} \boldsymbol{v}_h^1\right\|^2 \\
&\qquad \leq \frac{1}{2} \left\|\boldsymbol{\nabla} \boldsymbol{m}_h^0\right\|^2 + \frac{k}{2\alpha} \left\|\boldsymbol{h}_{\mathrm{m}}[\boldsymbol{u}_h^0, \boldsymbol{m}_h^0]\right\|^2 + \frac{\alpha k}{2} \left\|\boldsymbol{v}_h^1\right\|^2 \\
&\qquad\qquad \leq \frac{1}{2} \left\|\boldsymbol{\nabla} \boldsymbol{m}_h^0\right\|^2 + \frac{\alpha k}{2} \left\|\boldsymbol{v}_h^1\right\|^2 \\
&\qquad\qquad + \frac{4k}{\alpha} \left\|\mathbb{Z}\right\|_{\boldsymbol{L}^\infty(\Omega)}^2 \left\|\mathbb{C}\right\|_{\boldsymbol{L}^\infty(\Omega)}^2 \left(\left\|\boldsymbol{\varepsilon}(\boldsymbol{u}_h^0)\right\|^2 + \left\|\mathbb{Z}\right\|_{\boldsymbol{L}^\infty(\Omega)}^2 |\Omega| \right) .
\end{aligned}$$

Moving the $\alpha k \left\|\boldsymbol{v}_h^1\right\|^2/2$ to the left-hand side yields

$$\begin{aligned}
&\frac{1}{2} \left\|\boldsymbol{\nabla} \boldsymbol{m}_h^1\right\|^2 + \frac{\alpha k}{2} \left\|\boldsymbol{v}_h^1\right\|^2 + (\theta - 1/2) k^2 \left\|\boldsymbol{\nabla} \boldsymbol{v}_h^1\right\|^2 \\
&\quad \leq \frac{1}{2} \left\|\boldsymbol{\nabla} \boldsymbol{m}_h^0\right\|^2 + \frac{4k}{\alpha} \left\|\mathbb{Z}\right\|_{\boldsymbol{L}^\infty(\Omega)}^2 \left\|\mathbb{C}\right\|_{\boldsymbol{L}^\infty(\Omega)}^2 \left(\left\|\boldsymbol{\varepsilon}(\boldsymbol{u}_h^0)\right\|^2 + \left\|\mathbb{Z}\right\|_{\boldsymbol{L}^\infty(\Omega)}^2 |\Omega| \right) . \quad (6.11)
\end{aligned}$$

Now we insert $\boldsymbol{\psi}_h = (\mathrm{d}_t \boldsymbol{u}_h^1)/k$ into (6.6), so that

$$\begin{aligned}
&\left\|\mathrm{d}_t \boldsymbol{u}_h^1\right\|^2 + \beta \left\langle \mathbb{C}\boldsymbol{\varepsilon}(\boldsymbol{u}_h^1), \boldsymbol{\varepsilon}(k \mathrm{d}_t \boldsymbol{u}_h^1) \right\rangle + \left(\frac{1}{2} - \beta \right) \left\langle \mathbb{C}\boldsymbol{\varepsilon}(\boldsymbol{u}_h^0), \boldsymbol{\varepsilon}(k \mathrm{d}_t \boldsymbol{u}_h^1) \right\rangle \\
&= \left\langle \dot{\boldsymbol{u}}_h^0, \mathrm{d}_t \boldsymbol{u}_h^1 \right\rangle + \left(\frac{1}{2} - \beta \right) \left\langle \mathbb{C}\boldsymbol{\varepsilon}_{\mathrm{m}}(\boldsymbol{m}_h^0), \boldsymbol{\varepsilon}(k \mathrm{d}_t \boldsymbol{u}_h^1) \right\rangle + \beta \left\langle \mathbb{C}\boldsymbol{\varepsilon}_{\mathrm{m}}(\Pi_h \boldsymbol{m}_h^1), k \mathrm{d}_t \boldsymbol{\varepsilon}(\boldsymbol{u}_h^1) \right\rangle .
\end{aligned}$$

We can write out

$$\beta \left\langle \mathbb{C}\boldsymbol{\varepsilon}(\boldsymbol{u}_h^1), \boldsymbol{\varepsilon}(k \mathrm{d}_t \boldsymbol{u}_h^1) \right\rangle = \frac{\beta}{2} \left\|\boldsymbol{\varepsilon}(\boldsymbol{u}_h^1)\right\|_{\mathbb{C}}^2 - \frac{\beta}{2} \left\|\boldsymbol{\varepsilon}(\boldsymbol{u}_h^0)\right\|_{\mathbb{C}}^2 + \frac{\beta k^2}{2} \left\|\boldsymbol{\varepsilon}(\mathrm{d}_t \boldsymbol{u}_h^1)\right\|_{\mathbb{C}}^2$$

and

$$\left(\frac{1}{2}-\beta\right)\left\langle \mathbb{C}\boldsymbol{\varepsilon}(\boldsymbol{u}_h^0),\boldsymbol{\varepsilon}(k\mathrm{d}_t\boldsymbol{u}_h^1)\right\rangle \\ = \frac{1}{4}\left\|\boldsymbol{\varepsilon}(\boldsymbol{u}_h^1)\right\|_{\mathbb{C}}^2-\frac{1}{4}\left\|\boldsymbol{\varepsilon}(\boldsymbol{u}_h^0)\right\|_{\mathbb{C}}^2-\frac{k^2}{4}\left\|\boldsymbol{\varepsilon}(\mathrm{d}_t\boldsymbol{u}_h^1)\right\|_{\mathbb{C}}^2 \\ -\frac{\beta}{2}\left\|\boldsymbol{\varepsilon}(\boldsymbol{u}_h^1)\right\|_{\mathbb{C}}^2+\frac{\beta}{2}\left\|\boldsymbol{\varepsilon}(\boldsymbol{u}_h^0)\right\|_{\mathbb{C}}^2+\frac{\beta k^2}{2}\left\|\boldsymbol{\varepsilon}(\mathrm{d}_t\boldsymbol{u}_h^1)\right\|_{\mathbb{C}}^2$$

which implies that

$$\left\|\mathrm{d}_t\boldsymbol{u}_h^1\right\|^2+\frac{1}{4}\left\|\boldsymbol{\varepsilon}(\boldsymbol{u}_h^1)\right\|_{\mathbb{C}}^2-\frac{1}{4}\left\|\boldsymbol{\varepsilon}(\boldsymbol{u}_h^0)\right\|_{\mathbb{C}}^2+k^2\left(\beta-\frac{1}{4}\right)\left\|\boldsymbol{\varepsilon}(\mathrm{d}_t\boldsymbol{u}_h^1)\right\|_{\mathbb{C}}^2 \\ =\left\langle\dot{\boldsymbol{u}}_h^0,\mathrm{d}_t\boldsymbol{u}_h^1\right\rangle+\left(\frac{1}{2}-\beta\right)\left\langle\mathbb{C}\boldsymbol{\varepsilon}_{\mathrm{m}}(\boldsymbol{m}_h^0),\boldsymbol{\varepsilon}(k\mathrm{d}_t\boldsymbol{u}_h^1)\right\rangle+\beta\left\langle\mathbb{C}\boldsymbol{\varepsilon}_{\mathrm{m}}(\Pi_h\boldsymbol{m}_h^1),k\mathrm{d}_t\boldsymbol{\varepsilon}(\boldsymbol{u}_h^1)\right\rangle.$$

The first term on the right-hand side is easily estimated via

$$\left\langle\dot{\boldsymbol{u}}_h^0,\mathrm{d}_t\boldsymbol{u}_h^1\right\rangle\leq\frac{1}{2}\left\|\dot{\boldsymbol{u}}_h^0\right\|^2+\frac{1}{2}\left\|\mathrm{d}_t\boldsymbol{u}_h^1\right\|^2$$

so that

$$\frac{1}{2}\left\|\mathrm{d}_t\boldsymbol{u}_h^1\right\|^2+\frac{1}{4}\left\|\boldsymbol{\varepsilon}(\boldsymbol{u}_h^1)\right\|_{\mathbb{C}}^2-\frac{1}{4}\left\|\boldsymbol{\varepsilon}(\boldsymbol{u}_h^0)\right\|_{\mathbb{C}}^2+k^2\left(\beta-\frac{1}{4}\right)\left\|\boldsymbol{\varepsilon}(\mathrm{d}_t\boldsymbol{u}_h^1)\right\|_{\mathbb{C}}^2 \\ \leq\frac{1}{2}\left\|\dot{\boldsymbol{u}}_h^0\right\|^2+\left(\frac{1}{2}-\beta\right)\left\langle\mathbb{C}\boldsymbol{\varepsilon}_{\mathrm{m}}(\boldsymbol{m}_h^0),\boldsymbol{\varepsilon}(k\mathrm{d}_t\boldsymbol{u}_h^1)\right\rangle+\beta\left\langle\mathbb{C}\boldsymbol{\varepsilon}_{\mathrm{m}}(\Pi_h\boldsymbol{m}_h^1),k\mathrm{d}_t\boldsymbol{\varepsilon}(\boldsymbol{u}_h^1)\right\rangle.$$

Lastly, for the remaining right-hand side terms we note that $\beta,|\beta-1/2|\leq 1$, and apply Cauchy–Schwarz and weighted Young inequalities yielding for arbitrary $\nu>0$

$$\left(\frac{1}{2}-\beta\right)\left\langle\mathbb{C}\boldsymbol{\varepsilon}_{\mathrm{m}}(\boldsymbol{m}_h^0),\boldsymbol{\varepsilon}(k\mathrm{d}_t\boldsymbol{u}_h^1)\right\rangle\leq\frac{1}{8\nu}\left\|\boldsymbol{\varepsilon}_{\mathrm{m}}(\boldsymbol{m}_h^0)\right\|_{\mathbb{C}}^2+\frac{\nu k^2}{2}\left\|\boldsymbol{\varepsilon}(\mathrm{d}_t\boldsymbol{u}_h^1)\right\|_{\mathbb{C}}^2, \\ \beta\left\langle\mathbb{C}\boldsymbol{\varepsilon}_{\mathrm{m}}(\Pi_h\boldsymbol{m}_h^1),k\mathrm{d}_t\boldsymbol{\varepsilon}(\boldsymbol{u}_h^1)\right\rangle\leq\frac{1}{8\nu}\left\|\boldsymbol{\varepsilon}_{\mathrm{m}}(\Pi_h\boldsymbol{m}_h^1)\right\|_{\mathbb{C}}^2+\frac{\nu k^2}{2}\left\|\boldsymbol{\varepsilon}(\mathrm{d}_t\boldsymbol{u}_h^1)\right\|_{\mathbb{C}}^2.$$

We finally have

$$\frac{1}{2}\left\|\mathrm{d}_t\boldsymbol{u}_h^1\right\|^2+\frac{1}{4}\left\|\boldsymbol{\varepsilon}(\boldsymbol{u}_h^1)\right\|_{\mathbb{C}}^2+k^2\left(\beta-\nu-\frac{1}{4}\right)\left\|\boldsymbol{\varepsilon}(\mathrm{d}_t\boldsymbol{u}_h^1)\right\|_{\mathbb{C}}^2 \\ \leq\frac{1}{2}\left\|\dot{\boldsymbol{u}}_h^0\right\|^2+\frac{1}{4}\left\|\boldsymbol{\varepsilon}(\boldsymbol{u}_h^0)\right\|_{\mathbb{C}}^2+\frac{1}{8\nu}\left\|\boldsymbol{\varepsilon}_{\mathrm{m}}(\boldsymbol{m}_h^0)\right\|_{\mathbb{C}}^2+\frac{1}{8\nu}\left\|\boldsymbol{\varepsilon}_{\mathrm{m}}(\Pi_h\boldsymbol{m}_h^1)\right\|_{\mathbb{C}}^2.$$

To ensure positivity of all coefficients on the left-hand side we must choose $\beta>1/4$, and we can then choose $\nu=(\beta+1/4)/2$. Then, $1/(8\nu)=1/(4\beta+1)\leq 1$, yielding the stability

$$\frac{1}{2}\left\|\mathrm{d}_t\boldsymbol{u}_h^1\right\|^2+\frac{1}{4}\left\|\boldsymbol{\varepsilon}(\boldsymbol{u}_h^1)\right\|_{\mathbb{C}}^2+\frac{k^2}{2}\left(\beta-\frac{1}{4}\right)\left\|\boldsymbol{\varepsilon}(\mathrm{d}_t\boldsymbol{u}_h^1)\right\|_{\mathbb{C}}^2 \\ \leq\frac{1}{2}\left\|\dot{\boldsymbol{u}}_h^0\right\|^2+\frac{1}{4}\left\|\boldsymbol{\varepsilon}(\boldsymbol{u}_h^0)\right\|_{\mathbb{C}}^2+\left\|\boldsymbol{\varepsilon}_{\mathrm{m}}(\boldsymbol{m}_h^0)\right\|_{\mathbb{C}}^2+\left\|\boldsymbol{\varepsilon}_{\mathrm{m}}(\Pi_h\boldsymbol{m}_h^1)\right\|_{\mathbb{C}}^2. \quad (6.12)$$

Summing up (6.11) and (6.12) and noting that $\|\boldsymbol{\varepsilon}_{\mathrm{m}}(\boldsymbol{m}_h^0)\|_{\mathbb{C}}^2, \|\boldsymbol{\varepsilon}_{\mathrm{m}}(\Pi_h \boldsymbol{m}_h^1)\|_{\mathbb{C}}^2 \lesssim 1$ completes the proof. □

We now show an estimate for the midpoint scheme.

Proposition 6.4.3. *The midpoint scheme satisfies for each $j \geq 1$ the estimate*

$$\left\|\boldsymbol{\nabla} \boldsymbol{m}_h^j\right\|^2 + k \sum_{i=1}^{j-1} \left\|\boldsymbol{v}_h^{i+1}\right\|^2 \lesssim \left\|\boldsymbol{\nabla} \boldsymbol{m}_h^1\right\|^2 + k \sum_{i=0}^{j-1} \left(1 + \left\|\boldsymbol{\varepsilon}(\boldsymbol{u}_h^i)\right\|^2\right), \tag{6.13}$$

where the hidden constant is dependent upon the problem data, and is independent of the discretization parameters.

As mentioned in Remark 6.4.2, if we use an inverse estimate $\|\boldsymbol{\varepsilon}(\boldsymbol{u}_h^i)\| \lesssim h^{-1} \|\boldsymbol{u}_h^i\|$, then (6.13) would be of the form

$$\left\|\boldsymbol{\nabla} \boldsymbol{m}_h^j\right\|^2 + k \sum_{i=1}^{j-1} \left\|\boldsymbol{v}_h^{i+1}\right\|^2 \lesssim \left\|\boldsymbol{\nabla} \boldsymbol{m}_h^1\right\|^2 + k \sum_{i=0}^{j-1} \left(1 + h^{-2} \left\|\boldsymbol{u}_h^i\right\|^2\right),$$

which is very problematic. It is not clear how one would estimate the right-hand side, as the time-step k would be spent entirely upon the summation, and no CFL condition could be established to bound the strain term as $h \to 0$.

Proof. Inserting $\boldsymbol{\phi}_h = k \boldsymbol{v}_h^{i+1}$ into (6.7) yields

$$\alpha k \left\|\boldsymbol{v}_h^{i+1}\right\|^2 + \frac{k^2}{2} \left\|\boldsymbol{\nabla} \boldsymbol{v}_h^{i+1}\right\|^2 = -k \left\langle \boldsymbol{\nabla} \boldsymbol{m}_h^i, \boldsymbol{\nabla} \boldsymbol{v}_h^{i+1} \right\rangle + \left\langle \boldsymbol{h}_{\mathrm{m}}[\widehat{\boldsymbol{u}}_h^{i+1/2}, \Pi_h \widehat{\boldsymbol{m}}_h^{i+1/2}], \boldsymbol{v}_h^{i+1} \right\rangle,$$

and applying the time-stepping (6.8) we can rewrite this as

$$\frac{1}{2} \left\|\boldsymbol{\nabla} \boldsymbol{m}_h^{i+1}\right\|^2 + \alpha k \left\|\boldsymbol{v}_h^{i+1}\right\|^2 = \frac{1}{2} \left\|\boldsymbol{\nabla} \boldsymbol{m}_h^i\right\|^2 + k \left\langle \boldsymbol{h}_{\mathrm{m}}[\widehat{\boldsymbol{u}}_h^{i+1/2}, \Pi_h \widehat{\boldsymbol{m}}_h^{i+1/2}], \boldsymbol{v}_h^{i+1} \right\rangle. \tag{6.14}$$

Again applying Lemma 5.6.1 we have

$$\begin{aligned}
&\frac{1}{2} \left\|\boldsymbol{\nabla} \boldsymbol{m}_h^{i+1}\right\|^2 + \frac{\alpha k}{2} \left\|\boldsymbol{v}_h^{i+1}\right\|^2 \\
&\qquad \leq \frac{1}{2} \left\|\boldsymbol{\nabla} \boldsymbol{m}_h^i\right\|^2 + \frac{k}{2\alpha} \left\|\boldsymbol{h}_{\mathrm{m}}[\widehat{\boldsymbol{u}}_h^{i+1/2}, \Pi_h \widehat{\boldsymbol{m}}_h^{i+1/2}]\right\|^2 \\
&\leq \frac{1}{2} \left\|\boldsymbol{\nabla} \boldsymbol{m}_h^i\right\|^2 + \frac{4k}{\alpha} \|\mathbb{Z}\|_{\boldsymbol{L}^\infty}^2 \|\mathbb{C}\|_{\boldsymbol{L}^\infty}^2 \left(\left\|\boldsymbol{\varepsilon}\left(\widehat{\boldsymbol{u}}_h^{i+1/2}\right)\right\|^2 + \|\mathbb{Z}\|_{\boldsymbol{L}^\infty}^2 |\Omega| \right) \\
&\qquad \leq \frac{1}{2} \left\|\boldsymbol{\nabla} \boldsymbol{m}_h^i\right\|^2 \\
&\qquad + \frac{4k}{\alpha} \|\mathbb{Z}\|_{\boldsymbol{L}^\infty}^2 \|\mathbb{C}\|_{\boldsymbol{L}^\infty}^2 \left(\frac{9}{2} \left\|\boldsymbol{\varepsilon}(\boldsymbol{u}_h^i)\right\|^2 + \frac{1}{4} \left\|\boldsymbol{\varepsilon}(\boldsymbol{u}_h^{i-1})\right\|^2 + \|\mathbb{Z}\|_{\boldsymbol{L}^\infty}^2 |\Omega| \right).
\end{aligned}$$

We can now sum up over $i = 1, \ldots, j-1$ for $j \geq 1$ yielding

$$\begin{aligned}
\frac{1}{2} \left\|\boldsymbol{\nabla} \boldsymbol{m}_h^j\right\|^2 + \frac{\alpha k}{2} \sum_{i=1}^{j-1} \left\|\boldsymbol{v}_h^{i+1}\right\|^2 &\leq \frac{1}{2} \left\|\boldsymbol{\nabla} \boldsymbol{m}_h^1\right\|^2 \\
&+ \frac{4k}{\alpha} \|\mathbb{Z}\|_{\boldsymbol{L}^\infty}^2 \|\mathbb{C}\|_{\boldsymbol{L}^\infty}^2 \sum_{i=1}^{j-1} \left(\frac{9}{2} \left\|\boldsymbol{\varepsilon}(\boldsymbol{u}_h^i)\right\|^2 + \frac{1}{4} \left\|\boldsymbol{\varepsilon}(\boldsymbol{u}_h^{i-1})\right\|^2 + \|\mathbb{Z}\|_{\boldsymbol{L}^\infty}^2 |\Omega| \right).
\end{aligned}$$

Now, the sum of the strains can be rewritten as

$$\frac{9}{2}\sum_{i=1}^{j-1}\left\|\boldsymbol{\varepsilon}(\boldsymbol{u}_h^i)\right\|^2+\frac{1}{4}\sum_{i=1}^{j-1}\left\|\boldsymbol{\varepsilon}(\boldsymbol{u}_h^{i-1})\right\|^2=\frac{9}{2}\sum_{i=1}^{j-1}\left\|\boldsymbol{\varepsilon}(\boldsymbol{u}_h^i)\right\|^2+\frac{1}{4}\sum_{i=0}^{j-2}\left\|\boldsymbol{\varepsilon}(\boldsymbol{u}_h^i)\right\|^2$$
$$=\frac{1}{4}\left\|\boldsymbol{\varepsilon}(\boldsymbol{u}_h^0)\right\|^2+\frac{9}{2}\sum_{i=1}^{j-2}\left(\left\|\boldsymbol{\varepsilon}(\boldsymbol{u}_h^i)\right\|^2+\frac{19}{4}\left\|\boldsymbol{\varepsilon}(\boldsymbol{u}_h^{j-1})\right\|^2\right)\leq 5\sum_{i=0}^{j-1}\left\|\boldsymbol{\varepsilon}(\boldsymbol{u}_h^i)\right\|^2$$

Combining the above yields (6.13). □

We now consider the stability of (6.9), basing the method on the one used in [FT02].

Proposition 6.4.4. *Let $\gamma=1/2$, $\beta>1/4$. Then there exists $k_0>0$ such that for $k<k_0$ we have for each $j\geq 1$ that*

$$\left\|\mathrm{d}_t\boldsymbol{u}_h^j\right\|^2+k^2\left\|\boldsymbol{\varepsilon}(\mathrm{d}_t\boldsymbol{u}_h^j)\right\|_{\mathbb{C}}^2+\left\|\boldsymbol{\varepsilon}(\boldsymbol{u}_h^j)\right\|_{\mathbb{C}}^2\lesssim 1+k\sum_{i=0}^{j-1}\left(1+\left\|\boldsymbol{\varepsilon}(\boldsymbol{u}_h^i)\right\|_{\mathbb{C}}^2\right),\qquad(6.15)$$

where the hidden constant is dependent upon the problem data, but independent of the discretization parameters h and k.

Proof. Let $i\geq 1$. Equation (6.9) yields

$$\begin{aligned}\left\langle\boldsymbol{u}_h^{i+1}-2\boldsymbol{u}_h^i+\boldsymbol{u}_h^{i-1},\boldsymbol{\psi}_h\right\rangle&+\beta k^2\left\langle\mathbb{C}\boldsymbol{\varepsilon}(\boldsymbol{u}_h^{i+1}),\boldsymbol{\varepsilon}(\boldsymbol{\psi}_h)\right\rangle\\&+\left(\frac{1}{2}+\gamma-2\beta\right)k^2\left\langle\mathbb{C}\boldsymbol{\varepsilon}(\boldsymbol{u}_h^i),\boldsymbol{\varepsilon}(\boldsymbol{\psi}_h)\right\rangle\\&+\left(\frac{1}{2}+\beta-\gamma\right)\left\langle\mathbb{C}\boldsymbol{\varepsilon}(\boldsymbol{u}_h^{i-1}),\boldsymbol{\varepsilon}(\boldsymbol{\psi}_h)\right\rangle\\&=\beta k^2\left\langle\mathbb{C}\boldsymbol{\varepsilon}_{\mathrm{m}}(\Pi_h\boldsymbol{m}_h^{i+1}),\boldsymbol{\varepsilon}(\boldsymbol{\psi}_h)\right\rangle\\&+\left(\frac{1}{2}+\gamma-2\beta\right)k^2\left\langle\mathbb{C}\boldsymbol{\varepsilon}_{\mathrm{m}}(\Pi_h\boldsymbol{m}_h^{i}),\boldsymbol{\varepsilon}(\boldsymbol{\psi}_h)\right\rangle\\&+\left(\frac{1}{2}+\beta-\gamma\right)k^2\left\langle\mathbb{C}\boldsymbol{\varepsilon}_{\mathrm{m}}(\Pi_h\boldsymbol{m}_h^{i-1}),\boldsymbol{\varepsilon}(\boldsymbol{\psi}_h)\right\rangle.\end{aligned}$$

Dividing by k we can refactor this into the form

$$\begin{aligned}k\left\langle\mathrm{d}_t^2\boldsymbol{u}_h^{i+1},\boldsymbol{\psi}_h\right\rangle&+\beta k^3\left\langle\mathbb{C}\boldsymbol{\varepsilon}(\mathrm{d}_t^2\boldsymbol{u}_h^{i+1}),\boldsymbol{\varepsilon}(\boldsymbol{\psi}_h)\right\rangle\\&+\left(\gamma-\frac{1}{2}\right)k^2\left\langle\mathbb{C}\boldsymbol{\varepsilon}(\mathrm{d}_t\boldsymbol{u}_h^i),\boldsymbol{\varepsilon}(\boldsymbol{\psi}_h)\right\rangle+k\left\langle\mathbb{C}\boldsymbol{\varepsilon}(\boldsymbol{u}_h^i),\boldsymbol{\varepsilon}(\boldsymbol{\psi}_h)\right\rangle\\&=\beta k^3\left\langle\mathbb{C}\mathrm{d}_t^2\boldsymbol{\varepsilon}_{\mathrm{m}}(\Pi_h\boldsymbol{m}_h^{i+1}),\boldsymbol{\varepsilon}(\boldsymbol{\psi}_h)\right\rangle\\&+\left(\gamma-\frac{1}{2}\right)k^2\left\langle\mathrm{d}_t\mathbb{C}\boldsymbol{\varepsilon}_{\mathrm{m}}(\Pi_h\boldsymbol{m}_h^{i}),\boldsymbol{\varepsilon}(\boldsymbol{\psi}_h)\right\rangle+k\left\langle\mathbb{C}\boldsymbol{\varepsilon}_{\mathrm{m}}(\Pi_h\boldsymbol{m}_h^{i}),\boldsymbol{\varepsilon}(\boldsymbol{\psi}_h)\right\rangle.\end{aligned}$$

If we now let $\gamma=1/2$, the velocity terms (responsible for damping) vanish, and we are left with

$$\begin{aligned}\left\langle\mathrm{d}_t\boldsymbol{u}_h^{i+1}-\mathrm{d}_t\boldsymbol{u}_h^i,\boldsymbol{\psi}_h\right\rangle+\beta k^2\left\langle\mathbb{C}\boldsymbol{\varepsilon}(\mathrm{d}_t\boldsymbol{u}_h^{i+1}-\mathrm{d}_t\boldsymbol{u}_h^i),\boldsymbol{\varepsilon}(\boldsymbol{\psi}_h)\right\rangle+k\left\langle\mathbb{C}\boldsymbol{\varepsilon}(\boldsymbol{u}_h^i),\boldsymbol{\varepsilon}(\boldsymbol{\psi}_h)\right\rangle\\=\beta k^3\left\langle\mathbb{C}\mathrm{d}_t^2\boldsymbol{\varepsilon}_{\mathrm{m}}(\Pi_h\boldsymbol{m}_h^{i+1}),\boldsymbol{\varepsilon}(\boldsymbol{\psi}_h)\right\rangle+k\left\langle\mathbb{C}\boldsymbol{\varepsilon}_{\mathrm{m}}(\Pi_h\boldsymbol{m}_h^{i}),\boldsymbol{\varepsilon}(\boldsymbol{\psi}_h)\right\rangle.\quad(6.16)\end{aligned}$$

If we choose the test function $\boldsymbol{\psi}_h = \mathrm{d}_t \boldsymbol{u}_h^{i+1} + \mathrm{d}_t \boldsymbol{u}_h^i$, we get with the symmetry of $\mathbb{C}$ that

$$\begin{aligned}
\left\|\mathrm{d}_t \boldsymbol{u}_h^{i+1}\right\|^2 - \left\|\mathrm{d}_t \boldsymbol{u}_h^{i}\right\|^2 + \beta k^2 \left\|\boldsymbol{\varepsilon}(\mathrm{d}_t \boldsymbol{u}_h^{i+1})\right\|_{\mathbb{C}}^2 - \beta k^2 \left\|\boldsymbol{\varepsilon}(\mathrm{d}_t \boldsymbol{u}_h^{i})\right\|_{\mathbb{C}}^2 \\
+ \left\langle \mathbb{C}\boldsymbol{\varepsilon}(\boldsymbol{u}_h^{i+1}), \boldsymbol{\varepsilon}(\boldsymbol{u}_h^i)\right\rangle - \left\langle \mathbb{C}\boldsymbol{\varepsilon}(\boldsymbol{u}_h^{i}), \boldsymbol{\varepsilon}(\boldsymbol{u}_h^{i-1})\right\rangle \\
= \beta k^2 \left\langle \mathbb{C}\mathrm{d}_t \boldsymbol{\varepsilon}_{\mathrm{m}}(\Pi_h \boldsymbol{m}_h^{i+1}), \boldsymbol{\varepsilon}(\mathrm{d}_t \boldsymbol{u}_h^{i+1} + \mathrm{d}_t \boldsymbol{u}_h^i)\right\rangle \\
- \beta k^2 \left\langle \mathbb{C}\mathrm{d}_t \boldsymbol{\varepsilon}_{\mathrm{m}}(\Pi_h \boldsymbol{m}_h^{i}), \boldsymbol{\varepsilon}(\mathrm{d}_t \boldsymbol{u}_h^{i+1} + \mathrm{d}_t \boldsymbol{u}_h^i)\right\rangle \\
+ k \left\langle \mathbb{C}\boldsymbol{\varepsilon}_{\mathrm{m}}(\Pi_h \boldsymbol{m}_h^{i}), \boldsymbol{\varepsilon}(\mathrm{d}_t \boldsymbol{u}_h^{i+1} + \mathrm{d}_t \boldsymbol{u}_h^i)\right\rangle . \quad (6.17)
\end{aligned}$$

The left-hand side of (6.17) is clearly ready to be summed, but the right-hand side requires some more work. We have

$$\begin{aligned}
\beta k^2 \left\langle \mathbb{C}\mathrm{d}_t \boldsymbol{\varepsilon}_{\mathrm{m}}(\Pi_h \boldsymbol{m}_h^{i+1}), \boldsymbol{\varepsilon}(\mathrm{d}_t \boldsymbol{u}_h^{i+1} + \mathrm{d}_t \boldsymbol{u}_h^i)\right\rangle \\
- \beta k^2 \left\langle \mathbb{C}\mathrm{d}_t \boldsymbol{\varepsilon}_{\mathrm{m}}(\Pi_h \boldsymbol{m}_h^{i}), \boldsymbol{\varepsilon}(\mathrm{d}_t \boldsymbol{u}_h^{i+1} + \mathrm{d}_t \boldsymbol{u}_h^i)\right\rangle \\
= \beta k^2 \left\langle \mathbb{C}\mathrm{d}_t \boldsymbol{\varepsilon}_{\mathrm{m}}(\Pi_h \boldsymbol{m}_h^{i+1}), \boldsymbol{\varepsilon}(\mathrm{d}_t \boldsymbol{u}_h^{i+1})\right\rangle \\
- \beta k^2 \left\langle \mathbb{C}\mathrm{d}_t \boldsymbol{\varepsilon}_{\mathrm{m}}(\Pi_h \boldsymbol{m}_h^{i}), \boldsymbol{\varepsilon}(\mathrm{d}_t \boldsymbol{u}_h^{i})\right\rangle \\
+ \beta k^2 \left\langle \mathbb{C}\mathrm{d}_t \boldsymbol{\varepsilon}_{\mathrm{m}}(\Pi_h \boldsymbol{m}_h^{i+1}), \boldsymbol{\varepsilon}(\mathrm{d}_t \boldsymbol{u}_h^{i})\right\rangle \\
- \beta k^2 \left\langle \mathbb{C}\mathrm{d}_t \boldsymbol{\varepsilon}_{\mathrm{m}}(\Pi_h \boldsymbol{m}_h^{i}), \boldsymbol{\varepsilon}(\mathrm{d}_t \boldsymbol{u}_h^{i+1})\right\rangle
\end{aligned}$$

Inserting this into (6.17) yields

$$\begin{aligned}
\left\|\mathrm{d}_t \boldsymbol{u}_h^{i+1}\right\|^2 - \left\|\mathrm{d}_t \boldsymbol{u}_h^{i}\right\|^2 + \beta k^2 \left\|\boldsymbol{\varepsilon}(\mathrm{d}_t \boldsymbol{u}_h^{i+1})\right\|_{\mathbb{C}}^2 - \beta k^2 \left\|\boldsymbol{\varepsilon}(\mathrm{d}_t \boldsymbol{u}_h^{i})\right\|_{\mathbb{C}}^2 \\
+ \left\langle \mathbb{C}\boldsymbol{\varepsilon}(\boldsymbol{u}_h^{i+1}), \boldsymbol{\varepsilon}(\boldsymbol{u}_h^i)\right\rangle - \left\langle \mathbb{C}\boldsymbol{\varepsilon}(\boldsymbol{u}_h^{i}), \boldsymbol{\varepsilon}(\boldsymbol{u}_h^{i-1})\right\rangle \\
= \beta k^2 \left\langle \mathbb{C}\mathrm{d}_t \boldsymbol{\varepsilon}_{\mathrm{m}}(\Pi_h \boldsymbol{m}_h^{i+1}), \boldsymbol{\varepsilon}(\mathrm{d}_t \boldsymbol{u}_h^{i+1})\right\rangle \\
- \beta k^2 \left\langle \mathbb{C}\mathrm{d}_t \boldsymbol{\varepsilon}_{\mathrm{m}}(\Pi_h \boldsymbol{m}_h^{i}), \boldsymbol{\varepsilon}(\mathrm{d}_t \boldsymbol{u}_h^{i})\right\rangle \\
+ \beta k^2 \left\langle \mathbb{C}\mathrm{d}_t \boldsymbol{\varepsilon}_{\mathrm{m}}(\Pi_h \boldsymbol{m}_h^{i+1}), \boldsymbol{\varepsilon}(\mathrm{d}_t \boldsymbol{u}_h^{i})\right\rangle \\
- \beta k^2 \left\langle \mathbb{C}\mathrm{d}_t \boldsymbol{\varepsilon}_{\mathrm{m}}(\Pi_h \boldsymbol{m}_h^{i}), \boldsymbol{\varepsilon}(\mathrm{d}_t \boldsymbol{u}_h^{i+1})\right\rangle \\
+ k \left\langle \mathbb{C}\boldsymbol{\varepsilon}_{\mathrm{m}}(\Pi_h \boldsymbol{m}_h^{i}), \boldsymbol{\varepsilon}(\mathrm{d}_t \boldsymbol{u}_h^{i+1} + \mathrm{d}_t \boldsymbol{u}_h^i)\right\rangle .
\end{aligned}$$

Now, summing up from $i = 1, \ldots, j-1$,

$$\begin{aligned}
\left\|\mathrm{d}_t \boldsymbol{u}_h^{j}\right\|^2 - \left\|\mathrm{d}_t \boldsymbol{u}_h^{1}\right\|^2 + \beta k^2 \left\|\boldsymbol{\varepsilon}(\mathrm{d}_t \boldsymbol{u}_h^{j})\right\|_{\mathbb{C}}^2 - \beta k^2 \left\|\boldsymbol{\varepsilon}(\mathrm{d}_t \boldsymbol{u}_h^{1})\right\|_{\mathbb{C}}^2 \\
+ \left\langle \mathbb{C}\boldsymbol{\varepsilon}(\boldsymbol{u}_h^{j}), \boldsymbol{\varepsilon}(\boldsymbol{u}_h^{j-1})\right\rangle - \left\langle \mathbb{C}\boldsymbol{\varepsilon}(\boldsymbol{u}_h^{1}), \boldsymbol{\varepsilon}(\boldsymbol{u}_h^{0})\right\rangle \\
= \beta k^2 \left\langle \mathbb{C}\mathrm{d}_t \boldsymbol{\varepsilon}_{\mathrm{m}}(\Pi_h \boldsymbol{m}_h^{j}), \boldsymbol{\varepsilon}(\mathrm{d}_t \boldsymbol{u}_h^{j})\right\rangle \\
- \beta k^2 \left\langle \mathbb{C}\mathrm{d}_t \boldsymbol{\varepsilon}_{\mathrm{m}}(\Pi_h \boldsymbol{m}_h^{1}), \boldsymbol{\varepsilon}(\mathrm{d}_t \boldsymbol{u}_h^{1})\right\rangle \\
+ \beta k^2 \sum_{i=1}^{j-1} \left\langle \mathbb{C}\mathrm{d}_t \boldsymbol{\varepsilon}_{\mathrm{m}}(\Pi_h \boldsymbol{m}_h^{i+1}), \boldsymbol{\varepsilon}(\mathrm{d}_t \boldsymbol{u}_h^{i})\right\rangle \\
- \beta k^2 \sum_{i=1}^{j-1} \left\langle \mathbb{C}\mathrm{d}_t \boldsymbol{\varepsilon}_{\mathrm{m}}(\Pi_h \boldsymbol{m}_h^{i}), \boldsymbol{\varepsilon}(\mathrm{d}_t \boldsymbol{u}_h^{i+1})\right\rangle \\
+ k \sum_{i=1}^{j-1} \left\langle \mathbb{C}\boldsymbol{\varepsilon}_{\mathrm{m}}(\Pi_h \boldsymbol{m}_h^{i}), \boldsymbol{\varepsilon}(\mathrm{d}_t \boldsymbol{u}_h^{i+1} + \mathrm{d}_t \boldsymbol{u}_h^i)\right\rangle . \quad (6.18)
\end{aligned}$$

We are then left with three summation terms on the right-hand side. The first two of these can be dealt with simply by expanding, noting that $|\beta| < 1$, i.e.

$$\begin{aligned}\beta k^2 \sum_{i=1}^{j-1} \left\langle \mathbb{C}\mathrm{d}_t \boldsymbol{\varepsilon}_{\mathrm{m}}(\Pi_h \boldsymbol{m}_h^{i+1}), \boldsymbol{\varepsilon}(\mathrm{d}_t \boldsymbol{u}_h^i) \right\rangle &= \beta k \sum_{i=1}^{j-1} \left\langle \mathbb{C}\mathrm{d}_t \boldsymbol{\varepsilon}_{\mathrm{m}}(\Pi_h \boldsymbol{m}_h^{i+1}), \boldsymbol{\varepsilon}(\boldsymbol{u}_h^i) \right\rangle \\ &\quad - \beta k \sum_{i=1}^{j-1} \left\langle \mathbb{C}\mathrm{d}_t \boldsymbol{\varepsilon}_{\mathrm{m}}(\Pi_h \boldsymbol{m}_h^{i+1}), \boldsymbol{\varepsilon}(\boldsymbol{u}_h^{i-1}) \right\rangle \\ &\leq k \sum_{i=1}^{j-1} \left\| \mathrm{d}_t \boldsymbol{\varepsilon}_{\mathrm{m}}(\Pi_h \boldsymbol{m}_h^{i+1}) \right\|_{\mathbb{C}}^2 \\ &\quad + k \sum_{i=0}^{j-1} \left\| \boldsymbol{\varepsilon}(\boldsymbol{u}_h^i) \right\|_{\mathbb{C}}^2\end{aligned}$$

and

$$\begin{aligned}-\beta k^2 \sum_{i=1}^{j-1} \left\langle \mathbb{C}\mathrm{d}_t \boldsymbol{\varepsilon}_{\mathrm{m}}(\Pi_h \boldsymbol{m}_h^{i}), \boldsymbol{\varepsilon}(\mathrm{d}_t \boldsymbol{u}_h^{i+1}) \right\rangle &= -\beta k \sum_{i=1}^{j-1} \left\langle \mathbb{C}\mathrm{d}_t \boldsymbol{\varepsilon}_{\mathrm{m}}(\Pi_h \boldsymbol{m}_h^{i}), \boldsymbol{\varepsilon}(\boldsymbol{u}_h^{i+1}) \right\rangle \\ &\quad + \beta k \sum_{i=1}^{j-1} \left\langle \mathbb{C}\mathrm{d}_t \boldsymbol{\varepsilon}_{\mathrm{m}}(\Pi_h \boldsymbol{m}_h^{i}), \boldsymbol{\varepsilon}(\boldsymbol{u}_h^{i}) \right\rangle \\ &\leq k \sum_{i=1}^{j-1} \left\| \mathrm{d}_t \boldsymbol{\varepsilon}_{\mathrm{m}}(\Pi_h \boldsymbol{m}_h^{i}) \right\|_{\mathbb{C}}^2 \\ &\quad + \frac{k}{2} \left\| \boldsymbol{\varepsilon}(\boldsymbol{u}_h^{j}) \right\|_{\mathbb{C}}^2 + k \sum_{i=1}^{j-1} \left\| \boldsymbol{\varepsilon}(\boldsymbol{u}_h^{i}) \right\|_{\mathbb{C}}^2 .\end{aligned}$$

The third summation in (6.18) requires a summation by parts akin to 5.6.5, in which

$$\begin{aligned}k \sum_{i=1}^{j-1} &\left\langle \mathbb{C}\boldsymbol{\varepsilon}_{\mathrm{m}}(\Pi_h \boldsymbol{m}_h^{i}), \boldsymbol{\varepsilon}(\mathrm{d}_t \boldsymbol{u}_h^{i+1} + \mathrm{d}_t \boldsymbol{u}_h^{i}) \right\rangle \\ &= \left\langle \mathbb{C}\boldsymbol{\varepsilon}_{\mathrm{m}}(\Pi_h \boldsymbol{m}_h^{j-1}), \boldsymbol{\varepsilon}(\boldsymbol{u}_h^{j}) \right\rangle + \left\langle \mathbb{C}\boldsymbol{\varepsilon}_{\mathrm{m}}(\Pi_h \boldsymbol{m}_h^{j-1}), \boldsymbol{\varepsilon}(\boldsymbol{u}_h^{j-1}) \right\rangle \\ &\quad - \left\langle \mathbb{C}\boldsymbol{\varepsilon}_{\mathrm{m}}(\Pi_h \boldsymbol{m}_h^{1}), \boldsymbol{\varepsilon}(\boldsymbol{u}_h^{1}) \right\rangle - \left\langle \mathbb{C}\boldsymbol{\varepsilon}_{\mathrm{m}}(\Pi_h \boldsymbol{m}_h^{1}), \boldsymbol{\varepsilon}(\boldsymbol{u}_h^{0}) \right\rangle \\ &\quad - k \sum_{i=2}^{j-1} \left\langle \mathbb{C}\mathrm{d}_t \boldsymbol{\varepsilon}_{\mathrm{m}}(\Pi_h \boldsymbol{m}_h^{i}), \boldsymbol{\varepsilon}(\boldsymbol{u}_h^{i}) \right\rangle - k \sum_{i=2}^{j-1} \left\langle \mathbb{C}\mathrm{d}_t \boldsymbol{\varepsilon}_{\mathrm{m}}(\Pi_h \boldsymbol{m}_h^{i}), \boldsymbol{\varepsilon}(\boldsymbol{u}_h^{i-1}) \right\rangle .\end{aligned}$$

There is only one problematic term, which can be rewritten as

$$\begin{aligned}\left\langle \mathbb{C}\boldsymbol{\varepsilon}_{\mathrm{m}}(\Pi_h \boldsymbol{m}_h^{j-1}), \boldsymbol{\varepsilon}(\boldsymbol{u}_h^{j-1}) \right\rangle &= \left\langle \mathbb{C}\boldsymbol{\varepsilon}_{\mathrm{m}}(\Pi_h \boldsymbol{m}_h^{j-1}), \boldsymbol{\varepsilon}(\boldsymbol{u}_h^{j}) \right\rangle \\ &\quad - \left\langle \mathbb{C}\boldsymbol{\varepsilon}_{\mathrm{m}}(\Pi_h \boldsymbol{m}_h^{j-1}), \boldsymbol{\varepsilon}(k\mathrm{d}_t \boldsymbol{u}_h^{j}) \right\rangle ,\end{aligned}$$

and so we can overestimate with the Cauchy–Schwarz inequality giving

$$
\begin{aligned}
k \sum_{i=1}^{j-1} & \left\langle \mathbb{C}\boldsymbol{\varepsilon}_{\mathrm{m}}(\Pi_h \boldsymbol{m}_h^i), \boldsymbol{\varepsilon}(\mathrm{d}_t \boldsymbol{u}_h^{i+1} + \mathrm{d}_t \boldsymbol{u}_h^i) \right\rangle \\
&\leq 2 \left\| \boldsymbol{\varepsilon}_{\mathrm{m}}(\Pi_h \boldsymbol{m}_h^{j-1}) \right\|_{\mathbb{C}} \left\| \boldsymbol{\varepsilon}(\boldsymbol{u}_h^j) \right\|_{\mathbb{C}} + \left\| \boldsymbol{\varepsilon}_{\mathrm{m}}(\Pi_h \boldsymbol{m}_h^{j-1}) \right\|_{\mathbb{C}} \left\| \boldsymbol{\varepsilon}(k\mathrm{d}_t \boldsymbol{u}_h^j) \right\|_{\mathbb{C}} \\
&\quad + \left\| \boldsymbol{\varepsilon}_{\mathrm{m}}(\Pi_h \boldsymbol{m}_h^1) \right\|_{\mathbb{C}} \left\| \boldsymbol{\varepsilon}(\boldsymbol{u}_h^1) \right\|_{\mathbb{C}} + \left\| \boldsymbol{\varepsilon}_{\mathrm{m}}(\Pi_h \boldsymbol{m}_h^1) \right\|_{\mathbb{C}} \left\| \boldsymbol{\varepsilon}(\boldsymbol{u}_h^0) \right\|_{\mathbb{C}} \\
&\quad + k \sum_{i=2}^{j-1} \left\| \mathrm{d}_t \boldsymbol{\varepsilon}_{\mathrm{m}}(\Pi_h \boldsymbol{m}_h^i) \right\|_{\mathbb{C}} \left\| \boldsymbol{\varepsilon}(\boldsymbol{u}_h^i) \right\|_{\mathbb{C}} + k \sum_{i=2}^{j-1} \left\| \mathrm{d}_t \boldsymbol{\varepsilon}_{\mathrm{m}}(\Pi_h \boldsymbol{m}_h^i) \right\|_{\mathbb{C}} \left\| \boldsymbol{\varepsilon}(\boldsymbol{u}_h^{i-1}) \right\|_{\mathbb{C}} .
\end{aligned}
$$

We can now apply the weighted Young inequality repeatedly, introducing two parameters $\nu_1, \nu_2 > 0$ for the first two terms on the left-hand side. We then have, after some index shifting on the sums,

$$
\begin{aligned}
k \sum_{i=1}^{j-1} & \left\langle \mathbb{C}\boldsymbol{\varepsilon}_{\mathrm{m}}(\Pi_h \boldsymbol{m}_h^i), \boldsymbol{\varepsilon}(\mathrm{d}_t \boldsymbol{u}_h^{i+1} + \mathrm{d}_t \boldsymbol{u}_h^i) \right\rangle \\
&\leq \left(\frac{1}{\nu_1} + \nu_2 \right) \left\| \boldsymbol{\varepsilon}_{\mathrm{m}}(\Pi_h \boldsymbol{m}_h^{j-1}) \right\|_{\mathbb{C}}^2 + \nu_1 \left\| \boldsymbol{\varepsilon}(\boldsymbol{u}_h^j) \right\|_{\mathbb{C}}^2 + \frac{k^2}{4\nu_2} \left\| \boldsymbol{\varepsilon}(\mathrm{d}_t \boldsymbol{u}_h^j) \right\|_{\mathbb{C}}^2 \\
&\quad + \left\| \boldsymbol{\varepsilon}_{\mathrm{m}}(\Pi_h \boldsymbol{m}_h^1) \right\|_{\mathbb{C}}^2 + \frac{1}{2} \left\| \boldsymbol{\varepsilon}(\boldsymbol{u}_h^1) \right\|_{\mathbb{C}}^2 + \frac{1}{2} \left\| \boldsymbol{\varepsilon}(\boldsymbol{u}_h^0) \right\|_{\mathbb{C}}^2 \\
&\quad + k \sum_{i=2}^{j-1} \left\| \mathrm{d}_t \boldsymbol{\varepsilon}_{\mathrm{m}}(\Pi_h \boldsymbol{m}_h^i) \right\|_{\mathbb{C}}^2 + k \sum_{i=1}^{j-1} \left\| \boldsymbol{\varepsilon}(\boldsymbol{u}_h^i) \right\|_{\mathbb{C}}^2 .
\end{aligned}
$$

To deal with the final terms of the left-hand side of (6.18), we have

$$
\left\langle \mathbb{C}\boldsymbol{\varepsilon}(\boldsymbol{u}_h^j), \boldsymbol{\varepsilon}(\boldsymbol{u}_h^{j-1}) \right\rangle = \left\| \boldsymbol{\varepsilon}(\boldsymbol{u}_h^j) \right\|_{\mathbb{C}}^2 - \left\langle \mathbb{C}\boldsymbol{\varepsilon}(\boldsymbol{u}_h^j), \boldsymbol{\varepsilon}(k\mathrm{d}_t \boldsymbol{u}_h^j) \right\rangle
$$

where we can apply Cauchy-Schwarz and the weighted Young inequality to the second term for some $\nu_3 > 0$, i.e.

$$
- \left\langle \mathbb{C}\boldsymbol{\varepsilon}(\boldsymbol{u}_h^j), \boldsymbol{\varepsilon}(k\mathrm{d}_t \boldsymbol{u}_h^j) \right\rangle \leq \nu_3 \left\| \boldsymbol{\varepsilon}(\boldsymbol{u}_h^j) \right\|_{\mathbb{C}}^2 + \frac{k^2}{4\nu_3} \left\| \boldsymbol{\varepsilon}(\mathrm{d}_t \boldsymbol{u}_h^j) \right\|_{\mathbb{C}}^2
$$

and

$$
\left\langle \mathbb{C}\boldsymbol{\varepsilon}(\boldsymbol{u}_h^1), \boldsymbol{\varepsilon}(\boldsymbol{u}_h^0) \right\rangle \leq \frac{1}{2} \left\| \boldsymbol{\varepsilon}(\boldsymbol{u}_h^1) \right\|_{\mathbb{C}}^2 + \frac{1}{2} \left\| \boldsymbol{\varepsilon}(\boldsymbol{u}_h^0) \right\|_{\mathbb{C}}^2 .
$$

The remaining terms on the right-hand side of (6.18) can be handled similarly, i.e. for some $\nu_4 > 0$

$$
\beta k^2 \left\langle \mathbb{C}\mathrm{d}_t \boldsymbol{\varepsilon}_{\mathrm{m}}(\Pi_h \boldsymbol{m}_h^j), \boldsymbol{\varepsilon}(\mathrm{d}_t \boldsymbol{u}_h^j) \right\rangle \leq \nu_4 k^2 \left\| \mathrm{d}_t \boldsymbol{\varepsilon}_{\mathrm{m}}(\Pi_h \boldsymbol{m}_h^j) \right\|_{\mathbb{C}}^2 + \frac{k^2}{4\nu_4} \left\| \boldsymbol{\varepsilon}(\mathrm{d}_t \boldsymbol{u}_h^j) \right\|_{\mathbb{C}}^2 ,
$$

and

$$
-\beta k^2 \left\langle \mathbb{C}\mathrm{d}_t \boldsymbol{\varepsilon}_{\mathrm{m}}(\Pi_h \boldsymbol{m}_h^1), \boldsymbol{\varepsilon}(\mathrm{d}_t \boldsymbol{u}_h^1) \right\rangle \leq \frac{k^2}{2} \left\| \mathrm{d}_t \boldsymbol{\varepsilon}_{\mathrm{m}}(\Pi_h \boldsymbol{m}_h^1) \right\|_{\mathbb{C}}^2 + \frac{k^2}{2} \left\| \boldsymbol{\varepsilon}(\mathrm{d}_t \boldsymbol{u}_h^1) \right\|_{\mathbb{C}}^2
$$

We can now combine each of these estimates together and apply them to (6.18) yielding

$$\begin{aligned}
\left\|\mathrm{d}_t \boldsymbol{u}_h^j\right\|^2 + \left(\beta - \frac{1}{4\nu_3} - \frac{1}{4\nu_4} - \frac{1}{4\nu_2}\right) k^2 \left\|\boldsymbol{\varepsilon}(\mathrm{d}_t \boldsymbol{u}_h^j)\right\|_{\mathbb{C}}^2 \\
+ \left(1 - \nu_3 - \nu_1 - \frac{k}{2}\right) \left\|\boldsymbol{\varepsilon}(\boldsymbol{u}_h^j)\right\|_{\mathbb{C}}^2 \\
\leq \left\|\boldsymbol{\varepsilon}(\boldsymbol{u}_h^1)\right\|_{\mathbb{C}}^2 + \left\|\boldsymbol{\varepsilon}(\boldsymbol{u}_h^0)\right\|_{\mathbb{C}}^2 + \left\|\mathrm{d}_t \boldsymbol{u}_h^1\right\|^2 + \beta k^2 \left\|\boldsymbol{\varepsilon}(\mathrm{d}_t \boldsymbol{u}_h^1)\right\|_{\mathbb{C}}^2 \\
+ \nu_4 k^2 \left\|\mathrm{d}_t \boldsymbol{\varepsilon}_{\mathrm{m}}(\Pi_h \boldsymbol{m}_h^j)\right\|_{\mathbb{C}}^2 + \frac{k^2}{2} \left\|\mathrm{d}_t \boldsymbol{\varepsilon}_{\mathrm{m}}(\Pi_h \boldsymbol{m}_h^1)\right\|_{\mathbb{C}}^2 + \frac{k^2}{2} \left\|\boldsymbol{\varepsilon}(\mathrm{d}_t \boldsymbol{u}_h^1)\right\|_{\mathbb{C}}^2 \\
+ \left(\frac{1}{\nu_1} + \nu_2\right) \left\|\boldsymbol{\varepsilon}_{\mathrm{m}}(\Pi_h \boldsymbol{m}_h^{j-1})\right\|_{\mathbb{C}}^2 \\
+ \left\|\boldsymbol{\varepsilon}_{\mathrm{m}}(\Pi_h \boldsymbol{m}_h^1)\right\|_{\mathbb{C}}^2 + 3k \sum_{i=0}^{j-1} \left\|\mathrm{d}_t \boldsymbol{\varepsilon}_{\mathrm{m}}(\Pi_h \boldsymbol{m}_h^{i+1})\right\|_{\mathbb{C}}^2 + 3k \sum_{i=1}^{j-1} \left\|\boldsymbol{\varepsilon}(\boldsymbol{u}_h^i)\right\|_{\mathbb{C}}^2
\end{aligned}$$

It is immediately obvious that any remaining non-summed terms on the right-hand side involving a projected magnetization are bounded, so we end up with

$$\begin{aligned}
\left\|\mathrm{d}_t \boldsymbol{u}_h^j\right\|^2 + \left(\beta - \frac{1}{4\nu_3} - \frac{1}{4\nu_4} - \frac{1}{4\nu_2}\right) k^2 \left\|\boldsymbol{\varepsilon}(\mathrm{d}_t \boldsymbol{u}_h^j)\right\|_{\mathbb{C}}^2 \\
+ \left(1 - \nu_3 - \nu_1 - \frac{k}{2}\right) \left\|\boldsymbol{\varepsilon}(\boldsymbol{u}_h^j)\right\|_{\mathbb{C}}^2 \\
\lesssim 1 + \left\|\boldsymbol{\varepsilon}(\boldsymbol{u}_h^1)\right\|_{\mathbb{C}}^2 + \left\|\boldsymbol{\varepsilon}(\boldsymbol{u}_h^0)\right\|_{\mathbb{C}}^2 + \left\|\mathrm{d}_t \boldsymbol{u}_h^1\right\|^2 \\
+ \beta k^2 \left\|\boldsymbol{\varepsilon}(\mathrm{d}_t \boldsymbol{u}_h^1)\right\|_{\mathbb{C}}^2 + k^2 \left\|\boldsymbol{\varepsilon}(\mathrm{d}_t \boldsymbol{u}_h^1)\right\|_{\mathbb{C}}^2 \\
+ k \sum_{i=0}^{j-1} \left\|\mathrm{d}_t \boldsymbol{\varepsilon}_{\mathrm{m}}(\Pi_h \boldsymbol{m}_h^{i+1})\right\|_{\mathbb{C}}^2 + k \sum_{i=1}^{j-1} \left\|\boldsymbol{\varepsilon}(\boldsymbol{u}_h^i)\right\|_{\mathbb{C}}^2
\end{aligned}$$

On the left-hand side, we require the coefficients to all be positive, i.e. we must choose $\nu_i > 0$ for $i = 1, 2, 3, 4$ such that

$$\begin{aligned}
4\beta - \frac{1}{\nu_3} - \frac{1}{\nu_4} - \frac{1}{\nu_2} > 0, \\
1 - \nu_1 - \nu_3 - \frac{k}{2} > 0.
\end{aligned}$$

Special attention must be paid to ν_3 which appears in both inequalities, and in the standard elastic case with no magnetization dependency, we would choose $\nu_3 = 1$. Here this is not possible, as we must spend a portion of β or 1 on the other terms. We find that we must choose ν_3 such that

$$\frac{1}{4\beta - \frac{1}{\nu_4} - \frac{1}{\nu_2}} < \nu_3 < 1 - \nu_1 - \frac{k}{2}.$$

It can be seen that we must have $k < 2$ and $\beta > 1/4$ for both inequalities to be consistent. We can now deal with the remaining magnetization terms, in a similar vein to Lemma 5.6.5. We have via Lemma 5.6.4 that for each $i \geq 0$

$$\begin{aligned}\left\|\mathrm{d}_t \boldsymbol{\varepsilon}_{\mathrm{m}}(\Pi_h \boldsymbol{m}_h^{i+1})\right\|_{\mathbb{C}} &= \frac{1}{k}\left\|\boldsymbol{\varepsilon}_{\mathrm{m}}(\Pi_h \boldsymbol{m}_h^{i+1}) - \boldsymbol{\varepsilon}_{\mathrm{m}}(\Pi_h \boldsymbol{m}_h^{i})\right\|_{\mathbb{C}} \\ &\lesssim \frac{1}{k}\left\|\boldsymbol{m}_h^{i+1} - \boldsymbol{m}_h^{i}\right\| \\ &= \left\|\boldsymbol{v}_h^{i+1}\right\|\end{aligned}$$

so it follows that

$$k\sum_{i=0}^{j-1}\left\|\mathrm{d}_t \boldsymbol{\varepsilon}_{\mathrm{m}}(\Pi_h \boldsymbol{m}_h^{i+1})\right\|_{\mathbb{C}}^2 \lesssim k\sum_{i=0}^{j-1}\left\|\boldsymbol{v}_h^{i+1}\right\|^2.$$

Then, we have from combining (6.10) (for $\boldsymbol{v}_h^1$ only) and (6.13) that

$$k\sum_{i=0}^{j-1}\left\|\boldsymbol{v}_h^{i+1}\right\|^2 \lesssim 1 + k\sum_{i=0}^{j-1}\left(1 + \left\|\boldsymbol{\varepsilon}(\boldsymbol{u}_h^i)\right\|^2\right),$$

Combining the above completes the proof. □

The proof of boundedness now flows from the previous propositions.

Proposition 6.4.5. *Let $\gamma = 1/2$, $\beta > 1/4$ and assume that k is sufficiently small. Then for every $j \geq 1$*

$$\left\|\mathrm{d}_t \boldsymbol{u}_h^j\right\|^2 + \left\|\boldsymbol{u}_h^j\right\|_{\boldsymbol{H}^1(\Omega)}^2 + \left\|\boldsymbol{m}_h^j\right\|_{\boldsymbol{H}^1(\Omega)}^2 + k^2\left\|\boldsymbol{\varepsilon}(\mathrm{d}_t \boldsymbol{u}_h^j)\right\|_{\mathbb{C}}^2 + k\sum_{i=0}^{j-1}\left\|\boldsymbol{v}_h^{i+1}\right\|^2 \lesssim 1, \quad (6.19)$$

and

$$\left\||\boldsymbol{m}_h^j|^2 - 1\right\|_{L^1} \lesssim k. \quad (6.20)$$

The hidden constants depend upon the problem data, Poincaré and Korn's constants and the time T, but are independent of the discretization parameters h, k.

Proof. Proposition 6.4.1, Proposition 6.4.3, Proposition 6.4.4, the boundedness from assumption (A1), and an application of a discrete Grönwall inequality imply that

$$\left\|\mathrm{d}_t \boldsymbol{u}_h^j\right\|^2 + \left\|\boldsymbol{\varepsilon}(\boldsymbol{u}_h^j)\right\|^2 + \left\|\boldsymbol{\nabla}\boldsymbol{m}_h^j\right\|^2 + k^2\left\|\boldsymbol{\varepsilon}(\mathrm{d}_t \boldsymbol{u}_h^j)\right\|_{\mathbb{C}}^2 + k\sum_{i=0}^{j-1}\left\|\boldsymbol{v}_h^{i+1}\right\|^2 \lesssim 1.$$

The proof of (6.20) then uses ideas from [ABRW25, Proposition 2.3] and the boundedness just derived. Combining these with the equivalence $\|\cdot\|_{\mathbb{C}} \simeq \|\cdot\|$, and Poincaré and Korn's inequalities yields (6.19). □

6.5 Numerical Experiments

In this section, we show the improvements of Algorithm 6.3.1 over the algorithms presented in [BPPR14] and Chapter 5. Specifically, we show the second-order behaviour in both the numerical error, and in the unit length constraint. We also investigate the energetic behaviour of Algorithm 6.3.1 and compare this to Algorithm 5.4.1. We will consider two algorithms:

1. Algorithm 6.3.1 with $\beta = 1/3, \gamma = 1/2$, denoted "Multi".
2. Algorithm 5.4.1. This uses an extension of the classical algorithm of [Alo08] combined with a Newmark-β scheme corresponding to $\beta = 1, \gamma = 3/2$, which we denote "NR".

We choose the parameters of FeCoSiB, shown in Table 5.1, and explicitly choose the damping parameter $\alpha = 0.1$, and the large magnetostriction parameter $\lambda_{100} = 0.003$, to increase the coupling behaviour for more interesting dynamics. The modified parameters are shown in Table 6.1.

The relative tolerance applied in this chapter, is 10^{-15} , as opposed to the relative tolerance of 10^{-8} applied in the previous chapter. This is to ensure the second-order convergence is detectable. Otherwise, all solver parameters are identical.

Symbol	Name	Value
A	Exchange constant	$1.5 \cdot 10^{-11}\mathrm{Jm}^{-1}$
α	Gilbert damping parameter	0.1*
γ	Gyromagnetic ratio	$1.761 \cdot 10^{11}$ rads^{-1}T^{-1}
μ_0	Permeability of free space	$1.255\,637\,06 \cdot 10^{-6}$
M_s	Saturation magnetization	$1.5 \cdot 10^{6}\mathrm{Am}^{-1}$
λ_{100}	Saturation magnetostrain	$3 \cdot 10^{-3}$*
ρ	Density	7900 kgm^{-3}
μ	First Lamé constant	172 GPa
λ	Second Lamé constant	54 GPa

Table 6.1: Material parameters of FeCoSiB from Table 5.1. Entries marked with an asterisk are chosen parameters.

6.5.1 Order of error in time

Due to the non-linear nature of the PDE system, analytical solutions are generally not available. For this reason, we produce multiple numerical solutions of different time-step size, and compute an error with respect to a reference solution with finer time-step size. We consider a unit cube $[0, 1]^3$, choose $h_{\max} \approx 0.43$, with 2217 nodes, and 3392 elements. For the initial conditions, we choose

$$\boldsymbol{m}_h^0 = \frac{\sqrt{85}}{10}(0.9, 0.2, 0)$$

for the magnetization, and $\boldsymbol{u}_h^0 = (10^{-3}x, 0, 0)$, $\dot{\boldsymbol{u}}_h^0 = \mathbf{0}$ for the displacement and its velocity. To encourage the same end state, we include in the energy a constant Zeeman field $f_{\text{zeeman}} = (1, 0, 0)$. We set $T = 1 \cdot 10^{-2}$, and consider $k_n = 1 \cdot 10^{-3} \cdot 2^{-n}$ for $n = 0, 1, 2, 3, 4, 5, 6$, comparing these to a reference solution computed for $n = 8$. Specifically, we calculate the $\boldsymbol{H}^1$ error at the final time, $t = T$, that is,

$$\text{err}^n_{\boldsymbol{H}^1}(\boldsymbol{\phi}_h) = \left\| \boldsymbol{\phi}_{h,k_8}(T) - \boldsymbol{\phi}_{h,k_n}(T) \right\|_{\boldsymbol{H}^1}.$$

In Figure 6.1, we see that the Algorithm 6.3.1 is of second-order in time for both the magnetization and displacement. Algorithm 5.4.1 is of first-order for both fields, as expected. The average number of GMRES iterations for this experiment was 4, independently of β and the time-step.

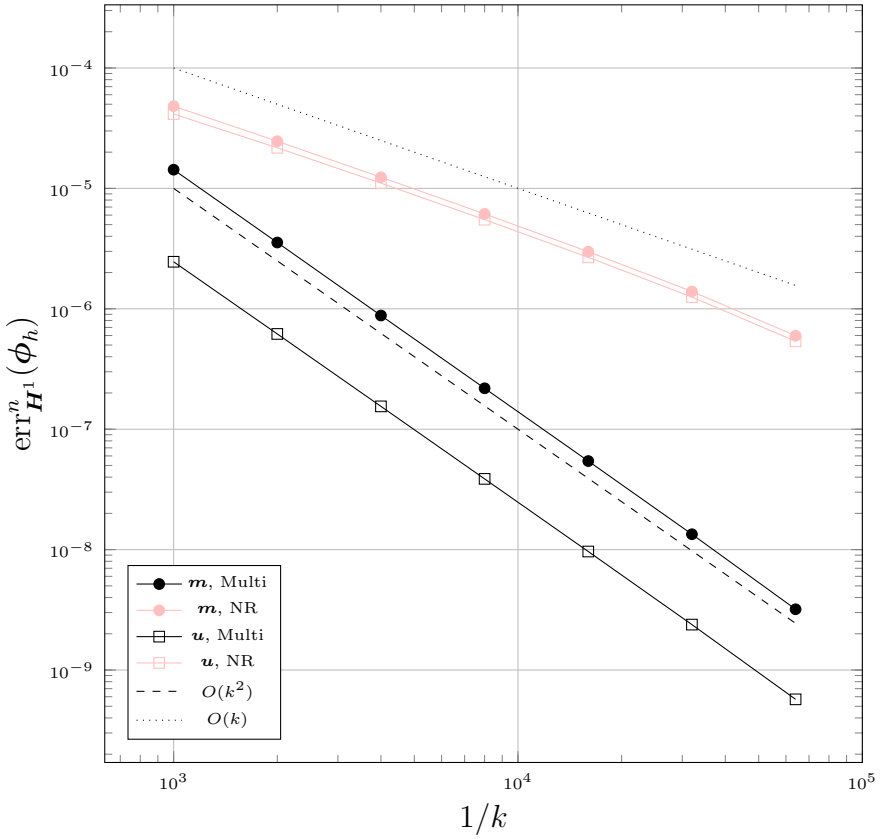

Figure 6.1: Experiment of Section 6.5.1. Experimental orders of convergence with respect to the $\boldsymbol{H}^1$ norm at the final time-step $t = T$ for Algorithm 6.3.1 and Algorithm 5.4.1.

6.5.2 Unit length constraint

To measure the unit length constraint error, we choose the same measure of error as in [Bar16], that is, for each $i \in \mathbb{N}$

$$\begin{aligned} \text{err}_{L^1}(\boldsymbol{m}_h^i) &= \left\| \mathcal{I}_h[|\boldsymbol{m}_h^i|^2] - 1 \right\|_{L^1}, \\ \text{err}_{\boldsymbol{L}^\infty}(\boldsymbol{m}_h^i) &= \left\| \boldsymbol{m}_h^i \right\|_{\boldsymbol{L}^\infty} - 1. \end{aligned}$$

We use the same mesh as in Section 6.5.1. For the initial magnetization, we consider

$$\boldsymbol{m}_h^0 = \frac{5}{\sqrt{26}}(0.2, \sin(4(x+y+z)), \cos(4(x+y+z)))$$

and set $\boldsymbol{u}_h^0 = \dot{\boldsymbol{u}}_h^0 = \boldsymbol{0}$, with $T = 1$ giving an initial energy of $\mathcal{E}[\boldsymbol{u}_h^0, \boldsymbol{m}_h^0] \approx 23$. The evolution in time of the unit length constraint for the three schemes are shown in Figure 6.2 for $k = 2.5 \cdot 10^{-4}$. The midpoint tangent plane scheme is not necessarily monotonically increasing in the unit length constraint (cf [ABRW25, Proposition 2.2]), and thus the unit length constraint violation may decrease with time. The first-order tangent plane scheme is always monotonically increasing.

To estimate the order of the constraint violation, we apply time-step sizes of $k = 1 \cdot 10^{-3} \cdot 2^{-n}$ for $n = 0, 1, 2, 3, 4, 5, 6$. The results are shown in Figure 6.3.

As expected, the midpoint scheme is significantly better at maintaining the unit length constraint, being almost two orders of magnitude smaller than for the first-order scheme. The constraint violation of the first-order algorithm increases greatly every step. The midpoint tangent plane scheme is not monotonically increasing in the unit length, unlike the standard tangent plane scheme.

As can be seen in Figure 6.3 the midpoint scheme is second-order in the unit length constraint, whilst the standard tangent plane is only first-order. The midpoint scheme is always at least first-order, but to be second-order a discrete regularity condition must be met (see [ABRW25, Proposition 2.3]).

To prove that the method is of second-order in a rigorous manner, we expect the required regularity on the solution to quite restrictive in terms of smoothness assumptions. The problem here is highly non-linear, and the nonconvex unit length constraint adds even more difficulty.

The average number of GMRES iterations for this experiment was 4, independently of β and the time-step.

6.5.3 Energy dissipation

According to the energy law (5.8), if the time derivative of the magnetization is small, or α is small, then the system is approximately energy conserving. The discrete energy law given in (5.4.4) includes several numerical dissipation terms, and some of these come directly from the displacement. This means that the numerical scheme will dissipate energy through the displacement, despite the physical model having no such mechanism for this. In systems where the magnetization is close to equilibrium (i.e. $\partial_t \boldsymbol{m} \approx 0$), the energy should be essentially conserved, but this places no restrictions on the time derivative of the displacement, $\dot{\boldsymbol{u}}$. Therefore, we can expect a scenario where for long times the displacement oscillates about the minima, stimulating small changes in the magnetization resulting in dissipation and thus eventual minimization.

We set $\boldsymbol{m}_h^0 = (1, 0, 0)$, and $\boldsymbol{u}_h^0, \dot{\boldsymbol{u}}_h^0 = \boldsymbol{0}$, and consider $T = 5 \cdot 10^{-11}$s. For the parameters, we choose $\beta = 1/3, \gamma = 1/2$, and select $k = 10^{-2}, 10^{-3}$, and compare this with Algorithm 5.4.1 with $k = 10^{-2}, 10^{-3}, 10^{-4}$. As can be seen in Figure 6.4,

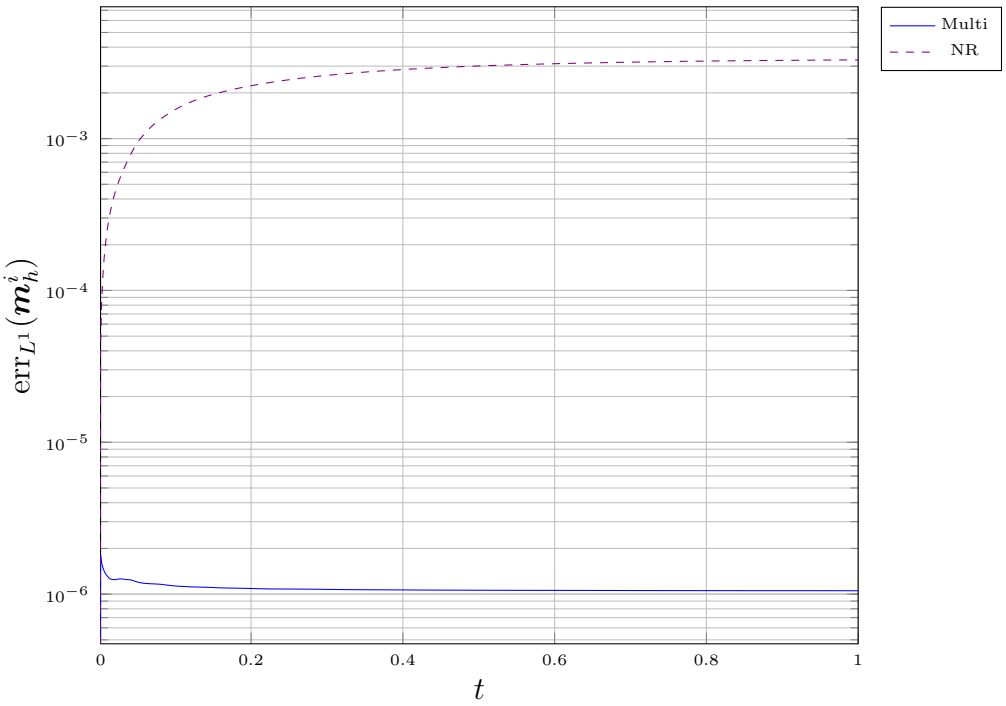

Figure 6.2: Experiment of Section 6.5.2. Algorithm 6.3.1 with $\gamma = 1/2$ and $\beta = 1/3$, or Algorithm 5.4.1 with time-step $k = 1.5625 \cdot 10^{-5}$.

Algorithm 5.4.1 dissipates energy very quickly, despite the magnetization being roughly constant. The dynamics of the numerical solution terminate much too quickly, requiring the time-step to be decreased sufficiently for a solution to behave correct energetically.

However, Algorithm 6.3.1 with $\beta = 1/3, \gamma = 1/2$ behaves robustly in terms of the energy as the time-step is changed. This results in the displacement slowly decreasing in amplitude over time utilizing the physical damping, modulated by the Gilbert damping constant. The disadvantage of 6.3.1, is that the energy is no longer monotonically decreasing, with the energy evolution oscillating around that of the limit. The oscillations decrease with the time-step, as shown in Figure 6.4. The oscillations come from the Newmark-β scheme being a variational scheme (in the sense that it can be derived from a discrete variational principle), meaning that the scheme conserves a pseudo energy quantity that is close to the energy of interest, with the difference between the pseudo and real energy being periodic and on the order of k^2, see for example [KMOW00].

6.5.4 Nutation

For this experiment, we use a unit cube. To detect nutation, we begin from a minimized energy state. To calculate the minimizer, we set $\gamma = 2, \beta = 1, \alpha = 1$, and eliminate the precession term resulting from (5.5). Setting $\gamma > 1/2$ incorporates some numerical dissipation (cf. Remark 6.3.3) which is useful for the minimization, and eliminating the precession term $\langle \boldsymbol{m} \times \boldsymbol{v}, \boldsymbol{\psi} \rangle$ does not affect the energy evolution explicitly, but reduces the unit length constraint violation (which

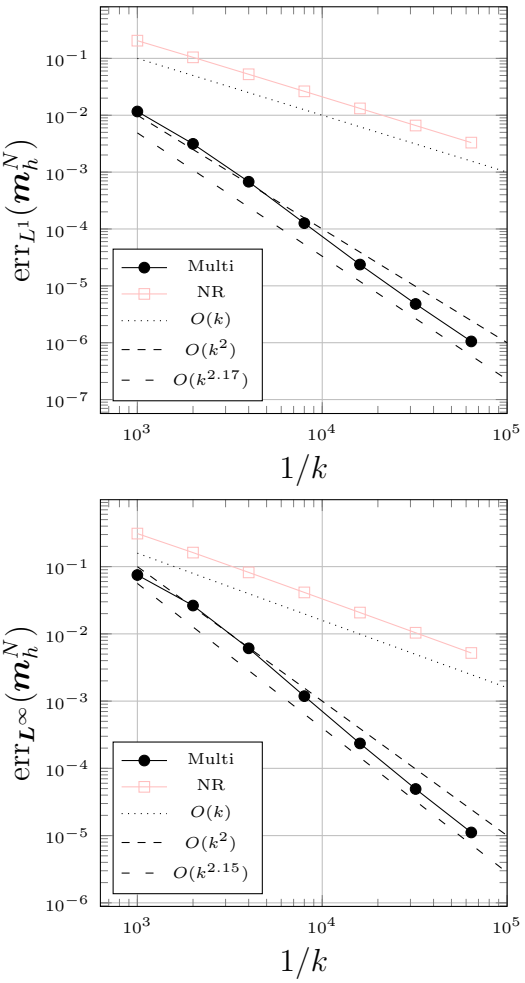

Figure 6.3: Experiment of Section 6.5.2. As predicted, Algorithm 5.4.1 is first-order in the unit length constraint. The midpoint scheme however is second-order in the unit length constraint, and in fact is super-second-order in this particular example. The effect of β is minimal.

does affect the energy) by reducing the amount of precession. For the initial condition of the minimization process, we select $\boldsymbol{m}_h^0 = (1, 0, 0), \boldsymbol{u}_h^0 = (\frac{1}{2}\lambda_m x, 0, 0)$, $\dot{\boldsymbol{u}}_h^0 = \mathbf{0}$, and use the time-step $k = 1 \cdot 10^{-2}$, and run the numerical scheme for $T = 20$ units of time. This is sufficiently long to reach a reasonable minimizer. We then apply a nodal projection to the minimizer and use it as an initial condition.

For the dynamical simulation, we apply a pulse Zeeman field of the form $f_{\text{zeeman}} = (1, H(t), 0)$, where $H(t)$ is defined as in Figure 6.6. We select $\beta = 1/3, \gamma = 1/2, \alpha = 0.1$ and choose the time-step $k = 1 \cdot 10^{-3}$. We run the simulation for $T = 20$ units of time.

The results are shown in Figure 6.7. We see in Figure 6.7a that the pulse field disturbs the magnetization away from its minimizer state, with $\langle m_x \rangle \approx 1$ falling to $\langle m_x \rangle \approx 0.98$, and $\langle m_y \rangle$ sharply increases to around 0.1 as shown in Figure 6.7b, and $\langle m_z \rangle$ sharply decreases to around -0.2 as shown in Figure 6.7c. Under pure LLG dynamics, the magnetization only precesses around $(1, 0, 0)$ as

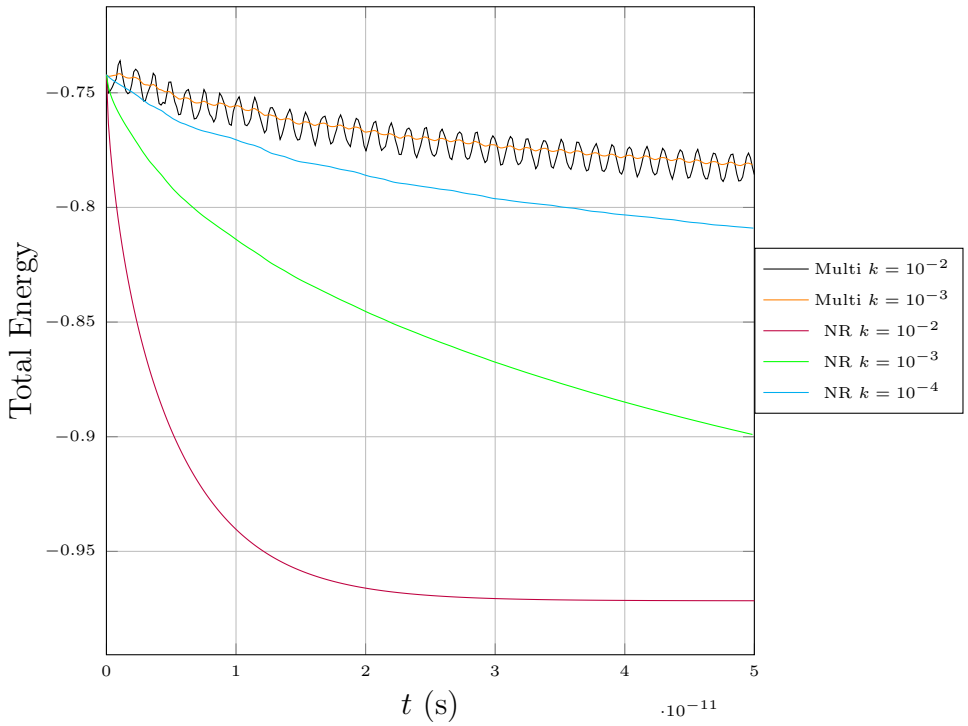

Figure 6.4: Experiment of Section 6.5.3. Energy evolution of Algorithm 6.3.1 and Algorithm 5.4.1.

the magnetization returns to the minimizer, but with the magnetoelastic effects included there is additional nutation. The displacement is slower to respond than the magnetization because of the wave nature of (5.4). The average displacement in the x-direction begins oscillating, with the average returning to the equilibrium point. The displacement in the y and z direction broadly mimic the magnetization in the y and z directions respectively. The energy evolution is shown in Figure 6.8, with the energy decreasing as the pulse field increases, and then decreasing as the field becomes weaker. When the field is disabled, the system begins a minimization process governed by the magnetoelastic PDEs.

6.5.5 Necessity of $\beta > 1/4$

As stated in Proposition 6.4.5, Algorithm 6.3.1 requires that $\beta > 1/4$ for stability. We expect that for $0 < \beta \leq 1/4$, a CFL condition is necessary for stability to remain, and in particular the CFL condition will be at least $k = O(h)$, coming from the solution of the displacement. To show that this is indeed the case, we design the following experiment with different mesh sizes and time-steps.

We choose a hemisphere of radius 0.05 and clamped planar face at $x = 0$. For the initial conditions, we choose $\boldsymbol{m}_h^0 = (1, 0, 0)$, and $\boldsymbol{u}_h^0 = \dot{\boldsymbol{u}}_h^0 = \mathbf{0}$, and apply an external field $(1, 0, 0)$. The final time is $T = 1$, and we choose $\alpha = 0.1$, and $\gamma = 1/2$. We vary the time-step size $k = 2.5 \cdot 10^{-3}$, $1 \cdot 10^{-3}$, $5 \cdot 10^{-4}$, $2.5 \cdot 10^{-4}$, $1 \cdot 10^{-4}$, mesh size $h_{\max} \approx 0.051$, 0.035, 0.015, and choose β to be either 0 or 1/3.

The final energy values are recorded in Table 6.2 and Table 6.3 for $\beta = 0$ and

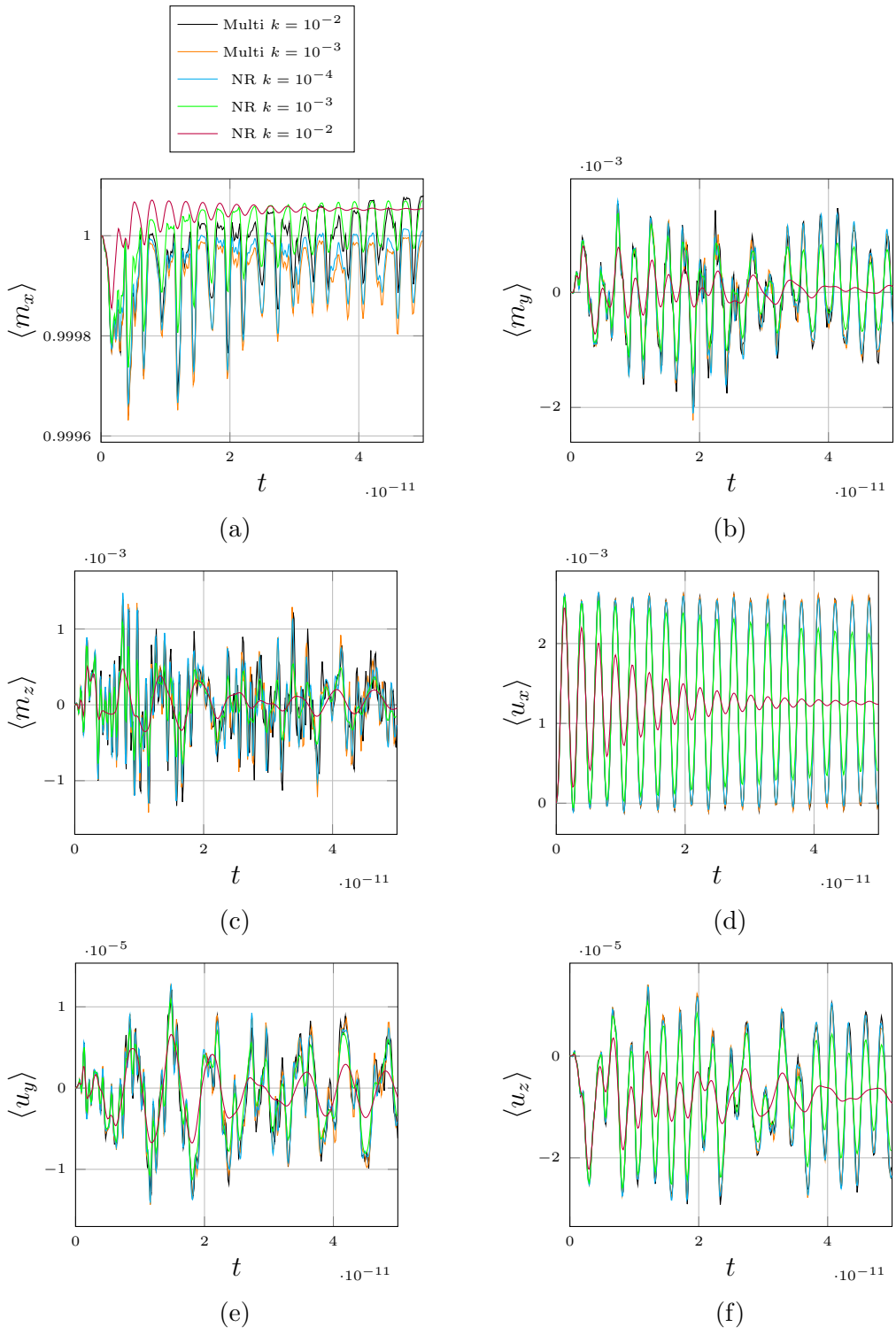

Figure 6.5: Experiment of Section 6.5.3. Averages of the magnetization and displacement in the x, y, z-directions.

$\beta = 1/3$ respectively. For some cases of k and $h_{\max}$ with $\beta = 0$, the algorithm was not stable and for these we record "Fail", indicating a divergence to $+\infty$ of the energy. For $\beta = 1/3$ we do not include the smaller time-steps for the fine mesh, as

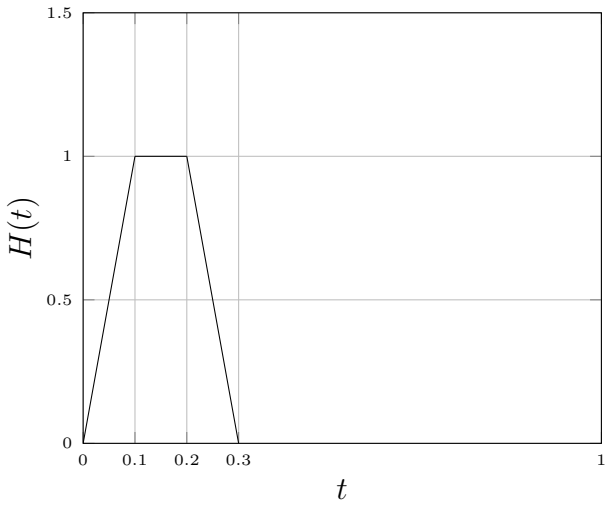

Figure 6.6: Pulse field of Section 6.5.4.

we already see stability for the larger time-steps. We see that using $\beta = 0$ imposes a CFL condition that appears to be at least linear, i.e., $k = O(h)$, but we see no such evidence for the implicit method with $\beta = 1/3$. For this reason, we do not recommend an explicit treatment of the displacement, and any implicit method should satisfy $\gamma = 1/2, \beta > 1/4$ to ensure stability of the method.

	$h_{\max}$		
	0.051	0.035	0.015
k			
$2.5 \cdot 10^{-3}$	Fail	Fail	Fail
$1 \cdot 10^{-3}$	$-1.72 \cdot 10^{-4}$	Fail	Fail
$5 \cdot 10^{-4}$	$-1.72 \cdot 10^{-4}$	$-1.88 \cdot 10^{-4}$	Fail
$2.5 \cdot 10^{-4}$	$-1.72 \cdot 10^{-4}$	$-1.87 \cdot 10^{-4}$	Fail
$1 \cdot 10^{-4}$			$-1.94 \cdot 10^{-4}$

Table 6.2: Experiment of Section 6.5.5. Final energy for $\beta = 0$.

	$h_{\max}$		
	0.051	0.035	0.015
k			
$2.5 \cdot 10^{-3}$	$-1.72 \cdot 10^{-4}$	$-1.86 \cdot 10^{-4}$	$-1.89 \cdot 10^{-4}$
$1 \cdot 10^{-3}$	$-1.72 \cdot 10^{-4}$	$-1.87 \cdot 10^{-4}$	$-1.93 \cdot 10^{-4}$
$5 \cdot 10^{-4}$	$-1.72 \cdot 10^{-4}$	$-1.87 \cdot 10^{-4}$	N/A
$2.5 \cdot 10^{-4}$	$-1.72 \cdot 10^{-4}$	$-1.87 \cdot 10^{-4}$	N/A

Table 6.3: Experiment of Section 6.5.5. Final energy for $\beta = 1/3$.

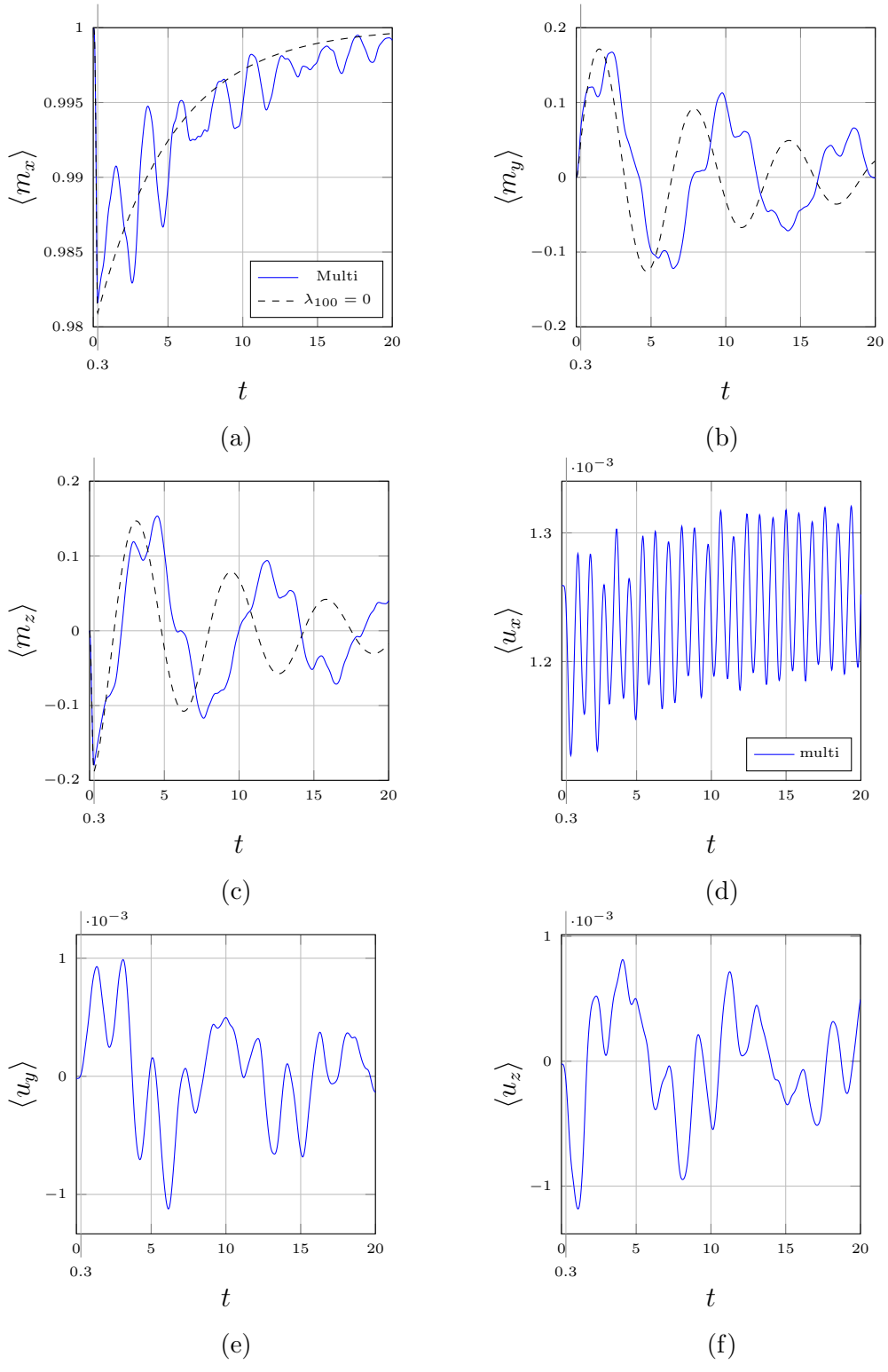

Figure 6.7: Experiment of Section 6.5.4. Parameters $k = 1 \cdot 10^{-3}$ and $\lambda_{100} = 3 \cdot 10^{-3}$.

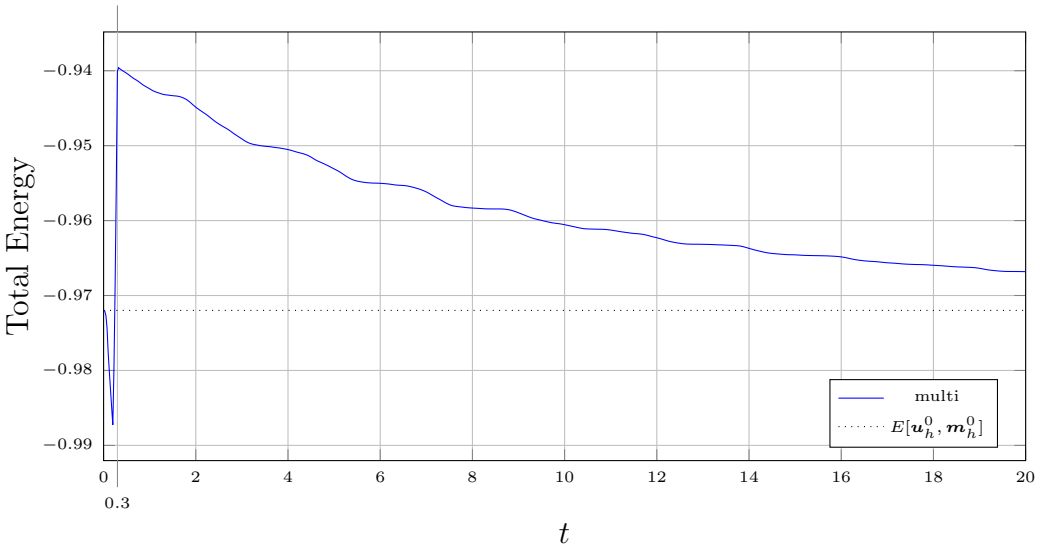

Figure 6.8: Experiment of Section 6.5.4. Parameters $k = 1 \cdot 10^{-3}$ and $\lambda_{100} = 3 \cdot 10^{-3}$. The energy of the system decreases as the pulse field becomes stronger, and then the energy increases as the pulse field becomes weaker, and when the pulse field is disabled the magnetization approaches the minimizer.

Chapter 7

Antiferromagnets/Ferrimagnets

For the paper that this chapter is based off of, see [NR25b].

7.1 Introduction

The novel contributions of this chapter are the following:

- We provide the first mathematically rigorous formulation of a state-of-the-art model currently used by applied scientists to simulate processes and devices involving AFM and FiM materials.
- Extending the techniques that have been developed for the approximation of the classical model of FM materials, we introduce and analyse the first convergent numerical schemes for this model of AFM and FiM materials.

The remainder of this chapter is organized as follows: In Section 7.2, we present the mathematical model of AFM and FiM materials. The algorithms for the static problem, their properties, and three numerical experiments are discussed in Section 7.3. In Section 7.4, we extend one of the algorithm and its analysis to the dynamic case, and use it to simulate the dynamics of magnetic skyrmions in AFM and FM materials. In Section 7.5, we collect the proofs of all results of the work. Finally, in Appendix C.2, we show how to pass from the formulation of the model in physical units to the dimensionless setting considered in this work.

7.2 Mathematical model

Let $\Omega \subset \mathbb{R}^3$ be a bounded Lipschitz domain representing the volume occupied by an AFM or a FiM material. The magnetic state of the material is described in terms of two unit-length vector fields, $\boldsymbol{m}_1$ and $\boldsymbol{m}_2$. The total magnetization of the sample is given by $\boldsymbol{m} = \eta_{\mathrm{s},1}\boldsymbol{m}_1 + \eta_{\mathrm{s},2}\boldsymbol{m}_2$, where $\eta_{\mathrm{s},1}, \eta_{\mathrm{s},2} > 0$ are dimensionless constants.

7.2.1 Static problem

Stable magnetic configurations of the sample are described by minimizers $\boldsymbol{m}_1, \boldsymbol{m}_2 : \Omega \to \mathbb{S}^2$ of the energy functional

$$\mathcal{E}[\boldsymbol{m}_1, \boldsymbol{m}_2] = \frac{1}{2} \sum_{\ell=1}^{2} a_{\ell\ell} \left\| \boldsymbol{\nabla} \boldsymbol{m}_\ell \right\|^2 + a_{12} \left\langle \boldsymbol{\nabla} \boldsymbol{m}_1, \boldsymbol{\nabla} \boldsymbol{m}_2 \right\rangle - a_0 \left\langle \boldsymbol{m}_1, \boldsymbol{m}_2 \right\rangle , \tag{7.1}$$

where the material constants $a_{11}, a_{22}, a_{12}, a_0 \in \mathbb{R}$ satisfy the inequalities

$$a_{11} + a_{22} > 0 \quad \text{and} \quad a_{11} a_{22} > a_{12}^2. \tag{7.2}$$

The three contributions in (7.1) are called *inhomogeneous intralattice exchange*, *inhomogeneous interlattice exchange*, and *homogeneous interlattice exchange*, respectively [STPKA+20]. Minimizers are sought in the set of admissible pairs of vector fields

$$\begin{aligned} \mathcal{X} :&= \boldsymbol{H}^1(\Omega; \mathbb{S}^2) \times \boldsymbol{H}^1(\Omega; \mathbb{S}^2) \\ &= \{(\boldsymbol{m}_1, \boldsymbol{m}_2) \in \boldsymbol{H}^1(\Omega) \times \boldsymbol{H}^1(\Omega) : |\boldsymbol{m}_1| = |\boldsymbol{m}_2| = 1 \text{ a.e. in } \Omega\}. \end{aligned} \tag{7.3}$$

Note that (7.2) guarantees that the energy is bounded from below in $\mathcal{X}$, as there holds the inequality $\mathcal{E}[\boldsymbol{m}_1, \boldsymbol{m}_2] \geq -|a_0|\,|\Omega|$ for all $(\boldsymbol{m}_1, \boldsymbol{m}_2) \in \mathcal{X}$, and that the energy functional is weakly sequentially lower semicontinuous in $\boldsymbol{H}^1(\Omega) \times \boldsymbol{H}^1(\Omega)$ (see Proposition 7.5.1 below). Hence, existence of minimizers follows from the direct method of calculus of variations.

Stationary points of the energy are admissible pairs $(\boldsymbol{m}_1, \boldsymbol{m}_2) \in \mathcal{X}$ which, for all $\ell = 1, 2$, solve

$$-\langle \boldsymbol{h}_{\mathrm{eff},\ell}[\boldsymbol{m}_1, \boldsymbol{m}_2], \boldsymbol{\varphi} - (\boldsymbol{m}_\ell \cdot \boldsymbol{\varphi}) \boldsymbol{m}_\ell \rangle = 0 \quad \text{for all } \boldsymbol{\varphi} \in \boldsymbol{H}^1(\Omega) \cap \boldsymbol{L}^\infty(\Omega), \tag{7.4}$$

where the effective field $\boldsymbol{h}_{\mathrm{eff},\ell}[\boldsymbol{m}_1, \boldsymbol{m}_2]$ is the (negative) Gateaux derivative of the energy with respect to $\boldsymbol{m}_\ell$, i.e.,

$$\begin{aligned} \langle \boldsymbol{h}_{\mathrm{eff},\ell}[\boldsymbol{m}_1, \boldsymbol{m}_2], \boldsymbol{\phi} \rangle \;:\; &= \left\langle -\frac{\delta \mathcal{E}[\boldsymbol{m}_1, \boldsymbol{m}_2]}{\delta \boldsymbol{m}_\ell}, \boldsymbol{\phi} \right\rangle \\ &\overset{(7.1)}{=} -a_{\ell\ell} \left\langle \boldsymbol{\nabla} \boldsymbol{m}_\ell, \boldsymbol{\nabla} \boldsymbol{\phi} \right\rangle - a_{12} \left\langle \boldsymbol{\nabla} \boldsymbol{m}_{3-\ell}, \boldsymbol{\nabla} \boldsymbol{\phi} \right\rangle + a_0 \left\langle \boldsymbol{m}_{3-\ell}, \boldsymbol{\phi} \right\rangle . \end{aligned} \tag{7.5}$$

Equivalently, a stationary point $(\boldsymbol{m}_1, \boldsymbol{m}_2) \in \mathcal{X}$ can be seen as the solution, for all $\ell = 1, 2$, of

$$-\langle \boldsymbol{h}_{\mathrm{eff},\ell}[\boldsymbol{m}_1, \boldsymbol{m}_2], \boldsymbol{\phi} \rangle = 0 \quad \text{for all } \boldsymbol{\phi} \in \boldsymbol{\mathcal{K}}[\boldsymbol{m}_\ell], \tag{7.6}$$

where the $\boldsymbol{m}_\ell$-dependent test space is given by

$$\boldsymbol{\mathcal{K}}[\boldsymbol{m}_\ell] = \{\boldsymbol{\psi} \in \boldsymbol{H}^1(\Omega) : \boldsymbol{m}_\ell \cdot \boldsymbol{\psi} = 0 \text{ a.e. in } \Omega\}. \tag{7.7}$$

Note that (7.4) and (7.6) can be interpreted as variational formulations of the boundary value problem

$$\begin{aligned} -\boldsymbol{m}_\ell \times \boldsymbol{h}_{\mathrm{eff},\ell}[\boldsymbol{m}_1, \boldsymbol{m}_2] &= \boldsymbol{0} \quad \text{in } \Omega, \\ \partial_{\boldsymbol{n}} \boldsymbol{m}_\ell &= \boldsymbol{0} \quad \text{on } \partial\Omega, \end{aligned} \tag{7.8}$$

where $\boldsymbol{n} : \partial\Omega \to \mathbb{S}^2$ denotes the outward-pointing unit normal vector to $\partial\Omega$.

7.2.2 Dynamic problem

Out of equilibrium, the dynamics of the time-dependent vector fields $\boldsymbol{m}_1, \boldsymbol{m}_2 : \Omega \times (0,\infty) \to \mathbb{S}^2$ is governed by a coupled system of two Landau–Lifshitz–Gilbert (LLG) equations, one for each vector field:

$$\partial_t \boldsymbol{m}_\ell = -\eta_\ell \, \boldsymbol{m}_\ell \times \boldsymbol{h}_{\mathrm{eff},\ell}[\boldsymbol{m}_1, \boldsymbol{m}_2] + \alpha_\ell \, \boldsymbol{m}_\ell \times \partial_t \boldsymbol{m}_\ell \quad \text{for all } \ell = 1, 2, \tag{7.9}$$

where $\eta_\ell, \alpha_\ell > 0$ are dimensionless constants. Note that the two LLG equations are coupled to each other via their effective fields. To complete the setting, (7.9) is supplemented with a suitable initial condition and the same boundary conditions as in (7.8), i.e.,

$$\boldsymbol{m}_\ell(0) = \boldsymbol{m}_\ell^0 \text{ in } \Omega \quad \text{and} \quad \partial_{\boldsymbol{n}} \boldsymbol{m}_\ell = \boldsymbol{0} \text{ on } \partial\Omega \times (0,\infty) \quad \text{for all } \ell = 1, 2, \tag{7.10}$$

for some admissible pair $(\boldsymbol{m}_1^0, \boldsymbol{m}_2^0) \in \mathcal{X}$.

In the following definition, we state the notion of a weak solution to the initial boundary value problem (7.9)–(7.10), which naturally extends to the present setting the notion introduced in [AS92] for the standard LLG equation.

Definition 7.2.1 (weak solution)**.** *Let $(\boldsymbol{m}_1^0, \boldsymbol{m}_2^0) \in \mathcal{X}$. A global weak solution of (7.9)–(7.10) is $(\boldsymbol{m}_1, \boldsymbol{m}_2) \in L^\infty(0,\infty;\mathcal{X})$ such that, for all $T > 0$, the following properties are satisfied:*

(i) *$\boldsymbol{m}_\ell|_{\Omega_T} \in \boldsymbol{H}^1(\Omega_T)$ for all $\ell = 1, 2$, where $\Omega_T := \Omega \times (0,T)$;*

(ii) *$\boldsymbol{m}_\ell(0) = \boldsymbol{m}_\ell^0$ in the sense of traces for all $\ell = 1, 2$;*

(iii) *for all $\ell = 1, 2$, for all $\boldsymbol{\varphi} \in \boldsymbol{H}^1(\Omega_T)$, it holds that*

$$\begin{aligned} &\int_0^T \langle \partial_t \boldsymbol{m}_\ell(t), \boldsymbol{\varphi}(t) \rangle \, \mathrm{d}t \\ &\quad = -\eta_\ell \int_0^T \langle \boldsymbol{h}_{\mathrm{eff},\ell}[\boldsymbol{m}_1(t), \boldsymbol{m}_2(t)], \boldsymbol{\varphi}(t) \times \boldsymbol{m}_\ell(t) \rangle \, \mathrm{d}t \\ &\qquad + \alpha_\ell \int_0^T \langle \boldsymbol{m}_\ell(t) \times \partial_t \boldsymbol{m}_\ell(t), \boldsymbol{\varphi}(t) \rangle \, \mathrm{d}t; \end{aligned} \tag{7.11}$$

(iv) *it holds that*

$$\mathcal{E}[\boldsymbol{m}_1(T), \boldsymbol{m}_2(T)] + \sum_{\ell=1}^2 \frac{\alpha_\ell}{\eta_\ell} \int_0^T \|\partial_t \boldsymbol{m}_\ell(t)\|^2 \, \mathrm{d}t \le \mathcal{E}[\boldsymbol{m}_1^0, \boldsymbol{m}_2^0]. \tag{7.12}$$

The variational formulations in (7.11) are weak formulations of the LLG equations in (7.9) in the space-time cylinder Ω_T, while (7.12) is a weak counterpart of the energy law

$$\frac{\mathrm{d}}{\mathrm{d}t} \mathcal{E}[\boldsymbol{m}_1(t), \boldsymbol{m}_2(t)] = -\sum_{\ell=1}^2 \frac{\alpha_\ell}{\eta_\ell} \|\partial_t \boldsymbol{m}_\ell(t)\|^2 \le 0 \quad \text{for all } t > 0,$$

satisfied by sufficiently smooth solutions of (7.9).

Remark 7.2.2. *For ease of presentation, we consider a dimensionless form of the energy functional. We refer to Appendix C.2.1 for its derivation (starting from the equations in physical units usually encountered in the physical literature). Moreover, we restrict ourselves to the case in which the energy comprises only the exchange contribution. This is sufficient to capture the main mathematical features of the model: First, the analytical and numerical treatment of standard lower-order energy contributions (e.g., magnetocrystalline anisotropy, Zeeman energy, magnetostatic energy, Dzyaloshinskii–Moriya interaction) is well understood (see, e.g., [BFF+14, HPP+19]). Second, lower-order terms do not entail the coupling of the fields (see Appendix C.2.2 for more details). Hence, even in the presence of lower-order terms, the Euler–Lagrange equations* (7.4) *and the system of LLG equations* (7.9) *are exchange-coupled only.*

7.3 Numerical energy minimization

In this section, we introduce a finite element discretization of the energy minimization problem and show its convergence in the sense of Γ-convergence. Then, we introduce two fully discrete algorithms to approximate stationary points of the energy functional (7.1). We state our results regarding well-posedness, stability, and convergence of the algorithms and underpin our theoretical results with numerical experiments. To make the presentation of the results concise, all proofs are postponed to Section 7.5.1.

7.3.1 Finite element discretization

To discretize the set of admissible pairs in (7.3), given a mesh $\mathcal{T}_h$ and a parameter $\delta > 0$, we consider the set

$$\mathcal{X}_{h,\delta} := \{(\boldsymbol{m}_{1,h,\delta}, \boldsymbol{m}_{2,h,\delta}) \in \mathcal{S}^1(\mathcal{T}_h)^3 \times \mathcal{S}^1(\mathcal{T}_h)^3 : \\ \big\|\mathcal{I}_h[|\boldsymbol{m}_{\ell,h,\delta}|^2] - 1\big\|_{L^1(\Omega)} \leq \delta \text{ for all } \ell = 1, 2\}.$$

Note that, at the discrete level, the unit-length constraint is relaxed [Bar16, AHP+14] as only a mild control in the L^1-norm of the error is enforced.

The discrete static problem consists of seeking a minimizer of the energy functional (7.1) in the set of discrete admissible pairs in $\mathcal{X}_{h,\delta}$. In the following theorem, we show that the discrete energy functional $\mathcal{E}_{h,\delta}[\cdot,\cdot] := \mathcal{E}|_{\mathcal{X}_{h,\delta}}[\cdot,\cdot]$ converges toward the continuous one in the sense of Γ-convergence. We note that our discretization is consistent, i.e., we do not modify the energy functional, but we restrict the set in which minimizers are sought.

Theorem 7.3.1 (Γ-convergence)**.** *The following two properties hold:*
(i) *Lim-inf inequality: For every sequence* $\{(\boldsymbol{m}_{1,h,\delta}, \boldsymbol{m}_{2,h,\delta})\}$ *with* $(\boldsymbol{m}_{1,h,\delta}, \boldsymbol{m}_{2,h,\delta}) \in \mathcal{X}_{h,\delta}$ *for all* $h, \delta > 0$ *such that, for some* $(\boldsymbol{m}_1, \boldsymbol{m}_2) \in \mathcal{X}$, $\boldsymbol{m}_{\ell,h,\delta} \rightharpoonup \boldsymbol{m}_\ell$ *in* $\boldsymbol{H}^1(\Omega)$ *as* $h, \delta \to 0$ *for all* $\ell = 1, 2$, *we have that* $\mathcal{E}[\boldsymbol{m}_1, \boldsymbol{m}_2] \leq \liminf_{h,\delta\to 0} \mathcal{E}_{h,\delta}[\boldsymbol{m}_{1,h,\delta}, \boldsymbol{m}_{2,h,\delta}]$.
(ii) *Existence of a recovery sequence: For every* $(\boldsymbol{m}_1, \boldsymbol{m}_2) \in \mathcal{X}$, *there exists a sequence* $\{(\boldsymbol{m}_{1,h,\delta}, \boldsymbol{m}_{2,h,\delta})\}$ *with* $(\boldsymbol{m}_{1,h,\delta}, \boldsymbol{m}_{2,h,\delta}) \in \mathcal{X}_{h,\delta}$ *for all* $h, \delta > 0$ *such*

that $(\boldsymbol{m}_{1,h,\delta}, \boldsymbol{m}_{2,h,\delta}) \to (\boldsymbol{m}_1, \boldsymbol{m}_2)$ *in* $\boldsymbol{H}^1(\Omega) \times \boldsymbol{H}^1(\Omega)$ *and* $\mathcal{E}_{h,\delta}[\boldsymbol{m}_{1,h,\delta}, \boldsymbol{m}_{2,h,\delta}] \to \mathcal{E}[\boldsymbol{m}_1, \boldsymbol{m}_2]$ *as* $h, \delta \to 0$.

A well-known consequence of Γ-convergence is the convergence of discrete global minimizers.

Corollary 7.3.2. *Let* $\{(\boldsymbol{m}_{1,h,\delta}, \boldsymbol{m}_{2,h,\delta})\}$ *be a sequence such that* $(\boldsymbol{m}_{1,h,\delta}, \boldsymbol{m}_{2,h,\delta}) \in \mathcal{X}_{h,\delta}$ *is a global minimizer of the discrete energy functional* $\mathcal{E}_{h,\delta}[\cdot,\cdot]$ *for all* $h, \delta > 0$. *Then, every accumulation point* $(\boldsymbol{m}_1, \boldsymbol{m}_2)$ *of the sequence belongs to* $\mathcal{X}$ *and is a global minimizer of the continuous energy functional* $\mathcal{E}[\cdot,\cdot]$.

We omit the proof of Corollary 7.3.2 as it is based on standard Γ-convergence arguments; see, e.g., [Bra02, Section 1.5]. Moreover, we recall that Γ-convergence does not imply the convergence of local minimizers.

7.3.2 Computation of low energy stationary points

Let $\boldsymbol{\mathcal{H}}$ be a Hilbert space with inner product $\langle\cdot,\cdot\rangle_{\boldsymbol{\mathcal{H}}}$ such that $\mathcal{X}$ is continuously embedded in $\boldsymbol{\mathcal{H}} \times \boldsymbol{\mathcal{H}}$. To find stationary points with low energy, we propose two iterative algorithms that are based on two discretizations of the dissipative dynamics governed by the $\boldsymbol{\mathcal{H}}$-gradient flow of the energy

$$\langle \partial_t \boldsymbol{m}_\ell, \boldsymbol{\phi}\rangle_{\boldsymbol{\mathcal{H}}} + \left\langle \frac{\delta \mathcal{E}[\boldsymbol{m}_1, \boldsymbol{m}_2]}{\delta \boldsymbol{m}_\ell}, \boldsymbol{\phi} \right\rangle = \boldsymbol{0} \quad \text{for all } \boldsymbol{\phi} \in \boldsymbol{\mathcal{K}}[\boldsymbol{m}_\ell] \quad (\ell = 1, 2). \tag{7.13}$$

The spatial discretization of both methods is based on first-order finite elements as described in Chapter 3. The time discretization is based on two different time-stepping methods.

Remark 7.3.3. *In this section, we refer to the variable* t *as* time *(accordingly, we refer to* k *below as the* time-step size*). However, note that we are considering the static setting, with the time variable* t *playing the role of a* pseudo-time*, introduced only for numerical purposes.*

The first method is proposed in the following algorithm.

Algorithm 7.3.4 (coupled discrete gradient flow)**.** ***Discretization parameters:*** *Mesh size* $h > 0$*, time-step size* $k > 0$*, tolerance* $\varepsilon > 0$.
Input: *Initial guess* $(\boldsymbol{m}^0_{1,h}, \boldsymbol{m}^0_{2,h}) \in \mathcal{S}^1(\mathcal{T}_h)^3 \times \mathcal{S}^1(\mathcal{T}_h)^3$ *such that, for all* $\ell = 1, 2$, $\left|\boldsymbol{m}^0_{\ell,h}(z)\right| = 1$ *for all* $z \in \mathcal{N}_h$.
Loop: *For all* $i \in \mathbb{N}_0$*, iterate* (i)–(ii) *until the stopping criterion* (stop) *is met:*

(i) *Given* $(\boldsymbol{m}^i_{1,h}, \boldsymbol{m}^i_{2,h}) \in \mathcal{S}^1(\mathcal{T}_h)^3 \times \mathcal{S}^1(\mathcal{T}_h)^3$*, compute* $(\boldsymbol{v}^i_{1,h}, \boldsymbol{v}^i_{2,h}) \in \boldsymbol{\mathcal{K}}_h[\boldsymbol{m}^i_{1,h}] \times \boldsymbol{\mathcal{K}}_h[\boldsymbol{m}^i_{2,h}]$ *such that, for all* $(\boldsymbol{\phi}_{1,h}, \boldsymbol{\phi}_{2,h}) \in \boldsymbol{\mathcal{K}}_h[\boldsymbol{m}^i_{1,h}] \times \boldsymbol{\mathcal{K}}_h[\boldsymbol{m}^i_{2,h}]$ *and* $\ell = 1, 2$*, it holds that*

$$\begin{aligned}
&\left\langle \boldsymbol{v}^i_{\ell,h}, \boldsymbol{\phi}_{\ell,h}\right\rangle_{\boldsymbol{\mathcal{H}}} + a_{\ell\ell} k \left\langle \boldsymbol{\nabla} \boldsymbol{v}^i_{\ell,h}, \boldsymbol{\nabla} \boldsymbol{\phi}_{\ell,h}\right\rangle \\
&\qquad + \frac{a_{12}}{2} k \left\langle \boldsymbol{\nabla} \boldsymbol{v}^i_{3-\ell,h}, \boldsymbol{\nabla} \boldsymbol{\phi}_{\ell,h}\right\rangle - \frac{a_0}{2} k \left\langle \boldsymbol{v}^i_{3-\ell,h}, \boldsymbol{\phi}_{\ell,h}\right\rangle \\
&= -a_{\ell\ell} \left\langle \boldsymbol{\nabla} \boldsymbol{m}^i_{\ell,h}, \boldsymbol{\nabla} \boldsymbol{\phi}_{\ell,h}\right\rangle - a_{12} \left\langle \boldsymbol{\nabla} \boldsymbol{m}^i_{3-\ell,h}, \boldsymbol{\nabla} \boldsymbol{\phi}_{\ell,h}\right\rangle + a_0 \left\langle \boldsymbol{m}^i_{3-\ell,h}, \boldsymbol{\phi}_{\ell,h}\right\rangle .
\end{aligned} \tag{7.14}$$

(ii) *Define*

$$\boldsymbol{m}_{\ell,h}^{i+1} := \boldsymbol{m}_{\ell,h}^{i} + k\boldsymbol{v}_{\ell,h}^{i} \quad \textit{for all } \ell = 1,2. \tag{7.15}$$

(stop) *Stop iterating* (i)–(ii) *if* $(\boldsymbol{v}_{1,h}^{i}, \boldsymbol{v}_{2,h}^{i}) \in \boldsymbol{\mathcal{K}}_h[\boldsymbol{m}_{1,h}^{i}] \times \boldsymbol{\mathcal{K}}_h[\boldsymbol{m}_{2,h}^{i}]$ *satisfies*

$$\max_{\ell=1,2} \left(\left\| \boldsymbol{v}_{\ell,h}^{i} \right\|_{\boldsymbol{\mathcal{H}}}^2 + k \left\| \boldsymbol{\nabla} \boldsymbol{v}_{\ell,h}^{i} \right\|^2 \right) \leq \varepsilon^2 \left| \Omega \right|. \tag{7.16}$$

Output: *If* $i^* \in \mathbb{N}_0$ *denotes the smallest integer satisfying the stopping criterion* (7.16)*, define the approximate stationary point* $(\boldsymbol{m}_{1,h}, \boldsymbol{m}_{2,h}) := (\boldsymbol{m}_{1,h}^{i^*}, \boldsymbol{m}_{2,h}^{i^*})$.

The second method is proposed in the following algorithm.

Algorithm 7.3.5 (decoupled discrete gradient flow)**.** ***Discretization parameters:*** *Mesh size* $h > 0$*, time-step size* $k > 0$*, tolerance* $\varepsilon > 0$.
Input: *Initial guess* $(\boldsymbol{m}_{1,h}^{0}, \boldsymbol{m}_{2,h}^{0}) \in \mathcal{S}^1(\mathcal{T}_h)^3 \times \mathcal{S}^1(\mathcal{T}_h)^3$ *such that, for all* $\ell = 1,2$, $\left| \boldsymbol{m}_{\ell,h}^{0}(z) \right| = 1$ *for all* $z \in \mathcal{N}_h$.
Loop: *For all* $i \in \mathbb{N}_0$*, iterate* (i)–(ii) *until the stopping criterion* (stop) *is met:*

(i) *Given* $(\boldsymbol{m}_{1,h}^{i}, \boldsymbol{m}_{2,h}^{i}) \in \mathcal{S}^1(\mathcal{T}_h)^3 \times \mathcal{S}^1(\mathcal{T}_h)^3$*, compute* $(\boldsymbol{v}_{1,h}^{i}, \boldsymbol{v}_{2,h}^{i}) \in \boldsymbol{\mathcal{K}}_h[\boldsymbol{m}_{1,h}^{i}] \times \boldsymbol{\mathcal{K}}_h[\boldsymbol{m}_{2,h}^{i}]$ *such that, for all* $(\boldsymbol{\phi}_{1,h}, \boldsymbol{\phi}_{2,h}) \in \boldsymbol{\mathcal{K}}_h[\boldsymbol{m}_{1,h}^{i}] \times \boldsymbol{\mathcal{K}}_h[\boldsymbol{m}_{2,h}^{i}]$ *and* $\ell = 1,2$*, it holds that*

$$\begin{aligned} &\left\langle \boldsymbol{v}_{\ell,h}^{i}, \boldsymbol{\phi}_{\ell,h} \right\rangle_{\boldsymbol{\mathcal{H}}} + a_{\ell\ell} k \left\langle \boldsymbol{\nabla} \boldsymbol{v}_{\ell,h}^{i}, \boldsymbol{\nabla} \boldsymbol{\phi}_{\ell,h} \right\rangle \\ &\quad = -a_{\ell\ell} \left\langle \boldsymbol{\nabla} \boldsymbol{m}_{\ell,h}^{i}, \boldsymbol{\nabla} \boldsymbol{\phi}_{\ell,h} \right\rangle - a_{12} \left\langle \boldsymbol{\nabla} \boldsymbol{m}_{3-\ell,h}^{i}, \boldsymbol{\nabla} \boldsymbol{\phi}_{\ell,h} \right\rangle + a_0 \left\langle \boldsymbol{m}_{3-\ell,h}^{i}, \boldsymbol{\phi}_{\ell,h} \right\rangle. \end{aligned} \tag{7.17}$$

(ii) *Define*

$$\boldsymbol{m}_{\ell,h}^{i+1} := \boldsymbol{m}_{\ell,h}^{i} + k\boldsymbol{v}_{\ell,h}^{i} \quad \textit{for all } \ell = 1,2. \tag{7.18}$$

(stop) *Stop iterating* (i)–(ii) *if* $(\boldsymbol{v}_{1,h}^{i}, \boldsymbol{v}_{2,h}^{i}) \in \boldsymbol{\mathcal{K}}_h[\boldsymbol{m}_{1,h}^{i}] \times \boldsymbol{\mathcal{K}}_h[\boldsymbol{m}_{2,h}^{i}]$ *satisfies*

$$\max_{\ell=1,2} \left(\left\| \boldsymbol{v}_{\ell,h}^{i} \right\|_{\boldsymbol{\mathcal{H}}}^2 + k \left\| \boldsymbol{\nabla} \boldsymbol{v}_{\ell,h}^{i} \right\|^2 \right) \leq \varepsilon^2 \left| \Omega \right|. \tag{7.19}$$

Output: *If* $i^* \in \mathbb{N}_0$ *denotes the smallest integer satisfying the stopping criterion* (7.19)*, define the approximate stationary point* $(\boldsymbol{m}_{1,h}, \boldsymbol{m}_{2,h}) := (\boldsymbol{m}_{1,h}^{i^*}, \boldsymbol{m}_{2,h}^{i^*})$.

In both Algorithm 7.3.4 and Algorithm 7.3.5 the iteration stops when the size of the updates is sufficiently small (according to (7.16) and (7.19), respectively). The algorithms are characterized by a different treatment of the inhomogeneous and homogeneous interlattice exchange contributions, which are treated implicitly in Algorithm 7.3.4 and explicitly in Algorithm 7.3.5.

One immediate consequence is that in Algorithm 7.3.4 the two equations are coupled (as they are in the continuous problem) and one iteration of the algorithm requires the solution of *one* $4N_h$-by-$4N_h$ linear system, whereas in Algorithm 7.3.5 the two equations are decoupled and one iteration of the algorithm requires the solution of *two* $2N_h$-by-$2N_h$ linear systems (that are independent of each other and thus can be solved in parallel, although we did not implement this). This

difference will affect the solvability and energetic behaviour of the algorithms, which will be the subject of the following propositions.

In the following proposition, we establish the properties of Algorithm 7.3.4.

Proposition 7.3.6 (properties of Algorithm 7.3.4)**.** *There hold the following statements:*

(i) *Suppose that k satisfies $c_{\boldsymbol{\mathcal{H}}}^2 \, |a_0| \, k < 2$, where a_0 is one of the coefficients in (7.1) and $c_{\boldsymbol{\mathcal{H}}}$ is the constant in (3.15). Then, for all $i \in \mathbb{N}_0$, (7.14) admits a unique solution $(\boldsymbol{v}_{1,h}^i, \boldsymbol{v}_{2,h}^i) \in \boldsymbol{\mathcal{K}}_h[\boldsymbol{m}_{1,h}^i] \times \boldsymbol{\mathcal{K}}_h[\boldsymbol{m}_{2,h}^i]$.*

(ii) *Under the assumption of part (i), suppose that k additionally satisfies $c_{\boldsymbol{\mathcal{H}}} c_{\mathcal{T}} \, |a_0| \, k < 1$, where $c_{\mathcal{T}} > 0$ is a constant which depends only on the shape-regularity of the family of meshes. Then, Algorithm 7.3.4 terminates within a finite number of iterations. In particular, the approximate stationary point $(\boldsymbol{m}_{1,h}, \boldsymbol{m}_{2,h})$ is well-defined.*

(iii) *Under the assumption of part (i), for all $i \in \mathbb{N}_0$, the iterates of Algorithm 7.3.4 satisfy*

$$\mathcal{E}[\boldsymbol{m}_{1,h}^{i+1}, \boldsymbol{m}_{2,h}^{i+1}] - \mathcal{E}[\boldsymbol{m}_{1,h}^{i}, \boldsymbol{m}_{2,h}^{i}] = -k \sum_{\ell=1}^{2} \left\| \boldsymbol{v}_{\ell,h}^i \right\|_{\boldsymbol{\mathcal{H}}}^2 - \frac{k^2}{2} \sum_{\ell=1}^{2} a_{\ell\ell} \left\| \boldsymbol{\nabla} \boldsymbol{v}_{\ell,h}^i \right\|^2 . \tag{7.20}$$

In particular, the sequence of energies generated by the algorithm is monotonically decreasing, i.e., it holds that $\mathcal{E}[\boldsymbol{m}_{1,h}^{i+1}, \boldsymbol{m}_{2,h}^{i+1}] \leq \mathcal{E}[\boldsymbol{m}_{1,h}^{i}, \boldsymbol{m}_{2,h}^{i}]$.

(iv) *Under the assumptions of part (ii), there exists $C > 0$ such that the approximate stationary point $(\boldsymbol{m}_{1,h}, \boldsymbol{m}_{2,h})$ satisfies*

$$\left\| \mathcal{I}_h[|\boldsymbol{m}_{\ell,h}|^2] - 1 \right\|_{L^1(\Omega)} \leq Ck \left(1 + \sum_{\ell=1}^{2} \left\| \boldsymbol{m}_{\ell,h}^0 \right\|_{\boldsymbol{H}^1(\Omega)}^2 \right) \quad \text{for all } \ell = 1, 2.$$

The constant $C > 0$ depends only on a_{11}, a_{12}, a_{22}, a_0, $c_{\boldsymbol{\mathcal{H}}}$, and the shape-regularity of the family of meshes.

Corresponding results for Algorithm 7.3.5 are the subject of the following proposition.

Proposition 7.3.7 (properties of Algorithm 7.3.5)**.** *There hold the following statements:*

(i) *For all $i \in \mathbb{N}_0$, (7.17) admits a unique solution $(\boldsymbol{v}_{1,h}^i, \boldsymbol{v}_{2,h}^i) \in \boldsymbol{\mathcal{K}}_h[\boldsymbol{m}_{1,h}^i] \times \boldsymbol{\mathcal{K}}_h[\boldsymbol{m}_{2,h}^i]$.*

(ii) *Suppose that k satisfies $c_{\boldsymbol{\mathcal{H}}}(c_{\boldsymbol{\mathcal{H}}}/2 + c_{\mathcal{T}}) \, |a_0| \, k < 1$, where a_0 is one of the coefficients in (7.1), $c_{\boldsymbol{\mathcal{H}}}$ is the constant in (3.15), and $c_{\mathcal{T}} > 0$ is a constant which depends only on the shape-regularity of the family of meshes. Then, Algorithm 7.3.5 terminates within a finite number of iterations. In particular, the approximate stationary point $(\boldsymbol{m}_{1,h}, \boldsymbol{m}_{2,h})$ is well-defined.*

(iii) *For all $i \in \mathbb{N}_0$, the iterates of Algorithm 7.3.5 satisfy*

$$\mathcal{E}[\boldsymbol{m}_{1,h}^{i+1}, \boldsymbol{m}_{2,h}^{i+1}] - \mathcal{E}[\boldsymbol{m}_{1,h}^{i}, \boldsymbol{m}_{2,h}^{i}] = -k \sum_{\ell=1}^{2} \left\| \boldsymbol{v}_{\ell,h}^{i} \right\|_{\boldsymbol{\mathcal{H}}}^2 - \frac{k^2}{2} \sum_{\ell=1}^{2} a_{\ell\ell} \left\| \boldsymbol{\nabla} \boldsymbol{v}_{\ell,h}^{i} \right\|^2 + a_{12} k^2 \left\langle \boldsymbol{\nabla} \boldsymbol{v}_{1,h}^{i}, \boldsymbol{\nabla} \boldsymbol{v}_{2,h}^{i} \right\rangle - a_0 k^2 \left\langle \boldsymbol{v}_{1,h}^{i}, \boldsymbol{v}_{2,h}^{i} \right\rangle . \quad (7.21)$$

Moreover, if k satisfies $c_{\boldsymbol{\mathcal{H}}}^2 |a_0| \, k \leq 2$, then the sequence of energies generated by the algorithm is monotonically decreasing, i.e., it holds that $\mathcal{E}[\boldsymbol{m}_{1,h}^{i+1}, \boldsymbol{m}_{2,h}^{i+1}] \leq \mathcal{E}[\boldsymbol{m}_{1,h}^{i}, \boldsymbol{m}_{2,h}^{i}]$.

(iv) *Under the assumptions of part* (ii)*, there exists $C > 0$ such that the approximate stationary point $(\boldsymbol{m}_{1,h}, \boldsymbol{m}_{2,h})$ satisfies*

$$\left\| \mathcal{I}_h[|\boldsymbol{m}_{\ell,h}|^2] - 1 \right\|_{L^1(\Omega)} \leq Ck \left(1 + \sum_{\ell=1}^{2} \left\| \boldsymbol{m}_{\ell,h}^{0} \right\|_{\boldsymbol{H}^1(\Omega)}^2 \right) \quad \text{for all } \ell = 1, 2.$$

The constant $C > 0$ depends only on a_{11}, a_{12}, a_{22}, a_0, $c_{\boldsymbol{\mathcal{H}}}$, and the shape-regularity of the family of meshes.

Each iteration of Algorithm 7.3.4 is well-defined if the time-step size is sufficiently small. Moreover, the algorithm unconditionally generates a monotonically decreasing sequence of energies. Conversely, each iteration of Algorithm 7.3.5 is unconditionally well-defined, but the sequence of energies it generates is monotonically decreasing only if the time-step size is sufficiently small. Furthermore, we note that the inequalities in point (iv) of both Proposition 7.3.6 and Proposition 7.3.7 show that if the initial guesses are uniformly bounded in $\boldsymbol{H}^1(\Omega)$ (in the sense of (7.22) below), then the approximate stationary points generated by the algorithms belong to the set of admissible pairs $\mathcal{X}_{h,\delta}$ with δ of the form $\delta = Ck$.

In the following theorem, we show that the sequence of approximate stationary points computed with both algorithms converges toward an admissible pair in $\mathcal{X}$ as the discretization parameters go to zero. If we neglect the inhomogeneous interlattice exchange contribution, we can identify the limit with a stationary point of the energy functional (7.1).

Theorem 7.3.8 (convergence of Algorithm 7.3.4 and Algorithm 7.3.5)**.** *Suppose that there exists $c_0 > 0$, independent of the discretization parameters h, k, and ε, such that*

$$\sup_{h>0} \left(\sum_{\ell=1}^{2} \left\| \boldsymbol{m}_{\ell,h}^{0} \right\|_{\boldsymbol{H}^1(\Omega)}^2 \right) \leq c_0. \quad (7.22)$$

Suppose that $k \to 0$ and $\varepsilon \to 0$ as $h \to 0$. Then, as $h \to 0$, the sequence of approximate stationary points $\{(\boldsymbol{m}_{1,h}, \boldsymbol{m}_{2,h})\}_{h>0}$ generated by either Algorithm 7.3.4 or Algorithm 7.3.5, upon extraction of a subsequence, converges weakly in $\boldsymbol{H}^1(\Omega) \times \boldsymbol{H}^1(\Omega)$ toward a point $(\boldsymbol{m}_1, \boldsymbol{m}_2) \in \mathcal{X}$. If $a_{12} = 0$, the limit $(\boldsymbol{m}_1, \boldsymbol{m}_2) \in \mathcal{X}$ is a stationary point of the energy functional (7.1)*.*

A byproduct of Theorem 7.3.8 is the existence of weak solutions to the Euler–Lagrange equations (7.4) for the case $a_{12} = 0$.

Remark 7.3.9. *In our analysis, we can identify the limit of the sequence of approximate stationary points with a stationary point of the energy only if we assume that $a_{12} = 0$, i.e., if we neglect the inhomogeneous interlattice exchange contribution from the energy. This restriction is related to the fact that, if $a_{12} \neq 0$, the weak formulation of the approximate Euler–Lagrange equations satisfied by $(\boldsymbol{m}_{1,h}, \boldsymbol{m}_{2,h})$ contains a term that involves the L^2-product of $\boldsymbol{\nabla}\boldsymbol{m}_{1,h}$ and $\boldsymbol{\nabla}\boldsymbol{m}_{2,h}$. Since $(\boldsymbol{m}_{1,h}, \boldsymbol{m}_{2,h})$ converges to $(\boldsymbol{m}_1, \boldsymbol{m}_2)$ only weakly in $\boldsymbol{H}^1(\Omega) \times \boldsymbol{H}^1(\Omega)$, we are not allowed to pass this term to the limit. We believe that this issue comes from the fact that our algorithms do not use any regularization, so that the stability analysis does not yield any additional regularity (and thus no stronger convergence properties) that would allow us to use arguments based on compensated compactness (see, e.g., [Eva90, Chapter 5] or [Str08, Section I.3]). However, we note that our numerical experiments suggest that the algorithms behave well even if $a_{12} \neq 0$. Moreover, in many situations (see, e.g., [PKC+19, SZT+20]), the inhomogeneous interlattice exchange contribution is of limited physical value and is omitted, so that the current theory already covers many applications.*

7.3.3 Numerical experiments

Before moving to the dynamic case, we show the effectivity of the proposed algorithms with two numerical experiments. The computations presented in this section (and in Section 7.4.2 below) have been performed with an implementation based on the open-source finite element library Netgen/NGSolve [Sch25] (version 6.2.2302). Lower-order energy contributions such as magnetocrystalline anisotropy, Dzyaloshinskii–Moriya interaction, and Zeeman energy (cf. Section C.2.2), omitted in our analysis, are treated explicitly (and thus contribute only to the right-hand-sides of (7.14) and (7.17)); see [BFF+14, AHP+14]. The orthogonality constraint in (7.14) and (7.17) is enforced using the null-space method discussed in Chapter 4, from [RGJ13, KPP+19]. To produce the linear systems, we apply the ideas shown in Chapter 4 to the larger system described here. For the decoupled system, we simply produce a null-space Q_1, Q_2 for each magnetization $\boldsymbol{m}_{1,h}, \boldsymbol{m}_{2,h}$ respectively. Then we consider the pair of linear systems

$$\begin{aligned} Q_1 A_1 Q_1^\top \boldsymbol{z}_1 &= Q_1 F_1, \\ Q_2 A_2 Q_2^\top \boldsymbol{z}_2 &= Q_2 F_2. \end{aligned}$$

When we have the fully coupled system, we instead form a block matrix and solve the linear system

$$\begin{bmatrix} Q_1 A_1 Q_1^\top & Q_1 A_2 Q_2^\top \\ Q_2 A_1 Q_1^\top & Q_2 A_2 Q_2^\top \end{bmatrix} \begin{bmatrix} \boldsymbol{z}_1 \\ \boldsymbol{z}_1 \end{bmatrix} = \begin{bmatrix} Q_1 F_1 \\ Q_2 F_2 \end{bmatrix}.$$

The resulting linear systems are solved using the generalized minimal residual method (GMRES) with a relative tolerance of 10^{-8} with an incomplete LU decomposition preconditioner with a drop tolerance of 10^{-4} and fill factor of 10. We note that in the static case, the use of the conjugate gradient method is possible due to symmetry, but we use GMRES in these tests to maintain consistency with

the dynamic case (see Section 7.4.2 below). All computations have been made on an i5–9500 CPU with 16 GB of installed memory. Magnetization configurations are visualized with ParaView [AGL05].

7.3.3.1 Comparison of the algorithms

In this experiment, we aim to compare to each other Algorithm 7.3.4 and Algorithm 7.3.5, and to evaluate the impact on their performance of the choice of the gradient flow metric, i.e., the inner product $\langle \cdot, \cdot \rangle_{\boldsymbol{\mathcal{H}}}$ in (7.13).

For the dimensionless setting discussed in Section 7.2, we consider a toy problem on the unit cube $\Omega = (-1/2, 1/2)^3$. The total energy consists of exchange and uniaxial anisotropy, i.e.,

$$\mathcal{E}[\boldsymbol{m}_1, \boldsymbol{m}_2] = \frac{1}{2} \sum_{\ell=1}^{2} a_{\ell\ell} \int_\Omega |\boldsymbol{\nabla} \boldsymbol{m}_\ell|^2 + a_{12} \int_\Omega \boldsymbol{\nabla} \boldsymbol{m}_1 : \boldsymbol{\nabla} \boldsymbol{m}_2 - a_0 \int_\Omega \boldsymbol{m}_1 \cdot \boldsymbol{m}_2 + \frac{q_1^2}{2} \int_\Omega [1 - (\boldsymbol{a} \cdot \boldsymbol{m}_1)^2] + \frac{q_2^2}{2} \int_\Omega [1 - (\boldsymbol{a} \cdot \boldsymbol{m}_2)^2],$$

with exchange constants $a_{11} = 2$, $a_{22} = 1$, $a_{12} = -1/2$, and $a_0 = -100$, anisotropy constants $q_1 = 5$ and $q_2 = 10$, and easy axis $\boldsymbol{a} = (1, 1, 1)/\sqrt{3}$. It is easy to see that for this setup the energy minimization problem admits two global minimizers $(\boldsymbol{m}_1^\pm, \boldsymbol{m}_2^\pm) \equiv \pm(\boldsymbol{a}, -\boldsymbol{a})$ and that the energy value at the minimizers is $\mathcal{E}[\boldsymbol{m}_1^\pm, \boldsymbol{m}_2^\pm] = -100$.

For the discretization, we consider a tetrahedral mesh generated by Netgen with mesh size $h \approx 0.209$ (1433 vertices and 6201 elements), and we set $k = 10^{-3}$ and $\varepsilon = 10^{-4}$. Starting from the constant initial guess $\boldsymbol{m}_{1,h}^0 \equiv (1, 0, 0)$ and $\boldsymbol{m}_{2,h}^0 \equiv (0, 1, 0)$, we run Algorithm 7.3.4 and Algorithm 7.3.5 for three different choices for the gradient flow metric: the L^2-metric $\langle \cdot, \cdot \rangle_{\boldsymbol{\mathcal{H}}} = \langle \cdot, \cdot \rangle$, the mass-lumped L^2-metric $\langle \cdot, \cdot \rangle_{\boldsymbol{\mathcal{H}}} = \langle \cdot, \cdot \rangle_h$ (see (3.4)), and the H^1-metric $\langle \cdot, \cdot \rangle_{\boldsymbol{\mathcal{H}}} = \langle \cdot, \cdot \rangle + \langle \boldsymbol{\nabla}(\cdot), \boldsymbol{\nabla}(\cdot) \rangle$. For all six runs (two algorithms, three metrics each), the iterative algorithm returns as an approximate stationary point, an approximation of the minimizer $(\boldsymbol{m}_1^-, \boldsymbol{m}_2^-) \equiv (-\boldsymbol{a}, \boldsymbol{a})$.

In Table 7.1, we compare the performance of each combination in terms of

- the final energy $\mathcal{E}[\boldsymbol{m}_{1,h}, \boldsymbol{m}_{2,h}]$ of the approximate stationary point (*energy*);
- the difference $\mathcal{E}[\widehat{\boldsymbol{m}}_{1,h}, \widehat{\boldsymbol{m}}_{2,h}] + 100$ between the final energy $\mathcal{E}[\widehat{\boldsymbol{m}}_{1,h}, \widehat{\boldsymbol{m}}_{2,h}]$ of the normalized approximate stationary point (*proj. energy err.*) and the expected energy -100, where $\widehat{\boldsymbol{m}}_{\ell,h} = \mathcal{I}_h[\boldsymbol{m}_{\ell,h} / |\boldsymbol{m}_{\ell,h}|]$ for all $\ell = 1, 2$;
- the number of iterations necessary to meet the stopping criterion (*num. iter.*);
- the average solve time per iteration (*solve time*), measured in s, where the solve time is defined as the time needed to solve the linear system (7.14) for Algorithm 7.3.4 and as the sum of the times needed to solve the two linear systems (7.17) (one for $\ell = 1$ and one for $\ell = 2$) for Algorithm 7.3.5;

- the error in the unit-length constraint measured in the L^1-norm, i.e., $\mathrm{err}_{L^1} := \max_{\ell=1,2} \left\| \mathcal{I}_h \left[\left| \boldsymbol{m}_{\ell,h} \right|^2 \right] - 1 \right\|_{L^1(\Omega)}$;
- the error in the unit-length constraint measured in the L^∞-norm, i.e., $\mathrm{err}_{\boldsymbol{L}^\infty} := \max_{\ell=1,2} \|\boldsymbol{m}_{\ell,h}\|_{\boldsymbol{L}^\infty(\Omega)} - 1$.
- The average number of GMRES iterations per linear solve.

Moreover, in Figure 7.1, for all six combinations of algorithms and metrics, we plot the evolution of the energy during the iteration.

	Algorithm 7.3.4 (coupled)			Algorithm 7.3.5 (decoupled)		
$\mathcal{H}$	$(\boldsymbol{L}^2(\Omega), \|\cdot\|)$	$(\boldsymbol{L}^2(\Omega), \|\cdot\|_h)$	$\boldsymbol{H}^1(\Omega)$	$(\boldsymbol{L}^2(\Omega), \|\cdot\|)$	$(\boldsymbol{L}^2(\Omega), \|\cdot\|_h)$	$\boldsymbol{H}^1(\Omega)$
energy	-111.59	-111.59	-111.59	-111.38	-111.38	-111.38
proj. energy err.	$8.56 \cdot 10^{-11}$	$8.56 \cdot 10^{-11}$	$8.56 \cdot 10^{-11}$	$9.90 \cdot 10^{-11}$	$9.90 \cdot 10^{-11}$	$9.90 \cdot 10^{-11}$
num. iter.	249	249	249	275	275	275
solve time	0.223	0.232	0.376	0.095	0.094	0.209
$\mathrm{err}_{\boldsymbol{L}^\infty}$	0.049	0.049	0.049	0.047	0.047	0.047
err_{L^1}	0.100	0.100	0.100	$9.61 \cdot 10^{-2}$	$9.61 \cdot 10^{-2}$	$9.61 \cdot 10^{-2}$
Avg. GMRES	2	2	3	2	2	29

Table 7.1: Experiment of Section 7.3.3.1: Comparison of algorithms and gradient flow metrics (constant initial guess).

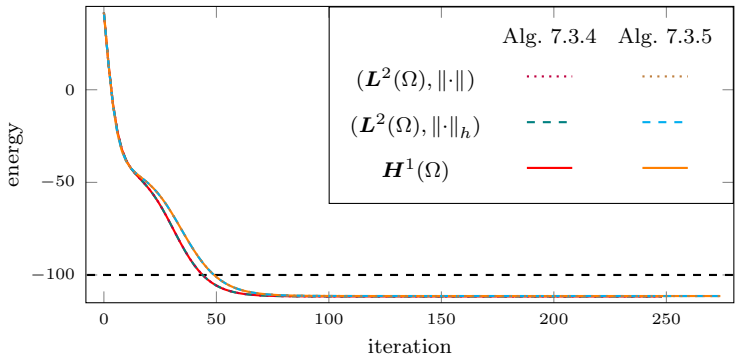

Figure 7.1: Experiment of Section 7.3.3.1: Evolution of the energy with different algorithms and gradient flow metrics (constant initial guess).

In the very first part of the gradient flow dynamics (corresponding roughly to the first 15 iterations), the constant initial guess with $\boldsymbol{m}_1$ and $\boldsymbol{m}_2$ perpendicular to each other evolves to reach a constant state with an antiparallel alignment of the fields. This yields a strong reduction of the a_0-modulated homogeneous interlattice exchange contribution (with the total energy abruptly dropping from an initial value of about 41 to -42). The rest of the dynamics is slower and consists of a rotation of the pair of constant fields which make them align to the direction of the easy axis as prescribed by the anisotropy energy contribution.

Looking at the results, we observe that Algorithm 7.3.4 and Algorithm 7.3.5 require approximately the same number of iterations to fulfil the stopping criterion (those of Algorithm 7.3.4 are slightly less than those of Algorithm 7.3.5). The

energy decay of Algorithm 7.3.4 is faster than the one of Algorithm 7.3.5, but this does not lead to a significantly smaller number of iterations. On the other hand, the average solve time of Algorithm 7.3.5 is about half of the one of Algorithm 7.3.4, which makes the simulations performed with the decoupled algorithm significantly faster. The different metrics are practically identical (except for a minimal difference in the average solve time). For the L^2- and mass-lumped L^2-metric, this is unsurprising, since they are equivalent to each other; see (3.5). We believe that the equivalence to the H^1-metric in this example (with constant initial guess) is due to the fact that the updates $\boldsymbol{v}_{\ell,h}^i$ are essentially uniform, and hence their gradients $\boldsymbol{\nabla} \boldsymbol{v}_{\ell,h}^i$ are essentially zero. It follows that in the numerical scheme, the gradient part of the H^1-metric is small, reducing to the L^2-metric. We note that the only significant deviation in the number of GMRES iterations was for the decoupled system with the $\boldsymbol{H}^1$-metric., with all others taking around 2 iterations.

There is a significant discrepancy between the value of the energy at the minimizer ($\mathcal{E}[\boldsymbol{m}_1^+, \boldsymbol{m}_2^+] = -100$) and the one of its approximation ($\mathcal{E}[\boldsymbol{m}_{1,h}, \boldsymbol{m}_{2,h}] \approx$ -111). However, if we remove the error in the unit-length constraint by normalizing the fields at the vertices of the mesh, we obtain the desired value up to the tenth digit. This shows that our projection-free algorithms are perfectly able to identify the minimizers. However, for a quantitative match of the energy values, the error in the constraint needs to be removed or reduced (applying a nodal projection to the final configuration or decreasing the time-step size).

	Algorithm 7.3.4 (coupled)			Algorithm 7.3.5 (decoupled)		
$\boldsymbol{\mathcal{H}}$	$(\boldsymbol{L}^2(\Omega), \|\cdot\|)$	$(\boldsymbol{L}^2(\Omega), \|\cdot\|_h)$	$\boldsymbol{H}^1(\Omega)$	$(\boldsymbol{L}^2(\Omega), \|\cdot\|)$	$(\boldsymbol{L}^2(\Omega), \|\cdot\|_h)$	$\boldsymbol{H}^1(\Omega)$
energy	-182.36	-158.04	-100.38	-182.70	-158.03	-100.38
proj. energy err.	$5.70 \cdot 10^{-11}$	$6.33 \cdot 10^{-11}$	$6.02 \cdot 10^{-9}$	$6.54 \cdot 10^{-11}$	$7.70 \cdot 10^{-11}$	$6.02 \cdot 10^{-9}$
num. iter.	231	231	13713	252	254	13718
solve time	0.220	0.227	0.347	0.093	0.092	0.170
$\mathrm{err}_{\boldsymbol{L}^\infty}$	1.185	0.923	0.004	1.196	0.905	0.004
err_{L^1}	0.668	0.433	$2.51 \cdot 10^{-3}$	0.670	0.428	$2.51 \cdot 10^{-3}$
Avg. GMRES	2	2	1	3	3	2

Table 7.2: Experiment of Section 7.3.3.1: Comparison of algorithms and gradient flow metrics (random initial guess).

Next, we repeat the experiment, but this time we start from a random initial guess (the same for all simulations). For all six runs, the iterative algorithm again returns as an approximate stationary point, an approximation of the minimizer $(\boldsymbol{m}_1^-, \boldsymbol{m}_2^-) \equiv (-\boldsymbol{a}, \boldsymbol{a})$. The results are displayed in Table 7.2. The faster average solve time of Algorithm 7.3.5 observed for the case of a constant initial guess is confirmed. However, in this case, we observe a clear difference between the L^2-metrics (with and without mass lumping) and the H^1-metric, with the latter requiring a significantly larger number of iterations (ca 13700 against 200–300), which results in longer computational times. However, as far as the unit-length constraint is concerned, the H^1-metric is characterized by a much better accuracy.

Overall, our experiments show that the decoupled approach of Algorithm 7.3.5, due to its computational efficiency, is preferable over the coupled one of Algorithm 7.3.4. On the other hand, the choice of the gradient flow metric is more

delicate. While for a constant initial guess (with low exchange energy) the metrics are essentially equivalent, for a random initial guess (with large exchange energy) the H^1-metric guarantees a significantly smaller violation of the unit-length constraint at the discrete level (which, however, is obtained at the price of higher computational costs).

In this respect, we conclude by observing that, for any metric, the solvability of Algorithm 7.3.4 and the stability of Algorithm 7.3.5 require k to be sufficiently small (see Proposition 7.3.6(i)–(ii) and Proposition 7.3.7(ii)–(iii), respectively). This is different from what happens for similar algorithms to approximate harmonic maps [Bar16] (or energy minimizers of the standard micromagnetic energy for FM materials), where the stabilizing effect of the H^1-metric allows the use of very large time-step sizes, which usually yields a significant reduction of the number of iterations needed to achieve convergence.

7.3.3.2 AFM skyrmion formation

In this experiment, we aim to highlight the capability of our algorithms to compute stable magnetization configurations in AFM materials.

The domain is an AFM nanodisk of thickness 1 nm (aligned with x_3-axis) and diameter 60 nm (aligned with the x_1x_2-plane). The energy consists of exchange, out-of-plane uniaxial anisotropy, and interfacial Dzyaloshinskii–Moriya interaction, and reads as

$$\begin{aligned}\mathcal{E}[\boldsymbol{m}_1, \boldsymbol{m}_2] = \frac{1}{2}\sum_{\ell=1}^{2} a_{\ell\ell}\int_\Omega |\boldsymbol{\nabla}\boldsymbol{m}_\ell|^2 - a_0\int_\Omega \boldsymbol{m}_1\cdot\boldsymbol{m}_2 + \frac{q^2}{2}\int_\Omega [1-(\boldsymbol{a}\cdot\boldsymbol{m}_1)^2] \\ + \frac{q^2}{2}\int_\Omega [1-(\boldsymbol{a}\cdot\boldsymbol{m}_2)^2] + \int_\Omega \widehat{\boldsymbol{D}} : (\boldsymbol{\nabla}\boldsymbol{m}_1\times\boldsymbol{m}_1) + \int_\Omega \widehat{\boldsymbol{D}} : (\boldsymbol{\nabla}\boldsymbol{m}_2\times\boldsymbol{m}_2),\end{aligned}$$

where the dimensionless parameters a_{11}, a_{22}, a_0, q and $\widehat{\boldsymbol{D}}$ are obtained from the material parameters collected in Table 7.3 as explained in Appendix C.2.

For the discretization, we consider a tetrahedral mesh $\mathcal{T}_h$ generated by Netgen with mesh size 3.36 nm (1660 vertices and 4694 elements), i.e., well below the exchange length of $\ell_{\mathrm{ex}} = \sqrt{2A_{11}/(\mu_0 M_{\mathrm{s},1}^2)} = 8.61\,\mathrm{nm}$, Here, $\mu_0 > 0$ denotes the vacuum permeability (in $\mathrm{N/A^2}$).

As an initial guess, we consider a perturbed skyrmion-like AFM state; see Figure 7.2a. More precisely, we consider the auxiliary function

$$f_{\mathrm{init}}(x,y,z) := \frac{1}{1+\exp\left(20\left(\sqrt{x^2+y^2}-10\right)\right)} - \frac{1}{2}$$

and start from the initial condition $\boldsymbol{m}_{1,2} = (0,0,\pm f_{\mathrm{init}})$. This is then interpolated using the built-in Oswald-type interpolation of NGSolve before undergoing a nodal projection, random perturbation (up to 0.3 in each component) and another nodal projection. The value 10 in the expression of f_{init} corresponds to 10 nm and refers

Parameter	Value
$M_{\mathrm{s},1},\ M_{\mathrm{s},2}$	$376\,\mathrm{kA/m}$
$A_{11},\ A_{22}$	$6.59\,\mathrm{pJ/m}$
A_{12}	0
A_0	$-6.59\,\mathrm{pJ/m}$
a	$1\,\mathrm{nm}$
K	$0.15\,\mathrm{MJ/m^3}$
$\boldsymbol{a}$	$\boldsymbol{e}_3$
$\boldsymbol{D}$	$D(-\boldsymbol{e}_1 \otimes \boldsymbol{e}_2 + \boldsymbol{e}_2 \otimes \boldsymbol{e}_1)$
D	$3\,\mathrm{mJ/m^2}$

Table 7.3: Experiment of Section 7.3.3.2: Material parameters. All values are taken from [SZT+20], except those of a and D. Here, we denote by $\{\boldsymbol{e}_1, \boldsymbol{e}_2, \boldsymbol{e}_3\}$ the canonical basis of $\mathbb{R}^3$.

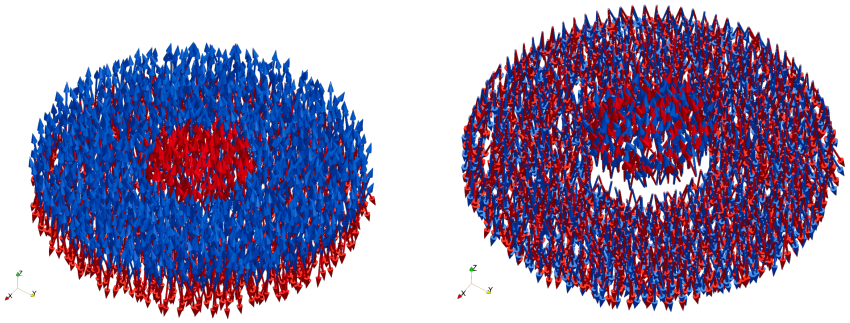

(a) AFM initial guess. (b) FM initial guess.

Figure 7.2: Experiments of Sections 7.3.3.2–7.3.3.3: Initial guesses for Algorithm 7.3.5. The orientation of $\boldsymbol{m}_{h,1}^0$ (resp., $\boldsymbol{m}_{h,2}^0$) is shown in red (resp., blue). In (a), we have $\boldsymbol{m}_{h,1}^0 \approx \boldsymbol{e}_1$ in the internal region, $\boldsymbol{m}_{h,1}^0 \approx -\boldsymbol{e}_1$ in the external region, and $\boldsymbol{m}_{h,2}^0 \approx -\boldsymbol{m}_{h,1}^0$ in the entire domain (AFM alignment). In (b), we have $\boldsymbol{m}_{h,1}^0$ as in (a), but $\boldsymbol{m}_{h,2}^0 \approx \boldsymbol{m}_{h,1}^0$ (FM alignment).

to the radius of the inner circle. The decay constant 20 makes the transition reasonably sharp before projecting.

Starting from this configuration, we run Algorithm 7.3.5 (in our opinion, the best performing one in Section 7.3.3.1) with dimensionless time-step size k and stopping tolerance ε both equal to $1 \cdot 10^{-3}$.

In Figures 7.3a–7.3b below, we show the stable configurations obtained running Algorithm 7.3.5 with H^1-metric. We see that both fields are Néel-type skyrmions [FRC17] (with the cores pointing up for $\boldsymbol{m}_{h,1}$ and down for $\boldsymbol{m}_{h,2}$, in line with the orientation of the field in the internal region for the corresponding initial condition), which is typical for magnetic systems characterized by interfacial Dzyaloshinskii–Moriya interaction. Moreover, as expected for an AFM material, we have that $\boldsymbol{m}_{h,1} \approx -\boldsymbol{m}_{h,2}$.

In Table 7.4, we compare the performance of the three gradient flow metrics

	Algorithm 7.3.5		
$\mathcal{H}$	$(\boldsymbol{L}^2(\Omega), \|\cdot\|)$	$(\boldsymbol{L}^2(\Omega), \|\cdot\|_h)$	$\boldsymbol{H}^1(\Omega)$
energy	$-4.362 \cdot 10^5$	$-4.287 \cdot 10^5$	$-4.256 \cdot 10^5$
num. iter.	17 552	17 704	17 784
solve time	0.060	0.050	0.058
$\mathrm{err}_{\boldsymbol{L}^\infty}$	0.165	0.100	0.061
err_{L^1}	95.134	44.173	23.411
Avg. GMRES	2	2	2

Table 7.4: Experiment of Section 7.3.3.2: Comparison of gradient flow metrics for Algorithm 7.3.5.

considered in Section 7.3.3.1. We see that, in terms of final energy value, number of iterations, and average solve time, the performance of the three metrics is comparable. On the other hand, as far as the violation of the unit-length constraint is concerned, the H^1-metric exhibits the best performance.

7.3.3.3 The role of a_0

The interaction of $\boldsymbol{m}_1$ and $\boldsymbol{m}_2$ with each other is incorporated into the model by means of two contributions of the energy functional (7.1): the a_{12}-modulated inhomogeneous interlattice exchange contribution and the a_0-modulated homogeneous interlattice exchange contribution. The first one is of limited physical value (that is why it is often omitted as, e.g., in [PKC$^+$19, SZT$^+$20]) and is mathematically dominated by the inhomogeneous intralattice exchange contributions (cf. assumption (7.2)).

As far as the coupling of the fields is concerned, the main player is indeed the a_0-modulated energy term. In particular, it is easily seen that negative values of a_0 (as those considered in all experiments presented so far) favours minimizers with an antiparallel alignment of the fields (typical for AFM and FiM materials), whereas positive values of a_0 induce a parallel alignment. Moreover, if $a_0 > 0$, the energy functional (7.1) yields, up to positive multiplicative and additive constants, a weighted squared H^1-norm for the total magnetization $\boldsymbol{m} = \eta_{\mathrm{s},1}\boldsymbol{m}_1 + \eta_{\mathrm{s},2}\boldsymbol{m}_2$, which resembles (and therefore behaves like) the standard micromagnetic energy for FM materials.

In this experiment, we investigate these aspects numerically. To this end, we repeat the experiment of Section 7.3.3.2 with combinations of the following modifications. On the one hand, we test positive and negative values of a_0 (by setting $A_0 = \pm\, 6.59\,\mathrm{pJ/m}$, cf. Table 7.3). On the other hand, we use either the previous AFM initial guess or its FM sister in which the fields are almost aligned with each other (shown in Figure 7.2b). For these four setup combinations (two values for a_0, two initial guesses), but otherwise the same material and discretization parameters as in Section 7.3.3.2, we run Algorithm 7.3.5 with H^1-metric and mass-lumped L^2-metric.

The results are shown in Table 7.5, where we compare the results of the eights simulations (two values of a_0, two initial guesses, two gradient flow metrics), whereas in Figure 7.3 we show the approximate stationary points computed by

	$a_0 < 0$, AFM initial guess		$a_0 > 0$, AFM initial guess	
$\mathcal{H}$	$(\boldsymbol{L}^2(\Omega), \|\cdot\|_h)$	$\boldsymbol{H}^1(\Omega)$	$(\boldsymbol{L}^2(\Omega), \|\cdot\|_h)$	$\boldsymbol{H}^1(\Omega)$
energy	$-4.287 \cdot 10^5$	$-4.256 \cdot 10^5$	$-4.913 \cdot 10^5$	$-4.817 \cdot 10^5$
num. iter.	17 704	17 784	58 518	41 319
solve time	0.060	0.069	0.072	0.070
err_{L^∞}	0.100	0.061	0.252	0.121
err_{L^1}	44.173	23.541	451.584	386.488
final state	Fig. 7.3a	Fig. 7.3b	Fig. 7.3g	Fig. 7.3h
Avg. GMRES	2	2	2	2
	$a_0 < 0$, FM initial guess		$a_0 > 0$, FM initial guess	
$\mathcal{H}$	$(\boldsymbol{L}^2(\Omega), \|\cdot\|_h)$	$\boldsymbol{H}^1(\Omega)$	$(\boldsymbol{L}^2(\Omega), \|\cdot\|_h)$	$\boldsymbol{H}^1(\Omega)$
energy	$-4.911 \cdot 10^5$	$-4.805 \cdot 10^5$	$-4.287 \cdot 10^5$	$-4.256 \cdot 10^5$
num. iter.	220 489	17 849	16 547	16 523
solve time	0.066	0.067	0.060	0.068
err_{L^∞}	0.174	0.148	0.108	0.069
err_{L^1}	452.250	381.746	44.018	23.551
final state	Fig. 7.3c	Fig. 7.3d	Fig. 7.3e	Fig. 7.3f
Avg. GMRES	2	2	2	2

Table 7.5: Experiment of Section 7.3.3.3: Comparison of gradient flow metrics for Algorithm 7.3.5 using varied initial guess (cf. Figure 7.2), and positive or negative a_0.

Algorithm 7.3.5 with H^1-metric (the mass-lumped L^2-metric led to the same approximate stationary points). In all cases, the expected FM/AFM coupling of the fields is observed. We see that, if the sign of a_0 and the mutual alignment of the fields in the initial guess match, i.e., either $a_0 < 0$ with AFM initial guess or $a_0 > 0$ with FM initial guess, both fields in the final state are Néel-type skyrmions, with $\boldsymbol{m}_{h,2} \approx -\boldsymbol{m}_{h,1}$ if $a_0 < 0$ (see Figures 7.3a–7.3b) and $\boldsymbol{m}_{h,2} \approx \boldsymbol{m}_{h,1}$ if $a_0 > 0$ (see Figures 7.3e–7.3f).

In terms of final energy value, number of iterations, and average solve time, the results for the two metrics are very similar, whereas the performance is different in terms of constraint violation error, with the one of the H^1-metric being smaller. On the other hand, in the *nonmatching* setups, i.e., either $a_0 > 0$ with AFM initial guess or $a_0 < 0$ with FM initial guess, the number of iterations required to meet the stopping criterion is generically greater (which is not surprising, as the gradient flow dynamics must enforce also the mutual alignment of the fields prescribed by the sign of a_0).

Moreover, the performance of the two metrics is different not only in terms of constraint violation error (which is the case for the *matching* setups), but also in terms of number of iterations needed to reach the stopping criterion. This is particularly extreme for the case $a_0 < 0$ with FM initial guess, for which the mass-lumped L^2-metric requires over 200k iterations, despite the H^1-metric taking only 17k.

Furthermore, the final states obtained for the nonmatching setups are not pairs of skyrmions, but different configurations characterized by larger energy values. We see that, if $a_0 < 0$ with FM initial guess, the disk is divided in half, with a transition between generally pointing up and generally pointing down (see Figures 7.3c–7.3d). On the other hand, if $a_0 > 0$ with AFM initial guess, the final

state exhibits for both fields a line in the middle pointing down, with two parallel sections pointing upwards (see Figures 7.3g–7.3h). A similar stable state can be observed in [TSTLD+20, Figure 2].

7.4 Numerical approximation of the LLG system

In this section, starting from Algorithm 7.3.5, we introduce a fully discrete algorithm to approximate solutions of the initial boundary value problem (7.9)–(7.10) for the coupled system of LLG equations modelling the dynamics of AFM and FiM materials. We state well-posedness, stability, and unconditional convergence of the approximations toward a weak solution of the problem, and present numerical experiments to show its applicability for the simulation of the dynamics of magnetic skyrmions in AFM materials. To make the presentation of the results concise, all proofs are postponed to Section 7.5.2.

7.4.1 Numerical algorithm and main results

The method we propose, stated in the following algorithm, is based on the projection-free tangent plane scheme from [AHP+14, Bar16, HPP+19] and employs the decoupled approach of Algorithm 7.3.5. Like in the static case, the spatial discretization is based on first-order finite elements (see Chapter 3).

Algorithm 7.4.1 (tangent plane scheme)**.** ***Discretization parameters:*** *Mesh size $h > 0$, time-step size $k > 0$.*
Input: *Approximate initial condition $(\boldsymbol{m}_{1,h}^0, \boldsymbol{m}_{2,h}^0) \in \mathcal{S}^1(\mathcal{T}_h)^3 \times \mathcal{S}^1(\mathcal{T}_h)^3$ such that, for all $\ell = 1, 2$, $\left|\boldsymbol{m}_{\ell,h}^0(z)\right| = 1$ for all $z \in \mathcal{N}_h$.*
Loop: *For all $i \in \mathbb{N}_0$, iterate* (i)–(ii) *until the stopping criterion* (stop) *is met:*

(i) *Given $(\boldsymbol{m}_{1,h}^i, \boldsymbol{m}_{2,h}^i) \in \mathcal{S}^1(\mathcal{T}_h)^3 \times \mathcal{S}^1(\mathcal{T}_h)^3$, compute $(\boldsymbol{v}_{1,h}^i, \boldsymbol{v}_{2,h}^i) \in \boldsymbol{\mathcal{K}}_h[\boldsymbol{m}_{1,h}^i] \times \boldsymbol{\mathcal{K}}_h[\boldsymbol{m}_{2,h}^i]$ such that, for all $\ell = 1, 2$, for all $(\boldsymbol{\phi}_{1,h}, \boldsymbol{\phi}_{2,h}) \in \boldsymbol{\mathcal{K}}_h[\boldsymbol{m}_{1,h}^i] \times \boldsymbol{\mathcal{K}}_h[\boldsymbol{m}_{2,h}^i]$, it holds that*

$$\begin{aligned} &\alpha_\ell \left\langle \boldsymbol{v}_{\ell,h}^i, \boldsymbol{\phi}_{\ell,h} \right\rangle_h + \left\langle \boldsymbol{m}_{\ell,h}^i \times \boldsymbol{v}_{\ell,h}^i, \boldsymbol{\phi}_{\ell,h} \right\rangle_h + \eta_\ell a_{\ell\ell} k \left\langle \boldsymbol{\nabla} \boldsymbol{v}_{\ell,h}^i, \boldsymbol{\nabla} \boldsymbol{\phi}_{\ell,h} \right\rangle \\ &= -\eta_\ell a_{\ell\ell} \left\langle \boldsymbol{\nabla} \boldsymbol{m}_{\ell,h}^i, \boldsymbol{\nabla} \boldsymbol{\phi}_{\ell,h} \right\rangle - \eta_\ell a_{12} \left\langle \boldsymbol{\nabla} \boldsymbol{m}_{3-\ell,h}^i, \boldsymbol{\nabla} \boldsymbol{\phi}_{\ell,h} \right\rangle + \eta_\ell a_0 \left\langle \boldsymbol{m}_{3-\ell,h}^i, \boldsymbol{\phi}_{\ell,h} \right\rangle . \end{aligned} \tag{7.23}$$

(ii) *Define*

$$\boldsymbol{m}_{\ell,h}^{i+1} := \boldsymbol{m}_{\ell,h}^i + k \boldsymbol{v}_{\ell,h}^i \quad \text{for all } \ell = 1, 2. \tag{7.24}$$

Output: *Sequence of approximations $\{(\boldsymbol{m}_{1,h}^i, \boldsymbol{m}_{2,h}^i)\}_{i \in \mathbb{N}_0}$.*

Starting from approximations $\boldsymbol{m}_{1,h}^0, \boldsymbol{m}_{2,h}^0 \in \mathcal{S}^1(\mathcal{T}_h)^3$ of the initial conditions, in each step of Algorithm 7.4.1, the new approximations are computed updating the current ones using a predictor-corrector approach. In the predictor step, (7.23) are discretizations of

$$\begin{aligned} \alpha_\ell \, \partial_t \boldsymbol{m}_\ell + \boldsymbol{m}_\ell \times \partial_t \boldsymbol{m}_\ell = \eta_\ell \, \boldsymbol{h}_{\mathrm{eff},\ell}[\boldsymbol{m}_1, \boldsymbol{m}_2] \\ - \eta_\ell \left(\boldsymbol{h}_{\mathrm{eff},\ell}[\boldsymbol{m}_1, \boldsymbol{m}_2] \cdot \boldsymbol{m}_\ell \right) \boldsymbol{m}_\ell \quad \text{for all } \ell = 1, 2, \end{aligned}$$

an equivalent reformulation of (7.9) that can be obtained using standard vector identities as well as the relations $|\boldsymbol{m}_\ell| = 1$ and $\boldsymbol{m}_\ell \cdot \partial_t \boldsymbol{m}_\ell = 0$ [AJ06]. The discrete problems are posed in the discrete tangent space (3.14), which yields a natural linearization. Like in Algorithm 7.3.5, the inhomogeneous intralattice exchange contribution is treated implicitly, whereas the interlattice contributions are treated explicitly. By doing this, the system of LLG equations is decoupled and one has to solve two, independent of each other, $2N_h$-by-$2N_h$ linear systems per time-step. The corrector step (7.24) is a simple projection-free first-order time-stepping.

In the following proposition, we show that Algorithm 7.4.1 is well-defined.

Proposition 7.4.2 (well-posedness of Algorithm 7.4.1)**.** *For all $i \in \mathbb{N}_0$, (7.23) admits a unique solution $(\boldsymbol{v}_{1,h}^i, \boldsymbol{v}_{2,h}^i) \in \boldsymbol{\mathcal{K}}_h[\boldsymbol{m}_{1,h}^i] \times \boldsymbol{\mathcal{K}}_h[\boldsymbol{m}_{2,h}^i]$. In particular, each iteration of Algorithm 7.4.1 is well-defined.*

In the following proposition, we characterize the energy behaviour of Algorithm 7.4.1.

Proposition 7.4.3 (discrete energy law and stability of Algorithm 7.4.1)**.** *There hold the following statements:*

(i) *For all $i \in \mathbb{N}_0$, the approximations generated by Algorithm 7.4.1 satisfy the identity*

$$\mathcal{E}[\boldsymbol{m}_{1,h}^{i+1}, \boldsymbol{m}_{2,h}^{i+1}] - \mathcal{E}[\boldsymbol{m}_{1,h}^{i}, \boldsymbol{m}_{2,h}^{i}] = -k \sum_{\ell=1}^{2} \frac{\alpha_\ell}{\eta_\ell} \left\|\boldsymbol{v}_{\ell,h}^i\right\|_h^2 - \frac{k^2}{2} \sum_{\ell=1}^{2} a_{\ell\ell} \left\|\boldsymbol{\nabla} \boldsymbol{v}_{\ell,h}^i\right\|^2 + a_{12} k^2 \left\langle \boldsymbol{\nabla} \boldsymbol{v}_{1,h}^i, \boldsymbol{\nabla} \boldsymbol{v}_{2,h}^i \right\rangle - a_0 k^2 \left\langle \boldsymbol{v}_{1,h}^i, \boldsymbol{v}_{2,h}^i \right\rangle. \quad (7.25)$$

(ii) *If $k < 2 \min\{\alpha_1, \alpha_2\} / |a_0|$, for all $j \in \mathbb{N}$, the approximations generated by Algorithm 7.4.1 satisfy the inequality*

$$\sum_{\ell=1}^{2} \left\|\boldsymbol{m}_{\ell,h}^j\right\|_{\boldsymbol{H}^1(\Omega)}^2 + k \sum_{i=0}^{j-1} \sum_{\ell=1}^{2} \left\|\boldsymbol{v}_{\ell,h}^i\right\|_h^2 + k^2 \sum_{i=0}^{j-1} \sum_{\ell=1}^{2} \left\|\boldsymbol{\nabla} \boldsymbol{v}_{\ell,h}^i\right\|^2 \leq C. \quad (7.26)$$

The constant $C > 0$ depends only on the problem data and the shape-regularity of the family of meshes.

The discrete energy law of Algorithm 7.4.1 is an approximation of the one satisfied by weak solutions (see (7.12)). The LLG-inherent energy dissipation, modulated by the damping parameters α_1 and α_2, is enhanced by the dissipation coming from the second term on the right-hand side, which is due to the implicit treatment of the homogeneous intralattice exchange contribution. The last two terms on the right-hand side of (7.25), in general unsigned, are perturbations arising from the explicit treatment of the interlattice exchange contributions.

With the sequence of approximations delivered by Algorithm 7.4.1, for $\ell = 1, 2$, we define the piecewise affine time reconstruction $\boldsymbol{m}_{\ell,hk} : [0, \infty) \to \mathcal{S}^1(\mathcal{T}_h)^3$ as

$$\boldsymbol{m}_{\ell,hk}(t) := \frac{t - t_i}{k} \boldsymbol{m}_{\ell,h}^{i+1} + \frac{t_{i+1} - t}{k} \boldsymbol{m}_{\ell,h}^{i} \quad \text{for all } i \in \mathbb{N}_0 \text{ and } t \in [t_i, t_{i+1}]$$

(see (3.3)). In the following theorem, we state the convergence of the finite element approximations toward a weak solution of (7.9) in the sense of Definition 7.2.1.

Theorem 7.4.4 (convergence of Algorithm 7.4.1)**.** *Suppose that* $\boldsymbol{m}_{1,h}^0 \to \boldsymbol{m}_1^0$ *and* $\boldsymbol{m}_{2,h}^0 \to \boldsymbol{m}_2^0$ *in* $\boldsymbol{H}^1(\Omega)$ *as* $h \to 0$*. Then, there exist* $(\boldsymbol{m}_1, \boldsymbol{m}_2) \in L^\infty(0,\infty;\mathcal{X})$ *and a (nonrelabeled) subsequence of* $\{(\boldsymbol{m}_{1,hk}, \boldsymbol{m}_{2,hk})\}$ *which converges toward* $(\boldsymbol{m}_1, \boldsymbol{m}_2)$ *as* $h, k \to 0$*. In particular, as* $h, k \to 0$*, for all* $\ell = 1, 2$ *it holds that* $\boldsymbol{m}_{\ell,hk} \overset{*}{\rightharpoonup} \boldsymbol{m}_\ell$ *in* $L^\infty(0,\infty;\boldsymbol{H}^1(\Omega))$*. If* $a_{12} = 0$*, the limit* $(\boldsymbol{m}_1, \boldsymbol{m}_2)$ *is a weak solution of* (7.9) *in the sense of Definition 7.2.1.*

Like in the stationary case, we need to assume that $a_{12} = 0$ to be able to show that the limit toward which the finite element approximations are converging satisfies the variational formulation (7.11) (cf. Remark 7.3.9). Under this assumption, Theorem 7.4.4 shows existence of a weak solution to (7.9) and convergence (without rates) of the time reconstructions generated using the snapshots computed using Algorithm 7.4.1 toward it.

7.4.2 Numerical experiments

In this section, we aim to show the capability of Algorithm 7.4.1 to simulate dynamic processes involving AFM materials and how the nature of the coupling of the fields (FM vs. AFM coupling) affects the dynamics of the total magnetization.

7.4.2.1 LLG-based energy minimization

Starting from the observation that the dynamics of $\boldsymbol{m}_1$ and $\boldsymbol{m}_2$ governed by the system of LLG equations (7.9) is dissipative, with the energy dissipation being modulated by the damping parameters α_1 and α_2, we repeat the experiment of Section 7.3.3.1, but to compute low-energy stationary points we use Algorithm 7.4.1 (instead of the gradient flow-based approaches of Algorithm 7.3.4 and Algorithm 7.3.5).

More precisely, we consider the same setup and the same spatial discretization of Section 7.3.3.1 and run Algorithm 7.4.1 with $\eta_1 = \eta_2 = 1$, different damping parameters $\alpha_1 = \alpha_2 = \alpha \in \{1, 1/2, 1/4, 1/8, 1/16\}$, and $k = 10^{-3}$, using the constant fields $\boldsymbol{m}_{1,h}^0 \equiv (1,0,0)$ and $\boldsymbol{m}_{2,h}^0 \equiv (0,1,0)$ as initial condition. The iteration is stopped when the α-independent stopping criterion (7.16) with $\|\cdot\|_{\boldsymbol{\mathcal{H}}}^2 = \|\cdot\|_h^2$ and $\varepsilon = 10^{-4}$ is satisfied.

	Alg. 7.3.5	Algorithm 7.4.1				
α	1	1	1/2	1/4	1/8	1/16
energy	-111.38	-112.26	-126.64	-160.60	-214.79	-998.44
proj. energy err.	$9.90 \cdot 10^{-11}$	$1.03 \cdot 10^{-10}$	$4.81 \cdot 10^{-11}$	$8.27 \cdot 10^{-11}$	$6.13 \cdot 10^{-11}$	$3.64 \cdot 10^{-11}$
num. iter.	275	310	334	600	2954	46698
solve time	0.094	0.093	0.095	0.098	0.097	0.094
err_{L^∞}	0.047	$3.932 \cdot 10^{-2}$	$9.497 \cdot 10^{-2}$	0.219	0.408	6.705
err_{L^1}	$9.61 \cdot 10^{-2}$	$8.019 \cdot 10^{-2}$	0.199	0.486	0.982	3.995
Avg. GMRES	2	3	3	3	3	3

Table 7.6: Experiment of Section 7.4.2.1: Comparison of Algorithm 7.3.5 (with mass-lumped L^2-metric and $\alpha = 1$) with Algorithm 7.4.1 (with $\alpha = 1, 1/2, 1/4, 1/8, 1/16$).

We display the results of our computations in Table 7.6. Noting that Algorithm 7.4.1 coincides with Algorithm 7.3.5 with mass-lumped L^2-metric if $\eta_1 = \eta_2 = \alpha_1 = \alpha_2 = 1$ and the precession term $\langle \boldsymbol{m}^i_{\ell,h} \times \boldsymbol{v}^i_{\ell,h}, \boldsymbol{\phi}_{\ell,h} \rangle_h$ is omitted from (7.23), in the first column of the table we include the results from Section 7.3.3.1 of this instance of Algorithm 7.3.5 for the sake of comparison.

We see that as α is lowered, the final energy is further from the expected value of -100, which is due to the slower dissipation resulting in lengthier dynamics (larger number of iterations) and more rotations (as the precession term is made stronger in a relative sense) before reaching the minimizing state, thereby increasing the average length of $\boldsymbol{m}_{h,1}$ and $\boldsymbol{m}_{h,2}$ (as seen in the error rows). Similarly to Table 7.1 we see that after applying a nodal projection, the energy is within 10 decimal places of -100, indicating that a minimizer is still identified. As expected the average solve time is independent of α.

For $\alpha = 1/16$ we see that the violation of the unit-length constraint and the number of iterations are significantly larger. We suppose that this is related to a possible instability of Algorithm 7.4.1, since, as shown Proposition 7.4.3(ii), stability requires k to be sufficiently small, with the threshold for the time-step size being proportional to the damping parameter. Indeed, for $\alpha = 1/16$, we observe that it is sufficient to reduce k to regain a good performance of the algorithm.

The fact that lowering the value of α results in less dissipation can also be seen in Figure 7.4, where we display the evolution of the average first component of both fields, i.e., $\langle \boldsymbol{m}_\ell(t) \cdot \boldsymbol{e}_1 \rangle = |\Omega|^{-1} \int_\Omega \boldsymbol{m}_\ell(t) \cdot \boldsymbol{e}_1$ for all $\ell = 1, 2$, for all cases. Interestingly, we see that the gradient flow dynamics and the LLG dynamics for $\alpha = 1/8, 1/16$ return as approximate stationary point an approximation of the minimizer $(\boldsymbol{m}_1^-, \boldsymbol{m}_2^-) \equiv (-\boldsymbol{a}, \boldsymbol{a})$, whereas the LLG dynamics for $\alpha = 1, 1/2, 1/4$ return an approximation of $(\boldsymbol{m}_1^+, \boldsymbol{m}_2^+) \equiv (\boldsymbol{a}, -\boldsymbol{a})$. This is not surprising, since different dynamics can result in convergence to different stationary points, even with the same initial condition. As far as the LLG dynamics is concerned, we see that the oscillations of the average first components increase as α is lowered, which can be explained by the greater relative weight of the precessional term on the right-hand side of the LLG equation for smaller values of α.

7.4.2.2 Skyrmion dynamics

Inspired by the experiment in [HPP+19, Section 4.3], we simulate the dynamics of isolated magnetic skyrmions in an AFM or FM nanodisk in response to an applied field pulse.

The setup (domain, energy, and material parameters) is the same as in Sections 7.3.3.2–7.3.3.3, which we complete with the additional parameters needed for the dynamic case, i.e., the rescaled gyromagnetic ratios $\gamma_1 = \gamma_2 = \gamma_0 \approx 2.21 \cdot 10^5\,\mathrm{m/(A\,s)}$ and the Gilbert damping parameters $\alpha_1 = \alpha_2 = 0.01$ (see (C.2) below). We consider both the case of an AFM material ($A_0 = -6.59\,\mathrm{pJ/m}$) and the case of an FM material ($A_0 = 6.59\,\mathrm{pJ/m}$). Given the same spatial discretization (mesh) as in Sections 7.3.3.2–7.3.3.3, as initial conditions $\boldsymbol{m}^0_{1,h}$ and $\boldsymbol{m}^0_{2,h}$ for Algorithm 7.4.1, we consider the nodal projections of the Néel-type skyrmions

shown in Figure 7.3. More precisely, we start from the skyrmions in Figures 7.3a–7.3b for the AFM dynamics ($A_0 < 0$) and from those in Figures 7.3e–7.3f for the FM dynamics ($A_0 > 0$). Moreover, for the time discretization, we use of a constant time-step size of 1 fs.

Starting from these configurations, we perturb the system from its equilibrium by applying an in-plane pulse field of the form $\boldsymbol{H}_{\text{ext}}(t) = (H(t), 0, 0)$ of maximum intensity $\mu_0 H_{\max} = 50\,\text{mT}$ for 150 ps; see Figure 7.5a. Then, we turn off the applied external field, i.e., $\boldsymbol{H}_{\text{ext}}(t) \equiv (0, 0, 0)$, and let the system relax. The overall simulation time is 0.5 ns. The average number of GMRES iterations for this experiment was 3.

In Figures 7.5b–7.5c, we show the time evolution of the average first component of the total magnetization $\boldsymbol{m} = \boldsymbol{m}_1 + \boldsymbol{m}_2$. For the AFM material ($A_0 < 0$), we see a perfect match between the applied pulse field and the total magnetization. When the field is turned off, the state immediately comes back to the initial configuration, which confirms its stability. For the FM material ($A_0 > 0$), the total magnetization still roughly follows the applied field, but the response pulse is around 2 orders of magnitude larger than for the AFM material. Additionally, the FM system receives more energy from the Zeeman field (as the total magnetization is around magnitude 2, compared to almost 0 for the case of the AFM material), resulting in a large visible precession (manifesting itself as oscillations in the plot of the average magnetization). In particular, the return of the total magnetization to the initial stable state is slower.

This experiment provides a demonstration, for a simple setup, of the weaker response of AFM materials (compared to FM materials) to external magnetic fields. This enhanced robustness against external perturbations is one of the properties which makes this class of materials outstanding candidates for the next generation of spintronic devices [BMT+18].

7.5 Proofs

In this section, we collect the proofs of the propositions claimed throughout this chapter.

7.5.1 Static problem

We start with showing the weak sequential lower semicontinuity of the energy functional.

Proposition 7.5.1. *The energy functional* (7.1) *is weakly sequentially lower semicontinuous in* $\boldsymbol{H}^1(\Omega) \times \boldsymbol{H}^1(\Omega)$*, i.e., if* $\{(\boldsymbol{m}_{1,k}, \boldsymbol{m}_{2,k})\}_{k\in\mathbb{N}} \subset \boldsymbol{H}^1(\Omega) \times \boldsymbol{H}^1(\Omega)$ *and* $(\boldsymbol{m}_1, \boldsymbol{m}_2) \in \boldsymbol{H}^1(\Omega) \times \boldsymbol{H}^1(\Omega)$ *are such that* $(\boldsymbol{m}_{1,k}, \boldsymbol{m}_{2,k}) \rightharpoonup (\boldsymbol{m}_1, \boldsymbol{m}_2)$ *in* $\boldsymbol{H}^1(\Omega) \times \boldsymbol{H}^1(\Omega)$ *as* $k \to \infty$*, then* $\mathcal{E}[\boldsymbol{m}_1, \boldsymbol{m}_2] \leq \liminf_{k\to\infty} \mathcal{E}[\boldsymbol{m}_{1,k}, \boldsymbol{m}_{2,k}]$.

The result is a special case of the following lemma.

Lemma 7.5.2. *Let* V *and* H *two Hilbert spaces such that* $V \subset H$ *with compact inclusion. Let* $a : V \times V \to \mathbb{R}$ *be a continuous bilinear form satisfying a so-called*

Gårding inequality, i.e., there exists $C_1 > 0$ and $C_2 \in \mathbb{R}$ such that

$$a(v,v) \geq C_1 \|v\|_V^2 - C_2 \|v\|_H^2 \quad \text{for all } v \in V. \tag{7.27}$$

Then, the quadratic functional $\mathcal{J} : V \to \mathbb{R}$ defined by $\mathcal{J}[v] := a(v,v)$ for all $v \in V$ is weakly sequentially lower semicontinuous in V, i.e., if $\{v_k\}_{k\in\mathbb{N}} \subset V$ and $v \in V$ are such that $v_k \rightharpoonup v$ in V as $k \to \infty$, then $\mathcal{J}[v] \leq \liminf_{k\to\infty} \mathcal{J}[v_k]$.

Proof. Let $\{v_k\}_{k\in\mathbb{N}} \subset V$ and $v \in V$ be such that $v_k \rightharpoonup v$ in V as $k \to \infty$. From the compact inclusion $V \subset H$, it follows that $v_k \to v$ in H. Using (7.27), we see that

$$\begin{aligned} C_1 \|v - v_k\|_V^2 - C_2 \|v - v_k\|_H^2 &\leq a(v - v_k, v - v_k) \\ &= a(v,v) - a(v_k,v) - a(v,v_k) + a(v_k,v_k). \end{aligned}$$

We now take the lim-inf as $k \to \infty$ of this inequality. For the left-hand side we have that

$$\liminf_{k\to\infty} \left(C_1 \|v - v_k\|_V^2 - C_2 \|v - v_k\|_H^2 \right) \geq 0.$$

For the right-hand side, noting that $v_k \rightharpoonup v$ in V implies that $a(v_k, v) \to a(v,v)$ as $k \to \infty$, we have that

$$\begin{aligned} \liminf_{k\to\infty} \left[a(v,v) - a(v_k,v) - a(v,v_k) + a(v_k,v_k) \right] &= -a(v,v) + \liminf_{k\to\infty} a(v_k,v_k) \\ &= -\mathcal{J}[v] + \liminf_{k\to\infty} \mathcal{J}[v_k]. \end{aligned}$$

This shows that $\mathcal{J}[v] \leq \liminf_{k\to\infty} \mathcal{J}[v_k]$ and thus concludes the proof. □

We now prove Theorem 7.3.1 establishing the Γ-convergence of our finite element discretization.

Proof of Theorem 7.3.1. Part (i) of the theorem immediately follows from the weak sequential lower semicontinuity of the energy functional established in Proposition 7.5.1. To show part (ii), let $P_h : \boldsymbol{H}^1(\Omega) \to \mathcal{S}^1(\mathcal{T}_h)^3$ be the quasi-interpolation operator from [SZ90] (applied componentwise). It is well known that P_h is a linear and continuous operator, which is H^1-convergent and satisfies a first-order L^2-convergence property [SZ90]. In particular, given an arbitrary $(\boldsymbol{m}_1, \boldsymbol{m}_2) \in \mathcal{X}$, for all $\ell = 1, 2$ it holds that

$$\begin{aligned} \|P_h \boldsymbol{m}_\ell\|_{\boldsymbol{H}^1(\Omega)} &\leq C \|\boldsymbol{m}_\ell\|_{\boldsymbol{H}^1(\Omega)}, \\ \lim_{h\to 0} \|\boldsymbol{m}_\ell - P_h \boldsymbol{m}_\ell\|_{\boldsymbol{H}^1(\Omega)} &= 0, \\ \|\boldsymbol{m}_\ell - P_h \boldsymbol{m}_\ell\| &\leq Ch \|\boldsymbol{\nabla} \boldsymbol{m}_\ell\|, \end{aligned}$$

where $C > 0$ depends only on the shape-regularity of the mesh. From the triangle inequality, it follows that

$$\left\| \mathcal{I}_h[|P_h \boldsymbol{m}_\ell|^2] - 1 \right\|_{L^1(\Omega)} \leq \left\| \mathcal{I}_h[|P_h \boldsymbol{m}_\ell|^2] - |P_h \boldsymbol{m}_\ell|^2 \right\|_{L^1(\Omega)} + \left\| |P_h \boldsymbol{m}_\ell|^2 - 1 \right\|_{L^1(\Omega)}.$$

For the first term on the right-hand side, the argument used in the proof of [Bar15b, Lemma 7.2], combined with the continuity of P_h, yields that

$$\left\|\mathcal{I}_h[|P_h\boldsymbol{m}_\ell|^2] - |P_h\boldsymbol{m}_\ell|^2\right\|_{L^1(\Omega)} \leq Ch^2 \left\|\boldsymbol{\nabla} P_h\boldsymbol{m}_\ell\right\|^2 \leq Ch^2 \left\|\boldsymbol{m}_\ell\right\|^2_{\boldsymbol{H}^1(\Omega)}.$$

For the second term, using the continuity of Π_h and its L^2-approximation property, we have that

$$\begin{aligned}\left\||P_h\boldsymbol{m}_\ell|^2 - 1\right\|_{L^1(\Omega)} &= \left\||P_h\boldsymbol{m}_\ell|^2 - |\boldsymbol{m}_\ell|^2\right\|_{L^1(\Omega)} \leq \left\|\boldsymbol{m}_\ell + P_h\boldsymbol{m}_\ell\right\| \left\|\boldsymbol{m}_\ell - P_h\boldsymbol{m}_\ell\right\| \\ &\leq \left(\left\|\boldsymbol{m}_\ell\right\| + \left\|P_h\boldsymbol{m}_\ell\right\|\right) \left\|\boldsymbol{m}_\ell - P_h\boldsymbol{m}_\ell\right\| \leq Ch \left\|\boldsymbol{m}_\ell\right\|^2_{\boldsymbol{H}^1(\Omega)}.\end{aligned}$$

Altogether, we thus obtain that

$$\left\|\mathcal{I}_h[|P_h\boldsymbol{m}_\ell|^2] - 1\right\|_{L^1(\Omega)} \leq C(h^2 + h) \left\|\boldsymbol{m}_\ell\right\|^2_{\boldsymbol{H}^1(\Omega)}. \tag{7.28}$$

For all $\delta > 0$, we define $\boldsymbol{m}_{\ell,h,\delta} = P_h[\boldsymbol{m}_\ell]$ for all $\ell = 1, 2$, where $h > 0$ is chosen in such a way that $\left\|\mathcal{I}_h[|P_h\boldsymbol{m}_\ell|^2] - 1\right\|_{L^1(\Omega)} \leq \delta$ (which is possible thanks to (7.28)). Then, $(\boldsymbol{m}_{1,h,\delta}, \boldsymbol{m}_{2,h,\delta})$ belongs to $\mathcal{X}_{h,\delta}$. We thus obtain a sequence $\{(\boldsymbol{m}_{1,h,\delta}, \boldsymbol{m}_{2,h,\delta})\} \subset \mathcal{X}_{h,\delta}$ satisfying the desired convergence properties $(\boldsymbol{m}_{1,h,\delta}, \boldsymbol{m}_{2,h,\delta}) \to (\boldsymbol{m}_1, \boldsymbol{m}_2)$ in $\boldsymbol{H}^1(\Omega) \times \boldsymbol{H}^1(\Omega)$ and $\mathcal{E}_{h,\delta}[\boldsymbol{m}_{1,h,\delta}, \boldsymbol{m}_{2,h,\delta}] \to \mathcal{E}[\boldsymbol{m}_1, \boldsymbol{m}_2]$ as $h, \delta \to 0$ (with the second convergence being a consequence of the first one). This concludes the proof. □

In view of the analysis of the discrete gradient flows presented in Section 7.3, we now introduce the following algorithm.

Algorithm 7.5.3 (general discrete gradient flow)**.** ***Discretization parameters:*** *Mesh size $h > 0$, time-step size $k > 0$, tolerance $\varepsilon > 0$, parameters $0 \leq \theta_1, \theta_2, \theta_3 \leq 1$.*

Input: *Initial guess $(\boldsymbol{m}^0_{1,h}, \boldsymbol{m}^0_{2,h}) \in \mathcal{S}^1(\mathcal{T}_h)^3 \times \mathcal{S}^1(\mathcal{T}_h)^3$ such that, for all $\ell = 1, 2$, $\left|\boldsymbol{m}^0_{\ell,h}(z)\right| = 1$ for all $z \in \mathcal{N}_h$.*

Loop: *For all $i \in \mathbb{N}_0$, iterate* (i)–(ii) *until the stopping criterion* (stop) *is met:*

(i) *Given $(\boldsymbol{m}^i_{1,h}, \boldsymbol{m}^i_{2,h}) \in \mathcal{S}^1(\mathcal{T}_h)^3 \times \mathcal{S}^1(\mathcal{T}_h)^3$, compute $(\boldsymbol{v}^i_{1,h}, \boldsymbol{v}^i_{2,h}) \in \boldsymbol{\mathcal{K}}_h[\boldsymbol{m}^i_{1,h}] \times \boldsymbol{\mathcal{K}}_h[\boldsymbol{m}^i_{2,h}]$ such that, for all $(\boldsymbol{\phi}_{1,h}, \boldsymbol{\phi}_{2,h}) \in \boldsymbol{\mathcal{K}}_h[\boldsymbol{m}^i_{1,h}] \times \boldsymbol{\mathcal{K}}_h[\boldsymbol{m}^i_{2,h}]$ and $\ell = 1, 2$, it holds that*

$$\begin{aligned}&\left\langle \boldsymbol{v}^i_{\ell,h}, \boldsymbol{\phi}_{\ell,h}\right\rangle_{\boldsymbol{\mathcal{H}}} + a_{\ell\ell}\theta_1 k \left\langle \boldsymbol{\nabla}\boldsymbol{v}^i_{\ell,h}, \boldsymbol{\nabla}\boldsymbol{\phi}_{\ell,h}\right\rangle \\ &\qquad + a_{12}\theta_2 k \left\langle \boldsymbol{\nabla}\boldsymbol{v}^i_{3-\ell,h}, \boldsymbol{\nabla}\boldsymbol{\phi}_{\ell,h}\right\rangle - a_0\theta_3 k \left\langle \boldsymbol{v}^i_{3-\ell,h}, \boldsymbol{\phi}_{\ell,h}\right\rangle \\ &\qquad = -a_{\ell\ell} \left\langle \boldsymbol{\nabla}\boldsymbol{m}^i_{\ell,h}, \boldsymbol{\nabla}\boldsymbol{\phi}_{\ell,h}\right\rangle - a_{12} \left\langle \boldsymbol{\nabla}\boldsymbol{m}^i_{3-\ell,h}, \boldsymbol{\nabla}\boldsymbol{\phi}_{\ell,h}\right\rangle \\ &\qquad\qquad + a_0 \left\langle \boldsymbol{m}^i_{3-\ell,h}, \boldsymbol{\phi}_{\ell,h}\right\rangle. \end{aligned} \tag{7.29}$$

(ii) *Define*

$$\boldsymbol{m}^{i+1}_{\ell,h} := \boldsymbol{m}^i_{\ell,h} + k\boldsymbol{v}^i_{\ell,h} \quad \text{for all } \ell = 1, 2. \tag{7.30}$$

(stop) *Stop iterating* (i)–(ii) *if $(\boldsymbol{v}^i_{1,h}, \boldsymbol{v}^i_{2,h}) \in \boldsymbol{\mathcal{K}}_h[\boldsymbol{m}^i_{1,h}] \times \boldsymbol{\mathcal{K}}_h[\boldsymbol{m}^i_{2,h}]$ satisfies*

$$\sum_{\ell=1}^{2} \left(\left\|\boldsymbol{v}^i_{\ell,h}\right\|^2_{\boldsymbol{\mathcal{H}}} + k \left\|\boldsymbol{\nabla}\boldsymbol{v}^i_{\ell,h}\right\|^2\right) \leq \varepsilon^2 \left|\Omega\right|. \tag{7.31}$$

Output: *If $i^* \in \mathbb{N}_0$ denotes the smallest integer satisfying the stopping criterion* (7.31)*, define the approximate stationary point* $(\boldsymbol{m}_{1,h}, \boldsymbol{m}_{2,h}) := (\boldsymbol{m}_{1,h}^{i^*}, \boldsymbol{m}_{2,h}^{i^*})$.

The parameters $0 \leq \theta_1, \theta_2, \theta_3 \leq 1$ modulates the 'degree of implicitness' in the treatment of the three contributions of the energy. It is easy to see that Algorithm 7.3.4 and Algorithm 7.3.5 are special instances of Algorithm 7.5.3, where $\theta_1 = 1$ (backward Euler) and $\theta_2 = \theta_3 = 1/2$ (Crank–Nicolson) in Algorithm 7.3.4, whereas $\theta_1 = 1$ (backward Euler) and $\theta_2 = \theta_3 = 0$ (forward Euler) in Algorithm 7.3.5.

For ease of presentation, in Section 7.3, we have decided not to present Algorithm 7.5.3 in its full generality, but we have restricted ourselves to two of its instances. This has been motivated by the following two reasons: First, we believe that the two proposed cases are the most relevant in practical computations. Second, the properties and the analysis of the algorithm for general $\theta_1, \theta_2, \theta_3$ resemble the ones of the two presented prototypical cases (excluding the combinations involving values $\theta_1, \theta_2 < 1/2$, which require severe restrictions of the form $k = \mathcal{O}(h^2)$ for stability and therefore have been ignored).

In the following proposition, we show well-posedness of each iteration of Algorithm 7.5.3.

Proposition 7.5.4. *Suppose that θ_1, θ_2, θ_3, and k satisfy the following conditions:*

$$\theta_1 > 0, \quad a_{11}a_{22}\theta_1^2 > a_{12}^2\theta_2^2, \quad \text{and} \quad c_{\boldsymbol{\mathcal{H}}}^2 \,|a_0|\, \theta_3 k < 1, \tag{7.32}$$

where a_{11}, a_{22}, a_{12}, and a_0 are the coefficients in (7.1)*, whereas $c_{\boldsymbol{\mathcal{H}}}$ is the constant in* (3.15)*. Then, for all $i \in \mathbb{N}_0$,* (7.29) *admits a unique solution $(\boldsymbol{v}_{1,h}^i, \boldsymbol{v}_{2,h}^i) \in \boldsymbol{\mathcal{K}}_h[\boldsymbol{m}_{1,h}^i] \times \boldsymbol{\mathcal{K}}_h[\boldsymbol{m}_{2,h}^i]$.*

Proof. Let $i \in \mathbb{N}_0$. The sum of the left-hand sides of (7.29) for $\ell = 1, 2$ yields a bilinear form $b_i : (\boldsymbol{\mathcal{K}}_h[\boldsymbol{m}_{1,h}^i] \times \boldsymbol{\mathcal{K}}_h[\boldsymbol{m}_{2,h}^i]) \times (\boldsymbol{\mathcal{K}}_h[\boldsymbol{m}_{1,h}^i] \times \boldsymbol{\mathcal{K}}_h[\boldsymbol{m}_{2,h}^i]) \to \mathbb{R}$, which is defined by

$$\begin{aligned} b_i((\boldsymbol{\psi}_{1,h}, \boldsymbol{\psi}_{2,h}), (\boldsymbol{\phi}_{1,h}, \boldsymbol{\phi}_{2,h})) = {} & \left\langle \boldsymbol{\psi}_{1,h}, \boldsymbol{\phi}_{1,h} \right\rangle_{\boldsymbol{\mathcal{H}}} + \left\langle \boldsymbol{\psi}_{2,h}, \boldsymbol{\phi}_{2,h} \right\rangle_{\boldsymbol{\mathcal{H}}} \\ & + a_{11}\theta_1 k \left\langle \boldsymbol{\nabla}\boldsymbol{\psi}_{1,h}, \boldsymbol{\nabla}\boldsymbol{\phi}_{1,h} \right\rangle + a_{22}\theta_1 k \left\langle \boldsymbol{\nabla}\boldsymbol{\psi}_{2,h}, \boldsymbol{\nabla}\boldsymbol{\phi}_{2,h} \right\rangle \\ & + a_{12}\theta_2 k \left\langle \boldsymbol{\nabla}\boldsymbol{\psi}_{2,h}, \boldsymbol{\nabla}\boldsymbol{\phi}_{1,h} \right\rangle + a_{12}\theta_2 k \left\langle \boldsymbol{\nabla}\boldsymbol{\psi}_{1,h}, \boldsymbol{\nabla}\boldsymbol{\phi}_{2,h} \right\rangle \\ & - a_0\theta_3 k \left\langle \boldsymbol{\psi}_{2,h}, \boldsymbol{\phi}_{1,h} \right\rangle - a_0\theta_3 k \left\langle \boldsymbol{\psi}_{1,h}, \boldsymbol{\phi}_{2,h} \right\rangle \end{aligned}$$

for all $(\boldsymbol{\psi}_{1,h}, \boldsymbol{\psi}_{2,h}), (\boldsymbol{\phi}_{1,h}, \boldsymbol{\phi}_{2,h}) \in \boldsymbol{\mathcal{K}}_h[\boldsymbol{m}_{1,h}^i] \times \boldsymbol{\mathcal{K}}_h[\boldsymbol{m}_{2,h}^i]$. Owing to the second inequality in (3.15), the bilinear form is bounded with respect to the H^1-norm. To show coercivity, for an arbitrary $(\boldsymbol{\phi}_{1,h}, \boldsymbol{\phi}_{2,h}) \in \boldsymbol{\mathcal{K}}_h[\boldsymbol{m}_{1,h}^i] \times \boldsymbol{\mathcal{K}}_h[\boldsymbol{m}_{2,h}^i]$, we first compute

$$\begin{aligned} b_i((\boldsymbol{\phi}_{1,h}, \boldsymbol{\phi}_{2,h}), (\boldsymbol{\phi}_{1,h}, \boldsymbol{\phi}_{2,h})) = {} & \left\|\boldsymbol{\phi}_{1,h}\right\|_{\boldsymbol{\mathcal{H}}}^2 + \left\|\boldsymbol{\phi}_{2,h}\right\|_{\boldsymbol{\mathcal{H}}}^2 - 2a_0\theta_3 k \left\langle \boldsymbol{\phi}_{2,h}, \boldsymbol{\phi}_{1,h} \right\rangle \\ & + a_{11}\theta_1 k \left\|\boldsymbol{\nabla}\boldsymbol{\phi}_{1,h}\right\|^2 + a_{22}\theta_1 k \left\|\boldsymbol{\nabla}\boldsymbol{\phi}_{2,h}\right\|^2 \\ & + 2a_{12}\theta_2 k \left\langle \boldsymbol{\nabla}\boldsymbol{\phi}_{2,h}, \boldsymbol{\nabla}\boldsymbol{\phi}_{1,h} \right\rangle. \end{aligned}$$

The terms involving the gradients of $(\boldsymbol{\phi}_{1,h}, \boldsymbol{\phi}_{2,h})$ make up a quadratic form, which is positive definite if and only if the underlying 2-by-2 matrix is positive definite, which is true if and only if the first two inequalities in (7.32) hold.

Thanks to (3.15), it holds that

$$\left\|\boldsymbol{\phi}_{1,h}\right\|_{\boldsymbol{\mathcal{H}}}^2+\left\|\boldsymbol{\phi}_{2,h}\right\|_{\boldsymbol{\mathcal{H}}}^2-2a_0\theta_3k\left\langle\boldsymbol{\phi}_{2,h},\boldsymbol{\phi}_{1,h}\right\rangle\geq(c_{\boldsymbol{\mathcal{H}}}^{-2}-|a_0|\,\theta_3k)\left(\left\|\boldsymbol{\phi}_{1,h}\right\|^2+\left\|\boldsymbol{\phi}_{2,h}\right\|^2\right).$$

This shows that the L^2-part of the bilinear form is coercive if the third inequality in (7.32) holds.

Hence, we conclude that the bilinear form $b_i(\cdot,\cdot)$ is coercive with respect to the H^1-norm if (7.32) is satisfied. Observing that the sum over $\ell=1,2$ of the right-hand sides of (7.29) defines a bounded linear form, well-posedness of (7.29) then follows from the Lax–Milgram theorem. □

In the following proposition, we establish the discrete energy law satisfied by the approximations generated by Algorithm 7.5.3.

Proposition 7.5.5. *Let θ_1, θ_2, θ_3, and k satisfy the assumptions of Proposition 7.5.4. For all $i\in\mathbb{N}_0$, the iterates of Algorithm 7.5.3 satisfy*

$$\begin{aligned}\mathcal{E}[\boldsymbol{m}_{1,h}^{i+1},\boldsymbol{m}_{2,h}^{i+1}]-\mathcal{E}[\boldsymbol{m}_{1,h}^{i},\boldsymbol{m}_{2,h}^{i}]=-k\sum_{\ell=1}^{2}\left\|\boldsymbol{v}_{\ell,h}^{i}\right\|_{\boldsymbol{\mathcal{H}}}^2-\frac{(2\theta_1-1)}{2}k^2\sum_{\ell=1}^{2}a_{\ell\ell}\left\|\boldsymbol{\nabla}\boldsymbol{v}_{\ell,h}^{i}\right\|^2\\-a_{12}(2\theta_2-1)k^2\left\langle\boldsymbol{\nabla}\boldsymbol{v}_{1,h}^{i},\boldsymbol{\nabla}\boldsymbol{v}_{2,h}^{i}\right\rangle+a_0(2\theta_3-1)k^2\left\langle\boldsymbol{v}_{1,h}^{i},\boldsymbol{v}_{2,h}^{i}\right\rangle.\end{aligned}\tag{7.33}$$

Suppose that θ_1, θ_2, θ_3, and k satisfy also the following conditions:

$$\theta_1\geq1/2,\quad a_{11}a_{22}(2\theta_1-1)^2\geq a_{12}^2(2\theta_2-1)^2,\quad\text{and } c_{\boldsymbol{\mathcal{H}}}^2\,|a_0|\,|2\theta_3-1|\,k\leq2.\tag{7.34}$$

Then, the sequence of energies generated by Algorithm 7.5.3 is monotonically decreasing, i.e., it holds that $\mathcal{E}[\boldsymbol{m}_{1,h}^{i+1},\boldsymbol{m}_{2,h}^{i+1}]\leq\mathcal{E}[\boldsymbol{m}_{1,h}^{i},\boldsymbol{m}_{2,h}^{i}]$ for all $i\in\mathbb{N}_0$.

Proof. Let $i\in\mathbb{N}_0$. Testing (7.29) with $\boldsymbol{\phi}_{\ell,h}=\boldsymbol{v}_{\ell,h}^{i}\in\boldsymbol{\mathcal{K}}_h[\boldsymbol{m}_{\ell,h}^{i}]$ for $\ell=1,2$ and summing the resulting equations, we obtain that

$$\begin{aligned}&\sum_{\ell=1}^{2}\left(\left\|\boldsymbol{v}_{\ell,h}^{i}\right\|_{\boldsymbol{\mathcal{H}}}^2+a_{\ell\ell}\theta_1k\left\|\boldsymbol{\nabla}\boldsymbol{v}_{\ell,h}^{i}\right\|^2\right)+2a_{12}\theta_2k\left\langle\boldsymbol{\nabla}\boldsymbol{v}_{1,h}^{i},\boldsymbol{\nabla}\boldsymbol{v}_{2,h}^{i}\right\rangle-2a_0\theta_3k\left\langle\boldsymbol{v}_{1,h}^{i},\boldsymbol{v}_{2,h}^{i}\right\rangle\\&\quad=\sum_{\ell=1}^{2}\left(-a_{\ell\ell}\left\langle\boldsymbol{\nabla}\boldsymbol{m}_{\ell,h}^{i},\boldsymbol{\nabla}\boldsymbol{v}_{\ell,h}^{i}\right\rangle-a_{12}\left\langle\boldsymbol{\nabla}\boldsymbol{m}_{3-\ell,h}^{i},\boldsymbol{\nabla}\boldsymbol{v}_{\ell,h}^{i}\right\rangle+a_0\left\langle\boldsymbol{m}_{3-\ell,h}^{i},\boldsymbol{v}_{\ell,h}^{i}\right\rangle\right).\end{aligned}\tag{7.35}$$

It follows that

$$\begin{aligned}&\mathcal{E}[\boldsymbol{m}_{1,h}^{i+1},\boldsymbol{m}_{2,h}^{i+1}]\\&\overset{(7.30)}{=}\mathcal{E}[\boldsymbol{m}_{1,h}^{i},\boldsymbol{m}_{2,h}^{i}]+\frac{1}{2}k\sum_{\ell=1}^{2}a_{\ell\ell}\big(2\left\langle\boldsymbol{\nabla}\boldsymbol{m}_{\ell,h}^{i},\boldsymbol{\nabla}\boldsymbol{v}_{\ell,h}^{i}\right\rangle+k\left\|\boldsymbol{\nabla}\boldsymbol{v}_{\ell,h}^{i}\right\|^2\big)\\&\qquad+a_{12}k\Big(\left\langle\boldsymbol{\nabla}\boldsymbol{m}_{1,h}^{i},\boldsymbol{\nabla}\boldsymbol{v}_{2,h}^{i}\right\rangle+\left\langle\boldsymbol{\nabla}\boldsymbol{m}_{2,h}^{i},\boldsymbol{\nabla}\boldsymbol{v}_{1,h}^{i}\right\rangle+k\left\langle\boldsymbol{\nabla}\boldsymbol{v}_{1,h}^{i},\boldsymbol{\nabla}\boldsymbol{v}_{2,h}^{i}\right\rangle\Big)\\&\qquad-a_0k\Big(\left\langle\boldsymbol{m}_{1,h}^{i},\boldsymbol{v}_{2,h}^{i}\right\rangle+\left\langle\boldsymbol{m}_{2,h}^{i},\boldsymbol{v}_{1,h}^{i}\right\rangle+k\left\langle\boldsymbol{v}_{1,h}^{i},\boldsymbol{v}_{2,h}^{i}\right\rangle\Big)\\&\overset{(7.35)}{=}\mathcal{E}[\boldsymbol{m}_{1,h}^{i},\boldsymbol{m}_{2,h}^{i}]-k\sum_{\ell=1}^{2}\left\|\boldsymbol{v}_{\ell,h}^{i}\right\|_{\boldsymbol{\mathcal{H}}}^2-\frac{(2\theta_1-1)}{2}k^2\sum_{\ell=1}^{2}a_{\ell\ell}\left\|\boldsymbol{\nabla}\boldsymbol{v}_{\ell,h}^{i}\right\|^2\\&\qquad-a_{12}(2\theta_2-1)k^2\left\langle\boldsymbol{\nabla}\boldsymbol{v}_{1,h}^{i},\boldsymbol{\nabla}\boldsymbol{v}_{2,h}^{i}\right\rangle+a_0(2\theta_3-1)k^2\left\langle\boldsymbol{v}_{1,h}^{i},\boldsymbol{v}_{2,h}^{i}\right\rangle,\end{aligned}$$

which is (7.33). Arguing as in the proof of Proposition 7.5.4, it is easy to see the right-hand side of (7.33) is nonpositive if the inequalities in (7.34) are satisfied. This shows that the sequence of energies generated by the algorithm is monotonically decreasing and concludes the proof. □

In the following lemma, we prove two auxiliary estimates, which will be useful in the proof of convergence of Algorithm 7.5.3.

Lemma 7.5.6. *For all $\ell = 1, 2$, for all $j \in \mathbb{N}$, the iterates of Algorithm 7.5.3 satisfy*

$$c_{\mathcal{T}}^{-1} \left\| \mathcal{I}_h[\left|\boldsymbol{m}_{\ell,h}^j\right|^2] - 1 \right\|_{L^1(\Omega)} \leq k^2 \sum_{i=0}^{j-1} \left\|\boldsymbol{v}_{\ell,h}^i\right\|^2 \tag{7.36}$$

$$c_{\mathcal{T}}^{-1} \left\|\boldsymbol{m}_{\ell,h}^j\right\|^2 \leq |\Omega| + k^2 \sum_{i=0}^{j-1} \left\|\boldsymbol{v}_{\ell,h}^i\right\|^2, \tag{7.37}$$

where $c_{\mathcal{T}} > 0$ depends only on the shape-regularity of the family of meshes.

Proof. We follow [Bar16]. Let $\ell = 1, 2$ and $j \in \mathbb{N}$. For all $i = 0, \dots, j-1$, from (7.30), since $\boldsymbol{v}_{\ell,h}^i \in \boldsymbol{\mathcal{K}}_h[\boldsymbol{m}_{\ell,h}^i]$, we deduce that $\left|\boldsymbol{m}_{\ell,h}^{i+1}(z)\right|^2 = \left|\boldsymbol{m}_{\ell,h}^i(z)\right|^2 + k^2 \left|\boldsymbol{v}_{\ell,h}^i(z)\right|^2$ for all $z \in \mathcal{N}_h$. Iterating in i and using that $\left|\boldsymbol{m}_{\ell,h}^0(z)\right| = 1$ for all $z \in \mathcal{N}_h$, we obtain that

$$\left|\boldsymbol{m}_{\ell,h}^j(z)\right|^2 = 1 + k^2 \sum_{i=0}^{j-1} \left|\boldsymbol{v}_{\ell,h}^i(z)\right|^2.$$

Then, both (7.36) and (7.37) follow from the equivalence of the L^p-norm of discrete functions with the weighted ℓ^p-norm of the vector collecting their nodal values (with equivalence constants depending only on the shape-regularity of the family of meshes); see, e.g., [Bar15b, Lemma 3.4]. □

In the following lemma, we prove stability of Algorithm 7.5.3.

Lemma 7.5.7. *Let θ_1, θ_2, θ_3, and k satisfy the assumptions of Proposition 7.5.4 as well as the inequalities*

$$\theta_1 > 1/2, \quad a_{11}a_{22}(2\theta_1 - 1)^2 > a_{12}^2(2\theta_2 - 1)^2, \quad \text{and } c_{\boldsymbol{\mathcal{H}}}^2 |a_0| \, |2\theta_3 - 1| \, k < 2. \tag{7.38}$$

Then, there exists a threshold $k_0 > 0$ such that, if $k < k_0$, the iterates of Algorithm 7.5.3 satisfy, for all $j \in \mathbb{N}$, the stability estimate

$$\sum_{\ell=1}^{2} \left\|\boldsymbol{m}_{\ell,h}^j\right\|_{\boldsymbol{H}^1(\Omega)}^2 + k \sum_{i=0}^{j-1} \sum_{\ell=1}^{2} \left\|\boldsymbol{v}_{\ell,h}^i\right\|_{\boldsymbol{\mathcal{H}}}^2 + k^2 \sum_{i=0}^{j-1} \sum_{\ell=1}^{2} \left\|\boldsymbol{\nabla} \boldsymbol{v}_{\ell,h}^i\right\|^2 \leq C \left(1 + \sum_{\ell=1}^{2} \left\|\boldsymbol{m}_{\ell,h}^0\right\|_{\boldsymbol{H}^1(\Omega)}^2\right). \tag{7.39}$$

The threshold k_0 depends on a_0, θ_3, $c_{\boldsymbol{\mathcal{H}}}$, and the shape-regularity of the family of meshes, whereas the constant $C > 0$ depends only on $|\Omega|$, a_{11}, a_{12}, a_{22}, a_0, θ_1, θ_2, θ_3, $c_{\boldsymbol{\mathcal{H}}}$, and the shape-regularity of the family of meshes.

Proof. Let $j \in \mathbb{N}$. For all $i = 0, \dots, j-1$, we apply Proposition 7.5.5, which yields (7.33). Summing (7.33) over $i = 0, \dots, j-1$, we obtain that

$$\begin{aligned}\mathcal{E}[\boldsymbol{m}_{1,h}^j, \boldsymbol{m}_{2,h}^j] + k \sum_{i=0}^{j-1} \sum_{\ell=1}^{2} \left\| \boldsymbol{v}_{\ell,h}^i \right\|_{\boldsymbol{\mathcal{H}}}^2 + \frac{(2\theta_1 - 1)}{2} k^2 \sum_{i=0}^{j-1} \sum_{\ell=1}^{2} a_{\ell\ell} \left\| \boldsymbol{\nabla} \boldsymbol{v}_{\ell,h}^i \right\|^2 \\ + a_{12}(2\theta_2 - 1) k^2 \sum_{i=0}^{j-1} \left\langle \boldsymbol{\nabla} \boldsymbol{v}_{1,h}^i, \boldsymbol{\nabla} \boldsymbol{v}_{2,h}^i \right\rangle - a_0(2\theta_3 - 1) k^2 \sum_{i=0}^{j-1} \left\langle \boldsymbol{v}_{1,h}^i, \boldsymbol{v}_{2,h}^i \right\rangle \\ = \mathcal{E}[\boldsymbol{m}_{1,h}^0, \boldsymbol{m}_{2,h}^0].\end{aligned}$$

Using (7.38) and arguing as in the proof of Proposition 7.5.4, one can show that

$$\mathcal{E}[\boldsymbol{m}_{1,h}^j, \boldsymbol{m}_{2,h}^j] + \lambda_1 k \sum_{i=0}^{j-1} \sum_{\ell=1}^{2} \left\| \boldsymbol{v}_{\ell,h}^i \right\|_{\boldsymbol{\mathcal{H}}}^2 + \lambda_2 k^2 \sum_{i=0}^{j-1} \sum_{\ell=1}^{2} \left\| \boldsymbol{\nabla} \boldsymbol{v}_{\ell,h}^i \right\|^2 \leq \mathcal{E}[\boldsymbol{m}_{1,h}^0, \boldsymbol{m}_{2,h}^0]$$

for some positive values $\lambda_1 = \lambda_1(a_0, \theta_3)$ and $\lambda_2 = \lambda_2(a_{11}, a_{12}, a_{22}, \theta_1, \theta_2)$. From (7.2) and Young's inequality, it follows that

$$\mathcal{E}[\boldsymbol{m}_{1,h}^j, \boldsymbol{m}_{2,h}^j] \geq \lambda_3 \sum_{\ell=1}^{2} \left\| \boldsymbol{\nabla} \boldsymbol{m}_{\ell,h}^j \right\|^2 - \frac{|a_0|}{2} \sum_{\ell=1}^{2} \left\| \boldsymbol{m}_{\ell,h}^j \right\|^2$$

for some $\lambda_3 = \lambda_3(a_{11}, a_{12}, a_{22}) > 0$. Moreover, it holds that

$$\mathcal{E}[\boldsymbol{m}_{1,h}^0, \boldsymbol{m}_{2,h}^0] \leq \lambda_4 \sum_{\ell=1}^{2} \left\| \boldsymbol{m}_{\ell,h}^0 \right\|_{\boldsymbol{H}^1(\Omega)}^2$$

for some $\lambda_4 = \lambda_3(a_{11}, a_{12}, a_{22}, a_0) > 0$. Altogether, we thus obtain that

$$\begin{aligned}\lambda_3 \sum_{\ell=1}^{2} \left\| \boldsymbol{\nabla} \boldsymbol{m}_{\ell,h}^j \right\|^2 - \frac{|a_0|}{2} \sum_{\ell=1}^{2} \left\| \boldsymbol{m}_{\ell,h}^j \right\|^2 \\ + \lambda_1 k \sum_{i=0}^{j-1} \sum_{\ell=1}^{2} \left\| \boldsymbol{v}_{\ell,h}^i \right\|_{\boldsymbol{\mathcal{H}}}^2 + \lambda_2 k^2 \sum_{i=0}^{j-1} \sum_{\ell=1}^{2} \left\| \boldsymbol{\nabla} \boldsymbol{v}_{\ell,h}^i \right\|^2 \\ \leq \lambda_4 \sum_{\ell=1}^{2} \left\| \boldsymbol{m}_{\ell,h}^0 \right\|_{\boldsymbol{H}^1(\Omega)}^2 . \quad (7.40)\end{aligned}$$

From Lemma 7.5.6 and (3.15), we deduce that

$$|a_0| \sum_{\ell=1}^{2} \left\| \boldsymbol{m}_{\ell,h}^j \right\|^2 \leq 2 c_{\mathcal{T}} |a_0| |\Omega| + c_{\mathcal{T}} |a_0| c_{\boldsymbol{\mathcal{H}}} k^2 \sum_{i=0}^{j-1} \sum_{\ell=1}^{2} \left\| \boldsymbol{v}_{\ell,h}^i \right\|_{\boldsymbol{\mathcal{H}}}^2 , \quad (7.41)$$

where $c_{\mathcal{T}} > 0$ is the constant appearing in (7.37) (which depends only on the shape-regularity of the family of meshes). Combining (7.40) and (7.41), we thus

obtain that

$$\lambda_3 \sum_{\ell=1}^{2} \left\|\boldsymbol{\nabla} \boldsymbol{m}_{\ell,h}^{j}\right\|^2 + \frac{|a_0|}{2} \sum_{\ell=1}^{2} \left\|\boldsymbol{m}_{\ell,h}^{j}\right\|^2 + (\lambda_1 - c_{\mathcal{T}} |a_0| \, c_{\boldsymbol{\mathcal{H}}} k) k \sum_{i=0}^{j-1} \sum_{\ell=1}^{2} \left\|\boldsymbol{v}_{\ell,h}^{i}\right\|_{\boldsymbol{\mathcal{H}}}^2 + \lambda_2 k^2 \sum_{i=0}^{j-1} \sum_{\ell=1}^{2} \left\|\boldsymbol{\nabla} \boldsymbol{v}_{\ell,h}^{i}\right\|^2 \leq 2 c_{\mathcal{T}} |a_0| \, |\Omega| + \lambda_4 \sum_{\ell=1}^{2} \left\|\boldsymbol{m}_{\ell,h}^{0}\right\|_{\boldsymbol{H}^1(\Omega)}^2 .$$

Hence, if $k < k_0 := \lambda_1 / (c_{\mathcal{T}} |a_0| \, c_{\boldsymbol{\mathcal{H}}})$, all terms on the left-hand side are nonnegative, and we obtain (7.39), where the (explicitly computable) constant $C > 0$ depends only on $|\Omega|$, a_{11}, a_{12}, a_{22}, a_0, θ_1, θ_2, θ_3, $c_{\boldsymbol{\mathcal{H}}}$, and $c_{\mathcal{T}}$. □

In the following proposition, combining the results we have proved so far, we establish the main properties of Algorithm 7.5.3

Proposition 7.5.8. *Let θ_1, θ_2, θ_3, and k satisfy the assumptions of Lemma 7.5.7. If the time-step size k is sufficiently small, then Algorithm 7.5.3 is well-defined: Each iteration is well-defined and the stopping criterion* (7.31) *is met in a finite number of iterations. In particular, the approximate stationary point $(\boldsymbol{m}_{1,h}, \boldsymbol{m}_{2,h})$ is well-defined. Moreover, for all $\ell = 1, 2$, it holds that*

$$\left\|\mathcal{I}_h[|\boldsymbol{m}_{\ell,h}|^2] - 1\right\|_{L^1(\Omega)} \leq Ck \left(1 + \sum_{\ell=1}^{2} \left\|\boldsymbol{m}_{\ell,h}^{0}\right\|_{\boldsymbol{H}^1(\Omega)}^2\right), \tag{7.42}$$

where the constant $C > 0$ depends only on $|\Omega|$, a_{11}, a_{12}, a_{22}, a_0, θ_1, θ_2, θ_3, $c_{\boldsymbol{\mathcal{H}}}$, and the shape-regularity of the family of meshes.

Proof. The well-posedness of each iteration of the algorithm is a consequence of Proposition 7.5.4. Now, let $k_0 > 0$ be the threshold guaranteed by Lemma 7.5.7. If $k < k_0$, then (7.39) holds. Since the left-hand side of (7.39) is nonnegative and the right-hand side is independent of j, we deduce that the series

$$\sum_{i=0}^{\infty} \sum_{\ell=1}^{2} \left(\left\|\boldsymbol{v}_{\ell,h}^{i}\right\|_{\boldsymbol{\mathcal{H}}}^2 + k \left\|\boldsymbol{\nabla} \boldsymbol{v}_{\ell,h}^{i}\right\|^2\right)$$

is convergent. It follows that $\sum_{\ell=1,2} \left\|\boldsymbol{v}_{\ell,h}^{i}\right\|_{\boldsymbol{\mathcal{H}}}^2 + k \left\|\boldsymbol{\nabla} \boldsymbol{v}_{\ell,h}^{i}\right\|^2 \to 0$ as $i \to \infty$, which guarantees that the stopping criterion (7.31) is satisfied if i is sufficiently large. Estimate (7.42) is a consequence of (7.39) and (7.36) from Lemma 7.5.6. This concludes the proof. □

In the following theorem, we show the convergence of the sequence generated by Algorithm 7.5.3.

Theorem 7.5.9. *Let θ_1 and θ_2 satisfy the inequalities*

$$\theta_1 > 1/2, \quad a_{11} a_{22} \theta_1^2 > a_{12}^2 \theta_2^2, \quad \text{and} \quad a_{11} a_{22} (2\theta_1 - 1)^2 > a_{12}^2 (2\theta_2 - 1)^2.$$

Suppose that there exists $c_0 > 0$, independent of the discretization parameters h, k, and ε, such that

$$\sup_{h>0} \left(\sum_{\ell=1}^{2} \left\|\boldsymbol{m}_{\ell,h}^{0}\right\|_{\boldsymbol{H}^1(\Omega)}^2\right) \leq c_0. \tag{7.43}$$

Suppose that $k \to 0$ and $\varepsilon \to 0$ as $h \to 0$. Then, as $h \to 0$, the sequence of approximate stationary points $\{(\boldsymbol{m}_{1,h}, \boldsymbol{m}_{2,h})\}_{h>0}$ generated by Algorithm 7.5.3, upon extraction of a subsequence, converges weakly in $\boldsymbol{H}^1(\Omega) \times \boldsymbol{H}^1(\Omega)$ toward a point $(\boldsymbol{m}_1, \boldsymbol{m}_2) \in \mathcal{X}$. If $a_{12} = 0$, the limit $(\boldsymbol{m}_1, \boldsymbol{m}_2)$ is a stationary point of the energy functional (7.1).

Proof. Since $k \to 0$, we can assume that it is sufficiently small such that the algorithm is well-defined (cf. Proposition 7.5.8) and that the stability estimate (7.39) holds (cf. Lemma 7.5.7). Together with (7.43), it thus follows that the sequence $\{(\boldsymbol{m}_{1,h}, \boldsymbol{m}_{2,h})\}_{h>0}$ is uniformly bounded in $\boldsymbol{H}^1(\Omega) \times \boldsymbol{H}^1(\Omega)$. Hence, there exists $(\boldsymbol{m}_1, \boldsymbol{m}_2) \in \boldsymbol{H}^1(\Omega) \times \boldsymbol{H}^1(\Omega)$ and a (nonrelabeled) weakly convergent subsequence of $\{(\boldsymbol{m}_{1,h}, \boldsymbol{m}_{2,h})\}_{h>0}$ such that $(\boldsymbol{m}_{1,h}, \boldsymbol{m}_{2,h}) \rightharpoonup (\boldsymbol{m}_1, \boldsymbol{m}_2)$ in $\boldsymbol{H}^1(\Omega) \times \boldsymbol{H}^1(\Omega)$ and $(\boldsymbol{m}_{1,h}, \boldsymbol{m}_{2,h}) \to (\boldsymbol{m}_1, \boldsymbol{m}_2)$ in $\boldsymbol{L}^2(\Omega) \times \boldsymbol{L}^2(\Omega)$. Combining (7.43) with (7.42), we see that, for all $\ell = 1, 2$, $\big\|\mathcal{I}_h[|\boldsymbol{m}_{\ell,h}|^2] - 1\big\|_{L^1(\Omega)} \to 0$ as $h \to 0$. Hence, applying [Bar15b, Lemma 7.2], we obtain that $(\boldsymbol{m}_1, \boldsymbol{m}_2) \in \mathcal{X}$.

To conclude the proof, it remains to show that, if $a_{12} = 0$, $(\boldsymbol{m}_1, \boldsymbol{m}_2) \in \mathcal{X}$ satisfies (7.4). We start with observing that each approximate stationary point $(\boldsymbol{m}_{1,h}, \boldsymbol{m}_{2,h})$ generated by Algorithm 7.5.3 satisfies the variational formulation

$$-a_{\ell\ell} \left\langle \boldsymbol{\nabla} \boldsymbol{m}_{\ell,h}, \boldsymbol{\nabla} \boldsymbol{\phi}_{\ell,h} \right\rangle + a_0 \left\langle \boldsymbol{m}_{3-\ell,h}, \boldsymbol{\phi}_{\ell,h} \right\rangle = \mathcal{R}_{\ell,h}(\boldsymbol{\phi}_{\ell,h})$$

for all $\boldsymbol{\phi}_{\ell,h} \in \boldsymbol{\mathcal{K}}_h[\boldsymbol{m}_{\ell,h}]$ and $\ell = 1, 2$, where the remainder terms on the right-hand side are given by

$$\mathcal{R}_{\ell,h}(\boldsymbol{\phi}_{\ell,h}) = \left\langle \boldsymbol{v}_{\ell,h}^{i^*}, \boldsymbol{\phi}_{\ell,h} \right\rangle_{\boldsymbol{\mathcal{H}}} + a_{\ell\ell}\theta_1 k \left\langle \boldsymbol{\nabla} \boldsymbol{v}_{\ell,h}^{i^*}, \boldsymbol{\nabla} \boldsymbol{\phi}_{\ell,h} \right\rangle - a_0\theta_3 k \left\langle \boldsymbol{v}_{3-\ell,h}^{i^*}, \boldsymbol{\phi}_{\ell,h} \right\rangle$$

and satisfy $\big|\mathcal{R}_{\ell,h}(\boldsymbol{\phi}_{\ell,h})\big| \leq C\varepsilon \big\|\boldsymbol{\phi}_{\ell,h}\big\|_{\boldsymbol{H}^1(\Omega)}$ for all $\boldsymbol{\phi}_{\ell,h} \in \boldsymbol{H}^1(\Omega)$; see equations (7.29) and (7.31). Here, $C > 0$ depends only on a_{11}, a_{22}, a_0, and $|\Omega|$. Note that, since $\varepsilon \to 0$ as $h \to 0$, we have that $\mathcal{R}_{\ell,h} \to 0$ in $\boldsymbol{H}^1(\Omega)^*$ as $h \to 0$. Let $\boldsymbol{\psi} \in \boldsymbol{C}^\infty(\overline{\Omega})$. Choosing the test function $\boldsymbol{\phi}_{\ell,h} = \mathcal{I}_h[\boldsymbol{m}_{\ell,h} \times \boldsymbol{\psi}] \in \boldsymbol{\mathcal{K}}_h[\boldsymbol{m}_{\ell,h}]$ in (7.29) and passing to the limit as $h \to 0$ (using the available convergence results as in the proof of [Bar15b, Theorem 7.6]), we obtain that

$$-a_{\ell\ell} \left\langle \boldsymbol{\nabla} \boldsymbol{m}_\ell, \boldsymbol{m}_\ell \times \boldsymbol{\nabla} \boldsymbol{\psi} \right\rangle + a_0 \left\langle \boldsymbol{m}_{3-\ell}, \boldsymbol{m}_\ell \times \boldsymbol{\psi} \right\rangle = 0 \tag{7.44}$$

for all $\ell = 1, 2$. Since $\boldsymbol{\psi}$ was arbitrary, by density we have that this identity holds for all $\boldsymbol{\psi} \in \boldsymbol{H}^1(\Omega)$. Finally, let $\boldsymbol{\varphi} \in \boldsymbol{H}^1(\Omega) \cap \boldsymbol{L}^\infty(\Omega)$ be arbitrary. Choosing $\boldsymbol{\psi} = \boldsymbol{m}_\ell \times \boldsymbol{\varphi}$ in (7.44) and performing simple algebraic manipulations based on the identities $\boldsymbol{a} \times (\boldsymbol{b} \times \boldsymbol{c}) = (\boldsymbol{a} \cdot \boldsymbol{c})\boldsymbol{b} - (\boldsymbol{a} \cdot \boldsymbol{b})\boldsymbol{c}$ (for all $\boldsymbol{a}, \boldsymbol{b}, \boldsymbol{c} \in \mathbb{R}^3$), $|\boldsymbol{m}_\ell| = 1$ (a.e. in Ω, for all $\ell = 1, 2$) and $\partial_i \boldsymbol{m}_\ell \cdot \boldsymbol{m}_\ell = 0$ (a.e. in Ω, for all $i = 1, 2, 3$ and $\ell = 1, 2$), we obtain that $(\boldsymbol{m}_1, \boldsymbol{m}_2) \in \mathcal{X}$ solves (7.4) for the case $a_{12} = 0$. This shows that $(\boldsymbol{m}_1, \boldsymbol{m}_2)$ is a stationary point of the energy and concludes the proof. □

7.5.2 Dynamic problem

In this section, we aim to present the proofs of the results concerning Algorithm 7.4.1 discussed in Section 7.4. However, for the sake of brevity, we omit

those of Proposition 7.4.2 and Proposition 7.4.3, because they can be obtained following line by line those of Proposition 7.5.4, Proposition 7.5.5, and Lemma 7.5.7. We focus on the proof of the main convergence result.

Proof of Theorem 7.4.4. We follow the argument of the seminal paper on the tangent plane scheme [Alo08], which we adapt in order to take the projection-free update (7.24) (see also [AHP+14, HPP+19]) and the different expression of the energy into account. For the sake of clarity, we split the proof into three steps:

- *Step 1:* Existence of the limit $(\boldsymbol{m}_1, \boldsymbol{m}_2) \in L^\infty(0,\infty;\mathcal{X})$.

Let $T > 0$ be arbitrary. From the stability estimate (7.26) (cf. Proposition 7.4.3), which holds uniformly in h and k (if k is sufficiently small), it follows that, for all $\ell = 1, 2$, the piecewise affine time reconstruction $\boldsymbol{m}_{\ell,hk}$ and the piecewise constant time reconstructions $\boldsymbol{m}^{\pm}_{\ell,hk}$ (defined according to (3.3)) are both uniformly bounded in $L^\infty(0,\infty;\boldsymbol{H}^1(\Omega))$.

Moreover, $\boldsymbol{m}_{\ell,hk}|_{\Omega_T}$ is uniformly bounded in $\boldsymbol{H}^1(\Omega_T)$. By compactness, successive extractions of (nonrelabeled) subsequences and standard Sobolev embeddings yield the existence of $\boldsymbol{m}_1, \boldsymbol{m}_2 \in L^\infty(0,\infty;\boldsymbol{H}^1(\Omega)) \cap \boldsymbol{H}^1(\Omega_T)$ such that, for all $\ell = 1, 2$, as $h, k \to 0$ we have the convergences

- $\boldsymbol{m}_{\ell,hk}|_{\Omega_T} \rightharpoonup \boldsymbol{m}|_{\Omega_T}$ in $\boldsymbol{H}^1(\Omega_T)$,
- $\boldsymbol{m}_{\ell,hk}|_{\Omega_T} \to \boldsymbol{m}|_{\Omega_T}$ in $\boldsymbol{H}^s(\Omega_T)$ for all $s \in (0,1)$,
- $\boldsymbol{m}_{\ell,hk}, \boldsymbol{m}^{\pm}_{\ell,hk} \overset{*}{\rightharpoonup} \boldsymbol{m}_\ell$ in $L^\infty(0,\infty;\boldsymbol{H}^1(\Omega))$,
- $\boldsymbol{m}_{\ell,hk}, \boldsymbol{m}^{\pm}_{\ell,hk} \rightharpoonup \boldsymbol{m}_\ell$ in $L^2(0,\infty;\boldsymbol{H}^1(\Omega))$,
- $\boldsymbol{m}_{\ell,hk}|_{\Omega_T}, \boldsymbol{m}^{\pm}_{\ell,hk}|_{\Omega_T} \to \boldsymbol{m}_\ell$ in $L^2(0,T;\boldsymbol{H}^s(\Omega))$ for all $s \in (0,1)$,
- $\boldsymbol{m}_{\ell,hk}|_{\Omega_T}, \boldsymbol{m}^{\pm}_{\ell,hk}|_{\Omega_T} \to \boldsymbol{m}_\ell$ in $\boldsymbol{L}^2(\Omega_T)$, and pointwise almost everywhere in Ω_T.

From the projection-free updates (7.24), arguing as in the proof of Lemma 7.5.6, we obtain that (7.36) holds for all $\ell = 1, 2$ and for all $j \in \mathbb{N}$, from which it follows (see Step 3 of the proof of [HPP+19, Proposition 6]) that $|\boldsymbol{m}_1| = |\boldsymbol{m}_2| = 1$ a.e. in $\Omega \times (0,\infty)$. This shows that $(\boldsymbol{m}_1, \boldsymbol{m}_2) \in L^\infty(0,\infty;\mathcal{X})$. Finally, from the stability estimate, it also follows that, for all $\ell = 1, 2$, $k\boldsymbol{\nabla}(\partial_t \boldsymbol{m}_{\ell,hk})|_{\Omega_T} \to 0$ in $\boldsymbol{L}^2(\Omega_T)$ as $h, k \to 0$.

- *Step 2:* If $a_{12} = 0$, $(\boldsymbol{m}_1, \boldsymbol{m}_2)$ satisfies the variational formulation (7.11).

Let $\boldsymbol{\varphi} \in \boldsymbol{C}^\infty(\overline{\Omega_T})$ be an arbitrary smooth test function. We consider the smallest integer $j \in \mathbb{N}$ satisfying $T \le jk$ and extend $\boldsymbol{\varphi}$ by zero in (T, t_j). Let $\ell = 1, 2$. For all $i = 0, \dots, j-1$, we choose $\boldsymbol{\phi}_{\ell,h} = \mathcal{I}_h[\boldsymbol{m}^i_{\ell,h} \times \boldsymbol{\varphi}(t_i)] \in \boldsymbol{\mathcal{K}}_h[\boldsymbol{m}^i_h]$ in (7.23), we obtain

$$\begin{aligned}
&\alpha_\ell \left\langle \boldsymbol{v}^i_{\ell,h}, \mathcal{I}_h[\boldsymbol{m}^i_{\ell,h} \times \boldsymbol{\varphi}(t_i)] \right\rangle_h + \left\langle \boldsymbol{m}^i_{\ell,h} \times \boldsymbol{v}^i_{\ell,h}, \mathcal{I}_h[\boldsymbol{m}^i_{\ell,h} \times \boldsymbol{\varphi}(t_i)] \right\rangle_h \\
&\quad + \eta_\ell a_{\ell\ell} k \left\langle \boldsymbol{\nabla} \boldsymbol{v}^i_{\ell,h}, \boldsymbol{\nabla} \mathcal{I}_h[\boldsymbol{m}^i_{\ell,h} \times \boldsymbol{\varphi}(t_i)] \right\rangle \\
&\qquad = -\eta_\ell a_{\ell\ell} \left\langle \boldsymbol{\nabla} \boldsymbol{m}^i_{\ell,h}, \boldsymbol{\nabla} \mathcal{I}_h[\boldsymbol{m}^i_{\ell,h} \times \boldsymbol{\varphi}(t_i)] \right\rangle + \eta_\ell a_0 \left\langle \boldsymbol{m}^i_{3-\ell,h}, \mathcal{I}_h[\boldsymbol{m}^i_{\ell,h} \times \boldsymbol{\varphi}(t_i)] \right\rangle,
\end{aligned}$$

Due to the properties of the mass-lumped scalar product, we can remove the nodal interpolant from the first two terms on the left-hand side without altering the

value of the integrals. Multiplication by k and summation over $i = 0, \dots, j-1$ then yield

$$\begin{aligned}
&\alpha_\ell \int_0^{t_j} \left\langle \partial_t \boldsymbol{m}_{\ell,hk}(t), \boldsymbol{m}^-_{\ell,hk}(t) \times \boldsymbol{\varphi}^-_k(t) \right\rangle_h \mathrm{d}t \\
&\quad + \int_0^{t_j} \left\langle \boldsymbol{m}^-_{\ell,hk}(t) \times \partial_t \boldsymbol{m}_{\ell,hk}(t), \boldsymbol{m}^-_{\ell,hk}(t) \times \boldsymbol{\varphi}^-_k(t) \right\rangle_h \mathrm{d}t \\
&\qquad + \eta_\ell a_{\ell\ell} k \int_0^{t_j} \left\langle \boldsymbol{\nabla} \partial_t \boldsymbol{m}_{\ell,hk}(t), \boldsymbol{\nabla} \mathcal{I}_h[\boldsymbol{m}^-_{\ell,hk}(t) \times \boldsymbol{\varphi}^-_k(t)] \right\rangle \mathrm{d}t \\
&\qquad\quad = -\eta_\ell a_{\ell\ell} \int_0^{t_j} \left\langle \boldsymbol{\nabla} \boldsymbol{\varphi}^-_k(t), \boldsymbol{\nabla} \mathcal{I}_h[\boldsymbol{m}^-_{\ell,hk}(t) \times \boldsymbol{\varphi}^-_k(t)] \right\rangle \mathrm{d}t \\
&\qquad\qquad + \eta_\ell a_0 \int_0^{t_j} \left\langle \boldsymbol{m}^-_{3-\ell,hk}(t), \mathcal{I}_h[\boldsymbol{m}^-_{\ell,hk}(t) \times \boldsymbol{\varphi}^-_k(t)] \right\rangle \mathrm{d}t,
\end{aligned}$$

where we note that we have rewritten the equation in terms of the time reconstructions (3.3). Using (3.4) and the approximation properties (3.6) of the nodal interpolant, in all integrals we substitute the mass-lumped inner products by L^2-products and remove the nodal interpolant (see [Alo08]). Moreover, exploiting the fact that the integrands are all uniformly bounded, we modify the domain in integration in time from $(0, t_j)$ to $(0, T)$. All these actions generate an error which goes to zero in the limit as $h, k \to 0$. In particular, we obtain

$$\begin{aligned}
&\alpha_\ell \int_0^{T} \left\langle \partial_t \boldsymbol{m}_{\ell,hk}(t), \boldsymbol{m}^-_{\ell,hk}(t) \times \boldsymbol{\varphi}^-_k(t) \right\rangle \mathrm{d}t \\
&\quad + \int_0^{T} \left\langle \boldsymbol{m}^-_{\ell,hk}(t) \times \partial_t \boldsymbol{m}_{\ell,hk}(t), \boldsymbol{m}^-_{\ell,hk}(t) \times \boldsymbol{\varphi}^-_k(t) \right\rangle \mathrm{d}t \\
&\qquad + \eta_\ell a_{\ell\ell} k \int_0^{T} \left\langle \boldsymbol{\nabla} \partial_t \boldsymbol{m}_{\ell,hk}(t), \boldsymbol{\nabla} [\boldsymbol{m}^-_{\ell,hk}(t) \times \boldsymbol{\varphi}^-_k(t)] \right\rangle \mathrm{d}t \\
&\qquad\quad = -\eta_\ell a_{\ell\ell} \int_0^{T} \left\langle \boldsymbol{\nabla} \boldsymbol{\varphi}^-_k(t), \boldsymbol{\nabla} [\boldsymbol{m}^-_{\ell,hk}(t) \times \boldsymbol{\varphi}^-_k(t)] \right\rangle \mathrm{d}t \\
&\qquad\qquad + \eta_\ell a_0 \int_0^{T} \left\langle \boldsymbol{m}^-_{3-\ell,hk}(t), \boldsymbol{m}^-_{\ell,hk}(t) \times \boldsymbol{\varphi}^-_k(t) \right\rangle \mathrm{d}t + o(1).
\end{aligned}$$

Using the convergence results available from Step 1, we can pass this formulation to the limit as $h, k \to 0$ and obtain that the last term on the left-hand side goes to zero, whereas all other terms converge toward the corresponding ones in (7.11).

For the details of the argument, we refer to [Alo08] for all terms but the second one on the left-hand side, which, due to the omission of the nodal projection from (7.24), requires a more careful treatment (see Step 2 of the proof of [HPP+19, Theorem 1]). This shows that, for all $\ell = 1, 2$, $\boldsymbol{m}_\ell$ satisfies (7.11) for all $\boldsymbol{\varphi} \in \boldsymbol{C}^\infty(\overline{\Omega_T})$. By density, the result then holds for all $\boldsymbol{\varphi} \in \boldsymbol{H}^1(\Omega_T)$.

- *Step 3:* $(\boldsymbol{m}_1, \boldsymbol{m}_2)$ satisfies the energy inequality (7.12).

We start from the discrete energy law (7.25) established in Proposition 7.4.3. Using (7.2) and a combination of Cauchy–Schwarz' and Young's inequalities, we

obtain that

$$\mathcal{E}[\boldsymbol{m}_{1,h}^j, \boldsymbol{m}_{2,h}^j] + k \sum_{i=0}^{j-1} \sum_{\ell=1}^{2} \left(\frac{\alpha_\ell}{\eta_\ell} - \frac{|a_0|\, k}{2} \right) \left\| \boldsymbol{v}_{\ell,h}^i \right\|_h^2 + \lambda k^2 \sum_{i=0}^{j-1} \sum_{\ell=1}^{2} \left\| \boldsymbol{\nabla} \boldsymbol{v}_{\ell,h}^i \right\|^2 \leq \mathcal{E}[\boldsymbol{m}_{1,h}^0, \boldsymbol{m}_{2,h}^0],$$

where $\lambda > 0$ is the minimum eigenvalue of the 2×2 matrix $\left(\begin{smallmatrix} a_{11} & a_{12} \\ a_{12} & a_{22} \end{smallmatrix}\right)$. The last term on the left-hand side is nonnegative and can be omitted. Rewriting the inequality in terms of the time reconstructions (3.3), we get

$$\mathcal{E}[\boldsymbol{m}_{1,hk}^+(T), \boldsymbol{m}_{2,hk}^+(T)] + \sum_{\ell=1}^{2} \left(\frac{\alpha_\ell}{\eta_\ell} - \frac{|a_0|\, k}{2} \right) \int_0^T \left\| \partial_t \boldsymbol{m}_{\ell,hk}(t) \right\|_h^2 \, \mathrm{d}t \leq \mathcal{E}[\boldsymbol{m}_{1,hk}^-(0), \boldsymbol{m}_{2,hk}^-(0)].$$

Passing to the limit as $h, k \to 0$, using the convergence results available from Step 1, standard lower semicontinuity arguments yield (7.12). This concludes the proof. □

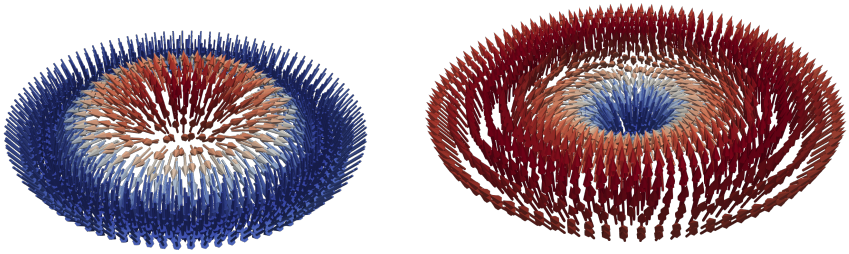

(a) $\boldsymbol{m}_{h,1}$, $a_0 < 0$, AFM initial guess

(b) $\boldsymbol{m}_{h,2}$, $a_0 < 0$, AFM initial guess

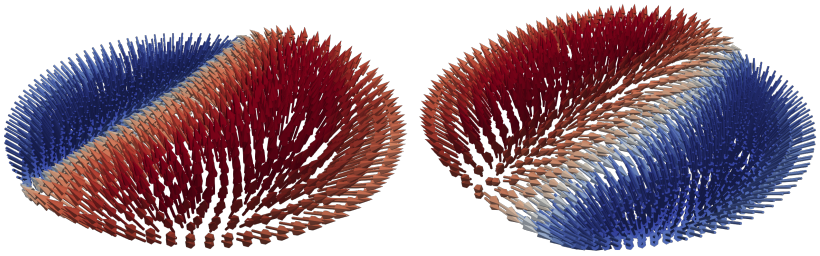

(c) $\boldsymbol{m}_{h,1}$, $a_0 < 0$, FM initial guess

(d) $\boldsymbol{m}_{h,2}$, $a_0 < 0$, FM initial guess

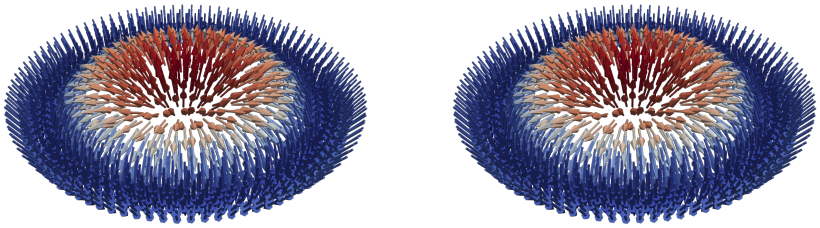

(e) $\boldsymbol{m}_{h,1}$, $a_0 > 0$, FM initial guess

(f) $\boldsymbol{m}_{h,2}$, $a_0 > 0$, FM initial guess

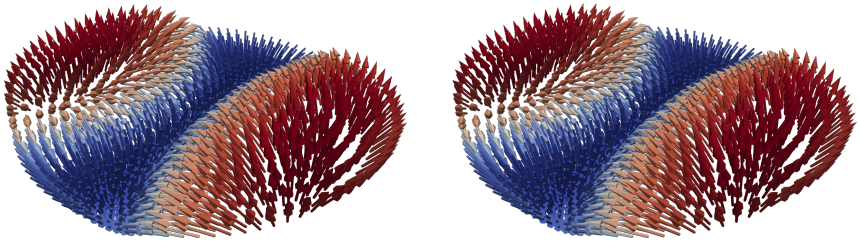

(g) $\boldsymbol{m}_{h,1}$, $a_0 > 0$, AFM initial guess

(h) $\boldsymbol{m}_{h,2}$, $a_0 > 0$, AFM initial guess

Figure 7.3: Experiments of Sections 7.3.3.2-7.3.3.3: Stable configurations computed using Algorithm 7.3.5 with H^1-metric, using varied initial guess (cf. Figure 7.2), and positive or negative a_0. In the pictures, the colour scale refers to the third component of the fields, which attains values between -1 (blue) and 1 (red).

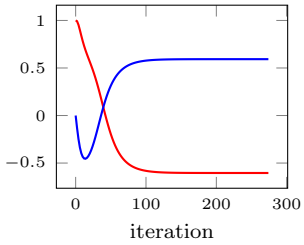

(a) Alg. 7.3.5, $\alpha = 1$.

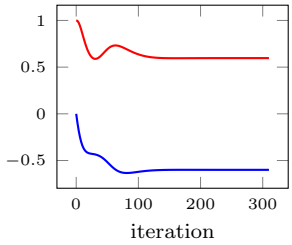

(b) Alg. 7.4.1, $\alpha = 1$.

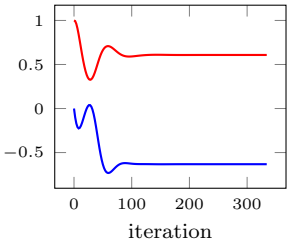

(c) Alg. 7.4.1, $\alpha = 1/2$.

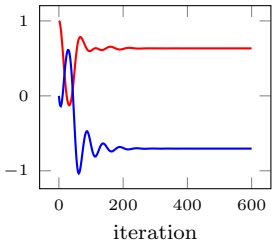

(d) Alg. 7.4.1, $\alpha = 1/4$.

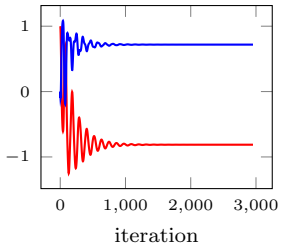

(e) Alg. 7.4.1, $\alpha = 1/8$.

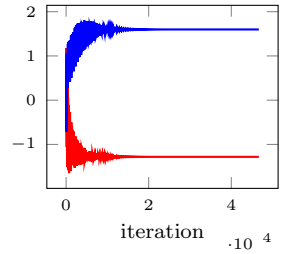

(f) Alg. 7.4.1, $\alpha = 1/16$.

Figure 7.4: Experiment of Section 7.4.2: Evolution of $\langle \boldsymbol{m}_1(t) \cdot \boldsymbol{e}_1 \rangle$ (red) and $\langle \boldsymbol{m}_2(t) \cdot \boldsymbol{e}_1 \rangle$ (blue). (a) Algorithm 7.3.5 with mass-lumped L^2-metric and $\alpha = 1$. (b)–(f) Algorithm 7.4.1 with $\alpha = 1, 1/2, 1/4, 1/8, 1/16$.

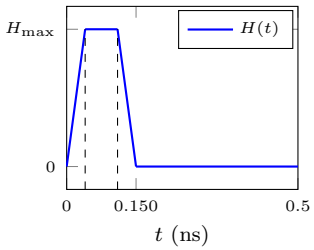

(a) Applied pulse field.

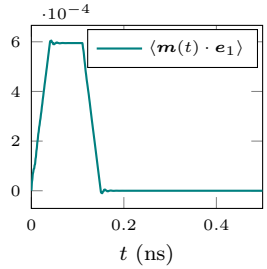

(b) AFM coupling.

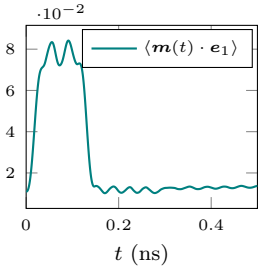

(c) FM coupling.

Figure 7.5: Experiment of Section 7.4.2.2: (a) Structure of the applied pulse field. (b) Time evolution of $\langle \boldsymbol{m}(t) \cdot \boldsymbol{e}_1 \rangle$ for an AFM material. (c) Time evolution of $\langle \boldsymbol{m}(t) \cdot \boldsymbol{e}_1 \rangle$ for an FM material.

Chapter 8

Ultrafast Dynamics

8.1 Introduction

In recent years, significant interest has developed on the dynamics of magnetization at extremely small timescales. Previous work in this area has focused either on basic tangent plane schemes, which suffer from significant artificial damping and the requirement of weakly acute meshes, or non-linear iterative methods that rely on CFL conditions for their solvability. In this chapter, we make the following novel contributions:

- We design and analyse a fully discrete numerical scheme for the iLLG initial value problem, parameterized by an interpolation parameter β between BDF2 and BDF1 for the acceleration term. This algorithm is a novel improvement upon previous work [Rug22], improving the energetic behaviour of the first-order tangent plane scheme therein described. Moreoever, our method suggests a second-order in time method for the iLLG problem.
- For $\beta \in (0, 1]$ the scheme stated below is unconditionally stable, and the unit length constraint violation is unconditionally of second-order in time thanks to a BDF2 scheme for the magnetization and exploting the improved time regularity from the iLLG equation. Under a discrete time regularity condition and stationary initial condition, the unit length constraint violation is super-second-order in time. Lastly, the discrete scheme is fully linear for every $\beta \in [0, 1]$, and does not require weakly acute meshes for stability.
- We prove that under a suitable CFL-like condition, a weakly convergent subsequence approaches a solution of the iLLG problem. This provides another constructive proof of existence of weak solutions to iLLG.
- Numerical experiments demonstrate our theoretical results.
- We include numerical experiments for the fully BDF2 scheme with $\beta = 0$, which we conjecture to be formally second-order in time.

8.2 Model problem

Consider a ferromagnetic body $\Omega \subset \mathbb{R}^3$, let $T > 0$ and define $\Omega_T = \Omega \times [0, T]$. If we consider subpicosecond time scales, when ultrafast motion is taken into account, the time evolution of the magnetization $\boldsymbol{m} \in \mathbb{S}^2 := \{\boldsymbol{x} \in \mathbb{R}^3 \colon |\boldsymbol{x}| = 1\}$, satisfying the unit length constraint $|\boldsymbol{m}| = 1$, is governed by the inertial Landau–Lifshitz–Gilbert (iLLG) equation: Find $\boldsymbol{m}(t) \colon \Omega_T \to \mathbb{S}^2$ such that

$$\partial_t \boldsymbol{m} = -\boldsymbol{m} \times \boldsymbol{h}_{\text{eff}}[\boldsymbol{m}] + \alpha \boldsymbol{m} \times \partial_t \boldsymbol{m} + \tau \boldsymbol{m} \times \partial_{tt} \boldsymbol{m} \quad \text{in} \quad \Omega \times [0, T], \tag{8.1a}$$

$$\partial_{\boldsymbol{n}} \boldsymbol{m} = \boldsymbol{0} \quad \text{on} \quad \partial\Omega \times [0, T], \tag{8.1b}$$

$$\boldsymbol{m}(0) = \boldsymbol{m}^0 \quad \text{in} \quad \Omega, \tag{8.1c}$$

$$\partial_t \boldsymbol{m}(0) = \boldsymbol{v}^0 \quad \text{in} \quad \Omega. \tag{8.1d}$$

Here, $\tau > 0$ is the angular momentum relaxation time (in seconds) and $\alpha > 0$ denotes the dimensionless Gilbert damping parameter. The right-hand side of (8.1a) includes, beyond the classical precession and damping terms an additional term with the second time derivative of the magnetization. This extra term is responsible for nutation dynamics: rapid oscillations of the magnetization superimposed on the slower damped precession, occurring at much higher frequencies. Note that setting formally $\tau = 0$ in (8.1a) recovers the classical LLG equation.

The initial condition satisfies $|\boldsymbol{m}^0| = 1$, with the compatibility condition $\boldsymbol{m}^0 \cdot \boldsymbol{v}^0 = 0$. Noting that for $t \in [0, T]$

$$\frac{\mathrm{d}}{\mathrm{d}t} |\boldsymbol{m}(t)|^2 = 2\boldsymbol{m}(t) \cdot \partial_t \boldsymbol{m}(t) \overset{(8.1a)}{=} 0,$$

we see that the magnitude of $\boldsymbol{m}$ is conserved, and if $|\boldsymbol{m}^0| = 1$ we have that $|\boldsymbol{m}(t)| = 1$ for all time $t \in [0, T]$. Here we consider only the highest order contribution to the energy, the exchange energy, given by

$$\mathcal{E}[\boldsymbol{m}] = \frac{1}{2} \int_\Omega |\boldsymbol{\nabla} \boldsymbol{m}|^2 \, \mathrm{d}\boldsymbol{x}, \tag{8.2}$$

so that it holds that

$$\boldsymbol{h}_{\text{eff}}[\boldsymbol{m}] = -\frac{\delta \mathcal{E}[\boldsymbol{m}]}{\delta \boldsymbol{m}} = \boldsymbol{\Delta} \boldsymbol{m}. \tag{8.3}$$

As opposed to the LLG equation, the iLLG equation is associated with a "kinetic energy", given by $\tau \left\| \partial_t \boldsymbol{m} \right\|^2 / 2$, which motivates the definition of the extended energy functional [Rug22]

$$\mathcal{J}[\boldsymbol{m}, \boldsymbol{\phi}] = \mathcal{E}[\boldsymbol{m}] + \frac{\tau}{2} \left\| \boldsymbol{\phi} \right\|^2. \tag{8.4}$$

Within the kinematic framework, the quantity $\mathcal{J}[\boldsymbol{m}, \partial_t \boldsymbol{m}]$ can be interpreted as the total energy of the magnetization, consisting of the potential energy $\mathcal{E}[\boldsymbol{m}]$ and the kinetic energy $\tau \left\| \partial_t \boldsymbol{m} \right\|^2 / 2$. Sufficiently smooth solutions to the iLLG equation satisfy a dissipative energy law

$$\frac{\mathrm{d}}{\mathrm{d}t} \mathcal{J}[\boldsymbol{m}, \partial_t \boldsymbol{m}] = -\alpha \int |\partial_t \boldsymbol{m}|^2 \mathrm{d}\boldsymbol{x} \leq 0 \tag{8.5}$$

which is interpreted as the total energy of the system being non-increasing in time, where the dissipation is modulated by the Gilbert α parameter. The definition of a weak solution is the following, from [Rug22]:

Definition 8.2.1 (Weak solution)**.** *Let $\boldsymbol{m}^0 \in \boldsymbol{H}^1(\Omega;\mathbb{S}^2)$ and $\boldsymbol{v}^0 \in \boldsymbol{L}^2(\Omega)$ such that $\boldsymbol{m}^0 \cdot \boldsymbol{v}^0 = 0$ a.e. in Ω. A vector field $\boldsymbol{m} : \Omega \times (0,\infty) \to \mathbb{R}^3$ is called a* global weak solution *of iLLG (8.1) if $\boldsymbol{m} \in L^\infty(0,\infty;\boldsymbol{H}^1(\Omega)) \cap W^{1,\infty}(0,\infty;\boldsymbol{L}^2(\Omega))$ and, for all $T > 0$, the following properties are satisfied:*

(i) $\boldsymbol{m} \in \boldsymbol{H}^1(\Omega_T) \quad \text{and} \quad |\boldsymbol{m}| = 1 \quad \text{a.e. in} \quad \Omega_T$;

(ii) $\boldsymbol{m}(0) = \boldsymbol{m}^0$ *and* $\partial_t \boldsymbol{m}(0) = \boldsymbol{v}^0$ *in the sense of traces;*

(iii) For all $\boldsymbol{\phi} \in C_c^\infty([0,T);\boldsymbol{H}^1(\Omega))$, it holds that

$$\begin{aligned}\int_0^T \langle \partial_t \boldsymbol{m}(t), \boldsymbol{\phi}(t)\rangle \,\mathrm{d}t = &- \int_0^T \langle \boldsymbol{h}_{\mathrm{eff}}[\boldsymbol{m}(t)], \boldsymbol{\phi}(t) \times \boldsymbol{m}(t)\rangle \,\mathrm{d}t \\ &+ \alpha \int_0^T \langle \boldsymbol{m}(t) \times \partial_t \boldsymbol{m}(t), \boldsymbol{\phi}(t)\rangle \,\mathrm{d}t \\ &- \tau \int_0^T \langle \boldsymbol{m}(t) \times \partial_t \boldsymbol{m}(t), \partial_t \boldsymbol{\phi}(t)\rangle \,\mathrm{d}t \\ &- \tau \left\langle \boldsymbol{m}^0 \times \boldsymbol{v}^0, \boldsymbol{\phi}(0)\right\rangle ;\end{aligned} \tag{8.6}$$

(iv) It holds that

$$\mathcal{J}[\boldsymbol{m}(T), \partial_t \boldsymbol{m}(T)] + \alpha \int_0^T \|\partial_t \boldsymbol{m}(t)\|^2 \,\mathrm{d}t \le \mathcal{J}[\boldsymbol{m}^0, \boldsymbol{v}^0]. \tag{8.7}$$

Equation (8.6) is based on a variational formulation of (8.1) over the space-time domain Ω_T, and is derived by integrating by parts in time, which reduces the regularity requirements on $\boldsymbol{m}$. In particular, we use the identity

$$\partial_t(\boldsymbol{m} \times \partial_t \boldsymbol{m}) = \partial_t \boldsymbol{m} \times \partial_t \boldsymbol{m} + \boldsymbol{m} \times \partial_{tt} \boldsymbol{m} = \boldsymbol{m} \times \partial_{tt} \boldsymbol{m}.$$

Inequality (8.7) is a weak energy law, being the weak counterpart of the energy law (8.5).

8.3 Preliminaries

In this section, we collect some notation and preliminary results that will be necessary to introduce and analyse the fully discrete algorithm we propose to approximate solutions to the initial boundary value problem (8.1). For general preliminaries, see Chapter 3.

8.3.1 Time discretization

Let $0 = t_0 < t_1 < \cdots < t_N = T$ be a uniform partition of the time interval into N uniform intervals with constant time-step size $k = T/N$, i.e. $t_j = jk$

for all $j = 0, \dots, N$. Let x and y be elements of a general inner product space. Given values $\{\phi^j\}_{0\le j\le N}$ and $\dot\phi^0$, we define the BDF2 second-order time derivative approximation, given for $j \ge 2$ by

$$\dot\phi^j = \frac{1}{2k}(3\phi^j - 4\phi^{j-1} + \phi^{j-2}), \tag{8.8}$$

which implies that

$$\phi^j = \frac{1}{3}(4\phi^{j-1} - \phi^{j-2} + 2k\dot\phi^j). \tag{8.9}$$

Moreover, defining $\Phi^j := (\phi^j, \phi^{j-1})$ it is possible to define the BDF2-adapted G-norm

$$|\Phi^j|_G^2 = (G\Phi^j)\cdot\Phi^j = g_{11}|\phi^j|^2 + 2g_{12}\phi^j\cdot\phi^{j-1} + g_{22}|\phi^{j-1}|^2 \tag{8.10}$$

via the symmetric matrix $G = (g_{ij})$ with entries $g_{11} = 5/4, g_{12} = -1/2, g_{22} = 1/4$. This symmetric positive definite matrix has eigenvalues $\mu_\pm = (3\pm2\sqrt{2})/4$, yielding the norm equivalence,

$$\mu_-(|x|^2 + |y|^2) \le |(x,y)|_G^2 \le \mu_+(|x|^2 + |y|^2). \tag{8.11}$$

Moreover as in [ABP24], the G norm satisfies the identities,

$$\dot\phi^j\cdot\phi^j = \mathrm{d}_t|\Phi^j|_G^2 + \frac{k^3}{4}|\mathrm{d}_t^2\phi^j|^2, \tag{8.12}$$

$$|(x,y)|_G^2 = \frac{3}{4}|x|^2 - \frac{1}{4}|y^2| + \frac{1}{2}|x-y|^2. \tag{8.13}$$

8.4 Algorithm and main results

We will now present the full-discretization algorithm to approximate solutions to the iLLG equation (8.1), along with the main results. The proofs are postponed to Section 8.6.

Firstly, we make the following assumptions on the initial data of the problem (8.1):

(A1) $\boldsymbol{m}_h^0 \in \boldsymbol{\mathcal{M}}_h$ satisfies $\boldsymbol{m}_h^0 \to \boldsymbol{m}^0$ in $\boldsymbol{H}^1(\Omega)$ as $h \to 0$;

(A2) $\boldsymbol{v}_h^0 \in \boldsymbol{\mathcal{K}}_h(\boldsymbol{m}_h^0)$ satisfies $\boldsymbol{v}_h^0 \to \boldsymbol{v}^0$ in $\boldsymbol{L}^2(\Omega)$ as $h \to 0$.

Algorithm 8.4.1. ***Input:*** *Conforming mesh $\mathcal{T}_h$ of Ω, $\boldsymbol{m}_h^0 \in \boldsymbol{\mathcal{M}}_h$, $\boldsymbol{v}_h^0 \in \boldsymbol{\mathcal{K}}_h(\boldsymbol{m}_h^0)$, $\beta \in (0,1]$, $T > 0$, $N \in \mathbb{N}$, $k := T/N$, and $t_j := jk$ for all $j = 0, \dots, N$.*

i For $j = 0$

(a) Compute $\boldsymbol{v}_h^1 \in \boldsymbol{\mathcal{K}}_h(\boldsymbol{m}_h^0)$ such that, for all $\boldsymbol{\phi}_h \in \boldsymbol{\mathcal{K}}_h(\boldsymbol{m}_h^0)$,

$$\begin{aligned}\tau\left\langle \mathrm{d}_t\boldsymbol{v}_h^1, \boldsymbol{\phi}_h\right\rangle + \alpha\left\langle \boldsymbol{v}_h^1, \boldsymbol{\phi}_h\right\rangle \\ + \left\langle \boldsymbol{m}_h^0\times\boldsymbol{v}_h^1, \boldsymbol{\phi}_h\right\rangle + k\left\langle \boldsymbol{\nabla}\boldsymbol{v}_h^1, \boldsymbol{\nabla}\boldsymbol{\phi}_h\right\rangle = -\left\langle \boldsymbol{\nabla}\boldsymbol{m}_h^0, \boldsymbol{\nabla}\boldsymbol{\phi}_h\right\rangle\end{aligned} \tag{8.14}$$

(b) Set $\boldsymbol{m}_h^1 := \boldsymbol{m}_h^0 + k\boldsymbol{v}_h^1$.

(ii) For $j = 1, \dots, N-1$, repeat the following steps (a)–(c):

(a) Set $\widehat{\boldsymbol{m}}_h^{j+1} = 2\boldsymbol{m}_h^j - \boldsymbol{m}_h^{j-1}$.

(b) Compute $\boldsymbol{v}_h^{j+1} \in \boldsymbol{\mathcal{K}}_h(\widehat{\boldsymbol{m}}_h^{j+1})$ *such that, for all* $\boldsymbol{\phi}_h \in \boldsymbol{\mathcal{K}}_h(\widehat{\boldsymbol{m}}_h^{j+1})$,

$$\begin{aligned} &\beta\tau \left\langle \mathrm{d}_t \boldsymbol{v}_h^{j+1}, \boldsymbol{\phi}_h \right\rangle \\ &\quad + (1-\beta)\frac{\tau}{k}\left\langle \frac{3}{2}\boldsymbol{v}_h^{j+1} - 2\boldsymbol{v}_h^j + \frac{1}{2}\boldsymbol{v}_h^{j-1}, \boldsymbol{\phi}_h \right\rangle + \alpha \left\langle \boldsymbol{v}_h^{j+1}, \boldsymbol{\phi}_h \right\rangle \\ &\quad + \left\langle \widehat{\boldsymbol{m}}_h^{j+1} \times \boldsymbol{v}_h^{j+1}, \boldsymbol{\phi}_h \right\rangle + \frac{2}{3}k \left\langle \boldsymbol{\nabla}\boldsymbol{v}_h^{j+1}, \boldsymbol{\nabla}\boldsymbol{\phi}_h \right\rangle \\ &\quad = -\frac{1}{3}\left\langle \boldsymbol{\nabla}(4\boldsymbol{m}_h^j - \boldsymbol{m}_h^{j-1}), \boldsymbol{\nabla}\boldsymbol{\phi}_h \right\rangle. \end{aligned} \tag{8.15}$$

(c) Set $\boldsymbol{m}_h^{j+1} = \frac{4}{3}\boldsymbol{m}_h^j - \frac{1}{3}\boldsymbol{m}_h^{j-1} + \frac{2}{3}k\boldsymbol{v}_h^{j+1}$.

Output: *Sequences* $\boldsymbol{v}_h^j \approx \partial_t \boldsymbol{m}(t_j)$ *and* $\boldsymbol{m}_h^{j+1} \approx \boldsymbol{m}(t_{j+1})$ *for all* $j = 0, \dots, N-1$.

Algorithm 8.4.1 mimics the second-order BDF2 algorithm for LLG given in [AFP25], but has an extra term due to the iLLG inertial term. The usage of BDF2 for the magnetization and the extrapolation chosen means that unlike the midpoint scheme applied in Chapter 6, we can prove the following about the tangent space used in the discretization.

Proposition 8.4.2. *For every node* $\boldsymbol{z} \in \mathcal{N}_h$ *it holds that*

a) $|\boldsymbol{m}_h^{j+1}(\boldsymbol{z})|^2 = \frac{4}{3}|\boldsymbol{m}_h^j(\boldsymbol{z})|^2 - \frac{1}{3}|\boldsymbol{m}_h^{j-1}(\boldsymbol{z})|^2 + k^4|d_t^2 \boldsymbol{m}_h^{j+1}(\boldsymbol{z})|^2$ *for every* $j = 2, \dots, N-1$;

b) $|\boldsymbol{m}_h^{j+1}(\boldsymbol{z})|^2 \geq |\boldsymbol{m}_h^j(\boldsymbol{z})|^2$ *for every* $j = 0, \dots, N-1$;

c) $|\widehat{\boldsymbol{m}}_h^{j+1}(\boldsymbol{z})| \geq 1$ *for every* $j = 0, \dots, N-1$.

This implies that both the discrete tangent space $\boldsymbol{\mathcal{K}}_h(\widehat{\boldsymbol{m}}_h^{j+1})$ *for all* $j = 1, \dots, N$ *and* $\boldsymbol{\mathcal{K}}_h(\boldsymbol{m}_h^0)$ *are well-defined.*

To handle the extra inertial term, a parameter $0 < \beta \leq 1$ is introduced to split its discretization between two components: a β-weighted first-order finite difference derivative of $\boldsymbol{v}_h^{j+1}$, and a $(1-\beta)$-weighted second-order BDF2 finite difference derivative of $\boldsymbol{v}_h^{j+1}$. The β interpolation is motivated by complementary analytical and numerical considerations. This discretization yields the following energetic behaviour, parameterized by β.

Proposition 8.4.3. *Algorithm 8.4.1 is well-posed, and satisfies the discrete energy laws:*

- *For the initialization step,*

$$\mathcal{J}[\boldsymbol{m}_h^1, \boldsymbol{v}_h^1] + \alpha k \left\|\boldsymbol{v}_h^1\right\|^2 + \frac{\tau}{2}\left\|\boldsymbol{v}_h^1 - \boldsymbol{v}_h^0\right\|^2 + \frac{k^2}{2}\left\|\boldsymbol{\nabla}\boldsymbol{v}_h^1\right\|^2 = \mathcal{J}[\boldsymbol{m}_h^0, \boldsymbol{v}_h^0]; \tag{8.16}$$

- *For $j \geq 1$*

$$\begin{aligned}
&\beta\tau\Big(\frac{1}{2}\left\|\boldsymbol{v}_h^{j+1}\right\|^2 + \frac{k^2}{2}\left\|\mathrm{d}_t\boldsymbol{v}_h^{j+1}\right\|^2\Big) \\
&\quad + (1-\beta)\tau\Big(\left\|\boldsymbol{\mathcal{V}}_h^{j+1}\right\|_G^2 + \frac{k^4}{4}\left\|\mathrm{d}_t^2\boldsymbol{v}_h^{j+1}\right\|^2\Big) + \alpha k\left\|\boldsymbol{v}_h^{j+1}\right\|^2 \\
&\quad + \left\|\boldsymbol{\nabla}\boldsymbol{\mathcal{M}}_h^{j+1}\right\|_G^2 + \frac{k^4}{4}\left\|\mathrm{d}_t^2\boldsymbol{\nabla}\boldsymbol{m}_h^{j+1}\right\|^2 \\
&\quad = \beta\frac{\tau}{2}\left\|\boldsymbol{v}_h^{j}\right\|^2 + (1-\beta)\tau\left\|\boldsymbol{\mathcal{V}}_h^{j}\right\|_G^2 + \left\|\boldsymbol{\nabla}\boldsymbol{\mathcal{M}}_h^{j}\right\|_G^2,
\end{aligned} \tag{8.17}$$

where $\boldsymbol{\mathcal{M}}_h^j = (\boldsymbol{m}_h^j, \boldsymbol{m}_h^{j-1})$ and $\boldsymbol{\mathcal{V}}_h^j = (\boldsymbol{v}_h^j, \boldsymbol{v}_h^{j-1})$ for $1 \leq j \leq N$.

An alternative form of the energy law that resembles (8.16) is described in the following corollary. Notice that the two last terms of the left-hand side and of the right-hand side are unsigned terms.

Corollary 8.4.4. *For $N \geq 1$ it holds that*

$$\begin{aligned}
&\mathcal{J}[\boldsymbol{m}_h^N, \boldsymbol{v}_h^N] + \beta\frac{\tau k^2}{2}\sum_{j=0}^{N-1}\left\|\mathrm{d}_t\boldsymbol{v}_h^{j+1}\right\|^2 + (1-\beta)\frac{\tau k^4}{4}\sum_{j=1}^{N-1}\left\|\mathrm{d}_t^2\boldsymbol{v}_h^{j+1}\right\|^2 \\
&+ \alpha k\sum_{j=0}^{N-1}\left\|\boldsymbol{v}_h^{j+1}\right\|^2 + \frac{k^4}{4}\sum_{j=1}^{N-1}\left\|\mathrm{d}_t^2\boldsymbol{\nabla}\boldsymbol{m}_h^{j+1}\right\|^2 + (1-\beta)\frac{\tau k^2}{2}\left\|\mathrm{d}_t\boldsymbol{v}_h^N\right\|^2 \\
&+ \frac{k^2}{2}\left\|\mathrm{d}_t\boldsymbol{\nabla}\boldsymbol{m}_h^N\right\|^2 + (1-\beta)\frac{\tau k}{4}\mathrm{d}_t\left\|\boldsymbol{v}_h^N\right\|^2 + \frac{k}{4}\mathrm{d}_t\left\|\boldsymbol{\nabla}\boldsymbol{m}_h^N\right\|^2 \\
&= \mathcal{J}[\boldsymbol{m}_h^0, \boldsymbol{v}_h^0] + \frac{k}{4}\mathrm{d}_t\left\|\boldsymbol{\nabla}\boldsymbol{m}_h^1\right\|^2 + (1-\beta)\frac{\tau k}{4}\mathrm{d}_t\left\|\boldsymbol{v}_h^1\right\|^2.
\end{aligned} \tag{8.18}$$

These energy laws give rise to the following stability estimates.

Proposition 8.4.5. *Let $N \geq 1$. The time snapshots produced by Algorithm 8.4.1 satisfy the boundedness*

$$\begin{aligned}
\left\|\boldsymbol{v}_h^N\right\|^2 + \left\|\boldsymbol{m}_h^N\right\|_{\boldsymbol{H}^1(\Omega)}^2 &+ k\sum_{j=0}^{N-1}\left\|\boldsymbol{v}_h^{j+1}\right\|^2 \\
&+ k^2\sum_{j=0}^{N-1}\left\|\mathrm{d}_t\boldsymbol{v}_h^{j+1}\right\|^2 + k^4\sum_{j=1}^{N-1}\left\|\mathrm{d}_t^2\boldsymbol{v}_h^{j+1}\right\|^2 \\
&+ k^2\sum_{j=1}^{N-1}\left\|\mathrm{d}_t^2\boldsymbol{m}_h^{j+1}\right\|^2 + k^4\sum_{j=1}^{N-1}\left\|\mathrm{d}_t^2\boldsymbol{\nabla}\boldsymbol{m}_h^{j+1}\right\|^2 \leq C_1.
\end{aligned} \tag{8.19}$$

Moreover, the following unit length constraint violation estimate

$$\left\||\boldsymbol{m}^N|^2 - 1\right\|_{L^1(\Omega)} \leq C_2 k^2, \tag{8.20}$$

holds unconditionally. Furthermore, if $\boldsymbol{v}_h^0 = \boldsymbol{0}$ and the discrete regularity condition

$$k\left\|\mathrm{d}_t\boldsymbol{v}_h^1\right\|^2 + k\sum_{i=1}^{N-1}\left\|\mathrm{d}_t^2\boldsymbol{m}_h^{i+1}\right\|^2 \leq C_3$$

holds for some $C_3 > 0$, then we have

$$\left\| |\boldsymbol{m}^N|^2 - 1 \right\|_{L^1(\Omega)} \leq C_3 k^3. \tag{8.21}$$

The constants $C_1, C_2 > 0$ depend only upon the initial data and the shape regularity of the mesh.

As shown in Corollary 8.4.4 and Proposition 8.4.5, the first-order discretization of the inertial term ensures a bound on the quantity $k^2 \sum_{j=0}^{N-1} \left\| \mathrm{d}_t \boldsymbol{v}_h^{j+1} \right\|^2$, which is not guaranteed by the second-order BDF2 discretization alone. As shown in (8.32) in Proposition 8.6.2, this bound is crucial in order to bound the quantity $k^2 \sum_{j=1}^{N-1} \left\| \mathrm{d}_t^2 \boldsymbol{m}_h^{j+1} \right\|^2$, which is necessary to pass to the limit and verify Definition 8.2.1 (iii), as well as to guarantee *unconditional* second-order accuracy in the unit-length constraint violation, i.e., (8.20). We note that in practice using only the second-order BDF2 discretization (i.e. setting $\beta = 0$) still achieves the second-order accuracy in the unit-length constraint violation.

On the other hand, incorporating the second-order BDF2 discretization yields in experiments better accuracy, especially regarding the energy decay and order of convergence. The first-order discretization was used in [Rug22], where it was noted that the tangent plane scheme suffered from numerical dissipation when compared to a non-linear scheme. As the scheme in this work is formally second-order when $\beta = 0$, this dissipation is less restrictive, but still present. The use of the second-order BDF2 discretization for the velocity further reduces this dissipation, as will be shown in Section 8.5. This comes at a technical cost, as the analysis of convergence is more involved. When $\beta = 0$ we achieve a formally second-order scheme, but even for β sufficiently close to zero we achieve second-order convergence during numerical testing.

Using the sequence of snapshots $\{\boldsymbol{m}_h^j\}_{0 \leq j \leq N}$ and $\{\boldsymbol{v}_h^j\}_{0 \leq j \leq N-1}$ obtained by Algorithm 8.4.1, we define approximations

$$\boldsymbol{m}_{hk} \in \boldsymbol{H}^1(\Omega_T), \quad \boldsymbol{m}_{hk}^{\pm}, \widehat{\boldsymbol{m}}_{hk}^{+}, \boldsymbol{v}_{hk}^{\pm} \in L^2(0,T;\boldsymbol{H}^1(\Omega))$$

of $\boldsymbol{m}$ and $\boldsymbol{v} = \partial_t \boldsymbol{m}$ as follows: For all $0 \leq j \leq N-1$ and all $t \in [t_j, t_{j+1})$, let

$$\boldsymbol{m}_{hk}(t) \coloneqq \frac{t - t_j}{k} \boldsymbol{m}_h^{j+1} + \frac{t_{j+1} - t}{k} \boldsymbol{m}_h^j, \tag{8.22}$$

$$\boldsymbol{m}_{hk}^{-}(t) \coloneqq \boldsymbol{m}_h^j, \tag{8.23}$$

$$\boldsymbol{m}_{hk}^{+}(t) \coloneqq \boldsymbol{m}_h^{j+1}, \tag{8.24}$$

$$\widehat{\boldsymbol{m}}_{hk}^{+}(t) \coloneqq \begin{cases} \boldsymbol{m}_h^0 & \text{for } j = 0, \\ \widehat{\boldsymbol{m}}_h^{j+1} & \text{for } 1 \leq j \leq N-1, \end{cases} \tag{8.25}$$

$$\boldsymbol{v}_{hk}^{-}(t) \coloneqq \boldsymbol{v}_h^j. \tag{8.26}$$

$$\boldsymbol{v}_{hk}^{+}(t) \coloneqq \boldsymbol{v}_h^{j+1}. \tag{8.27}$$

The following theorem, which is the main theoretical result of this chapter, states that these interpolants converge weakly towards a weak solution of iLLG (8.1) as $(h,k) \to (0,0)$.

Theorem 8.4.6. *For $h > 0$, let $\mathcal{T}_h$ be a family of quasi-uniform meshes of Ω. Under assumptions (A1) and (A2), the sequences of discrete functions $\boldsymbol{m}_{hk}$, $\boldsymbol{m}_{hk}^{\pm}$ and $\widehat{\boldsymbol{m}}_{hk}^{+}$, admit subsequences (not relabelled) that unconditionally converge to a function $\boldsymbol{m}$ which is a weak solution of iLLG (8.1) in the sense of Definition 8.2.1(i)–(iii). More precisely, it holds that $\boldsymbol{m}_{hk} \rightharpoonup \boldsymbol{m}$ weakly in $\boldsymbol{H}^1(\Omega_T)$ (and hence $\boldsymbol{m}_{hk} \to \boldsymbol{m}$ strongly in $\boldsymbol{L}^2(\Omega_T)$) and $\boldsymbol{m}_{hk}, \boldsymbol{m}_{hk}^{\pm}, \widehat{\boldsymbol{m}}_{hk}^{+} \overset{*}{\rightharpoonup} \boldsymbol{m}$ in $L^\infty(0,T;\boldsymbol{H}^1(\Omega))$ as $(h,k) \to (0,0)$, where all convergences hold for the same subsequence. Moreover, under the CFL condition $k = o(h^2)$, the limit $\boldsymbol{m}$ satisfies also Definition 8.2.1(iv).*

8.5 Numerical experiments

To demonstrate the improvements of Algorithm 8.4.1 over the first-order tangent plane scheme applied in [Rug22] we present several numerical experiments. We once again apply the null-space method mentioned in Chapter 4 For solving the linears system, we apply GMRES with a relative tolerance of 10^{-15}, and a sparse incomplete LU decomposition with a fill ratio of 10 and a drop tolerance of 10^{-4} as a preconditioner. For each experiment, independently of β, the average number of GMRES iterations was between 2 and 4.

8.5.1 Unit length constraint

As a first experiment, we investigate the order of convergence in the unit length constraint for different values of $\beta \in \{0, 0.4, 0.6, 1\}$. Notice that $\beta = 0$ is not covered by the analysis. We choose $\Omega = [0,1]^3$, and select as the initial conditions

$$\boldsymbol{m}_h^0 = \frac{2}{\sqrt{5}} \mathcal{I}_h \left[\left(\frac{1}{2}, \sin\big(4(x+y+z)\big), \cos\big(4(x+y+z)\big) \right) \right] \quad \text{and} \quad \boldsymbol{v}_h^0 = \boldsymbol{0},$$

yielding an initial total energy of $\mathcal{J}[\boldsymbol{m}_h^0, \boldsymbol{v}_h^0] \approx 19$. We fix $\alpha = 0.1$ and $\tau = 0.013\,276$. The body is discretized with a mesh with mesh size $h_{\max} \approx 0.41$, and we vary the time-step for $n = 0, \dots, 5$ as $k_n = 10^{-2} \cdot 2^{-n}$. The total time for this simulation is $T \approx 0.995$. To measure the unit length constraint violation, we use

$$\begin{aligned} \operatorname{err}_{L^1} &= \big\| \mathcal{I}_h[|\boldsymbol{m}_h^N|^2 - 1] \big\|_{L^1(\Omega)} \\ \operatorname{err}_{\boldsymbol{L}^\infty} &= \big\| \boldsymbol{m}_h^N \big\|_{\boldsymbol{L}^\infty(\Omega)} - 1. \end{aligned}$$

The results are shown in Figure 8.1. The second-order convergence in time as predicted by (8.20) is verified, even for $\beta = 0$, and we see that the third-order convergence as predicted by (8.21) is nearly attained for all choices of β, with precisely third-order in the case of $\beta = 0$. If β is closer to 1, we see that the unit length constraint is more precise, which is because the second derivative term $k^2 \sum_{j=1}^{N-1} \big\| \mathrm{d}_t^2 \boldsymbol{m}_h^{j+1} \big\|^2$ responsible for the unconditional quadratic consistency in (8.20) has a larger coefficient in the stability estimate (8.17).

To see the precise slopes, we estimate the order of the unit length constraint violation using the two largest values of $1/k$ to compute the logarithmic slope. The results are shown in Table 8.1. We see that the orders of convergence for both

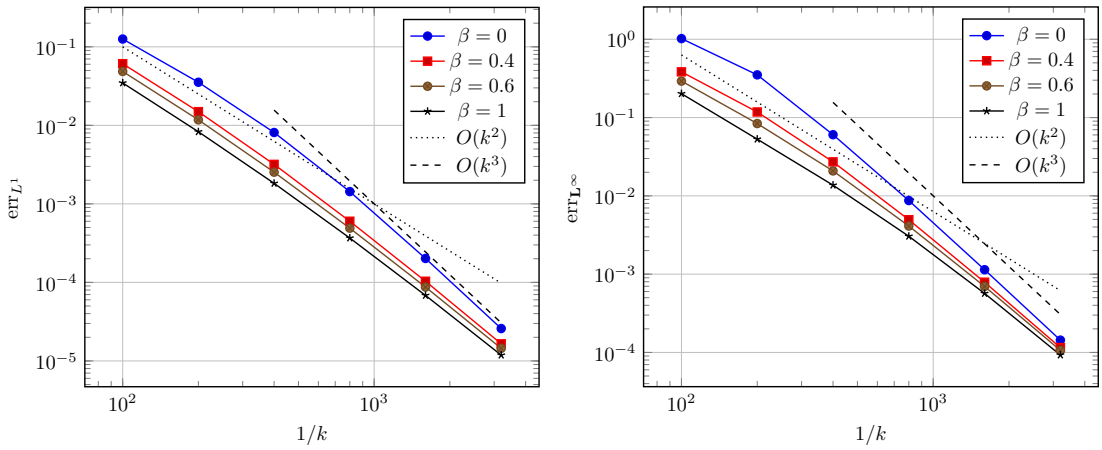

(a) L^1 error (b) $\boldsymbol{L}^\infty$ error

Figure 8.1: Experiment of Section 8.5.1. Unit length constraint violation $\mathrm{err}_{L^1}, \mathrm{err}_{\boldsymbol{L}^\infty}$ vs $1/k$, with varied β.

measures are almost 3 for $\beta = 0$, and the orders of convergence drop to about 2.5 and 2.6 for L^1 and $\boldsymbol{L}^\infty$ respectively as β approaches 1.

β	Order L^1	Order $\boldsymbol{L}^\infty$
0	2.965 572 787 672 859 2	2.987 775 632 873 702 1
0.4	2.646 623 217 734 211 6	2.774 586 566 423 436
0.6	2.592 797 959 527 271	2.712 119 536 758 021
1	2.525 844 289 414 931	2.613 694 223 552 76

Table 8.1: Experiment of Section 8.5.1. Experimental order of convergence for L^1 and $\boldsymbol{L}^\infty$ errors.

8.5.2 Effects of the β-parameter

We shall now demonstrate the effects of β on the energy dissipation. We apply the same mesh, but change $T = 1, \tau = 0.1$, keeping $\alpha = 0.1$, and consider the larger time-step $k = 10^{-2}$. The initial conditions we consider are

$$\boldsymbol{m}_h^0 = \frac{10}{\sqrt{85}}(0.9, 0.2, 0) \quad \text{and} \quad \boldsymbol{v}_h^0 \equiv \boldsymbol{0}.$$

We supplement the energy with a Zeeman field $(1, 0, 0)$. We now plot the evolution in time of the inertial energy $\|\partial_t \boldsymbol{m}_{hk}(t)\|^2/2$ in Figure 8.2, and the average magnetization in the x-direction i.e. $\langle m_x(t)\rangle := 1/|\Omega| \int_\Omega \boldsymbol{m}_{hk}(t)\cdot\boldsymbol{e}_1 \,\mathrm{d}\boldsymbol{x}$ in Figure 8.3. In Figure 8.2 we see that values of β closer to zero have larger peaks in inertial energy, and dissipate energy at a slower rate. At $t = 3.5$ in Figure 8.2 we see that for $\beta = 1$, the inertial energy curve is almost linear, but for $\beta = 0$ the inertial energy is still oscillating. This can be seen similarly in Figure 8.3, where $\langle m_x(t)\rangle$ is almost linearly increasing from $t = 2.5$ onwards, whereas for $\beta = 0, 0.2$ we clearly

see that $\langle m_x(t) \rangle$ is still oscillating in addition to increasing. The dissipation here is time-step dependent, and lowering the time-step would result in a correspondence of the curves in both figures, although we do not plot this here. We can observe that the period of oscillation is essentially the same, independently of the value of β, with all curves regularly meeting at the inflection points.

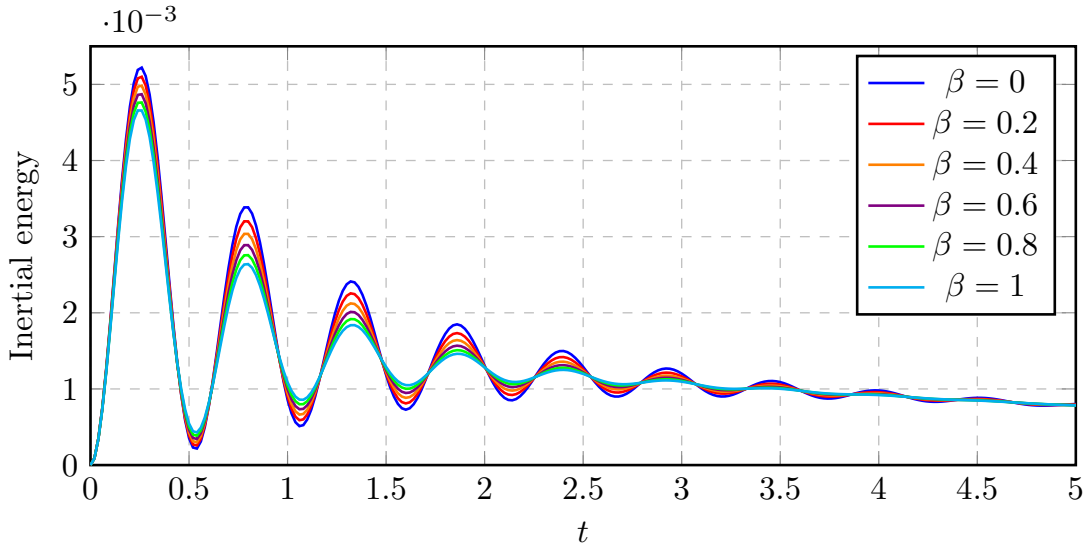

Figure 8.2: Experiment of Section 8.5.2. Time-step of $k = 10^{-2}$.

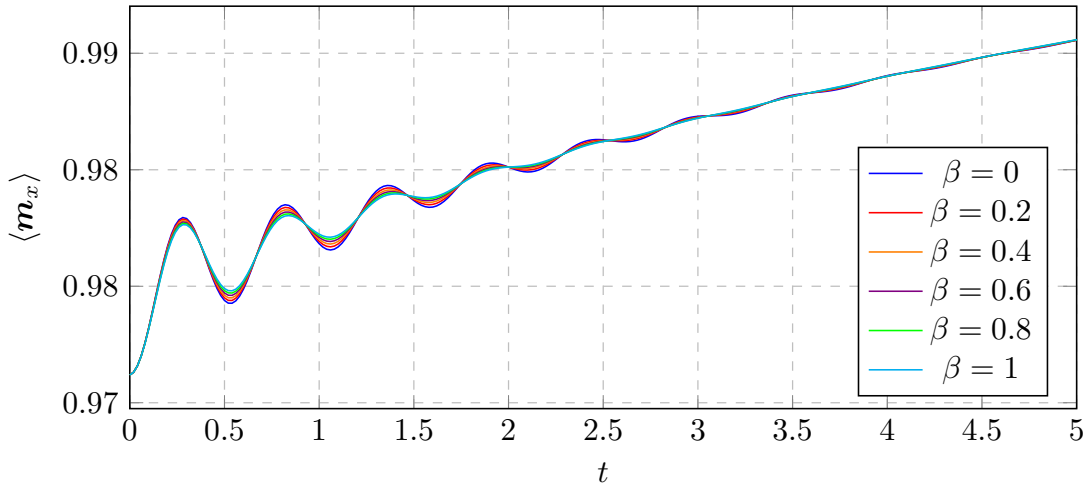

Figure 8.3: Experiment of Section 8.5.2. Time-step of $k = 1 \cdot 10^{-2}$. Average magnetization in x-direction, $\langle m_x \rangle$. Values of β close to one dissipate energy more quickly. The magnetization stops oscillation sooner, and curves less.

8.5.3 Order of Convergence

To estimate the order of convergence, we consider two on a triangulation of $[0, 1]^3$. The 3D mesh satisfies $h_{\max} \approx 0.41$. We set $T = 1/2$, $\alpha = \tau = 0.1$, and consider

the two following initial conditions. The constant initial condition

$$\boldsymbol{m}_h^0 = \frac{10}{\sqrt{85}}(0.9, 0.2, 0) \quad \text{and} \quad \boldsymbol{v}_h^0 \equiv \mathbf{0},$$

and the high energy initial condition

$$\boldsymbol{m}_h^0 = \frac{2}{\sqrt{5}}\Big(\frac{1}{2}, \sin\big(4(x+y+z)\big), \cos\big(4(x+y+z)\big)\Big) \quad \text{and} \quad \boldsymbol{v}_h^0 = \mathbf{0}. \tag{8.28}$$

We supplement the energy with a Zeeman field $(1, 0, 0)$ in both cases. We consider time step-sizes $k_n = 5 \cdot 10^{-3} \cdot 2^{-n}$ for $n = 0, \ldots, 6$, and compare this to a reference solution (computed for each value of β) corresponding to $n = 8$. The error is computed with the $\boldsymbol{H}^1$-norm at the final time-step $t = T$, that is

$$\mathrm{err}_{\boldsymbol{H}^1}^n = \|\boldsymbol{m}_{h,k_n}(T) - \boldsymbol{m}_{h,k_8}(T)\|_{\boldsymbol{H}^1(\Omega)}.$$

In Figure 8.4 we show the results. We notice that for $\beta = 0$ we obtain second-order convergence despite only applying linear operations, unlike the non-linear methods of [Rug22, dPS24]. This second-order convergence is kept for very small values of β. As β increases, the order of convergence decreases to first-order. However, the estimated order of convergence depends upon both the initial condition and the value of β. Indeed, notice that for the constant initial condition we obtain second-order convergence until $\beta = 10^{-3}$, and it starts to drop to first-order from $\beta = 5 \times 10^{-3}$ (see Figure 8.4a), while for the high energy initial condition the situation is slightly better, where we obtain second-order convergence until $\beta = 10^{-2}$, and it starts to drop to first-order from $\beta = 5 \times 10^{-2}$ (see Figure 8.4b), i.e., there is one order of magnitude of difference between the two cases. We conjecture that for any $\beta > 0$, the scheme is formally of first-order as $k \to 0$.

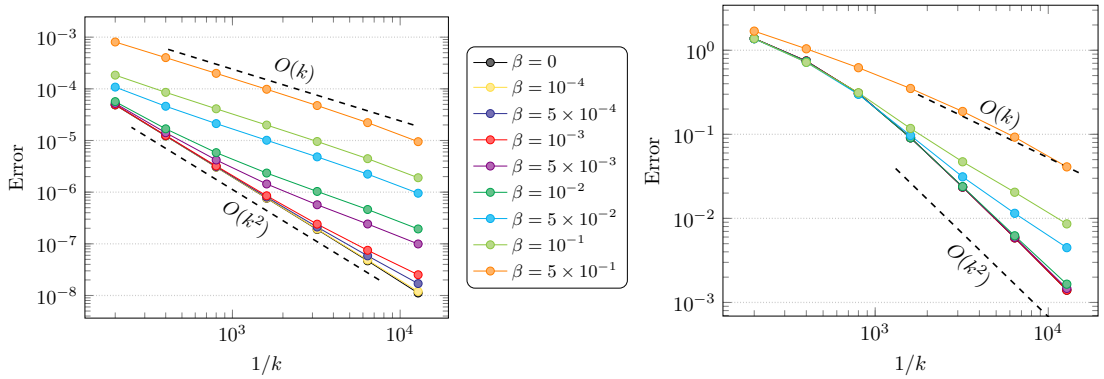

(a) Constant initial condition. (b) High energy initial condition

Figure 8.4: Experiment of Section 8.5.3. $\boldsymbol{H}^1$-norm of error $\mathrm{err}_{\boldsymbol{H}^1}$ vs $1/k$, with varied β. For small values of β we see second-order convergence, but as β increases the order of convergence drops to first-order.

To see the dependence upon β of the order, we instead plot the estimated order of convergence against β, using the two greatest values of $1/k$ in Figure 8.4. The

order of convergence is estimated using the formula

$$\text{Order of convergence} \approx -\log_2\left(\frac{\text{err}^6_{\boldsymbol{H}^1}}{\text{err}^5_{\boldsymbol{H}^1}}\right).$$

The results are shown in Figure 8.5, where we see that for smaller values of β, we clearly have second-order convergence in time.

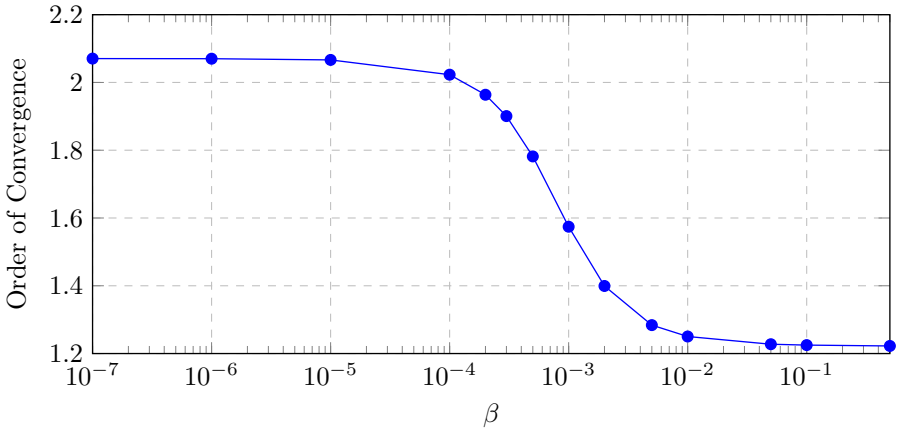

Figure 8.5: Experiment of Section 8.5.3. Estimated order of convergence against value of β. We see that the estimated order of convergence approaches 2 as β becomes smaller.

8.6 Proofs

We first show some properties of well-posedness.

Proof of Proposition 8.4.2. The proof of *a)* follows by the proof of [AFP25, Lemma 13, equation (36)]. An immediate consequence of *a)* is that

$$|\boldsymbol{m}_h^{j+1}(\boldsymbol{z})|^2 \geq |\boldsymbol{m}_h^{j+1}(\boldsymbol{z})|^2 + \frac{1}{3}\big(|\boldsymbol{m}_h^{j}(\boldsymbol{z})|^2 - |\boldsymbol{m}_h^{j-1}(\boldsymbol{z})|^2\big),$$

and since $|\boldsymbol{m}_h^1(\boldsymbol{z})|^2 = |\boldsymbol{m}_h^0(\boldsymbol{z})|^2 + k^2|\boldsymbol{v}_h^0(\boldsymbol{z})|^2 \geq |\boldsymbol{m}_h^0(\boldsymbol{z})|^2 = 1$ by induction we obtain *b)*. Finally, since

$$4\boldsymbol{m}_h^j(\boldsymbol{z}) \cdot \boldsymbol{m}_h^{j-1}(\boldsymbol{z}) \leq 2|\boldsymbol{m}_h^j(\boldsymbol{z})|^2 + 2|\boldsymbol{m}_h^{j-1}(\boldsymbol{z})|^2,$$

it holds that

$$\begin{aligned}
|\widehat{\boldsymbol{m}}_h^{j+1}(\boldsymbol{z})|^2 &= \left|2\boldsymbol{m}_h^j(\boldsymbol{z}) - \boldsymbol{m}_h^{j-1}(\boldsymbol{z})\right|^2 \\
&= 4|\boldsymbol{m}_h^j(\boldsymbol{z})|^2 - 4\boldsymbol{m}_h^j(\boldsymbol{z}) \cdot \boldsymbol{m}_h^{j-1}(\boldsymbol{z}) + |\boldsymbol{m}_h^{j-1}(\boldsymbol{z})|^2 \\
&\geq 4|\boldsymbol{m}_h^j(\boldsymbol{z})|^2 - 2|\boldsymbol{m}_h^j(\boldsymbol{z})|^2 - 2|\boldsymbol{m}_h^{j-1}(\boldsymbol{z})|^2 + |\boldsymbol{m}_h^{j-1}(\boldsymbol{z})|^2 \\
&= |\boldsymbol{m}_h^j(\boldsymbol{z})|^2 + \left(|\boldsymbol{m}_h^j(\boldsymbol{z})|^2 - |\boldsymbol{m}_h^{j-1}(\boldsymbol{z})|^2\right),
\end{aligned}$$

and applying *b)* yields $|\widehat{\boldsymbol{m}}_h^{j+1}(\boldsymbol{z})|^2 \geq 1$, concluding the proof of *c)*. □

Proof of Proposition 8.4.3. For the initialization step, we have the linear system

$$\tau \left\langle \mathrm{d}_t \boldsymbol{v}_h^1, \boldsymbol{\phi}_h \right\rangle + \alpha \left\langle \boldsymbol{v}_h^1, \boldsymbol{\phi}_h \right\rangle + \left\langle \boldsymbol{m}_h^0 \times \boldsymbol{v}_h^1, \boldsymbol{\phi}_h \right\rangle + k \left\langle \boldsymbol{\nabla} \boldsymbol{v}_h^1, \boldsymbol{\nabla} \boldsymbol{\phi}_h \right\rangle = - \left\langle \boldsymbol{\nabla} \boldsymbol{m}_h^0, \boldsymbol{\nabla} \boldsymbol{\phi}_h \right\rangle .$$

This is easily seen to have a unique solution via the Lax–Milgram lemma. Inserting $\boldsymbol{\phi}_h = k\boldsymbol{v}_h^1$ in (8.14) yields

$$\tau \left\langle \boldsymbol{v}_h^1 - \boldsymbol{v}_h^0, \boldsymbol{v}_h^1 \right\rangle + \alpha k \left\| \boldsymbol{v}_h^1 \right\|^2 + k \left\langle \boldsymbol{\nabla} \boldsymbol{m}_h^1, \boldsymbol{\nabla} \boldsymbol{v}_h^1 \right\rangle . = 0$$

Using $\boldsymbol{m}_h^1 = \boldsymbol{m}_h^0 + k\boldsymbol{v}_h^1$ it is possible to see that

$$\begin{aligned} \left\langle \boldsymbol{\nabla} \boldsymbol{m}_h^1, k \boldsymbol{\nabla} \boldsymbol{v}_h^1 \right\rangle &= \left\langle \boldsymbol{\nabla} \Big(\frac{\boldsymbol{m}_h^1 + \boldsymbol{m}_h^0}{2} \Big) + \boldsymbol{\nabla} \Big(\frac{\boldsymbol{m}_h^1 - \boldsymbol{m}_h^0}{2} \Big), \boldsymbol{\nabla} (\boldsymbol{m}_h^1 - \boldsymbol{m}_h^0) \right\rangle \\ &= \frac{1}{2} \left\| \boldsymbol{\nabla} \boldsymbol{m}_h^1 \right\|^2 - \frac{1}{2} \left\| \boldsymbol{\nabla} \boldsymbol{m}_h^0 \right\|^2 + \frac{k^2}{2} \left\| \boldsymbol{\nabla} \boldsymbol{v}_h^1 \right\|^2 , \end{aligned}$$

and we also have by the vector identity $2(\boldsymbol{a} - \boldsymbol{b}) \cdot \boldsymbol{a} = |\boldsymbol{a}|^2 - |\boldsymbol{b}|^2 + |\boldsymbol{a} - \boldsymbol{b}|^2$ that

$$\left\langle \boldsymbol{v}_h^1 - \boldsymbol{v}_h^0, \boldsymbol{v}_h^1 \right\rangle = \frac{1}{2} \left\| \boldsymbol{v}_h^1 \right\|^2 - \frac{1}{2} \left\| \boldsymbol{v}_h^0 \right\|^2 + \frac{k^2}{2} \left\| \mathrm{d}_t \boldsymbol{v}_h^1 \right\|^2 , \tag{8.29}$$

hence we have

$$\mathcal{J}[\boldsymbol{m}_h^1, \boldsymbol{v}_h^1] + \alpha k \left\| \boldsymbol{v}_h^1 \right\|^2 + \frac{\tau k^2}{2} \left\| \mathrm{d}_t \boldsymbol{v}_h^1 \right\|^2 + \frac{k^2}{2} \left\| \boldsymbol{\nabla} \boldsymbol{v}_h^1 \right\|^2 = \mathcal{J}[\boldsymbol{m}_h^0, \boldsymbol{v}_h^0].$$

For the loop, we have from (8.15)

$$\begin{aligned} \beta \frac{\tau}{k} \left\langle \boldsymbol{v}_h^{j+1}, \boldsymbol{\phi}_h \right\rangle + (1-\beta) \frac{3\tau}{2k} \left\langle \boldsymbol{v}_h^{j+1}, \boldsymbol{\phi}_h \right\rangle + \alpha \left\langle \boldsymbol{v}_h^{j+1}, \boldsymbol{\phi}_h \right\rangle \\ + \left\langle \widehat{\boldsymbol{m}}_h^{j+1} \times \boldsymbol{v}_h^{j+1}, \boldsymbol{\phi}_h \right\rangle + \frac{2k}{3} \left\langle \boldsymbol{\nabla} \boldsymbol{v}_h^{j+1}, \boldsymbol{\nabla} \boldsymbol{\phi}_h \right\rangle \\ = \beta \frac{\tau}{k} \left\langle \boldsymbol{v}_h^{j}, \boldsymbol{\phi}_h \right\rangle + (1-\beta) \frac{\tau}{2k} \left\langle 4\boldsymbol{v}_h^{j} - \boldsymbol{v}_h^{j-1}, \boldsymbol{\phi}_h \right\rangle \\ - \frac{1}{3} \left\langle \boldsymbol{\nabla} (4\boldsymbol{m}_h^{j} - \boldsymbol{m}_h^{j-1}), \boldsymbol{\nabla} \boldsymbol{\phi}_h \right\rangle , \end{aligned}$$

for which the left-hand side is clearly coercive in $\boldsymbol{H}^1(\Omega)$, and positive definite, with the right hand side being bounded. It follows that a unique solution $\boldsymbol{v}_h^{j+1}$ exists, and inserting $\boldsymbol{\phi}_h = k\boldsymbol{v}_h^{j+1}$ yields

$$\begin{aligned} \beta\tau \left\langle \boldsymbol{v}_h^{j+1} - \boldsymbol{v}_h^{j}, \boldsymbol{v}_h^{j+1} \right\rangle + (1-\beta) \frac{\tau}{2} \left\langle 3\boldsymbol{v}_h^{j+1} - 4\boldsymbol{v}_h^{j} + \boldsymbol{v}_h^{j-1}, \boldsymbol{v}_h^{j+1} \right\rangle + \alpha k \left\| \boldsymbol{v}_h^{j+1} \right\|^2 \\ + \frac{k}{3} \left\langle \boldsymbol{\nabla} (4\boldsymbol{m}_h^{j} - \boldsymbol{m}_h^{j-1} + 2k\boldsymbol{v}_h^{j+1}), \boldsymbol{\nabla} \boldsymbol{v}_h^{j+1} \right\rangle = 0. \end{aligned}$$

Applying (8.12) yields

$$\frac{1}{2} \left\langle 3\boldsymbol{v}_h^{j+1} - 4\boldsymbol{v}_h^{j} + \boldsymbol{v}_h^{j-1}, \boldsymbol{v}_h^{j+1} \right\rangle = \left\| \boldsymbol{\mathcal{V}}_h^{j+1} \right\|_G^2 - \left\| \boldsymbol{\mathcal{V}}_h^{j} \right\|_G^2 + \frac{k^4}{4} \left\| \mathrm{d}_t^2 \boldsymbol{v}_h^{j+1} \right\|^2$$

and analogously

$$\begin{aligned}
&\frac{k}{3}\left\langle \boldsymbol{\nabla}(4\boldsymbol{m}_h^j - \boldsymbol{m}_h^{j-1} + 2k\boldsymbol{v}_h^{j+1}), \boldsymbol{\nabla}\boldsymbol{v}_h^{j+1}\right\rangle \\
&\qquad = k\left\langle \boldsymbol{\nabla}\boldsymbol{m}_h^{j+1}, \boldsymbol{\nabla}\frac{1}{k}\Big(\frac{3}{2}\boldsymbol{m}_h^{j+1} - 2\boldsymbol{m}_h^j + \frac{1}{2}\boldsymbol{m}_h^{j-1}\Big)\right\rangle \\
&\qquad = \left\|\boldsymbol{\nabla}\boldsymbol{\mathcal{M}}_h^{j+1}\right\|_G^2 - \left\|\boldsymbol{\nabla}\boldsymbol{\mathcal{M}}_h^{j}\right\|_G^2 + \frac{k^4}{4}\left\|\mathrm{d}_t^2\boldsymbol{\nabla}\boldsymbol{m}_h^{j+1}\right\|^2.
\end{aligned}$$

Putting this all together and applying the same vector identity as the initialization (8.29) yields

$$\begin{aligned}
\beta\tau\Big(\frac{1}{2}\left\|\boldsymbol{v}_h^{j+1}\right\|^2 - \frac{1}{2}\left\|\boldsymbol{v}_h^{j}\right\|^2 + \frac{k^2}{2}\left\|\mathrm{d}_t\boldsymbol{v}_h^{j+1}\right\|^2\Big) \\
+ (1-\beta)\tau\Big(\left\|\boldsymbol{\mathcal{V}}_h^{j+1}\right\|_G^2 - \left\|\boldsymbol{\mathcal{V}}_h^{j}\right\|_G^2 + \frac{k^4}{4}\left\|\mathrm{d}_t^2\boldsymbol{v}_h^{j+1}\right\|^2\Big) \\
+ \alpha k\left\|\boldsymbol{v}_h^{j+1}\right\|^2 + \left\|\boldsymbol{\nabla}\boldsymbol{\mathcal{M}}_h^{j+1}\right\|_G^2 - \left\|\boldsymbol{\nabla}\boldsymbol{\mathcal{M}}_h^{j}\right\|_G^2 + \frac{k^4}{4}\left\|\mathrm{d}_t^2\boldsymbol{\nabla}\boldsymbol{m}_h^{j+1}\right\|^2 = 0
\end{aligned}$$

and concludes the proof. □

Proof of Corollary 8.4.4. Summing the energy law (8.17) over $j = 1, \dots, N-1$ yields

$$\begin{aligned}
&\beta\frac{\tau}{2}\left\|\boldsymbol{v}_h^N\right\|^2 + (1-\beta)\tau\left\|\boldsymbol{\mathcal{V}}_h^N\right\|_G^2 + \left\|\boldsymbol{\nabla}\boldsymbol{\mathcal{M}}_h^N\right\|_G^2 + \beta\frac{\tau k^2}{2}\sum_{j=1}^{N-1}\left\|\mathrm{d}_t\boldsymbol{v}_h^{j+1}\right\|^2 \\
&\qquad + (1-\beta)\frac{\tau k^4}{4}\sum_{j=1}^{N-1}\left\|\mathrm{d}_t^2\boldsymbol{v}_h^{j+1}\right\|^2 + \alpha k\sum_{j=1}^{N-1}\left\|\boldsymbol{v}_h^{j+1}\right\|^2 \\
&\qquad + \frac{k^4}{4}\sum_{j=1}^{N-1}\left\|\mathrm{d}_t^2\boldsymbol{\nabla}\boldsymbol{m}_h^{j+1}\right\|^2 \\
&\qquad = \beta\frac{\tau}{2}\left\|\boldsymbol{v}_h^1\right\|^2 + (1-\beta)\tau\left\|\boldsymbol{\mathcal{V}}_h^1\right\|_G^2 + \left\|\boldsymbol{\nabla}\boldsymbol{\mathcal{M}}_h^1\right\|_G^2.
\end{aligned} \tag{8.30}$$

Using (8.13) we see that it holds that

$$\left\|\boldsymbol{\nabla}\boldsymbol{\mathcal{M}}_h^\ell\right\|_G^2 = \frac{1}{2}\left\|\boldsymbol{\nabla}\boldsymbol{m}_h^\ell\right\|^2 + \frac{k}{4}\mathrm{d}_t\left\|\boldsymbol{\nabla}\boldsymbol{m}_h^\ell\right\|^2 + \frac{k^2}{2}\left\|\mathrm{d}_t\boldsymbol{\nabla}\boldsymbol{m}_h^\ell\right\|^2$$

and

$$\left\|\boldsymbol{\mathcal{V}}_h^\ell\right\|_G^2 = \frac{1}{2}\left\|\boldsymbol{v}_h^\ell\right\|^2 + \frac{k}{4}\mathrm{d}_t\left\|\boldsymbol{v}_h^\ell\right\|^2 + \frac{k^2}{2}\left\|\mathrm{d}_t\boldsymbol{v}_h^\ell\right\|^2.$$

Inserting these relations for $\ell \in \{1, N\}$ yields

$$\begin{aligned}
&\frac{\beta\tau}{2}\left\|\boldsymbol{v}_h^N\right\|^2 + (1-\beta)\tau\Big[\frac{1}{2}\left\|\boldsymbol{v}_h^N\right\|^2 + \frac{k}{4}\mathrm{d}_t\left\|\boldsymbol{v}_h^N\right\|^2 + \frac{k^2}{2}\left\|\mathrm{d}_t\boldsymbol{v}_h^N\right\|^2\Big] \\
&\quad + \frac{1}{2}\left\|\boldsymbol{\nabla}\boldsymbol{m}_h^N\right\|^2 + \frac{k}{4}\mathrm{d}_t\left\|\boldsymbol{\nabla}\boldsymbol{m}_h^N\right\|^2 + \frac{k^2}{2}\left\|\mathrm{d}_t\boldsymbol{\nabla}\boldsymbol{m}_h^N\right\|^2 + \beta\frac{\tau k^2}{2}\sum_{j=1}^{N-1}\left\|\mathrm{d}_t\boldsymbol{v}_h^{j+1}\right\|^2 \\
&\quad + (1-\beta)\frac{\tau k^4}{4}\sum_{j=1}^{N-1}\left\|\mathrm{d}_t^2\boldsymbol{v}_h^{j+1}\right\|^2 + \alpha k\sum_{j=1}^{N-1}\left\|\boldsymbol{v}_h^{j+1}\right\|^2 + \frac{k^4}{4}\sum_{j=1}^{N-1}\left\|\mathrm{d}_t^2\boldsymbol{\nabla}\boldsymbol{m}_h^{j+1}\right\|^2 \\
&\quad = \beta\frac{\tau}{2}\left\|\boldsymbol{v}_h^1\right\|^2 + (1-\beta)\tau\Big[\frac{1}{2}\left\|\boldsymbol{v}_h^1\right\|^2 + \frac{k}{4}\mathrm{d}_t\left\|\boldsymbol{v}_h^1\right\| + \frac{k^2}{2}\left\|\mathrm{d}_t\boldsymbol{v}_h^1\right\|^2\Big] \\
&\quad + \frac{1}{2}\left\|\boldsymbol{\nabla}\boldsymbol{m}_h^1\right\|^2 + \frac{k}{4}\mathrm{d}_t\left\|\boldsymbol{\nabla}\boldsymbol{m}_h^1\right\|^2 + \frac{k^2}{2}\left\|\mathrm{d}_t\boldsymbol{\nabla}\boldsymbol{m}_h^1\right\|^2.
\end{aligned}$$

Considering the definition of the energy functional (8.4) we have for $1 \le i \le N$

$$\frac{1}{2}\left\|\boldsymbol{\nabla}\boldsymbol{m}_h^i\right\|^2 + \frac{\beta\tau}{2}\left\|\boldsymbol{v}_h^i\right\|^2 + \frac{(1-\beta)\tau}{2}\left\|\boldsymbol{v}_h^i\right\|^2 = \mathcal{J}[\boldsymbol{m}_h^i, \boldsymbol{v}_h^i]$$

and therefore

$$\begin{aligned}
&\mathcal{J}[\boldsymbol{m}_h^N, \boldsymbol{v}_h^N] + (1-\beta)\frac{\tau k^2}{2}\left\|\mathrm{d}_t\boldsymbol{v}_h^N\right\|^2 + (1-\beta)\frac{\tau k}{4}\mathrm{d}_t\left\|\boldsymbol{v}_h^N\right\|^2 \\
&+ \frac{k}{4}\mathrm{d}_t\left\|\boldsymbol{\nabla}\boldsymbol{m}_h^N\right\|^2 + \frac{k^2}{2}\left\|\mathrm{d}_t\boldsymbol{\nabla}\boldsymbol{m}_h^N\right\|^2 \\
&+ \beta\frac{\tau k^2}{2}\sum_{j=1}^{N-1}\left\|\mathrm{d}_t\boldsymbol{v}_h^{j+1}\right\|^2 + (1-\beta)\frac{\tau k^4}{4}\sum_{j=1}^{N-1}\left\|\mathrm{d}_t^2\boldsymbol{v}_h^{j+1}\right\|^2 \\
&+ \alpha k\sum_{j=1}^{N-1}\left\|\boldsymbol{v}_h^{j+1}\right\|^2 + \frac{k^4}{4}\sum_{j=1}^{N-1}\left\|\mathrm{d}_t^2\boldsymbol{\nabla}\boldsymbol{m}_h^{j+1}\right\|^2 \\
&= \mathcal{J}[\boldsymbol{m}_h^1, \boldsymbol{v}_h^1] + \frac{k^2}{2}\left\|\mathrm{d}_t\boldsymbol{\nabla}\boldsymbol{m}_h^1\right\|^2 + \frac{k}{4}\mathrm{d}_t\left\|\boldsymbol{\nabla}\boldsymbol{m}_h^1\right\|^2 \\
&\quad + (1-\beta)\frac{\tau k}{4}\mathrm{d}_t\left\|\boldsymbol{v}_h^1\right\|^2 + (1-\beta)\frac{\tau k^2}{2}\left\|\mathrm{d}_t\boldsymbol{v}_h^1\right\|^2.
\end{aligned}$$

Inserting the energy law for the first time step (8.16)

$$\mathcal{J}[\boldsymbol{m}_h^1, \boldsymbol{v}_h^1] = \mathcal{J}[\boldsymbol{m}_h^0, \boldsymbol{v}_h^0] - \alpha k\left\|\boldsymbol{v}_h^1\right\|^2 - \frac{\tau k^2}{2}\left\|\mathrm{d}_t\boldsymbol{v}_h^1\right\|^2 - \frac{k^2}{2}\left\|\boldsymbol{\nabla}\boldsymbol{v}_h^1\right\|^2$$

and noting that $\mathrm{d}_t\boldsymbol{m}_h^1 = \boldsymbol{v}_h^1$ concludes the proof. □

Remark 8.6.1. *Notice that the energy law* (8.18) *contains the unsigned terms*

$$(1-\beta)\frac{\tau k}{4}\mathrm{d}_t\left\|\boldsymbol{v}_h^\ell\right\|^2 + \frac{k}{4}\mathrm{d}_t\left\|\boldsymbol{\nabla}\boldsymbol{m}_h^\ell\right\|^2 \quad \textit{for} \quad \ell \in \{1, N\},$$

which will require a CFL condition on the first and last time step when passing to the limit to the continuous energy inequality in the proof of Theorem 8.4.6.

If $\beta = 0$, i.e., the problem is discretized with full BDF2 method, we can write those unsigned terms in a compact form as

$$\frac{k}{2}\mathrm{d}_t\mathcal{J}[\boldsymbol{m}_h^\ell, \boldsymbol{v}_h^\ell], \qquad \ell \in \{1, N\}.$$

In particular, the term $\frac{k}{2}\mathrm{d}_t\mathcal{J}[\boldsymbol{m}_h^1, \boldsymbol{v}_h^1]$ is always negative, by the initialization step (8.16)*, and can be discarded from the energy law* (8.18) *at the cost of an inequality. This would save us from having to impose a CFL condition in the first time step, when passing to the limit to the continuous energy inequality. Nevertheless, the term at the N-th step $\frac{k}{2}\mathrm{d}_t\mathcal{J}[\boldsymbol{m}_h^N, \boldsymbol{v}_h^N]$ would still require the CFL condition. On the other hand, as aforementioned, notice that if $\beta = 0$ we would lose the boundedness of $k^2\sum_{j=0}^{N-1}\left\|\mathrm{d}_t\boldsymbol{v}_h^{j+1}\right\|$ and consequently the boundedness of $k^2\sum_{j=1}^{N-1}\left\|\mathrm{d}_t^2\boldsymbol{m}_h^{j+1}\right\|^2$, see Proposition 8.6.2, which is (analytically, but not numerically) crucial for the second-order in time unit length constraint and to pass to the limit in the variational formulation in the proof of Theorem 8.4.6.*

In the case $\beta = 1$, i.e., first-order discrete derivative for the inertial term, the unsigned terms take the form

$$\frac{k}{4}\mathrm{d}_t\left\|\boldsymbol{\nabla}\boldsymbol{m}_h^\ell\right\|^2, \qquad \ell \in \{1, N\},$$

which require the CFL condition. In the special case in which $\boldsymbol{v}_h^0 \equiv \mathbf{0}$, from (8.16)

$$\mathcal{J}[\boldsymbol{m}_h^1, \boldsymbol{v}_h^1] + \alpha k\left\|\boldsymbol{v}_h^1\right\|^2 + \frac{\tau}{2}\left\|\boldsymbol{v}_h^1\right\|^2 + \frac{k^2}{2}\left\|\boldsymbol{\nabla}\boldsymbol{v}_h^1\right\|^2 = \frac{1}{2}\left\|\boldsymbol{\nabla}\boldsymbol{m}_h^0\right\|^2$$

we can gather

$$\frac{1}{2}\left\|\boldsymbol{\nabla}\boldsymbol{m}_h^1\right\|^2 \leq \frac{1}{2}\left\|\boldsymbol{\nabla}\boldsymbol{m}_h^0\right\|^2,$$

and therefore we can remove the unsigned term at the first time step at cost of an inequality, since it is non-positive, and only the unsigned term at the last N-th time step requires a CFL condition.

The case $\beta = 1$, i.e., is excellent analytically, since it guarantees the needed boundedness of $k^2\sum_{j=1}^{N-1}\left\|\mathrm{d}_t^2\boldsymbol{m}_h^{j+1}\right\|^2$, but $\beta = 0$ (i.e. BDF2 discretization for the inertial term) performs better numerically, especially in the case where the time step is large in terms of energy conservation (this is a problem noticed in [Rug22], and it is why the author recommends using the non-linear method instead of the tangent plane scheme).

Both issues are addressed via a weighted mixing of the two discretizations for the inertial term.

The following proposition, based upon [DGXY24, Lemma 4.5], provides us with useful bounds and allows us to prove unconditional second-order consistency for the modulus one constraint $\left\||\boldsymbol{m}_h^N|^2 - 1\right\|_{L^1(\Omega)} \lesssim k^2$.

Proposition 8.6.2. *Let $j \geq 1$ and $N \geq 3$. It holds that*

$$\left\|\mathrm{d}_t\boldsymbol{m}_h^{j+1}\right\|^2 \leq \left(\frac{2}{3}\left\|\boldsymbol{v}_h^{j+1}\right\| + \frac{1}{3}\left\|\mathrm{d}_t\boldsymbol{m}_h^j\right\|\right)^2 \leq \frac{8}{9}\left\|\boldsymbol{v}_h^{j+1}\right\|^2 + \frac{2}{9}\left\|\mathrm{d}_t\boldsymbol{m}_h^j\right\|^2 \qquad (8.31)$$

and

$$\sum_{j=2}^{N-1} \left\| \mathrm{d}_t^2 \boldsymbol{m}_h^{j+1} \right\|^2 \leq \frac{2}{7} \left\| \mathrm{d}_t^2 \boldsymbol{m}_h^2 \right\|^2 + \frac{8}{7} \sum_{j=2}^{N-1} \left\| \mathrm{d}_t \boldsymbol{v}_h^{j+1} \right\|^2. \tag{8.32}$$

Proof of Proposition 8.6.2. For $j \geq 1$ it holds that

$$3\mathrm{d}_t \boldsymbol{m}_h^{j+1} = 2\boldsymbol{v}_h^{j+1} + \mathrm{d}_t \boldsymbol{m}_h^j.$$

Using this and the relation $(2a+b)^2 \leq 8a^2 + 2b^2$ we immediately get that

$$\left\| \mathrm{d}_t \boldsymbol{m}_h^{j+1} \right\|^2 \leq \left(\frac{2}{3} \left\| \boldsymbol{v}_h^{j+1} \right\| + \frac{1}{3} \left\| \mathrm{d}_t \boldsymbol{m}_h^j \right\| \right)^2 \leq \frac{8}{9} \left\| \boldsymbol{v}_h^{j+1} \right\|^2 + \frac{2}{9} \left\| \mathrm{d}_t \boldsymbol{m}_h^j \right\|^2$$

and (8.31) follows. Moreover, for $j \geq 2$ it holds that

$$3\mathrm{d}_t^2 \boldsymbol{m}_h^{j+1} = 2\mathrm{d}_t \boldsymbol{v}_h^{j+1} + \mathrm{d}_t^2 \boldsymbol{m}_h^j$$

and using again the relation $(2a+b)^2 \leq 8a^2 + 2b^2$, it follows that

$$\left\| \mathrm{d}_t^2 \boldsymbol{m}_h^{j+1} \right\|^2 \leq \left(\frac{2}{3} \left\| \mathrm{d}_t \boldsymbol{v}_h^{j+1} \right\| + \frac{1}{3} \left\| \mathrm{d}_t^2 \boldsymbol{m}_h^j \right\| \right)^2 \leq \frac{8}{9} \left\| \mathrm{d}_t \boldsymbol{v}_h^{j+1} \right\|^2 + \frac{2}{9} \left\| \mathrm{d}_t^2 \boldsymbol{m}_h^j \right\|^2$$

which after summing over $j = 2, \ldots, N-1$ yields

$$\sum_{j=2}^{N-1} \left\| \mathrm{d}_t^2 \boldsymbol{m}_h^{j+1} \right\|^2 - \frac{2}{9} \sum_{j=2}^{N-1} \left\| \mathrm{d}_t^2 \boldsymbol{m}_h^j \right\|^2 \leq \frac{8}{9} \sum_{j=2}^{N-1} \left\| \mathrm{d}_t \boldsymbol{v}_h^{j+1} \right\|^2.$$

Performing the computation of the terms on the left-hand side yields

$$\left\| \mathrm{d}_t^2 \boldsymbol{m}_h^N \right\|^2 + \frac{7}{9} \sum_{j=3}^{N-1} \left\| \mathrm{d}_t^2 \boldsymbol{m}_h^j \right\|^2 \leq \frac{2}{9} \left\| \mathrm{d}_t^2 \boldsymbol{m}_h^2 \right\|^2 + \frac{8}{9} \sum_{j=2}^{N-1} \left\| \mathrm{d}_t \boldsymbol{v}_h^{j+1} \right\|^2.$$

Multiplying both sides by $\frac{9}{7}$ and weakening the inequality gives

$$\sum_{j=3}^{N} \left\| \mathrm{d}_t^2 \boldsymbol{m}_h^j \right\|^2 \leq \frac{2}{7} \left\| \mathrm{d}_t^2 \boldsymbol{m}_h^2 \right\|^2 + \frac{8}{7} \sum_{j=2}^{N-1} \left\| \mathrm{d}_t \boldsymbol{v}_h^{j+1} \right\|^2.$$

This concludes the proof. □

Proof of Proposition 8.4.5. Notice that thanks to the available norm equivalences (8.11) and (3.5), we have

$$\begin{aligned} \left\| \boldsymbol{v}_h^1 \right\|^2 + \left\| \boldsymbol{\mathcal{V}}_h^1 \right\|_G^2 + \left\| \boldsymbol{\nabla} \boldsymbol{\mathcal{M}}_h^1 \right\|_G^2 &\overset{(8.11),\,(3.5)}{\lesssim} \left\| \boldsymbol{v}_h^1 \right\|^2 + \left\| \boldsymbol{v}_h^0 \right\|^2 + \left\| \boldsymbol{\nabla} \boldsymbol{m}_h^1 \right\|^2 + \left\| \boldsymbol{\nabla} \boldsymbol{m}_h^0 \right\|^2 \\ &\overset{(8.16)}{\lesssim} \left\| \boldsymbol{v}_h^0 \right\|^2 + \left\| \boldsymbol{\nabla} \boldsymbol{m}_h^0 \right\|^2. \end{aligned}$$

This gives an upper bound for (8.30), i.e.

$$\left\|\boldsymbol{v}_h^N\right\|^2 + \left\|\boldsymbol{\mathcal{V}}_h^N\right\|_G^2 + \left\|\boldsymbol{\nabla}\boldsymbol{\mathcal{M}}_h^N\right\|_G^2 + k\sum_{j=0}^{N-1}\left\|\boldsymbol{v}_h^{j+1}\right\|^2 + k^2\sum_{j=0}^{N-1}\left\|\mathrm{d}_t\boldsymbol{v}_h^{j+1}\right\|^2 + k^4\sum_{j=1}^{N-1}\left\|\mathrm{d}_t^2\boldsymbol{v}_h^{j+1}\right\|^2 + k^4\sum_{j=1}^{N-1}\left\|\mathrm{d}_t^2\boldsymbol{\nabla}\boldsymbol{m}_h^{j+1}\right\|^2 \lesssim \left\|\boldsymbol{v}_h^0\right\|^2 + \left\|\boldsymbol{\nabla}\boldsymbol{m}_h^0\right\|^2.$$

Using the norm equivalences once more, we get for $N \geq 2$

$$\left\|\boldsymbol{v}_h^N\right\|^2 + \left\|\boldsymbol{\nabla}\boldsymbol{m}_h^N\right\|^2 + k\sum_{j=1}^{N-1}\left\|\boldsymbol{v}_h^{j+1}\right\|^2 + k^2\sum_{j=1}^{N-1}\left\|\mathrm{d}_t\boldsymbol{v}_h^{j+1}\right\|^2 + k^4\sum_{j=1}^{N-1}\left\|\mathrm{d}_t^2\boldsymbol{v}_h^{j+1}\right\|^2 + k^4\sum_{j=1}^{N-1}\left\|\mathrm{d}_t^2\boldsymbol{\nabla}\boldsymbol{m}_h^{j+1}\right\|^2 \lesssim \left\|\boldsymbol{v}_h^0\right\|^2 + \left\|\boldsymbol{\nabla}\boldsymbol{m}_h^0\right\|^2 \lesssim 1. \tag{8.33}$$

Moreover, thanks to Proposition 8.6.2, we have

$$k^2\sum_{j=2}^{N-1}\left\|\mathrm{d}_t^2\boldsymbol{m}_h^{j+1}\right\|^2 \lesssim k^2\left\|\mathrm{d}_t^2\boldsymbol{m}_h^2\right\|^2 + k^2\sum_{j=2}^{N-1}\left\|\mathrm{d}_t\boldsymbol{v}_h^{j+1}\right\|^2 \overset{(8.33)}{\lesssim} k^2\left\|\mathrm{d}_t^2\boldsymbol{m}_h^2\right\|^2 + 1.$$

The term $k^2\left\|\mathrm{d}_t^2\boldsymbol{m}_h^2\right\|^2$ is also bounded. Indeed,

$$k^2\mathrm{d}_t^2\boldsymbol{m}_h^2 = \boldsymbol{m}_h^2 - 2\boldsymbol{m}_h^1 + \boldsymbol{m}_h^0 = \frac{2}{3}k(\boldsymbol{v}_h^2 - \mathrm{d}_t\boldsymbol{m}_h^1) = \frac{2}{3}k(\boldsymbol{v}_h^2 - \boldsymbol{v}_h^1)$$

and therefore

$$k^4\left\|\mathrm{d}_t^2\boldsymbol{m}_h^2\right\|^2 \lesssim k^2\big(\left\|\boldsymbol{v}_h^1\right\|^2 + \left\|\boldsymbol{v}_h^2\right\|^2\big) \overset{(8.33)}{\lesssim} k^2.$$

All together, we have that

$$k^2\sum_{j=1}^{N-1}\left\|\mathrm{d}_t^2\boldsymbol{m}_h^{j+1}\right\|^2 \lesssim 1. \tag{8.34}$$

Combining (8.33) and (8.34) gives (8.19) and concludes the first part of the proof.

To get the unit length constraint violation we use [ABP24, Lemma 3.4], noting that $|\boldsymbol{m}_h^0|^2 = 1$ and $|\boldsymbol{m}_h^1|^2 = |\boldsymbol{m}_h^0|^2 + k^2|\boldsymbol{v}_h^1|^2$, which shows that for $N \geq 2$

$$\left\||\boldsymbol{m}_h^N|^2 - 1\right\|_{L^1(\Omega)} \lesssim k^2\left\|\boldsymbol{v}_h^1\right\|^2 + k^4\sum_{i=1}^{N-1}\left\|\mathrm{d}_t^2\boldsymbol{m}_h^{i+1}\right\|^2 \overset{(8.19)}{\lesssim} k^2. \tag{8.35}$$

The boundedness of $\left\|\boldsymbol{m}_h^i\right\|^2$ follows immediately by the triangular inequality. Furthermore, since $\boldsymbol{v}_h^1 = \boldsymbol{v}_h^0 + k\mathrm{d}_t\boldsymbol{v}_h^1$, we have from (8.35) that

$$\left\||\boldsymbol{m}_h^N|^2 - 1\right\|_{L^1(\Omega)} \lesssim k^2\left\|\boldsymbol{v}_h^0\right\|^2 + k^4\left\|\mathrm{d}_t\boldsymbol{v}_h^1\right\|^2 + k^4\sum_{i=1}^{N-1}\left\|\mathrm{d}_t^2\boldsymbol{m}_h^{i+1}\right\|^2$$

so, if $\boldsymbol{v}_h^0 = \mathbf{0}$, we have

$$\left\| |\boldsymbol{m}_h^N|^2 - 1 \right\|_{L^1(\Omega)} \lesssim k^3 \Big(k \left\| \mathrm{d}_t \boldsymbol{v}_h^1 \right\|^2 + k \sum_{i=1}^{N-1} \left\| \mathrm{d}_t^2 \boldsymbol{m}_h^{i+1} \right\|^2 \Big),$$

which is of third order in time if the quantity in parentheses is uniformly bounded. This completes the proof. □

Proof of Theorem 8.4.6 (Definition 8.2.1* (i)*). The uniform boundedness guaranteed by (8.19) yields the uniform boundedness of the reconstructed interpolants (8.22)–(8.27), and therefore we can prove that there exists $\boldsymbol{m} \in L^\infty(0,T;\boldsymbol{H}^1(\Omega)) \cap W^{1,\infty}(0,T;\boldsymbol{L}^2(\Omega))$ such that, upon extraction of subsequences, there holds convergences $\boldsymbol{m}_{hk}, \boldsymbol{m}_{hk}^\pm, \widehat{\boldsymbol{m}}_{hk}^+ \overset{*}{\rightharpoonup} \boldsymbol{m}$ in $L^\infty(0,T;\boldsymbol{H}^1(\Omega))$, $\boldsymbol{m}_{hk} \rightharpoonup \boldsymbol{m}$ in $\boldsymbol{H}^1(\Omega_T)$ and $\boldsymbol{m}_{hk}, \boldsymbol{m}_{hk}^\pm, \widehat{\boldsymbol{m}}_{hk}^+ \to \boldsymbol{m}$ in $\boldsymbol{L}^2(\Omega_T)$, see [AFP25] for further details. □

Proof of Theorem 8.4.6 (Definition 8.2.1* (ii)*). We have that $\boldsymbol{m}_{hk} \rightharpoonup \boldsymbol{m}$ in $\boldsymbol{H}^1(\Omega_T)$, so it follows $\boldsymbol{m}_{hk}(0) \rightharpoonup \boldsymbol{m}(0)$ in $\boldsymbol{H}^{1/2}(\Omega)$. By assumption (8.4), it holds that $\boldsymbol{m}_{hk}(0) = \boldsymbol{m}_h^0 \to \boldsymbol{m}^0$ strongly and hence weakly in $\boldsymbol{H}^1(\Omega)$. It follows that $\boldsymbol{m}(0) = \boldsymbol{m}^0$ in the sense of traces which verifies Definition 8.2.1(ii) for $\boldsymbol{m}$. The proof that $\partial_t \boldsymbol{m}(t) \to \boldsymbol{v}^0$ in $\boldsymbol{L}^2(\Omega)$ as $t \to 0$ is more complicated, and for this we refer to [BFP08, p.72]. □

Proof of Theorem 8.4.6 (Limit $\boldsymbol{m}$ satisfies Definition 8.2.1 (iii)*).* We have split the proof into five steps, where the core argument is summarized in Step 1.

Step 1 (Discrete variational formulation). Following the approach of [AFP25] let $\boldsymbol{\varphi} \in C_C^\infty([0,T), \boldsymbol{C}(\Omega))$ be a smooth test function and fix $j \in \{0, 1, \dots, N-1\}$. We choose the test function

$$\boldsymbol{\zeta}_h = \mathcal{I}_h[\widehat{\boldsymbol{m}}_h^{j+1} \times \boldsymbol{\varphi}(t_j)] \in \boldsymbol{\mathcal{K}}_h(\widehat{\boldsymbol{m}}_h^{j+1})$$

where $\widehat{\boldsymbol{m}}_h^1 = \boldsymbol{m}_h^0$ for uniform notation. Testing the variational formulations (8.14)–(8.15) with $k\boldsymbol{\zeta}_h$, we obtain for $j = 0$

$$\begin{aligned} &\tau k \left\langle \mathrm{d}_t \boldsymbol{v}_h^1, \mathcal{I}_h[\boldsymbol{m}_h^0 \times \boldsymbol{\varphi}(0)] \right\rangle + \alpha k \left\langle \boldsymbol{v}_h^1, \mathcal{I}_h[\boldsymbol{m}_h^0 \times \boldsymbol{\varphi}(0)] \right\rangle \\ &\qquad + k \left\langle \boldsymbol{m}_h^0 \times \boldsymbol{v}_h^1, \mathcal{I}_h[\boldsymbol{m}_h^0 \times \boldsymbol{\varphi}(0)] \right\rangle = -k \left\langle \boldsymbol{\nabla}(\boldsymbol{m}_h^0 + k\boldsymbol{v}_h^1), \boldsymbol{\nabla} \mathcal{I}_h[\boldsymbol{m}_h^0 \times \boldsymbol{\varphi}(0)] \right\rangle \end{aligned}$$

and for $j \geq 1$

$$\begin{aligned} &\beta\tau k \left\langle \mathrm{d}_t \boldsymbol{v}_h^{j+1}, \mathcal{I}_h[\widehat{\boldsymbol{m}}_h^{j+1} \times \boldsymbol{\varphi}(t_j)] \right\rangle \\ &\qquad + (1-\beta)\frac{\tau}{2} \left\langle 3\boldsymbol{v}_h^{j+1} - 4\boldsymbol{v}_h^j + \boldsymbol{v}_h^{j-1}, \mathcal{I}_h[\widehat{\boldsymbol{m}}_h^{j+1} \times \boldsymbol{\varphi}(t_j)] \right\rangle \\ &\qquad + \alpha k \left\langle \boldsymbol{v}_h^{j+1}, \mathcal{I}_h[\widehat{\boldsymbol{m}}_h^{j+1} \times \boldsymbol{\varphi}(t_j)] \right\rangle + k \left\langle \widehat{\boldsymbol{m}}_h^{j+1} \times \boldsymbol{v}_h^{j+1}, \mathcal{I}_h[\widehat{\boldsymbol{m}}_h^{j+1} \times \boldsymbol{\varphi}(t_j)] \right\rangle \\ &\qquad = -\frac{k}{3} \left\langle \boldsymbol{\nabla}(4\boldsymbol{m}_h^j - \boldsymbol{m}_h^{j-1} + 2k\boldsymbol{v}_h^{j+1}), \boldsymbol{\nabla} \mathcal{I}_h[\widehat{\boldsymbol{m}}_h^{j+1} \times \boldsymbol{\varphi}(t_j)] \right\rangle. \end{aligned}$$

On the left-hand sides, we can remove the nodal interpolant subject to an error that vanishes in the limit (cf. [Alo08]), and summing the two equations over

$j = 0, \dots, N-1$ yields

$$
\begin{aligned}
&\beta\tau k \sum_{j=0}^{N-1} \left\langle \mathrm{d}_t \boldsymbol{v}_h^{j+1}, \widehat{\boldsymbol{m}}_h^{j+1} \times \boldsymbol{\varphi}(t_j) \right\rangle \\
&\quad + (1-\beta)\frac{\tau}{2} \sum_{j=1}^{N-1} \left\langle 3\boldsymbol{v}_h^{j+1} - 4\boldsymbol{v}_h^{j} + \boldsymbol{v}_h^{j-1}, \widehat{\boldsymbol{m}}_h^{j+1} \times \boldsymbol{\varphi}(t_j) \right\rangle \\
&\quad + (1-\beta)\tau k \left\langle \mathrm{d}_t \boldsymbol{v}_h^{1}, \boldsymbol{m}_h^{0} \times \boldsymbol{\varphi}(t_0) \right\rangle + \alpha k \sum_{j=0}^{N-1} \left\langle \boldsymbol{v}_h^{j+1}, \widehat{\boldsymbol{m}}_h^{j+1} \times \boldsymbol{\varphi}(t_j) \right\rangle \qquad (8.36) \\
&\quad + k \sum_{j=0}^{N-1} \left\langle \widehat{\boldsymbol{m}}_h^{j+1} \times \boldsymbol{v}_h^{j+1}, \widehat{\boldsymbol{m}}_h^{j+1} \times \boldsymbol{\varphi}(t_j) \right\rangle \\
&\qquad = -k \sum_{j=0}^{N-1} \left\langle \boldsymbol{\nabla} \boldsymbol{m}_h^{j+1}, \boldsymbol{\nabla} \mathcal{I}_h[\widehat{\boldsymbol{m}}_h^{j+1} \times \boldsymbol{\varphi}(t_j)] \right\rangle .
\end{aligned}
$$

The following steps (2)–(5) will show that the terms in (8.36) converge to the following limit equation

$$
\begin{aligned}
\int_0^T \langle \partial_t \boldsymbol{m}(t), \boldsymbol{\varphi}(t) \rangle \,\mathrm{d}t &= -\int_0^T \langle \boldsymbol{h}_{\mathrm{eff}}[\boldsymbol{m}(t)], \boldsymbol{\varphi}(t) \rangle \,\mathrm{d}t \\
&\quad + \alpha \int_0^T \langle \boldsymbol{m}(t) \times \partial_t \boldsymbol{m}(t), \boldsymbol{\varphi}(t) \rangle \,\mathrm{d}t \qquad (8.37) \\
- \tau \int_0^T \langle \boldsymbol{m}(t) \times \partial_t \boldsymbol{m}(t), \partial_t \boldsymbol{\varphi}(t) \rangle \,\mathrm{d}t &- \tau \left\langle \boldsymbol{m}^0 \times \boldsymbol{v}^0, \boldsymbol{\varphi}(0) \right\rangle
\end{aligned}
$$

Overall, we have then proved that (8.37) holds for all $\boldsymbol{\varphi} \in C^\infty(\Omega_T)$ and hence, by density, for all $\boldsymbol{\varphi} \in \boldsymbol{H}^1(\Omega_T)$. Consequently, this verifies Definition 8.2.1 (iii).

Step 2 (Convergence of the last three terms of (8.36)). The term on the right-hand side and the last two terms on the left-hand side of (8.36) converge exactly as in the proof of this result in [AFP25]. Indeed, see [AFP25] for further details, it holds that

$$
\begin{aligned}
&\alpha k \sum_{j=0}^{N-1} \left\langle \boldsymbol{v}_h^{j+1}, \widehat{\boldsymbol{m}}_h^{j+1} \times \boldsymbol{\varphi}(t_j) \right\rangle = \alpha \int_0^T \left\langle \boldsymbol{v}_{hk}^{+}(t), \widehat{\boldsymbol{m}}_{hk}^{+}(t) \times \boldsymbol{\varphi}(t) \right\rangle \mathrm{d}t \\
&\xrightarrow{(h,k)\to(0,0)} \alpha \int_0^T \langle \partial_t \boldsymbol{m}(t), \boldsymbol{m}(t) \times \boldsymbol{\varphi}(t) \rangle \,\mathrm{d}t = -\alpha \int_0^T \langle \boldsymbol{m}(t) \times \partial_t \boldsymbol{m}(t), \boldsymbol{\varphi}(t) \rangle \,\mathrm{d}t;
\end{aligned}
$$

$$
\begin{aligned}
&k \sum_{j=0}^{N-1} \left\langle \widehat{\boldsymbol{m}}_h^{j+1} \times \boldsymbol{v}_h^{j+1}, \widehat{\boldsymbol{m}}_h^{j+1} \times \boldsymbol{\varphi}(t_j) \right\rangle = \int_0^T \left\langle \widehat{\boldsymbol{m}}_{hk}^{+}(t) \times \boldsymbol{v}_{hk}^{+}(t), \widehat{\boldsymbol{m}}_{hk}^{+}(t) \times \boldsymbol{\varphi}(t) \right\rangle \mathrm{d}t \\
&\xrightarrow{(h,k)\to(0,0)} \int_0^T \langle \partial_t \boldsymbol{m}(t), \boldsymbol{\varphi}(t) \rangle \,\mathrm{d}t;
\end{aligned}
$$

and

$$
\begin{aligned}
&- k \sum_{j=0}^{N-1} \left\langle \boldsymbol{\nabla} \boldsymbol{m}_h^{j+1}, \boldsymbol{\nabla} \mathcal{I}_h[\widehat{\boldsymbol{m}}_h^{j+1} \times \boldsymbol{\varphi}(t_j)] \right\rangle \\
&\qquad = - \int_0^T \left\langle \boldsymbol{\nabla} \boldsymbol{m}_{hk}^+(t), \boldsymbol{\nabla} \mathcal{I}_h[\widehat{\boldsymbol{m}}_{hk}^+(t) \times \boldsymbol{\varphi}(t)] \right\rangle \mathrm{d}t \\
&\xrightarrow{(h,k)\to(0,0)} - \int_0^T \langle \boldsymbol{\nabla} \boldsymbol{m}(t), \boldsymbol{m}(t) \times \boldsymbol{\nabla} \boldsymbol{\varphi}(t) \rangle \, \mathrm{d}t \\
&\qquad = - \int_0^T \langle \boldsymbol{h}_{\mathrm{eff}}[\boldsymbol{m}(t)], \boldsymbol{\varphi}(t) \times \boldsymbol{m}(t) \rangle \, \mathrm{d}t.
\end{aligned}
$$

Therefore, in the remaining part of the proof, we will focus on the first three terms of the left-hand side of (8.36), which are the terms raising from the adding of the inertial term.

Step 3 (Convergence of the first term of (8.36)). To deal with the first term, we take inspiration from [Rug22]. Using a summation by parts formula and some algebraic manipulations, we have

$$
\begin{aligned}
\beta\tau k \sum_{j=0}^{N-1} \left\langle \mathrm{d}_t \boldsymbol{v}_h^{j+1}, \widehat{\boldsymbol{m}}_h^{j+1} \times \boldsymbol{\varphi}(t_j) \right\rangle &= \beta\tau \sum_{j=0}^{N-1} \left\langle \boldsymbol{v}_h^{j+1} - \boldsymbol{v}_h^j, \widehat{\boldsymbol{m}}_h^{j+1} \times \boldsymbol{\varphi}(t_j) \right\rangle \\
&= -\beta\tau \sum_{j=0}^{N-1} \left\langle \boldsymbol{v}_h^{j+1}, \widehat{\boldsymbol{m}}_h^{j+2} \times \boldsymbol{\varphi}(t_{j+1}) - \widehat{\boldsymbol{m}}_h^{j+1} \times \boldsymbol{\varphi}(t_j) \right\rangle \\
&\quad + \beta\tau \left\langle \boldsymbol{v}_h^N, \widehat{\boldsymbol{m}}_h^{N+1} \times \boldsymbol{\varphi}(t_N) \right\rangle \\
&\quad - \beta\tau \left\langle \boldsymbol{v}_h^0, \widehat{\boldsymbol{m}}_h^1 \times \boldsymbol{\varphi}(t_0) \right\rangle
\end{aligned}
$$

and noting that $\boldsymbol{\varphi}(t_N) = 0$ and $\widehat{\boldsymbol{m}}_h^1 = \boldsymbol{m}_h^0$, we have

$$
\begin{aligned}
&\beta\tau k \sum_{j=0}^{N-1} \left\langle \mathrm{d}_t \boldsymbol{v}_h^{j+1}, \widehat{\boldsymbol{m}}_h^{j+1} \times \boldsymbol{\varphi}(t_j) \right\rangle \\
&= -\beta\tau \sum_{j=0}^{N-1} \left\langle \boldsymbol{v}_h^{j+1}, \widehat{\boldsymbol{m}}_h^{j+2} \times \boldsymbol{\varphi}(t_{j+1}) - \widehat{\boldsymbol{m}}_h^{j+1} \times \boldsymbol{\varphi}(t_j) \right\rangle - \beta\tau \left\langle \boldsymbol{v}_h^0, \boldsymbol{m}_h^0 \times \boldsymbol{\varphi}(t_0) \right\rangle. \\
&= -\beta\tau k \sum_{j=0}^{N-1} \left\langle \boldsymbol{v}_h^{j+1}, \widehat{\boldsymbol{m}}_h^{j+1} \times \mathrm{d}_t \boldsymbol{\varphi}(t_{j+1}) \right\rangle - \beta\tau k \sum_{j=0}^{N-1} \left\langle \boldsymbol{v}_h^{j+1}, \mathrm{d}_t \widehat{\boldsymbol{m}}_h^{j+2} \times \boldsymbol{\varphi}(t_{j+1}) \right\rangle \\
&\qquad\qquad - \beta\tau \left\langle \boldsymbol{v}_h^0, \boldsymbol{m}_h^0 \times \boldsymbol{\varphi}(t_0) \right\rangle.
\end{aligned}
$$

Using that $\boldsymbol{a}\cdot(\boldsymbol{a}\times\boldsymbol{b})=0$ it holds that

$$\begin{aligned}\beta\tau k\sum_{j=0}^{N-1}\left\langle \mathrm{d}_t\boldsymbol{v}_h^{j+1},\widehat{\boldsymbol{m}}_h^{j+1}\times\boldsymbol{\varphi}(t_j)\right\rangle &= -\beta\tau k\sum_{j=0}^{N-1}\left\langle \boldsymbol{v}_h^{j+1},\widehat{\boldsymbol{m}}_h^{j+1}\times\mathrm{d}_t\boldsymbol{\varphi}(t_{j+1})\right\rangle\\ &\quad-\beta\tau k\sum_{j=0}^{N-1}\left\langle \boldsymbol{v}_h^{j+1},(\mathrm{d}_t\widehat{\boldsymbol{m}}_h^{j+2}-\boldsymbol{v}_h^{j+1})\times\boldsymbol{\varphi}(t_{j+1})\right\rangle\\ &\quad-\beta\tau\left\langle \boldsymbol{v}_h^0,\boldsymbol{m}_h^0\times\boldsymbol{\varphi}(t_0)\right\rangle. \end{aligned}\tag{8.38}$$

The first term of the right-hand side of (8.38) converges to

$$\begin{aligned}-\beta\tau k\sum_{j=0}^{N-1}\left\langle \boldsymbol{v}_h^{j+1},\widehat{\boldsymbol{m}}_h^{j+1}\times\mathrm{d}_t\boldsymbol{\varphi}(t_{j+1})\right\rangle &= -\beta\tau\int_0^T\left\langle \boldsymbol{v}_{hk}^+(t),\widehat{\boldsymbol{m}}_{hk}^+(t)\times\mathrm{d}_t\boldsymbol{\varphi}(t)\right\rangle\mathrm{d}t\\ &\xrightarrow{(h,k)\to(0,0)} -\beta\tau\int_0^T\langle\partial_t\boldsymbol{m}(t),\boldsymbol{m}(t)\times\partial_t\boldsymbol{\varphi}(t)\rangle\,\mathrm{d}t\\ &= \beta\tau\int_0^T\langle\boldsymbol{m}(t)\times\partial_t\boldsymbol{m}(t),\partial_t\boldsymbol{\varphi}(t)\rangle\,\mathrm{d}t.\end{aligned}$$

Regarding the second term of the right-hand side of (8.38), observing that for $j=0$ we get $\mathrm{d}_t\widehat{\boldsymbol{m}}_h^2=2\boldsymbol{v}_h^1$, it holds that

$$\left\langle \boldsymbol{v}_h^1,(\mathrm{d}_t\widehat{\boldsymbol{m}}_h^2-\boldsymbol{v}_h^1)\times\boldsymbol{\varphi}(t_0)\right\rangle=\left\langle \boldsymbol{v}_h^1,\boldsymbol{v}_h^1\times\boldsymbol{\varphi}(t_0)\right\rangle=0,$$

and thus we can ignore the $j=0$ term of the second sum. Moreover, notice that for $j\geq 1$

$$\mathrm{d}_t\widehat{\boldsymbol{m}}_h^{j+2}-\boldsymbol{v}_h^{j+1}=\frac{k}{2}\mathrm{d}_t^2\boldsymbol{m}_h^{j+1}.$$

Thus, we have that

$$-k\sum_{j=1}^{N-1}\left\langle \boldsymbol{v}_h^{j+1},(\mathrm{d}_t\widehat{\boldsymbol{m}}_h^{j+2}-\boldsymbol{v}_h^{j+1})\times\boldsymbol{\varphi}(t_{j+1})\right\rangle=-\frac{k^2}{2}\sum_{j=1}^{N-1}\left\langle \boldsymbol{v}_h^{j+1},\mathrm{d}_t^2\boldsymbol{m}_h^{j+1}\times\boldsymbol{\varphi}(t_{j+1})\right\rangle.$$

Applying the weighted Young's inequality (with $\varepsilon=k^{1/2}$), we have that

$$\left|\left\langle \boldsymbol{v}_h^{j+1},\mathrm{d}_t^2\boldsymbol{m}_h^{j+1}\times\boldsymbol{\varphi}(t_{j+1})\right\rangle\right|\leq\frac{\left\|\boldsymbol{v}_h^{j+1}\right\|^2}{2k^{1/2}}+k^{1/2}\frac{\left\|\mathrm{d}_t^2\boldsymbol{m}_h^{j+1}\times\boldsymbol{\varphi}(t_{j+1})\right\|^2}{2},$$

so that

$$\begin{aligned}\left|k\sum_{j=1}^{N-1}\left\langle \boldsymbol{v}_h^{j+1},(\mathrm{d}_t\widehat{\boldsymbol{m}}_h^{j+2}-\boldsymbol{v}_h^{j+1})\times\boldsymbol{\varphi}(t_{j+1})\right\rangle\right| &= \left|\frac{k^2}{2}\sum_{j=1}^{N-1}\left\langle \boldsymbol{v}_h^{j+1},\mathrm{d}_t^2\boldsymbol{m}_h^{j+1}\times\boldsymbol{\varphi}(t_{j+1})\right\rangle\right|\\ &\leq\frac{k^{3/2}}{4}\sum_{j=1}^{N-1}\left\|\boldsymbol{v}_h^{j+1}\right\|^2+\frac{k^{5/2}}{4}\sum_{j=1}^{N-1}\left\|\mathrm{d}_t^2\boldsymbol{m}_h^{j+1}\times\boldsymbol{\varphi}(t_{j+1})\right\|^2\\ &\overset{(8.19)}{\lesssim} k^{1/2}+k^{1/2}\left\|\boldsymbol{\varphi}\right\|_{\boldsymbol{L}^\infty(\Omega)}^2\xrightarrow{(h,k)\to(0,0)}0.\end{aligned}\tag{8.39}$$

Finally, the last term of the right-hand side of (8.38) converges to

$$-\beta\tau\left\langle \boldsymbol{v}_h^0, \boldsymbol{m}_h^0 \times \boldsymbol{\varphi}(t_0)\right\rangle \xrightarrow{(h,k)\to(0,0)} -\beta\tau\left\langle \boldsymbol{v}^0, \boldsymbol{m}^0 \times \boldsymbol{\varphi}(0)\right\rangle,$$

and thus we have shown that

$$\begin{aligned}\beta\tau k\sum_{j=0}^{N-1}\left\langle \mathrm{d}_t\boldsymbol{v}_h^{j+1}, \widehat{\boldsymbol{m}}_h^{j+1}\times\boldsymbol{\varphi}(t_j)\right\rangle \xrightarrow{(h,k)\to(0,0)} &\beta\tau\int_0^T \langle \boldsymbol{m}(t)\times\partial_t\boldsymbol{m}(t), \partial_t\boldsymbol{\varphi}(t)\rangle\,\mathrm{d}t\\ &-\beta\tau\left\langle \boldsymbol{v}^0, \boldsymbol{m}^0\times\boldsymbol{\varphi}(0)\right\rangle.\end{aligned} \tag{8.40}$$

This concludes the proof of convergence for the first term of (8.36).

Step 4 (Convergence of the second and third terms of (8.36)). To treat the second and third term of (8.36), we notice that

$$\frac{3}{2}\boldsymbol{v}_h^{j+1} - 2\boldsymbol{v}_h^j + \frac{1}{2}\boldsymbol{v}_h^{j-1} = \frac{3}{2}k\mathrm{d}_t\boldsymbol{v}_h^{j+1} - \frac{1}{2}k\mathrm{d}_t\boldsymbol{v}_h^j,$$

and therefore we can split the second and third terms of (8.36) as follows

$$\begin{aligned}&(1-\beta)\tau\sum_{j=1}^{N-1}\left\langle \frac{3}{2}\boldsymbol{v}_h^{j+1} - 2\boldsymbol{v}_h^j + \frac{1}{2}\boldsymbol{v}_h^{j-1}, \widehat{\boldsymbol{m}}_h^{j+1}\times\boldsymbol{\varphi}(t_j)\right\rangle\\ &\qquad + (1-\beta)\tau k\left\langle \mathrm{d}_t\boldsymbol{v}_h^1, \boldsymbol{m}_h^0\times\boldsymbol{\varphi}(t_0)\right\rangle\\ &= \frac{3}{2}(1-\beta)\tau k\sum_{j=1}^{N-1}\left\langle \mathrm{d}_t\boldsymbol{v}_h^{j+1}, \widehat{\boldsymbol{m}}_h^{j+1}\times\boldsymbol{\varphi}(t_j)\right\rangle\\ &\qquad - \frac{1}{2}(1-\beta)\tau k\sum_{j=1}^{N-1}\left\langle \mathrm{d}_t\boldsymbol{v}_h^{j}, \widehat{\boldsymbol{m}}_h^{j+1}\times\boldsymbol{\varphi}(t_j)\right\rangle\\ &\qquad + \frac{3}{2}(1-\beta)\tau k\left\langle \mathrm{d}_t\boldsymbol{v}_h^1, \boldsymbol{m}_h^0\times\boldsymbol{\varphi}(t_0)\right\rangle - \frac{1}{2}(1-\beta)\tau k\left\langle \mathrm{d}_t\boldsymbol{v}_h^1, \boldsymbol{m}_h^0\times\boldsymbol{\varphi}(t_0)\right\rangle\\ &= \frac{3}{2}(1-\beta)\tau k\sum_{j=0}^{N-1}\left\langle \mathrm{d}_t\boldsymbol{v}_h^{j+1}, \widehat{\boldsymbol{m}}_h^{j+1}\times\boldsymbol{\varphi}(t_j)\right\rangle\\ &\qquad - \frac{1}{2}(1-\beta)\tau k\sum_{j=1}^{N-1}\left\langle \mathrm{d}_t\boldsymbol{v}_h^{j}, \widehat{\boldsymbol{m}}_h^{j+1}\times\boldsymbol{\varphi}(t_j)\right\rangle\\ &\qquad - \frac{1}{2}(1-\beta)\tau k\left\langle \mathrm{d}_t\boldsymbol{v}_h^1, \boldsymbol{m}_h^0\times\boldsymbol{\varphi}(t_0)\right\rangle.\end{aligned} \tag{8.41}$$

The first time of the right-hand side of (8.41) is exactly the same term of Step 3 (up to a factor of 3/2), and thus converges to

$$\begin{aligned}&\frac{3}{2}(1-\beta)\tau k\sum_{j=0}^{N-1}\left\langle \mathrm{d}_t\boldsymbol{v}_h^{j+1}, \widehat{\boldsymbol{m}}_h^{j+1}\times\boldsymbol{\varphi}(t_j)\right\rangle\\ \xrightarrow{(h,k)\to(0,0)}\quad &\frac{3}{2}(1-\beta)\tau\int_0^T\langle \boldsymbol{m}(t)\times\partial_t\boldsymbol{m}(t), \partial_t\boldsymbol{\varphi}(t)\rangle\,\mathrm{d}t\\ &-\frac{3}{2}(1-\beta)\tau\left\langle \boldsymbol{v}^0, \boldsymbol{m}^0\times\boldsymbol{\varphi}(0)\right\rangle.\end{aligned} \tag{8.42}$$

For the second term of the right-hand side of (8.41) we follow the same argument as in Step 3, with the difference that now we have $\mathrm{d}_t \boldsymbol{v}_h^j$ instead of $\mathrm{d}_t \boldsymbol{v}_h^{j+1}$. In particular, following the same lines, we have

$$
\begin{aligned}
-\frac{1}{2}(1-\beta)\tau k \sum_{j=1}^{N-1} \Big\langle \mathrm{d}_t \boldsymbol{v}_h^j, \widehat{\boldsymbol{m}}_h^{j+1} \times \boldsymbol{\varphi}(t_j) \Big\rangle & \\
&= \frac{1}{2}(1-\beta)\tau k \sum_{j=0}^{N-1} \Big\langle \boldsymbol{v}_h^j, \widehat{\boldsymbol{m}}_h^{j+1} \times \mathrm{d}_t \boldsymbol{\varphi}(t_{j+1}) \Big\rangle \\
&\quad + \frac{1}{2}(1-\beta)\tau k \sum_{j=0}^{N-1} \Big\langle \boldsymbol{v}_h^j, (\mathrm{d}_t \widehat{\boldsymbol{m}}_h^{j+2} - \boldsymbol{v}_h^j) \times \boldsymbol{\varphi}(t_{j+1}) \Big\rangle \\
&\quad + \frac{1}{2}(1-\beta)\tau k \left\langle \boldsymbol{v}_h^0, \boldsymbol{m}_h^0 \times \boldsymbol{\varphi}(t_0) \right\rangle
\end{aligned}
$$

and therefore, following the same lines as in Step 3, we have that

$$
\begin{aligned}
\frac{1}{2}(1-\beta)\tau k \sum_{j=0}^{N-1} \Big\langle \boldsymbol{v}_h^j, \widehat{\boldsymbol{m}}_h^{j+1} \times \mathrm{d}_t \boldsymbol{\varphi}(t_{j+1}) \Big\rangle & \\
&= \frac{1}{2}(1-\beta)\tau \int_0^T \left\langle \boldsymbol{v}_{hk}^-(t), \widehat{\boldsymbol{m}}_{hk}^+(t) \times \mathrm{d}_t \boldsymbol{\varphi}(t) \right\rangle \mathrm{d}t \\
&\xrightarrow{(h,k)\to(0,0)} \frac{1}{2}(1-\beta)\tau \int_0^T \langle \partial_t \boldsymbol{m}(t), \boldsymbol{m}(t) \times \partial_t \boldsymbol{\varphi}(t) \rangle \, \mathrm{d}t \\
&= -\frac{1}{2}(1-\beta)\tau \int_0^T \langle \boldsymbol{m}(t) \times \partial_t \boldsymbol{m}(t), \partial_t \boldsymbol{\varphi}(t) \rangle \, \mathrm{d}t
\end{aligned}
$$

and

$$
\frac{1}{2}(1-\beta)\tau k \left\langle \boldsymbol{v}_h^0, \boldsymbol{m}_h^0 \times \boldsymbol{\varphi}(t_0) \right\rangle \xrightarrow{(h,k)\to(0,0)} \frac{1}{2}(1-\beta)\tau \left\langle \boldsymbol{v}^0, \boldsymbol{m}^0 \times \boldsymbol{\varphi}(0) \right\rangle .
$$

The term

$$
\frac{1}{2}(1-\beta)\tau k \sum_{j=0}^{N-1} \Big\langle \boldsymbol{v}_h^j, (\mathrm{d}_t \widehat{\boldsymbol{m}}_h^{j+2} - \boldsymbol{v}_h^j) \times \boldsymbol{\varphi}(t_{j+1}) \Big\rangle
$$

requires a more careful analysis, due to the different definition of $\mathrm{d}_t \widehat{\boldsymbol{m}}_h^{j+2} - \boldsymbol{v}_h^j$ if $j = 0$, $j = 1$ or $j \geq 2$.

For $j = 0$, since

$$
\mathrm{d}_t \widehat{\boldsymbol{m}}_h^2 - \boldsymbol{v}_h^0 = \frac{1}{k}(\widehat{\boldsymbol{m}}_h^2 - \widehat{\boldsymbol{m}}_h^1) - \boldsymbol{v}_h^0 = \frac{1}{k}(2\boldsymbol{m}_h^1 - \boldsymbol{m}_h^0 - \boldsymbol{m}_h^0) - \boldsymbol{v}_h^0 = 2\boldsymbol{v}_h^1 - \boldsymbol{v}_h^0,
$$

we can proceed as in (8.39) in Step 3, obtaining

$$\begin{aligned}
&\frac{1}{2}(1-\beta)\tau k\left\langle \boldsymbol{v}_h^0, (\mathrm{d}_t\widehat{\boldsymbol{m}}_h^2-\boldsymbol{v}_h^0)\times\boldsymbol{\varphi}(t_1)\right\rangle\\
&\qquad=\frac{1}{2}(1-\beta)\tau k\left\langle \boldsymbol{v}_h^0, (2\boldsymbol{v}_h^1-\boldsymbol{v}_h^0)\times\boldsymbol{\varphi}(t_1)\right\rangle\\
&\qquad=\frac{1}{2}(1-\beta)\tau k\left\langle \boldsymbol{v}_h^0, (2\boldsymbol{v}_h^1-2\boldsymbol{v}_h^0)\times\boldsymbol{\varphi}(t_1)\right\rangle\\
&\qquad=\frac{1}{2}(1-\beta)\tau k^2\left\langle \boldsymbol{v}_h^0, 2\mathrm{d}_t\boldsymbol{v}_h^1\times\boldsymbol{\varphi}(t_1)\right\rangle\\
&\qquad\lesssim(1-\beta)\tau k^2\Big[\frac{1}{k^{1/2}}\left\|\boldsymbol{v}_h^0\right\|^2+k^{1/2}\left\|\mathrm{d}_t\boldsymbol{v}_h^1\right\|^2\|\boldsymbol{\varphi}\|^2_{\boldsymbol{L}^\infty(\Omega)}\Big]\\
&\qquad\overset{(8.19)}{\lesssim}k^{1/2}\xrightarrow{(h,k)\to(0,0)}0.
\end{aligned}$$

Similarly, for $j=1$, since

$$\mathrm{d}_t\widehat{\boldsymbol{m}}_h^3-\boldsymbol{v}_h^1=\frac{1}{k}(\widehat{\boldsymbol{m}}_h^3-\widehat{\boldsymbol{m}}_h^2)-\boldsymbol{v}_h^1=\frac{1}{k}(2\boldsymbol{m}_h^2-\boldsymbol{m}_h^1-2\boldsymbol{m}_h^1+\boldsymbol{m}_h^0)-\boldsymbol{v}_h^1=2k\mathrm{d}_t^2\boldsymbol{m}_h^2$$

we have

$$\begin{aligned}
&\frac{1}{2}(1-\beta)\tau k\left\langle \boldsymbol{v}_h^1, (\mathrm{d}_t\widehat{\boldsymbol{m}}_h^3-\boldsymbol{v}_h^1)\times\boldsymbol{\varphi}(t_2)\right\rangle\\
&\qquad=(1-\beta)\tau k^2\left\langle \boldsymbol{v}_h^1, \mathrm{d}_t^2\boldsymbol{m}_h^2\times\boldsymbol{\varphi}(t_2)\right\rangle\\
&\qquad\lesssim k^2\Big[\frac{1}{k^{1/2}}\left\|\boldsymbol{v}_h^1\right\|^2+k^{1/2}\left\|\mathrm{d}_t^2\boldsymbol{m}_h^2\right\|^2\|\boldsymbol{\varphi}\|^2_{\boldsymbol{L}^\infty(\Omega)}\Big]\\
&\qquad\overset{(8.19)}{\lesssim}k^{1/2}\xrightarrow{(h,k)\to(0,0)}0.
\end{aligned}$$

Finally, for $j\geq 2$, since

$$\mathrm{d}_t\widehat{\boldsymbol{m}}_h^{j+2}-\boldsymbol{v}_h^j=\frac{1}{k}(\widehat{\boldsymbol{m}}_h^{j+2}-\widehat{\boldsymbol{m}}_h^{j+1})-\boldsymbol{v}_h^j=2k\mathrm{d}_t^2\boldsymbol{m}_h^{j+1}-\frac{k}{2}\mathrm{d}_t^2\boldsymbol{m}_h^j$$

we have

$$\begin{aligned}
&\frac{1}{2}(1-\beta)\tau k\sum_{j=2}^{N-1}\left\langle \boldsymbol{v}_h^j, (\mathrm{d}_t\widehat{\boldsymbol{m}}_h^{j+2}-\boldsymbol{v}_h^j)\times\boldsymbol{\varphi}(t_{j+1})\right\rangle\\
&\quad=(1-\beta)\tau k^2\sum_{j=2}^{N-1}\Big[\left\langle \boldsymbol{v}_h^j, \mathrm{d}_t^2\boldsymbol{m}_h^{j+1}\times\boldsymbol{\varphi}(t_{j+1})\right\rangle-\frac{1}{4}\left\langle \boldsymbol{v}_h^j, \mathrm{d}_t^2\boldsymbol{m}_h^j\times\boldsymbol{\varphi}(t_{j+1})\right\rangle\Big],
\end{aligned}$$

and the right-hand side converges to 0 exactly as in (8.39).

All of this gives

$$\begin{aligned}
&-\frac{1}{2}(1-\beta)\tau k\sum_{j=1}^{N-1}\left\langle \mathrm{d}_t\boldsymbol{v}_h^j, \widehat{\boldsymbol{m}}_h^{j+1}\times\boldsymbol{\varphi}(t_j)\right\rangle\\
&\xrightarrow{(h,k)\to(0,0)}-\frac{1}{2}(1-\beta)\tau\int_0^T\langle\boldsymbol{m}(t)\times\partial_t\boldsymbol{m}(t),\partial_t\boldsymbol{\varphi}(t)\rangle\,\mathrm{d}t\\
&\qquad+\frac{1}{2}(1-\beta)\tau\left\langle \boldsymbol{v}^0, \boldsymbol{m}^0\times\boldsymbol{\varphi}(0)\right\rangle.
\end{aligned}\tag{8.43}$$

To conclude, we still need to consider the third term of the right-hand side of (8.41), i.e.,

$$-\frac{1}{2}(1-\beta)\tau k\left\langle \mathrm{d}_t \boldsymbol{v}_h^1, \boldsymbol{m}_h^0 \times \boldsymbol{\varphi}(t_0)\right\rangle.$$

This is the only term that needs a CFL condition $k = o(h^2)$ to converge to zero. Firstly, notice that

$$\left\|\boldsymbol{v}_h^1\right\|^2 - \left\|\boldsymbol{v}_h^0\right\|^2 \overset{(8.16)}{\lesssim} \left\|\boldsymbol{\nabla} \boldsymbol{m}_h^0\right\|^2 - \left\|\boldsymbol{\nabla} \boldsymbol{m}_h^1\right\|^2. \tag{8.44}$$

This implies that

$$\begin{aligned} k^2\left\|\mathrm{d}_t \boldsymbol{v}_h^1\right\|^2 &\overset{(8.16)}{\lesssim} \left\|\boldsymbol{v}_h^1\right\|^2 - \left\|\boldsymbol{v}_h^0\right\|^2 + \left\|\boldsymbol{\nabla} \boldsymbol{m}_h^0\right\|^2 - \left\|\boldsymbol{\nabla} \boldsymbol{m}_h^1\right\|^2 \\ &\overset{(8.44)}{\lesssim} 2\big(\left\|\boldsymbol{\nabla} \boldsymbol{m}_h^0\right\|^2 - \left\|\boldsymbol{\nabla} \boldsymbol{m}_h^1\right\|^2\big) \\ &\lesssim k\left\|\mathrm{d}_t \boldsymbol{\nabla} \boldsymbol{m}_h^1\right\| \lesssim k h^{-1}\left\|\mathrm{d}_t \boldsymbol{m}_h^1\right\| \lesssim \sqrt{k} h^{-1} \xrightarrow{(h,k)\to(0,0)} 0. \end{aligned}$$

This implies that

$$-\frac{1}{2}(1-\beta)\tau k\left\langle \mathrm{d}_t \boldsymbol{v}_h^1, \boldsymbol{m}_h^0 \times \boldsymbol{\varphi}(t_0)\right\rangle \lesssim k\left\|\mathrm{d}_t \boldsymbol{v}_h^1\right\|\left\|\boldsymbol{m}_h^0\right\|\|\boldsymbol{\varphi}\|_{\boldsymbol{L}^\infty(\Omega)} \xrightarrow{(h,k)\to(0,0)} 0. \tag{8.45}$$

Combining (8.42), (8.43) and (8.45), we obtain that

$$\begin{aligned} &(1-\beta)\tau \sum_{j=1}^{N-1}\left\langle \frac{3}{2}\boldsymbol{v}_h^{j+1} - 2\boldsymbol{v}_h^j + \frac{1}{2}\boldsymbol{v}_h^{j-1}, \widehat{\boldsymbol{m}}_h^{j+1} \times \boldsymbol{\varphi}(t_j)\right\rangle \\ &\qquad + (1-\beta)\tau k\left\langle \mathrm{d}_t \boldsymbol{v}_h^1, \boldsymbol{m}_h^0 \times \boldsymbol{\varphi}(t_0)\right\rangle \qquad (8.46) \\ &\xrightarrow{(h,k)\to(0,0)} \frac{3}{2}(1-\beta)\tau \int_0^T \langle \boldsymbol{m}(t) \times \partial_t \boldsymbol{m}(t), \partial_t \boldsymbol{\varphi}(t)\rangle \,\mathrm{d}t \\ &\qquad - \frac{3}{2}(1-\beta)\tau\left\langle \boldsymbol{v}^0, \boldsymbol{m}^0 \times \boldsymbol{\varphi}(0)\right\rangle \qquad (8.47) \\ &\qquad - \frac{1}{2}(1-\beta)\tau \int_0^T \langle \boldsymbol{m}(t) \times \partial_t \boldsymbol{m}(t), \partial_t \boldsymbol{\varphi}(t)\rangle \,\mathrm{d}t \\ &\qquad + \frac{1}{2}(1-\beta)\tau\left\langle \boldsymbol{v}^0, \boldsymbol{m}^0 \times \boldsymbol{\varphi}(0)\right\rangle \qquad (8.48) \\ &\qquad = (1-\beta)\tau \int_0^T \langle \boldsymbol{m}(t) \times \partial_t \boldsymbol{m}(t), \partial_t \boldsymbol{\varphi}(t)\rangle \,\mathrm{d}t \qquad (8.49) \\ &\qquad - (1-\beta)\tau\left\langle \boldsymbol{v}^0, \boldsymbol{m}^0 \times \boldsymbol{\varphi}(0)\right\rangle. \qquad (8.50) \end{aligned}$$

Step 5 (Convergence of the discrete variational summation). Combin-

ing (8.40) and (8.49) we obtain that

$$\begin{aligned}
&\beta\tau k\sum_{j=0}^{N-1}\left\langle \mathrm{d}_t\boldsymbol{v}_h^{j+1},\widehat{\boldsymbol{m}}_h^{j+1}\times\boldsymbol{\varphi}(t_j)\right\rangle\\
&\qquad+(1-\beta)\tau\sum_{j=1}^{N-1}\left\langle\frac{3}{2}\boldsymbol{v}_h^{j+1}-2\boldsymbol{v}_h^{j}+\frac{1}{2}\boldsymbol{v}_h^{j-1},\widehat{\boldsymbol{m}}_h^{j+1}\times\boldsymbol{\varphi}(t_j)\right\rangle\\
&\qquad+(1-\beta)\tau k\left\langle \mathrm{d}_t\boldsymbol{v}_h^{1},\boldsymbol{m}_h^{0}\times\boldsymbol{\varphi}(t_0)\right\rangle\\
&\xrightarrow{(h,k)\to(0,0)}\beta\tau\int_0^T\langle\boldsymbol{m}(t)\times\partial_t\boldsymbol{m}(t),\partial_t\boldsymbol{\varphi}(t)\rangle\,\mathrm{d}t-\beta\tau\left\langle\boldsymbol{v}^0,\boldsymbol{m}^0\times\boldsymbol{\varphi}(0)\right\rangle\\
&\qquad+(1-\beta)\tau\int_0^T\langle\boldsymbol{m}(t)\times\partial_t\boldsymbol{m}(t),\partial_t\boldsymbol{\varphi}(t)\rangle\,\mathrm{d}t-(1-\beta)\tau\left\langle\boldsymbol{v}^0,\boldsymbol{m}^0\times\boldsymbol{\varphi}(0)\right\rangle\\
&\qquad=\tau\int_0^T\langle\boldsymbol{m}(t)\times\partial_t\boldsymbol{m}(t),\partial_t\boldsymbol{\varphi}(t)\rangle\,\mathrm{d}t-\tau\left\langle\boldsymbol{v}^0,\boldsymbol{m}^0\times\boldsymbol{\varphi}(0)\right\rangle. \qquad (8.51)
\end{aligned}$$

As noticed in Step 1, the convergences from Step 2 and (8.51) imply that the discrete variational formulation (8.36) tends to its continuous counterpart (8.37) as $(h,k)\to(0,0)$. This concludes this shows that the limit $\boldsymbol{m}$ satisfies Definition 8.2.1**(iii)**. □

Proof of Theorem 8.4.6 (Definition 8.2.1*(iv)*). We have split the proof into four steps.

Step 1 (Discrete energy inequality). We consider the discrete energy equality from Corollary 8.18, and ignore some positive terms in the left-hand side to obtain

$$\begin{aligned}
&\mathcal{J}[\boldsymbol{m}_h^N,\boldsymbol{v}_h^N]+\alpha k\sum_{j=0}^{N-1}\left\|\boldsymbol{v}_h^{j+1}\right\|^2+(1-\beta)\frac{\tau k}{4}\mathrm{d}_t\left\|\boldsymbol{v}_h^N\right\|^2+\frac{k}{4}\mathrm{d}_t\left\|\boldsymbol{\nabla}\boldsymbol{m}_h^N\right\|^2\\
&\qquad\le\mathcal{J}[\boldsymbol{m}_h^0,\boldsymbol{v}_h^0]+(1-\beta)\frac{\tau k}{4}\mathrm{d}_t\left\|\boldsymbol{v}_h^1\right\|^2+\frac{k}{4}\mathrm{d}_t\left\|\boldsymbol{\nabla}\boldsymbol{m}_h^1\right\|^2.
\end{aligned}$$

We define the unsigned terms as

$$\gamma_\ell\coloneqq(1-\beta)\frac{\tau k}{4}\mathrm{d}_t\left\|\boldsymbol{v}_h^\ell\right\|^2+\frac{k}{4}\mathrm{d}_t\left\|\boldsymbol{\nabla}\boldsymbol{m}_h^\ell\right\|^2,$$

therefore we can re-write this last equation in integral form as

$$\mathcal{J}[\boldsymbol{m}_{hk}^+(T),\boldsymbol{v}_{hk}^+(T)]+\alpha\int_0^T\left\|\boldsymbol{v}_{hk}^+(t)\right\|^2\mathrm{d}t+\gamma_N\le\mathcal{J}[\boldsymbol{m}_{hk}^-(0),\boldsymbol{v}_{hk}^-(0)]+\gamma_1. \quad (8.52)$$

Step 2 (Convergence of the signed terms of (8.52)). Since $\boldsymbol{m}_{hk}^+\to\boldsymbol{m}$ in $\boldsymbol{L}^2(\Omega_T)$ and $\boldsymbol{v}_{hk}^+\rightharpoonup\partial_t\boldsymbol{m}$ in $\boldsymbol{L}^2(\Omega_T)$, it holds by weakly lower semicontinuity that

$$\mathcal{J}[\boldsymbol{m}(T),\partial_t\boldsymbol{m}(T)]\le\liminf_{(h,k)\to(0,0)}\mathcal{J}[\boldsymbol{m}_{hk}^+(T),\boldsymbol{v}_{hk}^+(T)]. \quad (8.53)$$

The strong convergence of the initial data $\boldsymbol{m}_h^0 \to \boldsymbol{m}^0$ in $\boldsymbol{H}^1(\Omega)$ and $\boldsymbol{v}_h^0 \to \boldsymbol{v}^0$ in $\boldsymbol{L}^2(\Omega)$ by assumptions (8.4) and (8.4) imply that

$$\mathcal{J}[\boldsymbol{m}^0, \boldsymbol{v}^0] = \lim_{h\to 0} \mathcal{J}[\boldsymbol{m}_h^0, \boldsymbol{v}_h^0] = \liminf_{(h,k)\to(0,0)} \mathcal{J}[\boldsymbol{m}_{hk}^-(0), \boldsymbol{v}_{hk}^-(0)]. \tag{8.54}$$

Finally, by convergence of $\boldsymbol{v}_{hk}^+ \rightharpoonup \partial_t \boldsymbol{m}$ in $\boldsymbol{L}^2(\Omega_T)$, we have that weakly lower semicontinuity yields

$$\int_0^T \|\partial_t \boldsymbol{m}(t)\|^2 \,\mathrm{d}t \le \liminf_{(h,k)\to(0,0)} \int_0^T \left\|\boldsymbol{v}_{hk}^+(t)\right\|^2 \mathrm{d}t. \tag{8.55}$$

Step 3 (Convergence of the unsigned terms of (8.52)). The unsigned terms γ_ℓ require a CFL condition $k = o(h^2)$ on the first and last step for $\ell \in \{1, N\}$, similarly to [AFP25]. Firstly, notice that

$$k \left\|\mathrm{d}_t \boldsymbol{m}_h^N\right\|^2 \le \|\partial_t \boldsymbol{m}\|_{\Omega_T}^2 \le \|\boldsymbol{m}_{hk}\|_{\boldsymbol{H}^1(\Omega)}^2 \lesssim 1;$$

therefore $\sqrt{k}\left\|\mathrm{d}_t \boldsymbol{m}_h^N\right\| \lesssim 1$. Moreover, with $\ell \in \{1, N\}$, it holds

$$\begin{aligned}
\gamma_\ell &= (1-\beta)\frac{\tau k}{4}\mathrm{d}_t \left\|\boldsymbol{v}_h^\ell\right\|^2 + \frac{k}{4}\mathrm{d}_t \left\|\boldsymbol{\nabla} \boldsymbol{m}_h^\ell\right\|^2 \\
&= (1-\beta)\frac{\tau}{4}\left(\left\|\boldsymbol{v}_h^\ell\right\|^2 - \left\|\boldsymbol{v}_h^{\ell-1}\right\|^2\right) + \frac{1}{4}\left(\left\|\boldsymbol{\nabla} \boldsymbol{m}_h^\ell\right\|^2 - \left\|\boldsymbol{\nabla} \boldsymbol{m}_h^{\ell-1}\right\|^2\right) \\
&= (1-\beta)\frac{\tau k}{4}\left\langle \boldsymbol{v}_h^\ell + \boldsymbol{v}_h^{\ell-1}, \mathrm{d}_t \boldsymbol{v}_h^\ell \right\rangle + \frac{k}{4}\left\langle \boldsymbol{\nabla} \boldsymbol{m}_h^\ell + \boldsymbol{\nabla} \boldsymbol{m}_h^{\ell-1}, \mathrm{d}_t \boldsymbol{\nabla} \boldsymbol{m}_h^\ell \right\rangle \\
&\lesssim k\left(\left\|\mathrm{d}_t \boldsymbol{v}_h^\ell\right\| + \left\|\mathrm{d}_t \boldsymbol{\nabla} \boldsymbol{m}_h^\ell\right\|\right) \\
&\lesssim k\left\|\mathrm{d}_t \boldsymbol{v}_h^\ell\right\| + kh^{-1}\left\|\mathrm{d}_t \boldsymbol{m}_h^\ell\right\|.
\end{aligned}$$

Let us fix $\ell = N$. To deal with the first term we notice that thanks to (8.19)

$$\sum_{j=0}^{N-1} \left(k\left\|\mathrm{d}_t \boldsymbol{v}_h^{j+1}\right\|\right)^2 \lesssim 1$$

and therefore as a necessary condition

$$k\left\|\mathrm{d}_t \boldsymbol{v}_h^N\right\| \xrightarrow{N\to\infty} 0.$$

Under the CFL condition $k = o(h^2)$ on the last step it holds that

$$kh^{-1}\left\|\mathrm{d}_t \boldsymbol{m}_h^N\right\| \lesssim \sqrt{k}h^{-1} \xrightarrow{(h,k)\to(0,0)} 0.$$

Let us now consider $\ell = 1$ and

$$\gamma_1 = (1-\beta)\frac{\tau k}{4}\mathrm{d}_t \left\|\boldsymbol{v}_h^1\right\|^2 + \frac{k}{4}\mathrm{d}_t \left\|\boldsymbol{\nabla} \boldsymbol{m}_h^1\right\|^2.$$

Arguing as before, under the CFL condition $k = o(h^2)$ on the first step, it holds that

$$k\mathrm{d}_t \left\|\boldsymbol{\nabla} \boldsymbol{m}_h^1\right\|^2 \lesssim k\left\|\mathrm{d}_t \boldsymbol{\nabla} \boldsymbol{m}_h^1\right\| \lesssim kh^{-1}\left\|\mathrm{d}_t \boldsymbol{m}_h^1\right\| \lesssim \sqrt{k}h^{-1} \xrightarrow{(h,k)\to(0,0)} 0.$$

Finally, as before, under the same CFL condition it holds that

$$\begin{aligned}\left\|\boldsymbol{v}_h^1\right\|^2 - \left\|\boldsymbol{v}_h^0\right\|^2 &\overset{(8.16)}{\lesssim} -\left\|\boldsymbol{\nabla}\boldsymbol{m}_h^1\right\|^2 - k\left\|\boldsymbol{v}_h^1\right\|^2 \\ &\qquad - k^2\left\|\mathrm{d}_t\boldsymbol{v}_h^1\right\|^2 - k^2\left\|\boldsymbol{\nabla}\boldsymbol{v}_h^1\right\|^2 + \left\|\boldsymbol{\nabla}\boldsymbol{m}_h^0\right\|^2 \\ &\lesssim -k\mathrm{d}_t\left\|\boldsymbol{\nabla}\boldsymbol{m}_h^1\right\|^2 \leq k\big|\mathrm{d}_t\left\|\boldsymbol{\nabla}\boldsymbol{m}_h^1\right\|^2\big| \\ &= k\big|\left\langle\boldsymbol{\nabla}\boldsymbol{m}_h^1 + \boldsymbol{\nabla}\boldsymbol{m}_h^0, \mathrm{d}_t\boldsymbol{\nabla}\boldsymbol{m}_h^1\right\rangle\big| \\ &\lesssim kh^{-1}\left\|\mathrm{d}_t\boldsymbol{m}_h^1\right\|^2 \lesssim \sqrt{k}h^{-1} \xrightarrow{(h,k)\to(0,0)} 0.\end{aligned}$$

This shows that

$$\lim_{(h,k)\to(0,0)} \gamma_\ell = 0, \quad \text{with} \quad \ell \in \{1, N\}.$$

Step 4 (Continuous energy inequality). The convergence statements from Step 2–3 prove

$$\begin{aligned}&\mathcal{J}(\boldsymbol{m}(T), \partial_t\boldsymbol{m}(T)) + \alpha\int_0^T \left\|\partial_t\boldsymbol{m}(t)\right\|^2 \mathrm{d}t \\ &\leq \liminf_{(h,k)\to(0,0)} \Big[\mathcal{J}[\boldsymbol{m}_{hk}^+(T), \boldsymbol{v}_{hk}^+(T)] + \alpha\int_0^T \left\|\boldsymbol{v}_{hk}^+(t)\right\|^2 \mathrm{d}t\Big] \\ &\overset{(8.52)}{\leq} \liminf_{(h,k)\to(0,0)} \Big[\mathcal{J}[\boldsymbol{m}_{hk}^-(0), \boldsymbol{v}_{hk}^-(0)] + \gamma_1 - \gamma_N\Big] = \mathcal{J}[\boldsymbol{m}^0, \boldsymbol{v}^0].\end{aligned}$$

This shows that the limit $\boldsymbol{m}$ satisfies the energy inequality from Definition 8.2.1 (iv) and thus concludes the proof of Theorem 8.4.6. □

Chapter 9

Conclusion

With this thesis, we have contributed to the numerical analysis of reliable and efficient methods for simulating coupled (magnetoelastic and AFM/FiM) and ultrafast (iLLG) micromagnetic phenomena. The primary focus has been on integrators that are stable/convergent unconditionally. We believe that the integrators stated in the previous chapters can be extended further to include more complicated non-local effects, and the subjects of different chapters can be mixed together, e.g. to yield magnetoelastic antiferromagnetic materials governed by the iLLG equation. To this end, we gather a few ideas that we did not have time to investigate, but we feel are worthwhile.

We have a few suggestions for future work:

- The analysis of the numerical schemes presented in this thesis was performed at the minimal regularity, that is, without assuming any regularity of the exact solution beyond what is necessary to define it. As a result, we have been able to prove weak convergence results of a subsequence without explicit rates of convergence. Each algorithm we have mentioned in this thesis deserves a rigorous error analysis in line with the analysis in [BKW24] for the projection-free tangent plane scheme, or [ALS24] for the tangent plane scheme with a projection step, where, at the price of (sometimes very strong) regularity assumptions on the exact solution, error estimates have been derived. Work has been done in this area already for several magnetoelastic integrators with [BS06, Baň05, BS05].
- A more careful investigation of the energetic behaviour given in Chapter 5 may reduce the sufficient CFL condition $k = o(h^9)$ to a less severe, and necessary, CFL condition. We recommend extending the proofs of convergence, in particular the proof of the energy law, of Chapter 5 to the algorithms of Chapter 6. The CFL condition that appears in the proof of the energy law in Chapter 5 may be relieved given a particular choice of γ or β.
- It would be interesting to compare more closely the iLLG model with the magnetoelastic model, in line with the research by H. Suhl [Suh98, Suh07]. Specifically, one could compare the nutation generated by the inertial LLG model to the nutation generated by the magnetoelastic interaction. We

also suggest modifying the iLLG system to include magnetostriction. This would be interesting from a mathematical perspective, but may be difficult to interpret from a physical standpoint, as the inertial LLG equation is partially modelled by the inclusion of magnetostriction, and thus separating these two effects may be difficult.

- The second-order methods of [ABRW25, ABP24] can be easily incorporated into the algorithms of Chapter 7 to give quadratic unit length constraint violation. In particular, the metric of gradient flow for the energy minimization schemes can be chosen to be the stronger H^1 metric, yielding additional improved performance.
- The iLLG model of Chapter 8 can be combined with the AFM/FiM model of Chapter 7. This is particularly interesting for physical investigation, as it is easier to detect nutation in antiferromagnetic materials due to them being exchange enhanced [Mon21]. The necessary extensions to both the inertial and Gilbert damping terms, to the ultrafast model have been considered by R. Mondal and others [DM24, MO21, MGRN21, Mon21, GCBM24, HWLC25, KTBB18]. This then allows for application of the methods of Chapter 8 in combination with the approach in Chapter 7. Furthermore, the iLLG formulation is very closely related to that used in accelerated gradient descent methods, so with suitable modification inline with ideas from [DGY25, DGXY24, CW22] the static energy minimization schemes could be significantly improved (in particular, with third order unit length constraint in both fields).
- We further recommend applying the midpoint scheme [ABRW25] as an alternative to the BDF2 approach of [ABP24] used in [DGY25, DGXY24, CW22] for the accelerated gradient descent methods, or for the solution of the iLLG equation. A central difference approximation (similar to a leapfrog method) for the acceleration term should yield second-order convergence in time, without being too difficult to analyse. It may also be possible to apply a Newmark-β method to the iLLG equation (as it is a PDE of second-order in time), but this will be much more difficult than for the elastic equations solved in Chapters 5 and 6. The conservation of momentum equation states that

$$\ddot{\boldsymbol{u}} = \boldsymbol{F}(\boldsymbol{u}),$$

which means that the velocity equation can be solved independently of the displacement but the iLLG equation is of the form

$$\ddot{\boldsymbol{m}} = \boldsymbol{F}(\boldsymbol{m}, \partial_t \boldsymbol{m}).$$

The dependence upon the velocity means that the resulting system of equations for iLLG is coupled. Alternatively, if considering the iLLG equation with $\alpha = 0$, we have

$$\ddot{\boldsymbol{m}} = \boldsymbol{F}(\boldsymbol{m}),$$

and the Newmark approach is likely an appropriate method to apply, at least for the energy conservation. We expect that the unit length constraint

should also be approximately conserved under this approach. The primary difficulty with these approaches is that the iLLG equation will likely become very stiff as the relaxation time τ becomes smaller, which is problematic as τ is typically very small.

- The model of Chapter 7 could be extended from two sublattices to n-sublattices for some integer $n \geq 2$. Some antiferromagnetic materials require more than 2 sublattices to describe them, e.g. $n = 3$ sublattices [RCP15, GL15], $n = 4$ sublattices [SPdS$^+$25] and even up to $n = 8$ sublattices [WKA$^+$18, MSG04]. The decoupled algorithm becomes significantly more useful, to avoid the solution of extremely large systems resulting from many magnetization fields. The decoupled systems can either be solved in parallel for very quick performance, or a Gauss–Seidel approach can be applied, updating $\boldsymbol{m}_{h,1}$ first, then $\boldsymbol{m}_{h,2}$ using the updated $\boldsymbol{m}_{h,1}$ in the spirit of the coupled algorithm, and then updating $\boldsymbol{m}_{h,3}$ using the updated values of $\boldsymbol{m}_{h,1}, \boldsymbol{m}_{h,2}$, and so on. This would appear in the energy law as a more complicated energy evolution, but with each subsequent magnetization receiving fewer error terms, thus potentially improving the performance of the algorithm energetically and in particular relaxing the time-step restriction as described in Proposition 7.4.3 (*ii*).
- The AFM model of Chapter 7 can also be extended to include magnetostriction, as in Chapters 5 and 6. The main ingredient is recognizing that the magnetostrain is now the sum of the individual magnetostrains from each sublattice as stated in [BDKC18], i.e.

$$\boldsymbol{\varepsilon}_{\mathrm{m}}(\boldsymbol{m}_1, \boldsymbol{m}_2) = \mathbb{Z}_1(\boldsymbol{m}_1 \otimes \boldsymbol{m}_1) + \mathbb{Z}_2(\boldsymbol{m}_2 \otimes \boldsymbol{m}_2).$$

  The antiferromagnetic model with magnetoelastic effects has been implemented in [MLDG$^+$24], incorporated in the software package mumax$^+$. Neither of the two solvers described in [BDKC18, MLDG$^+$24] contain any numerical analysis related to magnetoelastic effects, leaving an area open for rigorous investigation.

Bibliography

[Abe19] C. Abert. Micromagnetics and spintronics: models and numerical methods. *Eur. Phys. J. B*, 92(6):120, 2019. doi:10.1140/epjb/e2019-90599-6.

[ABH+15] M. Alnæs, J. Blechta, J. Hake, A. Johansson, B. Kehlet, A. Logg, C. Richardson, J. Ring, M. E. Rognes, and G. N. Wells. The FEniCS project version 1.5. *Arch. Numer. Softw.*, 3(100), 2015. doi:10.11588/ans.2015.100.20553.

[ABP24] G. Akrivis, S. Bartels, and C. Palus. Quadratic constraint consistency in the projection-free approximation of harmonic maps and bending isometries. *Math. of Comput.*, 2024. doi:10.1090/mcom/4035.

[ABRW25] G. Akrivis, S. Bartels, M. Ruggeri, and J. Wang. Projection-free approximation of flows of harmonic maps with quadratic constraint accuracy and variable step sizes. *arXiv prepr. arXiv:2505.05655*, 2025. doi:10.48550/arXiv.2505.05655.

[ACGK06] C. Amrouche, P. G. Ciarlet, L. Gratie, and S. Kesavan. On Saint Venant's compatibility conditions and Poincaré's lemma. *C. R. Acad. Sci. Paris, Ser. I*, 342(11):887–891, 2006. doi:10.1016/j.crma.2006.03.026.

[AEB+13] C. Abert, L. Exl, F. Bruckner, A. Drews, and D. Suess. magnum.fe: A micromagnetic finite-element simulation code based on FEniCS. *J. Magn. Magn. Mater.*, 345:29–35, 2013. doi:10.1016/j.jmmm.2013.05.051.

[AES+13] C. Abert, L. Exl, G. Selke, A. Drews, and T. Schrefl. Numerical methods for the stray-field calculation: A comparison of recently developed algorithms. *J. Magn. Magn. Mat.*, 326:176–185, 2013. doi:10.1016/j.jmmm.2012.08.041.

[AF05] R. J. Atkin and N. Fox. *An introduction to the theory of Elasticity*. Dover Publications Inc., 2005. URL `https://lccn.loc.gov/2005041433`.

[AFF+13] M. Aurada, M. Feischl, T. Führer, M. Karkulik, J. M. Melenk, and D. Praetorius. Classical FEM-BEM coupling methods: nonlinearities, well-posedness, and adaptivity. *Comput. Mech.*, 51(4):399–419,

2013. doi:10.1007/s00466-012-0779-6.

[AFKL21] G. Akrivis, M. Feischl, B. Kovács, and C. Lubich. Higher-order linearly implicit full discretization of the Landau–Lifshitz–Gilbert equation. *Math. Comput.*, 90(329):995–1038, 2021. doi:10.1090/mcom/3597.

[AFP25] M. Aldé, M. Feischl, and D. Praetorius. BDF2-type integrator for Landau–Lifshitz–Gilbert equation in micromagnetics. In preparation, 2025.

[AGL05] J. Ahrens, B. Geveci, and C. Law. ParaView: An End-User Tool for Large-Data Visualization. In C. D. Hansen and C. R. Johnson, editors, *Visualization Handbook*, pages 717–731. Butterworth-Heinemann, Burlington, 2005. doi:10.1016/B978-012387582-2/50038-1.

[Aha01] A. Aharoni. Micromagnetics: past, present and future. *Phys. B: Condens. Matter*, 306(1-4):1–9, 2001. doi:10.1016/S0921-4526(01)00954-1.

[Aha07] A. Aharoni. *Introduction to the Theory of Ferromagnetism*. Int. Ser. of Monogr. Phys. Reprint, Oxf. Univ. Press, second edition, (2001) 2007. doi:10.1093/oso/9780198508083.001.0001.

[AHP+14] C. Abert, G. Hrkac, M. Page, D. Praetorius, M. Ruggeri, and D. Suess. Spin-polarized transport in ferromagnetic multilayers: An unconditionally convergent FEM integrator. *Comput. Math. Appl.*, 68(6):639–654, 2014. doi:10.1016/j.camwa.2014.07.010.

[AJ06] F. Alouges and P. Jaisson. Convergence of a finite element discretization for the Landau–Lifshitz equations in micromagnetism. *Math. Models Methods Appl. Sci.*, 16(02):299–316, 2006. doi:10.1142/S0218202506001169.

[AKST14] F. Alouges, E. Kritsikis, J. Steiner, and J.-C. Toussaint. A convergent and precise finite element scheme for Landau–Lifschitz–Gilbert equation. *Numer. Math.*, 128(3):407–430, 2014. doi:10.1007/s00211-014-0615-3.

[AKT12] F. Alouges, E. Kritsikis, and J.-C. Toussaint. A convergent finite element approximation for Landau–Lifschitz–Gilbert equation. *Phys. B: Condens. Matter*, 407(9):1345–1349, 2012. doi:10.1016/j.physb.2011.11.031.

[Alo97] F. Alouges. A new algorithm for computing liquid crystal stable configurations: the harmonic mapping case. *SIAM J. on Numer. Anal.*, 34(5):1708–1726, 1997. doi:10.1137/S0036142994264249.

[Alo08] F. Alouges. A new finite element scheme for Landau–Lifchitz equations. *Discrete Contin. Dyn. Syst. Ser. S*, 1(2):187–196, 2008. doi:10.3934/dcdss.2008.1.187.

[ALS24] R. An, Y. Li, and W. Sun. Optimal error analysis of

the normalized tangent plane FEM for Landau–Lifshitz–Gilbert equation. *IMA J. Numer. Anal.*, pages 3109–3137, 2024. doi:10.1093/imanum/drae084.

[AS92] F. Alouges and A. Soyeur. On global weak solutions for Landau–Lifshitz equations: Existence and nonuniqueness. *Nonlinear Anal.*, 18(11):1071–1084, 1992. doi:10.1016/0362-546X(92)90196-L.

[Baň05] L. Baňas. A numerical method for the Landau–Lifshitz equation with magnetostriction. *Math. Methods Appl. Sci.*, 28(16):1939–1954, 2005. doi:10.1002/mma.651.

[Baň08] L. Baňas. Adaptive techniques for Landau–Lifshitz–Gilbert equation with magnetostriction. *J. Comput. Appl. Math.*, 215(2):304–310, 2008. doi:10.1016/j.cam.2006.03.043. Proceedings of the Third International Conference on Advanced Computational Methods in Engineering (ACOMEN 2005).

[Bar05] S. Bartels. Stability and convergence of finite-element approximation schemes for harmonic maps. *SIAM J. Numer. Anal.*, 43(1):220–238, 2005. doi:10.1137/040606594.

[Bar15a] S. Bartels. Fast and accurate finite element approximation of wave maps into spheres. *ESAIM: Math. Model. Numer. Anal.*, 49(2):551–558, 2015. doi:10.1051/m2an/2014044.

[Bar15b] S. Bartels. *Numerical Methods for Nonlinear Partial Differential Equations*, volume 47. Springer, 2015. doi:10.1007/978-3-319-13797-1.

[Bar16] S. Bartels. Projection-free approximation of geometrically constrained partial differential equations. *Math. Comput.*, 85(299):1033–1049, 2016. doi:10.1090/mcom/3008.

[BCGS92] F. Bethuel, J.-M. Coron, J.-M. Ghidaglia, and A. Soyeur. *Heat Flows and Relaxed Energies for Harmonic Maps*, pages 99–109. Birkhäuser Boston, Boston, MA, 1992. doi:10.1007/978-1-4612-0393-3_7.

[BCKO21] A. Bach, M. Cicalese, L. Kreutz, and G. Orlando. The antiferromagnetic XY model on the triangular lattice: chirality transitions at the surface scaling. *Calc. Var. Partial Differ. Equ.*, 60:149, 2021. doi:10.1007/s00526-021-02016-3.

[BCKO22] A. Bach, M. Cicalese, L. Kreutz, and G. Orlando. The antiferromagnetic XY model on the triangular lattice: topological singularities. *Ind. Univ. Math. J.*, 71(6):2411–2475, 2022. doi:10.1512/iumj.2022.71.9239.

[BDKC18] A. Barra, J. Domann, K. W. Kim, and G. Carman. Voltage control of antiferromagnetic phases at near-terahertz frequencies. *Phys. Rev. Appl.*, 9(3):034017, 2018. doi:10.1103/PhysRevApplied.9.034017.

[BEA24] M. Benmouane, E.-H. Essoufi, and C. Ayouch. A finite element scheme for the Landau–Lifshitz–Bloch equation. *Comput. Appl.*

Math., 43(7):394, 2024. doi:10.1103/PhysRevLett.76.4250.

[Ber] N. Berkov, D. amd Gorn. MicroMagus: Software package for micromagnetic simulations. `http://www.micromagus.de/`. Accessed on 19th July 2024.

[BFF+14] F. Bruckner, M. Feischl, T. Führer, P. Goldenits, M. Page, D. Praetorius, M. Ruggeri, and D. Suess. Multiscale modeling in micromagnetics: Existence of solutions and numerical integration. *Math. Models Methods Appl. Sci.*, 24(13):2627–2662, 2014. doi:10.1142/S0218202514500328.

[BFP08] S. Bartels, X. Feng, and A. Prohl. Finite element approximations of wave maps into spheres. *SIAM J. Numer. Anal.*, 46(1):61–87, 2008. doi:10.1137/060659971.

[BHB+14] B. Bergmair, T. Huber, F. Bruckner, C. Vogler, M. Fuger, and D. Suess. Fully coupled, dynamic model of a magnetostrictive amorphous ribbon and its validation. *J. Appl. Phys.*, 115(2):023905, 2014. doi:10.1063/1.4861735.

[BI15] V. G. Bar'yakhtar and B. A. Ivanov. The Landau–Lifshitz equation: 80 years of history, advances, and prospects. *Low Temp. Phys.*, 41(9):663–669, 09 2015, https://pubs.aip.org/aip/ltp/article-pdf/41/9/663/14705410/663_1_online.pdf. doi:10.1063/1.4931649.

[Bis20] M. A. Bisotti. *Research Software Engineering in Micromagnetics*. PhD thesis, University of Southampton, 2020. URL `https://eprints.soton.ac.uk/455863/`.

[BJ40] W. F. Brown Jr. Theory of the approach to magnetic saturation. *Phys. Rev.*, 58(8):736, 1940. doi:10.1103/PhysRev.58.736.

[BJ57] W. F. Brown Jr. Criterion for uniform micromagnetization. *Phys. Rev.*, 105(5):1479, 1957. doi:10.1103/PhysRev.105.1479.

[BK24] T. Z. Boulmezaoud and K. Kaliche. Stray field computation by inverted finite elements: a new method in micromagnetic simulations. *Adv. Comput. Math.*, 50(3):44, 2024. doi:10.1007/s10444-024-10139-2.

[BKK+20] J. Brandts, S. Korotov, M. Křížek, et al. *Simplicial Partitions with Applications to the Finite Element Method*. Springer Monogr. Math. Springer, 2020. doi:10.1007/978-3-030-55677-8.

[BKP08] S. Bartels, J. Ko, and A. Prohl. Numerical analysis of an explicit approximation scheme for the Landau–Lifshitz–Gilbert equation. *Math. Comp.*, 77(262):773–788, 2008. doi:10.1090/S0025-5718-07-02079-0.

[BKW24] S. Bartels, B. Kovács, and Z. Wang. Error analysis for the numerical approximation of the harmonic map heat flow with nodal constraints. *IMA J. Numer. Anal.*, 44(2):633–653, 2024. doi:10.1093/imanum/drad037.

[BL76] J. Bergh and J. Löfström. *Interpolation spaces: An introduction*, volume 223 of *Grundlehren der mathematischen Wissenschaften*. Springer, 1976. doi:10.1007/978-3-642-66451-9.

[BMDB96] E. Beaurepaire, J.-C. Merle, A. Daunois, and J.-Y. Bigot. Ultrafast spin dynamics in ferromagnetic nickel. *Phys. Rev. Lett.*, 76(22):4250, 1996. doi:10.1103/PhysRevLett.76.4250.

[BMT+18] V. Baltz, A. Manchon, M. Tsoi, T. Moriyama, T. Ono, and Y. Tserkovnyak. Antiferromagnetic spintronics. *Rev. Mod. Phys.*, 90(1):015005, 2018. doi:10.1103/RevModPhys.90.015005.

[BP06] S. Bartels and A. Prohl. Convergence of an implicit finite element method for the Landau–Lifshitz–Gilbert equation. *SIAM J. Numer. Anal.*, 44(4):1405–1419, 2006. doi:10.1137/050631070.

[BPNI21] R. Bjørk, E. B. Poulsen, K. K. Nielsen, and A. R. Insinga. Magtense: A micromagnetic framework using the analytical demagnetization tensor. *J. Magn. Magn. Mater.*, 535:168057, 2021. doi:10.1016/j.jmmm.2021.168057.

[BPPR14] L. Baňas, M. Page, D. Praetorius, and J. Rochat. A decoupled and unconditionally convergent linear FEM integrator for the Landau–Lifshitz–Gilbert equation with magnetostriction. *IMA J. Numer. Anal.*, 34(4):1361–1385, 2014. doi:10.1093/imanum/drt050.

[Bra02] A. Braides. Γ-*convergence for Beginners*, volume 22 of *Oxf. Lect. Ser. Math. Appl.* Oxford University Press, Oxford, 2002. doi:10.1093/acprof:oso/9780198507840.001.0001.

[Bro58] W. F. Brown, Jr. Rigorous approach to the theory of ferromagnetic microstructure. *J. Appl. Phys.*, 29(3):470–471, 1958. doi:10.1063/1.1723183.

[Bro62] W. F. Brown, Jr. *Magnetostatic Principles in Ferromagnetism*. Ser. Monogr. Sel. Top. Solid State Phys. North-Holland Publishing Company, 1962. URL `https://lccn.loc.gov/62051389`.

[Bro63] W. F. Brown, Jr. *Micromagnetics*, volume 18 of *Intersci. Tracts Phys. Astron.* Interscience Publishers, New York, 1963. URL `https://lccn.loc.gov/63018566`.

[Bro66] W. F. Brown, Jr. *Magnetoelastic Interactions*, volume 9 of *Springer Tracts Nat. Philos.* Springer, 1966. URL `https://lccn.loc.gov/66026600`.

[Bro78a] W. F. Brown, Jr. *Micromagnetics*. Reprint, Robert E. Krieger Publishing Company, New York, (1963) 1978.

[Bro78b] W. F. Brown, Jr. Domains, micromagnetics, and beyond: Reminiscences and assessments. *J. Appl. Phys.*, 49(3):1937–1942, 03 1978. doi:10.1063/1.324811.

[BS05] L. Baňas and M. Slodička. Space discretization for the Landau–Lifshitz–Gilbert equation with magnetostriction. *Com-*

put. Methods Appl. Mech. Eng., 194(2-5):467–477, 2005. doi:10.1016/j.cma.2004.06.021.

[BS06] L. Baňas and M. Slodička. Error estimates for Landau–Lifshitz–Gilbert equation with magnetostriction. *Appl. Numer. Math.*, 56(8):1019–1039, 2006. doi:10.1016/j.apnum.2005.09.003.

[BS08] S. C. Brenner and L. R. Scott. *The Mathematical Theory of Finite Element Methods*, volume 15 of *Texts Appl. Math.* Springer, New York, third edition, 2008. doi:10.1007/978-0-387-75934-0.

[CBM+22] M. Cherkasskii, I. Barsukov, R. Mondal, M. Farle, and A. Semisalova. Theory of inertial spin dynamics in anisotropic ferromagnets. *Phys. Rev. B*, 106(5):054428, 2022. doi:10.1103/PhysRevB.106.054428.

[CCV+17] S. Couture, R. Chang, I. Volvach, A. Goncharov, and V. Lomakin. Coupled Finite-Element Micromagnetic–Integral Equation Electromagnetic Simulator for Modeling Magnetization–Eddy Currents Dynamics. *IEEE Trans. Magn.*, 53(12):1–9, 2017. doi:10.1109/TMAG.2017.2745470.

[CEF11] G. Carbou, M. A. Efendiev, and P. Fabrie. Global weak solutions for the Landau–Lifschitz equation with magnetostriction. *Math. Methods Appl. Sci.*, 34(10):1274–1288, 2011. doi:10.1002/mma.1440.

[CF01a] G. Carbou and P. Fabrie. Regular solutions for Landau–Lifschitz equation in $\mathbb{R}^3$. *Commun. Appl. Anal.*, 5(1):17–30, 2001. URL `https://hal.science/hal-00296709v1`.

[CF01b] G. Carbou and P. Fabrie. Regular solutions for Landau–Lifschitz equation in a bounded domain. *Differ. Integral Equ.*, 14(2):213–229, 2001. doi:10.57262/die/1356123353.

[CFVD07] C. Chappert, A. Fert, and F. N. Van D. The emergence of spin electronics in data storage. *Nat. Mater.*, 6(11):813–823, 2007. doi:10.1038/nmat2024.

[CG05] S. Chikazumi and C. D. Graham. *Physics of Ferromagnetism*. Number 94 in Int. Ser. Monogr. Phys. Reprint, Oxford University Press, second edition, (1997) 2005. URL `https://lccn.loc.gov/2009497292`.

[Cim07a] I. Cimrák. Existence, regularity and local uniqueness of the solutions to the Maxwell–Landau–Lifshitz system in three dimensions. *J. Math. Anal. Appl.*, 329(2):1080–1093, 2007. doi:10.1016/j.jmaa.2006.06.080.

[Cim07b] I. Cimrák. A survey on the numerics and computations for the Landau–Lifshitz equation of micromagnetism. *Arch. Comput. Methods Eng.*, 15(3):1–37, 2007. doi:10.1007/BF03024947.

[Coe10] J. Coey. *Magnetism and Magnetic Materials*. Cambridge University Press, 2010. doi:10.1017/CBO9780511845000.

[CRW11] M.-C. Ciornei, J. Rubí, and J.-E. Wegrowe. Magnetization dynamics

in the inertial regime: Nutation predicted at short time scales. *Phys. Rev. B*, 83(2):020410, 2011. doi:10.1103/PhysRevB.83.020410.

[CS13] I. Chopra and J. Sirohi. *Smart structures theory*, volume 35. Cambridge University Press, 2013. doi:10.1017/CBO9781139025164.

[CSTT+21] F. Cutugno, L. Sanchez-Tejerina, R. Tomasello, M. Carpentieri, and G. Finocchio. Micromagnetic understanding of switching and self-oscillations in ferrimagnetic materials. *Appl. Phys. Lett.*, 118(5):052403, 2021. doi:10.1063/5.0038635.

[CW22] E. E. Chukwuemeka and S. W. Walker. Accelerated Gradient Descent Methods for the Uniaxially Constrained Landau–de Gennes model. *Adv. Appl. Math. Mech.*, 14(1):1–32, 2022. doi:10.4208/aamm.OA-2021-0075.

[DDAWE24] A. Dal Din, O. Amin, P. Wadley, and K. Edmonds. Antiferromagnetic spintronics and beyond. *npj Spintron.*, 2(1):25, 2024. doi:10.1038/s44306-024-00029-0.

[DDCF16] M. J. Dapino, Z. Deng, F. T. Calkins, and A. B. Flatau. *Magnetostrictive Devices*, pages 1–35. John Wiley & Sons, Ltd, 2016. doi:10.1002/047134608X.W4549.pub2.

[DDFPR22] E. Davoli, G. Di Fratta, D. Praetorius, and M. Ruggeri. Micromagnetics of thin films in the presence of Dzyaloshinskii–Moriya interaction. *Math. Models Methods Appl. Sci*, 32(05):911–939, 2022. doi:10.1142/S0218202522500208.

[DFIP20] G. Di Fratta, M. Innerberger, and D. Praetorius. Weak-strong uniqueness for the Landau–Lifshitz–Gilbert equation in micromagnetics. *Nonlinear Anal.: Real World Appl.*, 55:103122, 2020. doi:10.1016/j.nonrwa.2020.103122.

[DFPP+20] G. Di Fratta, C.-M. Pfeiler, D. Praetorius, M. Ruggeri, and B. Stiftner. Linear second order IMEX-type integrator for the (eddy current) Landau–Lifshitz–Gilbert equation. *IMA J. Numer. Anal.*, 40(4):2802–2838, 2020. doi:10.1093/imanum/drz046.

[DFPPR23] G. Di Fratta, C.-M. Pfeiler, D. Praetorius, and M. Ruggeri. The mass-lumped midpoint scheme for computational micromagnetics: Newton linearization and application to magnetic skyrmion dynamics. *Comput. Methods Appl. Math.*, 23(1):145–175, 2023. doi:10.1515/cmam-2022-0060.

[DGXY24] G. Dong, Z. Gong, Z. Xie, and S. Yang. BDF schemes for accelerated gradient flows in projection-free approximation of nonconvex constrained variational minimization. *arXiv prepr. arXiv:2409.14670*, 2024. doi:10.48550/arXiv.2409.14670.

[DGY25] G. Dong, H. Guo, and S. Yang. Accelerated gradient flows for large bending deformations of nonlinear plates. *SIAM J. Sci. Comput.*, 47(5):A2481–A2505, 2025. doi:10.1137/24M171904.

[DHD24] S. Dolui, A. Halder, and S. Dwivedi. Ultrafast domain wall motion in hexagonal magnetostrictive materials: role of inertial damping, magnetostriction, and dry-friction dissipation. *Acta Mech.*, 235(12):7121–7139, 2024. doi:10.1007/s00707-024-04069-9.

[DL22] A. De Laire. Recent results for the Landau–Lifshitz equation. *SeMA J.*, 79(2):253–295, 2022. doi:10.1007/s40324-021-00254-1.

[DM24] P. Dhali and R. Mondal. Theory of tensorial Gilbert damping in antiferromagnets. *J. Phys.: Condens. Matter*, 36(25):255804, 2024. doi:10.1088/1361-648X/ad353a.

[DMD24] S. Dolui, S. Maity, and S. Dwivedi. Strain-induced ultrafast magnetization dynamics in cubic magnetostrictive materials with inertial and nonlinear dissipative effects. *Z. für Angew. Math. Phys.*, 75(4):149, 2024. doi:10.1007/s00033-024-02289-6.

[DP] M. Donahue and D. G. Porter. The Object Oriented MicroMagnetic Framework (OOMMF) project at ITL/NIST. `https://math.nist.gov/oommf/`. Accessed on 18th July, 2024.

[DP99] M. J. Donahue and D. G. Porter. OOMMF user's guide: Version 1.0. Technical report, National Institute of Standards and Technology Gaithersburg, MD, 1999. URL `https://nvlpubs.nist.gov/nistpubs/Legacy/IR/nistir6376.pdf`.

[dPS24] M. d'Aquino, S. Perna, and C. Serpico. Midpoint geometric integrators for inertial magnetization dynamics. *J. Comput. Phys.*, 504:112874, 2024. doi:10.1016/j.jcp.2024.112874.

[DSL+25] A. De, J. Schlegel, A. Lentfert, L. Scheuer, B. Stadtmüller, P. Pirro, G. von Freymann, U. Nowak, and M. Aeschlimann. Magnetic nutation: Transient separation of magnetization from its angular momentum. *Phys. Rev. B*, 111(1):014432, 2025. doi:10.1103/PhysRevB.111.014432.

[dSM05] M. d'Aquino, C. Serpico, and G. Miano. Geometrical integration of Landau–Lifshitz–Gilbert equation based on the mid-point rule. *J. Comput. Phys.*, 209(2):730–753, 2005. doi:10.1016/j.jcp.2005.04.001.

[DSY18] C. Donaghy-Spargo and A. Yakovlev. Oliver heaviside's electromagnetic theory. *Philosophical Transactions of the Royal Society A: Mathematical, Physical and Engineering Sciences*, 376(2134), 2018. doi:10.1098/rsta.2018.0229.

[DW23a] C. Dorn and S. Wulfinghoff. Computing magnetic noise with micromagneto-mechanical simulations. *IEEE Trans. Magn.*, 59(2):1–4, 2023. doi:10.1109/TMAG.2022.3212764.

[DW23b] C. Dorn and S. Wulfinghoff. A magneto-mechanically coupled material model for magnetic sensor investigation. *PAMM*, 22(1):e202200008, 2023. doi:10.1002/pamm.202200008.

[Elm38] W. Elmore. The magnetic structure of cobalt. *Phys. Rev.*, 53(9):757,

1938. doi:10.1103/PhysRev.53.757.

[EMSS17] L. Exl, N. J. Mauser, T. Schrefl, and D. Suess. The extrapolated explicit midpoint scheme for variable order and step size controlled integration of the Landau–Lifschitz–Gilbert equation. *J. Comput. Phys.*, 346:14–24, 2017. doi:10.1016/j.jcp.2017.06.005.

[Ens09] D. Ensminger. *Magnetostriction: Materials and Transducers*. CRC Press, 2009. doi:10.1201/9781420020205-9.

[ESS20] L. Exl, D. Suess, and T. Schrefl. Micromagnetism. *Handbook of Magnetism and Magnetic Materials*, pages 1–44, 2020. doi:10.1007/978-3-030-63101-7_7-1.

[Eva90] L. C. Evans. *Weak convergence methods for nonlinear partial differential equations*, volume 74 of *CBMS Reg. Conf. Ser. Math.* Am. Math. Soc. Provid. RI, 1990. doi:10.1090/cbms/074.

[Eva10] L. C. Evans. *Partial differential equations*, volume 19 of *Grad. Stud. Math.* American Mathematical Society, second edition, 2010. doi:10.1090/gsm/019.

[FCV19] S. Federico, G. Consolo, and G. Valenti. Tensor representation of magnetostriction for all crystal classes. *Math. Mech. Solids*, 24(9):2814–2843, 2019. doi:10.1177/1081286518810741.

[FFBF07] T. Fischbacher, M. Franchin, G. Bordignon, and H. Fangohr. A systematic approach to multiphysics extensions of finite-element-based micromagnetic simulations: Nmag. *IEEE Trans. Magn.*, 43(6):2896–2898, 2007. doi:10.1109/TMAG.2007.893843.

[FI11] M. Fähnle and C. Illg. Electron theory of fast and ultrafast dissipative magnetization dynamics. *J. Phys.: Condens. Matter*, 23(49):493201, 2011. doi:10.1088/0953-8984/23/49/493201.

[FK90] D. R. Fredkin and T. R. Koehler. Hybrid method for computing demagnetizing fields. *IEEE Trans. Magn.*, 26(2):415–417, 1990. doi:10.1109/20.106342.

[FKS+25] P. Flauger, M. Küß, M. K. Steinbauer, F. Bruckner, B. Emhofer, E. Nysten, M. Weiß, D. Suess, H. J. Krenner, M. Albrecht, et al. Modeling magnetoelastic wave interactions in magnetic films and heterostructures: A finite-difference approach. *arXiv prepr. arXiv:2509.06007*, 2025. doi:10.48550/arXiv.2509.06007.

[FRC17] A. Fert, N. Reyren, and V. Cros. Magnetic skyrmions: advances in physics and potential applications. *Nat. Rev. Mater.*, 2:17031, 2017. doi:10.1038/natrevmats.2017.31.

[FSD+03] H. Forster, T. Schrefl, R. Dittrich, W. Scholz, and J. Fidler. Fast boundary methods for magnetostatic interactions in micromagnetics. *IEEE Trans. Magn.*, 39(5):2513–2515, 2003. doi:10.1109/TMAG.2003.816458.

[FT02] C. Fumihiro and K. Takashi. Newmark's Method and Discrete

Energy Applied to Resistive MHD Equation. *Vietnam J. Math.*, 30:501–520, 2002.

[FT17a] M. Feischl and T. Tran. The Eddy Current–LLG Equations: FEM-BEM Coupling and A Priori Error Estimates. *SIAM J. Numer. Anal.*, 55(4):1786–1819, 2017. doi:10.1137/16M1065161.

[FT17b] M. Feischl and T. Tran. Existence of Regular Solutions of the Landau–Lifshitz–Gilbert Equation in 3D with Natural Boundary Conditions. *SIAM J. Math. Anal.*, 49(6):4470–4490, 2017. doi:10.1137/16M1103427.

[GCBM24] S. Ghosh, M. Cherkasskii, I. Barsukov, and R. Mondal. Theory of tensorial magnetic inertia in terahertz spin dynamics. *Phys. Rev. B*, 110(17):174430, 2024. doi:10.1103/PhysRevB.110.174430.

[GCR06] C. J. García-Cervera and A. M. Roma. Adaptive mesh refinement for micromagnetics simulations. *IEEE Trans. Magn.*, 42(6):1648–1654, 2006. doi:10.1109/TMAG.2006.872199.

[GD08] B. Guo and S. Ding. *Landau–Lifshitz Equations*, volume 1. World Scientific, 2008. URL `https://lccn.loc.gov/2007044801`.

[GH93] B. Guo and M.-C. Hong. The Landau–Lifshitz equation of the ferromagnetic spin chain and harmonic maps. *Calc. Var. Partial Differ. Equ.*, 1(3):311–334, 1993. doi:10.1007/BF01191298.

[GHPS12] P. Goldenits, G. Hrkac, D. Praetorius, and D. Süss. An effective integrator for the Landau–Lifshitz–Gilbert equation. *IFAC Proc. Vol.*, 45(2):493–497, 2012. doi:10.3182/20120215-3-AT-3016.00086.

[Gil04] T. Gilbert. A phenomenological theory of damping in ferromagnetic materials. *IEEE Trans. Magn.*, 40(6):3443–3449, 2004. doi:10.1109/TMAG.2004.836740.

[GL15] O. Gomonay and V. Loktev. Using generalized Landau–Lifshitz equations to describe the dynamics of multi-sublattice antiferromagnets induced by spin-polarized current. *Low Temp. Phys.*, 41(9):698–704, 2015. doi:10.1063/1.4931648.

[HB05] B. Heinrich and J. Bland, editors. *Ultrathin Magnetic Structures IV*. Springer Berlin Heidelberg, 2005. doi:10.1007/b138704.

[HCB19] R. Hertel, S. Christophersen, and S. Börm. Large-scale magnetostatic field calculation in finite element micromagnetics with $\mathcal{H}^2$-matrices. *J. Magn. Magn. Mater.*, 477:118–123, 2019. doi:10.1016/j.jmmm.2018.12.103.

[Hea93] O. Heaviside. *Electromagnetic Theory*, volume 1. "The Electrician" Printing and Publishing Company, 1893. URL `https://archive.org/details/electromagnetict01heavrich/`. Accessed: 17-02-2026.

[HH12] B. J. Hunt and O. Heaviside. Oliver heaviside: A first-rate oddity. *Phys. Today*, 65(11):48–54, 2012. doi:10.1063/PT.3.1788.

[HK14] R. Hertel and A. Kákay. Hybrid finite-element/boundary-element method to calculate oersted fields. *J. Magn. Magn. Mater.*, 369:189–196, 2014. doi:10.1016/j.jmmm.2014.06.047.

[HLW03] E. Hairer, C. Lubich, and G. Wanner. Geometric numerical integration illustrated by the Störmer–Verlet method. *Acta Numer.*, 12:399–450, 2003. doi:10.1017/S0962492902000144.

[HPP+19] G. Hrkac, C.-M. Pfeiler, D. Praetorius, M. Ruggeri, A. Segatti, and B. Stiftner. Convergent tangent plane integrators for the simulation of chiral magnetic skyrmion dynamics. *Adv. Comput. Math.*, 45(3):1329–1368, 2019. doi:10.1007/s10444-019-09667-z.

[HS98] A. Hubert and R. Schäfer. *Magnetic domains: The analysis of magnetic microstructures*. Springer Berlin, Heidelberg, 1998. doi:10.1007/978-3-540-85054-0.

[HT14] M. Hadda and M. Tilioua. On magnetization dynamics with inertial effects. *J. Eng. Math.*, 88(1):197–206, 2014. doi:10.1007/s10665-014-9691-8.

[HWLC25] P.-B. He, R.-X. Wang, Z.-D. Li, and M. Cherkasskii. Inertial antiferromagnetic resonance driven by spin-orbit torques. *arXiv prepr. arXiv:2507.10323*, 2025. doi:10.48550/arXiv.2507.10323.

[HZJB23] W. Hu, L. Zhang, L. Jin, and F. Bai. Temperature dependent intrinsic Gilbert damping in magnetostrictive FeCoSiB thin film. *AIP Adv.*, 13(2), 2023. doi:10.1063/9.0000418.

[Jil16] D. Jiles. *Introduction to magnetism and magnetic materials*. CRC press, third edition, 2016. URL `https://lccn.loc.gov/2015510131`.

[JW98] R. D. James and M. Wuttig. Magnetostriction of martensite. *Philos. Mag. A*, 77(5):1273–1299, 1998. doi:10.1080/01418619808214252.

[Kac14] Z. Kaczkowski. Piezomagnetic parameters of the magnetostrictive materials. *Arch. Acoust.*, 23(2):307–29, 2014. URL `https://acoustics.ippt.pan.pl/index.php/aa/article/view/914`.

[KBL+22] S. K. Kim, G. S. D. Beach, K.-J. Lee, T. Ono, T. Rasing, and H. Yang. Ferrimagnetic spintronics. *Nat. Mater.*, 21:24–34, 2022. doi:10.1038/s41563-021-01139-4.

[KF75] E. A. Kearsley and J. T. Fong. Linearly independent sets of isotropic cartesian tensors of ranks up to eight. *J. Res. Natl. Bur. Stand.*, pages 49–58, 1975. doi:10.6028/jres.079B.005.

[Kit49] C. Kittel. Physical theory of ferromagnetic domains. *Rev. Mod. Phys.*, 21(4):541, 1949. doi:10.1103/RevModPhys.21.541.

[KKS19] M. Kalousek, J. Kortum, and A. Schlömerkemper. Mathematical analysis of weak and strong solutions to an evolutionary model for magnetoviscoelasticity. *arXiv prepr. arXiv:1904.07179*, 2019. doi:10.48550/arXiv.1904.07179.

[KMOW00] C. Kane, J. E. Marsden, M. Ortiz, and M. West. Variational integrators and the newmark algorithm for conservative and dissipative mechanical systems. *Int. J. Numer. Methods Eng.*, 49(10):1295–1325, 2000. doi:10.1002/1097-0207(20001210)49:10%3C1295::AID-NME993%3E3.0.CO;2-W.

[Kno00] H. E. Knoepfel. *Magnetic Fields: A Comprehensive Theoretical Treatise for Practical Use*. John Wiley & Sons, Inc, 2000. URL `https://lccn.loc.gov/99058796`.

[KNR25] M. Kružík, H. Normington, and M. Ruggeri. A decoupled, unconditionally stable and second-order integrator for the landau–lifshitz–gilbert equation with magnetoelastic effects. *arXiv preprint arXiv:2512.01741*, 2025. doi:10.48550/arXiv.2512.01741.

[KO85] O. Kohmoto and K. Ohya. Mass densities of amorphous Co-rich FeCo-SiB alloys. *J. Appl. Phys.*, 57(2):626–627, 1985. doi:10.1063/1.334752.

[KP06] M. Kružík and A. Prohl. Recent developments in the modeling, analysis, and numerics of ferromagnetism. *SIAM Rev.*, 48(3):439–483, 2006. doi:10.1137/S0036144504446187.

[KPP+19] J. Kraus, C. M. Pfeiler, D. Praetorius, M. Ruggeri, and B. Stiftner. Iterative solution and preconditioning for the tangent plane scheme in computational micromagnetics. *J. Comput. Phys.*, 398:108866, 2019. doi:10.1016/j.jcp.2019.108866.

[KR19] M. Kružík and T. Roubíček. *Mathematical methods in continuum mechanics of solids*. Interact. Mech. Math. Springer Cham, 2019. doi:10.1007/978-3-030-02065-1.

[Kre06] S. Krenk. Energy conservation in newmark based time integration algorithms. *Comput. Methods Appl. Mech. Eng.*, 195(44-47):6110–6124, 2006. doi:10.1016/j.cma.2005.12.001.

[KTBB18] A. Kamra, R. E. Troncoso, W. Belzig, and A. Brataas. Gilbert damping phenomenology for two-sublattice magnets. *Phys. Rev. B*, 98(18):184402, 2018. doi:10.1103/PhysRevB.98.184402.

[KVBP+14] E. Kritsikis, A. Vaysset, L. D. Buda-Prejbeanu, F. Alouges, and J.-C. Toussaint. Beyond first-order finite element schemes in micromagnetics. *J. Comput. Phys.*, 256:357–366, 2014. doi:10.1016/j.jcp.2013.08.035.

[KW14] T. K. Karper and F. Weber. A new angular momentum method for computing wave maps into spheres. *SIAM J. Numer. Anal.*, 52(4):2073–2091, 2014. doi:10.1137/130948823.

[KZ25] R. Kitengeso and Z. Zheng. A convergent numerical approximation for the coupled Maxwell–Landau–Lifshitz–Gilbert equations with inertia effects. *J. Appl. Anal. Comput.*, 15(3):1719–1741, 2025. doi:10.11948/20240364.

[LCDW20] P. Li, J. Chen, R. Du, and X.-P. Wang. Numerical methods for antiferromagnets. *IEEE Trans. Magn.*, 56(4):1–9, 2020. doi:10.1109/TMAG.2020.2971939.

[LDC+20] X. Liang, C. Dong, H. Chen, J. Wang, Y. Wei, M. Zaeimbashi, Y. He, A. Matyushov, C. Sun, and N. Sun. A review of thin-film magnetoelastic materials for magnetoelectric applications. *Sensors*, 20(5):1532, 2020. doi:10.3390/s20051532.

[LDM+18] J. Leliaert, M. Dvornik, J. Mulkers, J. De Clercq, M. Milošević, and B. Van Waeyenberge. Fast micromagnetic simulations on GPU—recent advances made with mumax3. *J. Phys. D: Appl. Phys.*, 51(12):123002, 2018. doi:10.1088/1361-6463/aaab1c.

[Lee55] E. W. Lee. Magnetostriction and magnetomechanical effects. *Rep. Prog. Phys.*, 18(1):184, 1955. doi:10.1088/0034-4885/18/1/305.

[LL35] L. D. Landau and E. Lifshitz. On the theory of the dispersion of magnetic permeability in ferromagnetic bodies. *Phys. Z. Sowjet.*, 8:153, 1935. doi:10.1016/B978-0-08-036364-6.50008-9.

[LN03] D. Lewis and N. Nigam. Geometric integration on spheres and some interesting applications. *J. Comput. Appl. Math.*, 151(1):141–170, 2003. doi:10.1016/S0377-0427(02)00743-4.

[LPPT15] K.-N. Le, M. Page, D. Praetorius, and T. Tran. On a decoupled linear fem integrator for eddy-current-LLG. *Appl. Anal.*, 94(5):1051–1067, 2015. doi:10.1080/00036811.2014.916401.

[LST24] K.-N. Le, A. L. Soenjaya, and T. Tran. The Landau–Lifshitz–Bloch equation: Unique existence and finite element approximation. *arXiv prepr. arXiv:2406.05808*, 2024. doi:10.48550/arXiv.2406.05808.

[LT13] K.-N. Le and T. Tran. A convergent finite element approximation for the quasi-static Maxwell–Landau–Lifshitz–Gilbert equations. *Comput. Math. Appl.*, 66(8):1389–1402, 2013. doi:10.1016/j.camwa.2013.08.009.

[LXD+20] P. Li, C. Xie, R. Du, J. Chen, and X. P. Wang. Two improved Gauss–Seidel projection methods for Landau–Lifshitz–Gilbert equation. *J. Comput. Phys.*, 401:109046, 2020. doi:10.1016/j.jcp.2019.109046.

[LYL+21] P. Li, L. Yang, J. Lan, R. Du, and J. Chen. A second-order semi-implicit method for the inertial Landau–Lifshitz–Gilbert equation. *arXiv prepr. arXiv:2108.03060*, 2021. doi:10.48550/arXiv.2108.03060.

[Mag] Magnetism.eu. Software and tools. URL `https://magnetism.eu/43-software.htm`. Accessed: 17-02-2026.

[MD+07] J. E. Miltat, M. J. Donahue, et al. Numerical micromagnetics: Finite difference methods. *Handbook of Magnetism and Advanced Magnetic Materials*, 2:742–764, 2007. doi:10.1002/9780470022184.hmm202.

[ME12] C. Miehe and G. Ethiraj. A geometrically consistent incremen-

tal variational formulation for phase field models in micromagnetics. *Comput. Methods Appl. Mech. Eng.*, 245:331–347, 2012. doi:10.1016/j.cma.2012.03.021.

[Mel12] C. Melcher. Global solvability of the cauchy problem for the Landau–Lifshitz–Gilbert equation in higher dimensions. *Ind. Univ. Math. J.*, pages 1175–1200, 2012. URL `https://www.jstor.org/stable/24904079`.

[MGRN21] R. Mondal, S. Großenbach, L. Rózsa, and U. Nowak. Nutation in antiferromagnetic resonance. *Phys. Rev. B*, 103(10):104404, 2021. doi:10.1103/PhysRevB.103.104404.

[MJ12] T. Miyazaki and H. Jin. *The Physics of Ferromagnetism*, volume 158 of *Springer Ser. Mater. Sci.* Springer Berlin, 2012. doi:10.1007/978-3-642-25583-0.

[MLDG+24] L. Moreels, I. Lateur, D. De Gusem, J. Mulkers, J. Maes, M. V. Milošević, J. Leliaert, and B. Van Waeyenberge. mumax+: extensible GPU-accelerated micromagnetics and beyond. *arXiv prepr. arXiv:2411.18194*, 2024. doi:10.48550/arXiv.2411.18194.

[MLP16] C. T. Ma, X. Li, and S. J. Poon. Micromagnetic simulation of ferrimagnetic TbFeCo films with exchange coupled nanophases. *J. Magn. Magn. Mater.*, 417:197–202, 2016. doi:10.1016/j.jmmm.2016.04.096.

[MMHH+14] F. S. Mballa-Mballa, O. Hubert, S. He, S. Depeyre, and P. Meilland. Micromagnetic modeling of magneto-mechanical behavior. *IEEE Trans. Magn.*, 50(4):1–4, 2014. doi:10.1109/TMAG.2013.2288911.

[MO21] R. Mondal and P. M. Oppeneer. Influence of intersublattice coupling on the terahertz nutation spin dynamics in antiferromagnets. *Phys. Rev. B*, 104(10):104405, 2021. doi:10.1103/PhysRevB.104.104405.

[Mon21] R. Mondal. Theroy of magnetic inertial dynamics in two-sublattice ferromagnets. *Journal of Physics: Condensed Matter*, 33(27):275804, 2021. doi:10.1088/1361-648X/abfc6d.

[MRA19] E. Martínez, V. Raposo, and Ó. Alejos. Current-driven domain wall dynamics in ferrimagnets: Micromagnetic approach and collective coordinates model. *J. Magn. Magn. Mater.*, 491:165545, 2019. doi:10.1016/j.jmmm.2019.165545.

[MRF+23] R. Mondal, L. Rózsa, M. Farle, P. M. Oppeneer, U. Nowak, and M. Cherkasskii. Inertial effects in ultrafast spin dynamics. *J. Magn. Magn. Mater.*, 579:170830, 2023. doi:10.1016/j.jmmm.2023.170830.

[MSG04] J. Milano, L. Steren, and M. Grimsditch. Effect of dipolar interaction on the antiferromagnetic resonance spectra of nio. *Phys. Rev. Lett.*, 93(7):077601, 2004. doi:10.1103/PhysRevLett.93.077601.

[MT16] M. Moumni and M. Tilioua. A finite-difference scheme for a model of magnetization dynamics with inertial effects. *Journal of Engineering Mathematics*, 100(1):95–106, 2016. doi:10.1007/s10665-015-9836-4.

[NAK+21] K. Neeraj, N. Awari, S. Kovalev, D. Polley, N. Z. Hagström, S. S. Arekapudi, A. Semisalova, K. Lenz, B. Green, J.-C. Deinert, I. Ilyakov, M. Chen, M. Bawatna, V. Scalera, M. d'Aquino, C. Serpico, O. Hellwig, J.-E. Wegrowe, M. Gensch, and S. Bonetti. Inertial spin dynamics in ferromagnets. *Nat. Phys.*, 17:245–250, 2021. doi:10.1038/s41567-020-01040-y.

[NE15] N. Ntallis and K. G. Efthimiadis. Micromagnetic simulation of an antiferromagnetic particle. *Comput. Mater. Sci.*, 97:42–47, 2015. doi:10.1016/j.commatsci.2014.10.010.

[New59] N. M. Newmark. A method of computation for structural dynamics. *J. Eng. Mech. Div.*, 85(3):67–94, 1959. doi:10.1061/JMCEA3.0000098.

[NIS] NIST. OOMMF Cites. `https://math.nist.gov/oommf/oommf_cites.html`. Accessed on 8th October, 2025.

[NPS+22] K. Neeraj, M. Pancaldi, V. Scalera, S. Perna, M. d'Aquino, C. Serpico, and S. Bonetti. Magnetization switching in the inertial regime. *Phys. Rev. B*, 105(5):054415, 2022. doi:10.1103/PhysRevB.105.054415.

[NR25a] N. A. Nguyen and A. Reusken. A comparative study of finite element methods for a class of harmonic map heat flow problems. *arXiv prepr. arXiv:2508.20590*, 2025. doi:10.48550/arXiv.2508.20590.

[NR25b] H. Normington and M. Ruggeri. Convergent finite element methods for antiferromagnetic and ferrimagnetic materials. *ESAIM: M2AN*, 59(1):167–199, 2025. doi:10.1051/m2an/2024065.

[NR25c] H. Normington and M. Ruggeri. A decoupled, convergent and fully linear algorithm for the Landau–Lifshitz–Gilbert equation with magnetoelastic effects. *Comput. Math. Appl.*, 187:1–29, 2025. doi:10.1016/j.camwa.2025.03.008.

[OLM+15] E. Olive, Y. Lansac, M. Meyer, M. Hayoun, and J.-E. Wegrowe. Deviation from the Landau–Lifshitz–Gilbert equation in the inertial regime of the magnetization. *J. Appl. Phys.*, 117(21), 2015. doi:10.1063/1.4921908.

[OLW12] E. Olive, Y. Lansac, and J.-E. Wegrowe. Beyond ferromagnetic resonance: The inertial regime of the magnetization. *Appl. Phys. Lett.*, 100(19), 2012. doi:10.1063/1.4712056.

[Osw93] P. Oswald. On a BPX-preconditioner for P1 elements. *Computing*, 51(2):125–133, 1993. doi:10.1007/BF02243847.

[Pas03] M. Pasquale. Mechanical sensors and actuators. *Sens. Actuator A Phys.*, 106(1):142–148, 2003. doi:10.1016/S0924-4247(03)00153-5.

[PKC+19] V. Puliafito, R. Khymyn, M. Carpentieri, B. Azzerboni, V. Tiberkevich, A. Slavin, and G. Finocchio. Micromagnetic modeling of terahertz oscillations in an antiferromagnetic material driven

by the spin Hall effect. *Phys. Rev. B*, 99(2):024405, 2019. doi:10.1103/PhysRevB.99.024405.

[PRS16] D. Praetorius, M. Ruggeri, and B. Stiftner. *Coupling and numerical integration of the Landau–Lifshitz–Gilbert equation*. PhD thesis, Vienna University of Technology, 2016. doi:10.34726/hss.2016.40261.

[PRS18] D. Praetorius, M. Ruggeri, and B. Stiftner. Convergence of an implicit-explicit midpoint scheme for computational micromagnetics. *Comput. Math. Appl.*, 75(5):1719–1738, 2018. doi:10.1016/j.camwa.2017.11.028.

[PRS+20] C.-M. Pfeiler, M. Ruggeri, B. Stiftner, L. Exl, M. Hochsteger, G. Hrkac, J. Schöberl, N. J. Mauser, and D. Praetorius. Computational micromagnetics with Commics. *Comput. Phys. Commun.*, 248:106965, 2020. doi:10.1016/j.cpc.2019.106965.

[PWH+15] R. C. Peng, J. J. Wang, J. M. Hu, L. Q. Chen, and C. W. Nan. Electric-field-driven magnetization reversal in square-shaped nanomagnet-based multiferroic heterostructure. *Appl. Phys. Lett*, 106(14):142901, 2015. doi:10.1063/1.4917228.

[RBJ21a] A. Renuka Balakrishna and R. D. James. A solution to the permalloy problem — A micromagnetic analysis with magnetostriction. *Appl. Phys. Lett.*, 118(21):212404, 2021. doi:10.1063/5.0051360.

[RBJ21b] A. Renuka Balakrishna and R. D. James. A tool to predict coercivity in magnetic materials. *Acta Mater.*, 208:116697, 2021. doi:10.1016/j.actamat.2021.116697.

[RCP15] H. D. Rosales, D. C. Cabra, and P. Pujol. Three-sublattice skyrmion crystal in the antiferromagnetic triangular lattice. *Phys. Rev. B*, 92(21):214439, 2015. doi:10.1103/PhysRevB.92.214439.

[RF10] H. L. Royden and P. Fitzpatrick. *Real Analysis*. Printice-Hall Inc, Boston, fourth edition, 2010.

[RGJ13] A. Ramage and E. C. Gartland Jr. A preconditioned nullspace method for liquid crystal director modeling. *SIAM J. Sci. Comput.*, 35(1):B226–B247, 2013. doi:10.1137/120870219.

[Rug22] M. Ruggeri. Numerical analysis of the Landau–Lifshitz–Gilbert equation with inertial effects. *ESAIM: Math. Model. Numer. Anal.*, 56(4):1199–1222, 2022. doi:10.1051/m2an/2022043.

[RV10] A. A. Rodríguez and A. Valli. *Eddy Current Approximation of Maxwell Equations: Theory, algorithms and applications*, volume 4. Springer Science & Business Media, 2010. doi:10.1007/978-88-470-1506-7.

[RXS22] M. Reichel, B.-X. Xu, and J. Schröder. A comparative study of finite element schemes for micromagnetic mechanically coupled simulations. *J. Appl. Phys.*, 132(18), 2022. doi:10.1063/5.0105613.

[Sad14] M. H. Sadd. *Elasticity: Theory, Applications, and Numerics*. Else-

vier Academic Press, third edition, 2014. URL https://lccn.loc.gov/2014498876.

[Sch25] J. Schöberl. Netgen/NGSolve, 2023-2025. https://ngsolve.org. v6.2.2301+.

[Sel13] G. Selke. *Design and Development of a GPU-accelerated Micromagnetic Simulator*. PhD thesis, Staats-und Universitätsbibliothek Hamburg Carl von Ossietzky, 2013. URL https://ediss.sub.uni-hamburg.de/handle/ediss/5407.

[SFS+03] W. Scholz, J. Fidler, T. Schrefl, D. Suess, H. Forster, V. Tsiantos, et al. Scalable parallel micromagnetic solvers for magnetic nanostructures. *Comput. Mater. Sci.*, 28(2):366–383, 2003. doi:10.1016/S0927-0256(03)00119-8.

[SLW04] Y. C. Shu, M. P. Lin, and K. C. Wu. Micromagnetic modeling of magnetostrictive materials under intrinsic stress. *Mech. Mater.*, 36(10):975–997, 2004. doi:10.1016/j.mechmat.2003.04.004.

[SPdS+25] J. Santos, E. Plaza, V. de Sousa, N. Moreno, et al. Metamagnetic transitions in R2RhIn8 (R= Nd, Tb, Dy, Ho) compounds: A four-sublattice model approach. *J. Magn. Magn. Mater.*, 622:172995, 2025. doi:10.1016/j.jmmm.2025.172995.

[Spe04] A. J. M. Spencer. *Continuum Mechanics*. Dover Publications, 2004. URL https://lccn.loc.gov/2003070116.

[SSB86] P.-L. Sulem, C. Sulem, and C. Bardos. On the continuous limit for a system of classical spins. *Commun. Math. Phys.*, 107(3):431–454, 1986. doi:10.1007/BF01220998.

[SSW] J. Schöberl, D. Seibel, and L. Weggler. NG-BEM. https://weggler.github.io/ngbem/intro.html. Accessed on 24th August 2024.

[ST23] A. L. Soenjaya and T. Tran. Global solutions of the Landau–Lifshitz–Baryakhtar equation. *J. Differ. Equ.*, 371:191–230, 2023. doi:10.1016/j.jde.2023.06.033.

[STPKA+20] L. Sánchez-Tejerina, V. Puliafito, P. Khalili Amiri, M. Carpentieri, and G. Finocchio. Dynamics of domain-wall motion driven by spin-orbit torque in antiferromagnets. *Phys. Rev. B*, 101(1):014433, 2020. doi:10.1103/PhysRevB.101.014433.

[Str08] M. Struwe. *Variational methods — Applications to nonlinear partial differential equations and Hamiltonian systems*, volume 34 of *Results in Mathematics and Related Areas. 3rd Series. A Series of Modern Surveys in Mathematics*. Springer-Verlag, Berlin, fourth edition, 2008. doi:10.1007/978-3-540-74013-1.

[Suh98] H. Suhl. Theory of the magnetic damping constant. *IEEE Trans. Magn.*, 34(4):1834–1838, 1998. doi:10.1109/20.706720.

[Suh07] H. Suhl. *Relaxation Processes in Micromagnetics*, volume 133. OUP

Oxford, 2007. doi:10.1093/acprof:oso/9780198528029.001.0001.

[SZ90] L. R. Scott and S. Zhang. Finite element interpolation of nonsmooth functions satisfying boundary conditions. *Math. Comp.*, 54(190):483–493, 1990. doi:10.1090/S0025-5718-1990-1011446-7.

[SZT+20] A. Salimath, F. Zhuo, R. Tomasello, G. Finocchio, and A. Manchon. Controlling the deformation of antiferromagnetic skyrmions in the high-velocity regime. *Phys. Rev. B*, 101(2):024429, 2020. doi:10.1103/PhysRevB.101.024429.

[TdL93] E. d. Trémolet de Lacheisserie. *Magnetostriction Theory and Applications of Magnetoelasticity*. CRC Press, 1993. URL `https://lccn.loc.gov/93007457`.

[Tho06] V. Thomée. *Galerkin finite element methods for parabolic problems*, volume 25 of *Springer Ser. Comput. Math.* Springer, second edition, 2006. doi:10.1007/3-540-33122-0.

[TSTLD+20] R. Tomasello, L. Sanchez-Tejerina, V. Lopez-Dominguez, F. Garescì, A. Giordano, M. Carpentieri, P. K. Amiri, and G. Finocchio. Domain periodicity in an easy-plane antiferromagnet with Dzyaloshinskii–Moriya interaction. *Phys. Rev. B*, 102(22):224432, 2020. doi:10.1103/PhysRevB.102.224432.

[VBAF16] M. Vousden, M. A. Bisotti, M. Albert, and H. Fangohr. Virtual micromagnetics: A framework for accessible and reproducible micromagnetic simulation, oct 2016. doi:10.5334/jors.141.

[VGO+20] P. Virtanen, R. Gommers, T. E. Oliphant, M. Haberland, T. Reddy, D. Cournapeau, E. Burovski, P. Peterson, W. Weckesser, J. Bright, et al. SciPy 1.0: fundamental algorithms for scientific computing in python. *Nat. Methods*, 17(3):261–272, 2020. doi:10.1038/s41592-019-0686-2.

[Vis85] A. Visintin. On Landau–Lifshitz' equations for ferromagnetism. *Japan J. Appl. Math.*, 2(1):69–84, 1985. doi:10.1007/BF03167039.

[VLD+14] A. Vansteenkiste, J. Leliaert, M. Dvornik, M. Helsen, F. Garcia-Sanchez, and B. Van Waeyenberge. The design and verification of mumax3. *AIP Adv.*, 4(10), 2014. doi:10.1063/1.4899186.

[VML+21] F. Vanderveken, J. Mulkers, J. Leliaert, B. Van Waeyenberge, B. Sorée, O. Zografos, F. Ciubotaru, and C. Adelmann. Finite difference magnetoelastic simulator. *Open Res. Eur.*, 1:35, 2021. doi:10.12688/openreseurope.13302.1.

[VVdW11] A. Vansteenkiste and B. Van de Wiele. Mumax: A new high-performance micromagnetic simulation tool. *J. Magn. Magn. Mater.*, 323(21):2585–2591, 2011. doi:10.1016/j.jmmm.2011.05.037.

[WC12] J.-E. Wegrowe and M.-C. Ciornei. Magnetization dynamics, gyromagnetic relation, and inertial effects. *American J. of Phys.*, 80(7):607–611, 2012. doi:10.1119/1.4709188.

[Wei12] D. Wei. *Micromagnetics and recording materials*. Springer Science & Business Media, 2012. doi:10.1007/978-3-642-28577-6.

[WGCE01] X.-P. Wang, C. J. García-Cervera, and W. E. A Gauss–Seidel projection method for micromagnetics simulations. *J. Comput. Phys.*, 171(1):357–372, 2001. doi:10.1006/jcph.2001.6793.

[WKA+18] Z. Wang, S. Kovalev, N. Awari, M. Chen, S. Germanskiy, B. Green, J.-C. Deinert, T. Kampfrath, J. Milano, and M. Gensch. Magnetic field dependence of antiferromagnetic resonance in NiO. *Appl. Phys. Lett.*, 112(25), 2018. doi:10.1063/1.5031213.

[WM16] J. Walowski and M. Münzenberg. Perspective: Ultrafast magnetism and thz spintronics. *J. Appl. Phys.*, 120(14), 2016. doi:10.1063/1.4958846.

[YFF13] H. D. Young, R. A. Freedman, and A. L. Ford. *University Physics with Modern Physics*. Pearson Education, second edition, 2013.

[ZG84] Y. Zhou and B. Guo. Existence of weak solution for boundary problems of systems of ferro-magnetic chain. *Sci. China, Ser. A*, 27(8), 1984. doi:10.1360/ya1984-27-8-799.

Appendix A

Constants and Units

> "Devotees of the Giorgi system will not be happy with my units; I can assure them that the unhappiness that my system inflicts on them will be no greater than the unhappiness that their system over the last thirty years has inflicted on me".
>
> W.F. Brown Jr. [Bro66, Section 1.5]

> "For some people, converting into SI units has become an obsession, bordering on a religious conviction to abolish heresy and make everybody use the "true" units".
>
> A. Aharoni [Aha07, Section 6.4]

Throughout the above work, where needed, we use the International System of Units (SI). To that end, we collect relevant quantities and physical constants here for the convenience of the reader in Table A.1. The relevant fundamental SI units are the second (s), metre (m), kilogram (kg), ampere (A), and kelvin (K). The additional two are the mole (mol) and candela (cd), which are not relevant. The unit of temperature is also almost irrelevant, as we assume that all systems are at zero temperature.

Quantity	Symbol
Mass Density	ρ
Displacement	$\boldsymbol{u}$
Elastic tensor	$\mathbb{C}$
Electric displacement	$\boldsymbol{D}$
Electric field	$\boldsymbol{E}$
Effective field	$\boldsymbol{H}_{\mathrm{eff}}$
Effective field (reduced)	$\boldsymbol{h}_{\mathrm{eff}}$
Exchange length	ℓ_{ex}
Exchange stiffness constants	$A, A_{11}, A_{12}, A_{22}, A_0$
Gilbert damping parameter	α
Gravitational acceleration	g
Gyromagnetic ratio	γ
Inertial response time	τ
Lamé constants	λ, μ
Magnetic field	$\boldsymbol{H}$
Magnetic intensity	$\boldsymbol{B}$
Magnetization	$\boldsymbol{M}$
Magnetization (reduced)	$\boldsymbol{m}$
Magnetostrain	$\boldsymbol{\varepsilon}_{\mathrm{m}}$
Magnetostriction tensor	$\mathbb{Z}$
Saturation magnetostrain	λ_{100}
Saturation magnetization	M_{s}
Strain	$\boldsymbol{\varepsilon}$
Stress	$\boldsymbol{\sigma}$
Time	t
Vacuum permeability	μ_0

Table A.1: Physical quantities and their respective symbols.

Appendix B

Auxiliary Results

B.1 Calculus of variations

We note a few useful definitions and theorems applied throughout the previous chapters. The main result we need is the Banach–Alaoglu Theorem [RF10, Section 15.1].

Theorem B.1.1 (Banach–Alaoglu)**.** *Let X be a normed linear space. Then the closed unit ball B^* of its dual space X^* is compact with respect to the weak* topology.*

If we also assume that X is separable, then we get Helley's Theorem.

Theorem B.1.2 (Helley's Theorem)**.** *Let X be a separable normed linear space. Then every bounded sequence $\{\psi_n\} \subset X^*$ has a (nonrelabelled) weakly* convergent subsequence such that $\psi_n \overset{*}{\rightharpoonup} \psi \in X^*$ as $n \to \infty$.*

We will need this for weak* convergence in the space $L^\infty((0,T);\boldsymbol{H}^1(\Omega))$. To apply Helley's Theorem requires noticing that the dual of $L^1(0,T;(\boldsymbol{H}^1(\Omega))^*)$ is $L^\infty(0,T;\boldsymbol{H}^1(\Omega))$, and as $L^1(0,T;\boldsymbol{H}^1(\Omega)^*)$ is separable (both $L^1(0,T)$ and $\boldsymbol{H}^1(\Omega)^*$ are separable) Helley's Theorem applies. A corollary of the Banach–Alaoglu Theorem is the following [RF10, Section 14.3, Theorem 17].

Theorem B.1.3. *Let X be a reflexive Banach space. Then any bounded sequence $\{x_n\} \subset X$ has a (nonrelabelled) weakly convergent subsequence such that $x_n \rightharpoonup x \in X$ as $n \to \infty$.*

As Hilbert spaces are reflexive Banach spaces, this result holds for spaces such as L^2 and H^1. To get stronger than weak convergence, we need a corollary of the [Eva10, Rellich–Kondrachov Compactness Theorem].

Theorem B.1.4. *Let Ω be a Lipschitz, bounded open subset of $\mathbb{R}^3$. Then $H^1(\Omega)$ is compactly embedded in $L^2(\Omega)$.*

This means that if we have weak convergence in $H^1(\Omega)$ we have strong convergence in $L^2(\Omega)$. We will also require Korn's inequality [BS08, Corollary 11.2.22] and the trace theorem [BS08, Theorem 1.6.6].

Theorem B.1.5 (Korn's Inequality)**.** *Let $\Omega \subset \mathbb{R}^3$ be an open bounded Lipschitz*

domain. Let $V = \{\boldsymbol{u} \in \boldsymbol{H}^1(\Omega) : \boldsymbol{u}|_{\Gamma_D}\}$ *where* $\Gamma_D \subset \partial\Omega$ *is of positive measure. Then there exists a constant* $C > 0$ *such that for all* $\boldsymbol{u} \in V$ *we have*

$$C \|\boldsymbol{u}\|_{\boldsymbol{H}^1(\Omega)} \leq \|\boldsymbol{\varepsilon}(\boldsymbol{u})\|_{\boldsymbol{L}^2(\Omega)}.$$

Theorem B.1.6 (Trace Theorem)**.** *Suppose that* Ω *has a Lipschitz boundary. Then there is a positive constant* C *such that for all* $\boldsymbol{u} \in \boldsymbol{H}^1(\Omega)$ *we have*

$$\|\boldsymbol{u}\|^2_{\boldsymbol{L}^2(\partial\Omega)} \leq C \|\boldsymbol{u}\|_{\boldsymbol{L}^2(\Omega)} \|\boldsymbol{u}\|_{\boldsymbol{H}^1(\Omega)}.$$

B.2 Linear algebra definitions and identities

In this section, for the convenience of the reader, we collect some definitions and vector/matrix/tensor identities from linear algebra that are used throughout the work.

We let $\boldsymbol{a}, \boldsymbol{b}, \boldsymbol{c} \in \mathbb{R}^3$ denote vectors. Then the following formulae hold:

$$\boldsymbol{a} \times \boldsymbol{a} = \boldsymbol{0}, \tag{B.1}$$
$$\boldsymbol{a} \times \boldsymbol{b} = -\boldsymbol{b} \times \boldsymbol{a}, \tag{B.2}$$
$$(\boldsymbol{a} \times \boldsymbol{b}) \cdot \boldsymbol{c} = (\boldsymbol{b} \times \boldsymbol{c}) \cdot \boldsymbol{a} = (\boldsymbol{c} \times \boldsymbol{a}) \cdot \boldsymbol{b} \tag{B.3}$$
$$\boldsymbol{a} \cdot (\boldsymbol{a} \times \boldsymbol{b}) = 0 \tag{B.4}$$
$$\boldsymbol{a} \times (\boldsymbol{b} \times \boldsymbol{c}) = (\boldsymbol{a} \cdot \boldsymbol{c})\boldsymbol{b} - (\boldsymbol{a} \cdot \boldsymbol{b})\boldsymbol{c}. \tag{B.5}$$

Definition B.2.1. *Let* $\mathbb{A} \in \mathbb{R}^{3^4}$ *be a fourth-order tensor (4-tensor) with components* $\mathbb{A}_{ij\ell m}$*, where* $i, j, \ell, m \in \{1, 2, 3\}$*. We say that*

1. $\mathbb{A}$ *is minorly symmetric if* $\mathbb{A}_{ij\ell m} = \mathbb{A}_{ji\ell m} = \mathbb{A}_{ijm\ell}$*,*
2. $\mathbb{A}$ *is majorly symmetric if* $\mathbb{A}_{ij\ell m} = \mathbb{A}_{\ell mji}$*,*
3. *and* $\mathbb{A}$ *is (fully) symmetric if the aforementioned two conditions hold together.*

The transpose of $\mathbb{A}$ *is the 4-tensor* $\mathbb{A}^\top \in \mathbb{R}^{3^4}$ *given by* $(\mathbb{A}^\top)_{ij\ell m} = \mathbb{A}_{\ell mji}$*. In particular,* $\mathbb{A}$ *is majorly symmetric if* $\mathbb{A}^\top = \mathbb{A}$*.*

Remark B.2.2. *In three dimensions, 4-tensors have* $3^4 = 81$ *components. Minorly symmetric 4-tensors have 36 independent components, majorly symmetric 4-tensors have 45 independent components, and fully symmetric 4-tensors have 21 independent components. Throughout this work the stiffness tensor* $\mathbb{C}$ *is assumed to be fully symmetric, whereas the magnetostriction tensor* $\mathbb{Z}$ *is assumed to be only minorly symmetric. In the numerical experiments of Section 5.5, we consider the isotropic case, in which* $\mathbb{C}$ *and* $\mathbb{Z}$ *have only two (the so-called Lamé constants) and one (the so-called saturation magnetostriction) independent components, respectively.*

In the following definition, we recall some operations between tensors.

Definition B.2.3. *Let* $\mathbb{A}, \mathbb{B} \in \mathbb{R}^{3^4}$ *be 4-tensors, let* $\boldsymbol{\nu}, \boldsymbol{\mu} \in \mathbb{R}^{3\times 3}$ *be 2-tensors (matrices), and let* $\boldsymbol{m}, \boldsymbol{w} \in \mathbb{R}^3$ *be 1-tensors (vectors). We denote the following operations:*

- *The double contraction between* $\mathbb{A}$ *and* $\mathbb{B}$ *is the 4-tensor* $\mathbb{A} : \mathbb{B} \in \mathbb{R}^{3^4}$ *given by*

$$(\mathbb{A} : \mathbb{B})_{ij\ell m} = \sum_{p,q} \mathbb{A}_{ijpq}\mathbb{B}_{pq\ell m};$$

- *The double contraction between* $\mathbb{A}$ *and* $\boldsymbol{\nu}$ *is the 2-tensor* $\mathbb{A} : \boldsymbol{\nu} \in \mathbb{R}^{3\times 3}$ *given by*

$$(\mathbb{A} : \boldsymbol{\nu})_{ij} = \sum_{\ell,m} \mathbb{A}_{ij\ell m}\nu_{\ell m};$$

- *The Frobenius product of* $\boldsymbol{\mu}$ *and* $\boldsymbol{\nu}$ *is the scalar* $\boldsymbol{\mu} : \boldsymbol{\nu} \in \mathbb{R}$ *given by*

$$\boldsymbol{\mu} : \boldsymbol{\nu} = \sum_{i,j} \mu_{ij}\nu_{ij};$$

- *The tensor product of* $\boldsymbol{m}$ *and* $\boldsymbol{w}$ *is the 2-tensor* $\boldsymbol{m} \otimes \boldsymbol{w} \in \mathbb{R}^{3\times 3}$ *given by*

$$(\boldsymbol{m} \otimes \boldsymbol{w})_{ij} = m_i w_j.$$

The following result is useful for manipulation of the magnetostrain terms.

Lemma B.2.4. *Let* $\mathbb{Z} \in \mathbb{R}^{3^4}$ *be a minorly symmetric 4-tensor, let* $\boldsymbol{\sigma} \in \mathbb{R}^{3\times 3}$ *be a symmetric 2-tensor, and let* $\boldsymbol{m}, \boldsymbol{w} \in \mathbb{R}^3$ *be two 1-tensors. We have the identity*

$$[(\mathbb{Z}^\top : \boldsymbol{\sigma})\boldsymbol{w}] \cdot \boldsymbol{m} = [(\mathbb{Z}^\top : \boldsymbol{\sigma})\boldsymbol{m}] \cdot \boldsymbol{w} = \boldsymbol{\sigma} : [\mathbb{Z} : (\boldsymbol{m} \otimes \boldsymbol{w})]. \tag{B.6}$$

Proof. We have by the minor symmetry of $\mathbb{Z}$ that

$$\begin{aligned}
(\mathbb{Z}^\top : \boldsymbol{\sigma})\boldsymbol{m} \cdot \boldsymbol{w} &= \sum_{i,j,\ell,m} \mathbb{Z}^\top_{ijk\ell}\sigma_{\ell m} m_j w_i \\
&= \sum_{i,j,\ell,m} \mathbb{Z}^\top_{jik\ell}\sigma_{\ell m} m_i w_j \quad \text{by relabelling} \\
&= \sum_{i,j,\ell,m} \mathbb{Z}^\top_{ijk\ell}\sigma_{\ell m} w_j m_i \quad \text{via minor symmetry} \\
&= (\mathbb{Z}^\top : \boldsymbol{\sigma})\boldsymbol{w} \cdot \boldsymbol{m}.
\end{aligned}$$

Furthermore, we have that

$$\begin{aligned}
(\mathbb{Z}^\top : \boldsymbol{\sigma})\boldsymbol{m} \cdot \boldsymbol{w} &= \sum_{i,j,\ell,m} \mathbb{Z}^\top_{ij\ell m}\sigma_{\ell m} m_j w_i = \sum_{i,j,\ell,m} \sigma_{\ell m}\mathbb{Z}^\top_{ij\ell m} m_j w_i \\
&= \sum_{i,j,\ell,m} \sigma_{\ell m}\mathbb{Z}_{\ell mji} m_j w_i \quad \text{via minor symmetry} \\
&= \sum_{\ell,m} \sigma_{\ell m}[\mathbb{Z} : (\boldsymbol{m} \otimes \boldsymbol{w})]_{\ell m} = \boldsymbol{\sigma} : [\mathbb{Z} : (\boldsymbol{m} \otimes \boldsymbol{w})].
\end{aligned}$$

This shows both identities in (B.6). □

The following identities are useful to show the stability of discrete numerical schemes. The first is Abel's lemma, in which we write a difference within an inner product as a difference of signed terms, and the second is a discrete form of Grönwalls lemma [Tho06, Lemma 10.5].

Lemma B.2.5 (Abel's Lemma)**.** *Let $\{\nu_i\}$ be a sequence in an inner product space with inner product $\langle \cdot, \cdot \rangle$ and associated norm $\|\cdot\|$. We have the identity*

$$\langle \nu_{i+1} - \nu_i, \nu_{i+1} \rangle = \frac{1}{2} \|\nu_{i+1}\|^2 - \frac{1}{2} \|\nu_i\|^2 + \frac{1}{2} \|\nu_{i+1} - \nu_i\|^2 . \tag{B.7}$$

Lemma B.2.6 (Discrete Grönwall's Lemma)**.** *Let $\{\alpha_n\}_{n\geq 0}$, $\{\beta_n\}_{n\geq 0}$, and $\{\gamma_n\}_{n\geq 0}$ be sequences of real numbers such that*

$$\alpha_i \leq \alpha_{i+1}, \quad 0 \leq \beta_i, \qquad \text{and } \gamma_i \leq \alpha_i \sum_{n=0}^{j-1} \beta_n \gamma_n \text{ for all } i \geq 0.$$

Then it holds that

$$\gamma_i \leq \alpha_i \sum_{n=0}^{j-1} \beta_n \text{ for all } i \geq 0.$$

Appendix C

Nondimensionalization

C.1 Magnetoelastics

In this section, we describe the nondimensionalisation of the model in Section 5.2 in physical units (used for physical investigations e.g. [SLW04, MMHH$^+$14, BHB$^+$14, PWH$^+$15, RBJ21b, RBJ21a, DW23a].) This justifies our choices of material parameters in Section 5.5.

C.1.1 Nondimensionalisation

Let $\Omega \subset \mathbb{R}^3$ denote the volume occupied by a ferromagnetic body (with the spatial variable $x \in \Omega$ measured in meter). Consider the magnetization $\boldsymbol{M}$ (measured in A/m), which satisfies the length constraint $|\boldsymbol{M}| = M_s$, where the saturation magnetization $M_s > 0$ is also measured in A/m, and the displacement $\boldsymbol{U}$ (measured in m). We denote by $\boldsymbol{\varepsilon}(\boldsymbol{U})$ the total strain given by

$$\boldsymbol{\varepsilon}(\boldsymbol{U}) = (\boldsymbol{\nabla U} + \boldsymbol{\nabla U}^\top)/2$$

and by $\boldsymbol{\varepsilon}_{\mathrm{m}}(\boldsymbol{M})$ the magnetostrain given by

$$\boldsymbol{\varepsilon}_{\mathrm{m}}(\boldsymbol{M}) = \mathbb{Z} : (\boldsymbol{M} \otimes \boldsymbol{M}/M_s^2),$$

where $\mathbb{Z}$ is a dimensionless fourth-order tensor.

The total energy of the system (measured in J) is given by

$$\begin{aligned}\mathcal{E}[\boldsymbol{U}, \boldsymbol{M}] = {} & \frac{A}{M_s^2} \int_\Omega |\boldsymbol{\nabla M}|^2 - \mu_0 \int_\Omega \boldsymbol{H}_{\mathrm{ext}} \cdot \boldsymbol{M} \\ & + \frac{1}{2} \int_\Omega [\boldsymbol{\varepsilon}(\boldsymbol{U}) - \boldsymbol{\varepsilon}_{\mathrm{m}}(\boldsymbol{M})] : \{\boldsymbol{C} : [\boldsymbol{\varepsilon}(\boldsymbol{U}) - \boldsymbol{\varepsilon}_{\mathrm{m}}(\boldsymbol{M})]\} - \int_\Omega \boldsymbol{F} \cdot \boldsymbol{U} - \int_{\Gamma_N} \boldsymbol{G} \cdot \boldsymbol{U},\end{aligned}$$

where A is the exchange constant (measured in $\mathrm{J\,m^{-1}}$), μ_0 is the permeability of free space (measured in $\mathrm{N\,A^{-2}}$), $\boldsymbol{H}_{\mathrm{ext}}$ is an applied external field (measured in A/m), $\boldsymbol{C}$ is the fourth-order stiffness tensor (measured in $\mathrm{N\,m^{-2}}$), $\boldsymbol{F}$ is a body force (measured in $\mathrm{N\,m^{-3}}$), and $\boldsymbol{G}$ is a surface force (measured in $\mathrm{N\,m^{-2}}$).

The dynamics of $\boldsymbol{M}$ is described by the LLG equation:

$$\partial_t \boldsymbol{M} = -\gamma\mu_0\, \boldsymbol{M} \times \boldsymbol{H}_{\text{eff}}[\boldsymbol{U}, \boldsymbol{M}] + \frac{\alpha}{M_s} \boldsymbol{M} \times \partial_t \boldsymbol{M},$$

where γ is the gyromagnetic ratio (measured in $\mathrm{rad\,s^{-1}T^{-1}}$), $\alpha > 0$ is the dimensionless Gilbert damping parameter, and the effective field $\boldsymbol{H}_{\text{eff}}$ (measured in A/m) reads as

$$\boldsymbol{H}_{\text{eff}}[\boldsymbol{U}, \boldsymbol{M}] = -\frac{1}{\mu_0} \frac{\delta \mathcal{E}[\boldsymbol{U}, \boldsymbol{M}]}{\delta \boldsymbol{M}} = \frac{2A}{\mu_0 M_s^2} \boldsymbol{\Delta} \boldsymbol{M} + \boldsymbol{H}_{\text{ext}} + \frac{2}{\mu_0 M_s^2} [\mathbb{Z}^\top : \boldsymbol{\Sigma}(\boldsymbol{U}, \boldsymbol{M})] \boldsymbol{M},$$

where $\boldsymbol{\Sigma}(\boldsymbol{U}, \boldsymbol{M}) = \boldsymbol{C} : [\boldsymbol{\varepsilon}(\boldsymbol{U}) - \boldsymbol{\varepsilon}_{\text{m}}(\boldsymbol{M})]$ is the stress (measured in $\mathrm{N\,m^{-2}}$). The LLG equation is coupled with the conservation of momentum equation satisfied by the displacement:

$$\rho\, \partial_{tt} \boldsymbol{U} = \boldsymbol{\nabla} \cdot \boldsymbol{\Sigma}(\boldsymbol{U}, \boldsymbol{M}) + \boldsymbol{F},$$

where ρ is the mass density (measured in $\mathrm{kg\,m^{-3}}$).

Let $\boldsymbol{m} = \boldsymbol{M}/M_s$ denote the normalized magnetization. We define the exchange length $\ell_{\text{ex}}^2 = 2A/\mu_0 M_s^2$ (measured in m) and use it to rescale the spatial variable and the displacement according to $x' = x/\ell_{\text{ex}}$ and $\boldsymbol{u} = \boldsymbol{U}/\ell_{\text{ex}}$, respectively. Additionally, we introduce the dimensionless domain $\Omega' = \Omega/\ell_{\text{ex}}$, the dimensionless time $t' = \gamma\mu_0 M_s t$, the dimensionless coupling parameter $\kappa = \rho \ell_{\text{ex}}^2 \gamma^2 \mu_0$, as well as the dimensionless differential operators $\boldsymbol{\nabla} = \boldsymbol{\nabla}'/\ell_{\text{ex}}$ and $\boldsymbol{\Delta} = \boldsymbol{\Delta}'/\ell_{\text{ex}}^2$. Further we define the dimensionless energy as

$$\begin{aligned}
\mathcal{E}'[\boldsymbol{u}, \boldsymbol{m}] &= \frac{\mathcal{E}[\ell_{\text{ex}} \boldsymbol{u}, M_s \boldsymbol{m}]}{\mu_0 M_s^2 \ell_{\text{ex}}^3} \\
&= \frac{1}{2} \int_{\Omega'} |\boldsymbol{\nabla}' \boldsymbol{m}|^2 - \int_{\Omega'} \boldsymbol{h}_{\text{ext}} \cdot \boldsymbol{m} \\
&\qquad + \frac{\kappa}{2} \int_{\Omega'} [\boldsymbol{\varepsilon}(\boldsymbol{u}) - \boldsymbol{\varepsilon}'_{\text{m}}(\boldsymbol{m})] : \{\mathbb{C} : [\boldsymbol{\varepsilon}(\boldsymbol{u}) - \boldsymbol{\varepsilon}'_{\text{m}}(\boldsymbol{m})] \\
&\qquad - \kappa \int_{\Omega'} \boldsymbol{f} \cdot \boldsymbol{u} - \kappa \int_{\Gamma'_N} \boldsymbol{g} \cdot \boldsymbol{u},
\end{aligned}$$

where $\boldsymbol{h}_{\text{ext}} = \boldsymbol{H}_{\text{ext}}/M_s$, $\boldsymbol{\varepsilon}_{\text{m}}(\boldsymbol{m}) = \mathbb{Z} : (\boldsymbol{m} \otimes \boldsymbol{m})$, $\boldsymbol{\Sigma} = \kappa\mu_0 M_s^2 \boldsymbol{\sigma}$, $\boldsymbol{G} = \kappa\mu_0 M_s^2 \boldsymbol{g}$, $\boldsymbol{F} = \kappa(\mu_0 M_s^2/\ell_{\text{ex}}) \boldsymbol{f}$, and $\boldsymbol{C} = \kappa\mu_0 M_s^2 \mathbb{C}$ (all dimensionless). The dimensionless effective field, defined by $\boldsymbol{h}_{\text{eff}}[\boldsymbol{u}, \boldsymbol{m}] = \boldsymbol{H}_{\text{eff}}[\ell_{\text{ex}} \boldsymbol{u}, M_s \boldsymbol{m}]/M_s$, satisfies the relation

$$\boldsymbol{h}_{\text{eff}}[\boldsymbol{u}, \boldsymbol{m}] = -\frac{\delta \mathcal{E}'[\boldsymbol{u}, \boldsymbol{m}]}{\delta \boldsymbol{m}} = \boldsymbol{\Delta}' \boldsymbol{m} + 2\kappa [\mathbb{Z}^\top : \boldsymbol{\sigma}(\boldsymbol{u}, \boldsymbol{m})] \boldsymbol{m} + \boldsymbol{h}_{\text{ext}}.$$

With all these definitions, we retrieve the coupled system

$$\begin{aligned}
\partial_{t't'} \boldsymbol{u} &= \boldsymbol{\nabla}' \cdot \boldsymbol{\sigma}(\boldsymbol{u}, \boldsymbol{m}) + \boldsymbol{f}, \\
\partial_{t'} \boldsymbol{m} &= -\boldsymbol{m} \times \boldsymbol{h}_{\text{eff}}[\boldsymbol{u}, \boldsymbol{m}] + \alpha\, \boldsymbol{m} \times \partial_{t'} \boldsymbol{m}.
\end{aligned}$$

Altogether, we thus obtain the dimensionless model problem discussed throughout this work. Note that, to simplify the notation, in Sections 5.2–5.6 we omit all 'primes' from the dimensionless quantities, we assume $\kappa = 1$, and we neglect the applied external field (unless otherwise mentioned).

C.2 AFM/FiM

In this appendix, for the convenience of all interdisciplinary readers, we present the model in physical units (used for physical investigations, e.g., in [NE15, MLP16, PKC+19, MRA19, SZT+20, STPKA+20, TSTLD+20, CSTT+21]) and show how to obtain from it the dimensionless setting described in Section 7.2 and analysed in the paper. By doing this, we also justify the setup and the choice of the material parameters in the numerical experiments presented in Section 7.3.3–7.4.2.

C.2.1 Nondimensionalisation

Let $\Omega \subset \mathbb{R}^3$ be the volume occupied by an AFM or FiM material. Let the vector field $\boldsymbol{M} : \Omega \to \mathbb{R}^3$ denote the total magnetization of the sample (in A/m). The total magnetization can be decomposed as $\boldsymbol{M} = \boldsymbol{M}_1 + \boldsymbol{M}_2$, where $\boldsymbol{M}_1, \boldsymbol{M}_2 : \Omega \to \mathbb{R}^3$, the magnetization vectors of two sublattices (in A/m), satisfy the constraints $|\boldsymbol{M}_1| = M_{\mathrm{s},1}$ and $|\boldsymbol{M}_2| = M_{\mathrm{s},2}$. The constants $M_{\mathrm{s},1}, M_{\mathrm{s},2} > 0$ are the sublattice saturation magnetizations (in A/m). Let $\boldsymbol{m}_1, \boldsymbol{m}_2 : \Omega \to \mathbb{S}^2$ be the dimensionless unit-length vector fields $\boldsymbol{m}_1 = \boldsymbol{M}_1/M_{\mathrm{s},1}$ and $\boldsymbol{m}_2 = \boldsymbol{M}_2/M_{\mathrm{s},2}$. The total Gibbs free energy (in J) of the system (assumed, for simplicity, to include only exchange contributions in this section) reads as

$$\begin{aligned} \mathcal{E}[\boldsymbol{m}_1, \boldsymbol{m}_2] &= \mathcal{E}_{\mathrm{ex}}[\boldsymbol{m}_1, \boldsymbol{m}_2] \\ &= \sum_{\ell=1}^{2} A_{\ell\ell} \int_\Omega |\boldsymbol{\nabla} \boldsymbol{m}_\ell|^2 + A_{12} \int_\Omega \boldsymbol{\nabla} \boldsymbol{m}_1 : \boldsymbol{\nabla} \boldsymbol{m}_2 \\ &\quad - \frac{4A_0}{a^2} \int_\Omega \boldsymbol{m}_1 \cdot \boldsymbol{m}_2, \end{aligned} \tag{C.1}$$

where the exchange constants $A_{11}, A_{22} > 0$ and $A_{12}, A_0 \in \mathbb{R}$ are in J/m, whereas $a > 0$ is the lattice constant (in m). The first contribution in (C.1) is called *inhomogeneous intra lattice exchange* and models the classical ferromagnetic exchange for $\boldsymbol{m}_1$ and $\boldsymbol{m}_2$. The second term is called *inhomogeneous interlattice exchange*, which arises from a nearest-neighbour approximation of the exchange interaction between spins. The last contribution is called *homogeneous interlattice exchange* and takes the local interaction between $\boldsymbol{m}_1$ and $\boldsymbol{m}_2$ into account.

The dynamics of $\boldsymbol{m}_1$ and $\boldsymbol{m}_2$ is governed by a coupled system of two LLG equations

$$\partial_t \boldsymbol{m}_\ell = -\gamma_\ell \, \boldsymbol{m}_\ell \times \boldsymbol{H}_{\mathrm{eff},\ell}[\boldsymbol{m}_1, \boldsymbol{m}_2] + \alpha_\ell \, \boldsymbol{m}_\ell \times \partial_t \boldsymbol{m}_\ell \quad \text{for } \ell = 1, 2, \tag{C.2}$$

where $\gamma_\ell > 0$ (in m/(A s)) and $\alpha_\ell > 0$ (dimensionless) are the sublattice rescaled gyromagnetic ratios and Gilbert damping parameters, respectively. In (C.2), the effective fields $\boldsymbol{H}_{\mathrm{eff},\ell}[\boldsymbol{m}_1, \boldsymbol{m}_2]$ (in A/m) are equal, up to a negative multiplicative constant, to the functional derivatives of the total energy with respect to $\boldsymbol{m}_\ell$, i.e.,

$$\boldsymbol{H}_{\mathrm{eff},\ell}[\boldsymbol{m}_1, \boldsymbol{m}_2] = -\frac{1}{\mu_0 M_{\mathrm{s},\ell}} \frac{\mathcal{E}[\boldsymbol{m}_1, \boldsymbol{m}_2]}{\delta m_\ell},$$

where μ_0 is the vacuum permeability (in $\mathrm{N/A^2}$). Assuming no flux boundary conditions, the strong form of the resulting effective fields reads as

$$\boldsymbol{H}_{\mathrm{eff},\ell}[\boldsymbol{m}_1,\boldsymbol{m}_2] = \frac{2A_{\ell\ell}}{\mu_0 M_{\mathrm{s},\ell}}\,\boldsymbol{\Delta}\boldsymbol{m}_\ell + \frac{A_{12}}{\mu_0 M_{\mathrm{s},\ell}}\,\boldsymbol{\Delta}\boldsymbol{m}_{3-\ell} + \frac{4A_0}{\mu_0 M_{\mathrm{s},\ell}\,a^2}\,\boldsymbol{m}_{3-\ell}.$$

We now start the nondimensionalization. Let $M_\mathrm{s} > 0$ and $\gamma_0 > 0$ be some reference saturation magnetization (in A/m) and rescaled gyromagnetic ratio (in $\mathrm{m/(A\,s)}$), respectively. For all $\ell = 1,2$, define the positive dimensionless parameters $\eta_{\mathrm{s},\ell} := M_{\mathrm{s},\ell}/M_\mathrm{s}$ and $\eta_{\gamma,\ell} := \gamma_\ell/\gamma_0$. The dimensionless total magnetization is given by $\boldsymbol{m} = \boldsymbol{M}/M_\mathrm{s} = \eta_{\mathrm{s},1}\boldsymbol{m}_1 + \eta_{\mathrm{s},2}\boldsymbol{m}_2$.

Let $L > 0$ be some intrinsic length of the problem. We rescale the space and time variables to obtain the dimensionless variables $x' = x/L$ and $t' = \gamma_0 M_\mathrm{s}\,t$. Accordingly, we rescale also the domain $\Omega' = \Omega/L$. We consider the rescaled unit-length vector fields $\boldsymbol{m}'_\ell(x',t') = \boldsymbol{m}_\ell(Lx', t'/(\gamma_0 M_\mathrm{s}))$ $(\ell = 1,2)$ and the rescaled total magnetization $\boldsymbol{m}'(x',t') = \boldsymbol{m}(Lx', t'/(\gamma_0 M_\mathrm{s}))$. Moreover, we rescale the energy as $\mathcal{E}'[\boldsymbol{m}'_1,\boldsymbol{m}'_2] = \mathcal{E}[\boldsymbol{m}_1,\boldsymbol{m}_2]/(\mu_0 M_\mathrm{s}^2 L^3)$, which yields the expression

$$\begin{aligned}\mathcal{E}'[\boldsymbol{m}'_1,\boldsymbol{m}'_2] &= \mathcal{E}'_{\mathrm{ex}}[\boldsymbol{m}'_1,\boldsymbol{m}'_2]\\ &= \frac{1}{2}\sum_{\ell=1}^{2}\frac{2A_{\ell\ell}}{\mu_0 M_\mathrm{s}^2 L^2}\int_{\Omega'}|\boldsymbol{\nabla}'\boldsymbol{m}'_\ell|^2 + \frac{A_{12}}{\mu_0 M_\mathrm{s}^2 L^2}\int_{\Omega'}\boldsymbol{\nabla}'\boldsymbol{m}'_1 : \boldsymbol{\nabla}'\boldsymbol{m}'_2\\ &\qquad - \frac{4A_0}{\mu_0 M_\mathrm{s}^2 a^2}\int_{\Omega'}\boldsymbol{m}'_1\cdot\boldsymbol{m}'_2.\end{aligned}$$

Defining the dimensionless coefficients $a_{\ell\ell} = 2A_{\ell\ell}/(\mu_0 M_\mathrm{s}^2 L^2) > 0$ $(\ell = 1,2)$, $a_{12} = A_{12}/(\mu_0 M_\mathrm{s}^2 L^2) \in \mathbb{R}$, and $a_0 = 4A_0/(\mu_0 M_\mathrm{s}^2 a^2) \in \mathbb{R}$, and omitting all 'primes' for simplicity, we obtain the dimensionless energy functional (7.1) of Section 7.2. By construction, the dimensionless rescaled effective fields defined in (7.5) are related to the ones in physical units according to the relation

$$\boldsymbol{h}_{\mathrm{eff},\ell}[\boldsymbol{m}'_1,\boldsymbol{m}'_2] \overset{(7.5)}{=} -\frac{\delta\mathcal{E}'[\boldsymbol{m}'_1,\boldsymbol{m}'_2]}{\delta\boldsymbol{m}'_\ell} = \frac{\eta_{\mathrm{s},\ell}^2}{M_{\mathrm{s},\ell}}\,\boldsymbol{H}_{\mathrm{eff},\ell}[\boldsymbol{m}_1,\boldsymbol{m}_2] \quad \text{for all } \ell = 1,2.$$

Rescaling the LLG equations in (C.2) according to the above change of variables and introducing all dimensionless quantities, we obtain

$$\partial_{t'}\boldsymbol{m}'_\ell = -\frac{\eta_{\gamma,\ell}}{\eta_{\mathrm{s},\ell}}\,\boldsymbol{m}'_\ell \times \boldsymbol{h}_{\mathrm{eff},\ell}[\boldsymbol{m}'_1,\boldsymbol{m}'_2] + \alpha_\ell\,\boldsymbol{m}'_\ell \times \partial_{t'}\boldsymbol{m}'_\ell \quad \text{for all } \ell = 1,2,$$

Defining the dimensionless parameter $\eta_\ell := \eta_{\gamma,\ell}/\eta_{\mathrm{s},\ell} > 0$ and omitting all 'primes', we obtain the dimensionless system (7.9) of LLG equations of Section 7.2.

C.2.2 Lower-order energy contributions

In practically relevant simulations, to be able to describe complex physical processes involving AFM and FiM materials, more energy contributions (in addition to the exchange ones) need to be taken into account in (C.1):

- The *magnetocrystalline anisotropy energy* incorporates the existence of preferred directions of alignment for the fields. In the uniaxial case, it reads as

$$\mathcal{E}_{\mathrm{ani}}[\boldsymbol{m}_1, \boldsymbol{m}_2] = K_1 \int_\Omega [1 - (\boldsymbol{a}_1 \cdot \boldsymbol{m}_1)^2] + K_2 \int_\Omega [1 - (\boldsymbol{a}_2 \cdot \boldsymbol{m}_2)^2],$$

  where $K_1, K_2 > 0$ are physical constants (in $\mathrm{J/m^3}$), whereas $\boldsymbol{a}_1, \boldsymbol{a}_2 \in \mathbb{S}^2$ are the so-called easy axes of the material (usually it holds that $K_1 = K_2$ and $\boldsymbol{a}_1 = \boldsymbol{a}_2$).

- The *Dzyaloshinskii–Moriya interaction* is used to incorporate chiral effects into the model. Its general expression for AFM and FiM materials is given by

$$\mathcal{E}_{\mathrm{DMI}}[\boldsymbol{m}_1, \boldsymbol{m}_2] = \int_\Omega \boldsymbol{D}_1 : (\boldsymbol{\nabla} \boldsymbol{m}_1 \times \boldsymbol{m}_1) + \int_\Omega \boldsymbol{D}_2 : (\boldsymbol{\nabla} \boldsymbol{m}_2 \times \boldsymbol{m}_2),$$

  where $\boldsymbol{D}_1, \boldsymbol{D}_2 \in \mathbb{R}^{3\times 3}$ are the so-called spiralization tensors (with coefficients in $\mathrm{J/m^2}$), whereas, for $\ell = 1, 2$, $\boldsymbol{\nabla} \boldsymbol{m}_\ell \times \boldsymbol{m}_\ell$ denotes the matrix with columns $\partial_j \boldsymbol{m} \times \boldsymbol{m}$ for $j = 1, 2, 3$ (again, usually it holds that $\boldsymbol{D}_1 = \boldsymbol{D}_2$).

- The *Zeeman energy* models the interaction of the total magnetization with an applied external field (assumed to be magnetization-independent) and reads as

$$\mathcal{E}_{\mathrm{ext}}[\boldsymbol{m}_1, \boldsymbol{m}_2] = -\mu_0 \int_\Omega \boldsymbol{H}_{\mathrm{ext}} \cdot (M_{\mathrm{s},1} \boldsymbol{m}_1 + M_{\mathrm{s},2} \boldsymbol{m}_2),$$

  where $\boldsymbol{H}_{\mathrm{ext}} \in \mathbb{R}^3$ denotes an applied external field (in $\mathrm{A/m}$).

- The *magnetostatic energy* can be understood as the energy associated with the interaction of the total magnetization with the stray field $\boldsymbol{H}_{\mathrm{s}} \in \mathbb{R}^3$, which solves the magnetostatic Maxwell–Heaviside equations

$$\nabla \cdot \boldsymbol{H}_{\mathrm{s}} = -\nabla \cdot [\chi_\Omega (M_{\mathrm{s},1} \boldsymbol{m}_1 + M_{\mathrm{s},2} \boldsymbol{m}_2)] \quad \text{and} \quad \nabla \times \boldsymbol{H}_{\mathrm{s}} = \boldsymbol{0} \quad \text{in } \mathbb{R}^3,$$

  where $\chi_\Omega : \mathbb{R}^3 \to \{0, 1\}$ denotes the indicator function of the domain Ω. The energy contribution is given by

$$\mathcal{E}_{\mathrm{static}}[\boldsymbol{m}_1, \boldsymbol{m}_2] = -\frac{\mu_0}{2} \int_\Omega \boldsymbol{H}_{\mathrm{s}} \cdot (M_{\mathrm{s},1} \boldsymbol{m}_1 + M_{\mathrm{s},2} \boldsymbol{m}_2).$$

Note that in all the above energy contributions the two fields are decoupled (for the magnetostatic energy, this is a consequence of the fact that the operator mapping the total magnetization to the solution of the magnetostatic Maxwell equations is linear). Hence, even in the presence of the above contributions, the system of Euler–Lagrange equations associated with the minimization problem and the system of LLG equations are only exchange-coupled.

In the numerical experiments of the work (see Sections 7.3.3 and 7.4.2), we considered dimensionless forms of magnetocrystalline anisotropy energy, Dzyaloshinskii–Moriya interaction and Zeeman energy, namely

$$\begin{aligned}
\mathcal{E}_{\mathrm{ani}}[\boldsymbol{m}_1, \boldsymbol{m}_2] &= \frac{q_1^2}{2} \int_\Omega [1 - (\boldsymbol{a}_1 \cdot \boldsymbol{m}_1)^2] + \frac{q_2^2}{2} \int_\Omega [1 - (\boldsymbol{a}_2 \cdot \boldsymbol{m}_2)^2], \\
\mathcal{E}_{\mathrm{DMI}}[\boldsymbol{m}_1, \boldsymbol{m}_2] &= \int_\Omega \widehat{\boldsymbol{D}}_1 : (\boldsymbol{\nabla} \boldsymbol{m}_1 \times \boldsymbol{m}_1) + \int_\Omega \widehat{\boldsymbol{D}}_2 : (\boldsymbol{\nabla} \boldsymbol{m}_2 \times \boldsymbol{m}_2), \\
\mathcal{E}_{\mathrm{ext}}[\boldsymbol{m}_1, \boldsymbol{m}_2] &= - \int_\Omega \boldsymbol{h}_{\mathrm{ext}} \cdot (\eta_{\mathrm{s},1} \boldsymbol{m}_1 + \eta_{\mathrm{s},2} \boldsymbol{m}_2) = - \int_\Omega \boldsymbol{h}_{\mathrm{ext}} \cdot \boldsymbol{m}.
\end{aligned}$$

In these expressions, which can be obtained rescaling the energy contributions as described in the previous section, the dimensionless parameters are related to the physical ones via the relationships $q_\ell = \sqrt{2K_\ell/(\mu_0 M_{\mathrm{s}}^2)}$, $\widehat{\boldsymbol{D}}_\ell = \boldsymbol{D}_\ell/(\mu_0 M_{\mathrm{s}}^2 L)$ ($\ell = 1, 2$), and $\boldsymbol{h}_{\mathrm{ext}} = \boldsymbol{H}_{\mathrm{ext}}/M_{\mathrm{s}}$.

To conclude, we note that for AFM and FiM materials, differently from what happens for FM materials, the Zeeman and the magnetostatic energies are usually of limited physical importance, because they depend on the total magnetization of the sample, which is in general very small.